Secondary Interaction of Fracturing Fluid and Shale Plays: A Reservoir Geomechanics Approach

by

Reza Keshavarzi

A thesis submitted in partial fulfillment of the requirements for the degree of

Doctor of Philosophy

in

Geotechnical Engineering

Department of Civil and Environmental Engineering
University of Alberta

Abstract

During hydraulic fracturing in unconventional tight formations a high percentage of the injected fluid may remain in the formation and only a small portion of the fracturing fluid is typically recovered. Although spontaneous imbibition is mainly introduced as the main dominating mechanism, a clear understanding of the fundamental mechanisms through which the fracturing fluid would interact with the formation remains a challenge. The impact of these mechanisms on rock property changes is even more challenging but is important to account for post-fracturing reservoir characterization.

In this study, an integrated analytical-experimental-numerical approach was adopted to study these issues using a case study within the Montney Formation in Farrell Creek field in northeast British Columbia. The results of experiments on Montney samples from different depths revealed that because of spontaneous water imbibition, the geomechanical properties of the samples were altered. Also, small scale heterogeneity in tight gas formations and shale results in these property changes occurring at various scales, such as beds. Property changes occurring along the beds and bedding planes, as a result of interaction with hydraulic fracturing fluid, can contribute to increased potential for shear failure along these planes. Therefore, a systematic micro-scale analysis (including micro-indentation and micro-scratch along the beds to capture micro-geomechanical responses) and macro-scale analysis (including ultrasonic measurements, uniaxial compressive loading in high and low capillary suctions and unloading-reloading cycles at varying capillary suction) have been developed and applied to capture the changes in rock behavior in different scales as a result of spontaneous water imbibition and how different behaviors in micro-scale would affect the responses in macro-scale. QEMSCAN analysis, nitrogen adsorption-desorption tests, thermogravimetric analysis (TGA), capillary condensation experiments, pressure-decay and

pulse-decay permeability measurements and direct shear tests were also completed for quantitative analysis of minerals, pore shapes and porosity, initial water saturation, capillary suction as a function of water saturation, permeability and strength parameters in both macro-scale and micro-scale (bed-scale).

QEMSCAN analysis indicated that mineral components were not the same in different beds and they could be categorized into quartz-rich and clay-rich. The results of the experimental phase indicated that the geomechanical and flow properties of Montney specimens were altered due to fluid imbibition. As the water saturation and capillary suction were changing in quartz-rich and clay-rich beds, they responded differently which would trigger some geomechanical behaviors in macro scale. In addition, it was observed that capillary suction would add extra stiffness and strength to the media and as it was diminishing, the media became weaker. A nonlinear response with hysteresis during unloading-reloading cycles at varying capillary suction implied that as a result of the water softening effect, the reduction in capillary suction and changing the local effective stress there is a high possibility of activation and propagation of pre-existing micro fractures.

In the numerical modeling phase of this research, fully coupled poro-elastoplastic partially saturated models were developed that included transversely isotropic matrix properties and bed-scale geometry. Inclusion of bed-scale features in the numerical approach provided better analysis options since different properties of the adjacent beds (including different capillary suction change) that can trigger the failure in the planes of weakness (such as the interface between the beds) can be directly included in the model while it is not possible to have that in transversely isotropic numerical modeling. This implies that conventional numerical analysis of geomechanical responses originated from spontaneous imbibition needs to be revisited. Beds-included numerical

analyses indicated that since the changes in local effective stress and rock mechanical properties were not the same in adjacent quartz-rich and clay-rich beds, differential volumetric strain along the interfaces between quartz-rich and clay-rich beds would take place which in turn generated induced shear stress components on the interface planes. For the interfaces where total shear stress along them exceeded the shear strength, failure occurred.

Comparing the result of micro-geomechanical (bed scale) and macro-geomechanical analysis with the results of numerical modeling at reservoir in-situ conditions would suggest that as a result of post-fracturing spontaneous water imbibition in the studied Montney Formation, the failures/micro fractures would be generated along the interfaces. Then because of the propagation of activated pre-existing micro fractures in the adjacent beds followed by coalescence with the failed interfaces, a complex micro fracture network can be formed. Accordingly, rock mass geomechanical responses and flow properties would be affected which means that any numerical modeling or analytical approach to account for the production, refracturing and any other reservoir-related analysis without considering this fact is under question mark.

Preface

The mini-cell described in chapter 5 was originally designed by Dr. Nathan Deisman. I was responsible for the modifications and calibrations done to the setup for this work. The analytical, experimental and numerical work and analysis in chapters 3, 4, 5 and 6 are my original work, as well as the literature review in chapter 2.

A part of chapter 3 of this thesis has been presented in "Keshavarzi, R., Moghadam A.A. & Chalaturnyk, R. 2016. Understanding the Implications of Changes in Shale Geomechanical Properties with Fracturing Fluid. AAPG Conference, Calgary, Canada, 19-22 June". Also, a part of chapter 6 of this thesis has been presented in "Keshavarzi, R. & Chalaturnyk, R. 2019. Understanding the Critical Role of Capillary Suction on Rock Mechanical Responses during Post-fracturing Spontaneous Imbibition in Tight Formations. Interpore 2019 (11th Annual Meeting), 6-10 May, Valencia, Spain".

Dedicated to my beloved wife, my dear father and my dear mother.

Acknowledgements

I would like to express my sincere gratitude to my supervisor, Dr. Rick Chalaturnyk, for his continuous support and his patience throughout my PhD. It was a great privilege for me to be a part of RG2 and being supervised by Dr. Rick Chalaturnyk. I have always enjoyed working with him and I appreciate him for all academic and life lessons that he taught me during this time. I am forever indebted to him.

Without support from the RG2 laboratory staff this research couldn't be done. I would like to thank Keivan Khaleghi and Gilbert Wong for their contributions. Also, support from Dr.Nathan Deisman and Jakob Brandl for designing the mini-cell and Mark Labbe for coring is gratefully acknowledged. I owe many thanks to all of my friends, colleagues and other people at the University of Alberta during my studies: Hope Walls, Dr. Kevin Hodder, Dr. Mahmoud Reza Yassin, Dr. Meisam nouri, Rouzbeh Reza Ahrabi…

Table of Contents

List of Tables

List of Figures

Chapter 1 : Introduction

Unconventional resources are the dominant source of hydrocarbon production in North America. Hydraulic fracturing to unlock shale plays and tight unconventional reservoirs has become quite disputable since a significant fraction of the injected fracturing fluid remains in the formation. The reasons for low water recovery and the effect of the remaining fracturing fluid on the formation rock properties and eventually production is still controversial.

To address this issue and increase our knowledge about how unconventional tight formations and shale would behave in the presence of fracturing fluid a combination of analytical, experimental, and numerical studies would be considered. The analytical phases of the research investigate the fundamentals and develop analytical approaches where needed. In the experimental phases, tests are performed on samples with different water saturations to investigate the role of water imbibition on rock mechanical and strength parameters in different scales. The results from this phase also serve as inputs of the numerical modeling phases where a three dimensional geomechanical fully coupled poro-elastoplastic partially saturated model is considered to account for the effect of imbibition on rock responses.

The results of this study enable us to understand how the changes of rock mechanical and failure parameters induced by fracturing fluid during shut-in time period would affect the rock behavior. Also, if the rock mass properties would be affected within or after fracturing then any numerical modeling or analytical approach to account for the production, refracturing and any other reservoir-related analysis without considering this fact would add uncertainties to the analysis.

1.1. Problem Statement

Most tight unconventional reservoirs including shale formations typically do not produce without performing hydraulic fracturing operations. However, only a small portion (5 to 50%) of fracturing fluid would be recovered (Figure 1-1) (King, 2012; Makhanov et al. 2014; Kondash et al., 2017) and the effect of that on rock behavior and production is a debatable issue. From one point of view (Guo and Gao, 2013; Dutta et al., 2014; Yan et al. 2015; Wang et al., 2020), water imbibition during shut-in time period may lead to gas flow restrictions and production reduction as a result of water blockage and gas entrapment in the pores as well as reduction in matrix relative permeability to gas by increasing the water saturation (as shown in Figure 1-2).

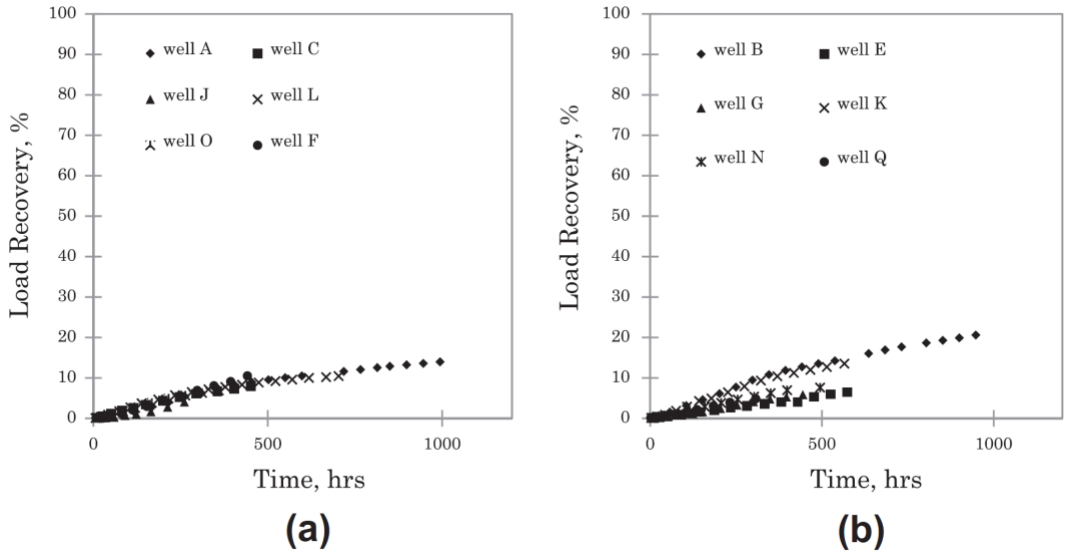

Figure 1-1. Decreasing water recovery with increasing shut-in time in Muskwa (a) and Otter Park (b) members of the Horn River Basin (Makhanov et al. (2014).

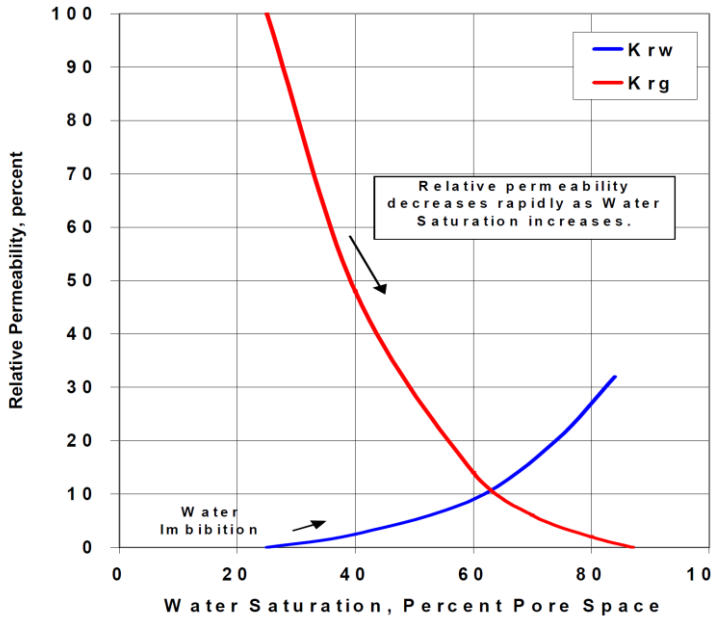

Figure 1-2. Effect of water saturation on relative permeability changes (Keelan, 1975).

Based on some other studies (Cheng, 2012; Agrawal and Sharma, 2013; Xu et al. 2015; Wang et al., 2018) extended shut-in time, would improve early gas production which are mainly attributed

to forming micro fractures taking place through capillary invasion (imbibition) and a counter-current imbibition through which water imbibition can push the gas out of the matrix pores towards the fractures (as shown in Figure 1-3).

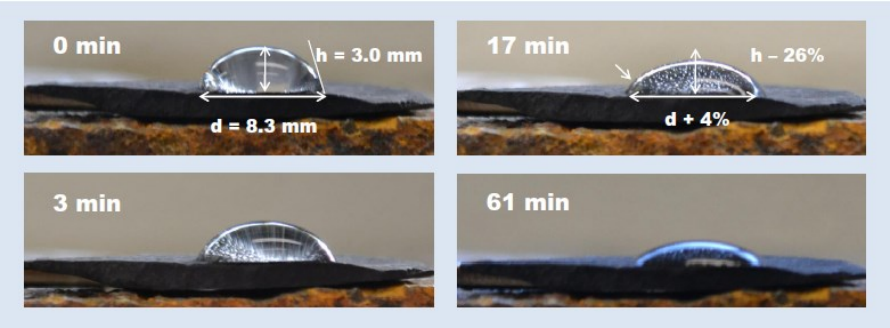

Figure 1-3. Water uptake through counter-current imbibition and releasing the gas bubbles from Marcellus shale sample (Engelder et al. 2014).

Therefore, a thorough understanding of how the remaining fracturing fluid and formation would interact especially during shut-in period is a key to optimize any prospective geomechanical or reservoir-related analysis.

1.2. Research Objectives

The main objective of this research is to understand the fundamentals behind the changes in the tight bedded partially saturated rock behavior as a result of water imbibition during shut-in time period and how it can affect further geomechanical or reservoir-related analysis. This mainly includes the followings:

- How would water imbibition take place and what are the phenomena observed as a function of time?
- How would increasing the water content affect the overall properties of the samples?
- What are the experimental approaches that can contribute more to account for samples-water interaction from geomechanical point of view?
- How can numerically water imbibition in this type of rocks (bedded partially saturated media) be handled to explain the geomechanical behaviors?

- How would the changes in water saturation affect the rock mechanical and strength parameters in the beds scale?
- Proposing an integrated workflow to explain the fundamentals of the behaviors in bedded partially saturated media as water imbibition is taking place.

1.3. Research Scope

The current research scope includes:

- Understanding the mechanisms that trigger the failure during the imbibition in partially saturated shale samples.
- Multi-scale tests to capture the fundamentals behind the responses observed as a function of water saturation (changes in elastic and plastic parameters as well as capillary suction).
- Creating and developing 3D geomechanical fully coupled poro-elastoplastic partially saturated model.

1.4. Thesis Structure

To fulfill the research objectives, an integrated analytical, numerical and experimental approach is considered through the following chapters:

1.4.1. Chapter 2: Literature review

A comprehensive and detailed review on theoretical, numerical and experimental studies done related to the interaction of shale and tight unconventional reservoirs with fracturing fluid as well as determining the dominating factors (mainly from geomechanical point of view).

1.4.2. Chapter 3: Qualitative Analysis of Geomechanical Behaviors Triggered by Spontaneous Imbibition

Performing spontaneous imbibition experiments on Montney samples (Farrell Creek field in northeast British Columbia) and determining the changes in geomechanical properties as water imbibition is taking place. This includes capturing the behaviors observed through spontaneous imbibition of fracturing fluid into Montney samples, changes in rock mechanical properties and capillary suction as well as how these changes would affect the stress state analysis and "fracability" (i.e. ability to hydraulically fracture formation". In addition, two fully coupled poro-

elastoplastic partially saturated isotropic numerical models have been introduced, developed and compared: 1) Transversely isotropic model and 2) Beds-included model.

1.4.3. Chapter 4: Reservoir Geomechanical Analysis of Spontaneous Water Imbibition in Tight Formations: Bed-scale Characterization

The properties of any bedded rock mass are dependent on the properties of the individual beds. This means that if changes in properties occur at the bed scale in a highly bedded rock, then it is very likely that this will significantly influence the overall behavior of the rock mass. To determine the properties at the bed-scale an integrated experimental and analytical approach has been developed. In other words, the existing methods for small-scale characterization have been modified/developed for partially saturated porous media and then based on that the results of experiments have been analyzed to capture the properties in the bed-scale. This includes performing QEMSCAN analyses to see how different the beds are from a mineralogy point of view, thermogravimetric analysis (TGA) to measure the initial saturation, nitrogen adsorption–desorption isotherms tests to understand pore structure, capillary condensation to determine the capillary pressure in each saturation, pressure decay and pulse decay tests for permeability measurements, micro-indentation and micro-scratch tests to capture the rock mechanical and strength properties of the beds in different saturations.

1.4.4. Chapter 5: Design, Calibration and Application of Mini-cell

Since the scale of the beds were very small (millimeter or less), small sample sizes (1cm diameter by 2 cm height) were selected to better study and capture the geomechanical mechanisms at this scale. To enable this component of the research, an innovative mini-cell was designed and built in Reservoir Geomechanics Research Group (RG2). One of the main advantages of applying the mini-cell is that it is applicable to explain and study the basic mechanisms which are taking place in small scale (e.g. bed-scale) but would affect the rock mass properties. Conventional triaxial-sized specimens create many challenges in studying small-scale specimen behavior and fundamental mechanisms. This chapter includes the design of the mini-cell, calibration procedure and application demonstration.

1.4.5. Chapter 6: Complex Geomechanical Responses during Spontaneous Water Imbibition in Tight Formations

After determination of the bed-scale geomechanical properties in Chapter 4, in this chapter larger scale tests have been considered to better understand how change in capillary pressure and rock mechanical and strength properties would impact rock response under stress. This includes investigating the response of Montney sample during capillary suction change (controlled wetting process) while the sample is under constant stress (uniaxial loading-unloading-reloading) followed by beds-included fully coupled poro-elastoplastic partially saturated model to investigate the possibility of failure generation during spontaneous water imbibition under reservoir condition for Montney Formation.

1.4.6. Chapter 7: Conclusions and Recommendations

This chapter includes the conclusions on the complicated behavior of tight gas formations and shale plays and why spontaneous imbibition of fracturing fluid is important in post fracturing reservoir characterization as well as how micro-geomechanics analysis contributes to explain the complex macro-geomechanics behaviors caused by spontaneous imbibition. In addition, recommendations have been made for improving the workflow and future studies.

1.4.7. Chapter 8: References

In this chapter the references used in this research are listed.

Chapter 2 : Literature review

During hydraulic fracturing in tight gas formations and shale plays, it is found that less than 50% of the injected fluid would be recovered and up to 95% of that may remain in the reservoir (Pagels et al. 2011; King, 2012; Striolo et al. 2012; Zhou et al. 2014; Kondash et al., 2017) which would start interacting with the formation. The most likely phenomena which can to some degree describe low water recovery is capillary invasion followed by spontaneous imbibition of fracturing fluid in the formation during and after fracturing (Roychaudhuri et al. 2011; Makhanov et al. (2012, 2013, 2014); Engelder et al. 2014; Dutta et al. 2014; Zhou et al. 2014; Shuai et al. 2016) and water retention in induced or pre-existing fractures (Fan et al., 2010; Ehlig-Economides and Economides, 2011; Ghanbari et al., 2013; Makhanov et al. 2014). In addition, imbibition is inversely proportional to water saturation (Li et al., 2006) which means that by increasing the water saturation the imbibition would reduce. The main concern is about the effect of the remaining fracturing fluid on production since matrix relative permeability to gas would change by increasing the water saturation in the media. The former concern would highlight the effect of shut-in time and positive or negative effects of that on the productivity (Taylor et al. 2009; Makhanov et al. (2013, 2014); Dutta et al. 2014; Yan et al. 2015; Wang et al., 2020). Some studies (Wang et al. 2012) indicate that a higher fracturing fluid recovery does not necessarily lead to higher gas production. Although increasing water saturation through imbibition would theoretically lead to decreasing the relative permeability of gas but based on some studies (Cheng, 2012; Agrawal and Sharma, 2013; Xu et al. 2015; Wang et al., 2018) extended shut-in time, would improve early gas production. This indirectly means that throughout the shut-in period there must be some dominating mechanisms which can result in increasing the productivity. The results of some studies (Gupta 2009; Fan et al. 2010; Shaoul et al., 2011; Wang et al. 2012; Guo and Gao, 2013; Yan et al. 2015; Wang et al., 2020), show that water imbibition as a result of high capillary pressure may lead to gas flow restrictions and production reduction while some other works imply that due to shear/tensile failures through capillary invasion (imbibition) in the matrix within shut-in period, micro fractures can be generated (Anderson et al. 2010, Caenn et al. 2011, Dehghanpour et al., 2012; Dehghanpour et al., 2013; Ji and Geehan, 2013; He et al. 2014) which can in turn lead to increasing the production. Dehghanpour et al. (2012) indicate that as a result of water imbibition moisture swelling would occur and internal stresses are generated which can increase the possibility of failure and micro fracture generation. In other words, from geomechanical point of

view, the mechanical properties of the rock as well as internal stress state would be affected as the capillary invasion is taking place which can increase the possibility of shear/tensile failures. Once the failure occurs due to capillary invasion, micro fractures will form which can lead to permeability increase. Some studies (Yan et al. 2015) imply that clay swelling would not only reduce the permeability but also permanently damages the absolute permeability. Even in such cases, based on the experimental studies (Bostrom et al. 2014) over time the permeability was rebounded between 30-100% several days after water exposure. Therefore, understanding how the remaining fracturing fluid would interact with tight gas formations through different mechanisms such as capillary invasion, tensile or shear failures is a key to account for the future reservoir-related analysis and characterization which can in turn affect the production.

2.1. The Effect of Fracturing Fluid Spontaneous Imbibition on Tight Gas Formations and Shale Properties

2.1.1. Observed Mechanisms and Behaviors

2.1.1.1. Capillary Invasion and Fluid Displacement

Bertoncello et al. (2014) considered two processes for water displacement within the formation while fracturing. First, the mechanism in which viscous force during hydraulic fracturing is a dominating parameter which forces the water to fill the larger and connected pores and second, imbibition into the small water-wet pores through capillary invasion (Figure 2-1. Schematic of water displacement processes in shale gas (Bertoncello et al. 2014).). Within shut-in period, displacing water from larger to small pores through capillary invasion decreases the water saturation in near the fracture face which can lead to facilitate gas flow and increasing gas productivity. They concluded that early production improvement is significantly affected by water invasion and immediate flowback would minimize it while the effect of water invasion on long-term production is limited. Dutta et al. (2014) have done a series of experimental tests to investigate the loss of fracturing fluid into tight formations. They concluded that permeability, capillarity and heterogeneities in the formation are the dominating factors which would play important roles in water uptake and redistribution of water and gas phase. Also, they believe that under reservoir conditions the fracturing fluid loss into the formation would be higher. On top of that, they observed up to 76% reduction in relative permeability to gas after 7 days shut-in period.

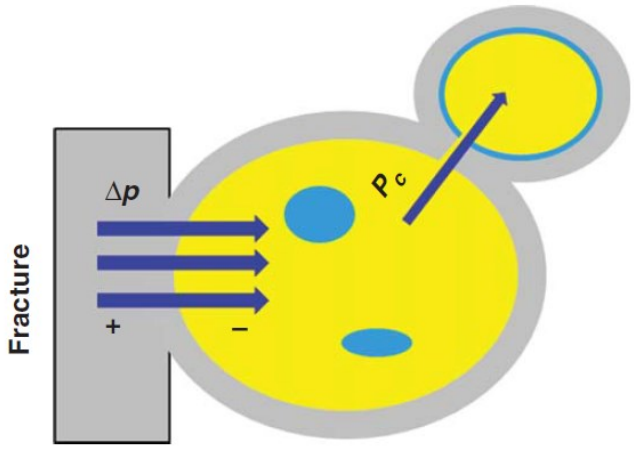

Figure 2-1. Schematic of water displacement processes in shale gas (Bertoncello et al. 2014). Viscous force during hydraulic fracturing which forces the water to fill the larger pores and imbibition into the small water-wet pores through capillary invasion.

To investigate the time-dependence permeability and optimize the shut-in time Bostrom et al. (2014) conducted experiments on gas saturated samples at reservoir conditions and observed the gas permeability before and after exposure to fracturing fluid. After the core was exposed to water, a significant permeability reduction was observed due to blockage but over time the permeability was rebounded due to water blockage dissipation. The permeability rebound which was observed in the experiments was between 30-100% several days after water exposure (Figure 2-2). Also according to Lan et al. (2014), the relationship between normalized volume imbibed and time for Montney samples was not necessarily linear and it showed a non-linear trend (as shown in Figure 2-3). Makhanov et al. (2014) conducted several spontaneous imbibition experiments on shale core samples collected from the Horn River shale basin. The results indicate that imbibition is the possible mechanism to describe low water recovery and early gas production after extended shut-in time. Also, they concluded that due to greater permeability parallel to the beds the imbibition rate in this direction is higher than the perpendicular direction which is followed by imbibition-induced micro fractures generated along and around the beds as shown in Figure 2-4. These results are consistent with the permeability measurements done on shale samples (Kwon et al. 2004; Pathi et al. 2008; Josh et al. 2012; Vermylen 2013; Yu et al. 2013; Polito et al. 2014;

Ghanizadeh et al. 2016; Zhao et al., 2020) in which the permeability parallel to the beds is higher than perpendicular direction (Figure 2-5).

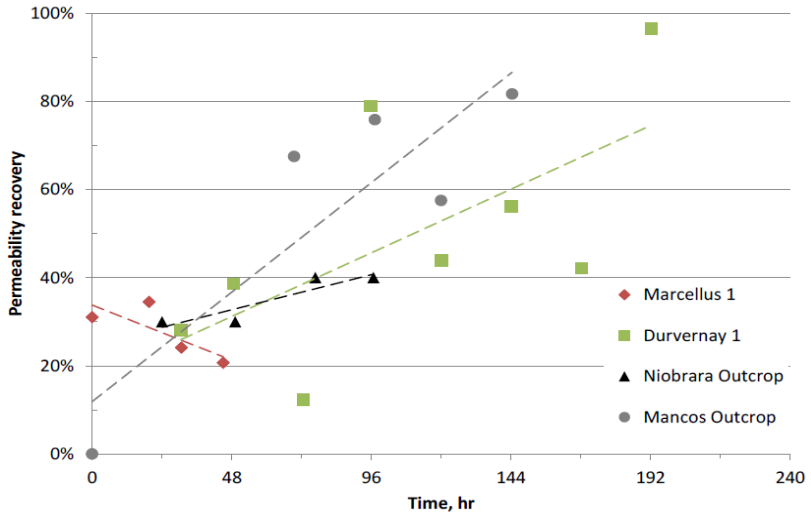

Figure 2-2. Permeability recovery as a function of time during water imbibition tests (Bostrom et al. 2014).

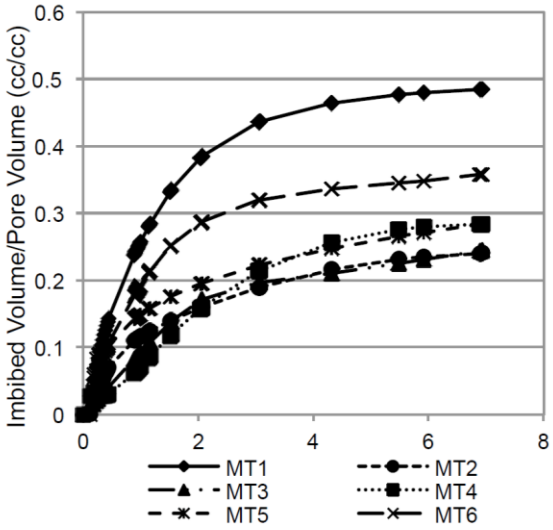

Figure 2-3. Normalized imbibed volume versus square root of time for Montney Formation samples (Makhanov et al. 2014).

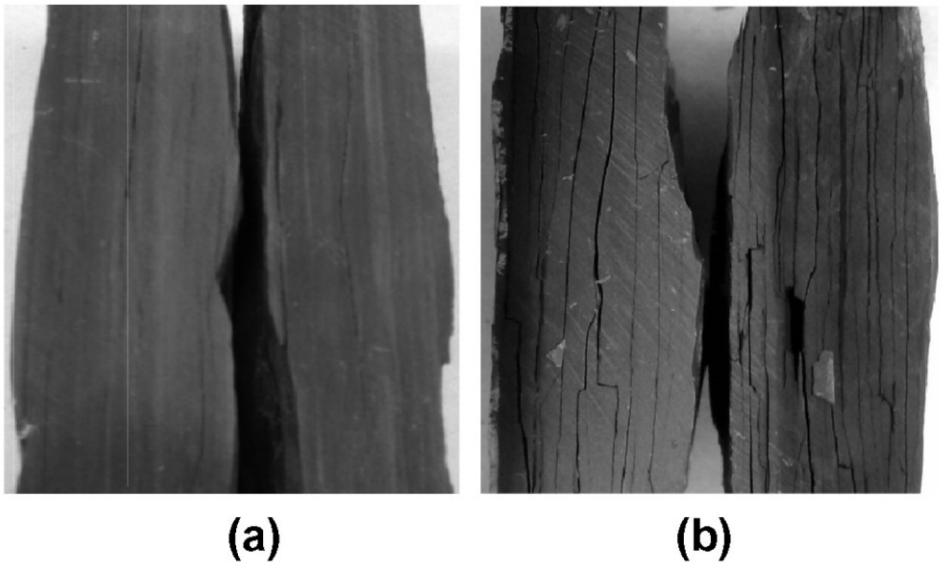

Figure 2-4. Imbibition-induced cracks due to one day fluid exposure in shale samples: (a) before water imbibition, (b) after water imbibitions (Makhanov et al. 2014).

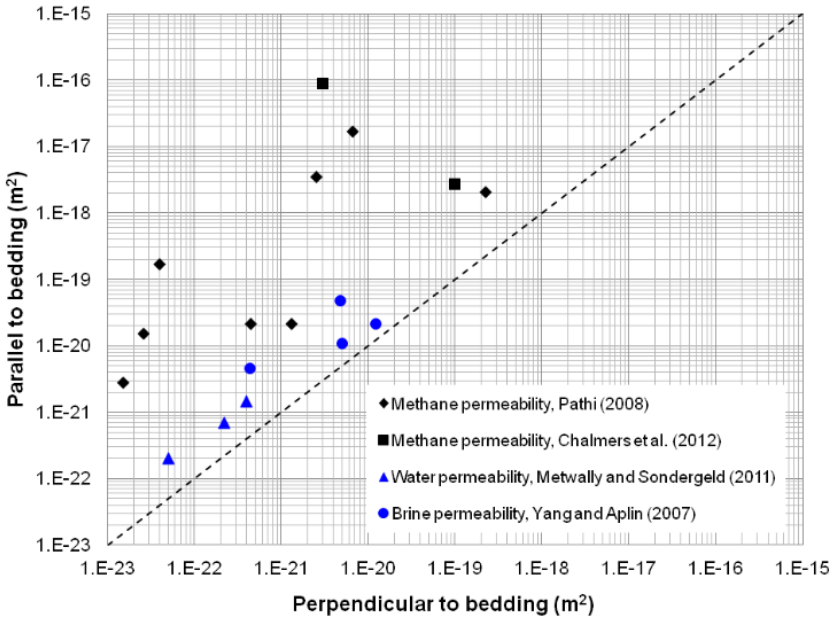

Figure 2-5. Permeability parallel and perpendicular to the beddings for Montney shale samples (Ghanizadeh, 2013).

2.1.1.2. Fracture Initiation and Propagation

In He et al. (2014) laboratory tests on shale samples fracture generation along bedding planes as well as extension or separation of fractures could also be observed (Figure 2-6).

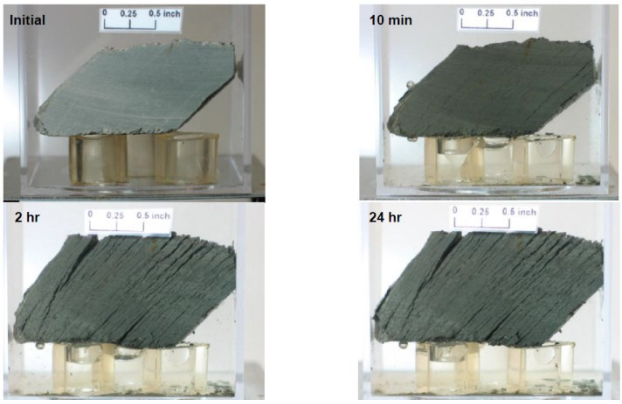

Figure 2-6. Fracture generation along beddings after water exposure (He et al. 2014).

In addition, the results of a test under confining pressure of 500 psi presents induced fractures mainly along bedding planes (Figure 2-7).

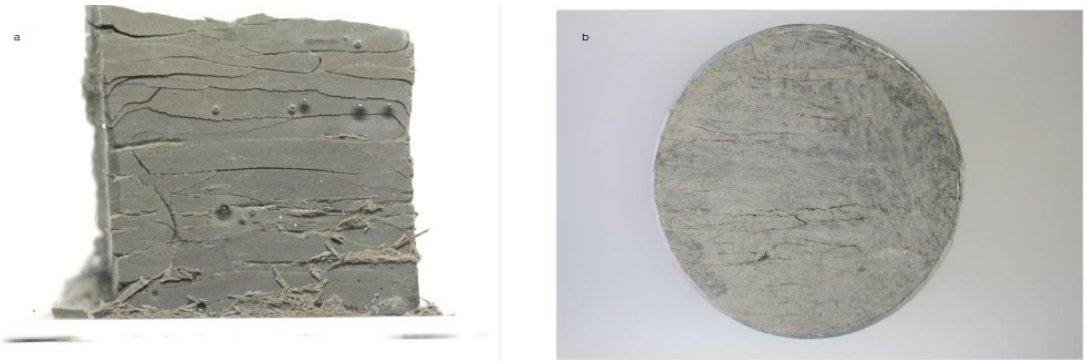

Figure 2-7. The effect of confining pressure on fracture generation in shale sample: a) without confining pressure and b) with confining pressure of 500 psi after one hour exposure to fluid (He et al. 2014).

The results of He et al. (2014) and Makhanov et al. (2014) agree with Morsy and Sheng (2014) studies on Barnett shale in which they concluded that recovery would increase due to generation of micro fractures along bedding. Also, Friedheim et al. (2011) investigated the failure in shale formation as a result of the interaction between fluid and low-reactive shale from 24 hours to few

days. They observed fracture generation and propagation in the samples which would suggest that some other parameters other than clay swelling are dominant as well (Figure 2-8).

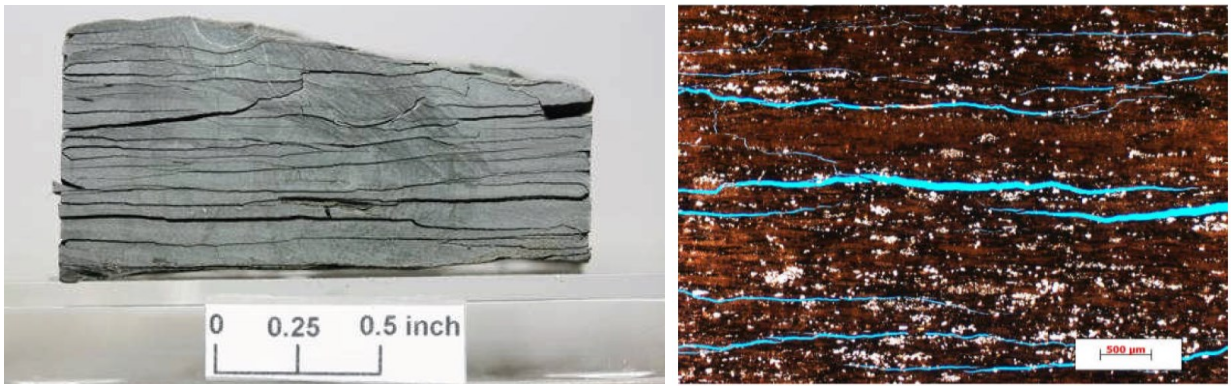

Figure 2-8. Low-reactive shale and fluid (water) interaction after around 24 hours in the samples (left) and thin section (right) (Friedheim et al. (2011)).

From another point of view Dyke and Dobereiner, (1991) concluded that surface fracture energy and the energy needed for crack propagation decreases with increasing the moisture content which results in the strength reduction in rocks and increasing the possibility of fracture generation and propagation. Also, Nara et al. (2012) state that fracture toughness would reduce as relative humidity is increasing and this reduction is more significant when the rock has expansive clay such as smectite which results in decreasing crack growth resistance.

Padin et al. (2014) investigated the mechanisms behind micro fractures propagation on ductile shales as well as the key factors that constrain its slippage in Eagle Ford (Texas) and Vaca Muerta (Neuquén, Argentina) formations. They stated that the most dominant factor affecting micro fracture propagation in shale is mainly related to anisotropy in fabric of the rock. They concluded that both horizontal and vertical micro fractures can be generated and horizontal micro fractures would follow the directions where the tensile strength is minimum (for example at the interfaces of bedding planes). Also, shear slippage and micro fracture propagation most likely happen in the interfaces between the different mineralogical components of the shale matrix.

Yang et al. (2015) studied the imbibition induced tensile fractures in shales. Based on their observations induced micro fractures are mainly formed near the organic-rich region (Figure 2-9). They also believe that swelling pressure and capillary pressure work together and induce the effective internal stress followed by micro fractures generation which leads to non-linearity and

hysteresis in imbibed volume versus square root of time plot at the later times stages (Figure 2-10). This is consistent with Roychaudhuri et al. (2013) where they concluded that a non-linear behavior at the later times implies that the shale itself develops micro fractures.

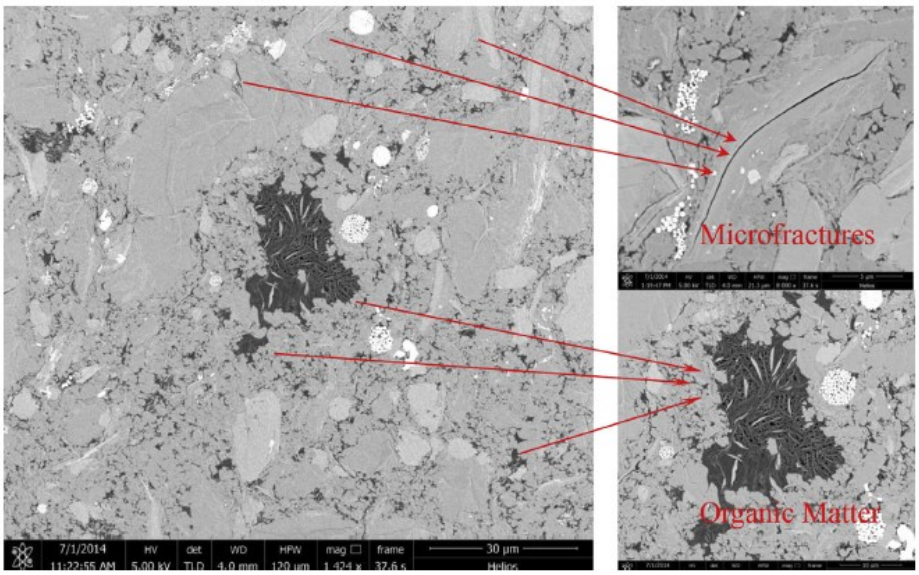

Figure 2-9. Scanning electron microscope image of a shale sample shows the generation of microfractures near the organic-rich regions (Yang et al. 2015).

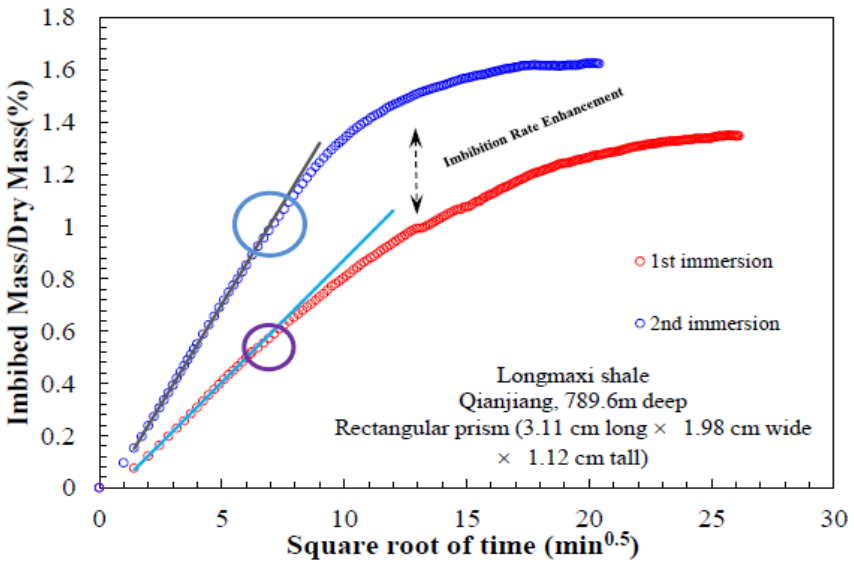

Figure 2-10. The cumulative imbibed weight per dry sample weight versus square root of Time (Yang et al. 2015).

Wang and Rahman (2015) studied the pressure increase due to gas entrapment and generation of micro fractures during fluid invasion (due to capillary suction) in shale formations. They conclude that as the internal pore pressure near the fracture face rises the possibility of tension and shear fractures generation would increase which in turn leads to increasing gas production. They believe that as the water is filling the smaller pores and throats, the gas also tends to move toward the nearest pore space and throats (larger pores or fractures) (as shown in Figure 2-11).

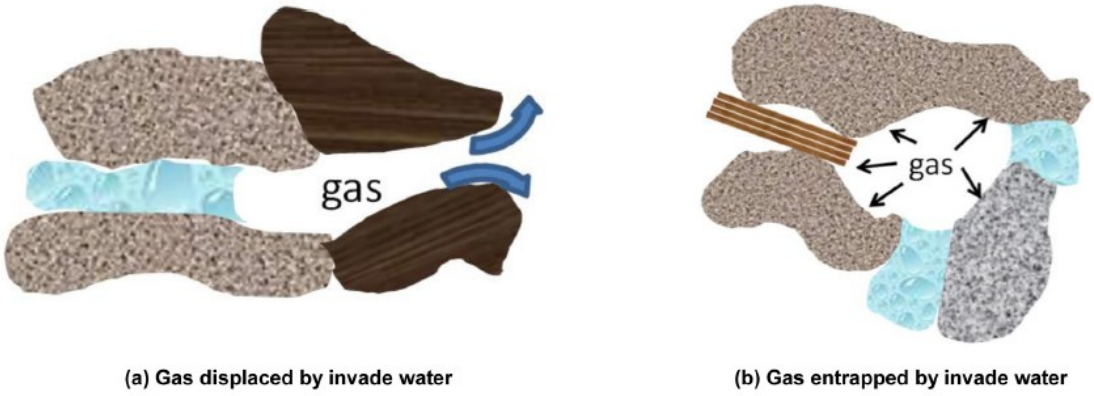

Figure 2-11. Effects of water invasion on gas displacement (Wang and Rahman 2015).

However, due to low porosity and permeability of shales, gas is likely to be trapped. Therefore, this gas entrapment would result in internal pressure increase and fracture generation. But the rise in pore pressure is not the same in all components and the amount of pore pressure increase in clay pores is higher than other components (Figure 2-12) which means that the effective stress of each component is different that can lead to a shear failure at the interface followed by generating micro fractures. This is consistent with Padin et al. (2014) investigation on micro fracture propagation in shale where they have suggested different size and strength properties of clay and non-clay minerals, differential horizontal stress as well as the orientation of pre-existing micro fractures would be the dominant parameters in micro fracture generation and propagation. Ghanbari et al. (2013) investigated the relationship between flowback efficiency and other parameters such as imbibition and generation of complex fracture network within the wells with low flowback and high gas production and the wells with high flowback and low gas production. They concluded that water blockage would take place in secondary induced fractures due to lower fracture conductivity. Then this water spreads away from the fracture face into the matrix. Within shut-in

time the gas in the matrix would be released and expelled from the matrix (through counter-current imbibition) and accumulates in the fracture network system (primary and secondary fractures) and flowback with water within the early steps.

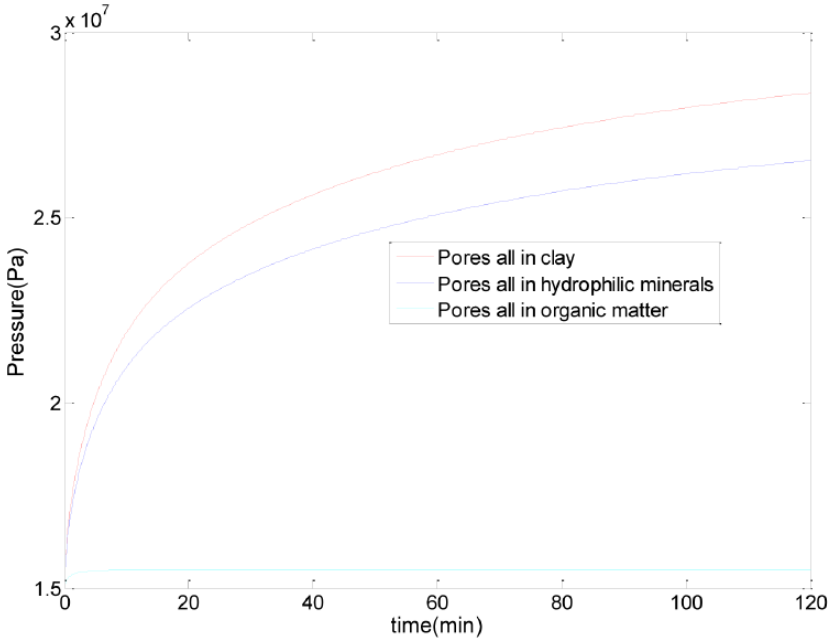

Figure 2-12. Pressure change versus time for different components (Wang and Rahman 2015).

Zhong and Leung (2020) studied on the impact of secondary fractures (pre-existing small fractures or induced fractures with low permeability than the main hydraulic fracture) distribution on shale gas production through integrating pressure-dependent matrix apparent permeability and 3D DFN model. They concluded that secondary fracture intensity would have a strong impact on fracturing fluid distribution in the reservoir but explaining water retention seems to be complicated because of compressibility of the fluids in gas-water system. They considered four regions: inside the hydraulic fracture, adjacent to the hydraulic fracture, the near-well region and far away region (Figure 2-13) and concluded that during the shut-in time there would be a water uptake from the main hydraulic fracture (Region 1) to the adjacent area (Region 2) as a result of capillary invasion and due to high capillary force in Region 2, less water imbibition would take place from Region 2 to Region 3 and then to Region 4 (Figure 2-14). They did not consider the changes on rock mechanical and strength properties as well as failure mechanisms which would affect the overall properties of the reservoir characterization.

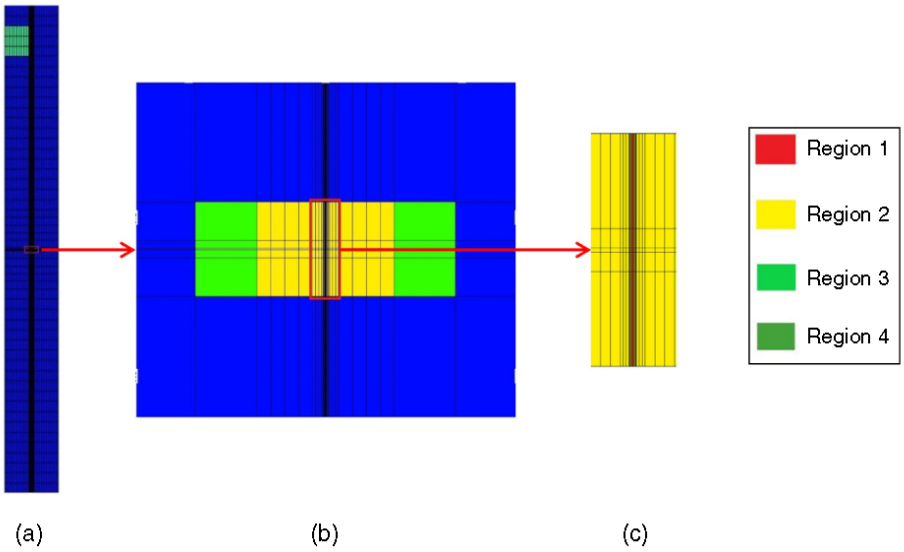

Figure 2-13. The regions considered for fluid distribution (Zhong and Leung (2020). Region1:inside the hydraulic fracture, Region 2: adjacent to the hydraulic fracture, Region 3: the near-well region and Region 4: far away region.

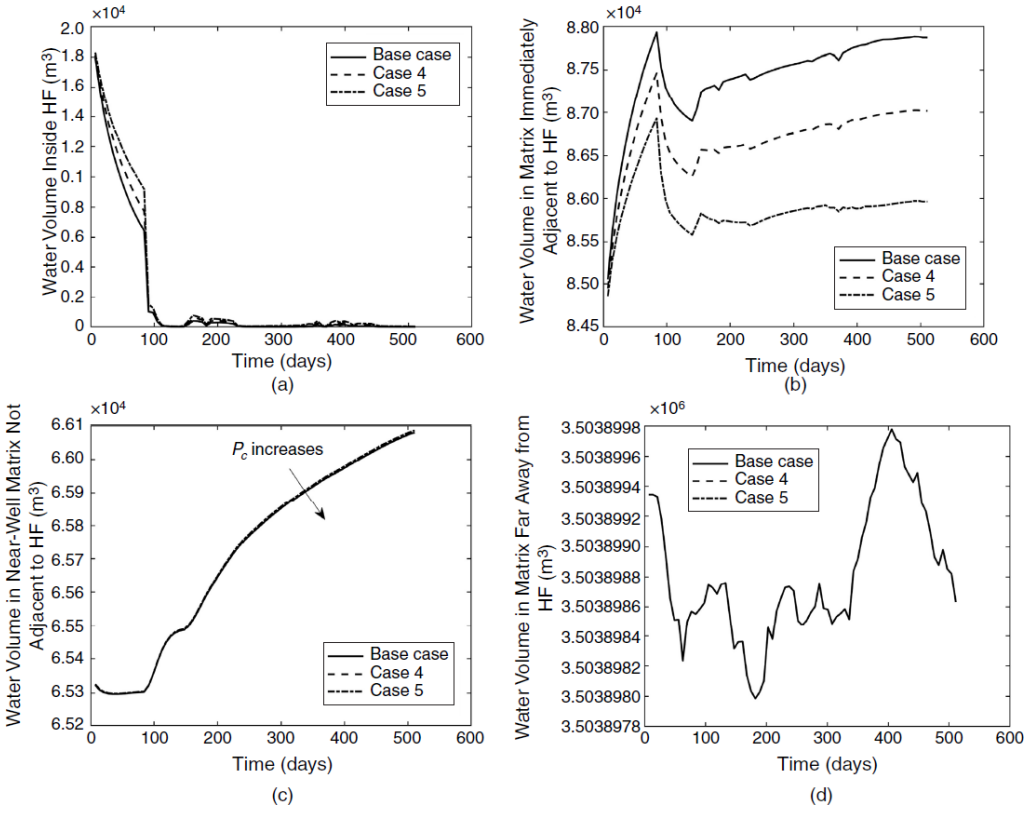

Figure 2-14. Water uptake in different regions from the fracture face : (a) Region 1, (b) Region 2, (c) Region 3, and (d) Region 4 (Zhong and Leung (2020).

Zhang et al. (2017) designed a triaxial setup equipped with CT scanner to investigate the hydration-induced fracture generation and propagation as a result of water imbibition under isotropic and anisotropic stress conditions. They clearly observed fracture generation and propagation as a result of water imbibition while the sample is under triaxial condition. Under isotropic stress condition as the confining stress increases from 2 MPa to 20 MPa no tensile fracture was observed while under anisotropic stress conditions shear-induced fractures were generated (Figure 2-15) which could increase the permeability to nearly 100 times higher in comparison with the base case.

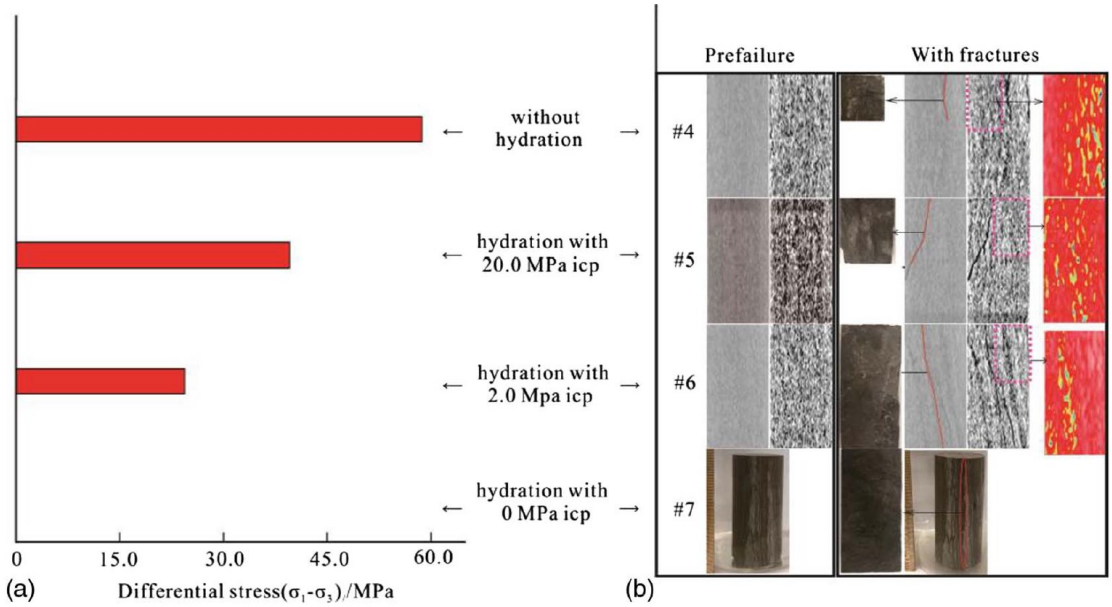

Figure 2-15. Hydration-Induced fracture generation in Mancos shale samples under anisotropic stress conditions:without hydration and confinement, with hydration and confienement 2 and 20MPa (Zhang et al. (2017).

2.1.2. Impacts of Fracturing Fluid Spontaneous Imbibition on Rock Mechanical and Strength Properties

As a result of the bedded structure of shale rocks the rock mechanical and strength properties may differ from one direction to another. Heng et al. (2015) conducted some direct shear experiments on shale samples to investigate the effect of bedding plane orientations (β) (or in other words "loading orientation") on shear strength and failure mechanisms in shale. The results indicate strength, cohesion and internal friction angle are maximum at β = 60 in comparison with other β

values (Figure 2-16). They put the failure modes into two categories: sliding mode, in which the anisotropy and plane discontinuity (such as bedding) dominates and non-sliding mode, in which the rock strength is dominant. It is recognized that main mechanism in β = 60 (in high normal stresses) is a combination of shear sliding across bedding planes accompanied by tensile splitting along bedding planes as shown in Figure 2-17.

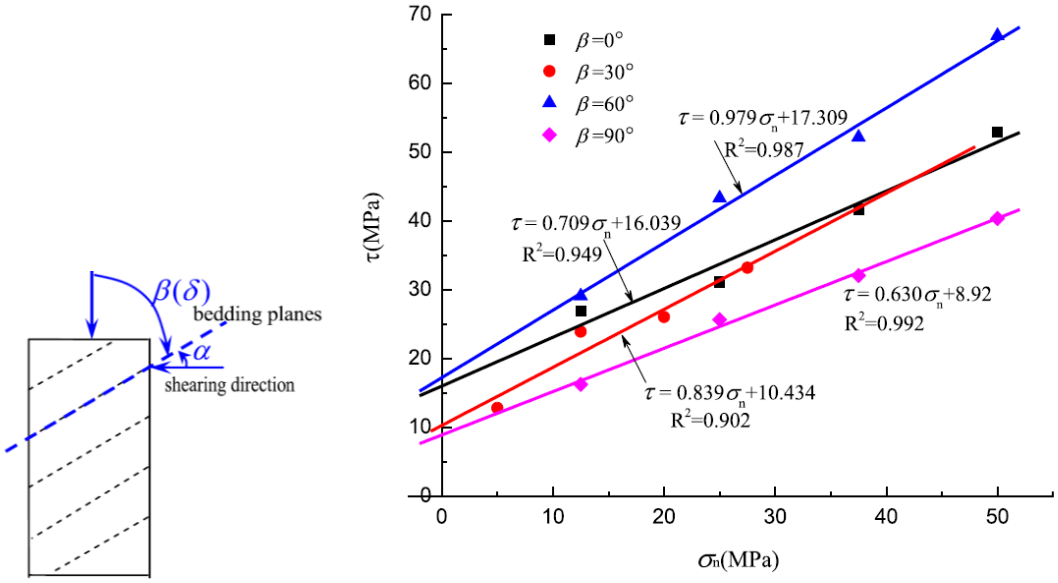

Figure 2-16. Failure envelopes, shear strength, cohesion and friction coefficient of shale samples with different bedding angle (Heng et al. 2015).

Mokhtari et al (2013) and Ambrose (2014) have conducted triaxial compression experiments on a series of shale samples with different bedding orientations to investigate the failure behavior in anisotropic shales. Mainly, the sample with bedding orientation of 90^{o} (parallel to the beddings) showed the highest strength where instead of a single sliding fracture, several fractures have been generated and intersected. Figure 2-18 and Figure 2-19 illustrate the effect of bedding orientation on shear strength of Mancos shale and Bossier shale respectively. Comparing the results of Heng et al. (2015) experiments with Mokhtari et al (2013) and Ambrose (2014) would show the complexity of the rock mechanical responses and failure patterns in tight bedded structure rock types. Due to interaction of fracturing fluid and shale formation, some rock mechanical properties and strength properties of shale would be affected. AL-Bazali (2013) performed experiments to see how water content would affect the uniaxial compressive strength (UCS) in shales.

Experimental data showed that water content has a detrimental effect on UCS in shale formations and UCS would significantly decrease as the water content rises which is not necessarily a linear relationship (as shown in Figure 2-20). He concluded that increasing water content can result in compressive strength reduction, elastic modulus reduction, cementing bonds weakening, matrix fabric deterioration, pore fluid composition alteration, initiation and generation of micro fractures and fissures, shale swelling, expansion and failure.

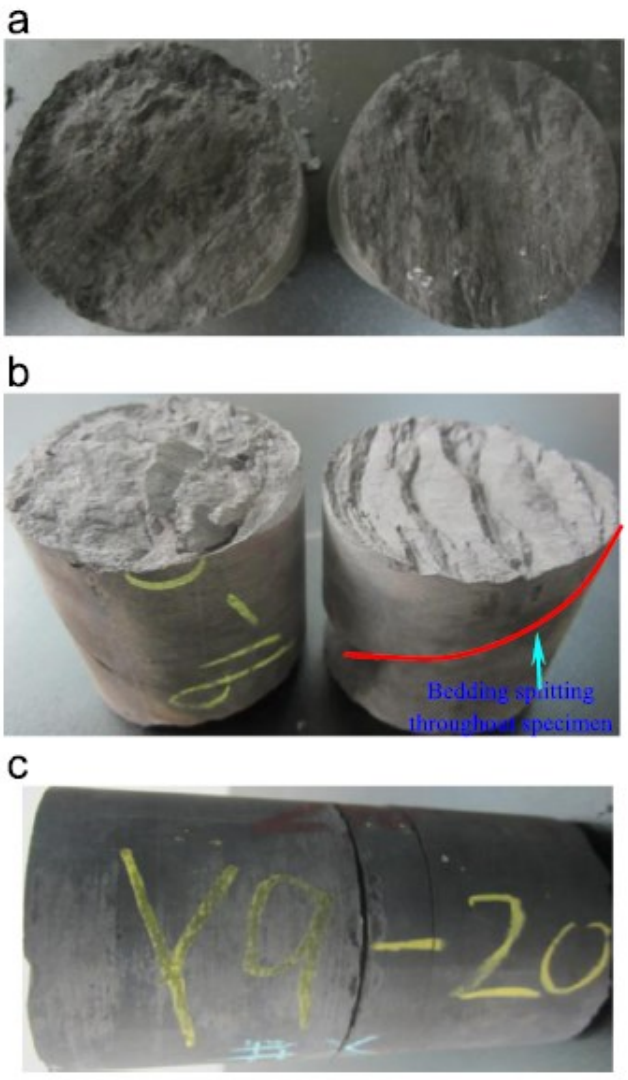

Figure 2-17. Failure mechanisms observed in different bedding orientations: a) β = 0 (non-sliding mode); b) 60 (combination of sliding and non-sliding mode) and c) 90 (sliding mode) (Heng et al. 2015).

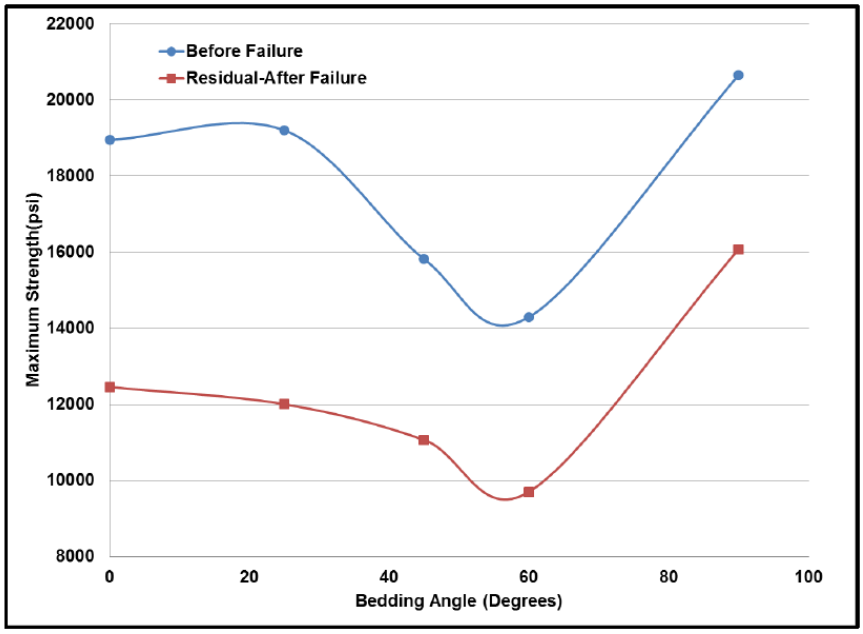

Figure 2-18. Shale strength in different bedding orientation in Mancos shale samples (Mokhtari et al 2013).

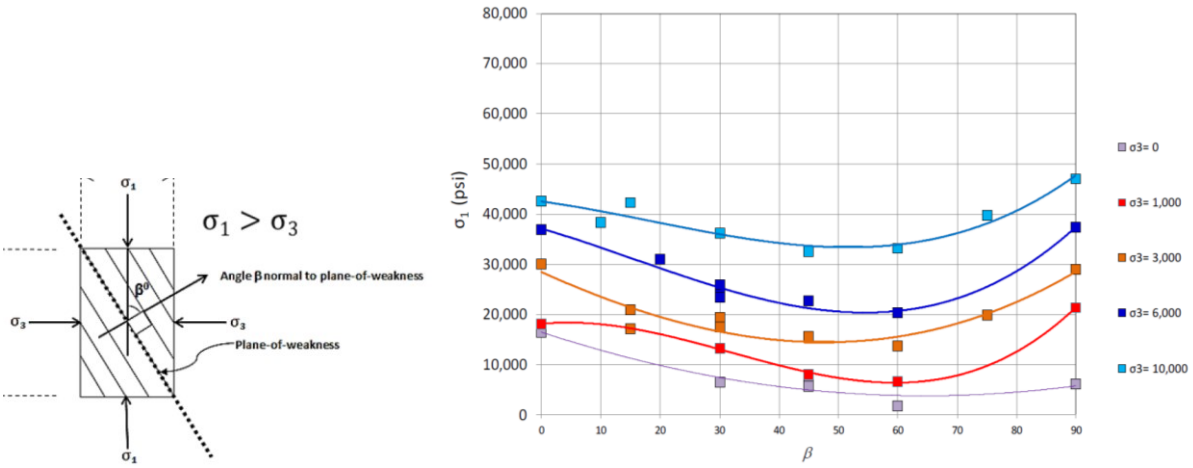

Figure 2-19. Shear strength of Bossier shale versus bedding angle (Ambrose, 2014)

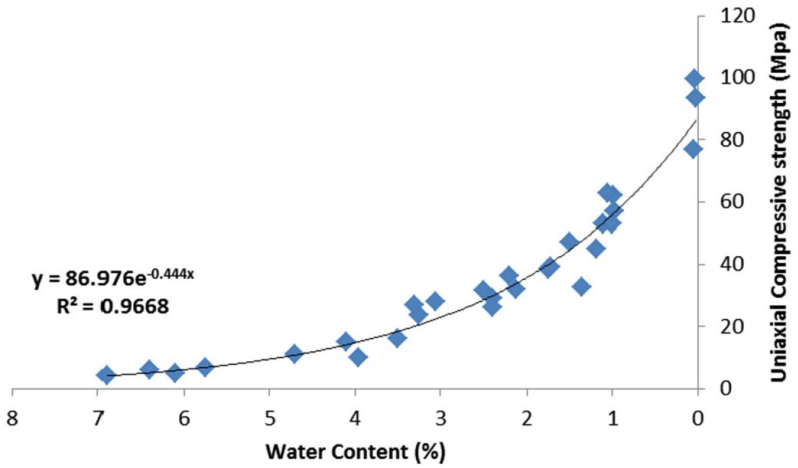

Figure 2-20. UCS measurements in shale samples under different water content AL-Bazali (2013).

Akrad et al. (2011) conducted experiments on samples from four shale formations: Bakken (middle and lower), Barnett, Eagle Ford and Haynesville to investigate the effect of fracturing fluid. They concluded that Young's modulus reduction due to fracturing fluid and shale interaction for calcite-rich shales is around 30-50%, for clay-rich shales 3-30%, and for quartz-rich shales 10-30%.

Also, Vale`s et al. (2004) performed uniaxial and triaxial experiments on Tournemire shale samples with different saturations and bedding orientations (0^o, 45^o, 90^o). It is recognized that for all degrees of saturation, the Young's modulus for triaxial tests are higher than uniaxial tests due to this fact that the confinement would stiffen the rock sample. Also, for all directions, as saturation increases triaxial compressive strength and Young's modulus decrease while Poisson ratio increases (as shown in Figure 2-21 and Figure 2-22). Interlayer swelling aperture for $\theta = 0^o$ and 90^o was observed which may also serve a path for water transfer. Water saturation increase would also lead to cohesion and friction angle reduction in both parallel and perpendicular samples (Figure 2-23).

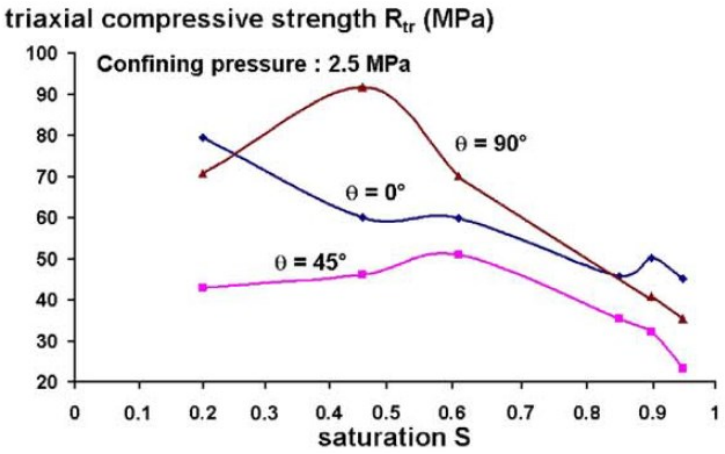

Figure 2-21. Triaxial compressive strength reduction as saturation rises in all directions (Vale`s et al. 2004).

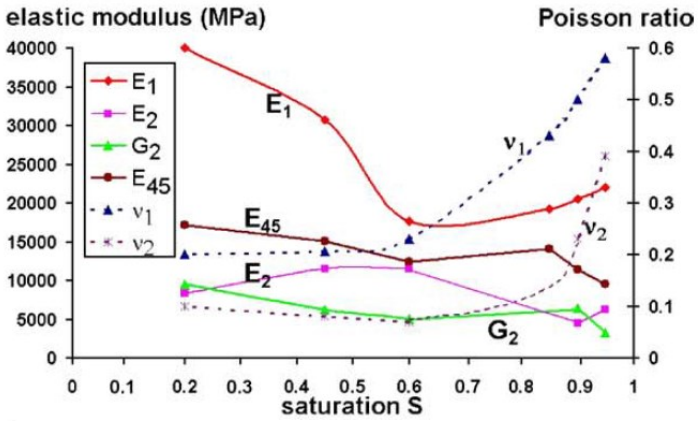

Figure 2-22. Changes in Young's modulus and Poisson ratio as saturation rises (Vale`s et al. 2004).

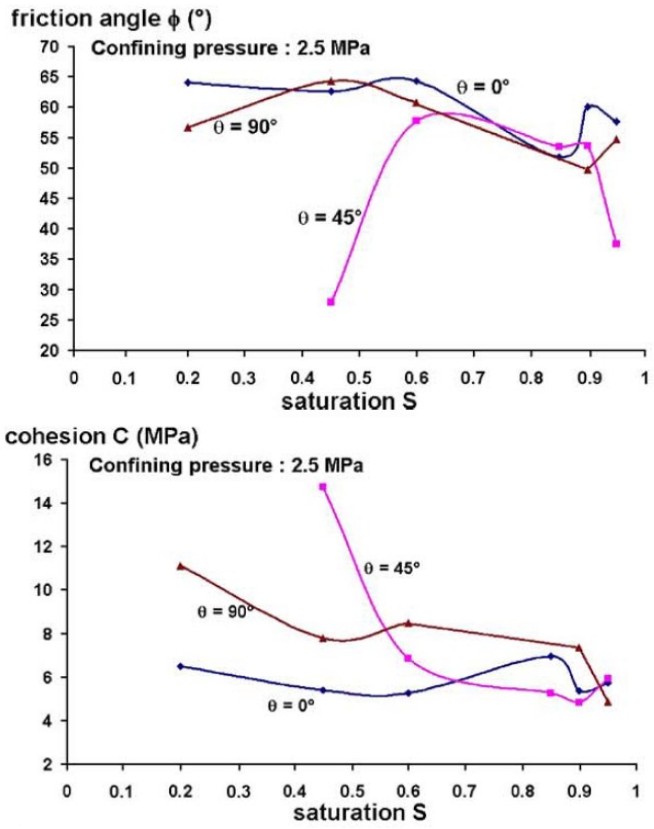

Figure 2-23. Changes in cohesion and friction angle as saturation rises (Vale`s et al. 2004).

Finally, they concluded that for $\theta = 0^o$, the failure is extensive with several parallel cracks when water is present. For $\theta = 45^o$, failure is associated with sliding in the direction of bedding planes. For this case also, the presence of water would result in generating several cracks parallel to the main fracture. In case of $\theta = 90^o$, the failure in the shale matrix is mainly related to shear bands and deformations taking place within shear bands result in severe damage and fracture generation. In addition, Figure 2-24 represents the failure modes observed in low and high saturation conditions for bedding orientation of 0^o, 45^o and 90^o. Holt et al. (2015) conducted rock mechanical laboratory experiments with Mancos and Pierre shale cores to account for the brittleness in anisotropic shales. It is observed that in anisotropic shale, brittleness mainly depends on the direction of loading (or in other words "bedding orientation"). It is recognized that, the highest brittleness value is observed when the failure plane coincides with the bedding plane which increases the possibility of micro fracture generation in this direction more than other directions.

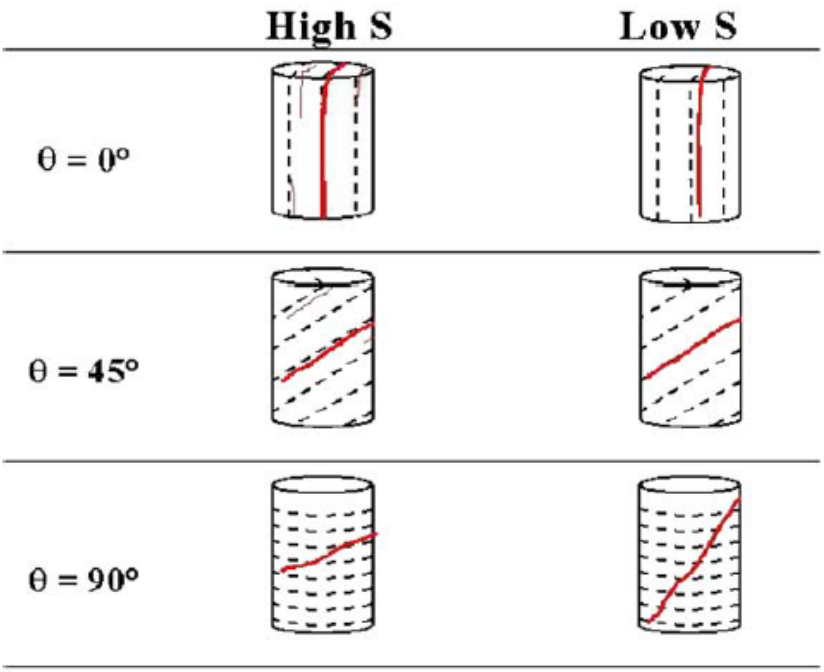

Figure 2-24. Failure modes observed in low and high saturation conditions for bedding orientation of 0°, 45° and 90° (Vale`s et al. 2004).

Based on the results of tensile failure tests conducted by Holt et al. (2015), the sample with 15° bedding inclination shows a pure tensile failure and a secondary splitting along the bedding plane while at 60° inclination, the tensile fracture follows a path between the direction of the maximum principal stress and the bedding plane (Figure 2-25).

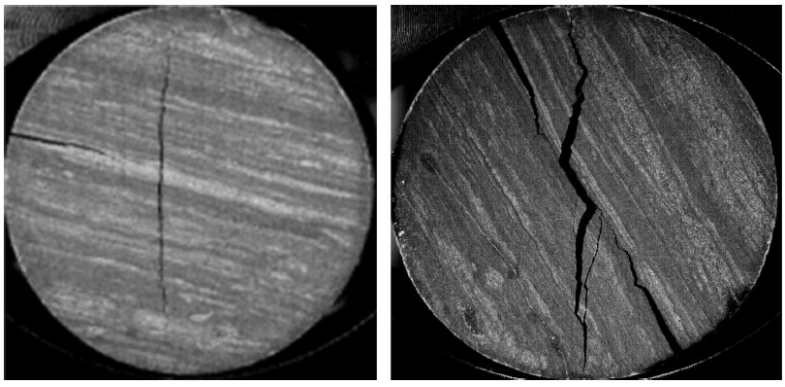

Figure 2-25. Failure pattern in shale samples within Brazilian test in 15o (left) and 60o (right) inclination (Holt et al. 2015).

Also, the results of ultrasonic tests by Gao et al. (2015) showed that both compression and shear wave velocities in shale samples followed strong anisotropic patterns and the minimum compression wave speed was in the direction perpendicular to the bedding plane.

Nygard et al. (2007) performed triaxial tests on the shale at different effective confining stress to account for brittle to ductile transition. They stated that both tensile fractures (when the pore pressure exceeds the sum of the minimum total stress and tensile strength) and shear fractures (when the shear stress exceeds the shear strength) can take place. The deformation can be brittle or ductile based on the effective confining stress. Brittle deformation is associated with dilatancy and sudden failure while ductile deformation is characterized by contractive response and gradual deformation to failure. In other words, in brittle deformation a distinct shear failure surfaces can be observed while ductile responses are usually with less distinct shear failure surface and no visible shear fractures could be observed in the ductile samples. It is recognized that brittle deformations in shales lead to permeability increase (due to the higher possibility of creation of complex fracture network) while shear failures in a ductile behavior would result in a contractive behavior which would decrease the permeability (due to lower possibility of secondary fracture generation near the main fracture face).

Das and Achalpurkar (2013) investigated the formation softening resulting from fracturing fluid and shale interaction and how changes in rock mechanical properties would affect brittleness and fracability of shales. In case of a high Young's modulus and low Poisson's ratio brittle fractures dominate, and in case of a low Young's modulus and high Poisson's ratio ductile fractures would take place which is in a good agreement with Rickman et al. (2008) studies (Figure 2-26). They believe that fracability of a shale formation is a function of brittleness and ductility in terms of Young's modulus and Poisson's ratio (Figure 2-27). In addition, Young's modulus measured parallel to the bedding plane is typically higher than in the vertical direction which agrees with Honarpour et al. (2012) studies. This means that the possibility of greater brittleness parallel to the bedding is higher. They also concluded that through transition the behavior from brittle to ductile bi-wing like fractures with less complexity would be created. In other words, higher brittleness in terms of high Young's modulus and low Pisson's ratio generally suggests the creation of a complex fracture network which agrees with Jian-chun et al (2014) studies. They considered formation softening and how the elastic properties (increasing or decreasing Young's modulus and Poisson's ratio) would be affected as a result of that as a key point to retain fracture complexity and long-term production.

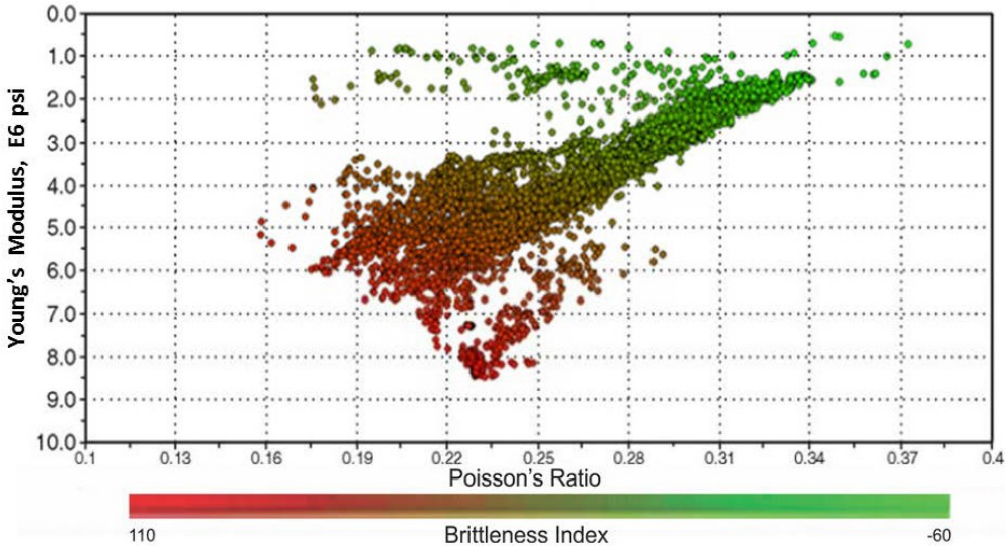

Figure 2-26. Relationship between brittleness and the values of Young's modulus and Poisson ratio: red is brittle and green is ductile (Rickman et al. 2008).

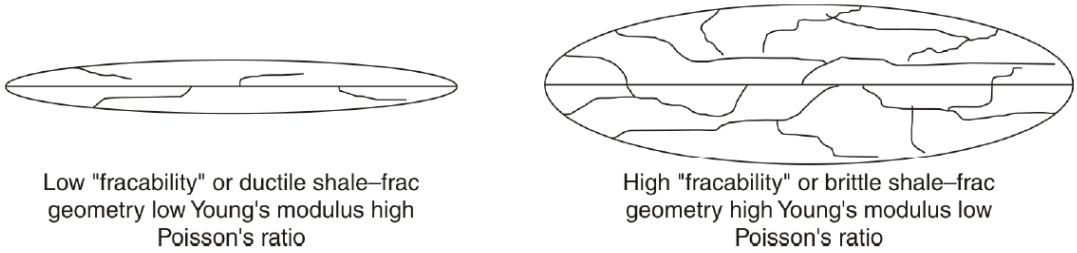

Figure 2-27. The role of fracability as a function of Young's modulus and Poisson's ratio on creating complex fracture network (Chong et al. 2010).

Jin et al. (2014) proposed and developed a new fracability index which includes not only brittleness but also energy dissipation during hydraulic fracturing. Based on the new fracability index, high brittleness and lower energy to create a new fracture surface are two optimal terms to have a complex fracture network. The lower the critical value of strain energy release rate the more fracture surface area will be created, and fractures will propagate in the direction which has the highest energy release rate.

In this regard, Holt et al. (2011) performed experiments to analyze the brittleness of North Sea shale based on changes in stress level, pore pressure and temperature. Based on the results of the experiments, at low confining stress shale samples behaves in a brittle manner and become less brittle as the stress level increases (As shown in Figure 2-28). They stated that brittleness is stress dependent and at high stresses a transition from brittle to ductile behavior can take place where the behavior of deformation also changes from dilatancy (in brittle manner) to contractive (in ductile manner).

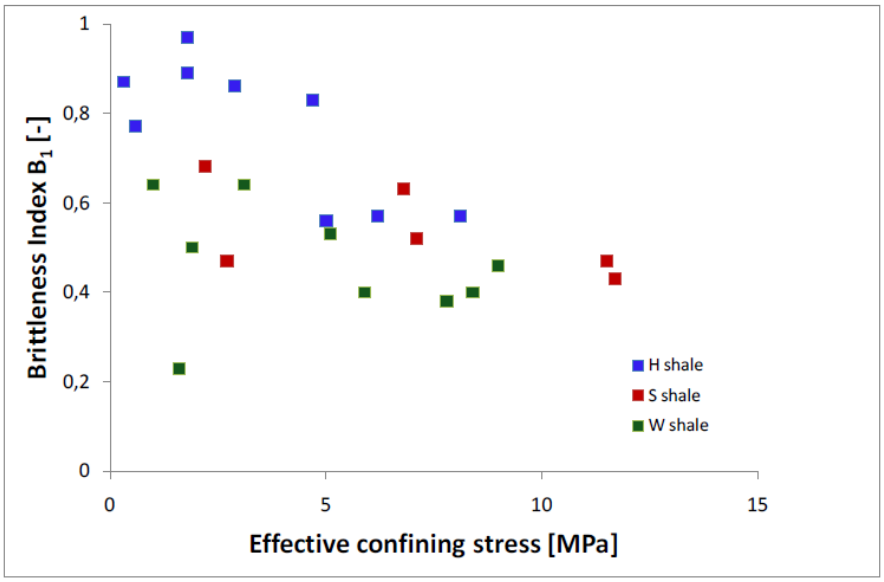

Figure 2-28. Changing the brittleness index by increasing the effective confining stress in triaxial tests performed on different North Sea shale samples (Holt et al. (2011).

Josh et al. (2012) stated that creation of complex fractures is linked to brittleness. Based on the results of their studies it is clearly observed that as water content rises, the elasticity significantly decreases which in turn leads to transitional brittle–ductile behavior.

From another point of view some researchers (Amann et al. 2014; Engelder et al. 2014; Wild et al. 2014; Yang et al. 2015) believe that imbibition into shale gas is related to the high capillary suction. They suggest that the strength primarily depends on the capillary suction associated with the pore size distribution where changing the capillary suction can facilitate the generation of micro fractures through locally affecting rock mechanical properties.

2.1.3. The Role of Capillary Suction on Rock Mechanical and Strength Properties

The total suction, of a partially saturated rock is made up of two components: the matric suction, and the osmotic suction. The matric suction is related to the difference between the non-wetting and wetting pressure and the osmotic suction comes from to the salt content in the pore fluid (Abedi-Koupai and Mehdizadeh, 2008). Changes in the total suction of the partially saturated rock may be caused by a change in either one or both components. Changes in the matric suction component are generally more significant than the changes in osmotic suction (Fredlund and Rahardjo, 1993). In addition, for partially saturated problems the changes in the matric suction can be substituted for the changes in total suction and vice versa (Fredlund and Rahardjo, 1993). Generally, when the pore space is filled with at least two immiscible fluids (for example water and gas), capillary suction can be considered based on the difference in the pressure for the wetting and non-wetting fluids as shown in Equation (1-1). In other words, the capillary suction is due to the surface tension which develops at the interface between the wetting (water) and the non-wetting (gas) fluids (Equation (1-2)) (Fjær et al. 2008):

$$P_{cp} = P_{nw} - P_{we} \tag{2-1}$$

$$P_{cp} = \frac{2\gamma\, cos\theta}{r} \tag{2-2}$$

where P_{cp} is capillary suction and P_{nw} and P_{we} are pressure for non-wetting and wetting phases, γ is the interfacial tension between the wetting and non-wetting phase, θ is the contact angle between the wetting phase and the solid, and r is the radius of pore. Therefore, parameters such as saturation (as shown in Figure 2-29), wettability, fluid type, interfacial tension and pore size distribution especially at the point where the two fluid phases meet would affect the capillary suction significantly (Fjær et al. 2008).

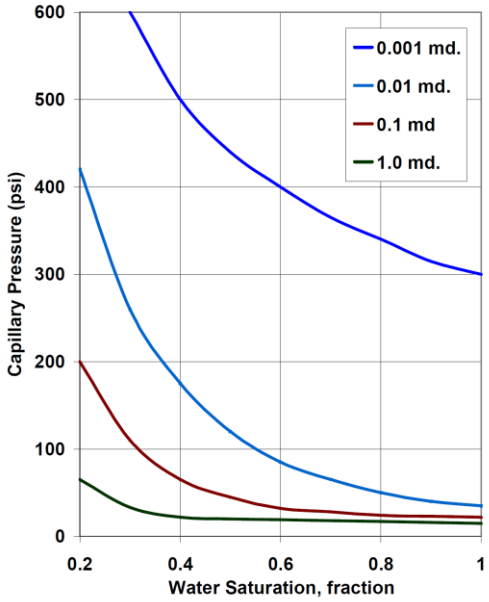

Figure 2-29. Relationship between capillarity and water saturation (Holditch, 1979).

Bishop (1959) developed an equation which demonstrates that the capillary suction has some effect on the effective stresses (Equation (1-3)).

$$\sigma' = \sigma - \alpha\,(P_{nw} - S_{we}P_{cp}) \qquad (2\text{-}3)$$

where σ' and σ are the effective and total stress respectively, S_{we} is the degree of saturation for wetting fluid and α is the effective stress coefficient. Based on Equation (2-3) at lower values of S_{we} the term $S_{we}P_{cp}$ typically increases while for $Swe = 0$ and $Swe = 1$ it disappears (Fjær et al. 2008). In addition, capillary suction which is a function of saturation would influence the rock properties such as cohesion (Papamichoes et al. 1997), strength and the stiffness.

Schmitt et al (1994) have investigated the role of saturation on capillary suction and strength of the rock both analytically and experimentally. Based on the results of their experiments on shale samples, as the saturation is increasing the capillary suction as well as the UCS of the shale is decreasing (Figure 2-30). Also, during water imbibition because of high internal overpressure generated inside the non–wetting fluid, tensile failure and expanding fracture faces are observed (Rozhko 2011a) as shown in Figure 2-31.

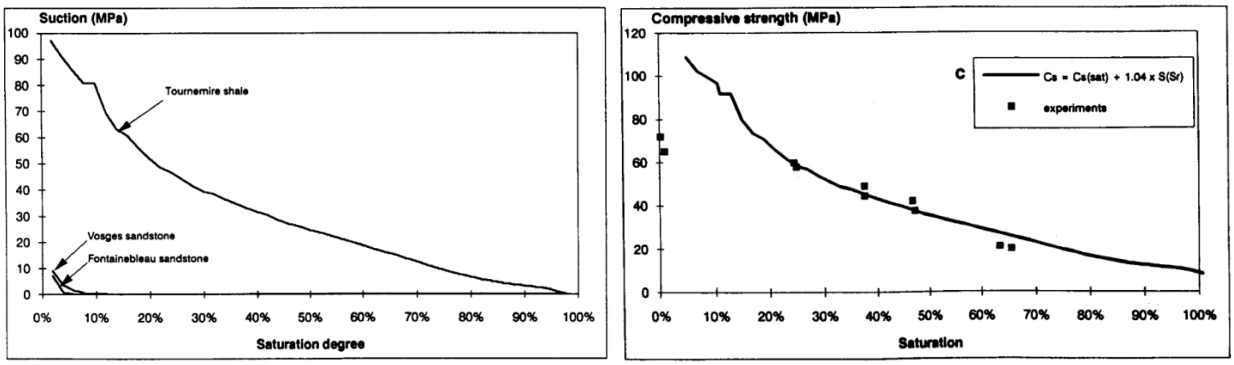

Figure 2-30. Effect of saturation on capillary suction (left) and UCS (right) of shale sample (Schmitt et al. 1994).

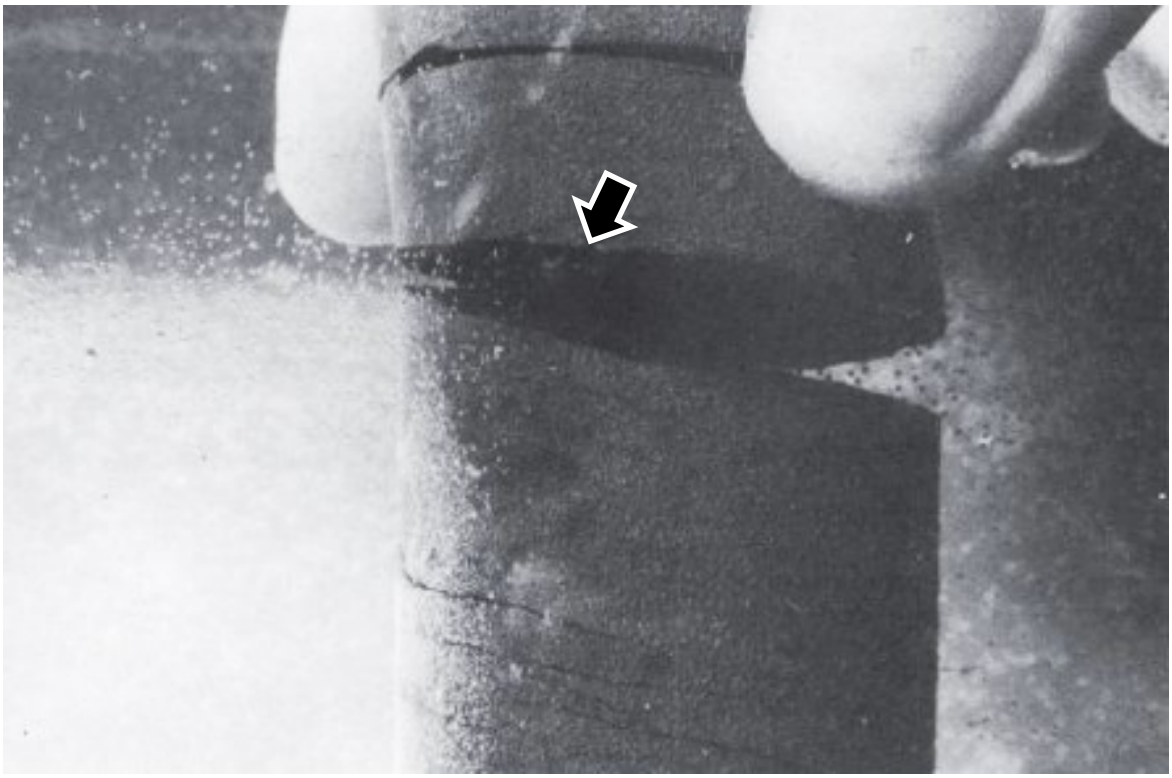

Figure 2-31. Tensile failure due to non-wetting phase (gas phase) entrapment: entrapped gas bubbles (indicated by by black arrow) are observed when manually lifting the shale fragments (Schmitt et al. 1994).

Roskho (2011b) investigated the capillary forces (suction) effect on the strength and deformation of a partially-saturated rock with two immiscible fluids using a fracture mechanics approach. He concluded that the effective stress coefficient is dependent on saturation degree, compressive stress, surface tension (between immiscible fluids), wetting angle, elastic parameters and fracture

toughness of the rock. He stated that capillary suction will lead to the overpressure condition at the reservoir which is equal to capillary pressure multiplied by saturation degree.

Amann et al. (2014) conducted experiments to investigate the role of capillary suction on mechanical properties of shale samples. Based on their observations, tensile strength, unconfined compressive strength and Young's modulus increase with increasing capillary suction (Figure 2-32). They suggested a non-linear relationship between saturation and capillary suction in their shale samples (Figure 2-33).

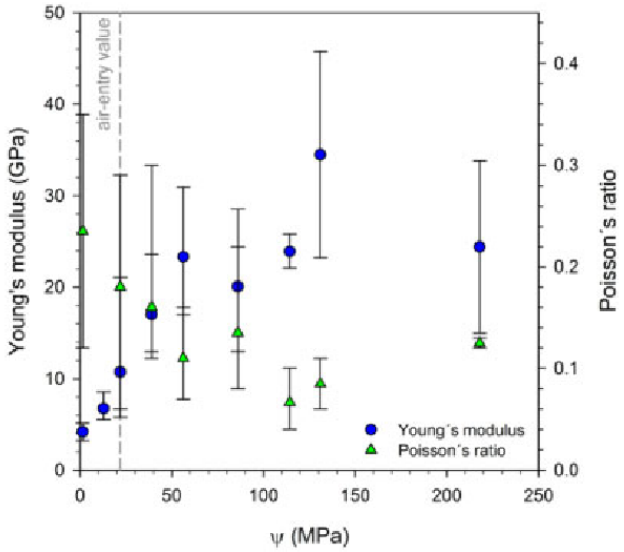

Figure 2-32. Young's modulus increases and Poisson's ratio decreases with increasing capillary suction (Amann et al. 2014).

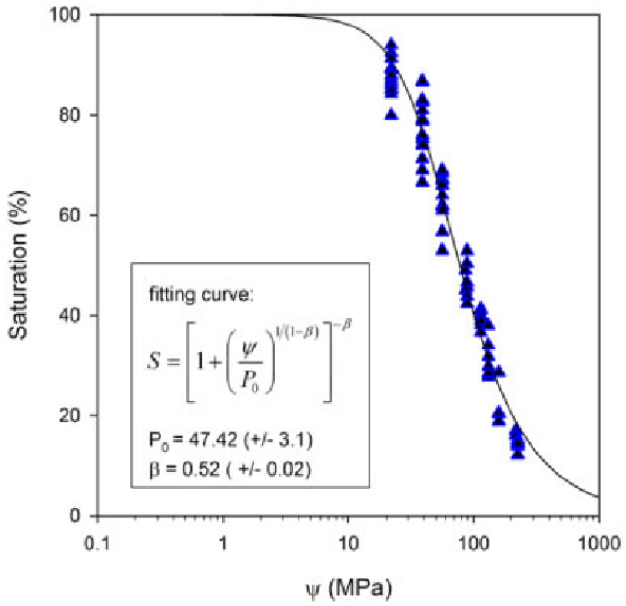

Figure 2-33. Nonlinear relationship between saturation and capillary suction in shale samples (Amann et al. 2014).

Vale`s et al. (2004) believe that higher capillary suction would change the mechanical behavior to more brittle. Also, Schmitt et al. (1994) and Fredlund et al. (1995) findings imply that increasing the capillary suction would result in increasing the frictional resistance.

Although the results of the existing theoretical, numerical and experimental studies in the literature shed light on some mechanisms observed during the interaction of shale and tight unconventional reservoirs with fracturing fluid but an integrated theoretical, numerical and experimental workflow to explain the fundamentals behind the responses observed is still lacking. That is why some researchers (Gupta 2009; Fan et al. 2010; Shaoul et al., 2011; Wang et al. 2012; Guo and Gao, 2013; Yan et al. 2015), believe that water imbibition leads to production reduction while some others (Anderson et al. 2010, Caenn et al. 2011, Dehghanpour et al., 2012; Dehghanpour et al., 2013; Ji and Geehan, 2013; He et al., 2014; Wang et al., 2018; Zhou et al., 2020) suggest that it can result in production increase.

This research aims to propose and develop a systematic theoretical, numerical and experimental workflow to fundamentally explain the geomechanical mechanisms and behaviors induced by fracturing fluid imbibition during shut-in time period.

Chapter 3 : Qualitative Analysis of Geomechanical Behaviors Triggered by Spontaneous Imbibition

As identified through the literature review presented in Chapter 2, the studies suggest that imbibition of fracturing fluids into partially saturated tight gas formations is an important mechanism which can affect not only the production but also the overall properties of the invaded zone. A deeper understanding of how the imbibed fracturing fluid would affect the rock properties and strength parameters and how fracturing fluid imbibition can be related to the behaviors observed is still lacking. The former can be attributed to extremely complex intrinsic rock mechanical properties of tight partially saturated bedded rocks which can be affected by many factors including anisotropy, water content and beds orientation. This would highlight the importance of investigating the weakening/softening mechanisms through which the rock properties can be affected which can in turn trigger some behaviors/mechanisms and eventually influence the production. Therefore, to understand the impacts, imbibition tests have been performed on Montney samples (Farrell Creek field in northeast British Columbia) to determine the changes in rock mechanical properties as water imbibition is occurring. This includes capturing the responses observed through spontaneous imbibition of fracturing fluid into Montney samples (such as micro fractures generation and gas phase releasing), changes in rock mechanical properties and capillary suction as well as how these changes would affect the stress state analysis and fracability. In addition, transversely isotropic and beds-included fully coupled poro-elastoplastic partially saturated models have been developed and compared.

3.1. Laboratory Experiments

3.1.1. Sample Description and Preparation

Our case study was the Lower Triassic Montney which is a siltstone reservoir in the Western Canada Sedimentary Basin. As illustrated in Figure 3-1, the Montney Formation is subdivided into Upper and Lower members. According to Figure 3-1, in the Farrell area, Lower and Upper Montney are mainly distinguished by argillaceous siltstone and carbonaceous siltstone, respectively (McLellan et al., 2014). To study the effect of water imbibition on rock properties, samples were drilled from Montney cores obtained from the well located in Farrell Creek field, northeast British Columbia (Figure 3-1). The samples are from different depths (2282m, 2290m,

2356m, 2415m and 2487m) and thin bedded structures are well developed in Montney cores (as shown in Figure 3-2). Although sedimentary layer with a thickness of less than 1 cm is categorized as laminae (McKee and Weir, 1953) but because generally beds are defined as the sedimentary layers that are different from the overlying and underlying layers (Campbell, 1967), for the purpose of this study "bed" and "bedding plane" are used.

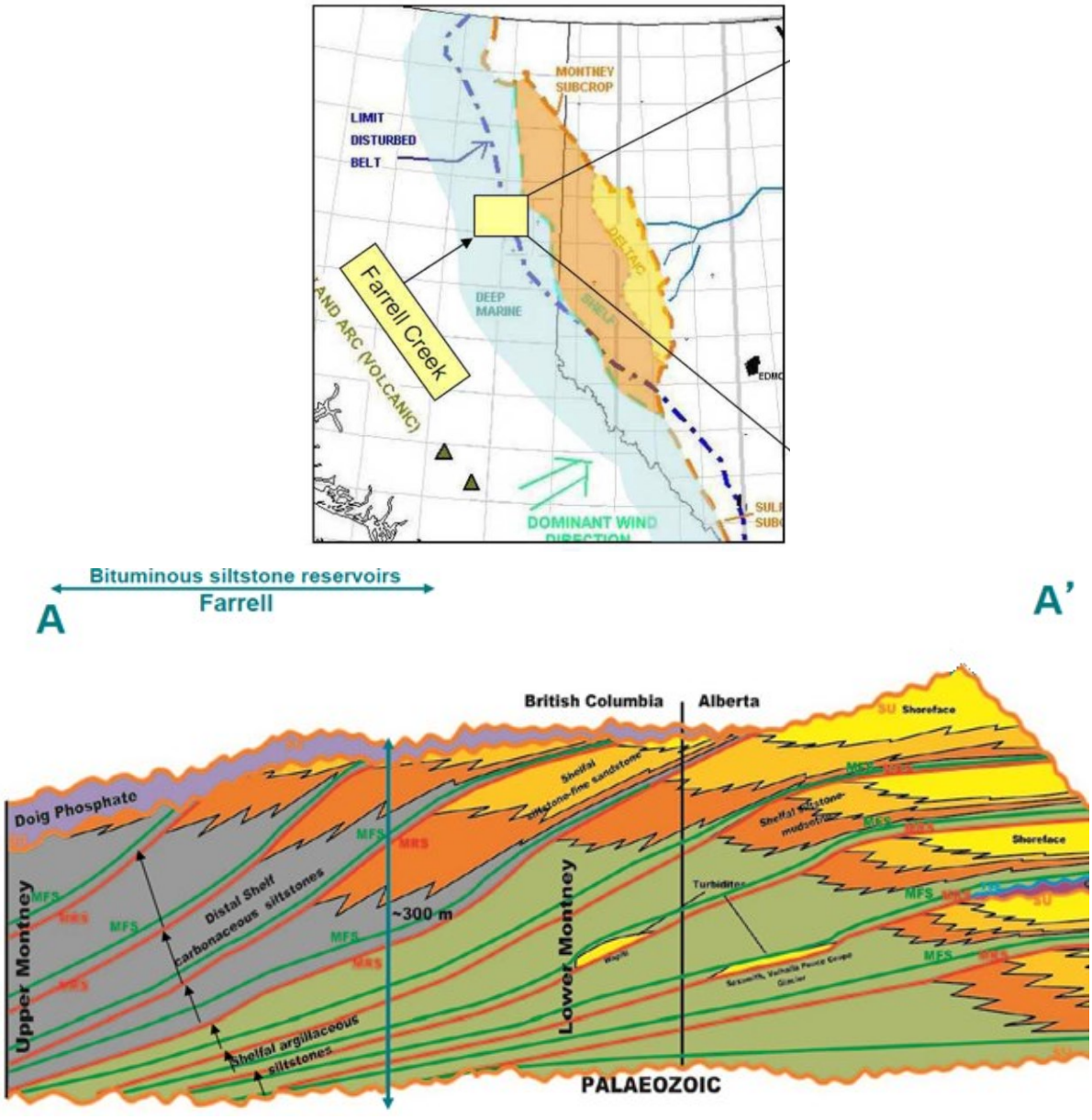

Figure 3-1.Top image: Farrell Creek field in northeast British Columbia (McLellan, 2012); Bottom image: Depositional environment of the Farrell Creek Montney Formation (McLellan et al., 2014)

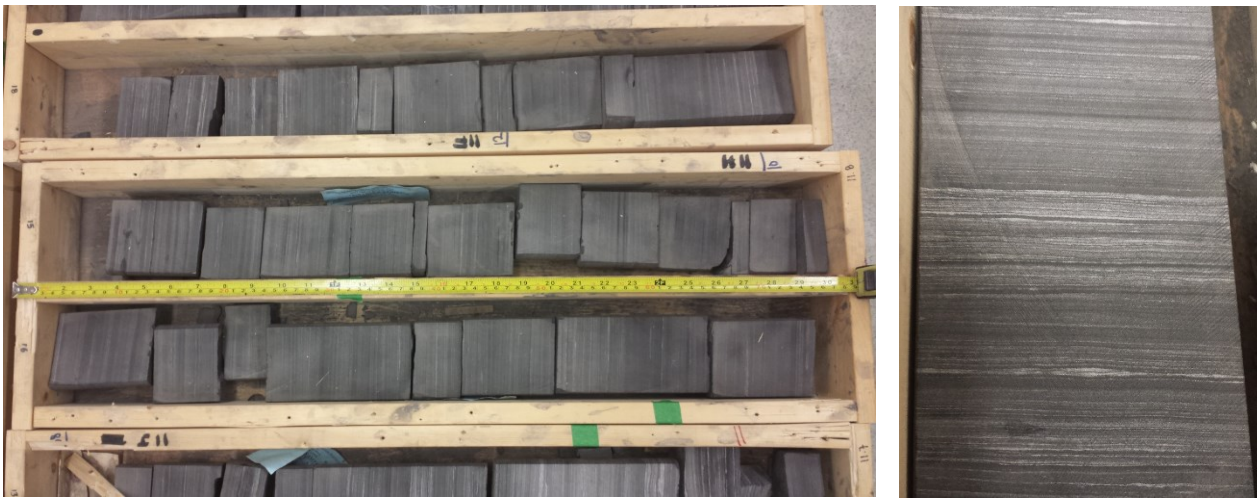

Figure 3-2. Bedded-structure of Montney samples.

The mineralogical compositions for the samples were obtained from QEMSCAN analysis conducted by SGS Canada (Vaisblat, 2020) which can be found in Table 3-1 and Figure 3-3. The samples mainly consist of varying amounts of quartz, clay and carbonates. All of the samples have significant amount of quartz while sample "5" has the highest amount of quartz with 37.18% and sample "2" has the lowest with 35.41%. Also, sample "1", "2" and "4" have more carbonates (calcite and dolomite) than sample "3" and "5". The minimum clay content is for sample "1" with 11.58% and the maximum is for sample "5" with 20.73%.

Table 3-1. Mineralogy (wt%) of Montney samples.

Sample No.	Depth (m)	Quartz	Total Carbonate	Total Clay	K Feldspar	Plagioclase	Muscovite	Pyrite	Biotite
1	2282	36.43	25.30	11.58	10.50	8.54	3.60	2.59	0.09
2	2290	35.41	24.19	13.88	10.23	8.70	3.97	2.38	0.10
3	2356	35.62	18.08	16.92	8.42	9.61	7.01	2.55	0.11
4	2415	36.17	24.17	19.05	3.49	6.83	5.52	2.71	1.10
5	2487	37.18	18.80	20.73	3.67	8.90	4.51	4.55	0.72

Regarding the type of clay, Table 3-2 and Figure 3-4, represents the clay types and as it can be clearly observed the majority of clay content is related to illite and illite-smectite type. Illite is a non-swelling clay and illite-smectite is a poor swellable clay (Chen et al., 2020) which means that hydration does not cause swelling (Aksu et al., 2015; Ahmad et al., 2018).

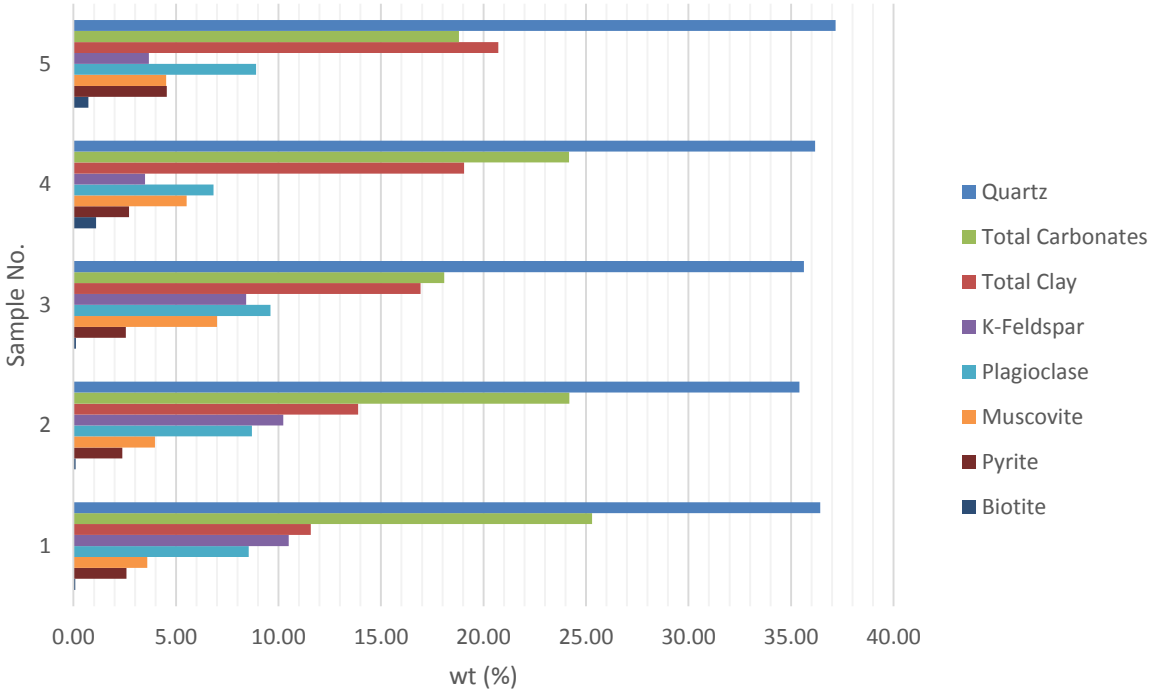

Figure 3-3. Mineral composition in Montney samples.

Table 3-2. Clay types in Montney samples.

Sample No.	Illite & Illite-Smectite (%)	Fe-Illite & Illite-Smectite (%)	Kaolinite (%)	Chlorite (%)
1	10.67	0.36	0.42	0.13
2	12.85	0.41	0.48	0.14
3	15.53	0.55	0.63	0.21
4	15.09	1.15	1.37	1.44
5	15.78	2.23	1.07	1.64

For capillary condensation tests, two small specimens were cut from the core at each depth and dried in the oven following ASTM D2216-19 standards. For spontaneous imbibition tests, one set of samples were cut perpendicular to the beds (shown with "PD" suffix), and the other set cut parallel to the beds (shown with "PR" suffix) as shown in Figure 3-5. Both parallel and perpendicular samples have a diameter of 2.54cm and a height of 1cm. Then, the bulk density of the dry samples was determined by measuring the weight by a digital scale with 0.1mg accuracy. The results showed a difference in density values for parallel and perpendicular samples of the same depth (Table 3-3).

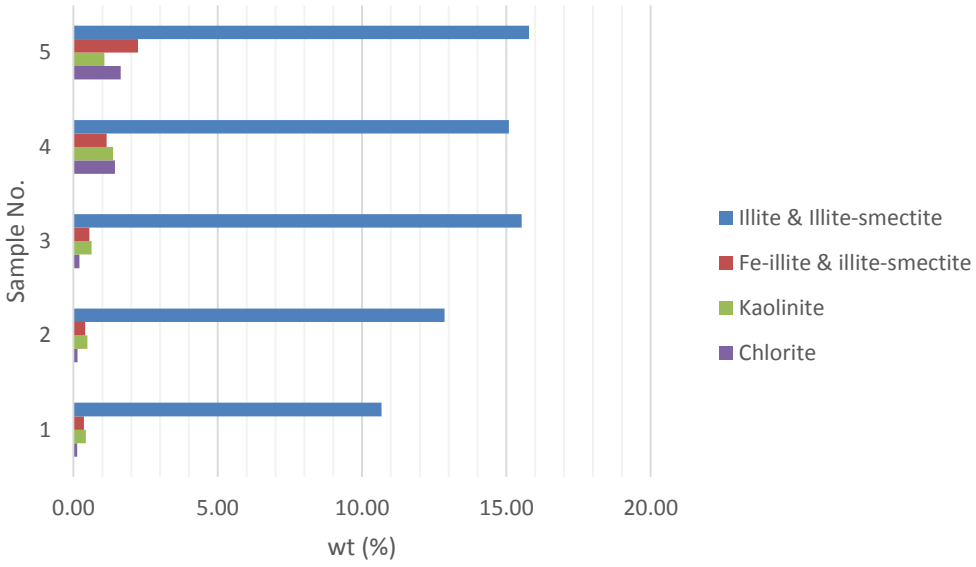

Figure 3-4. Clay content in Montney samples.

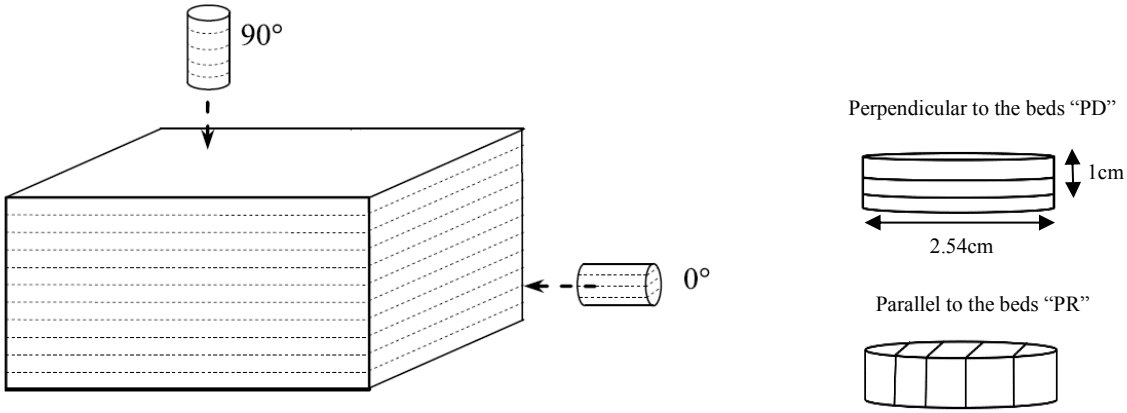

Figure 3-5. Coring orientations: a) Perpendicular to the beds (90°); b) parallel to the beds (0°).

Table 3-3. Density of Montney samples used in the spontaneous imbibition experiments.

Sample No.	Initial Weight (gr)	Density (gr/cc)
1-PD	12.5599	2.480
1-PR	13.1170	2.590
2-PD	12.6613	2.500
2-PR	12.7625	2.520
3-PD	12.8638	2.540
3-PR	13.2184	2.610
4-PD	13.5728	2.680
4-PR	13.7248	2.710
5-PD	12.9651	2.560
5-PR	13.3703	2.640

3.1.2. Experimental Procedures

3.1.2.1. Capillary Condensation Experiments

Capillary condensation is a mechanism of vapor phase condensation in small pores. For a given relative humidity, capillary condensation first starts in smaller pores and as relative humidity increases the water vapor condenses in the larger pores (Barsotti et al., 2016). Capillary suction would be calculated based on Equation (3-1) (Fredlund and Rahardjo 1993).

$$P_c = -\frac{M_w RT}{\rho_w}\ln(RH) \quad (3\text{-}1)$$

where P_c is the capillary suction, M_w is water molecular weight, R is the gas constant, T is the temperature, ρ_w is the water density and RH is relative humidity. Saturated salt solutions were used to maintain particular values of relative humidity inside sealed desiccator as shown in Figure 3-6. After reaching to equilibrium in each relative humidity, the weight of the samples was measured and the changes in water content were determined. Then, the relationship between the changes in the water content and the capillary suction was investigated. Capillary condensation tests were performed on 46 Montney samples from 2233m to 2518m to determine if the magnitude of capillary suction as a function of water content change varied for the Montney specimens. Two samples for each depth were considered and then an average of them was reported.

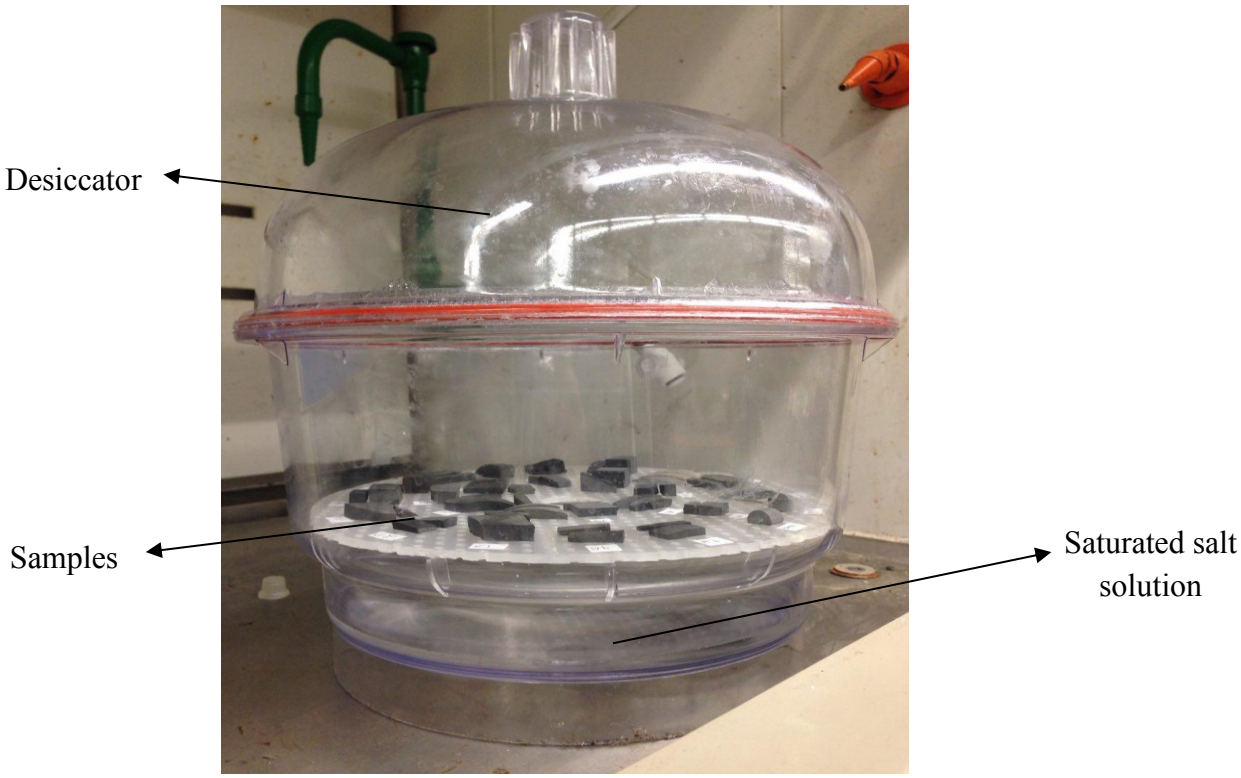

Figure 3-6. Capillary condensation experiment on Montney samples.

3.1.2.2. Spontaneous Imbibition Test and Rock Mechanical Measurements

To assess how Montney samples would behave in the presence of water, ultrasonic measurements were done in different water contents (as the water imbibition is taking place) and different

directions (parallel and perpendicular to the beds). Ultrasonic measurements followed ASTM D2845-08 standard. JSR DPR300 pulser-receiver system and Agilent DSO6014A oscilloscope with frequency bandwidth of 100 MHz were used. Ultrasonic measurements would be an effective and nondestructive approach to investigate the dynamic rock mechanical properties which relies on the propagation of compression and shear waves and then measuring the velocity (or time of travel) of these waves as they are traveling through the sample. So, the samples were submerged in 5000 ppm NaCl solution (as shown in Figure 3-7) for 24 hours and the normalized water content as well as compression and shear wave velocities parallel and perpendicular to the beds as a function of time were measured.

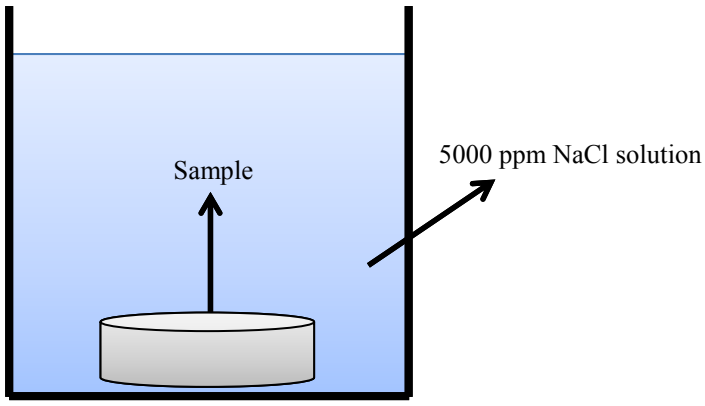

Figure 3-7. Spontaneous imbibition tests on Montney samples.

The experimental setup to measure the compression and shear wave velocities was comprised of compression and shear wave pulsers on one side and receivers on the other side as well as a digital oscilloscope (to digitize and store the signals as a wave form during the measurement procedure) (Figure 3-8). The sample is placed in the center (between the pulsers and receivers) and as the pulsers are generating compressive and shear waves, the receivers capture them after traveling through the sample. The signals are subsequently processed by receiver unit of the JSR DPR300 which makes them available for display in oscilloscope. Based on the values of compressive and shear wave velocities (or time of travel), dynamic elastic properties (Young's modulus, Poisson's

ratio and Shear modulus) could be measured in each time step by Equation (3-2), (3-3) and (3-4) (Fjær, 2008; Kate, 2012).

$$\boldsymbol{E}_{dyn} = \frac{\rho V_s^2(3V_p^2-4V_s^2)}{(V_p^2-V_s^2)} = \frac{\rho V_p^2(1+\boldsymbol{\nu_{dyn}})(1-2\boldsymbol{\nu_{dyn}})}{(1-\boldsymbol{\nu_{dyn}})} \quad (3\text{-}2)$$

$$\boldsymbol{\nu_{dyn}} = \frac{V_p^2-2V_s^2}{2(V_p^2-V_s^2)} = \frac{\frac{1}{2}-\frac{V_s^2}{V_p^2}}{1-\frac{V_s^2}{V_p^2}} \quad (3\text{-}3)$$

$$\boldsymbol{G_{dyn}} = \rho V_s^2 \quad (3\text{-}4)$$

where E_{dyn}, ν_{dyn} and G_{dyn} are dynamic Young's modulus, Poisson's ratio and Shear modulus, respectively. V_p is ultrasonic compressional velocity, and V_s is ultrasonic shear velocity and ρ is the density of the sample.

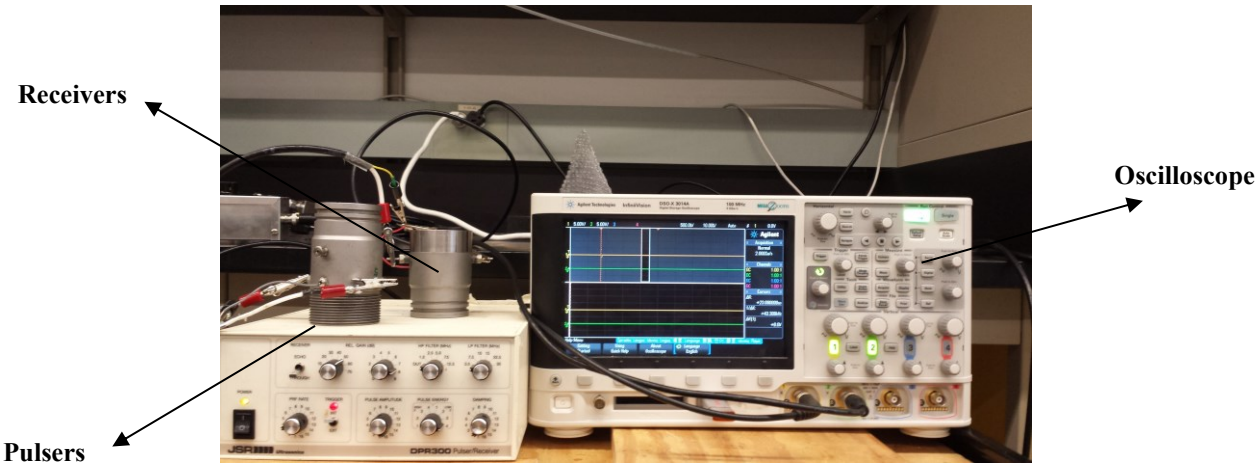

Figure 3-8. Ultrasonic setup for measuring compressive and shear wave velocities.

Also, the values of internal friction angle and brittleness were estimated using Equation (3-5) (Lal, 1999) and (3-6) (Grieser & Bray, 2007; Jin et al., 2014), respectively:

$$\varphi = sin^{-1}\left((V_p - 1000)/(V_p + 1000)\right) \quad (3\text{-}5)$$

$$BI = \frac{E_n+\nu_n}{2} * 100 \quad (3\text{-}6)$$

$$E_n = \frac{E-E_{min}}{E_{max}-E_{min}} \quad (3\text{-}7)$$

$$\nu_n = \frac{\nu_{max}-\nu}{\nu_{max}-\nu_{min}} \quad (3\text{-}8)$$

where *BI* is the brittleness index, E_n and ν_n are the normalized Young's modulus and Poisson's ratio, respectively, E_{min} and E_{max} are the minimum and maximum Young's modulus of the interval or formation, ν_{min}, and ν_{max} are the minimum and maximum Poisson's ratios, respectively. The main reason to choose Equation (3-6) for BI determination was related to the definition of a brittle material. Basically, brittle material is the material that breaks when subjected to stress but without a significant deformation before failure (Andreev, 1995). This means that the lower the strain at failure, the higher the brittleness. Also, the lower axial strain means the higher Young's modulus. In other words, the higher the Young's modulus means the higher brittleness. Generally, lateral strain is lower than axial strain and higher Poisson's ratio implies that the rock would have more lateral strain. Accordingly, lower Poisson's ratio means higher brittleness. Therefore, Equation (3-6) that includes both Young's modulus and Poisson's ratio would be a better representation of BI since it is directly related to the strain-stress relationship. According to Ye et al. (2020) the brittleness evaluation method based on stress-strain is the most reliable approach. Dynamic values of Young's modulus and Poisson's ratio of "PD" and "PR" samples were converted to static values by Equation (3-9) to (3-12) derived by Song and Hareland (2012) for Montney Formation wells in North East British Columbia.

$$E_{static-PD} = 0.8466\, E_{dynamic-PD} \quad (3\text{-}9)$$

$$E_{static-PR} = 0.6393\, E_{dynamic-PR} \quad (3\text{-}10)$$

$$\nu_{static-PD} = 1.2604\, \nu_{dynamic-PD} \quad (3\text{-}11)$$

$$\nu_{static-PR} = 1.1552\, \nu_{dynamic-PR} \quad (3\text{-}12)$$

3.1.3. Experimental Results and Discussions

3.1.3.1. Capillary Condensation Experiments

As explained in Chapter 2, since capillary invasion has been introduced as the dominating mechanism for water uptake during spontaneous imbibition of fracturing fluid into the formation, capillary condensation tests on 23 samples from different depths were performed. The following salts were used for the preparation of the saturated salt solutions: $MgCl_2$ (P_c = 152MPa), $Mg(NO_3)_2$ (P_c = 95MPa), NaCl (P_c = 39MPa) and K_2SO_4 (P_c = 7MPa) where the samples were exposed to 33%, 50%, 75% and 95% humidity (Greenspan, 1977) until they reached to equilibrium. Then, the

weight of the samples was measured and based on the initial weight of the samples (in dry condition) the normalized water content change versus capillary suction was determined (Figure 3-9). It is clearly observed that the values of capillary suction as a function of water content change differ in different samples where for example the normalized water content change to reach to 39MPa capillary suction for sample from depth 2253m is almost as twice as the sample related to depth 2290m. Table 3-4 represents a summary of the results of capillary condensation experiments for Montney samples.

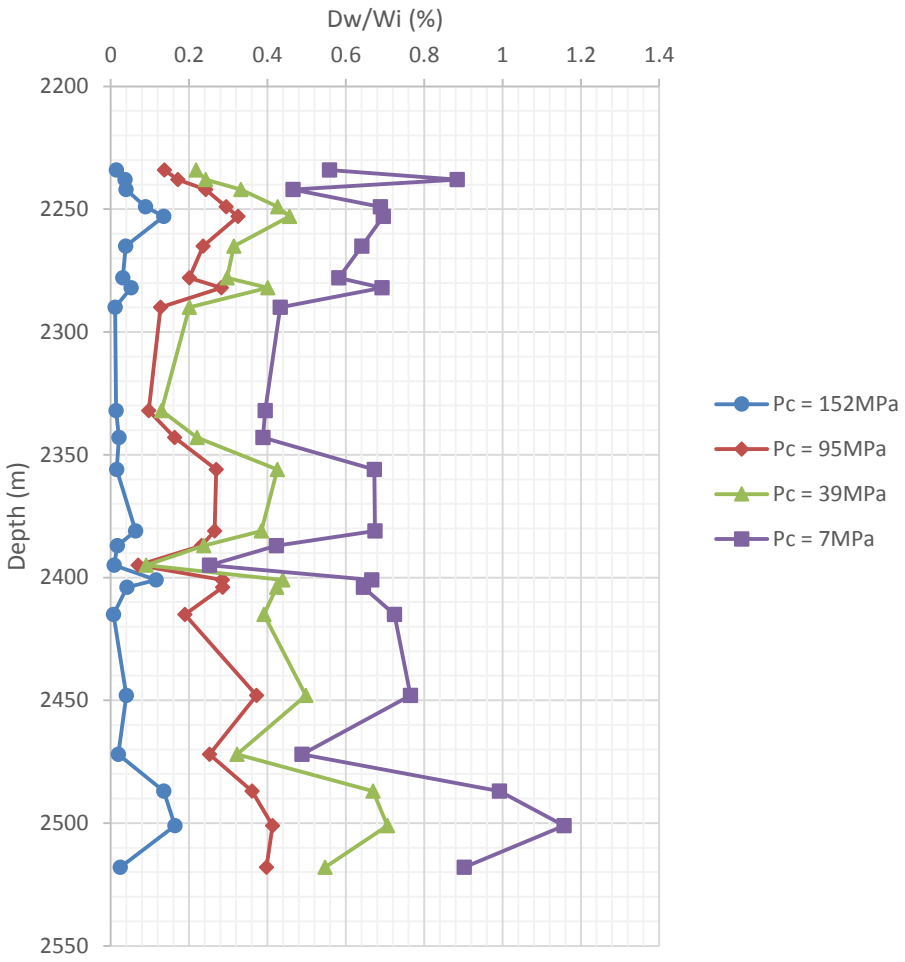

Figure 3-9. Changes in capillary suction in Montney samples as the water content is increasing through controlled humidity condition. (Dw is the difference between the initial (Wi) and the current weight of the sample).

Table 3-4. Summary of capillary condensation experiments on Montney samples (two samples for each depth: PD and PR means perpendicular and parallel sample, respectively).

Depth (m)	Initial Weight (gr)	(*Dw/Wi)*100 (RH = 33%) (Pc = 152 MPa)	(Dw/Wi)*100 (RH = 50%) (Pc = 95 MPa)	(Dw/Wi)*100 (RH = 75%) (Pc = 39 MPa)	(Dw/Wi)*100 (RH = 95%) (Pc = 7 MPa)
2234	5.4135[PD]	0.016	0.133	0.408	0.572
	8.7955[PD]	0.013	0.141	0.442	0.545
2238	4.314[PD]	0.034	0.243	0.256	0.867
	7.4575[PD]	0.039	0.271	0.228	0.902
2242	4.3775 [PR]	0.036	0.236	0.351	0.7
	4.5837 [PD]	0.041	0.249	0.312	0.647
2249	3.9913 [PD]	0.089	0.288	0.459	0.66
	7.2764 [PD]	0.088	0.302	0.403	0.716
2253	3.5231 [PD]	0.132	0.337	0.453	0.721
	5.8062 [PD]	0.138	0.313	0.45	0.671
2265	3.9535 [PD]	0.009	0.259	0.276	0.585
	4.0243 [PR]	0.008	0.213	0.352	0.696
2278	3.5621 [PD]	0.031	0.209	0.318	0.602
	4.2519 [PD]	0.03	0.192	0.276	0.561
2282	3.8241 [PR]	0.047	0.263	0.427	0.753
	6.6687 [PD]	0.056	0.301	0.373	0.631
2290	3.4926 [PR]	0.011	0.124	0.217	0.466
	7.4952 [PD]	0.012	0.13	0.183	0.399
2332	5.699 [PR]	0.012	0.101	0.142	0.445
	10.3227[PD]	0.016	0.093	0.117	0.345
2343	3.5308 [PD]	0.021	0.161	0.187	0.307
	5.2316 [PR]	0.02	0.166	0.253	0.469
2356	3.449 [PR]	0.014	0.236	0.482	0.746
	4.7091 [PD]	0.017	0.302	0.368	0.598
2381	4.1648 [PD]	0.063	0.249	0.361	0.692
	4.2537 [PD]	0.064	0.28	0.407	0.657
2387	4.5456 [PD]	0.018	0.255	0.229	0.486
	7.5753 [PR]	0.016	0.208	0.245	0.379
2395	4.7291 [PD]	0.008	0.067	0.086	0.244
	7.1283 [PD]	0.009	0.073	0.094	0.26
2401	4.3001 [PD]	0.121	0.27	0.461	0.695
	4.5327 [PD]	0.111	0.3	0.418	0.637
2404	4.0681 [PR]	0.04	0.307	0.46	0.719
	5.0982 [PD]	0.042	0.264	0.387	0.581
2415	3.9086 [PR]	0.009	0.179	0.427	0.812
	6.9072 [PD]	0.005	0.199	0.354	0.636
2448	4.0134 [PD]	0.038	0.362	0.527	0.785
	5.7817 [PD]	0.041	0.383	0.499	0.746
2472	3.5427 [PD]	0.019	0.276	0.326	0.403
	8.4559 [PR]	0.02	0.229	0.319	0.572
2487	4.5456 [PR]	0.13	0.301	0.759	1.083

	7.5753 PD	0.141	0.421	0.58	0.901
2501	4.0581PD	0.263	0.411	0.691	1.142
	6.1454 PD	0.265	0.416	0.722	1.172
2518	4.1341 PD	0.024	0.41	0.574	0.916
	7.6954 PD	0.025	0.385	0.52	0.888

* Dw = W-Wi; "Wi" is the initial weight of the sample.

The results from capillary condensation tests on "PR" and "PD" specimens at the depth intervals 2282m - sample "1", 2290m - sample "2", 2356m - sample "3", 2415m - sample "4" and 2487m - sample "5" can be found in Figure 3-10. To better compare the capillary suction values, the curve was fitted to the capillary suction versus normalized water content data for each of "PR" and "PD" samples and the regression equations are provided. These equations are used to compute and compare the values of capillary suction at normalized water content of 0.2%, 0.4% and 0.6% (Table 3-5).

3.1.3.2. Spontaneous Imbibition Test and Rock Mechanical Measurements

Following the capillary condensation tests, spontaneous imbibition tests were performed on the same samples listed in Table 3-3. As the imbibition was taking place, normalized water content change of each sample was measured (based on the initial weight of the sample and the weight measured during spontaneous imbibition). Figure 3-11 and Figure 3-12 represent the results of normalized water content as a function of time for "PR" and "PD" samples. It is clearly observed that in the first hours of the spontaneous imbibition the rate of imbibition in both "PR" and "PD" samples is higher and over time it decreases. These results are consistent with other spontaneous imbibition experiments on Montney samples (Lan et al., 2014; Lan et al., 2015). Based on Figure 3-11 and Figure 3-12 two main regions can be considered. The first region is related to the higher slope with higher imbibition rate which can be attributed to pre-existing or induced micro fractures and the second region which has a lower rate of imbibition indicates the water imbibition into the matrix. This would suggest that capillary suction and pre-existing/induced micro fractures are working together for water uptake during spontaneous imbibition. Although a similar observation was also noted by Roychaudhuri et al. (2011) and Ghanbari et al. (2013) but an extensive SEM analysis can give a thorough understanding about the pre-existing micro fractures which is not of course in the scope of this study.

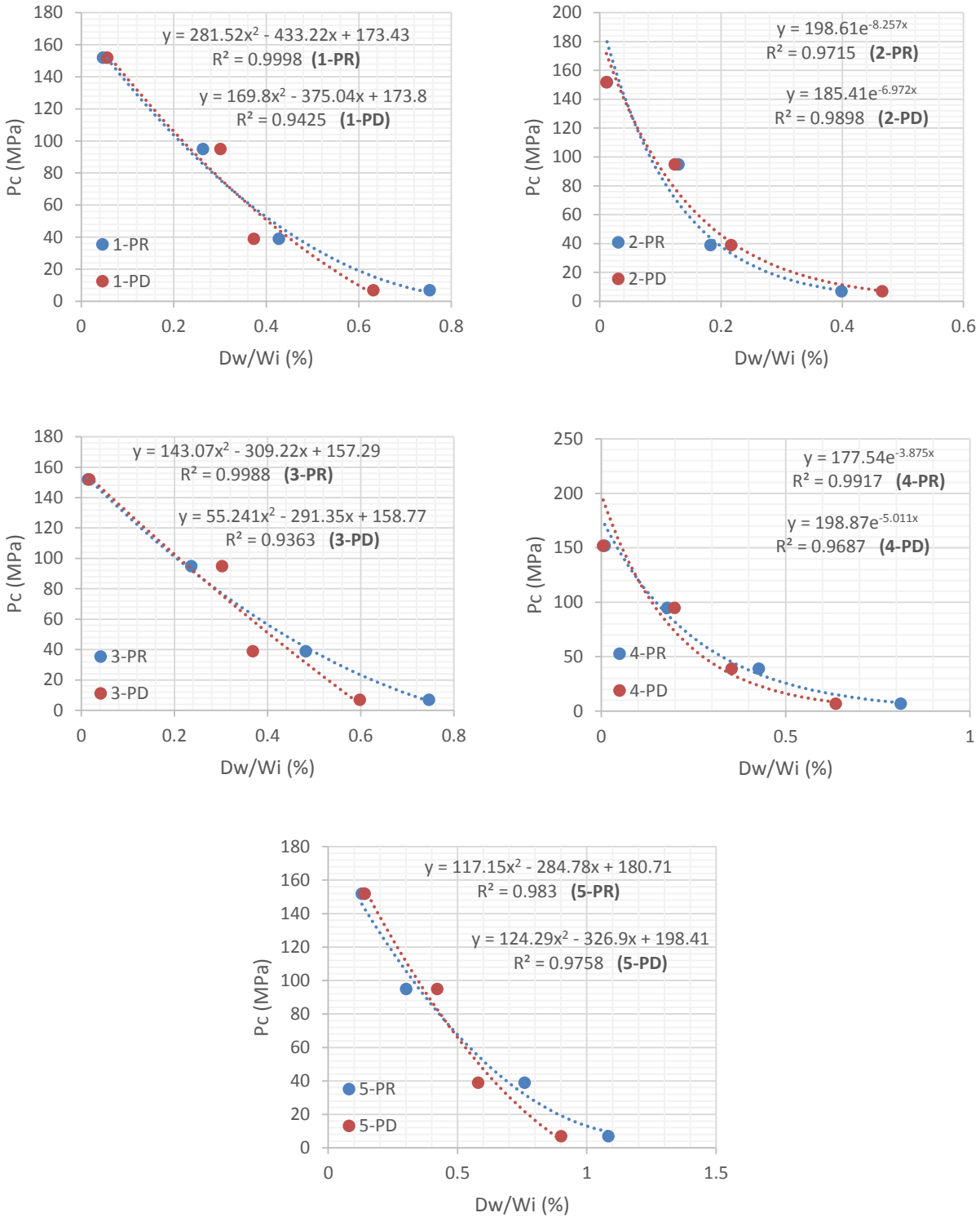

Figure 3-10. Capillary suction change as a function of normalized water content for "PR"and "PD"samples of "1", "2", "3", "4" and "5". Dotted lines are the fitted curves. Dw = W-Wi; "Wi" is the initial weight of the sample.

Table 3-5. Comparing capillary suction of "PR"and "PD"samples of "1", "2", "3", "4" and "5" specimens in the certain amounts of normalized water content.

Sample No.	P_c (MPa) Dw/Wi (%) = 0.2	P_c (MPa) Dw/Wi (%) = 0.4	P_c (MPa) Dw/Wi (%) = 0.6
1-PR	98.05	45.19	14.85
1-PD	105.58	50.95	9.90
2-PR	38.09	7.30	1.40
2-PD	45.98	11.40	2.83
3-PR	101.17	56.49	23.26
3-PD	102.71	51.07	3.85
4-PR	81.79	37.68	17.36
4-PD	73.00	26.80	9.84
5-PR	128.44	85.54	52.02
5-PD	138.00	87.54	47.01

Additionally, according to Figure 3-13 which represents the ratio of Dw/Wi for "PR" and "PD" samples of the same depth, "PR" samples show higher imbibition rates and higher imbibed volume than "PD" samples. Although based on Table 3-5, sample "5-PD" and "5-PR" show the highest capillary suction but the highest imbibition rate among all of the tested samples is related to sample "4-PR" with the highest number of beds (Figure 3-14). The lowest imbibition rate is related to sample "2-PD" with the lowest number of beds and capillary suction. It is clearly observed that as the number of the beds are increasing the rate of imbibition would increase. This is more obvious in the first hour of the imbibition test where Dw/Wi for sample "4-PR" and "3-PR" with 35 and 20 beds are the highest (blue dotted line in Figure 3-15). This can suggest that pre-existing/induced micro fractures or failures are higher in these samples and the failure mechanism to generate the induced fractures is related to the beds. As the time is progressing the rate of imbibition for these samples with higher number of beds are decreasing which can be an indication of water imbibition from the pre-existing/induced micro fractures into the matrix.

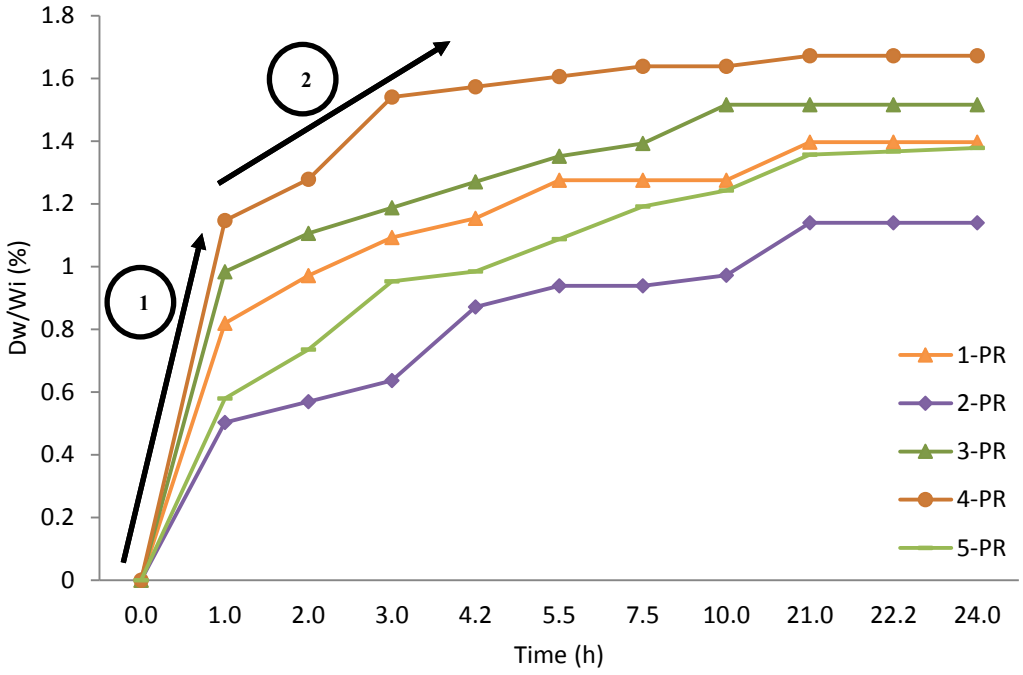

Figure 3-11. Changes in normalized water content change as a function of time for "PR" samples. Region 1 and 2 show higher and lower imbibition rates, respectively.

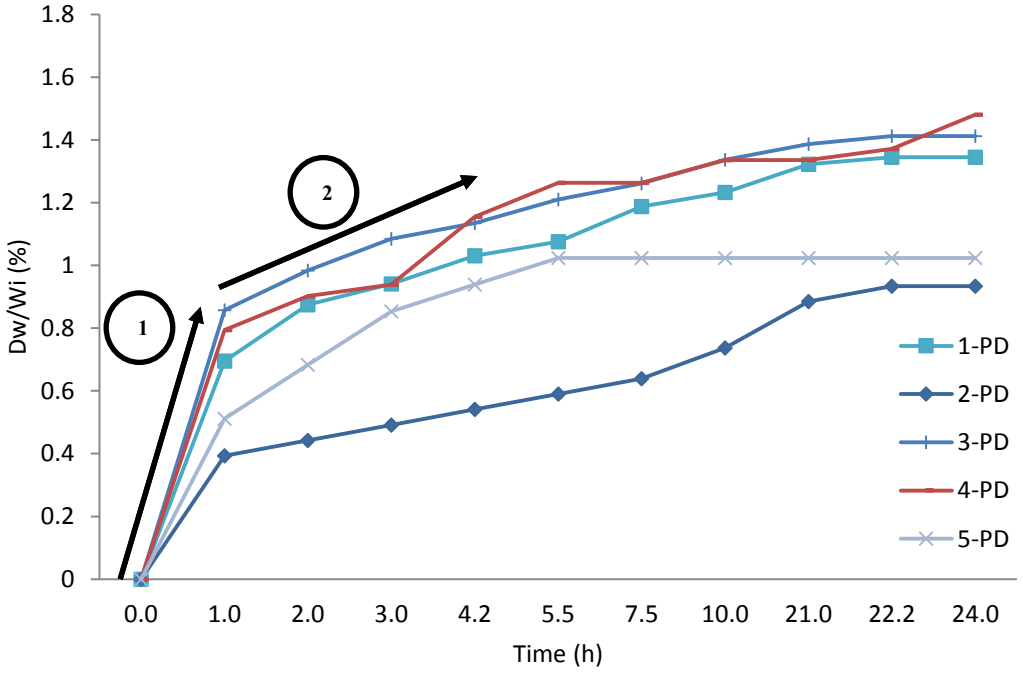

Figure 3-12. Changes in normalized water content change as a function of time for "PD" samples. Region 1 and 2 show higher and lower imbibition rates, respectively.

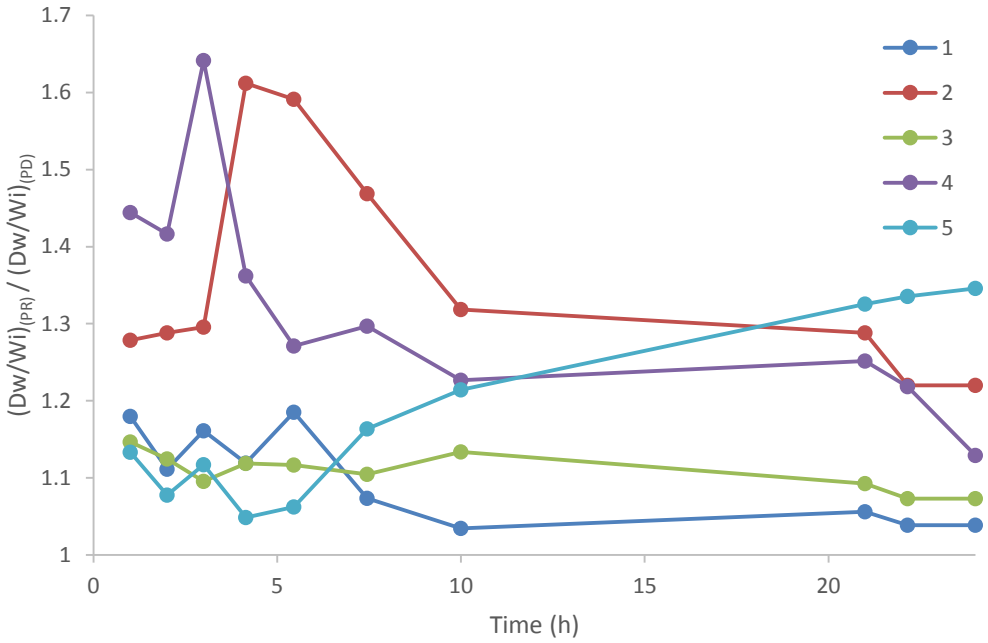

Figure 3-13. Comparing normalized water content change of "PR" and "PD" samples as a function of time.

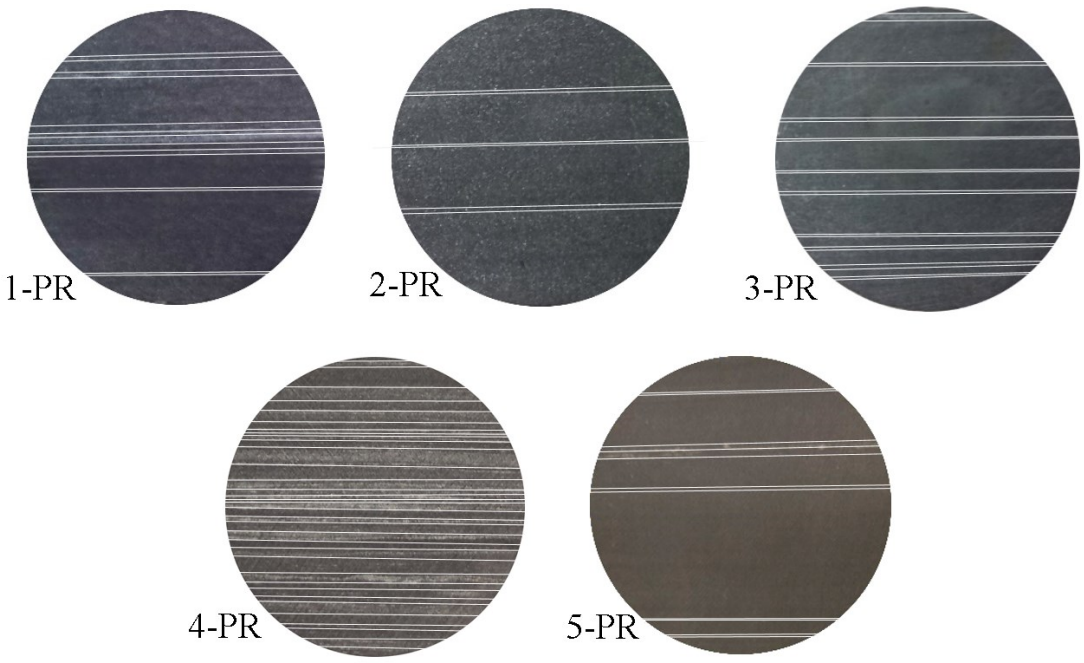

Figure 3-14. Number of the beds in different "PR" samples. 1-PR: 15 beds, 2-PR: 7 beds, 3-PR: 20 beds, 4-PR: 35 beds and 5-PR: 12 beds.

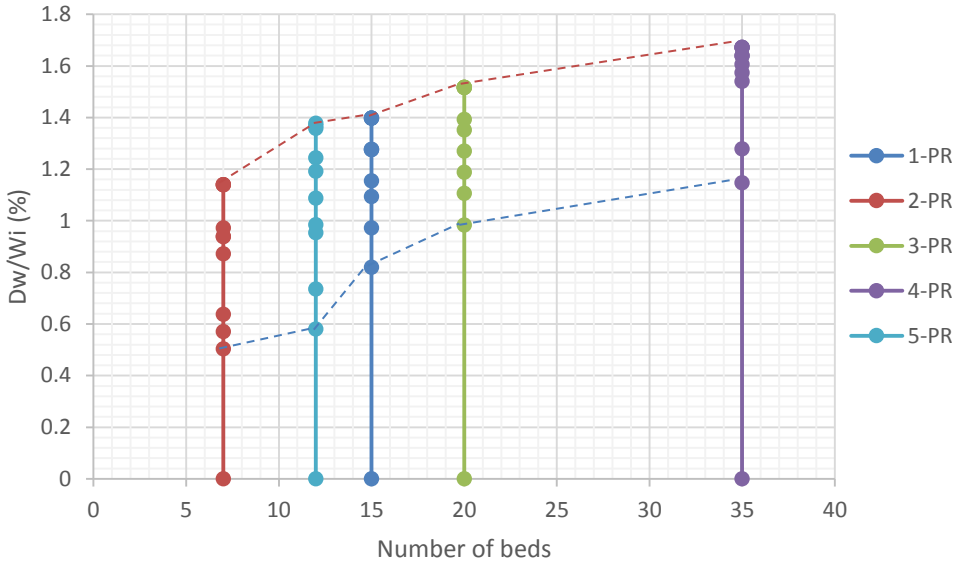

Figure 3-15. The role of number of the beds on imbibition rate and water content. Blue and red dotted lines are related to t = 1hour and t = 24hour, respectively.

3.1.3.2.1. Wave Velocity Measurements

Figure 3-16 and Figure 3-17 show compressional and shear wave velocities for "PD" and "PR" samples as the water content is increasing. The results of the spontaneous imbibition tests implies that the velocity of compressional waves in both "PD" and "PR" samples in dry condition are higher than shear waves (Figure 3-18 and Figure 3-19) which can be related to the impact of anisotropy where shear waves splitting would take place (Sondergeld and Rai, 1986). The compressional wave velocities in "PD" and "PR" samples are approximately 40-50% higher than shear wave velocities. In "PR" samples the velocity of the waves are higher than "PD" samples which is in agreement with previous studies (Wu and Tan, 2010; Schien, 2014). P-wave velocity mainly depends on the direction relative to the isotropic plane (Eitzenberger, 2012) which means that the velocity is higher in "PR" samples than "PD" samples. Based on the ultrasonic wave measurements during the imbibition, both compressional and shear waves would be affected. The rate of changes in wave velocities is more significant in "PR" samples. As the water content is rising, the ratio of compressional to shear wave velocity increases for both "PR" and "PD" samples but it is higher in "PR" samples (Figure 3-18 and Figure 3-19). This can be attributed to more anisotropy as a result of more beds as well as induced micro fractures which can in turn contribute

to more water uptake in "PR" samples (shear wave cannot propagate in water). Higher Vp/Vs values in water saturated media with higher micro fracture densities was also observed by Wang et al. (2012). If induced micro fractures are perpendicular to the wave propagation direction compressional wave velocity would decrease while shear wave velocity decreases if micro fractures are parallel with the wave propagation direction (Frederic L.P., 2007). Therefore, because both compressional and shear waves are decreased during the spontaneous imbibition tests it is expected to have induced micro fractures in both plane of isotropy and transverse plane (Figure 3-20). This is consistent with micro fracture generation and propagation pattern observed in the samples after spontaneous imbibition test where a complex micro fracture network has been formed (Figure 3-21).

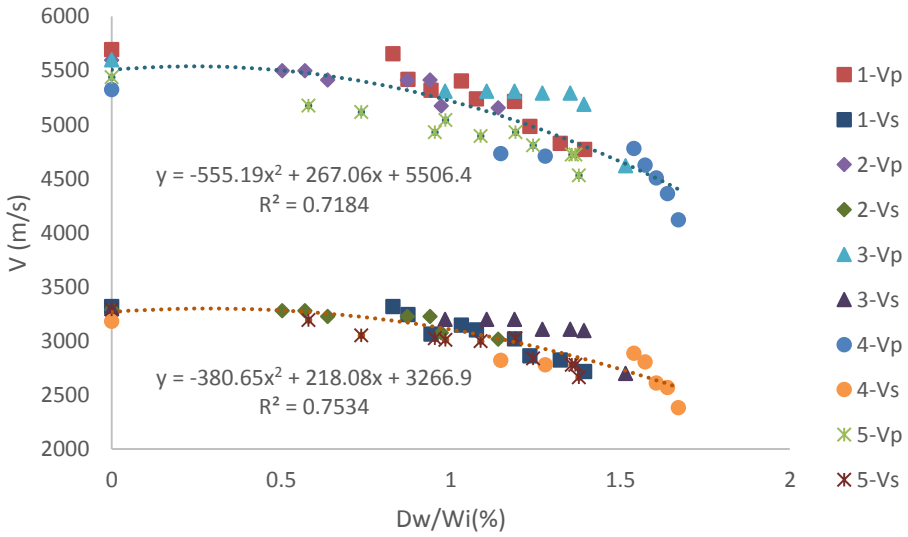

Figure 3-16. Velocity of Ultrasonic waves during spontaneous imbibition test on "PR" samples (Vp = velocity of compressional wave and Vs = velocity of shear waves)

.

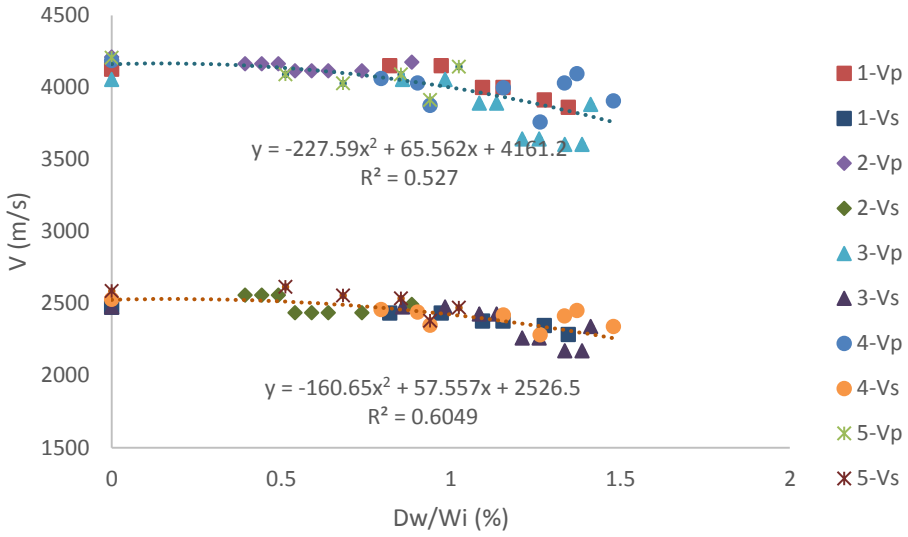

Figure 3-17. Velocity of Ultrasonic waves during spontaneous imbibition test on "PD" samples (Vp = velocity of compressional wave and Vs = velocity of shear waves).

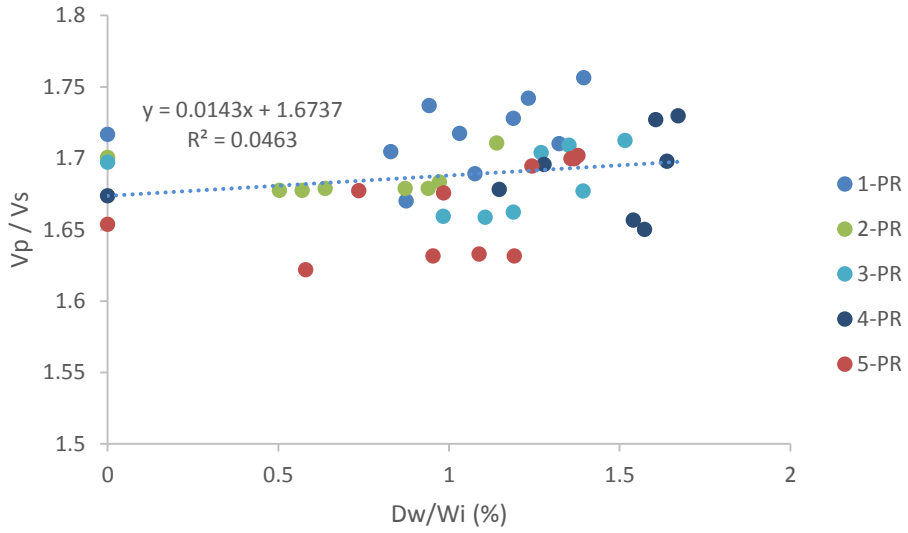

Figure 3-18. Changes in Vp/Vs as the water content is increasing during spontaneous water imbibition in "PR" Montney samples.

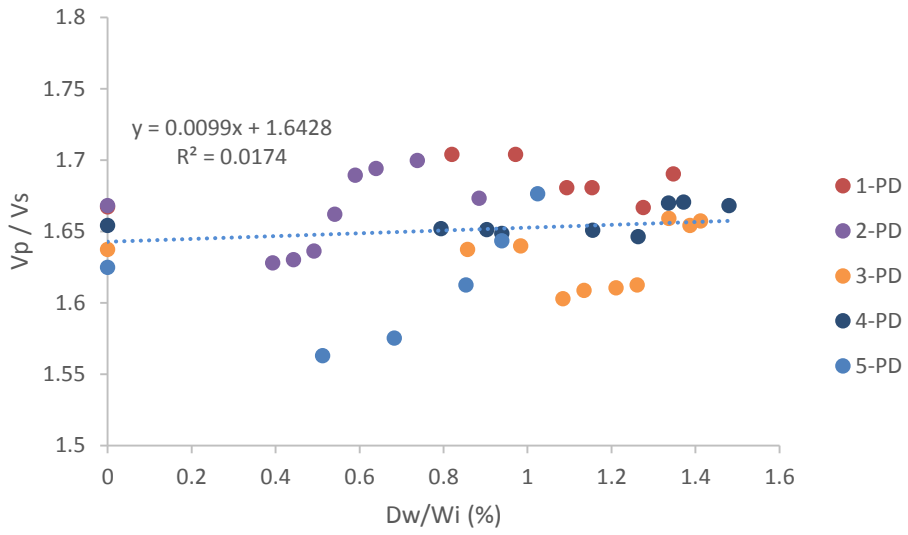

Figure 3-19. Changes in Vp/Vs as the water content is increasing during spontaneous water imbibition in "PD" Montney samples.

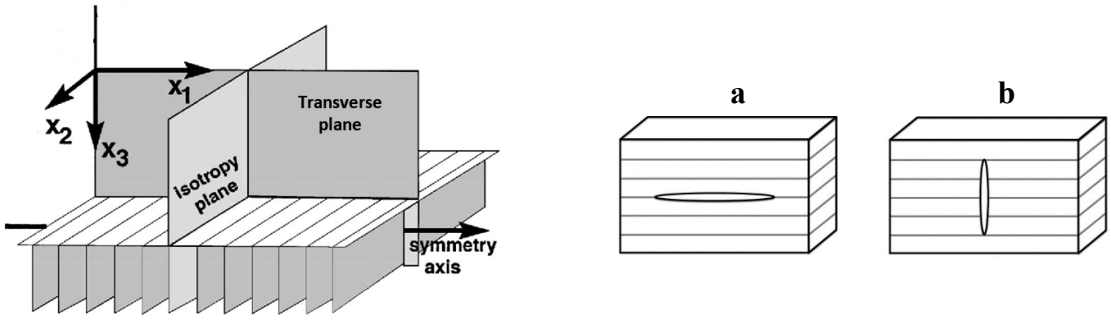

Figure 3-20. Micro fracture generation in a plane of isotropy and transverse plane: a) longitudinal fracture; b) transverse fracture.

A summary of spontaneous imbibition test and how it affected compressional and shear wave velocities in the samples is represented in Table 3-6.

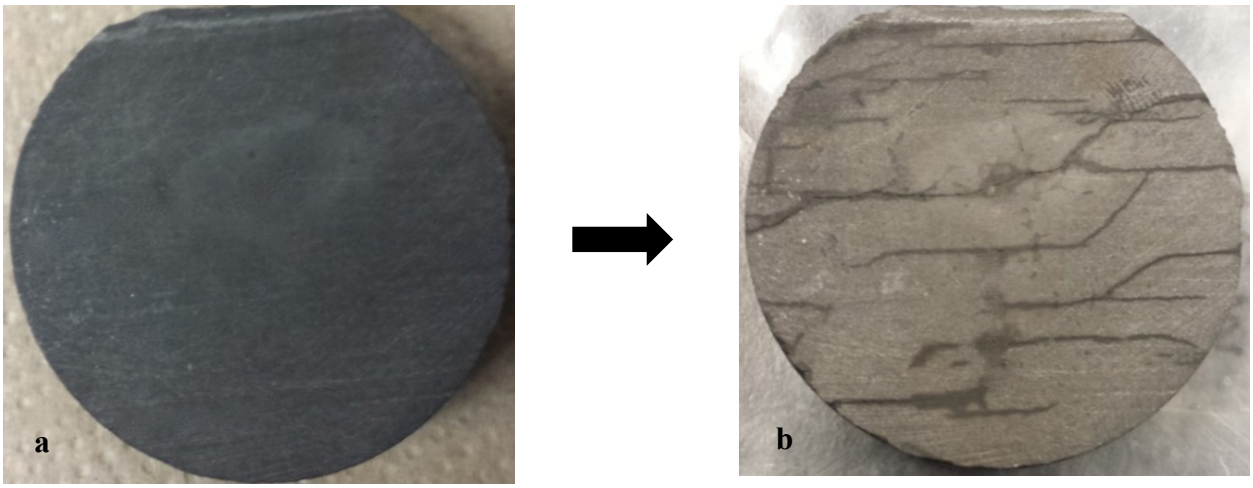

Figure 3-21. Induced complex micro fracture generation (sample 3-PR): a) pre-imbibition sample; b) post-imbibition sample.

Table 3-6. A summary of changes in samples weights and velocity of ultrasonic waves as a result of spontaneous imbibition. "Pre" and "Post" indicate pre-imbibition and post-imbibition.

Sample No.	"Pre" Weight (gr)	"Post" Weight (gr)	"Pre" V_p (m/s)	"Post" V_p (m/s)	"Pre" V_s (m/s)	"Post" V_s (m/s)	"Pre" V_p / V_s	"Post" V_p / V_s
1-PD	12.56	12.729	4126	3862	2475	2285	1.67	1.69
1-PR	13.117	13.3	5695	4770	3317	2716	1.72	1.76
2-PD	12.661	12.773	4211	4175	2524	2495	1.67	1.67
2-PR	12.763	12.908	5597	5155	3291	3013	1.70	1.71
3-PD	12.864	13.045	4054	3882	2476	2342	1.64	1.66
3-PR	13.218	13.418	5599	4620	3299	2698	1.70	1.71
4-PD	13.573	13.774	4186	3905	2531	2341	1.65	1.67
4-PR	13.725	13.954	5323	4119	3181	2382	1.67	1.73
5-PD	12.965	13.098	4206	4144	2589	2472	1.62	1.68
5-PR	13.37	13.554	5438	4531	3289	2663	1.65	1.70

3.1.3.2.2. Determination of Dynamic Elastic Properties

Elastic properties are critical parameters for describing rocks behavior under loading and before failure. In the next phase, based on the compressional and shear waves velocities captured during

spontaneous imbibition experiment, dynamic elastic values were determined. As it can be seen in Figure 3-22 to Figure 3-25, initially dynamic Young's modulus and shear modulus in "PR" samples are higher than "PD" samples. The results indicate that by increasing the water content, dynamic Young's modulus and shear modulus in both directions would decrease but the rate of decreasing in "PR" samples are higher than "PD" samples. This is consistent with Vale`s et al. (2004) experiments on shale samples in different water saturations. Figure 3-26 and Figure 3-27 represent dynamic Young's modulus and shear modulus reduction in both "PR" and "PD" samples where sample "4-PR" which has the highest number of beds (35 beds) and volume imbibed (Figure 3-11), shows the highest reduction in dynamic Young's modulus (42.72%) and shear modulus (43.94%). Also, the minimum reduction in dynamic Young's modulus (2.1%) and shear modulus (2.32%) is related to sample "2-PD" which has the lowest volume imbibed (Figure 3-12). This would suggest that the higher the water content the lower the Young's modulus and shear modulus while at the same time water content is related to the number of the beds (Figure 3-15) and it is reversely proportional to capillary suction (Table 3-5).This means that generation of induced micro fractures (which can be related to the number of beds) and more water uptake (more reduction in capillary suction) are working together to decrease Young's modulus and shear modulus. The results also indicate that initially dynamic Poisson's ratio values are higher in "PR" samples and as the water content is rising the dynamic Poisson's ratio parallel and perpendicular to the beds would generally increase although it might fluctuate to some degrees during the spontaneous imbibition test (Figure 3-28 and Figure 3-29). As shown in Figure 3-30, dynamic Poisson's ratio values increase more in "PR" samples except for sample "3" and "5" where dynamic Poisson's ratio increase is higher in "PD" samples. The highest and lowest dynamic Poisson's ratio increase as a result of spontaneous imbibition are related to sample "5-PD" 14.65% and "2-PD" 1.23%, respectively. Based on Equation (3-3), dynamic Poisson's ratio is dependent on the ratio of compressional and shear wave velocities. In other words, dynamic Poisson's ratio would not show a major variation as the compressional and shear wave velocities changes at a similar rate (as shown in Table 3-6). Therefore, highest, and lowest changes in dynamic Poisson's ratio can be attributed to generation of longitudinal and transverse micro fractures followed by water uptake.

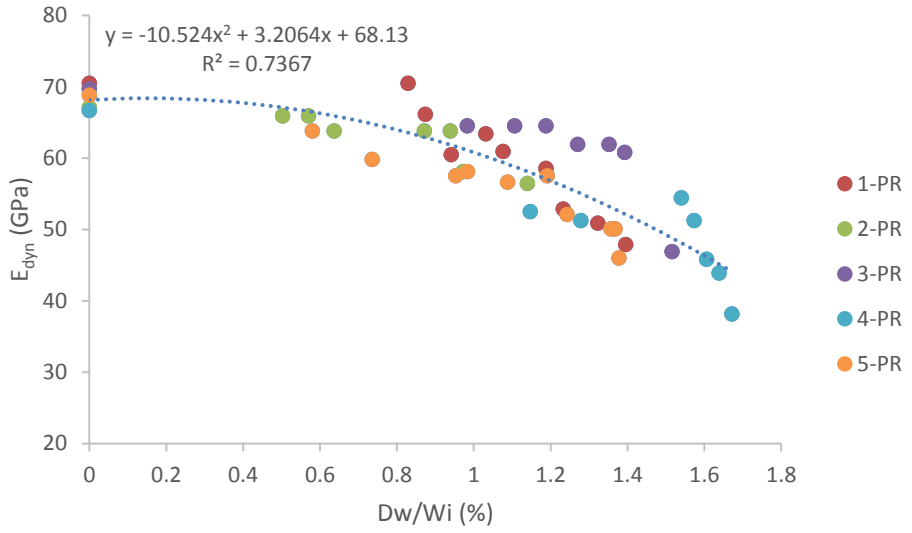

Figure 3-22. Changes in dynamic Young's modulus of "PR" samples as the water content in spontaneous imbibition is rising.

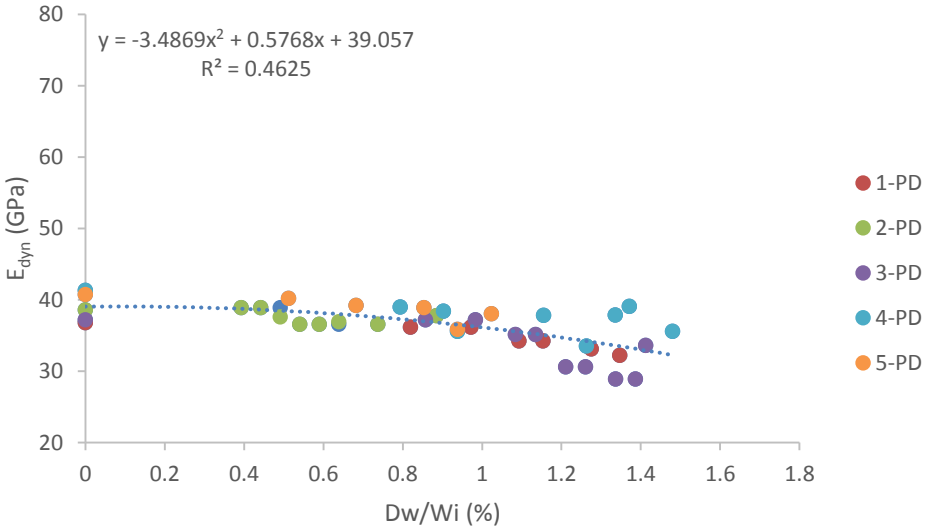

Figure 3-23. Changes in dynamic Young's modulus of "PD" samples as the water content in spontaneous imbibition is rising.

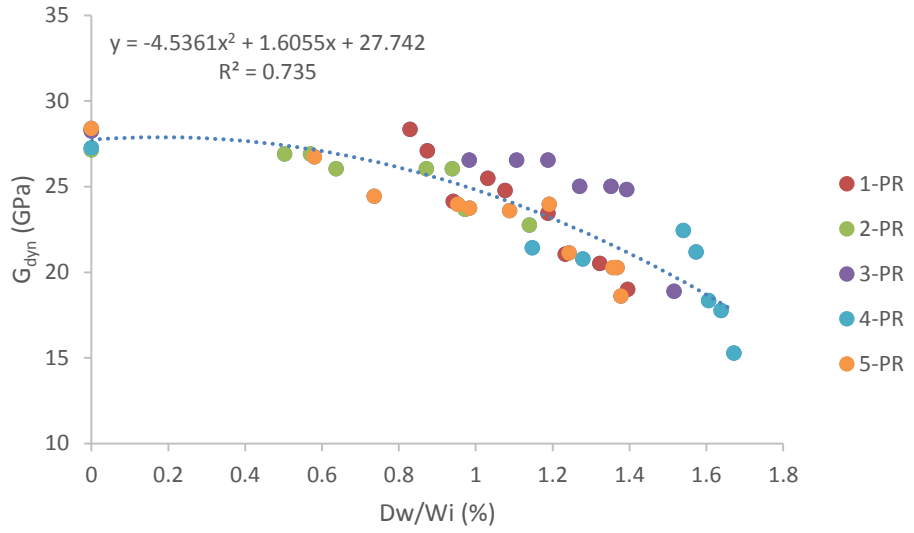

Figure 3-24. Changes in dynamic shear modulus of "PR" samples as the water content in spontaneous imbibition is rising.

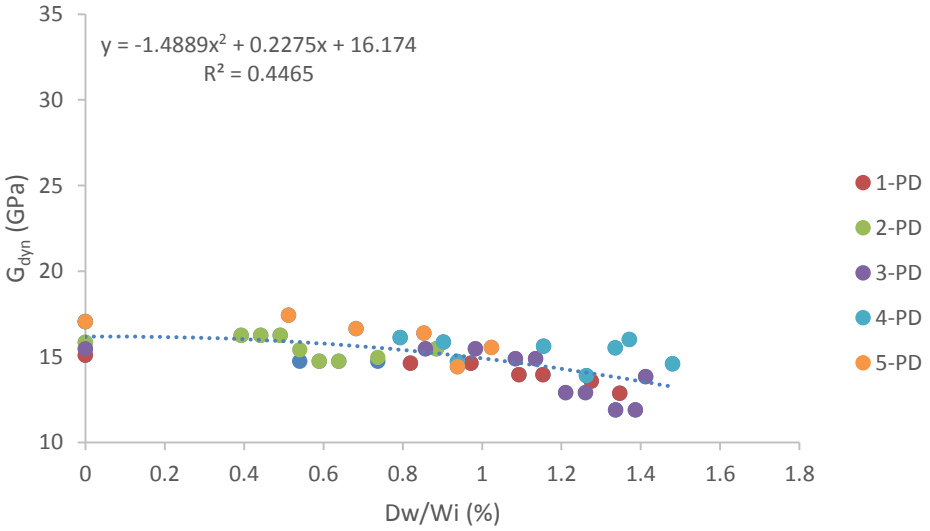

Figure 3-25. Changes in dynamic shear modulus of "PD" samples as the water content in spontaneous imbibition is rising.

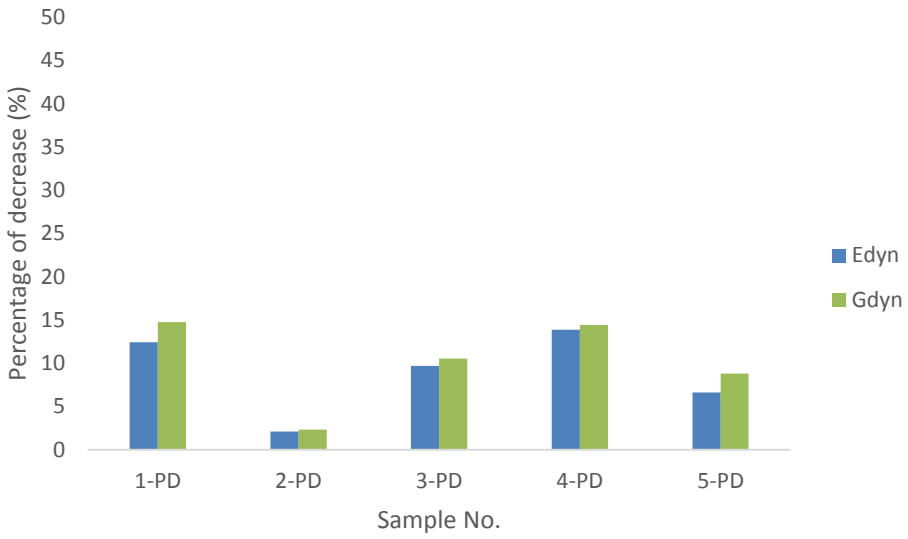

Figure 3-26. Reduction in dynamic Young's modulus and shear modulus of "PD" samples after spontaneous imbibition tests.

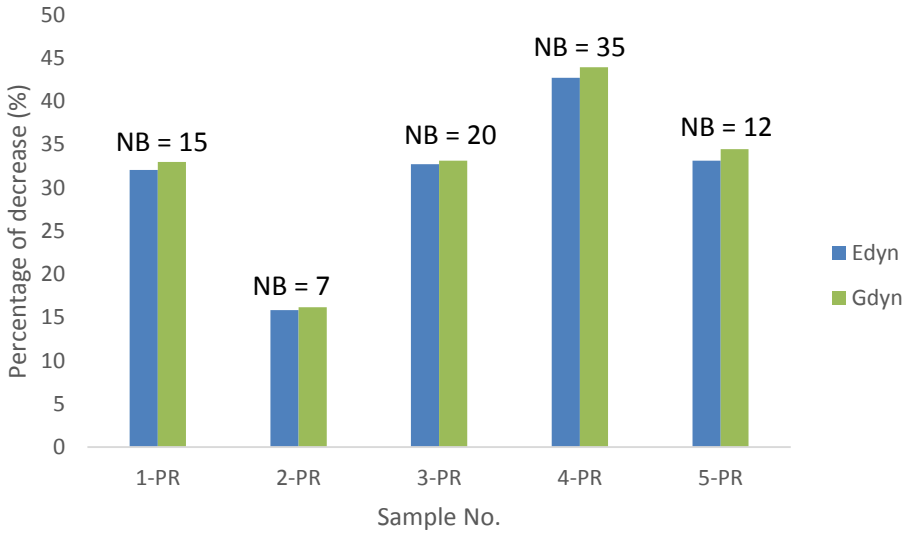

Figure 3-27. Reduction in dynamic Young's modulus and shear modulus of "PR" samples after spontaneous imbibition tests. "NB" represents the number of beds.

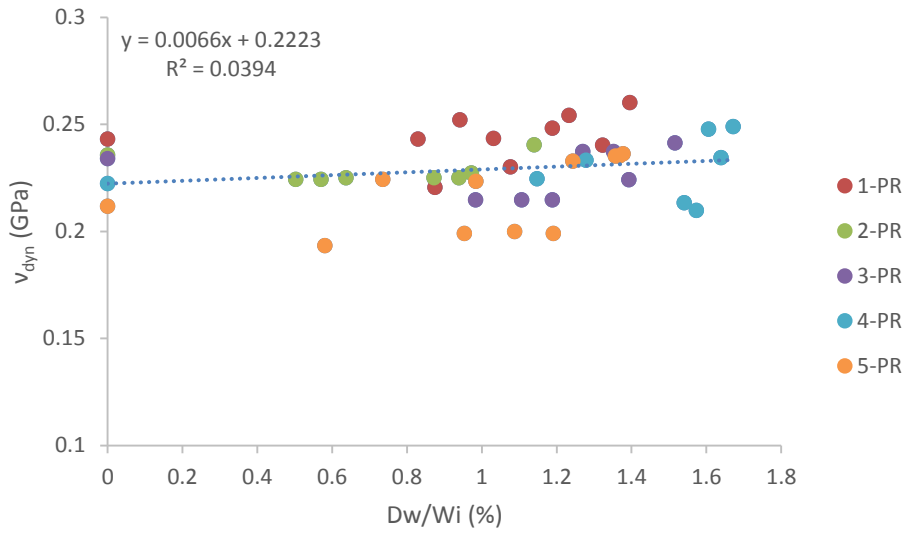

Figure 3-28. Changes in dynamic Poisson's ratio of "PR" samples as the water content in spontaneous imbibition is rising.

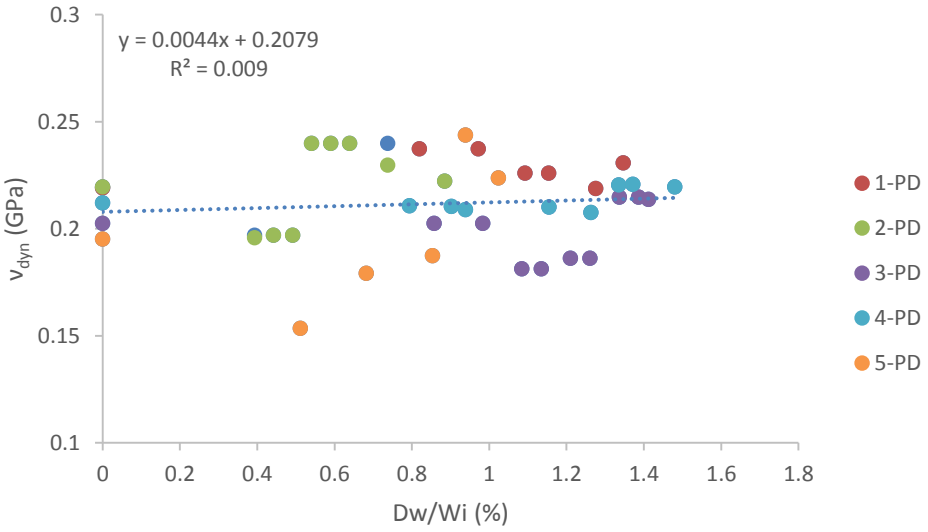

Figure 3-29. Changes in dynamic Poisson's ratio of "PD" samples as the water content in spontaneous imbibition is rising.

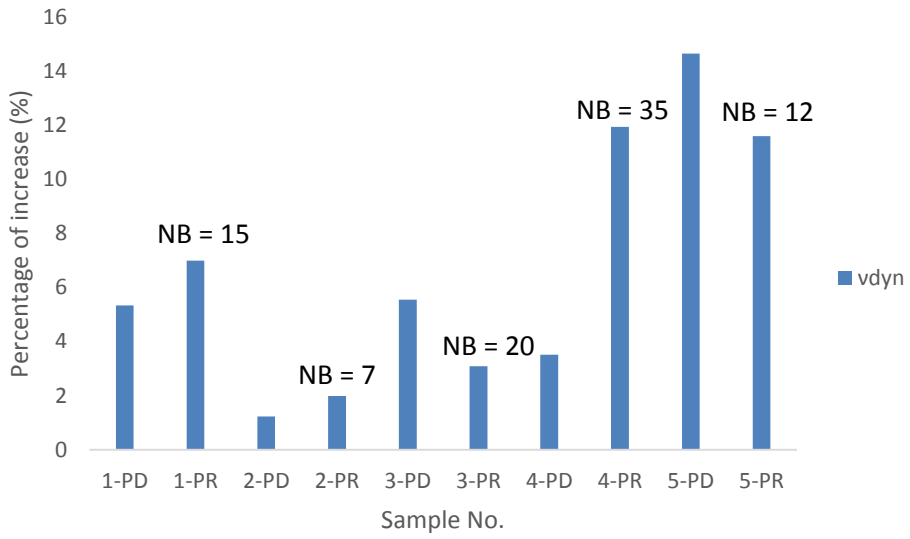

Figure 3-30. Increasing dynamic Poisson's ratio of the samples after spontaneous imbibition tests. "NB" represents the number of beds.

3.1.3.2.3. Determination of Brittleness Index (BI)

Brittleness index is an important mechanical parameter to evaluate whether complex fracture networks can be easily formed during hydraulic fracturing (King, 2010). To determine the brittleness index, E_n and ν_n were calculated by Equation (3-7) and (3-8) followed by brittleness index determination using Equation (3-6). The values of brittleness index as a function of normalized water content for "PR" and "PD" samples are represented in Figure 3-31 and Figure 3-32, respectively. The results imply that brittleness index in both "PR" and "PD" samples are decreasing as the water content is increasing while the rate of decrease is higher in "PR" samples. As shown in Figure 3-33, the highest change in brittleness index is related to sample "4-PR" 88.3% and the lowest is for sample "2-PD" 9.27%. Note that sample "4-PR" has the highest volume imbibed with the highest number of beds (35 beds) and sample "2-PD" has the lowest volume imbibed with the lowest capillary suction. Sample "3-PR" which has higher number of beds than "1-PR" and "5-PR" show a lower brittleness index reduction. The former would suggest that brittleness index which is a function of Young's modulus and Poisson's ratio, would be affected by the parameters that impact Young's modulus and Poisson's ratio including water uptake which is inversely proportional to capillary suction and directly proportional to generation

of induced micro fractures and the number of the beds as well as rate of longitudinal and transverse micro fractures generation (Vp/Vs).

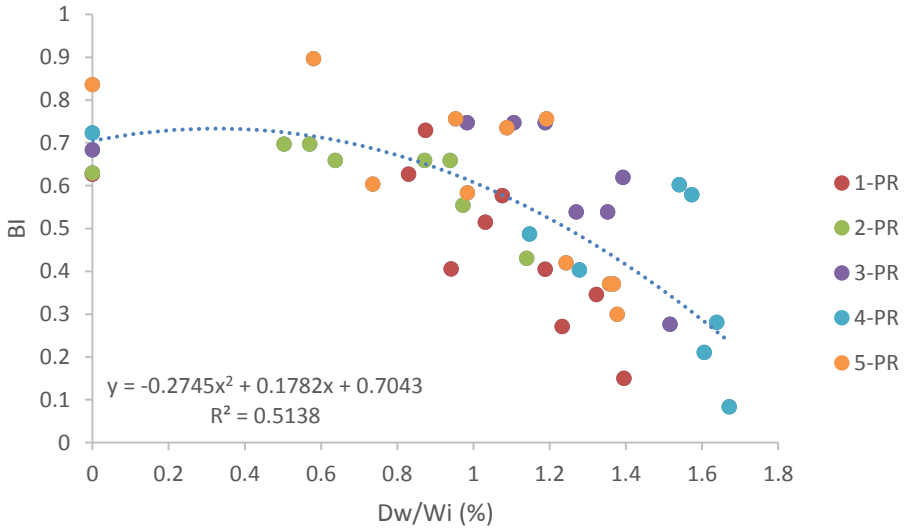

Figure 3-31. Changes in brittleness index (BI) of "PD" samples as the water content in spontaneous imbibition is rising.

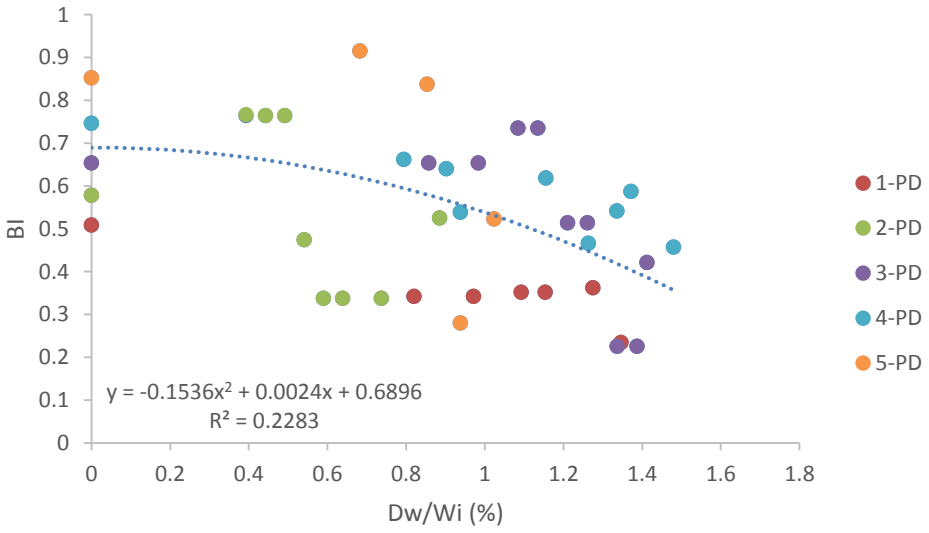

Figure 3-32. Changes in brittleness index (BI) of "PR" samples as the water content in spontaneous imbibition is rising.

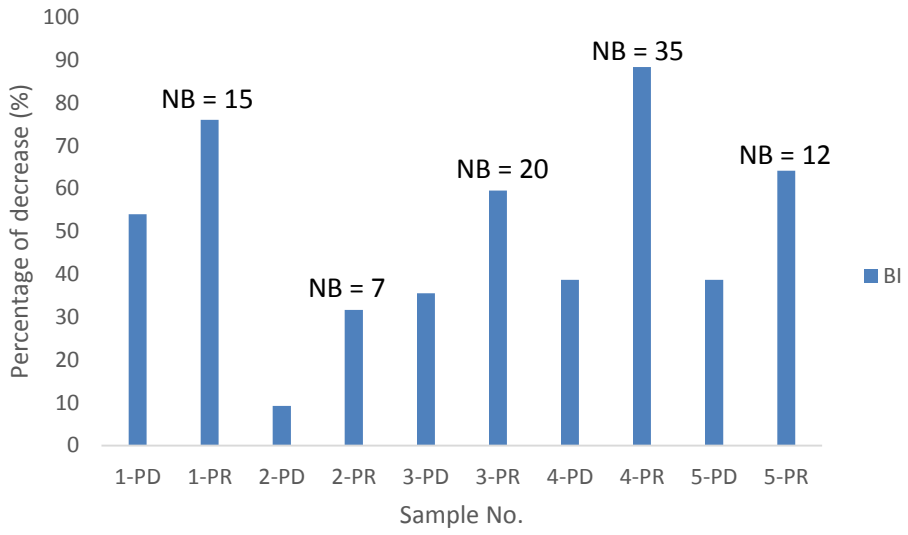

Figure 3-33. Reduction in brittleness index (BI) of the samples after spontaneous imbibition tests. "NB" represents the number of beds.

Brittleness index only corresponds to elastic deformation, but the failure of the rock refers also to plastic deformation (Bai, 2016). In this instance, fracability which is defined as "the rock failure under the ultimate rock strength in either brittle or ductile formation" becomes relevant (Mohamed et al., 2019). The higher the fracability of the formation, the smaller the strength of the formation and lower pressure is needed to induce fractures. Although fracturing of formations with more brittleness can lead to more complex fractures it doesn't necessarily mean that they are easier to fracture than ductile formations since brittle rocks may have higher strength than ductile rocks. Therefore, even if spontaneous water imbibition leads to decreasing brittleness, strength change as a result of water uptake should also be considered when assessing the complexity the induced fractures.

3.1.3.2.4. Determination of Internal Friction Angle

Friction angle is an important component of shear strength (as shown in Equation (3-15)). Any change in fiction angle would affect the shear strength. Consequently, it is of great significance to understand the change in failure parameters including friction angle as spontaneous water imbibition is taking place. By using Equation (3-5) the values of friction angle were estimated for both "PR" and "PD" samples (Figure 3-34 and Figure 3-35).

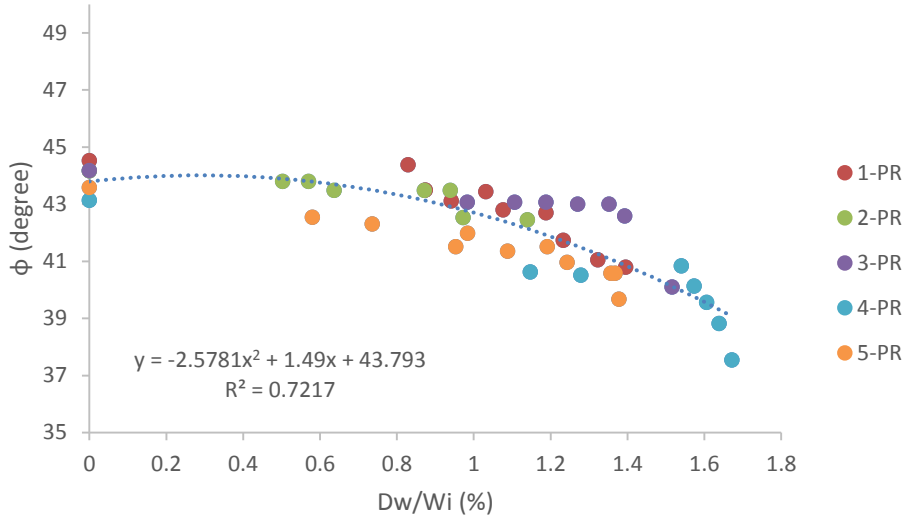

Figure 3-34. Changes in friction angles of "PR" samples as the water content in spontaneous imbibition is rising.

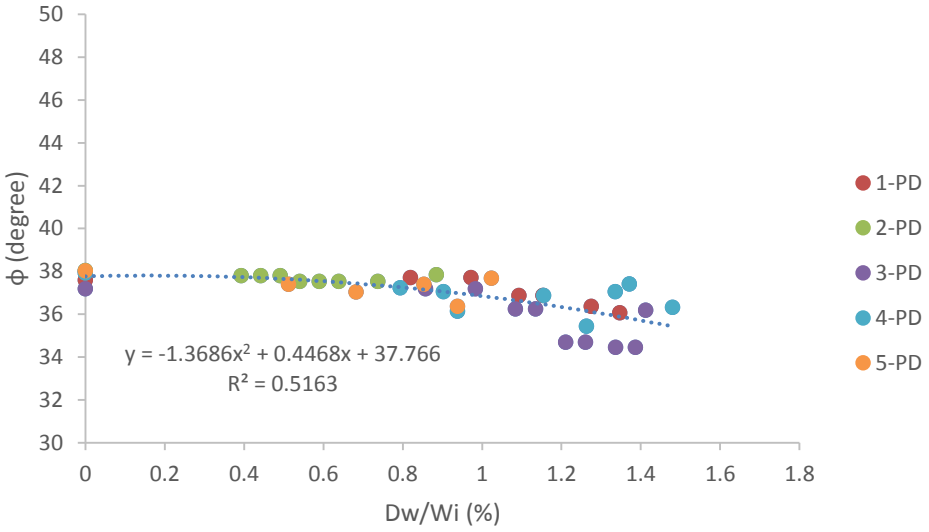

Figure 3-35. Changes in friction angles of "PD" samples as the water content in spontaneous imbibition is rising.

Initially internal friction angle is higher in "PR" samples and as a result of water uptake friction angle in both "PR" and "PD" samples decreases which agrees with He et al. (2016), Xia et al. (2018) and Ding et al. (2020) studies. As the water content increases as a result of spontaneous imbibition, friction angle in "PR" samples drop more than "PD" samples. As shown in Figure 3-36, the highest reduction in friction angle is for sample "4-PR" 12.97% and the lowest is for sample "2-PD" 0.51%.

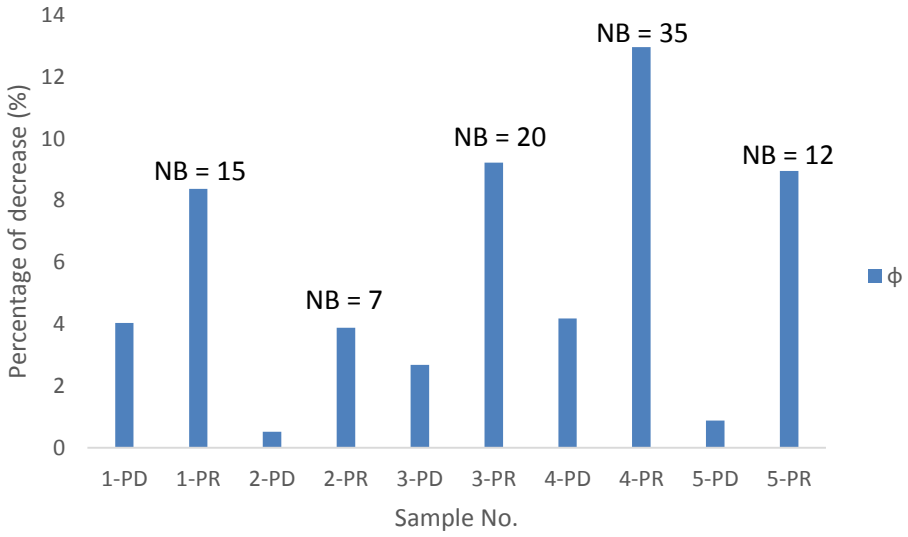

Figure 3-36. Reduction in friction angles of the samples after spontaneous imbibition tests. "NB" represents the number of beds.

There is a meaningful relationship between the number of the beds and the reduction in friction angle. As it can be observed in Figure 3-36 the samples with higher number of beds have higher reduction in friction angle. Figure 3-37 depicts the relationship between the number of the beds and Young's modulus, shear modulus, Poisson's ratio and friction angle for "PR" samples. Table 3-7 represents a summary of change in rock properties as a result of spontaneous imbibition.

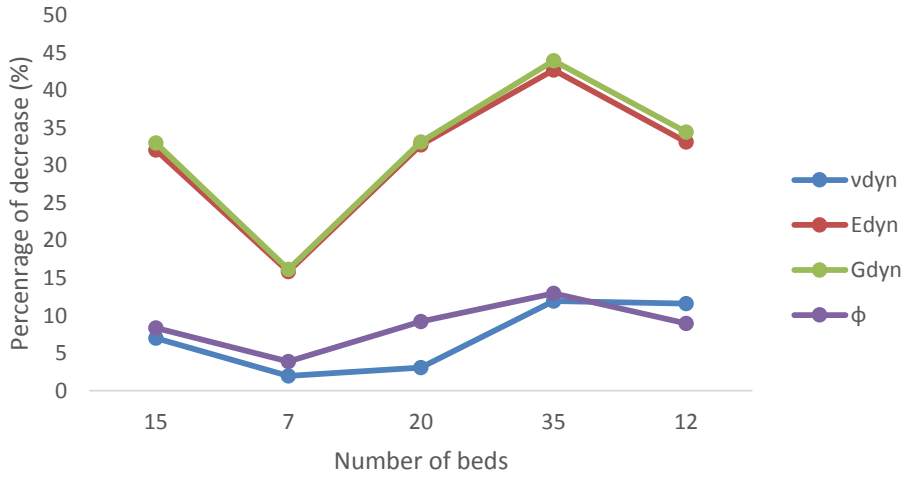

Figure 3-37. Relationship between the number of beds and Young's modulus, shear modulus, Poisson's ratio and friction angle for "PR" samples.

Table 3-7. A summary of changes in rock properties as a result of spontaneous imbibition. “Pre” and “Post” indicate pre-imbibition and post-imbibition.

Sample No.	“Pre” E_{dyn} (GPa)	“Post” E_{dyn} (GPa)	“Pre” G_{dyn} (GPa)	“Post” G_{dyn} (GPa)	“Pre” v_{dyn}	“Post” v_{dyn}	“Pre” BI	“Post” BI	“Pre” φ	“Post” φ
1-PD	36.83	32.25	15.11	12.87	0.219	0.231	50.89	23.41	37.58	36.06
1-PR	70.47	47.87	28.34	18.99	0.243	0.260	62.72	15.01	44.53	40.80
2-PD	38.64	37.83	15.84	15.47	0.220	0.222	57.83	52.47	38.04	37.84
2-PR	67.08	56.45	27.14	22.75	0.236	0.240	63.03	43.08	44.17	42.46
3-PD	37.24	33.63	15.48	13.85	0.203	0.214	65.33	42.10	37.18	36.18
3-PR	69.71	46.90	28.24	18.89	0.234	0.241	68.37	27.64	44.18	40.10
4-PD	41.37	35.63	17.07	14.61	0.212	0.220	74.58	45.69	37.91	36.32
4-PR	66.65	38.18	27.26	15.28	0.222	0.249	72.36	8.42	43.13	37.54
5-PD	40.77	38.07	17.06	15.56	0.195	0.224	85.25	52.25	38.01	37.68
5-PR	68.81	46.02	28.39	18.61	0.212	0.236	83.64	29.98	43.58	39.67

3.1.3.3. Geomechanical Mechanisms

The results of spontaneous imbibition tests described above show that it results in stiffness reduction and decreasing strength however, explaining the mechanisms is still lacking. From a geomechanical point of view, according to the experiments addressed above, it can be suggested that capillary suction pressure would add an apparent stiffness and strength to the rock and as it is decreasing as a result of increasing the water content, rock mechanical properties and strength parameters would be affected which can lead to weakening the rock and changing the local stress state. The following section utilizes the principles of poroelasticity to provide a framework for explain the property changes due to spontaneous imbibition. Coussy et al. (1998) and Chateau and Dormieux (2002) derived an incremental form of the general poroelastic framework for partially saturated media as shown in Equation (3-13):

$$d\left(\sigma_{ij} - bu_a\delta_{ij}\right) + S_r bd(u_a - u_w)\delta_{ij} = C_{ijkl}d\varepsilon_{kl} \quad (3\text{-}13)$$

where σ_{ij} is the total stress tensor, b is the Biot coefficient, u_a, u_w are pore air and water pressures, S_r is degree of saturation, C_{ijkl} is elasticity tensor and ε_{kl} is the strain tensor. From the left-hand side of Equation (3-13), (Equation (3-14) can be formed (Fredlund and Rahardjo 1993).

$$\sigma'_{ij} = \left(\sigma_{ij} - bu_a\delta_{ij}\right) + \chi b(u_a - u_w)\delta_{ij} \quad (3\text{-}14)$$

where it is assumed that $\chi = Sr$.

Based on Equation (3-14), water saturation increase, and capillary suction decrease would lead to reducing the effective stress. To better understand how these changes may affect the failure mechanisms (micro fracture initiation and propagation) a schematic view of Mohr- Coulomb circle is shown in Figure 3-38. As shown in Figure 3-38, any reduction in effective stress would shift the circle to the left where the possibility of touching the failure envelope and failure occurrence would increase.

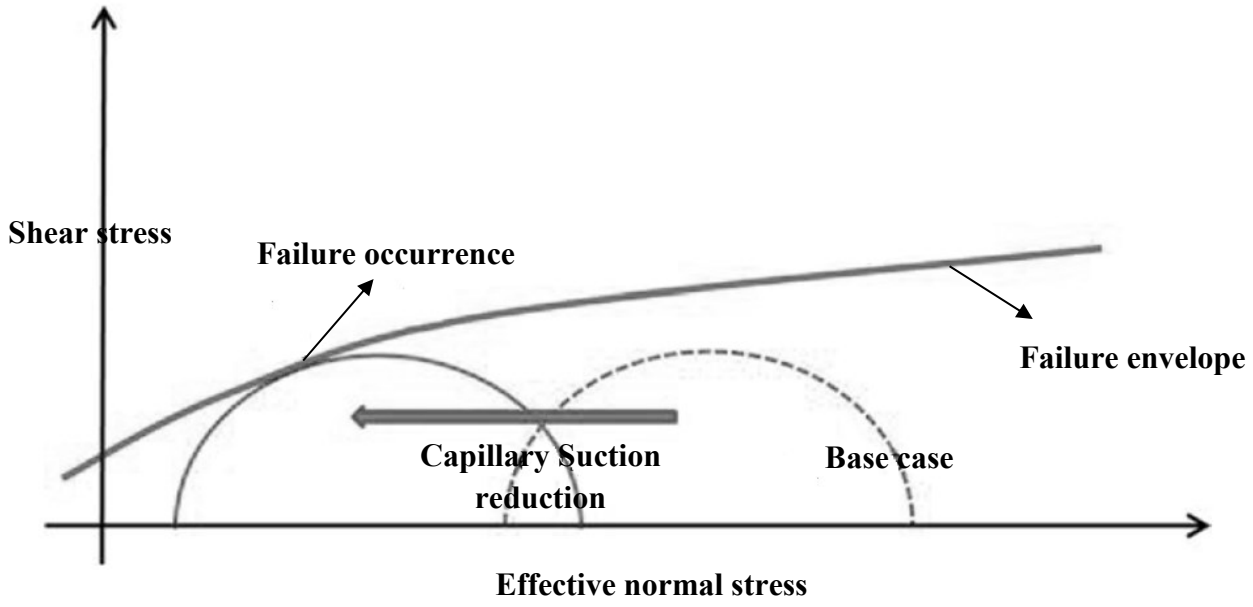

Figure 3-38. Effect of capillary suction change on shifting the Mohr- Coulomb circle toward the failure envelope.

Based on Equation (3-13), as the effective stress decreases, the medium tends to respond in a form of volumetric strain which would cause an expansion. Since heterogeneity in tight gas formations and shale begins from a very small scale, the volumetric strain of different components (such as beds) as a result of interaction with water may be different which can contribute to shear failure being triggered within planes of weaknesses (such as the interface between the beds). Also, by considering Mohr-Coulomb's failure criterion and substituting Equation (3-14), Equation (3-15) can be derived to handle the shear failure.

$$\tau = C + (\sigma_n - bu_a)tan\varphi' \quad (3\text{-}15)$$

$$C = (c' + (S_r b(u_a - u_w)tan\varphi'') \quad (3\text{-}16)$$

where φ' is the angle of internal friction with respect to changes in $(\sigma_n - bu_a)$, φ'' is friction angle associated with capillary suction $(u_a - u_w)$ and C is the total cohesion. The experimental investigations implied that the angle φ' is always equal or smaller than the internal friction angle φ' (Fredlund and Rahardjo 1993). Also, Fredlund et al. (1978) suggested that $(S_r b(u_a - u_w)tan\varphi'')$ in Equation (3-15) can be considered as an apparent cohesion for a given degree of saturation. Based on Equation 3-15 and 3-16, capillary suction would give an apparent cohesion to the media and as it reduces (as a result of increasing the water saturation) the total cohesion would decrease followed by a reduction in shear strength. Figure 3-39 represents a schematic view of Mohr- Coulomb circle where decreasing the cohesion would shift the failure envelop downward which would increase the possibility of touching the failure envelope by the Mohr- Coulomb circle followed by failure occurrence.

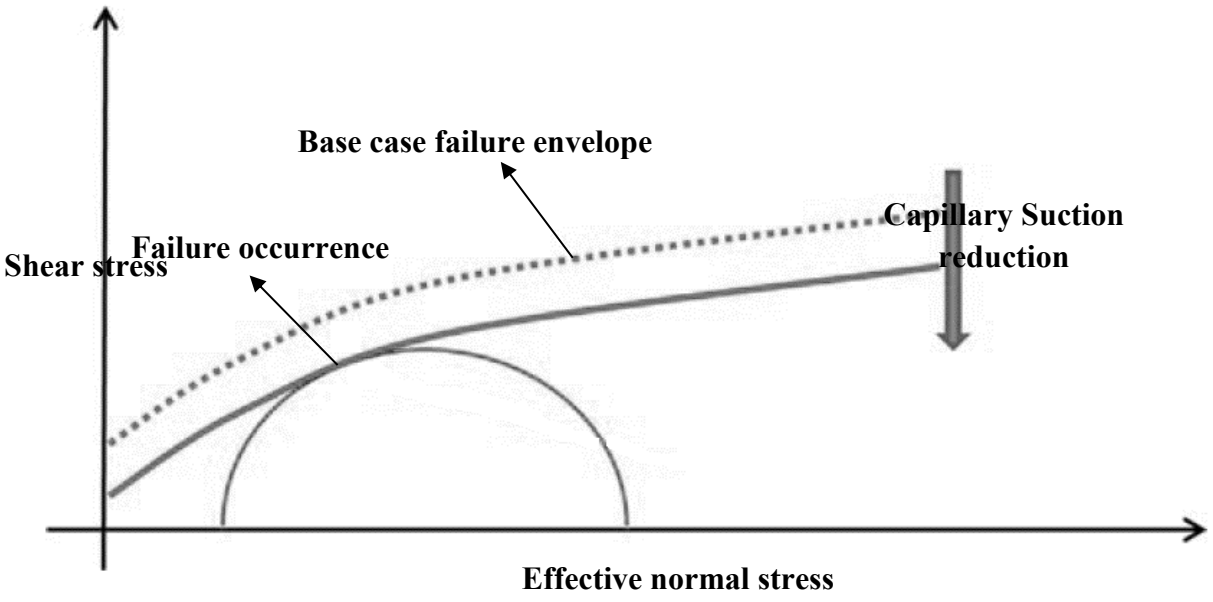

Figure 3-39. Effect of capillary suction change on shifting the failure envelope downward.

One of the behaviors that can be observed during spontaneous imbibition test is micro fracture generation. Based on the results from spontaneous imbibition test on Montney samples, the majority of the induced micro fractures are initiated and propagated near the interface between the

beds followed by propagation in the weaker adjacent bed as shown in Figure 3-40. This would suggest that the interface between the beds would act as a plane of weakness and as the water content increases it becomes weaker. In addition, as a result of changes in local effective stress (Equation (3-14)), both beds adjacent an interface would undergo volumetric responses concurrent with weakening of the rock mechanical and strength properties which can increase the possibility failure occurrence in the interface. Based on a visual interpretation of the microcracking shown in Figure 3-40, micro fracture initiation and propagation appears to occur at the interface between the beds and then (in our cases) propagate into the dark beds. This would imply that dark beds are weakening more than the white beds. In addition, during the tests it was clearly observed that gas phase is flowing out of the samples (especially near the interface between the beds) as the imbibition was taking place (Figure 3-41). This phenomenon implies that as the water is filling the pores and pushing the gas phase out of the pores, induced micro fractures (failures) may have provided additional conduits for the gas phase to flow out of the sample.

Figure 3-40. Micro fracture generation in the interface between the beds and within the beds. “a”, “b” and “c” are related to “3-PR”, “4-PR” and “4-PR”

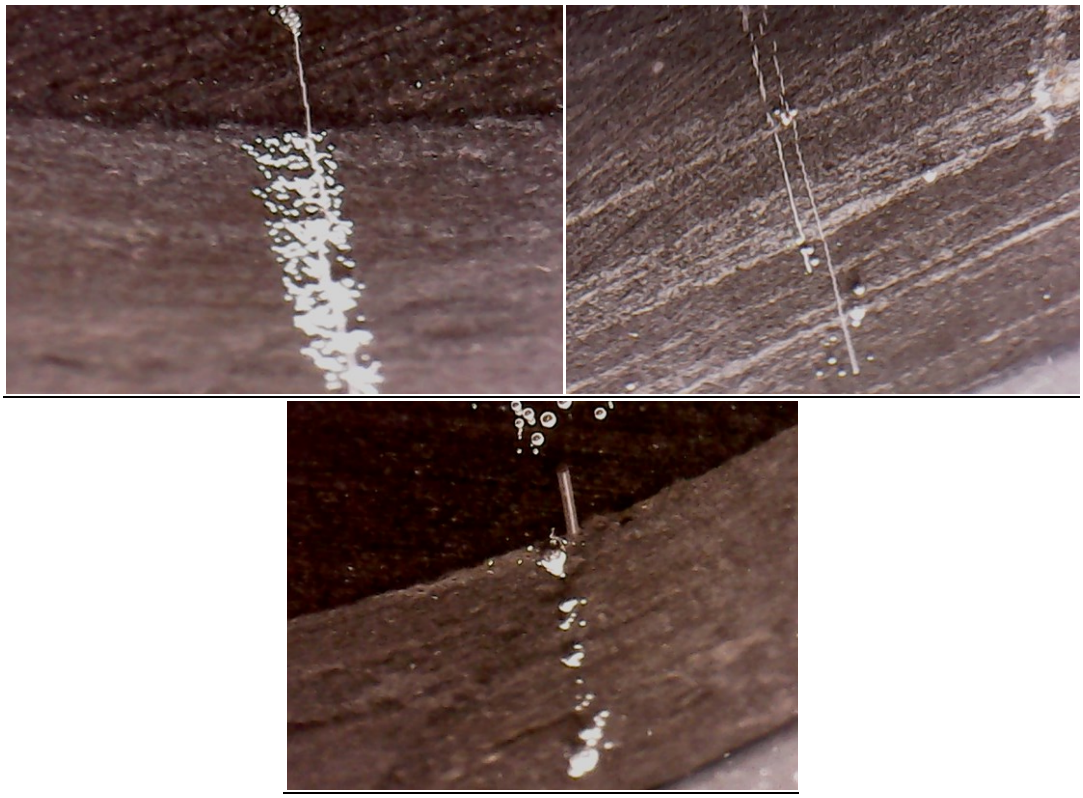

Figure 3-41. Gas phase flowing out of the samples during the imbibition test. “a”, “b” and “c” are related to “3-PD”, “4-PD” and “1-PD”.

From a fracability or fracture propagation point of view it is worth mentioning that while brittleness index can be used as a criterion for evaluation of fracability, it is not a well-defined parameter and remains the subject of research on how to best define fracability. Fracture toughness and strain energy release rate as well as rock strength and the fracture closure stress would be also influential (Economides and Nolte, 2000; Jin et al., 2015) in assessing fracability. Micro fracture generation pattern shown in Figure 3-40 would suggest that as a result of spontaneous imbibition, fracture toughness would decrease and the lower the fracture toughness the easier the fracture propagation. Also, mix-mode micro fracture propagation near the beds implies that not only Mode-I fracture toughness (opening) but also Mode-II fracture toughness (shearing) would be affected as the water content is increasing which would facilitate micro fracture generation. Additionally, changes in rock mechanical properties as a result of increasing water content (decreasing capillary suction) would significantly impact the stress state in the invaded zone. Theoretically, minimum

and maximum effective stress in transversely isotropic media can be measured by Equation (3-17) and (3-18) (Higgings et al., 2008).

$$\sigma_h - \alpha P = \left[\frac{E_h}{E_v}\frac{\vartheta_v}{1-\vartheta_h}\right](\sigma_v - \alpha P) + \frac{E_h}{1-\vartheta_h^2}\varepsilon_h + \frac{E_h\vartheta_h}{1-\vartheta_h^2}\varepsilon_H \quad (3\text{-}17)$$

$$\sigma_H - \alpha P = \left[\frac{E_h}{E_v}\frac{\vartheta_v}{1-\vartheta_h}\right](\sigma_v - \alpha P) + \frac{E_h}{1-\vartheta_h^2}\varepsilon_H + \frac{E_h\vartheta_h}{1-\vartheta_h^2}\varepsilon_h \quad (3\text{-}18)$$

where σ_H and σ_h are the maximum and minimum horizontal stress, respectively; σ_v is the vertical stress, P is the pore pressure, α is Boit's coefficient, ε_H and ε_h are the maximum and minimum horizontal tectonic strain, respectively. E_v is the vertical Young's modulus, E_h is the horizontal Young's modulus; ν_v is the vertical Poisson's ratio; and ν_h is the horizontal Poisson's ratio.

By assuming (Bishop, 1959):

$$P = S_w u_w + (1 - S_w)u_a \quad (3\text{-}19)$$

$$P_c = u_a - u_w \quad (3\text{-}20)$$

$$P = u_a - P_c S_w \quad (3\text{-}21)$$

where S_w is the water saturation and u_w, u_a and P_c are water pressure, gas pressure and capillary suction respectively. Then:

$$\sigma_h = \left[\frac{E_h}{E_v}\frac{\vartheta_v}{1-\vartheta_h}\right](\sigma_v - \alpha P_g + \alpha P_c S_w) + \frac{E_h}{1-\vartheta_h^2}\varepsilon_h + \frac{E_h\vartheta_h}{1-\vartheta_h^2}\varepsilon_H + \alpha P_g - \alpha P_c S_w \quad (3\text{-}22)$$

$$\sigma_H = \left[\frac{E_h}{E_v}\frac{\vartheta_v}{1-\vartheta_h}\right](\sigma_v - \alpha P_g + \alpha P_c S_w) + \frac{E_h}{1-\vartheta_h^2}\varepsilon_H + \frac{E_h\vartheta_h}{1-\vartheta_h^2}\varepsilon_h + \alpha P_g - \alpha P_c S_w \quad (3\text{-}23)$$

Rearranging:

$$\sigma_h = \left[\frac{E_h}{E_v}\frac{\vartheta_v}{1-\vartheta_h}\right](\sigma_v - \alpha P_g) + \alpha P_c S_w\left[\frac{E_h}{E_v}\frac{\vartheta_v}{1-\vartheta_h} - 1\right] + \frac{E_h}{1-\vartheta_h^2}\varepsilon_h + \frac{E_h\vartheta_h}{1-\vartheta_h^2}\varepsilon_H + \alpha P_g \quad (3\text{-}24)$$

$$\sigma_H = \left[\frac{E_h}{E_v}\frac{\vartheta_v}{1-\vartheta_h}\right](\sigma_v - \alpha P_g) + \alpha P_c S_w\left[\frac{E_h}{E_v}\frac{\vartheta_v}{1-\vartheta_h} - 1\right] + \frac{E_h}{1-\vartheta_h^2}\varepsilon_H + \frac{E_h\vartheta_h}{1-\vartheta_h^2}\varepsilon_h + \alpha P_g \quad (3\text{-}25)$$

Equation (3-24) and (3-25) indicate that in partially saturated media not only rock mechanical properties but also capillary suction would affect the overall stress state. Ignoring the changes in rock mechanical properties and capillary suction as a result of spontaneous imbibition and increasing water content would add uncertainty to stress measurements.

To assess the role of rock mechanical changes on in-situ stress measurements, the effective stress calculations based on the changes on rock mechanical properties of tested Montney samples are considered. Based on Equation (3-9) to (3-12) and Table 3-7 dynamic rock mechanical properties are converted to static values and then $\left[\frac{E_h}{E_v}\frac{\vartheta_v}{1-\vartheta_h}\right]$, $\frac{E_h}{1-\vartheta_h^2}$ and $\frac{E_h\vartheta_h}{1-\vartheta_h^2}$ terms have been calculated by first neglecting the effect of change in rock properties as a result of spontaneous imbibition and then considering those effects. Because of efficient water displacement during hydrocarbon migration stage, it is assumed that the water content of the tested Montney samples are close to irreducible water saturation (Wood, 2012). Also, pore pressure gradient of 17.2MPa/km for the Montney formation in Farrell Creek field (McLellan et al., 2014) were assumed. Even by ignoring the maximum and minimum horizontal tectonic strain terms, the effective stress values for the depth related to tested Montney samples would show at least 13.59% to 28.18% difference between the cases where the results of spontaneous imbibition are neglected and the cases where it is considered (Figure 3-42). This can lead to unrealistic stress and fracture geometry/propagation analysis as well as stress shadowing simulations. According to Narasimhan et al. (2015), 13-20% difference in calculated minimum horizontal stresses can lead to well integrity issues, predicting incorrect fracture geometry and communication between the child and the parent wells.

Table 3-8. Reduction in different terms of in-situ stress calculations (based on Equation(3-17) and (3-18)) as a result of spontaneous imbibition.

Sample No.	$\left[\frac{E_h}{E_v}\frac{\vartheta_v}{1-\vartheta_h}\right]$	Percentage of reduction (%)	$\frac{E_h}{1-\vartheta_h^2}$	Percentage of reduction (%)	$\frac{E_h\vartheta_h}{1-\vartheta_h^2}$	Percentage of reduction (%)
1 (dry)	0.55		48.91		13.76	
1 (wet)	0.46	16.07	33.63	31.27	10.11	26.56
2 (dry)	0.51		46.29		12.60	
2 (wet)	0.44	13.59	39.08	15.57	10.85	13.88
3 (dry)	0.49		48.06		12.99	
3 (wet)	0.39	20.47	32.49	32.39	9.056	30.30
4 (dry)	0.44		45.60		11.71	
4 (wet)	0.31	28.18	26.59	41.67	7.65	34.71
5 (dry)	0.41		46.76		11.44	
5 (wet)	0.35	14.68	31.77	32.06	8.67	24.17

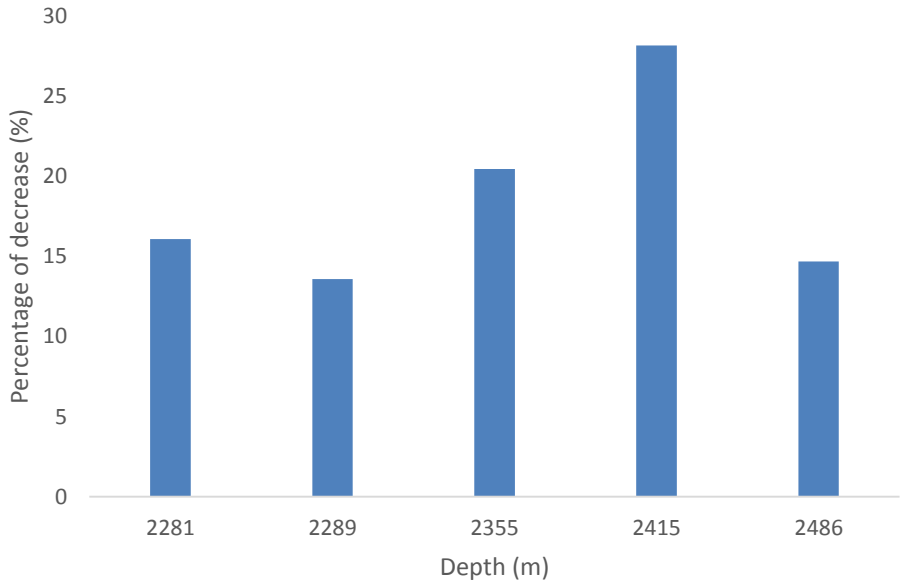

Figure 3-42. Reduction in in-situ stress calculation as a result of considering the effects of spontaneous imbibition.

3.2. Numerical Modeling

To investigate the possibility of micro fracture (failures) occurrence in triaxial conditions as a result of post-fracturing spontaneous imbibition, two three-dimensional fully coupled poro-elastoplastic partially saturated finite element models were developed using Abaqus/CAE. The first model is transversely isotropic (TVI) model which does not explicitly include bed structures but develops equivalent TVI properties based on parallel and perpendicular bedding structures. In the second numerical approach, a model is developed which explicitly includes the bed structure allowing them to be directly modeled with related rock mechanical and failure parameters assigned to each bed. The numerical analysis requires implementing the user defined subroutine (USDFLD) for Abaqus/CAE to achieve the water saturation and capillary suction dependency of rock mechanical properties and strength parameters. The subroutine USDFLD allows you to define field variables and can be used to introduce solution-dependent material properties since such properties can be defined as functions of field variables. This is a very critical step which adds complexities and challenges to numerical modeling. The aim to develop two different numerical modeling approaches in this chapter is to compare the results that can be obtained from them and evaluate which of them is appropriate for the scale that we are investigating. Since all of the input parameters for the numerical modeling of the Montney samples are not available in this chapter, the input parameters including rock mechanical properties, strength parameters and suction pressure as a function of water saturation are based on Vale's et al. (2004) experiments.

3.2.1. Transversely Isotropic Model (TVI)

Transversely isotropic is a special subclass of orthotropic behavior which is defined by the same properties in one plane and different properties in the direction normal to this plane. Thus, the compliance matrix would be as below (Abaqus (2017)).

$$\begin{Bmatrix} \varepsilon_{xx} \\ \varepsilon_{yy} \\ \varepsilon_{zz} \\ \varepsilon_{xy} \\ \varepsilon_{xz} \\ \varepsilon_{yz} \end{Bmatrix} = \begin{bmatrix} \frac{1}{E_p} & \frac{-\nu_p}{E_p} & \frac{-\nu_{tp}}{E_t} & 0 & 0 & 0 \\ \frac{-\nu_p}{E_p} & \frac{1}{E_p} & \frac{-\nu_{tp}}{E_t} & 0 & 0 & 0 \\ \frac{-\nu_{pt}}{E_p} & \frac{-\nu_{pt}}{E_p} & \frac{1}{E_t} & 0 & 0 & 0 \\ 0 & 0 & 0 & \frac{1}{G_p} & 0 & 0 \\ 0 & 0 & 0 & 0 & \frac{1}{G_t} & 0 \\ 0 & 0 & 0 & 0 & 0 & \frac{1}{G_t} \end{bmatrix} \begin{Bmatrix} \sigma_{xx} \\ \sigma_{yy} \\ \sigma_{zz} \\ \sigma_{xy} \\ \sigma_{xz} \\ \sigma_{yz} \end{Bmatrix}$$

where p and t stand for in-plane and transverse, $G_p = E_p/2(1+\nu_p)$ and $\nu_{tp}/E_t = \nu_{pt}/E_p$. Therefore, the total number of independent constants is five. The rock mechanical properties and strength parameters for transversely isotropic model are shown in Table 3-9.

Table 3-9. Rock mechanical properties and strength parameters as a function of water saturation and suction pressure for TVI model (Vale's et al., 2004).

Saturation	E ∥* (GPa)	E ⊥* (GPa)	ν ∥	ν ⊥	G_t (GPa)	C ∥ (MPa)	φ ∥	UCS ∥ (MPa)	P_c (MPa)
0.2	40	8.3	0.19	0.10	9.2	6.5	64.1	79.5	319.8
0.45	30.8	11.4	0.20	0.11	6	5.4	62.5	60	142.9
0.6	17.5	11.4	0.22	0.13	4.9	5.3	64.3	59.7	97
0.85	18.9	5.5	0.42	0.18	3.9	6.9	51.1	46.1	38.4
0.9	20.3	4.4	0.49	0.22	3.4	5.3	60.4	50.3	2.8
1	21.8	6.2	0.49	0.39	3	5.7	57.7	44.9	0

* ∥ and ⊥ means parallel and perpendicular to the beds, respectively.

Suction pressure for the fully saturated case was assumed to be zero. Although the suction pressure was reported as >419MPa for 0.2 water saturation by Vale's et al. (2004) but suction pressure for 0.2 water saturation was obtained from the correlation among the suction pressure values of 0.45, 0.6, 0.85, 0.9 and 1 water saturation addressed by Vale's et al. (2004) as shown in Figure 3-43.

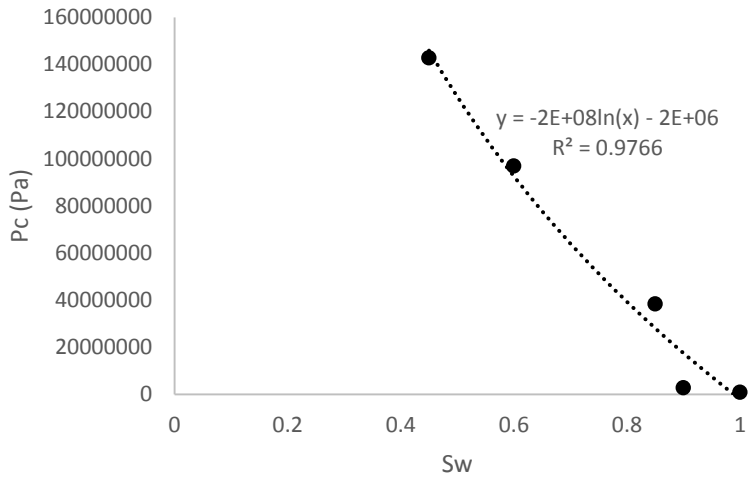

Figure 3-43. Correlation between water saturation and capillary suction pressure based on Vale's et al. (2004) experiments.

Also, the porosity was reported to be between 6.5% and 7.1% (Cabrera Nunez et al., 2001). For the simulation study, an average value of 6.8% was chosen. The permeability parallel and perpendicular to the beds was considered 4.88E-19 m^2 and 1.41E-19 m^2 , respectively (Nasseri and Young, 2016) and an average Biot's coefficient of 0.3 was assumed (Cosenza et al., 2002). The depth considered was 2000m while the overburden stress gradient was assumed to be 25MPa/km and the pore pressure gradient was assumed to be 13.5MPa/km (Zhang, 2019). Then, based on Equation 3-17 and neglecting ε_h and ε_H, the value of minimum horizontal stress was calculated to be 35.7MPa. The sample size in the numerical model is the same as Vale's et al. (2004) experiments which is 3.6cm by 7.2cm. A Drucker-Prager failure criteria was chosen and the boundary condition (as shown in Figure 3-44) is in such a way that the water is imbibed from the bottom surface through a pressure difference. In other words, a capillary suction pressure

(negative pore pressure) is defined inside the sample and in the bottom surface boundary 10Pa pressure is defined. As long as there is a pressure difference, the water is imbibed into the sample.

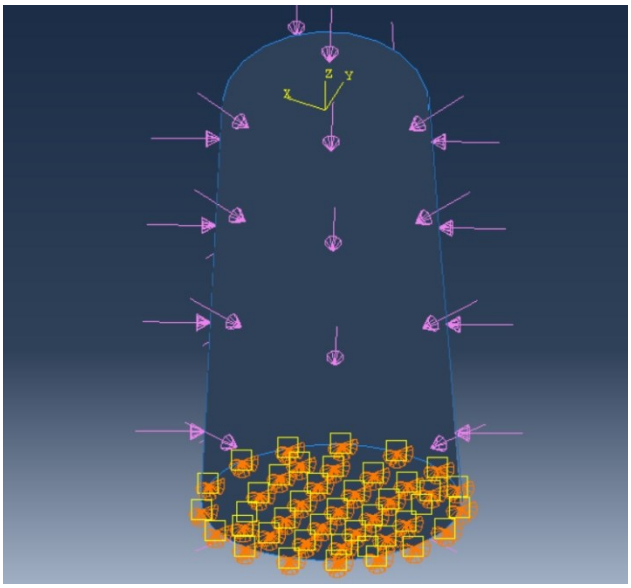

Figure 3-44. Boundary conditions of TVI model.Purple arrows indicate the loading on the sample and orange arrows show a pinned (zero deformation) boundary condition (U1=U2=U3=0).

As shown in Figure 3-45 as spontaneous imbibition is occurring, induced stress development can be observed especially near the region with 0.2-0.45 water saturation values which would affect the elastic strain values in transverse and in-plane directions (Figure 3-46) but does not result in plastic strain (failure). The former can be attributed to the effective stress reduction as a result of capillary suction decrease and water saturation increase as well as different rock mechanical properties at each water saturation level. One of the issues that cannot be addressed effectively during simulations adopting a TVI approach is lack of information on the interface between the beds, which is likely a weak plane where failure mechanisms can initiate.

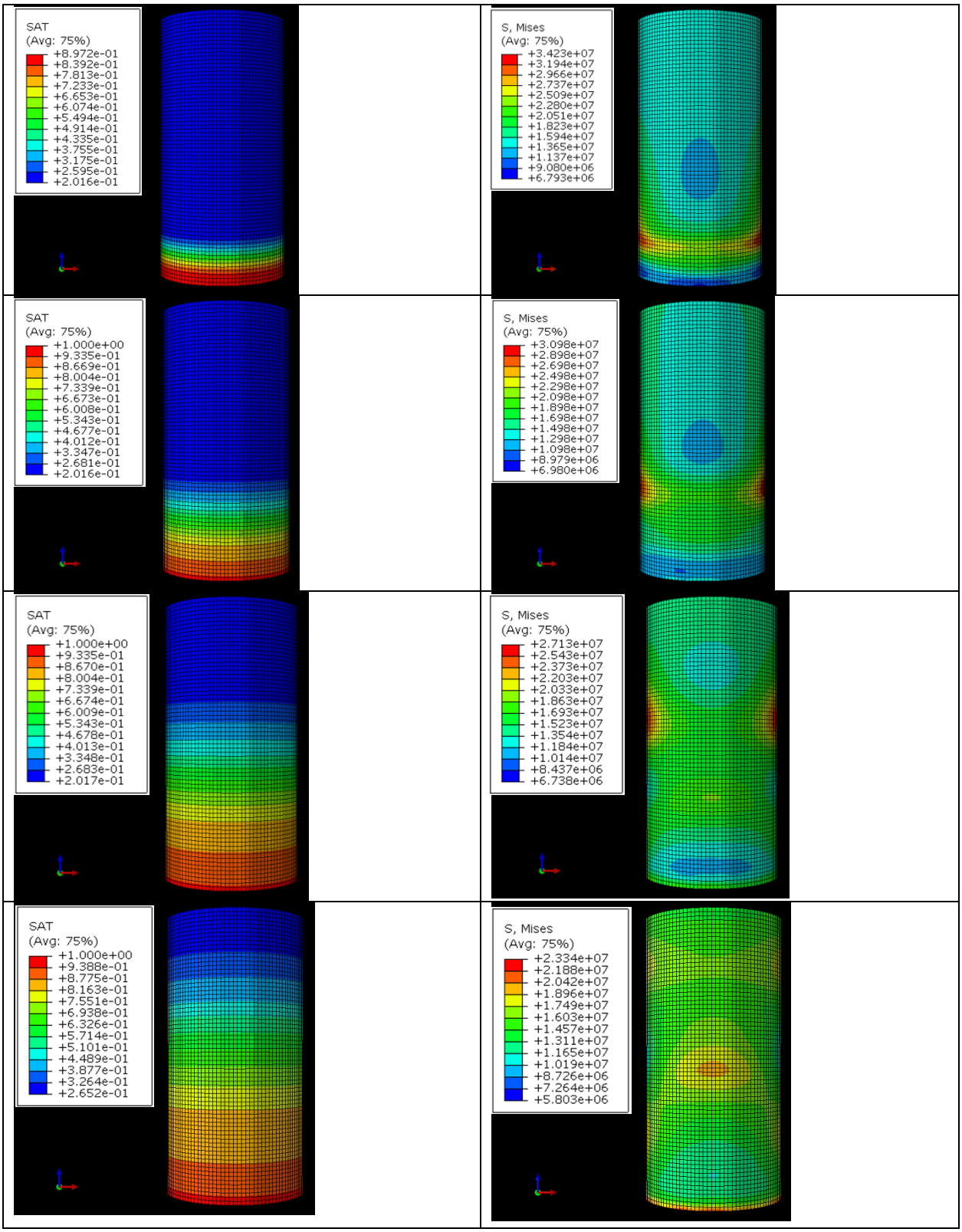

Figure 3-45. Changes in water saturation (on the left) and Mises stress (Pa) (on the right) during spontaneous water imbibition.

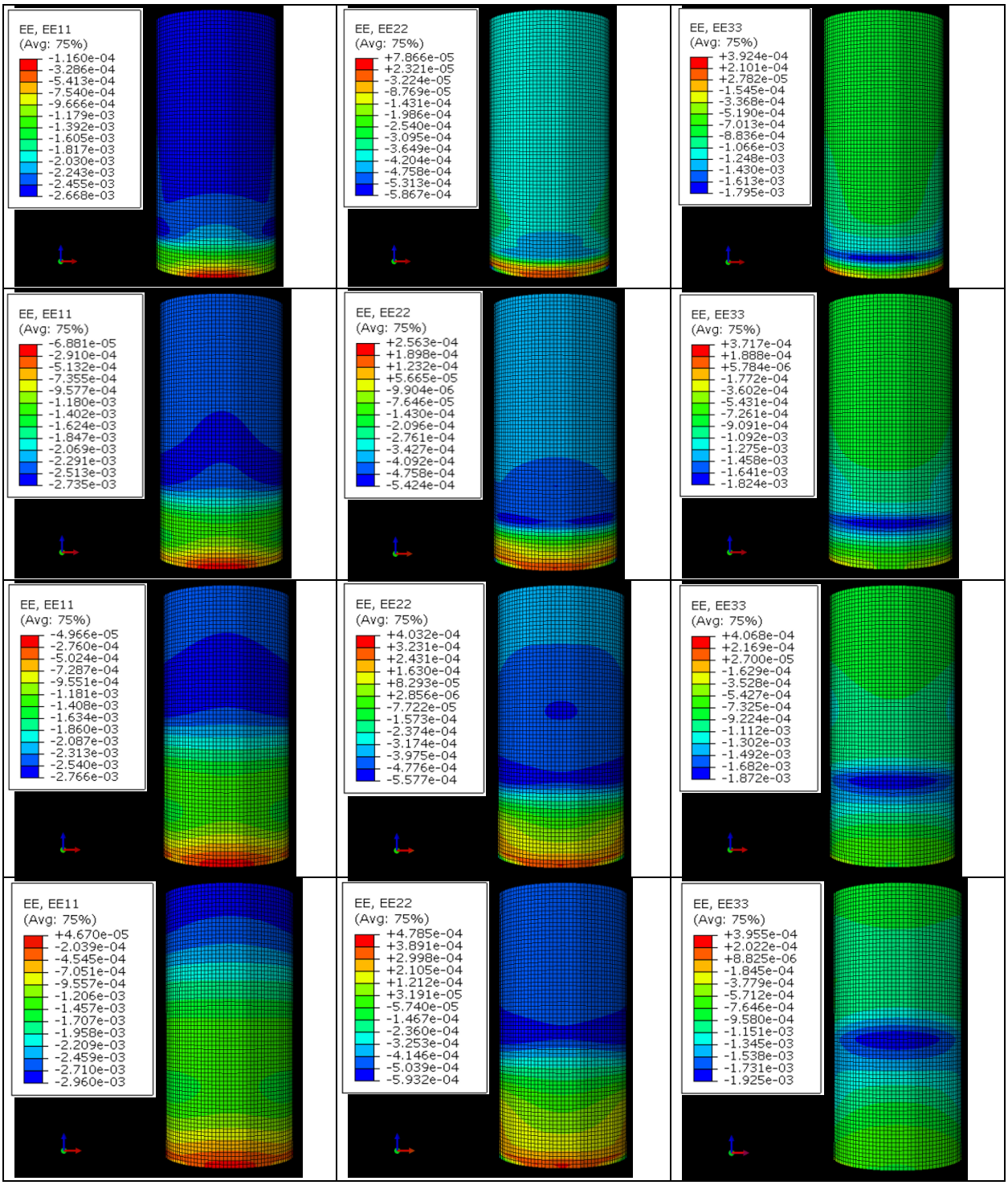

Figure 3-46. Changes in elastic strain values during spontaneous water imbibition: E11 (on the left), E22 (in the middle) and E33 (on the right).

Although the TVI approach did not explicitly include the interface between the beds, the development of shear stress along the interface plane between the beds within the model may still provide insight into the potential for failure along these interfaces. Since the normal direction relative to the interface between the beds would be "x" direction, the shear stress S12 and S13 which are shear stresses in "xy" and "xz" direction are considered and the resultant of these two vectors, which are perpendicular to each other, provide a proxy to investigate potential failure along the interface between the beds. Figure 3-47 depicts how S12 and S23 vary as spontaneous water saturation occurs. The induced shear stress can be related to the change in effective stress as well as different rock mechanical responses in transverse and in-plane directions. As the water saturation in the media is increasing the values of S12 and S13 decrease, which can be related to lower differences in the values of rock mechanical properties in higher water saturation levels. Based on the numerical analysis, the maximum value for S12 of 8.61MPa was observed at 0.38 water saturation. At the same time increment the maximum value for S13 was 4.83MPa, which means that the resultant shear stress would be 9.87MPa. In addition, based on to Equation (3-21) the gas phase pressure was estimated and then used for the calculation of shear strength of the interface between the beds (Equation (3-15)). The cohesion and friction angle of the interface was assumed to be respectively 50% and 75% of the cohesion and friction angle shown in Table 3-9. Figure 3-48 shows the shear strength of the interface between the beds in different water saturation degrees. According to Figure 3-48 and based on the results obtained from TVI numerical model no failure would be expected to happen since the shear strength of the interface in all saturation levels were higher than the maximum shear stress obtained in the numerical model.

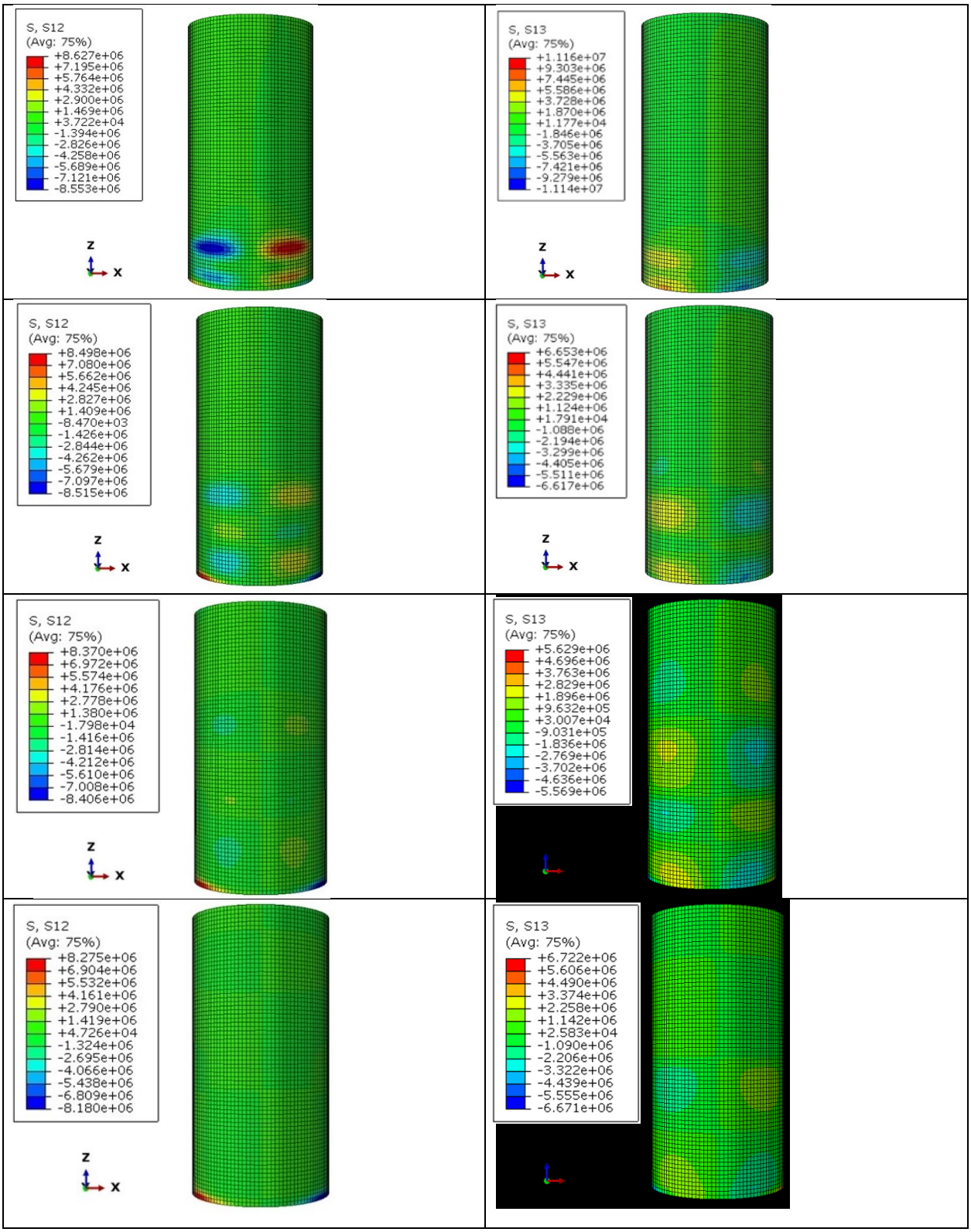

Figure 3-47. Induced shear stress (Pa) values during spontaneous water imbibition: S12 (on the left) and S13 (on the right).

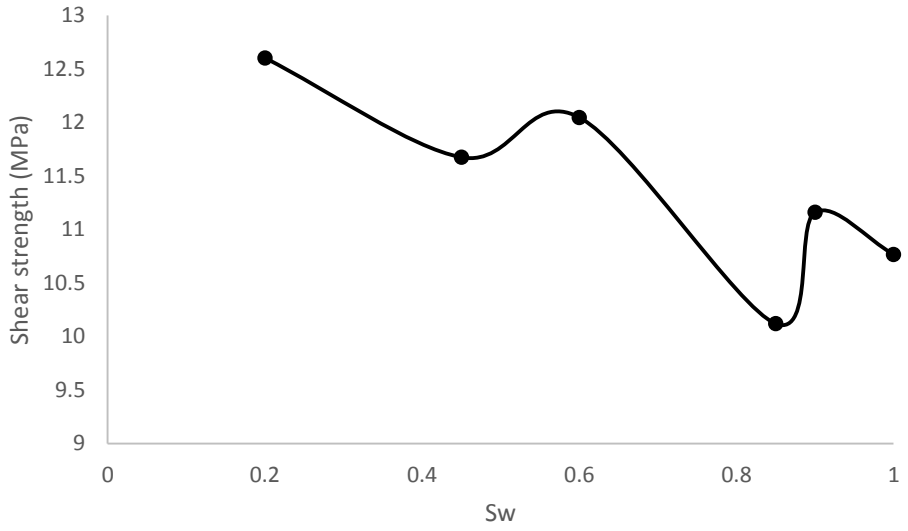

Figure 3-48. Shear strength calculated for the interface between the beds in different water saturation degrees.

3.2.2. Beds-Included Model

The "Beds-Included" model have the beds physically and individually modeled. To model the beds, it was assumed that the sample in Vale's et al. (2004) experiments had three 1mm individual beds (beds A) which were surrounded by other type of beds (beds B) as shown in Figure 3-49.

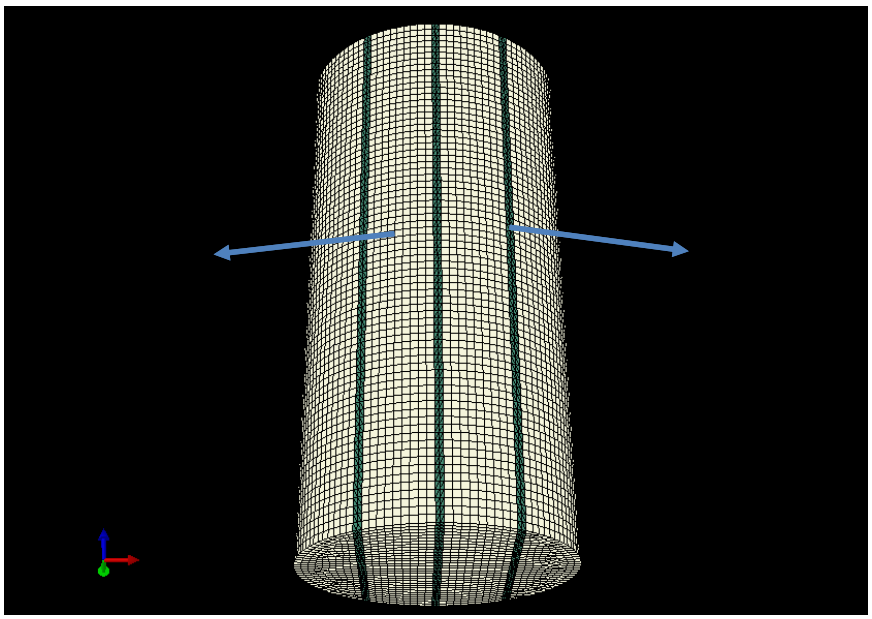

Figure 3-49. Geometry of the model in beds-included approach.

Also, it was assumed that each bed type would have different rock properties. To assign rock properties to each bed Ligang et al. (2017) approach was considered to determine Young's modulus and Poisson's ratio. Based on Ligang et al. (2017) approach, Young's modulus (E_r) and Poisson's ratio (v_r) of layered rock mass (E_r) with parallel beds would be determined by Equation (3-26) and (3-27).

$$E_r = E_1 \frac{h_1}{h} + E_2 \frac{h_2}{h} + E_3 \frac{h_3}{h} + \cdots + E_n \frac{h_n}{h} \tag{3-26}$$

$$v_r = v_1 \frac{h_1}{h} + v_2 \frac{h_2}{h} + v_3 \frac{h_3}{h} + \cdots + v_n \frac{h_n}{h} \tag{3-27}$$

where E_i (i = 1, 2, . . . , n) and v_i (i = 1, 2, . . . , n) are the Young's modulus and Poisson's ratio, of i layer, h is the sum thickness of the layers and hi (i = 1, 2, . . . , n) is the thickness of i layer. The total thickness of beds "A" and "B" constituted 11% and 89%, respectively, of the total thickness of the sample. Assuming that beds "A" were stiffer than beds "B" the values, the rock mechanical properties in beds "A" and beds "B" used in the modeling are provided in Table 3-10. Also, it was assumed that porosity in beds "B" was 0.06 and then based on the volumetric portions of beds "A" and "B" and considering the total porosity as 0.068, the porosity in beds "A" were 0.133. For permeability, according to the permeability value for parallel sample (4.88E-19 m^2) it was assumed that the permeability in beds "B" was 3.5E-19 m^2 and then based on $K_{avg} = \frac{\sum_{i=1}^{n} K_i A_i}{A_t}$ (where A_i is the cross section area of layer (i)) the permeability in beds "A" was calculated as 1.6E-18 m^2. Regarding capillary suction values, it was assumed that beds "B" had the capillary suction of 350MPa and then based on J-function concept (Equation 3-28) proposed by Leverett (1941) the value of capillary suction for beds "A" was calculated as 169.9MPa (Equation 3-29). The same procedure was done to capture the capillary suction values in different saturation levels.

$$J(S_w) = \frac{P_c(S_w)}{\sigma cos\theta} \sqrt{\frac{k}{\varphi}} \tag{3-28}$$

where $J(S_w)$ is the J-function, S_w is the wetting-phase saturation, $P_c(S_w)$ is the capillary pressure, σ is the interfacial tension, θ is the contact angle, k is permeability, and φ is porosity. Assuming beds "A" and "B" would have the same $J(S_w)$, σ and θ Equation (3-28) can be rewritten as Equation (3-29).

$$\frac{P_{c\,(B)}(S_w)}{P_{c}\,(A)(S_w)} = \sqrt{\frac{k_{(A)}\varphi_{(B)}}{k_{(B)}\varphi_{(A)}}} \tag{3-29}$$

Table 3-10. Rock mechanical properties of beds "A" and "B" as a function of water saturation and capillary suction.

Saturation	$E_{(A)}$ (GPa)	$E_{(B)}$ (GPa)	$\nu_{(A)}$	$\nu_{(B)}$	$P_{c\,(A)}$ (MPa)	$P_{c\,(B)}$ (MPa)
0.2	54.8	38	0.21	0.196	169.9	350
0.45	42.3	29.3	0.22	0.20	75.9	156.3
0.6	24.1	16.7	0.24	0.23	51.5	106.1
0.85	25.9	18	0.45	0.42	20.4	42
0.9	27.8	19.3	0.49	0.48	1.4	3.1
1	29.9	20.7	0.49	0.49	0	0

In addition, strength parameters of beds "A" and "B" were assumed to be as shown in Table 3-11 which was related to the strength parameters of perpendicular and parallel samples in Vale's et al. (2004) experiments. The boundary condition of beds-included model was the same as transversely isotropic approach.

Table 3-11. Strength parameters of beds "A" and "B" as a function of water saturation.

Saturation	$C_{(A)}$ (MPa)	$C_{(B)}$ (MPa)	$\varphi_{(A)}$	$\varphi_{(B)}$	$UCS_{(A)}$ (MPa)	$UCS_{(B)}$ (MPa)
0.2	11	6.5	64.1	56.5	70.4	79.5
0.45	7.7	5.4	62.5	64.1	91.4	60
0.6	8.4	5.3	64.3	60.7	69.6	59.7
0.85	7.5	6.9	51.1	51.4	44.6	46.1
0.9	7.3	5.3	60.4	49.5	40.4	50.3
1	4.7	5.7	57.7	54.6	35	44.9

One of the first issues that could be observed in beds-included numerical model was the difference of water elevation in beds "A" and "B" which would generate stress gradient. In other words, as it is illustrated in Figure 3-50 water saturation in beds "B" was higher than beds "A" which resulted in stress development along the beds and the interface between the beds. Figure 3-51 shows water saturation degrees in beds "A" and "B" at certain time increments. According to Figure 3-50 and Figure 3-51, the stress development was originated from the local difference of effective stress values in beds "B" and "A" which was a result of different water saturation and the relevant capillary suction values that based on Equation (3-14) would affect the local effective stress along beds "A" and "B".

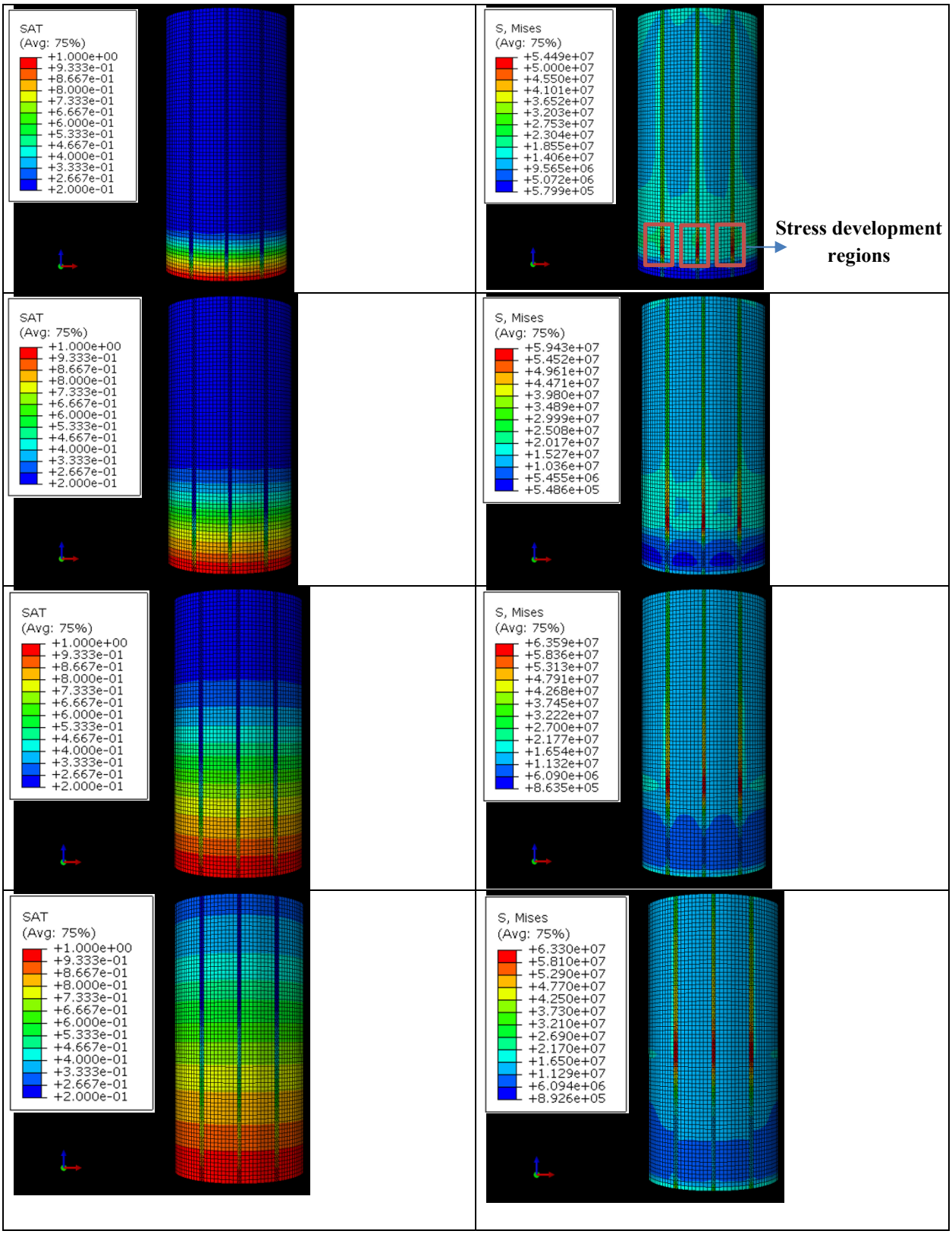

Figure 3-50. Changes in water saturation (on the left) and Mises stress (Pa) (on the right) in beds "A" and "B" during spontaneous water imbibition.

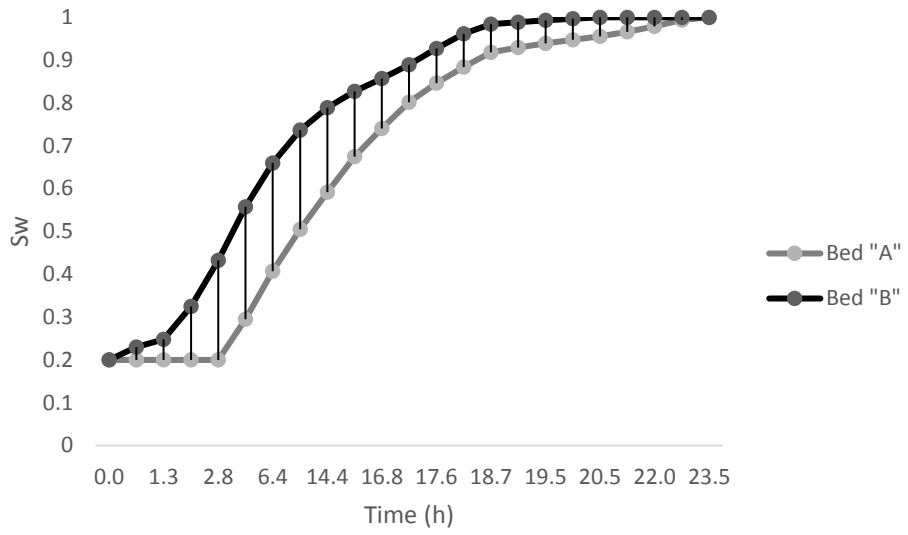

Figure 3-51. Water saturation in beds “A” and “B” in different time increments.

The generation of varying local-scale effective stresses along beds “A” and “B” would lead to differential local-scale volumetric response which can trigger the failure especially along the interface between the beds. Simulation results from the beds-included model indicate that no plastic strain was observed along the beds “A” and “B” but as the water saturation was changing in beds “A” and “B” during spontaneous water imbibition, the values of elastic strain also changed (Figure 3-52). To better investigate the volumetric response of beds “A” and “B” in certain time increments, the values of volumetric strain were represented in Figure 3-53 which shows that volumetric responses in beds “A” and “B” were indeed different. In addition, Figure 3-54 illustrates how the differential water saturation (difference between water saturation in beds “A” and “B” at the same elevation) and differential volumetric strain (difference between volumetric strain in beds “A” and “B” at the same elevation) can be related. According to Figure 3-54, the highest differential volumetric strain was related to the case where beds “A” had water saturation of 0.2 and in the same elevation the water saturation of the elements in beds “B” were 0.43 (differential water saturation of 0.23). In other words, capillary suction in beds “B” which was initially 350MPa reached 176.4MPa (49.6% reduction) but the capillary suction in beds “A” did not change. This means that locally the effective stress values in beds “A” and “B” changed differently followed by differential volumetric strain in the adjacent beds which would induce the shear stress especially near the interface between the beds.

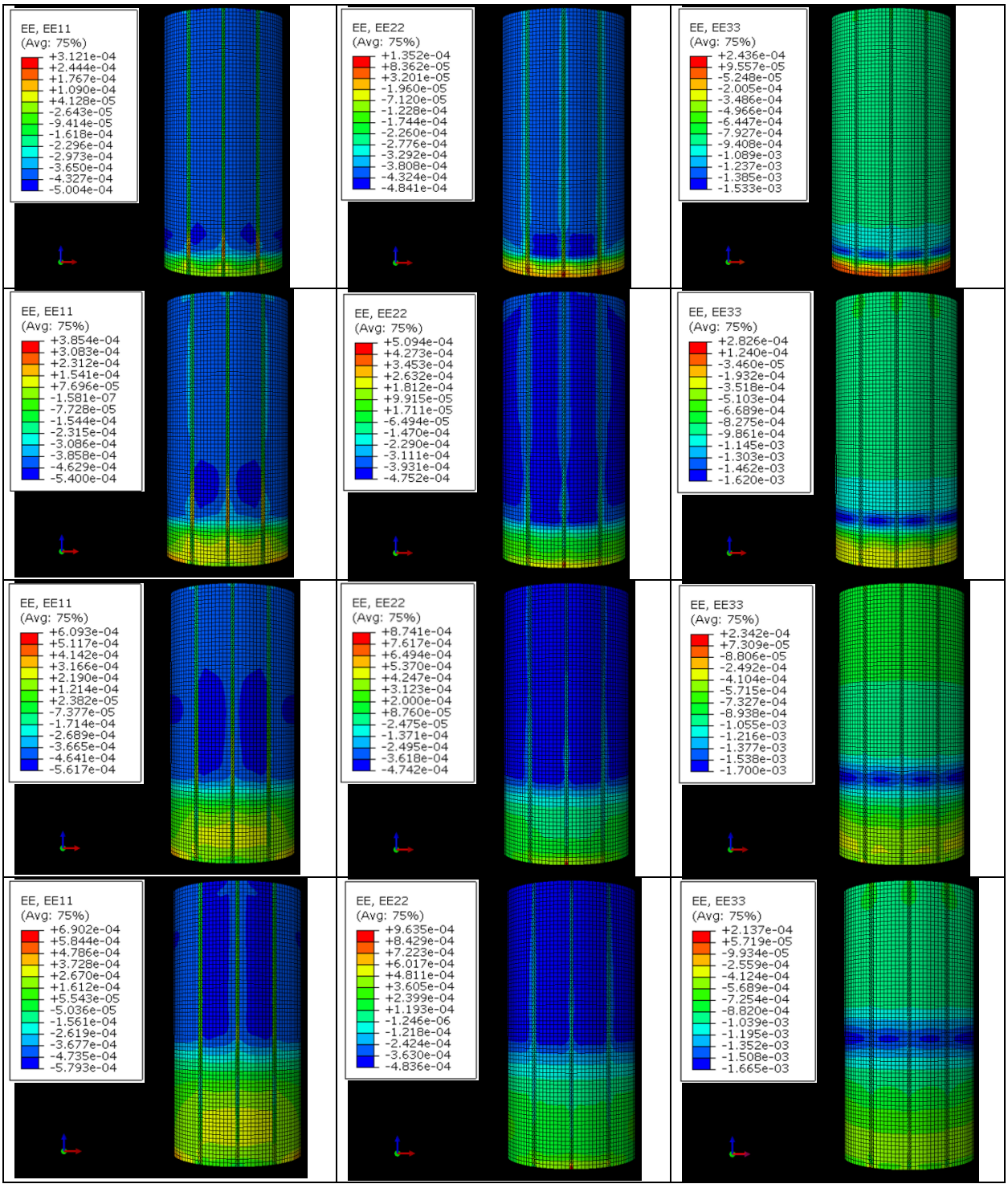

Figure 3-52. Changes in elastic strain values along beds “A” and “B” during spontaneous water imbibition: E11 (on the left), E22 (in the middle) and E33 (on the right).

As it is indicated in Figure 3-54, in the initial stages of spontaneous water imbibition where the water front and water saturation in beds “B” were higher than beds “A”, beds “B” would play a key role to induce shear stress especially near the interface between the beds. Oppositely, as the water saturation in beds “B” was increasing and the capillary suction was decreasing with a higher rate than beds “A”, it was time for beds “A” to gradually start to dominate the shear stress induction. Figure 3-55, depicts how dominating shear stress components (S12 and S13) were developing during spontaneous water imbibition.

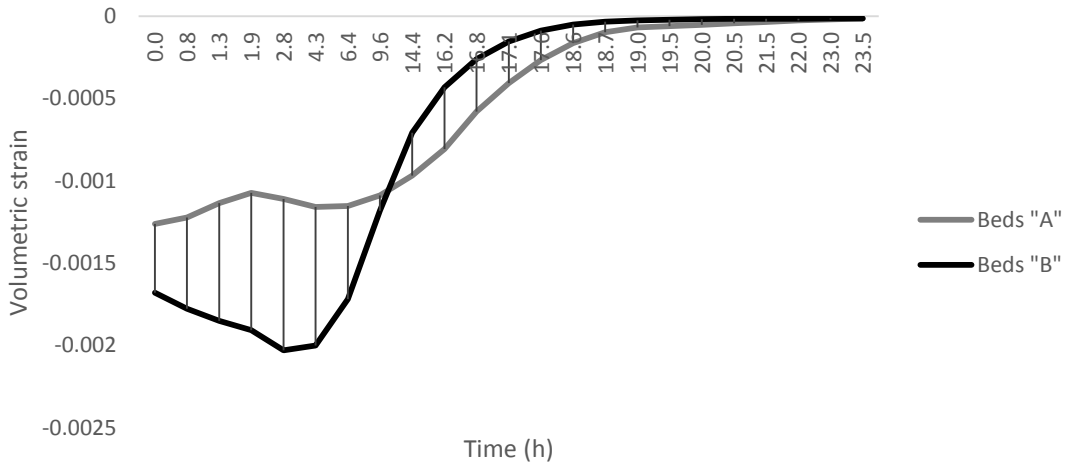

Figure 3-53. Volumetric strain of beds “A” and “B” in different time increments.

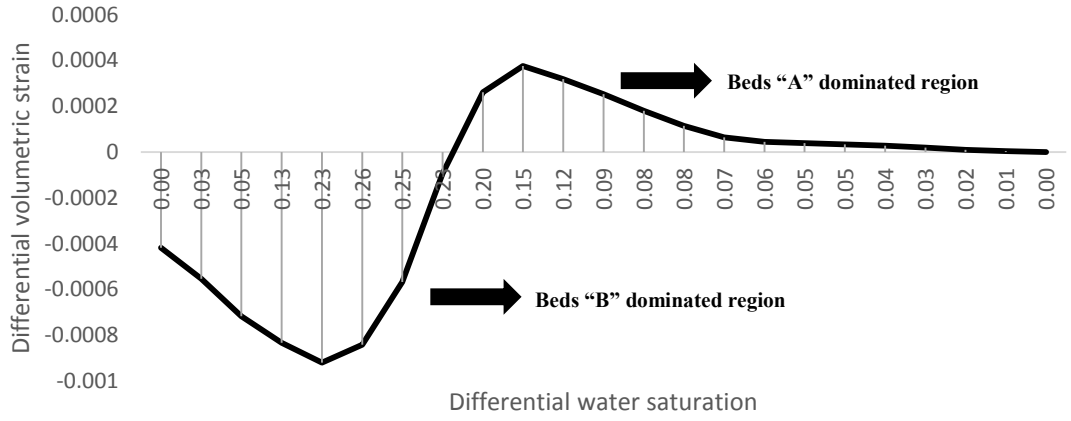

Figure 3-54. Changes in differential volumetric strain as a function of differential water saturation during spontaneous water imbibition.

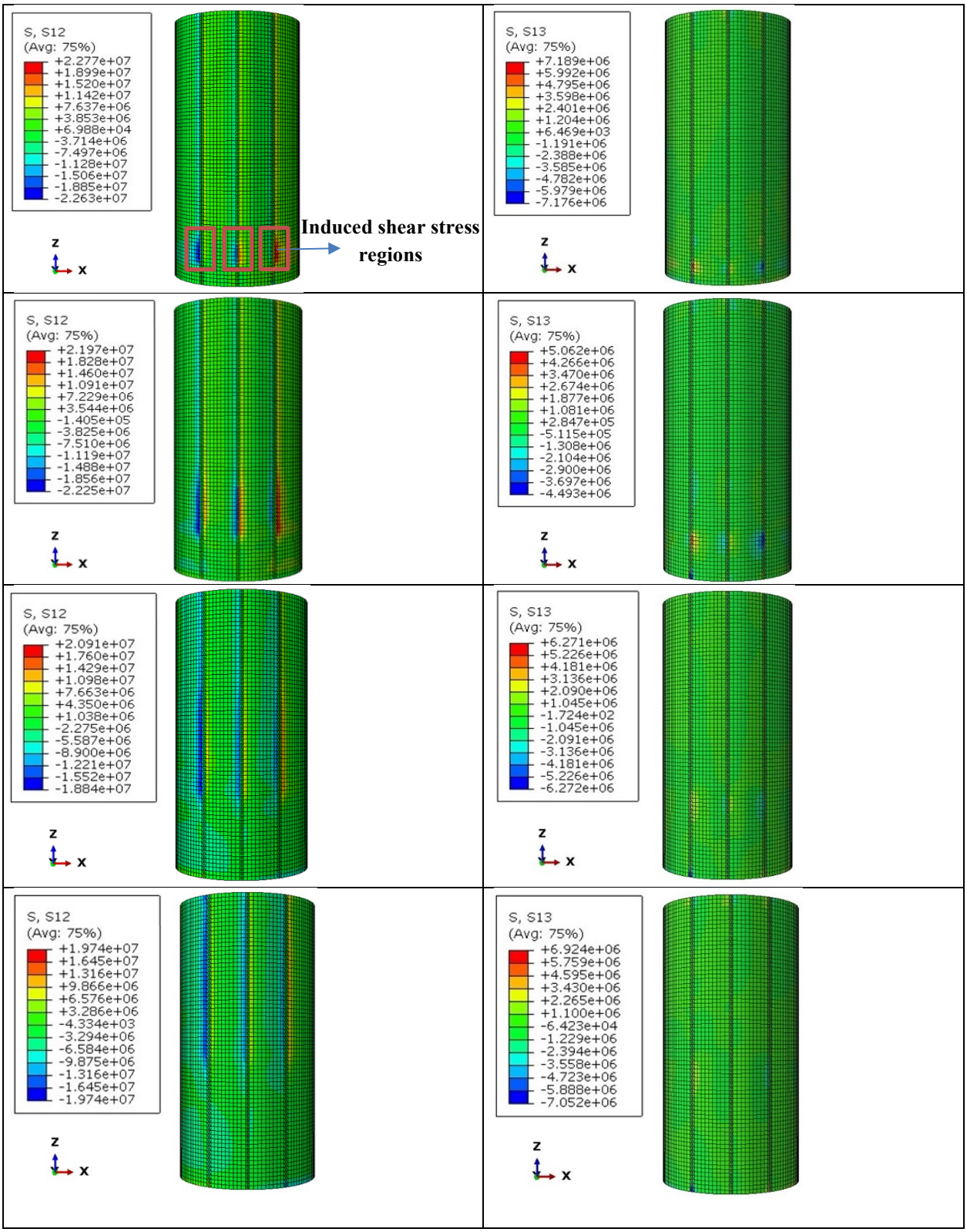

Figure 3-55. Induced shear stress values (Pa) along beds "A" and "B" and the interface between them during spontaneous water imbibition: S12 (on the left) and S13 (on the right).

The simulation results shown in Figure 3-55 indicate that as a result of spontaneous water imbibition, shear stress would be induced in the media especially near the interface between the beds where the volumetric strain on both sides of the interface are different. Shear stress induced along the interface was higher in the "Beds "B" dominated region" than "Beds "A" dominated region" (shown in Figure 3-54) and as the water saturation in beds "A" and "B" were getting closer to each other in higher water saturation levels, induced shear stress along the interface between the beds reduced significantly (shown in Figure 3-55) which could be related to lower differential volumetric strain. During spontaneous water imbibition in "Beds "B" dominated region" maximum value of S12 was 19.6MPa in different time increments while it was 3.2MPa for S13. The maximum values of total shear stress in each time increment were related to the regions along the interface where the maximum differential volumetric strain took place (Figure 3-56).

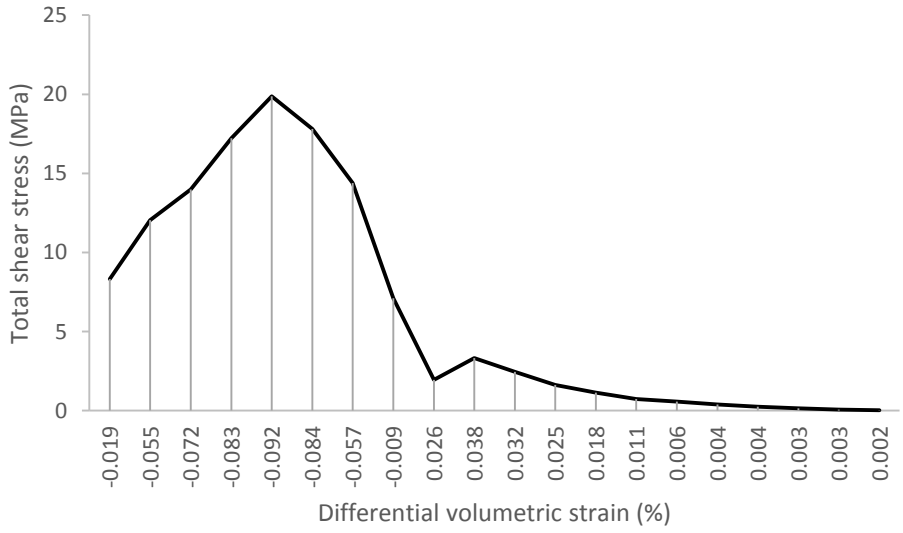

Figure 3-56. Total shear stress along the interface between the beds as a function of differential volumetric strain.

According to Figure 3-56 and based on the results obtained from beds-included numerical model the maximum value of total shear stress along the interface (19.86 MPa) were higher than shear strength of the interface between the beds (shown in Figure 3-48) which implied that failure would occur along the interface during spontaneous water imbibition.

3.3. Summary

Experimental and analytical analysis have been performed on Montney samples from different depths to investigate the role of spontaneous imbibition on geomechanical parameters and how the changes may affect the rock behavior. Two numerical approaches have been developed and analyzed to deal with micro fracture (failure) generation during spontaneous water imbibition in triaxial conditions. The results reveal that:

- Capillary suction measurements on 46 Montney samples from different depths indicate that the values of capillary suction differs from depth to depth.
- Capillary suction and pre-existing/induced micro fractures (which is a function of the number of beds) are working together for water uptake during spontaneous imbibition.
- Based on the ultrasonic wave measurements during spontaneous imbibition, the rate of changes in wave velocities is more significant parallel to the beds which can be attributed to induced micro fractures (both longitudinal and transverse fractures) and more water uptake.
- The rate of dynamic Young's modulus and shear modulus reduction during spontaneous imbibition in parallel samples are 2 to 5 times higher than perpendicular samples.
- The highest and lowest reduction in dynamic Young's modulus (42.72% and 2.1%) and shear modulus (43.94% and 2.32%) are related to the samples with the highest and lowest number of beds and volume imbibed, respectively.
- As the water content is increasing, dynamic Poisson's ratio parallel and perpendicular to the beds would generally increase which can be attributed to generation of longitudinal and transverse micro fractures followed by water uptake.
- Brittleness index in both perpendicular and parallel samples are decreasing as the water content is increasing while the rate of decrease is higher in parallel samples.
- Capillary suction would give apparent stiffness and strength to the rock. Decreasing capillary suction as a result of spontaneous imbibition would result in decreasing effective stress and total cohesion which can shift Mohr- Coulomb circle to the left and failure envelope downward followed by increasing the possibility of failure occurrence (micro fracture generation and propagation).

- It can be suggested that the volumetric response of different components (such as beds) as a result of interaction with water may not be the same which can contribute to trigger shear failure in the planes of weaknesses (such as the interface between the beds).
- Ignoring the changes in rock mechanical and capillary suction as a result of spontaneous imbibition would lead to miscalculations in stress measurements and fracability analysis.
- Beds-included numerical approach gives better analysis options than transversely isotropic approach to investigate the failure occurrence during spontaneous water imbibition. Beds-included numerical modeling shows the stress development and any possible failure especially along the interface between the beds (as a result of different water levels and capillary suctions in the adjacent beds) which is not possible to get captured in transversely isotropic approach.
- According to beds-included numerical model, as a result of different water front, water saturation and capillary suction values at the same elevation in the adjacent beds, different volumetric responses were observed that resulted in differential volumetric strain.
- Beds-included model indicated that differential volumetric strain would induce shear failure especially along the interface between the beds (known as a weak plane) which triggered the failure and micro fracture generation during spontaneous water imbibition.

Chapter 4 : Reservoir Geomechanical Analysis of Spontaneous Imbibition in Tight Formations: Bed-scale Characterization

The results of spontaneous imbibition tests on Montney samples indicate that the mechanisms through which rock behavior may be altered can initiate at the scale of bedding structures. Investigating the changes in the behavior of bedded, partially saturated tight rocks as a result of spontaneous water imbibition, an integrated workflow is defined (Figure 4-1). To determine reservoir geomechanical properties at the bed-scale, an integrated experimental and analytical approach for small-scale characterization of partially saturated porous media has been developed. To quantify bed scale mineralogy, Quantitative Evaluation of Materials by Scanning Electron Microscopy (QEMSCAN) analyses were completed followed by nitrogen adsorption–desorption isotherms tests to assess the pore size distribution and pore shape and porosity within individual beds. Thermogravimetric analysis (TGA) was done to measure the initial saturation of the beds. To determine the capillary suction over a range of fluid saturations, capillary condensation tests were conducted. For micro-geomechanical measurements, analytical solutions for micro-indentation and micro-scratch tests were developed and combined with experimental results to compute the rock mechanical and strength properties of the beds at different fluid saturations. To measure the permeability at the bed-scale, pressure decay and pulse decay tests were conducted for unconfined and confined conditions, respectively. Also, to determine the strength parameters of the interface between the beds in different saturations, direct shear tests were done. The results indicate that the beds have different properties, and they would show different behaviors as a result of increasing water saturation which can initiate a range of micro-geomechanical behavior and trigger failure processes (e.g., fracture generation).

es in the behavior of bedded, partially saturated

imbibition.

4.1. Laboratory Experiments

4.1.1. Specimen Description and Preparation

Specimens for bed-scale analysis and measurements are from the Montney Formation in Farrell Creek field, northeast British Columbia. Test specimens were taken from a core sample recovered from a depth of 2415 to 2416m. The bedded structure of the Montney Formation at a depth of 2415 to 2416m is shown in Figure 4-2.

.

Figure 4-2. Montney core from depth 2415m for bed-scale measurements and analysis.

Samples parallel and perpendicular to beds were cut from the core using a 1cm coring bit and air circulation. Air was used instead of water because water would weaken the core and significantly increase the possibility of micro fracture generation. Coring with air has its own challenges such as cooling the bit and selection of an appropriate air pressure during coring. All samples were cut and end faces leveled by surface grinder to prepare 1cm (diameter) to 1cm (height) samples (Figure 4-3)

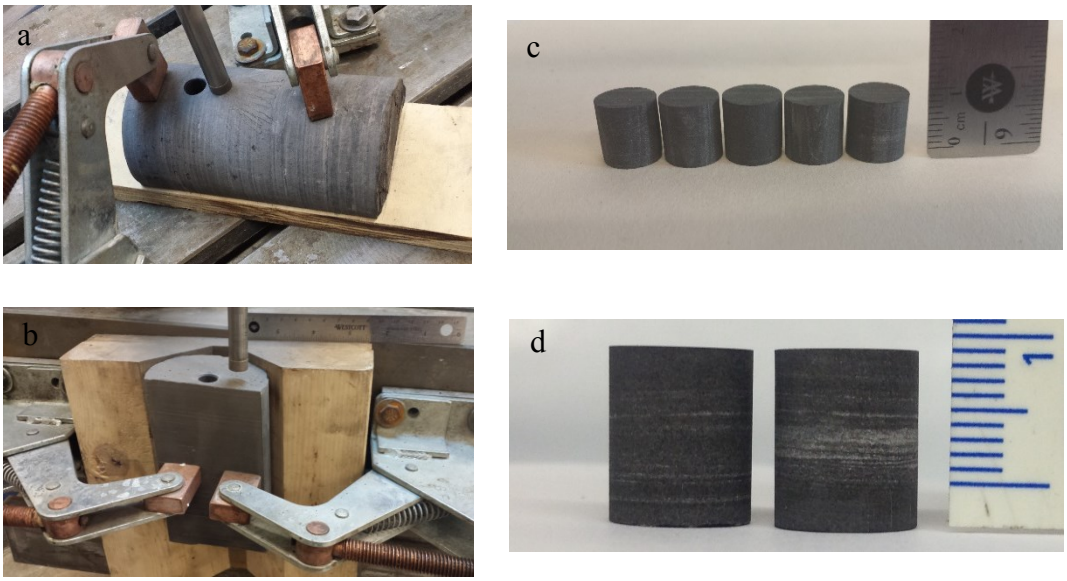

Figure 4-3. Coring parallel and perpendiculat to the beds and preparing 1cm to 1cm samples.

All samples were cut from a core at a depth of 2415m to 2416m to minimize any negative effect of larger scale heterogeneity on the measurements and subsequent analyses. Samples chosen for bed-scale measurements were selected from the same core slab or from the nearest core slab. For micro-indentation and micro-scratch tests on different beds (where the surface should be as smooth as possible) three levels of dry polishing after grinding were performed. This includes polishing on a rotating disk with sandpaper P600 (extra-fine (25.8µm)), P1200 (super-fine (15.3µm)) and P4000 (ultra-fine (2.5µm)). After sample preparation they were dried in the oven following ASTM D2216-19 standards. For nitrogen adsorption–desorption isotherms and TGA tests (where crushed samples <0.5cm from the beds were considered), first white and dark beds were cut and detached from the core and then they were crushed (Figure 4-4). For pressure-decay profile permeameter

test a piece of core slab was used. Sample for pulse-decay permeability measurements were cored with 2.54cm coring bit and then it was cut and leveled to reach 0.254cm in height (Figure 4-5). Capillary condensation experiments were performed on beds and 1cm to 1cm samples (with high and low number of beds) (Figure 4-3). Sample preparation and test procedure for direct shear tests followed ASTM D5607-16 standards. Since the diameter of parallel and perpendicular samples were 1cm, they were cut and leveled by surface grinder to reach to 0.5cm as shown in Figure 4-6.

a) b) c)

Figure 4-4. Bed-scale sample preparation for nitrogen adsorption–desorption isotherms and TGA tests. a) detaching the beds; b) crushed white color bed; c) crushed dark color bed.

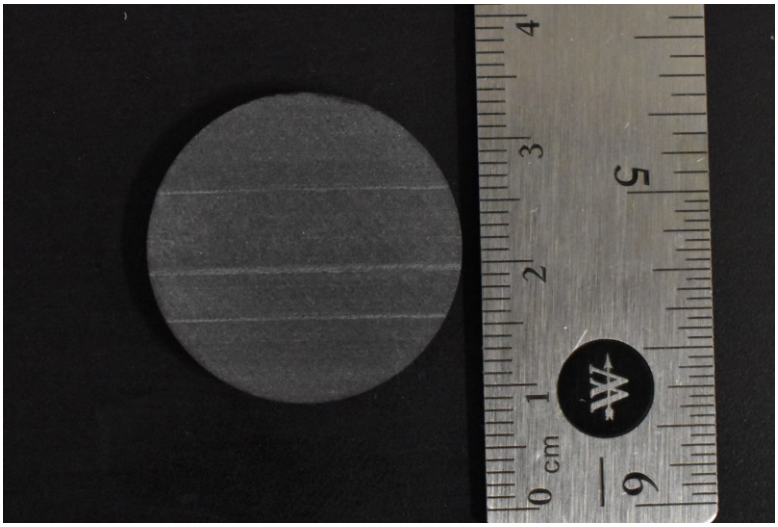

Figure 4-5. Sample for pulse-decay permeability test: 2.54cm in diameter and 0.254cm in height.

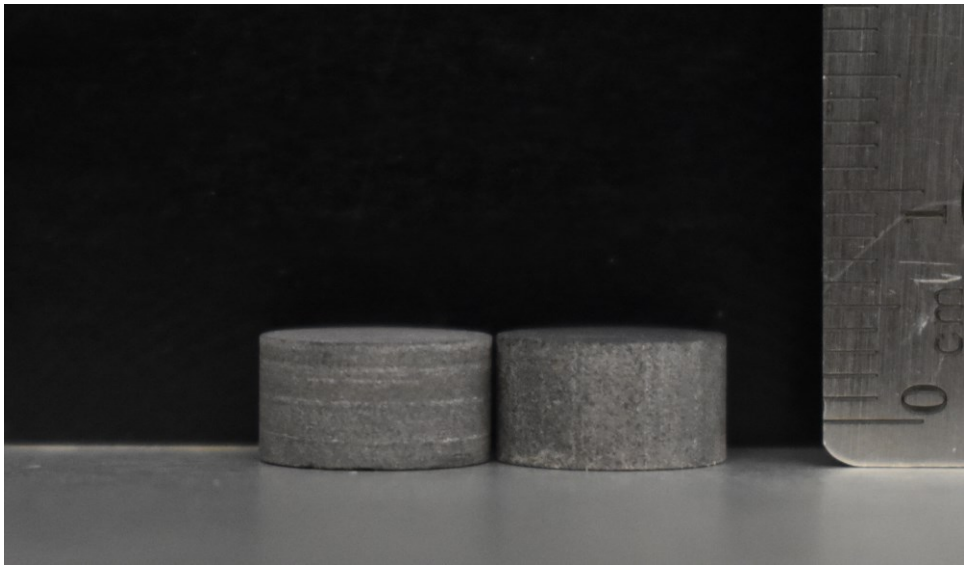

Figure 4-6. Preparing the samples of both parallel (right sample) and perpendicular (left sample) to the beds for direct shear tests.

4.1.2. Experimental Procedures

4.1.2.1. QEMSCAN Analysis

To determine a detailed understanding of the mineralogy in different beds, QEMSCAN (Quantitative Evaluation of Materials by Scanning Electron Microscopy) analysis was performed. This method provides better resolution than conventional thin section petrography to measure size

and distribution of different minerals (Ahmad and Haghighi, 2012). QEMSCAN provides automated, rapid and accurate mineralogical analysis by combining SEM (Scanning Electron Microscope), Energy-dispersive X-ray spectroscopy (EDS) detectors and a software to control automated data acquisition. As shown in Figure 4-7, SEM images would contribute to find the boundaries of the particles using Back-Scattered Electrons (BSE). Then, the spectrum related to each particles would be captured by EDS followed by analyzing the chemical composition, classification and eventually generating a mineralogy map (Ž Tonžetić et al., 2006; Sliwinski et al., 2010; Wood, 2013).

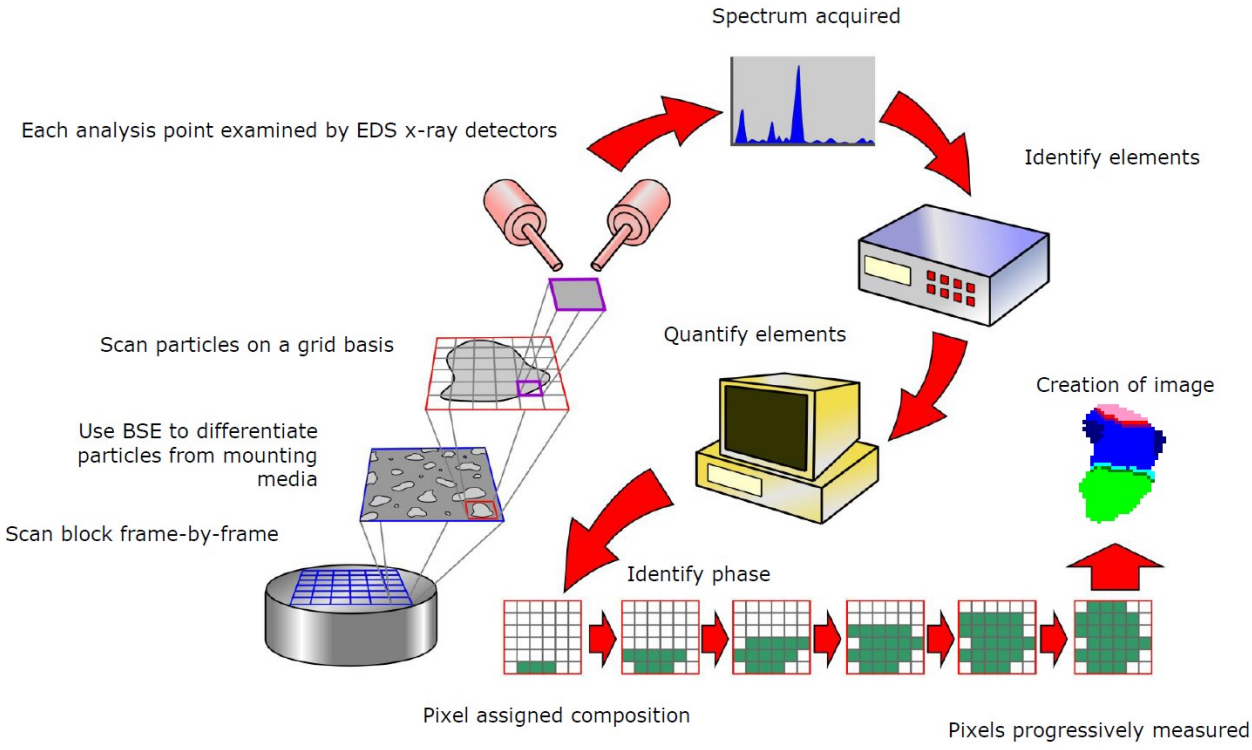

Figure 4-7. Schematic view of QEMSCAN measuring and analysis process (Ž Tonžetić et al., 2006).

4.1.2.2. Nitrogen Adsorption–Desorption Isotherms

Measuring gas adsorption isotherms is an effective method in the characterization of porous materials which is based on adsorption of gas on the surface within the porous media at constant temperature followed by recording the adsorbed amount of gas as a function of pressure. Nitrogen

is an inert gas that condenses in both organic and inorganic pores which means that nitrogen adsorption-desorption isotherms would give the total pore volume and pore size. Total pore volume can be obtained from the volume absorbed at a relative pressure close to unity and convert it to liquid volume as shown in Equation (4-1) (Anovitz and Cole, 2015).

$$V_{liq} = \frac{P_a V_{ads} V_m}{RT} \tag{4-1}$$

where V_{ads} is the gas volume adsorbed, V_m is the volume of adsorbate as a monolayer P_a is ambient pressure, R is the gas constant and T is temperature in Kelvin. Based on the pore volume, density and weight of the sample, the porosity can be also calculated. Therefore, pore diameter can be estimated from the pore volume by Equation (4-2) (Barrett et al., 1951).

$$D_p = \frac{4V_{liq}}{S} \tag{4-2}$$

where D_p is the pore diameter and S is the surface area which can be captured from Brunauer-Emmett-Teller (BET) surface area analysis. Although BET and BJH (Barrett–Joyner–Halenda) (1951) approach has become a popular method for shale rocks (Clarkson et al., 2012a; Li et al., 2016; Wang et al., 2018; Xu et al., 2020), Groen at al., (2003) reported that the BJH method is not sufficiently accurate for the assessment of pore size distribution in tight rocks. To capture pore size distributions in Montney samples, Density Functional Theory (DFT) molecular modelling has also been used (Qiang et al., 2020), which directly accounts for micropore filling process instead of a condensation process. DFT was applied in the current research. For our bed-scale analysis, Autosorb Quantachrome 1MP device was employed (Figure 4-8) to evaluate the nitrogen adsorption data as well as pore volume and pore size distribution of different beds. Before the tests samples are crushed into fine particles and then pre-treatments are conducted to remove gas and moisture. While the crushed sample is still under the vacuum it is cooled to -195^{o}C and nitrogen is dosed to the sample.

Figure 4-8. Autosorb Quantachrome 1MP device used for nitrogen adsorption–desorption Isotherms tests.

This process consists of four main stages. First stage is related to gas adsorption on the surface at low pressure followed by forming the monolayer coverage of the surface as the pressure is increasing in the second stage (Figure 4-9). In the third stage multilayer coverage would take place through further increase in gas pressure and eventually complete coverage of the sample occurs in the fourth stage where all the pores are filled (Figure 4-9). Also, desorption isotherm can be obtained by measuring the volume of gas removed from the sample as the pressure decreases. In addition, the hysteresis loop between adsorption and desorption isotherms would give some insights about the shape and characteristics of the pore structure (Li et al., 2016; Zhang et al., 2016; Chen et al., 2018; Wang et al., 2018; Xu et al., 2020). According to IUPAC guideline (Sing, 1985) hysteresis loops can be divided into four categories of H1, H2, H3 and H4 (Figure 4-10).

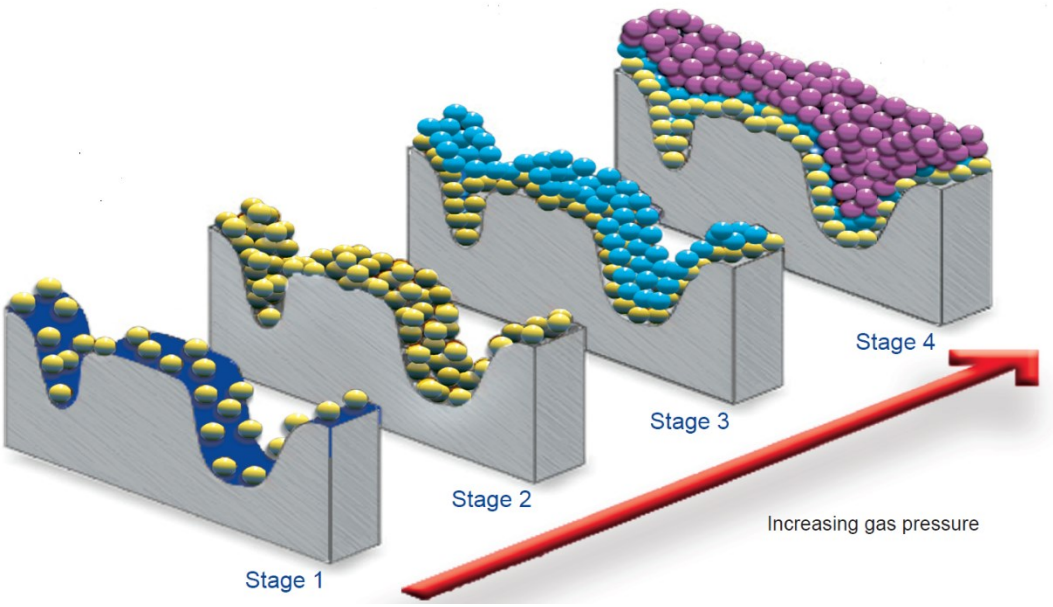

Figure 4-9. Stages in nitrogen adsorption isotherm test. Stage 1: gas adsorption on the surface; Stage 2: forming the monolayer coverage; Stage 3: multilayer coverage; Stage 4: complete coverage (White, 2012).

H1 hysteresis loop corresponds to porous materials consisting of cylindrical-like pore and H2 hysteresis mainly relates to ink-bottle-shaped pores where a pore mouth smaller than the pore body. H3 hysteresis shows parallel plate shaped pores and slit-like pores and H4 loop is generally associated with slit-like pores and wedge-shaped pores. In addition, based on the width of the hysteresis loop in each classification, more detailed discussions can be made about the pore structure.

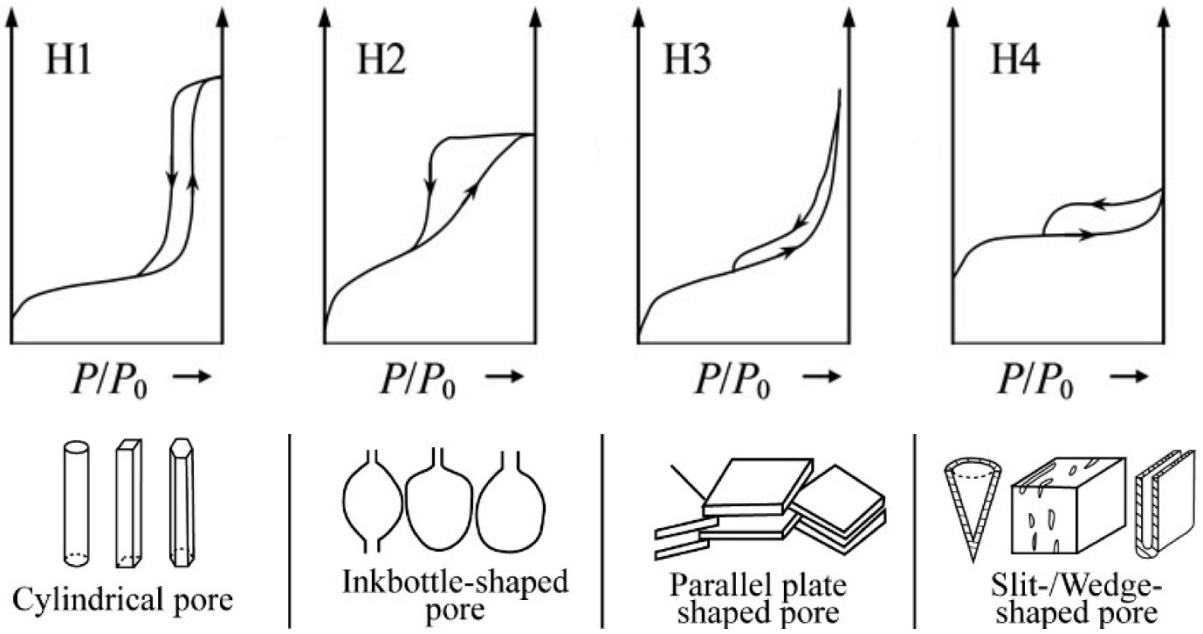

Figure 4-10. Classification of IUPAC for hystersis loops (modified from Sing, 1985)

4.1.2.3. Thermo-Gravimetric Analysis (TGA)

To measure the water saturation in different beds, Thermo-Gravimetric Analysis (TGA) was applied. TGA is a thermal analysis method that measures the amount of change in the weight of the sample as a function of sequential heating. One of the main advantages of TGA is that it is possible to differentiate between free water and bound water (as part of the clay structure). Generally, any water released before 120^{o}C corresponds to free water and by increasing the temperature the amount of water released by 350^{o}C is related to clay-bound water while any water extracted after that and before 700^{o}C is the structural water (Handwerger et al., 2012). Figure 4-11 represents an example of TGA on Marcellus shale sample where the green line shows the weight as a function of temperature and the blue line is the derivative of the weight curve. As it can be seen in Figure 4-11 by considering three temperature levels for water extraction (<120^{o}C, 120^{o}C - 350^{o}C and 350^{o}C - 700^{o}C) four main regions can be considered. The peak in "Region 2" at around 151^{o}C is related to releasing interlayer clay water and the peak in "Region 3" represents structural/hydroxyl water. To perform TGA, SDT Q600 instrument was used (Figure 4-12) where the saturation can be captured based on the weight loss (as a result of water loss) and pore volume measured in nitrogen adsorption–desorption isotherms (Equation 4-3).

$$Sw = \frac{TGA\ (V_w)}{Ads\ (PV)} * 100 \quad (4\text{-}3)$$

where *TGA (V_w)* is the volume of water measured in TGA and *Ads (PV)* is the pore volume captured in nitrogen adsorption–desorption isotherms.

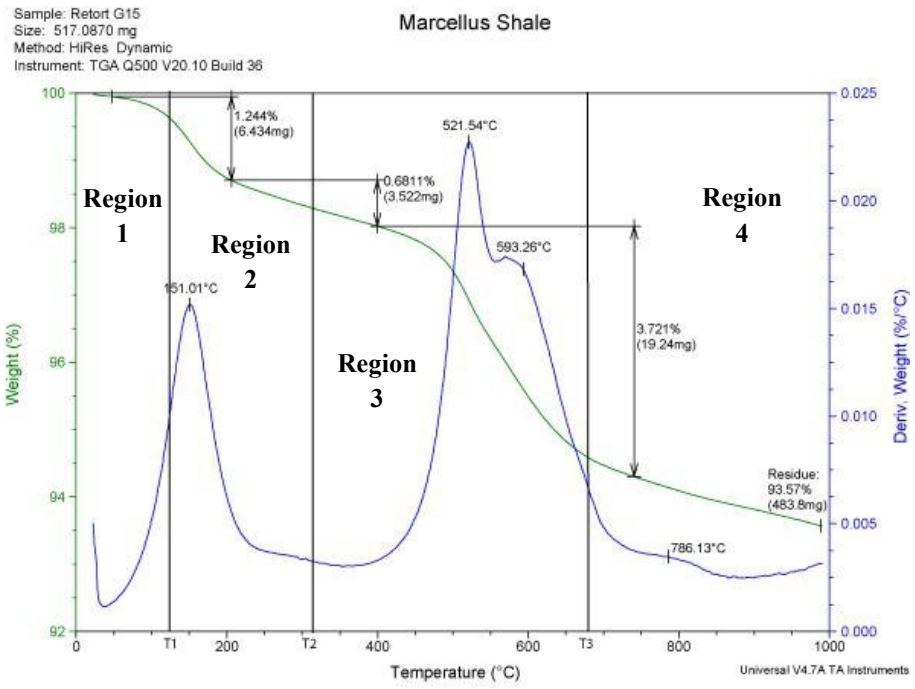

Figure 4-11. An example of TGA on Marcellus shale (Handweger et al., 2012).

4.1.2.4. Capillary Condensation Experiments

Capillary condensation is a process of vapor phase liquefaction in pore space at low vapor pressures. If the pores are small enough and the vapor phase sufficiently wets the pore surface, multilayer adsorption of vapor molecules in pore spaces would take place until the pores become filled with condensed liquid from the vapor phase. Figure 4-13 represents a schematic of slit-like pore condensation (which is a common pore structure in tights rocks containing clays (Li et al., 2016; Wang et al., 2018)).

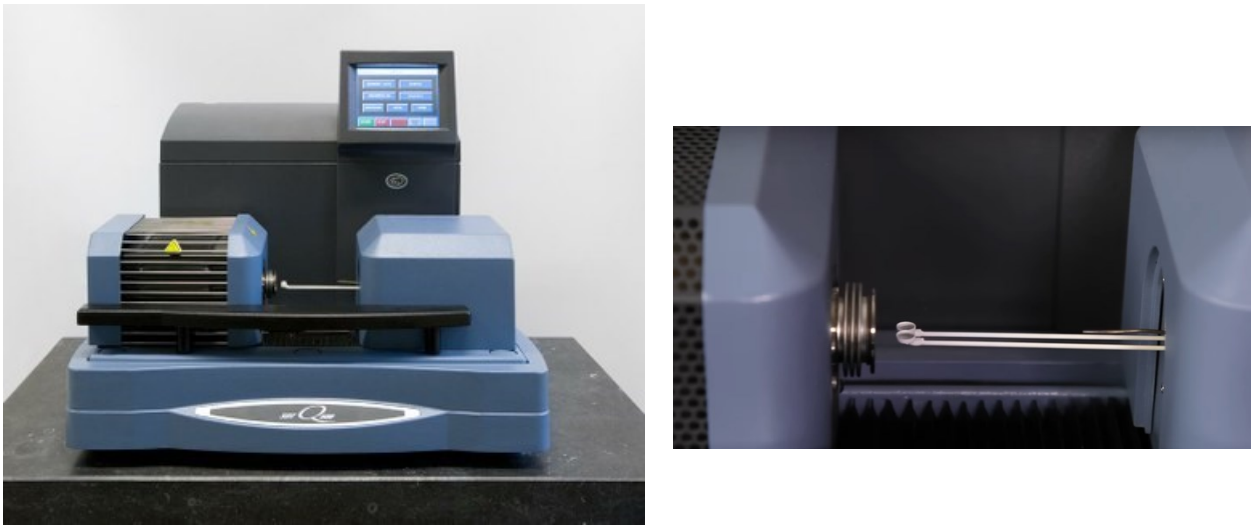

Figure 4-12. SDT Q600 used for Thermo-Gravimetric Analysis (TGA).

For a given relative humidity, capillary condensation first starts in smaller capillaries and as relative humidity increases the water vapor condenses in the larger capillaries. By considering the Kelvin equation the relationship between relative humidity and the size of the water-filled capillaries (or in other words capillary suction) can be obtained by Equation (4-4) (Camuffo 1984):

$$\ln(RH) = -\frac{\gamma V_m H}{RT} \tag{4-4}$$

where RH is relative humidity, H is mean curvature of meniscus, γ is liquid/vapor surface tension, V_m is liquid molar volume, R is ideal gas constant and T is temperature. To better understand how the capillary suction would change as a result of saturation, capillary condensation tests were performed to relate the saturation to relative humidity and capillary suction. First, according to the pore structure captured in nitrogen adsorption–desorption isotherms an analytical approach was developed for relating the saturation and capillary suction based on the results of the capillary condensation in different humidity values. In the experimental phase, samples were exposed to a certain amount of humidity in the humidity chamber attached to a humidifier (Figure 4-14). Certain amount of humidity can be obtained by adjusting the ventilation and vacuum valves as the humidifier is generating humidity and monitoring the humidity meter inside the humidity chamber. After maintaining the humidity level, the samples were left in the humidity chamber for 5 days to reach to equilibrium. In each humidity level the changes in the weight of the samples were monitored and recorded. Then, based on the pore volume captured from nitrogen adsorption–

desorption isotherms and the initial saturation measured in TGA, the values of water content as a result of increasing the humidity can be converted to saturation. Eventually, based on the relationship between the relative humidity and saturation in one hand and relative humidity and capillary suction in another hand the relationship between the saturation and capillary suction were generated.

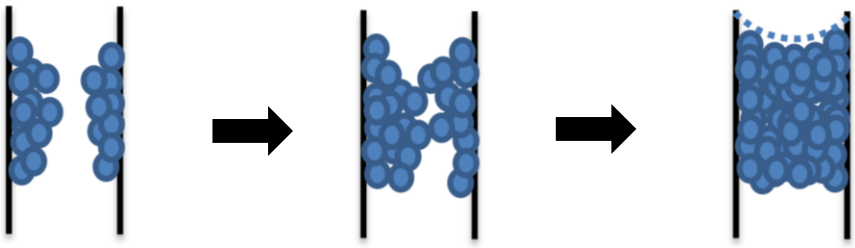

Figure 4-13. Schematic showing slit-like pore condensation.

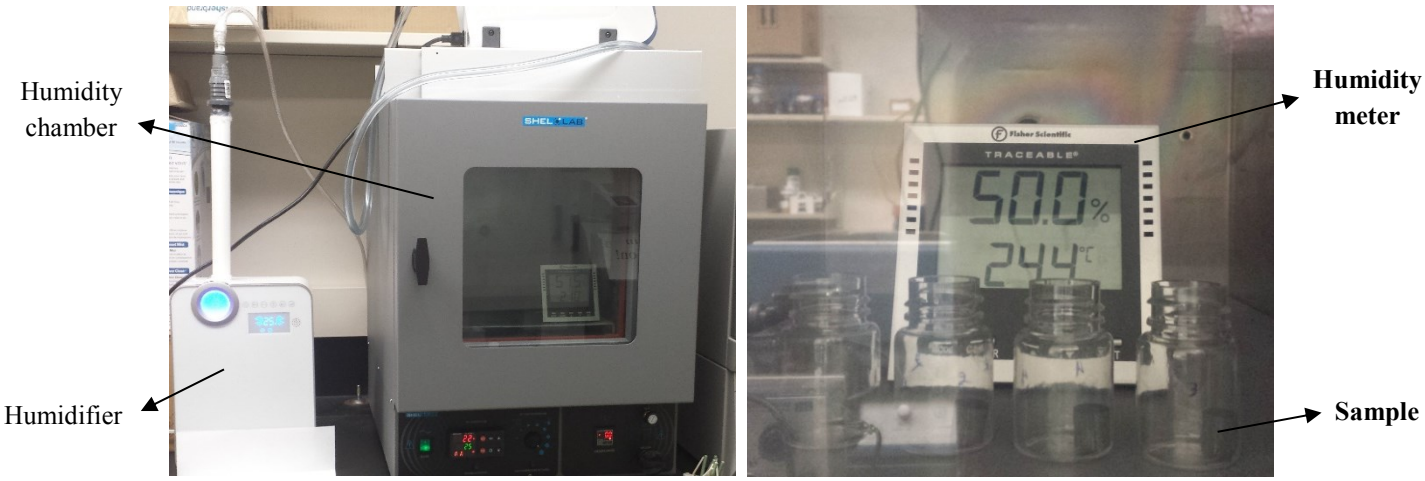

Figure 4-14. Capillary condensation experiments set up.

4.1.2.5. Micro-Geomechanical Measurements

Although typical mechanical parameters are obtained from conventional experiments such as uniaxial/ triaxial tests, micro-indentation and micro-scratch tests were performed to capture rock mechanical and strength properties due to the scale of existing compositional and microstructural features and beds as well as complex anisotropic behavior of tight gas rocks.

4.1.2.5.1. Micro-indentation

A micro- indentation test consists of penetrating an indenter into a material by applying a known load in a loading step and removing the indenter from the specimen during the unloading step (Figure 4-15). Bed-scale elastic properties of the samples at different saturations were captured by a Fischerscope H100C indentation apparatus with a Vickers indenter tip (Figure 4-16). The sample is fixed on the frame and using the microscope, indentation points on each of the white and dark beds are set followed by application of the indenter load. Utilizing the load versus displacement (indenter penetration depths) values in each step (especially during the unloading step), the mechanical properties are computed based on principles of elasticity and contact stiffness. Since elastic displacements occur in both the specimen and the indenter, a reduced elastic modulus (E_r) must be defined based on ASTM E2546–07, where the indentation reduced modulus Er and Young's modulus of the sample (E) would be calculated by Equation (4-5) and (4-6), respectively.

$$Er = \frac{\sqrt{\pi}}{2}\frac{S}{\sqrt{Ac}} \tag{4-5}$$

$$E = \left(\frac{1-\nu^2}{\frac{1}{Er}-\frac{1-\nu_i^2}{Ei}}\right) \tag{4-6}$$

where Ac is a contact area, $S= dP/dh$ is contact stiffness. E_i and ν_i are Young's modulus (1140GPa) and Poisson's ratio (0.07) of the indenter tip, respectively and ν is the Poisson's ratio of the sample. Based on Equation (4-6) not only Young's modulus and Poisson's ratio of the indenter tip are needed but also Poisson's ratio of the sample should be known to calculate Young's modulus of the sample. Therefore, a least-square method was developed based on Equation (4-5) and the definition of contact stiffness. In each saturation two sets of micro-indentation tests along the beds were done and an average values for Young's modulus and Poisson's ratio were considered.

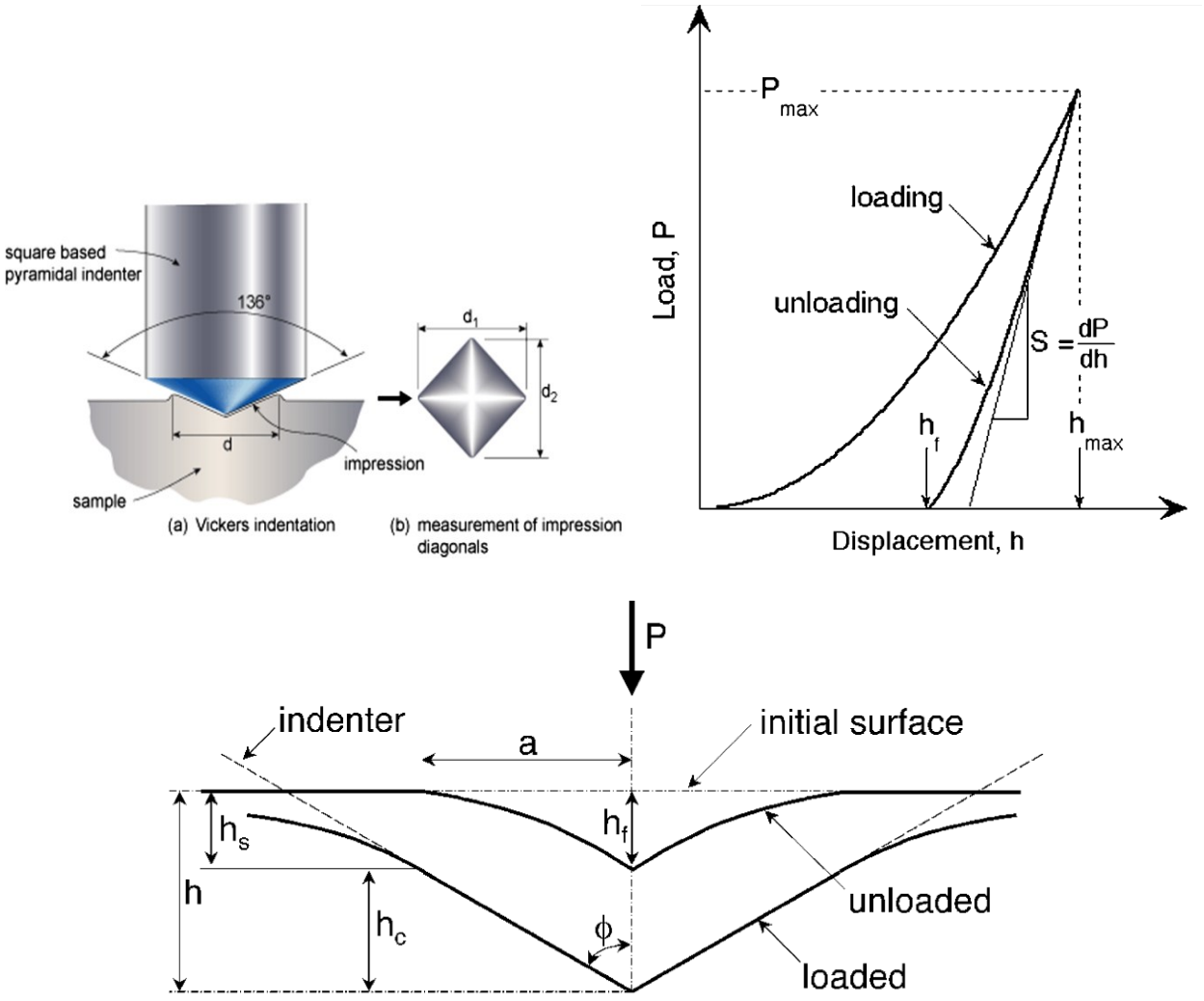

Figure 4-15. Schematic view of load–displacement curve and contact geometry during loading and unloading steps (Oliver and Pharr, 2004).

4.1.2.5.2. Micro-scratch

A micro-scratch test involves measuring the lateral and normal loads required to cut a narrow channel on the surface of a rock sample (Figure 4-17) with a blade (cutter) and using this load to infer strength properties of the rock.

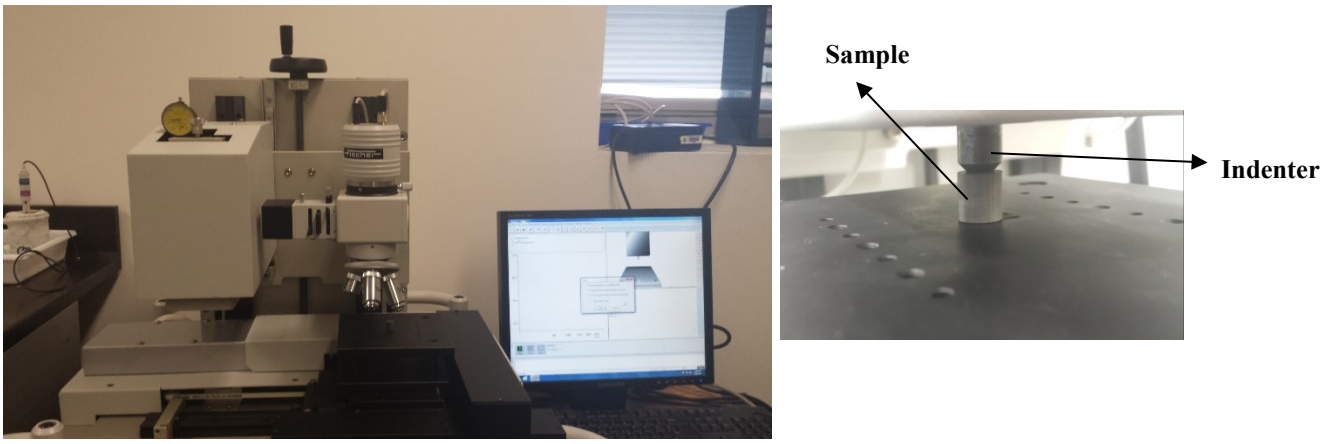

Figure 4-16. Fischerscope H100C indentation apparatus used for micro-indentation tests.

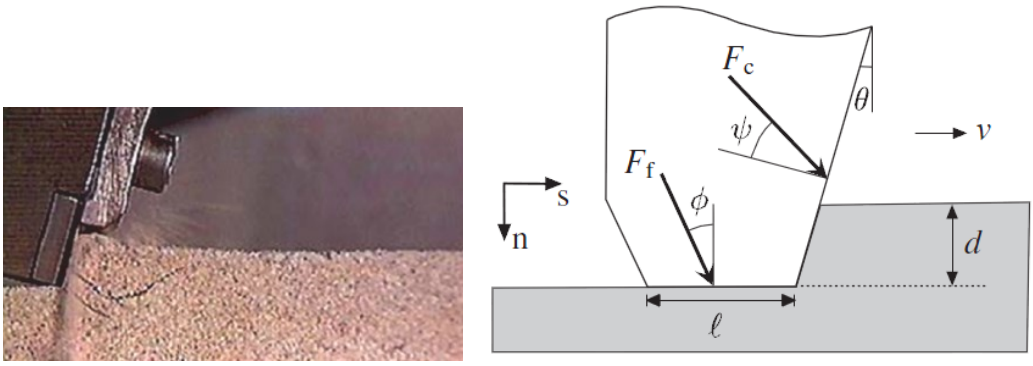

Figure 4-17.Schematic illustration of forces acting on a cutter. The force F acting on a blunt cutter results from the superposition of two forces F_c and F_f, acting on the cutting face and on the wear flat, respectively (Richard et al. 2012).

Richard et al. (2012), Fairhurst (2014) and Detournay (2014) have shown analytically and experimentally that in a scratch test the value of specific energy of the cutting (referred to nominal strength which is the tangential cutting force divided by the contact area between cutter and rock (Figure 4-17)) is in a 1:1 relationship (Figure 4-18) with UCS of the rock (Equation 4-7):

$$UCS = \frac{F_s}{wd} \tag{4-7}$$

where F_s is tangential cutting force, w is the width of a cutter and d is the depth of cut.

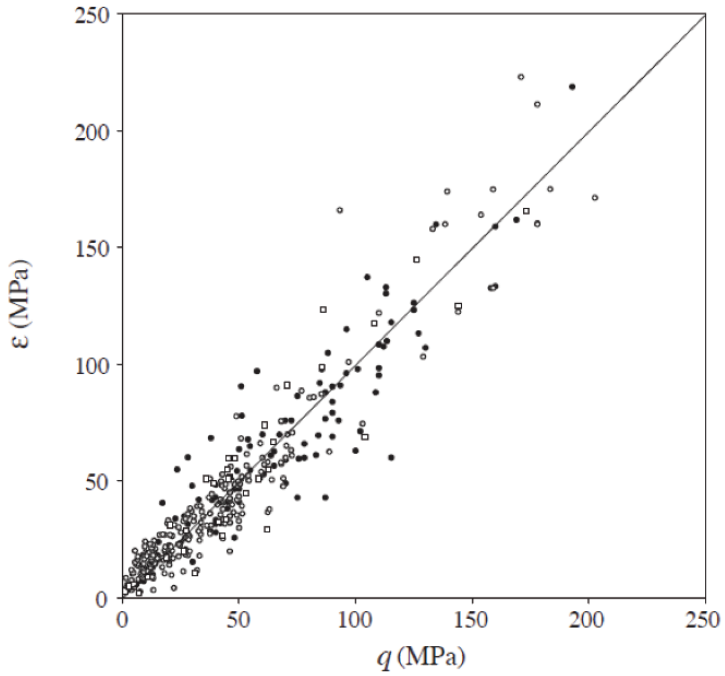

Figure 4-18. Scratch test experiments on different rock samples; ε is specific energy and q is uniaxial compressive strength of the rock (Fairhurst 2014).

To capture the strength parameters including UCS, internal friction angle and cohesion for partially saturated media an analytical approach was developed and verified. Micro-scratch tests were done using Rtec Tribometer Multi Function MFT-5000 (Figure 4-19) with two set of tests by Rockwell and conical tips in different degrees of water saturation. Rockwell diamond indenter has a cone of half-apex angle 60^o ending into a hemispherical tip of radius 200 micrometer. The transition from the sphere to the cone occurs at a depth of 26.8 micrometer. For the conical tip the half-apex angle is 30^o.To capture the parameters based on conical scratching tip the values of scratch hardness (H_T) and projected contact area (A_{LB}) should be calculated through Equation (4-8) and (4-9) (Akono & Ulm, 2012).

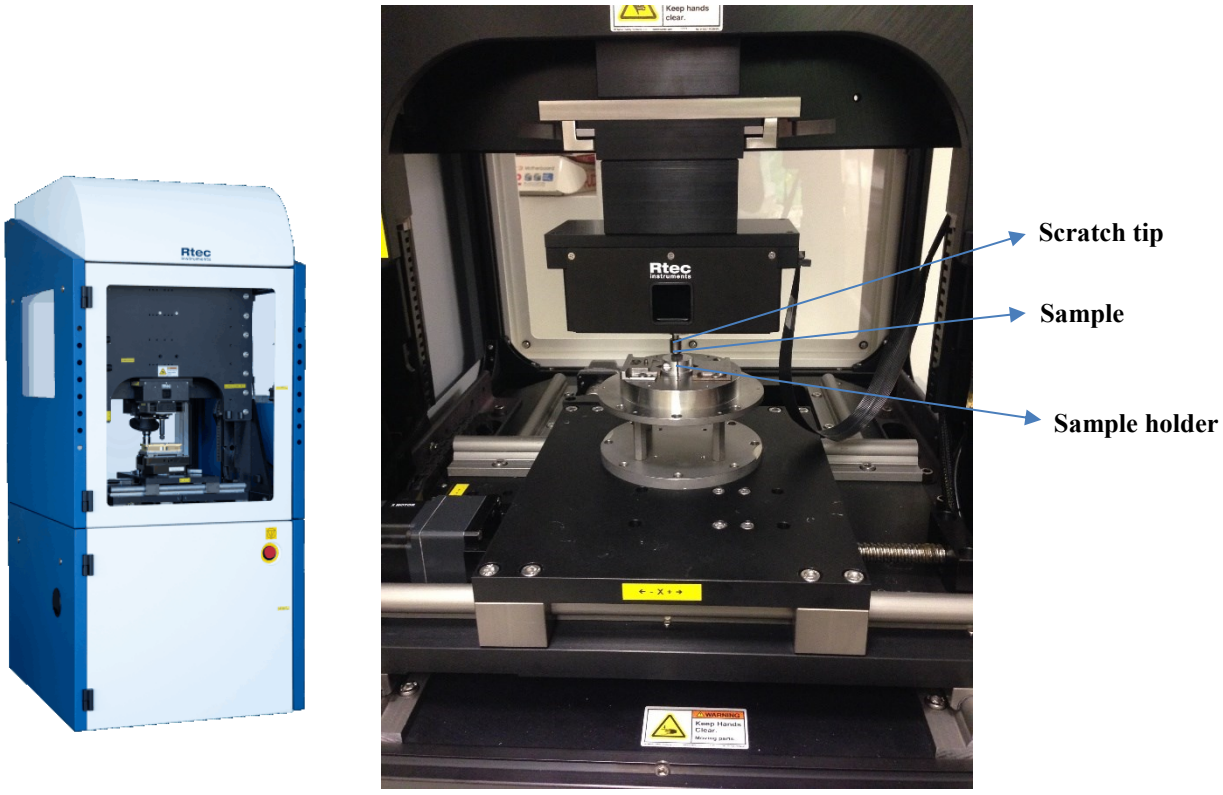

Figure 4-19. Rtec Tribometer Multi Function MFT-5000 used for micro-scratch tests.

$$H_T = \frac{F_T}{A_{LB}} \tag{4-8}$$

$$A_{LB} = \frac{d^2}{cot\theta} \tag{4-9}$$

where F_T is horizontal scratch force, θ is the back rake angle and d is depth of cut (Figure 4-20).

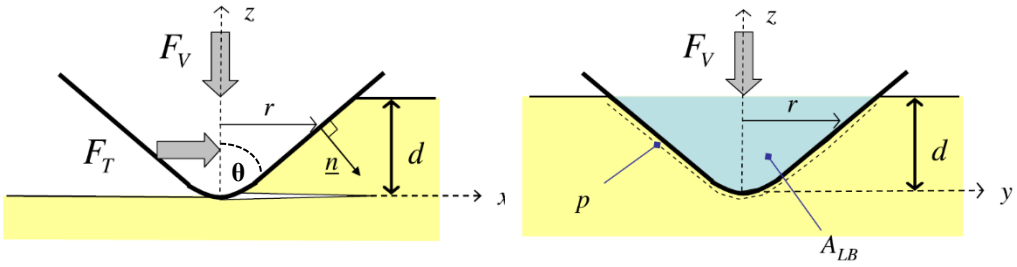

Figure 4-20.Force components and the geometry details of the scratching area (Akono & Ulm, 2012).

Also, based on the results of micro-scratch tests, fracture toughness can be determined by Equation (4-10) (Akono & Ulm, 2012):

$$K_c = \frac{F_{eq}\cos\theta}{2d^{\frac{3}{2}}\sqrt{\sin\theta}} \quad (4\text{-}10)$$

$$F_{eq} = \sqrt{F_T^2 + \frac{3}{5}F_V^2} \quad (4\text{-}11)$$

where F_V is vertical force and F_{eq} is an equivalent force for conical scratching tips.

4.1.2.6. Permeability Measurements

Analytical approaches based on Darcy's law can be developed to extract permeability values at the bed-scale from larger scale permeability measurements. To determine the permeability of layered beds with different permeability values, averaging method was used. Figure 4-21 represents a multilayer media with beds of different permeability values (K_1 and K_2).

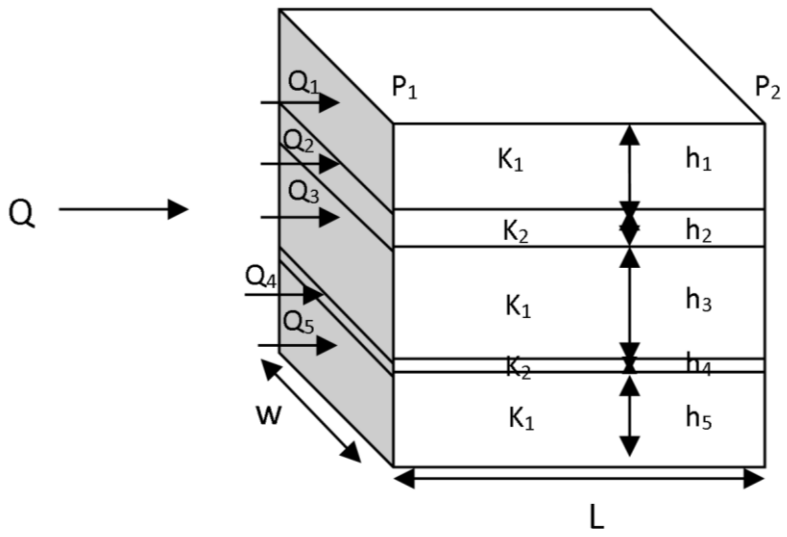

Figure 4-21. Shematic view of flow through layered media.

The flow from each layer (i) can be calculated using Equation (4-12) (assuming no cross flow).

$$Q_i = \frac{K_i w h_i}{\mu L}\,\Delta P \quad (4\text{-}12)$$

where Q is the flow rate, K is the permeability, w is the width, L is the length, μ is the viscosity and ΔP is the total pressure drop (P_1-P_2). By considering the same pressure drop for each layer and summation of flow rate for all layers to be the total flow rate, Equation (4-13) can be generated for total flow rate.

$$Q_t = \frac{K_{avg} w h_t}{\mu L} \Delta P \quad (4\text{-}13)$$

where $K_{avg} = \frac{\sum_{i=1}^{n} K_i h_i}{h_t}$ for the case of the same w for all of the layers and $K_{avg} = \frac{\sum_{i=1}^{n} K_i A_i}{A_t}$ with $A = w_i h_i$ (cross section area of layer (i)) for the case that each layer has its own width.

To capture the permeability of the beds, a back calculation was done based on K_{avg} obtained from the tests. To measure the permeability in a bed-scale two permeability measurement approaches were considered. In the first step, pressure-decay tests were conducted to see how different the permeability values are in white and dark beds in unconfined condition. In the next phase, to capture the permeability values as a function on confining pressure a pulse-decay experiment were performed.

4.1.2.6.1. Pressure-decay

To measure the permeability by pressure-decay method, PDPK-400 (Pressure-Decay Profile Permeameter) with 1cm x 1cm resolution was used (Figure 4-22). Initially, before starting the test on a core slab, it should be assured that the core slab is leveled and stabilized on a core rack. After choosing the location for permeability measurement (which is indicated by a laser beam that aligned with the axis of the probe), the probe tip is sealed against the core slab (its rubber seal is pressed against the sample with a controlled pressure) and the outlet valve which is connected to gas storage tank (nitrogen) is opened and the pressure in the tank is recorded as a function of time. Volumetric flow rate of gas entering the sample can be calculated based on the gas density and the mass flow rate of gas leaving the tank. The pressure decay response is continuously recorded with time followed by permeability estimation through interpretation of pressure decay curve (Jones, 1994). Slip-corrected gas permeability can be obtained using Equation 4-14 (Jones, 1994):

$$K_{g(cor)} = \frac{29392 \mu_g y}{(G_d r_i)(p+2p_a+2b)} \quad (4\text{-}14)$$

where μ_g is viscosity of the applied gas, p_a is atmospheric pressure, p is gauge pressure, b is the Klinkenberg gas slippage factor, r_i is the inner radius of the probe tip and G_d is geometric factor which is related to the ratio of inner and outer probe tip radius. In addition, y is calculated based on any two adjacent pressure-time points as shown in Equation 4-15 (Jones, 1994):

$$y_n = \frac{V_T \ln(\frac{p_{n-1}}{p_n})}{t_n - t_{n-1}} \tag{4-15}$$

where V_T is the gas volume injected. Also, b is approximated by Equation 4-16 (Jones, 1994):

$$b = 0.22\sqrt{\frac{G_d r_i}{\mu_g y}} \tag{4-16}$$

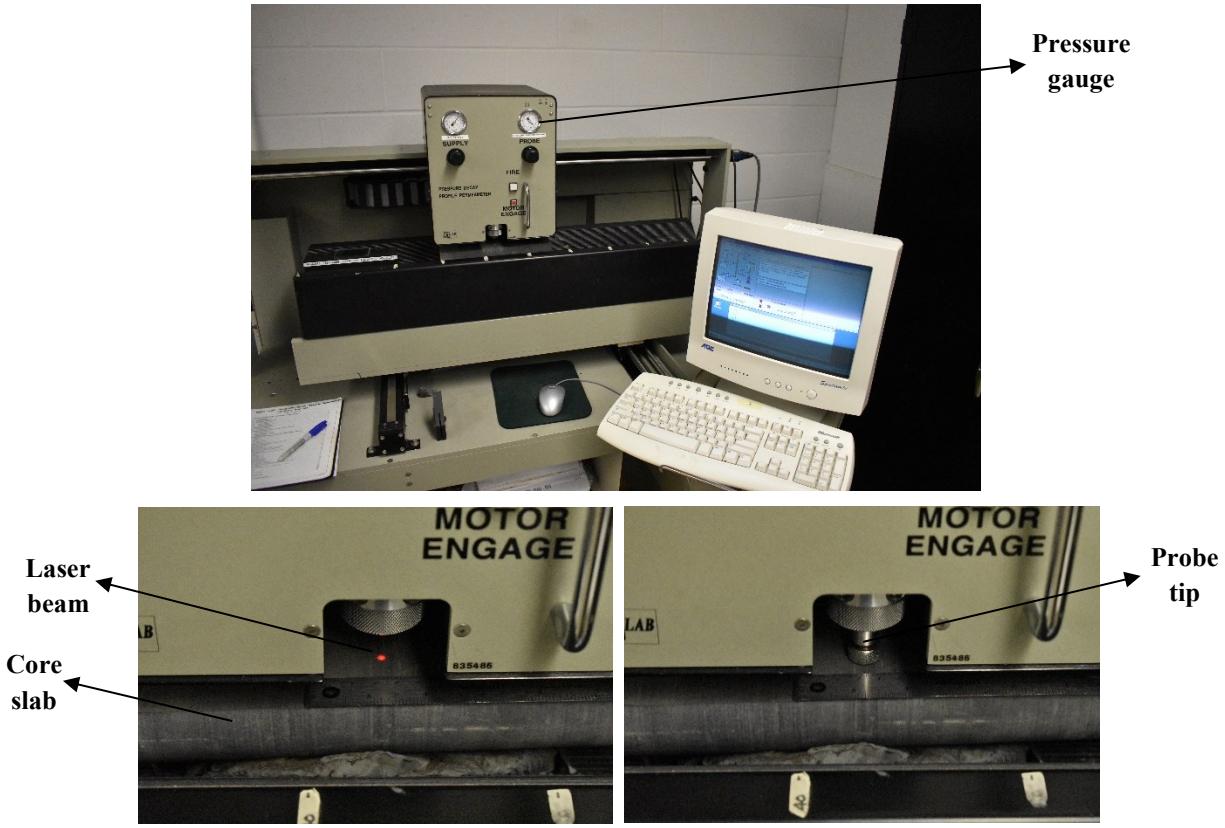

Figure 4-22. PDPK-400 (Pressure-Decay Profile Permeameter) used for permeability measurements.

4.1.2.6.2. Pulse-decay

One of the most common methods to capture the permeability of tight gas rocks in confined conditions is pulse-decay which is based on gas flow from one end of the sample and exit from the other end while some key parameters such as flow rate and upstream and downstream pressures are monitored and recorded. In our pulse-decay experiments, after placing the sample in the cell (Figure 4-23) the pressure in the upstream and downstream of the sample was kept constant and the rate was monitored untill it reached to a constant value while the sample was under a constant confining pressure. Gas flows into the bottom of the sample and exits at the top. For upstream pressure, a pump (Quizix Q-5000) was connected to the bottom of the sample and the top of the sample was connected to an accumulator to maintain downstream pressure and collect the gas passing through the sample (using an ISCO pump). Also, to ensure linear flow porous stones are placed at the top and bottom of the sample (Figure 4-23).

Figure 4-23. Pulse-decay permeability measurement cell (on the right) and porous stones on the top and bottom of the sample to ensure linear flow.

To calculate the gas permeability by pulse decay approach, Equation 4-17 was applied (Fink et al., 2017).

$$K_g = \frac{\Delta V}{\Delta T}\frac{2\mu(P_m,T)P_a L}{A(P_{down}^2 - P_{up}^2)} \quad (4\text{-}17)$$

where $\frac{\Delta V}{\Delta T}$ is flow rate, $\mu(P_m, T)$ is the viscosity as a function of mean pore pressure P_m, P_a is atmospheric pressure, L and A are the length and the cross-sectional area of the sample, P_{up} and P_{down} are the pressures on the upstream and downstream sides of the sample.

As a result of slip flow (Klinkenberg, 1941) the permeability coming from gas measurements (apparent permeability) needs to be corrected to get the intrinsic permeabilty. To do so, a modified version of Klinkenberg approach suggested by Ashrafi (2016) was used represented in Equation (4-18).

$$\dot{K}_{absolute} = \frac{K_{Apparent}}{(1+\frac{1}{\bar{P}}(b-\frac{a}{\bar{P}}))} \quad (4\text{-}18)$$

$$\bar{P} = \frac{P_{upstream}+P_{downstream}}{2} \quad (4\text{-}19)$$

$$b_{Klinkenberg} = (b - \frac{a}{\bar{P}}) \quad (4\text{-}20)$$

Based on Equation (4-18) the absolute permeability in zero effective stress ($\dot{K}_{absolute}$) can be calculated. To determine the absolute permeability in different effective stresses, Equation (4-21) was applied (Fink et al., 2017).

$$K_{absolute} = \dot{K}_{absolute} \exp(-\alpha_k \sigma') \quad (4\text{-}21)$$

where σ' is the effective stress and α_k is the compressibility coefficient which can be determined based on the mechanical properties (bulk modulus) measured in micro-geomechanical tests.

4.1.2.7. Direct Shear Measurements

The direct shear tests were carried out using a HUMBOLDT fully-automated pneumatic direct shear apparatus (Figure 4-24) with horizontal shear displacement at the rate of 0.002 mm/min. To measure the strength parameters both parallel and perpendicular to the beds as a function of saturation, samples were initially exposed to a desired amount of humidity through a saturated salt solution for 5 days (Figure 4-25) and then placed inside a special holder designed for 1cm samples

(Figure 4-26) in the shear box. The shear box was sealed from the outside where the same saturated salt solution containers were located on four corners of the shear box to maintain the humidity in the sample before the test and while the test was progressing (Figure 4-26). To monitor the humidity level a humidity meter was placed inside the sealed shear box. The normal load was applied followed by exerting a shear force on the sample until it failed. For each saturation, three constant normal stresses were considered and then based on the values of shear strength and normal stress for these three tests, friction angle and total cohesion were determined (Equation (3-15)), as shown in Figure 4-27.

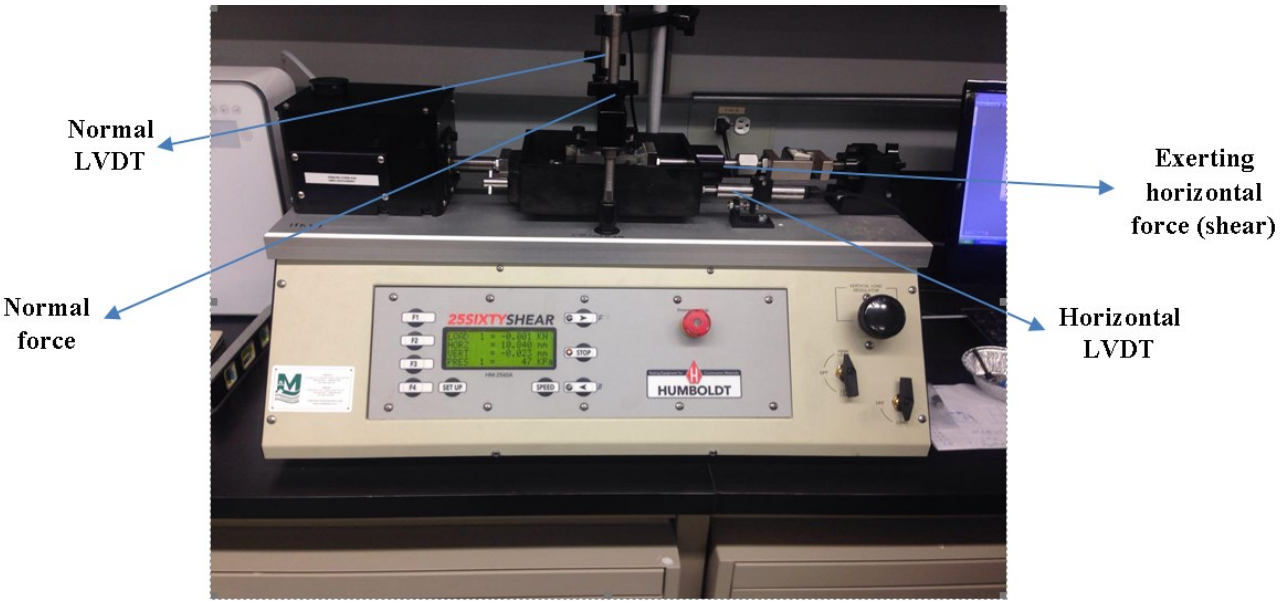

Figure 4-24. HUMBOLDT fully-automated pneumatic direct shear apparatus used for direct shear tests.

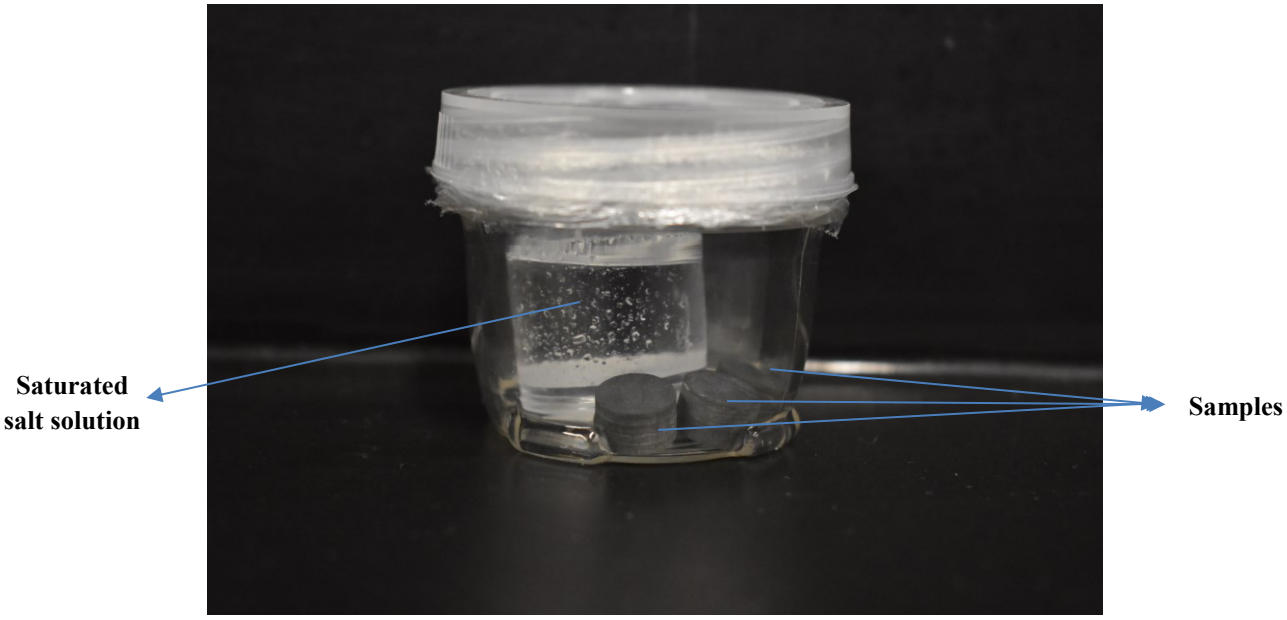

Figure 4-25. Saturating the samples through exposing to a certain level of humidity generated by a certain saturated salt solution.

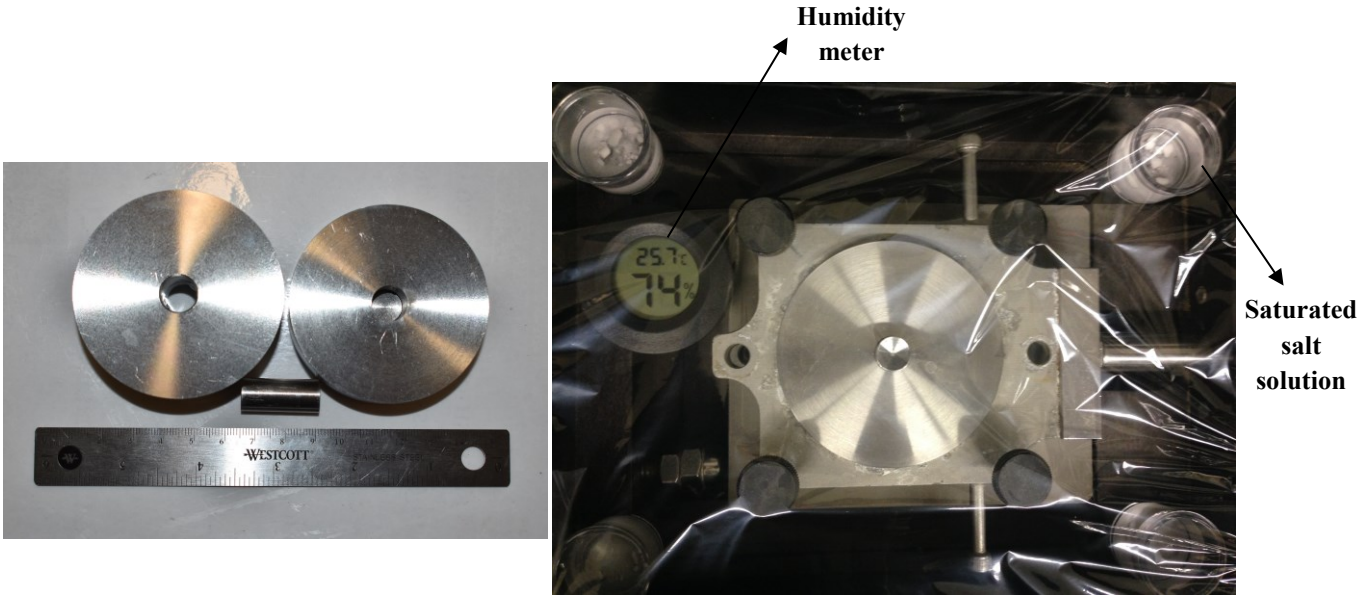

Figure 4-26. Special sample holder for 1cm samples (left image) and sealed shear box with saturated salt solution and humidity meter (right image).

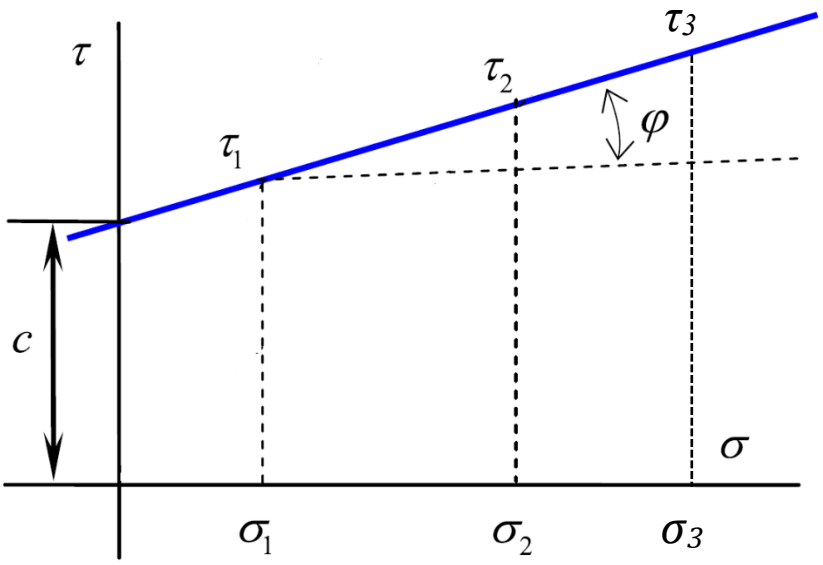

Figure 4-27. Schematic view of determining cohesion (c) and Intrnal friction angle (φ) using direct shear test.

4.1.3. Experimental Results and Discussions

4.1.3.1. QEMSCAN Analysis

The results of QEMSCAN analysis, which were completed by SGS Canada, on 1cm (in diameter) "PR" sample indicate that the mineralogy and even the mineral sizes in the white and dark beds were different. Figure 4-28, Figure 4-29 and Figure 4-30 represent the QEMSCAN analysis from the whole sample, dark beds and white beds, respectively. It can be clearly observed in Table 4-1and Figure 4-31 that the quartz and clay content of the white beds are respectively 10.2% higher and 56.4% lower than the dark beds. Therefore, one may conclude that white beds are quartz-rich beds and dark beds are clay-rich beds. The majority of clay content is related to illite and illite-smectite type. Illite is a non-swelling clay which means that hydration does not cause swelling (Aksu et al., 2015; Ahmad et al., 2018). The total carbonates in quartz-rich beds are 21.9% higher than clay-rich beds. Also, regarding the mineral size, generally the size of minerals in quartz-rich beds are bigger than the size of minerals in clay-rich beds and the size of quartz particles in quartz-rich beds are 19.3% bigger than clay-rich beds.

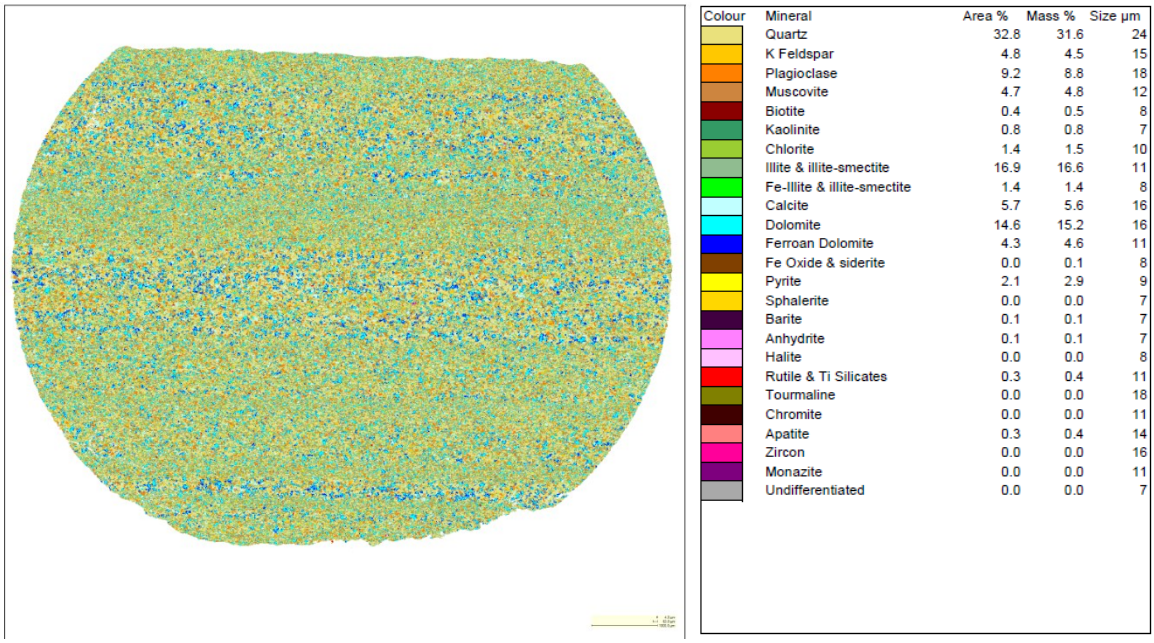

Colour	Mineral	Area %	Mass %	Size µm
	Quartz	32.8	31.6	24
	K Feldspar	4.8	4.5	15
	Plagioclase	9.2	8.8	18
	Muscovite	4.7	4.8	12
	Biotite	0.4	0.5	8
	Kaolinite	0.8	0.8	7
	Chlorite	1.4	1.5	10
	Illite & illite-smectite	16.9	16.6	11
	Fe-Illite & illite-smectite	1.4	1.4	8
	Calcite	5.7	5.6	16
	Dolomite	14.6	15.2	16
	Ferroan Dolomite	4.3	4.6	11
	Fe Oxide & siderite	0.0	0.1	8
	Pyrite	2.1	2.9	9
	Sphalerite	0.0	0.0	7
	Barite	0.1	0.1	7
	Anhydrite	0.1	0.1	7
	Halite	0.0	0.0	8
	Rutile & Ti Silicates	0.3	0.4	11
	Tourmaline	0.0	0.0	18
	Chromite	0.0	0.0	11
	Apatite	0.3	0.4	14
	Zircon	0.0	0.0	16
	Monazite	0.0	0.0	11
	Undifferentiated	0.0	0.0	7

Figure 4-28. QEMSCAN analysis of the whole sample.

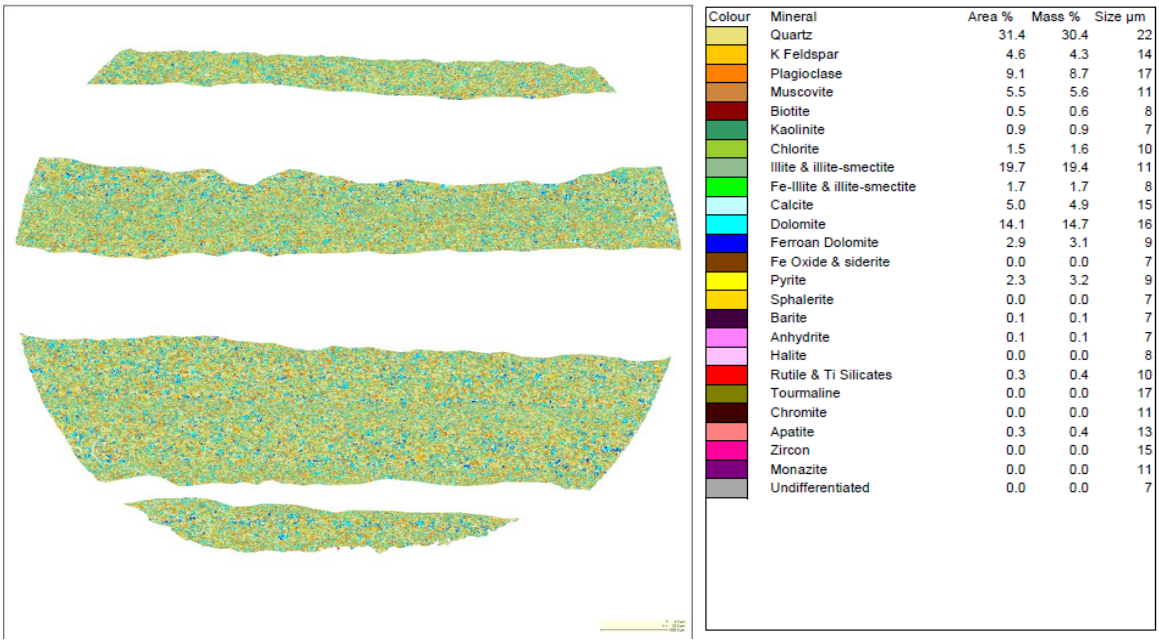

Colour	Mineral	Area %	Mass %	Size µm
	Quartz	31.4	30.4	22
	K Feldspar	4.6	4.3	14
	Plagioclase	9.1	8.7	17
	Muscovite	5.5	5.6	11
	Biotite	0.5	0.6	8
	Kaolinite	0.9	0.9	7
	Chlorite	1.5	1.6	10
	Illite & illite-smectite	19.7	19.4	11
	Fe-Illite & illite-smectite	1.7	1.7	8
	Calcite	5.0	4.9	15
	Dolomite	14.1	14.7	16
	Ferroan Dolomite	2.9	3.1	9
	Fe Oxide & siderite	0.0	0.0	7
	Pyrite	2.3	3.2	9
	Sphalerite	0.0	0.0	7
	Barite	0.1	0.1	7
	Anhydrite	0.1	0.1	7
	Halite	0.0	0.0	8
	Rutile & Ti Silicates	0.3	0.4	10
	Tourmaline	0.0	0.0	17
	Chromite	0.0	0.0	11
	Apatite	0.3	0.4	13
	Zircon	0.0	0.0	15
	Monazite	0.0	0.0	11
	Undifferentiated	0.0	0.0	7

Figure 4-29. QEMSCAN analysis of dark beds (Clay-rich beds).

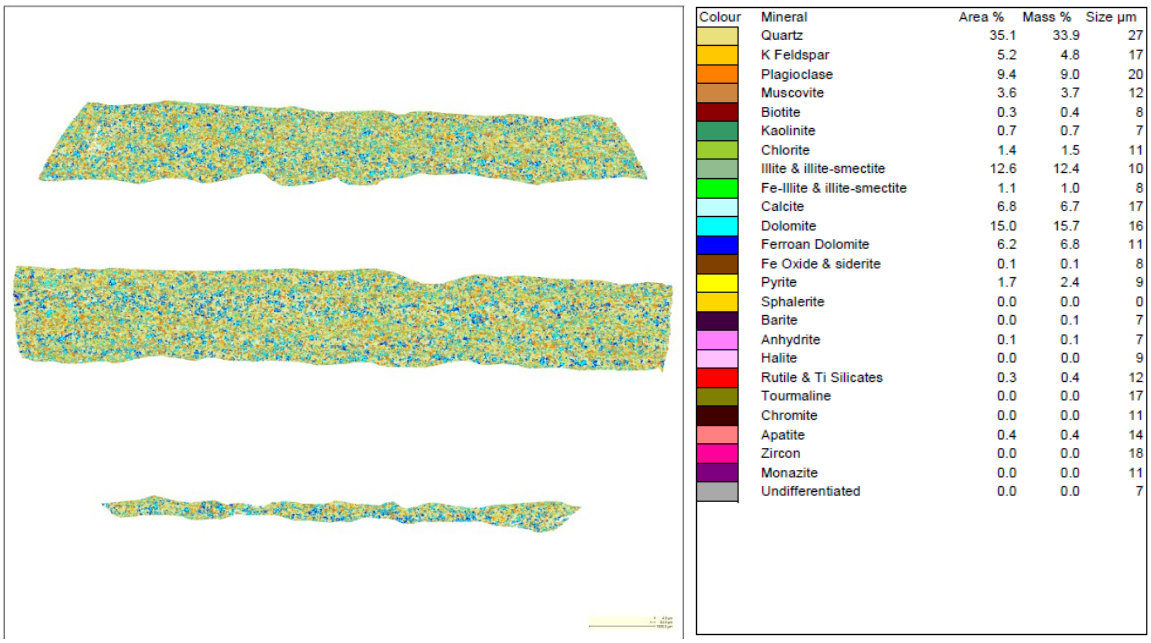

Figure 4-30. QEMSCAN analysis of white beds (Quartz-rich beds).

Table 4-1. Mineralogy of the whole sample, dark beds and white beds.

Section	Quartz	Total Carbonate	Total Clay	K Feldspar	Plagioclase	Muscovite	Pyrite	Biotite
Whole sample	31.64	25.44	20.41	4.50	8.78	4.82	2.88	0.49
Dark Beds	30.39	22.78	23.57	4.29	8.66	5.56	3.19	0.56
White beds	33.86	29.16	15.63	4.84	8.96	3.70	2.40	0.37

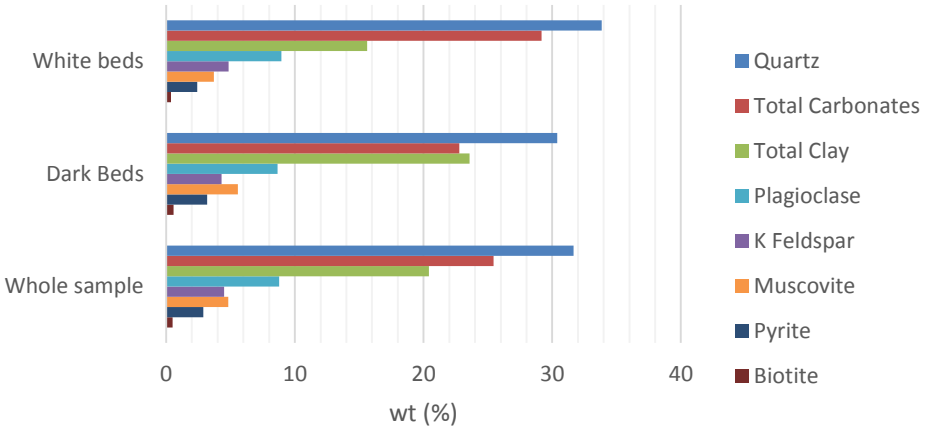

Figure 4-31. Mineral composition of the whole sample, dark beds (clay-rich beds) and white beds (quartz-rich beds).

Different mineralogy and mineral sizes in quartz-rich and clay-rich beds would lead to different rock mechanical and strength responses. More clay content would separate the contacts between the quartz particles leading to stress transmission hindrance (Dusseault et al., 1986). The former would most likely lead to more strain softening behavior and more ductility. Elastic modulus of clay minerals is generally lower than quartz particles and carbonates (Vanorio et al., 2003) which would suggest that the quartz-rich beds would be different from clay-rich beds in rock mechanical responses.

4.1.3.2. Nitrogen Adsorption–Desorption Isotherms

Based on nitrogen adsorption-desorption isotherm analysis it is clearly observed that quartz-rich and clay-rich beds have generated different responses. Figure 4-32 and Figure 4-33 show nitrogen adsorption-desorption isotherms for quartz-rich and clay-rich beds.

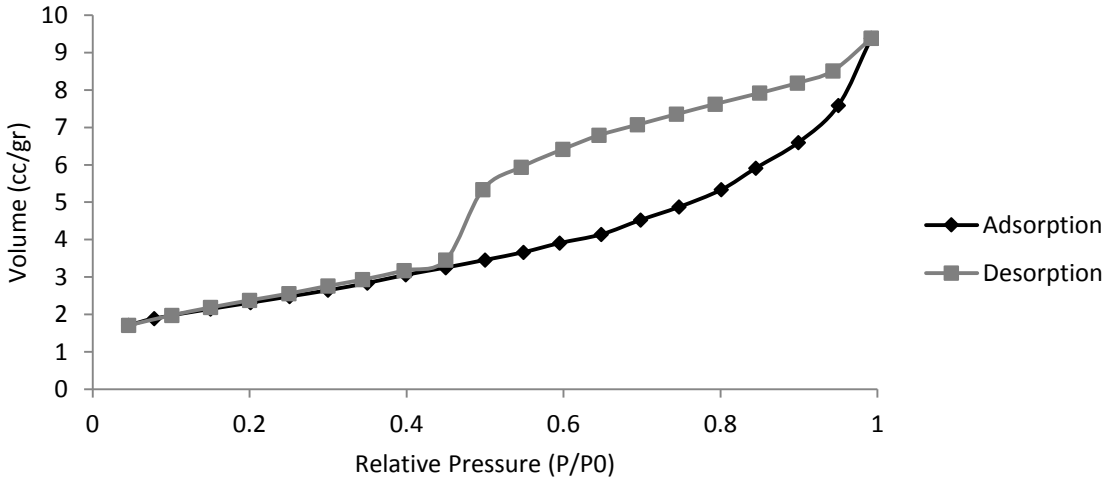

Figure 4-32. Nitrogen adsorption-desorption isotherm for quartz-rich bed.

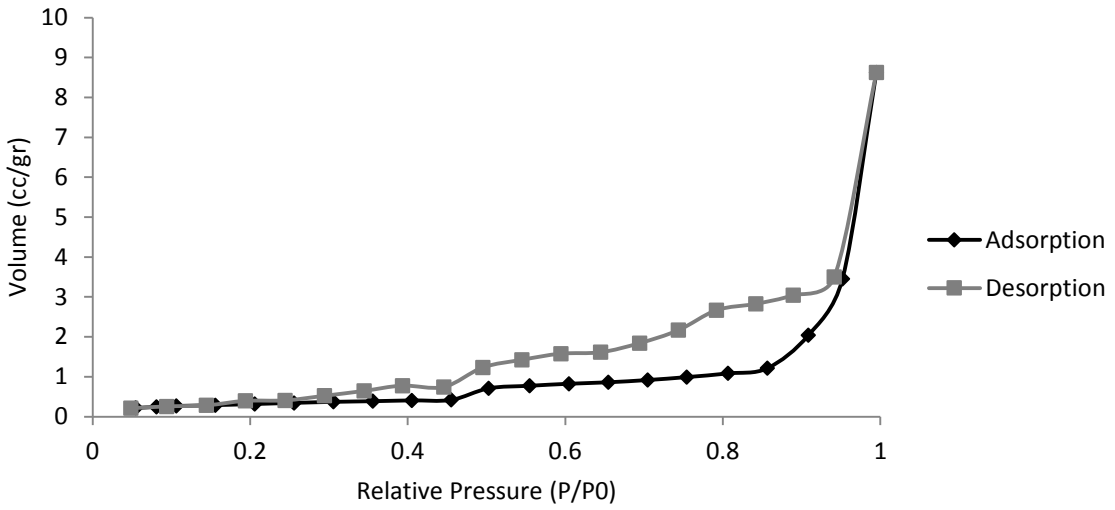

Figure 4-33. Nitrogen adsorption-desorption isotherm for clay-rich bed.

According to the pattern of hysteresis loops schematically shown in Figure 4-10, clay-rich beds can be categorized as H3 and quartz-rich beds as H4 which indicates that quartz-rich beds are slit-like pores and wedge-shaped pores dominated and clay-rich beds are parallel plate shaped pores and slit-like pores dominated. As shown in Figure 4-32 there is a wide hysteresis loop in nitrogen adsorption-desorption of quartz-rich bed which means that more gas is trapped in the pores during the desorption process. The pore system in both quartz-rich and clay-rich beds are dominated by slit-like pores within plate-like clay aggregates which is consistent with SEM analysis shown in Figure 4-34.

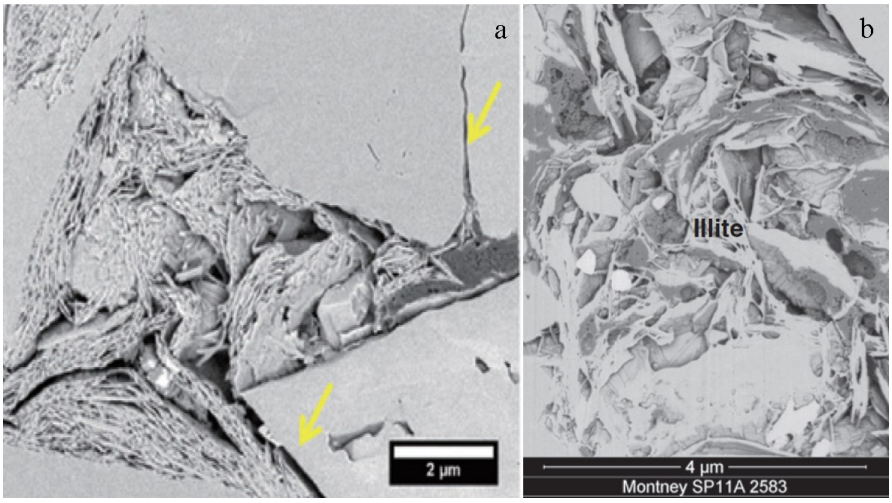

Figure 4-34. Slit-like pores within plate-like clay aggregates in Montney Samples. a) Akai et al. (2014) and b) Wood et al., (2015).

Pore volume and pore size distribution (PSD) of quartz-rich and clay-rich beds were calculated by the DFT method. According to the results of nitrogen adsorption-desorption isotherms, pore size distribution in quartz-rich and clay-rich beds are different (Figure 4-35 and Figure 4-36).

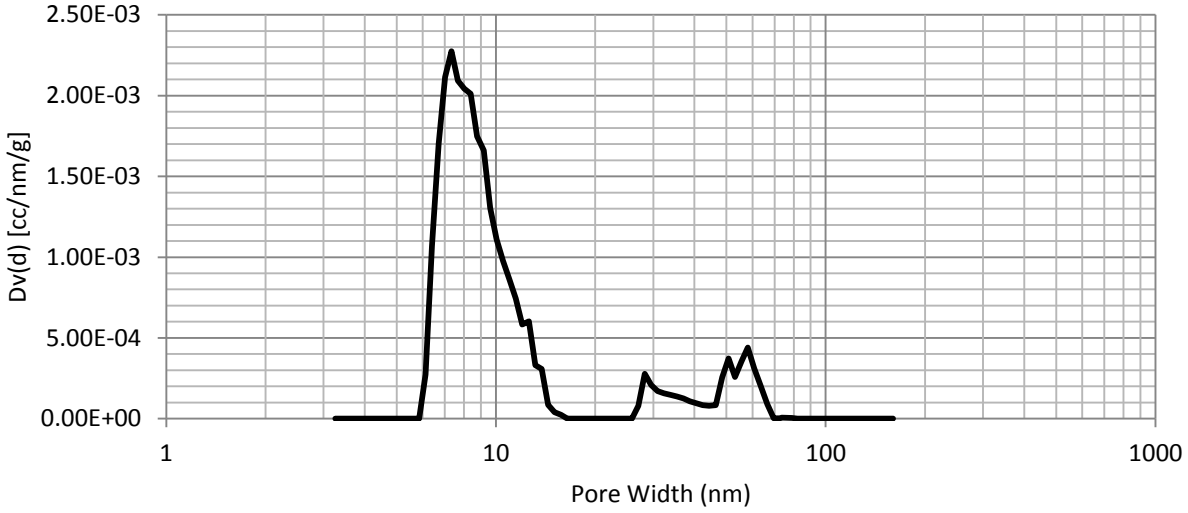

Figure 4-35. Pore size distribution in quartz-rich bed.

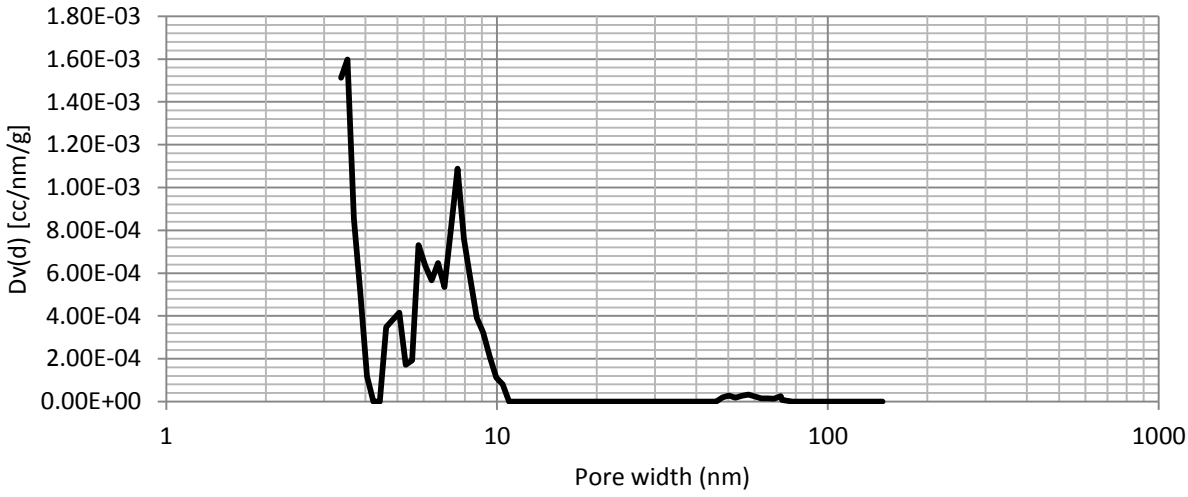

Figure 4-36. Pore size distribution in clay-rich bed.

In both quartz-rich and clay rich beds, pore of less than 15nm in width are predominant. For the quartz-rich beds PSD pore sizes range between 5.8nm to 14.4nm and the peak appears at 7.3nm while for the clay-rich beds, pore widths of 3.4nm to 10.9nm are dominant with a peak at 3.5nm width. However, in quartz-rich beds the second and third peaks for pore width are between 28.8nm to 69.5nm. The results demonstrate that the majority of the pore volume in quartz-rich and clay-rich beds is related to micro-pores and meso-pores. Measured pore volume and porosity for quartz-rich and clay-rich beds in nitrogen adsorption-desorption isotherm analysis is represented in Table 4-2.

Table 4-2. Pore volume and porosity of quartz-rich and clay-rich beds captured by nitrogen adsorption-desorption isotherm analysis

Sample	Weight (gr)	Density (gr/cm^3)	Pore volume (cm^3)	Porosity (%)
Quartz-rich bed	2.53	2.74	0.0143	3.92
Clay-rich bed	2.66	2.48	0.0083	2.06

As shown in Table 4-2, pore volume and porosity in quartz-rich bed are 41.9% and 47.4% higher than clay-rich bed. These results suggest that capillary behaviors in quartz-rich and clay-rich beds should be markedly different which can lead to different geomechanical responses and stress-induced phenomena during spontaneous imbibition.

4.1.3.3. Thermo-Gravimetric Analysis (TGA)

Before investigating the capillary suction in quartz-rich and clay-rich beds, it is necessary to determine the saturation of the beds. To measure the degree of saturation, the samples were tested by TGA through recording the weight as the sample was heated to 200^{o}C. Saturation is computed using Equation 4-3 based on the change in the weight and pore volume captured for the beds. Figure 4-37 and Figure 4-38 illustrate the change in weight with increasing temperature for quartz-rich and clay-rich bed samples where for both of the beds the peak appears at 118^{o}C. The results of TGA on quartz-rich and clay-rich beds can be found in Table 4-3. The results would suggest that initial water saturation (free water and water in pores) in quartz-rich and clay-rich beds are almost the same: 7.23% for clay-rich bed and 7.24% for quartz-rich bed.

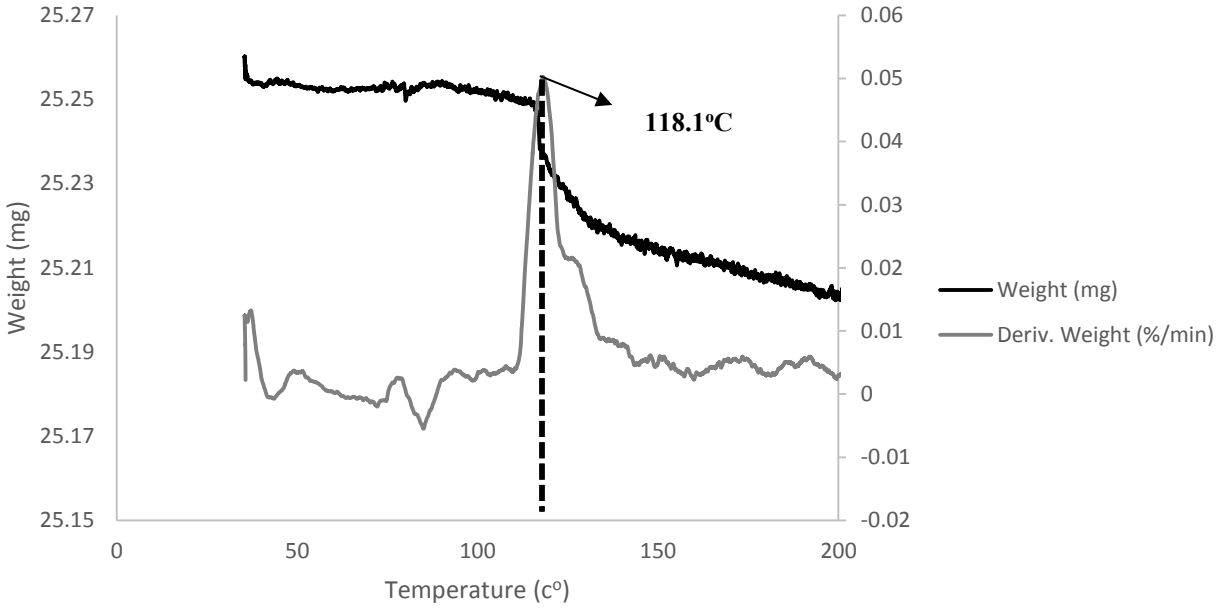

Figure 4-37. TGA results on quartz-rich bed.

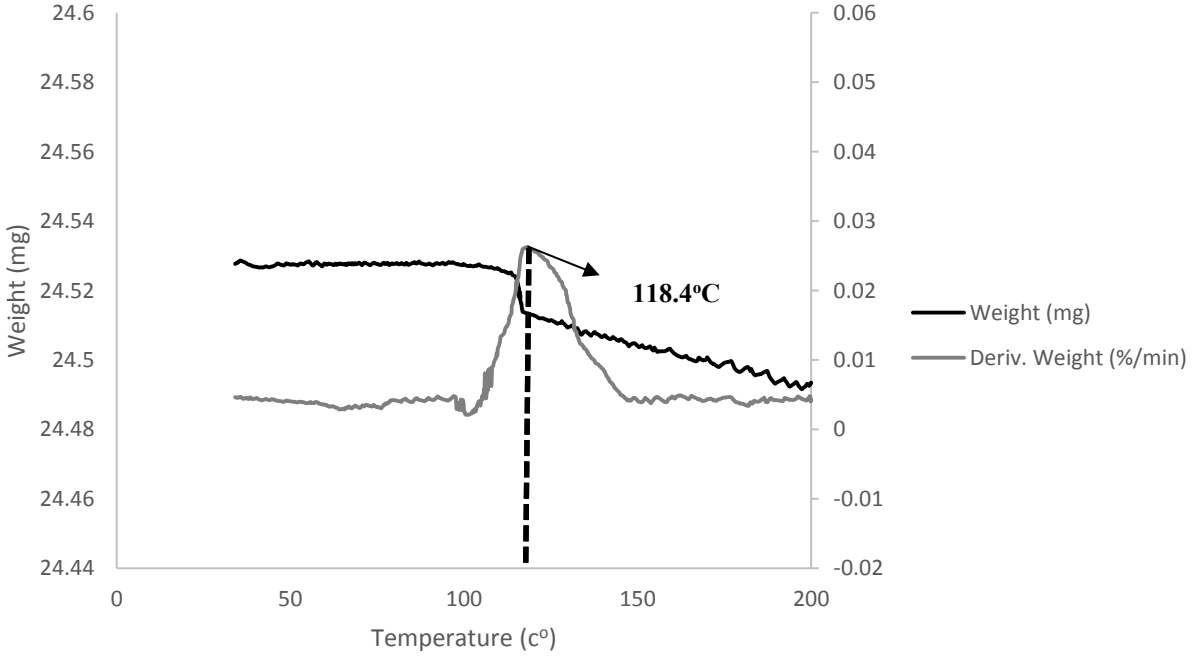

Figure 4-38. TGA result on clay-rich bed.

Table 4-3. Summary of TGA on quartz-rich and clay-rich beds.

Sample	Initial weight (mg)	Secondary weight (mg)	Water volume (cm^3)	Pore volume (cm^3)	Saturation (%)
Quartz-rich bed	25.24998	25.22383	2.615E-05	0.000361	7.24
Clay-rich bed	24.52767	24.51293	1.4736E-05	0.000204	7.23

4.1.3.4. Capillary Condensation Experiments

Based on nitrogen adsorption-desorption isotherm analysis it is clearly observed that the pore structure in quartz-rich and clay-rich beds is dominated by slit-like pores within plate-like clay aggregates. Therefore, the value of *H* in Equation (4-4) for slit-like pores can be defined based on Figure 4-39.

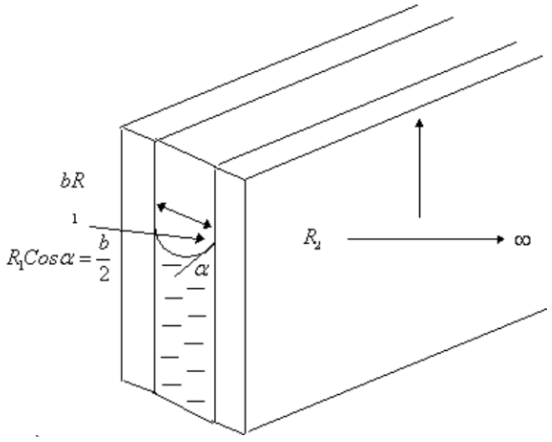

Figure 4-39. Schematic view of slit-like pores for capillary suction investigation in quartz-rich and clay-rich beds.

$$H = (\frac{1}{R_1} + \frac{1}{R_2}) ; \quad (4\text{-}22)$$

where $R_1 = (b/2\cos\alpha)$ and $R_2 = \infty$. Therefore:

$$H = (\frac{2cos\alpha}{b}) ; \quad (4\text{-}23)$$

where *b* is the separation between the plates. Substituting Equation (4-23) in Equation (4-4) and rearranging:

$$\ln(RH) = -\frac{\gamma V_m 2cos\alpha}{RTb} \Longrightarrow b = -\frac{\gamma V_m 2cos\alpha}{\ln(RH)*RT} \quad (4\text{-}24)$$

Also based on Young–Laplace equation, for slit-like pores (Figure 4-39) capillary suction (P_c) can be determined by Equation (4-25):

$$P_c = \gamma H = \gamma(\frac{1}{R1} + \frac{1}{R2}) \; ; \quad (4\text{-}25)$$

where γ is surface tension of the liquid phase. Substituting R_1, R_2 as well as b from Equation (4-24) to Equation (4-25) would generate Equation (4-26) where the capillary suction can be measured based on the humidity level in the pore structure which is dominated by slit-like pores

$$Pc = \frac{2\gamma cos\alpha}{b} \Longrightarrow Pc = -\frac{RT}{V_m} ln(RH) \; . \quad (4\text{-}26)$$

Capillary condensation experiments were conducted on quartz-rich and clay-rich bed Montney samples. Figure 4-3(d) illustrates the 1cm diameter by 1cm high specimens showing a clear variation in quartz-rich and clay-rich beds (with lower and higher number of quartz-rich beds). Pore volume and porosity of the samples with low and high number of beds were calculated based on the volumetric portion of quartz-rich and clay-rich beds. For the sample with lower number of quartz-rich beds the volumetric portion of clay-rich and quartz-rich beds were 85% and 15%, respectively, while for the sample with higher number of quartz-rich beds the volumetric portion of clay-rich and quartz-rich beds were 66% and 34%, respectively. Samples were placed in a humidity chamber and the amount of humidity level increased step by step to see where the weight of the samples would start changing. Initially the humidity level was fixed on 25% and the samples were exposed to that level of humidity for 5 days. No specific changes were observed to the weight of the samples. The humidity level was subsequently increased to 33%, which was corresponded to 152MPa capillary suction, which resulted in the clay-rich bed specimen to begin changing weight. The weight of quartz-rich bed specimen began to change once humidity was increased to 40%. The capillary condensation experiments continued through 50%, 75%, 85% and 90% humidity levels which corresponded to 95MPa, 39MPa, 22MPa and 14MPa capillary suction values. Based on the changes in the weight of the samples in each humidity level, the saturation of the samples was calculated and a relationship between the relative humidity and saturation for the samples was determined. Eventually, based on the relationship between the relative humidity and saturation (Table 4-4 and Figure 4-40) as well as the relationship between the relative humidity

and capillary suction, the values of capillary suction in different saturation were determined (Table 4-5 and Figure 4-41). Also, Table 4-6 represents a summary of capillary condensation experiments.

Table 4-4. Relationship between relative humidity (RH) and water saturation (S_w) for the tested samples.

Sample	Relationship between RH and S_w	R-squared value
Quartz-rich bed	S_w = 1.2516*RH - 0.3985	0.98
Clay-rich beds	S_w = 1.0965*RH - 0.2907	0.92
Lower number of Quartz-rich beds	S_w = 1.2697*RH - 0.3682	0.95
Higher number of Quartz-rich beds	S_w = 1.1778*RH - 0.3076	0.97

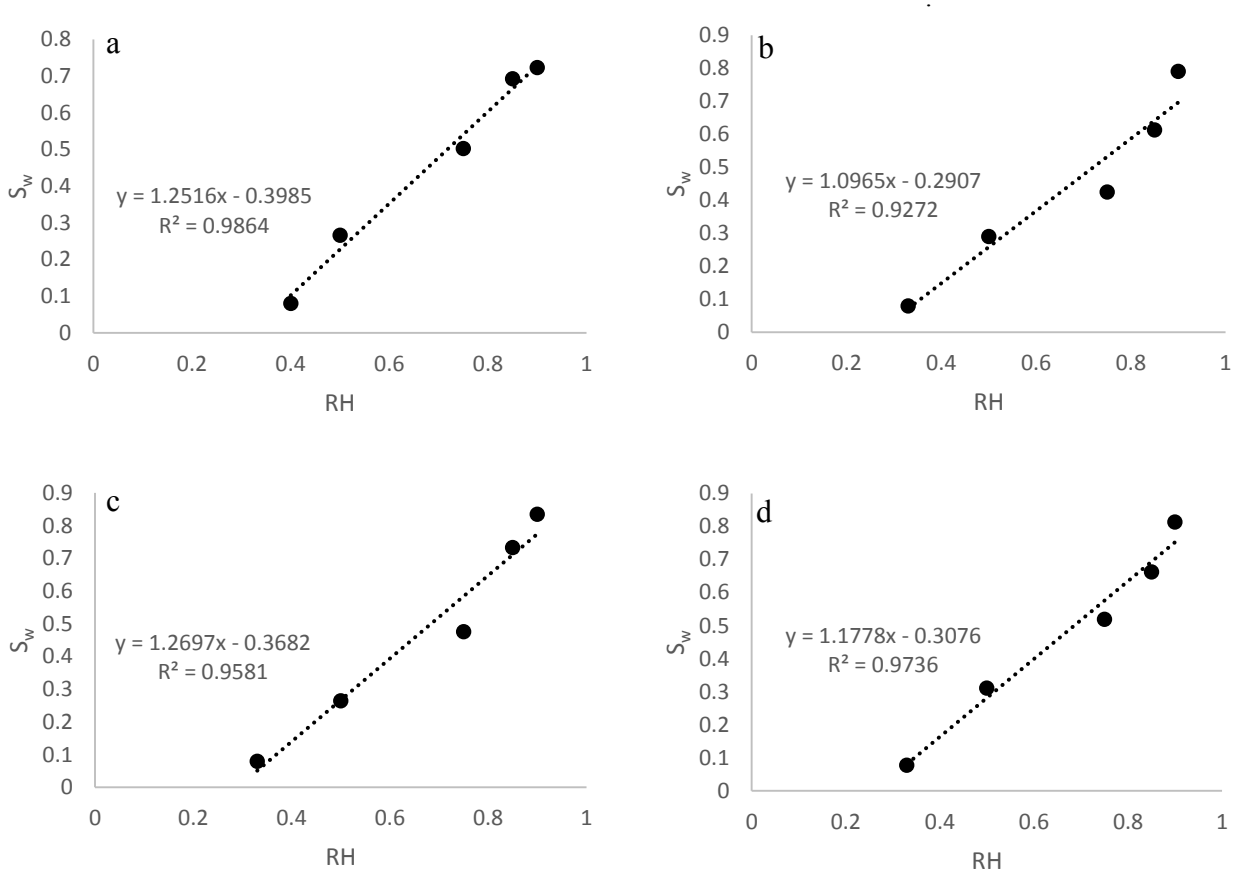

Figure 4-40. Relationship between relative humidity and saturation for the tested samples. a) quartz-rich sample; b) clay-rich sample; c) sample with lower number of quartz-rich beds; d) sample with higher number of quartz-rich beds.

Table 4-5. Relationship between capillary suction (P_c) and water saturation (S_w) for the tested samples.

Sample	Relationship between P_c and S_w	R-squared value
Quartz-rich bed	$P_c = -52.44\ln(S_w) + 3.8364$	0.95
Clay-rich beds	$P_c = -62.41\ln(S_w) - 1.7491$	0.96
Lower number of Quartz-rich beds	$P_c = -61.54\ln(S_w) - 1.7519$	0.97
Higher number of Quartz-rich beds	$P_c = -60.81\ln(S_w) - 2.2655$	0.98

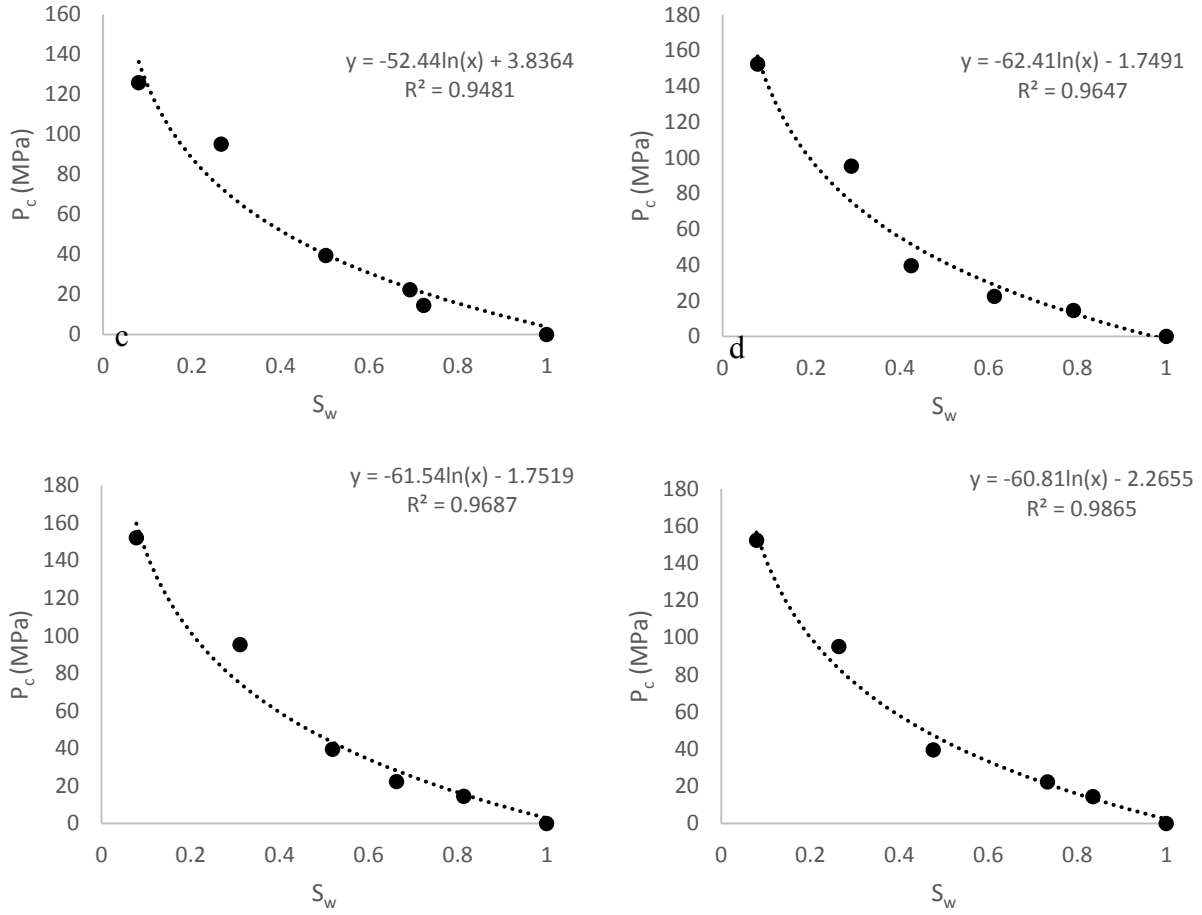

Figure 4-41. Relationship between capillary suction (P_c) and water saturation (S_w) for the tested samples. Top-left: quartz-rich bed sample; Top-right: clay-rich bed sample; Bottom-left: sample with lower number of quartz-rich beds; Bottom-right: sample with higher number of quartz-rich beds.

Table 4-6. Summary of capillary condensation experiments.

Sample	Pore volume (cm^3)	Initial water volume (cm^3)	Initial weight (gr)	RH (%)	Weight (gr)	Capillary suction (MPa)	Saturation (%)
Quartz-rich bed	0.0308	0.0022	2.5183	40	2.5186	125.8	8.0
				50	2.5243	95.2	26.6
				75	2.5316	39.5	50.2
				85	2.5374	22.3	69.2
				90	2.5384	14.5	72.3
Clay-rich beds	0.0162	0.0012	2.1755	33	2.1756	152.3	7.9
				50	2.1790	95.2	29.0
				75	2.1812	39.5	42.5
				85	2.1842	22.3	61.3
				90	2.1871	14.5	79.1
Sample with Lower number of Quartz-rich beds	0.0184	0.0013	2.2412	33	2.2413	152.3	7.8
				50	2.2456	95.2	31.1
				75	2.2494	39.5	51.9
				85	2.2521	22.3	66.2
				90	2.2549	14.5	81.4
Sample with Higher number of Quartz-rich beds	0.0211	0.0015	2.2108	33	2.2110	152.3	7.9
				50	2.2149	95.2	26.4
				75	2.2193	39.5	47.6
				85	2.2248	22.3	73.3
				90	2.2269	14.5	83.5

At low saturation levels, the capillary suction in clay-rich bed specimens is up to 17.7% higher than quartz-rich bed specimens. As water saturation increases in the specimens, however, the rate at which capillary suction decreases becomes markedly different between the two specimens. The clay-rich bed specimen displays a higher rate of reduction in capillary suction such that at around 58% water saturation, the capillary suction is actually lower than the quartz-rich bed specimen (Figure 4-42). This behavior reflects the difference in pore structure in the specimens and agrees with the results of the nitrogen adsorption-desorption isothermal analyses presented earlier.

The variations in capillary pressure as water saturation is increasing would also imply that local changes in effective stress in quartz-rich and clay-rich beds would be different leading to different volumetric responses and increasing the possibility of yielding near the interface between the beds.

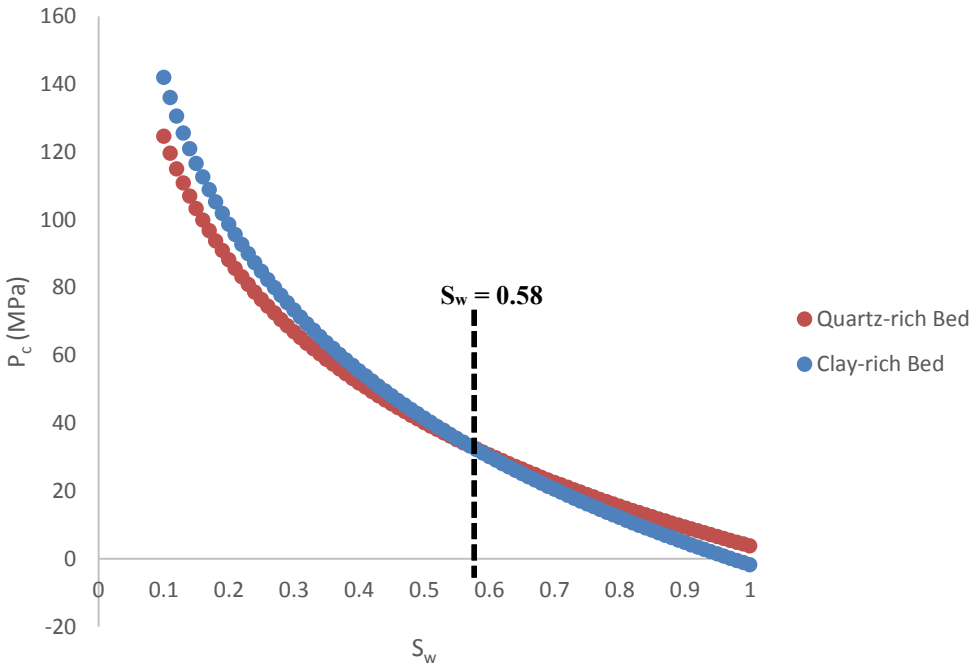

Figure 4-42. Comparing quartz-rich and clay-rich beds capillary suction as the water saturation is changing.

In addition, comparing the results of capillary condensation experiments on the samples with lower (15% in volume) and higher (34% in volume) quartz-rich beds indicate that as the number of quartz-rich beds increases the capillary suction would decrease as low as 14.4%.

4.1.3.5. Micro-Geomechanical Measurements

To investigate the changes in rock mechanical properties and strength parameters, micro-indentation tests and micro-scratch tests were performed on specimens at different levels of saturation and hence, capillary suction.

4.1.3.5.1. Micro-indentation

To capture both Young's modulus and Poisson's ratio simultaneously by micro-indentation tests first an analytical approach based on least-square method was developed based on Equation (4-5) and considering $S = dP/dh = (P_m - P)/(h_m - h)$, Equation (4-27) can be derived.

$$P = P_m - \frac{E_r * 2\beta * \sqrt{A_c} * (h_m - h)}{\pi} \tag{4-27}$$

where P_m and h_m are the maximum load and the depth at the maximum load, respectively. Er (indentation reduced modulus) can be determined by rearranging Equation (4-6).

$$\frac{1}{E_r} = \frac{1-v^2}{E} + \frac{1-v_i^2}{E_i^2} \tag{4-28}$$

For nonlinear least-square approach a function which is dependent on Young's modulus and Poisson's ratio is defined as shown in Equation (4-29).

$$F_k(E, v) = P_m - \frac{E_r * 2\beta * \sqrt{A_c} * (h_m - h_k)}{\pi} - P_k = 0 \tag{4-29}$$

where "k" indicates the points at which load P_k make the displacement h_k. The points are selected from the first 25% upper part of unloading curve. The correct values of Young's modulus (E) and Poisson's ratio (v) would make $F_k\ (E,v)$ zero for all values of k. By taking a Taylor series expansion of Equation (4-29), Equation (4-30) can be generated.

$$F_k^{i+1}(E, v) = F_k^i(E, v) + \frac{\partial F_k^i}{\partial E}\Delta E + \frac{\partial F_k^i}{\partial v}\Delta v \tag{4-30}$$

Rewriting Equation (4-30) for $F_k(E, v) = 0$:

$$-F_k^i(E, v) = \frac{\partial F_k^i}{\partial E}\Delta E + \frac{\partial F_k^i}{\partial v}\Delta v \tag{4-31}$$

where ΔE and Δv represents the corrections for E and v and "i" indicates the iteration step. For "n" data points Equation (4-32) can be represented in matrix form.

$$[F] = [G][H] \tag{4-32}$$

$$[F] = \begin{bmatrix} F_1 \\ F_2 \\ F_3 \\ \vdots \\ F_n \end{bmatrix} \quad [G] = \begin{bmatrix} \frac{\partial F_1}{\partial E} & \frac{\partial F_1}{\partial v} \\ \frac{\partial F_2}{\partial E} & \frac{\partial F_2}{\partial v} \\ \frac{\partial F_3}{\partial E} & \frac{\partial F_3}{\partial v} \\ \vdots & \vdots \\ \frac{\partial F_n}{\partial E} & \frac{\partial F_n}{\partial v} \end{bmatrix} \quad [H] = \begin{bmatrix} \Delta E \\ \Delta v \end{bmatrix}$$

Based on Equation (4-32) the correction terms can be determined as shown in Equation (4-33).

$$[H] = [G]^{-1}[F] \tag{4-33}$$

$$E_{i+1} = E_i + \Delta E \tag{4-34}$$

$$v_{i+1} = v_i + \Delta v \tag{4-35}$$

E_i and v_i in each iteration would be calculated and then according to the correction terms, the final values of E and v can be determined.

Two sets of micro-indentation tests (10 points) were completed along quartz-rich beds in at 8%, 26.6%, 5.2%, 72.3% and 97.8% water saturation and clay-rich beds at 7.9%, 29%, 42.5%, 79.1% and 96.2% water saturation. Saturating the samples was completed in the humidity chamber, which was used for capillary condensation experiments. To reach to a saturation value near 100% a quartz-rich bed sample, a clay-rich bed sample and one 1cm to 1cm cylindrical sample was pressurized to a 300psi pressure while they were submerged in the water. Although there might be the possibility of micro-fracture initiation or propagation as a result of saturating the samples under pressure. This procedure produced degrees of water saturation of 97.8% and 96.2% in the quartz-rich bed and clay-rich bed specimens, respectively.

For micro-indentation tests, the indentation load was 900mN and the loading rate was 45 mN/s. Micro-indentation results on quartz-rich and clay-rich beds in different water saturations are represented in Figure 4-43 and Figure 4-44, respectively. As it can be clearly observed, as the saturation increases, the average depth of penetration also increases in both quartz-rich and clay-rich beds but the rate of change in depth of penetration is higher in clay-rich beds. Initial stress state strongly affects the indenter depth of penetration. From geomechanical point of view, as the indenter is penetrating in the rock the pore pressure especially at higher water saturations would

build up which can lead to decreasing the local effective stresses followed by increasing the strains in both axial (parallel to the loading direction) and radial directions. The former would lead to increasing the depth of penetration with some strain softening. Based on micro-indentation analysis and the proposed non-linear least square method the mean values of Young's modulus and Poisson's ratio as a function of saturation were determined shown in Figure 4-45 and Figure 4-46. Additionally, Figure 4-49 to Figure 4-52 present the distribution of Young's modulus and Poisson's ratio measurements as well as the mean response on quartz-rich and clay-rich beds at different water saturation levels and capillary suction values. Based on the results of capillary condensation experiments and the values of capillary suction related to each saturation, the changes in Young's modulus and Poisson's ratio as a result of changing the capillary suction are shown in Figure 4-47 and Figure 4-48, respectively.

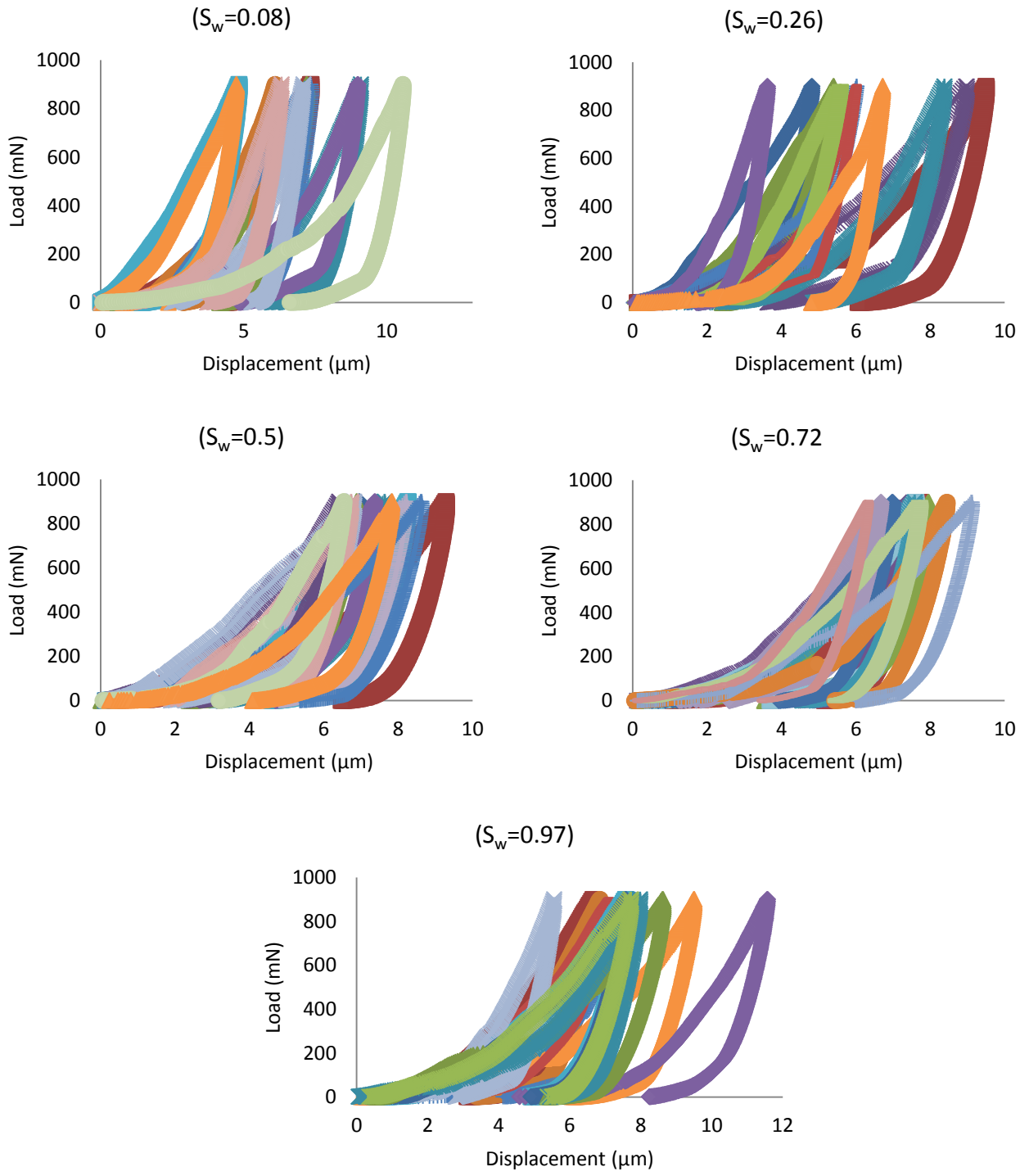

Figure 4-43. Micro-indentation load-displacement curves in different saturations along the quartz-rich beds. Each curve (color) is related to one indentation loading-unloading cycle.

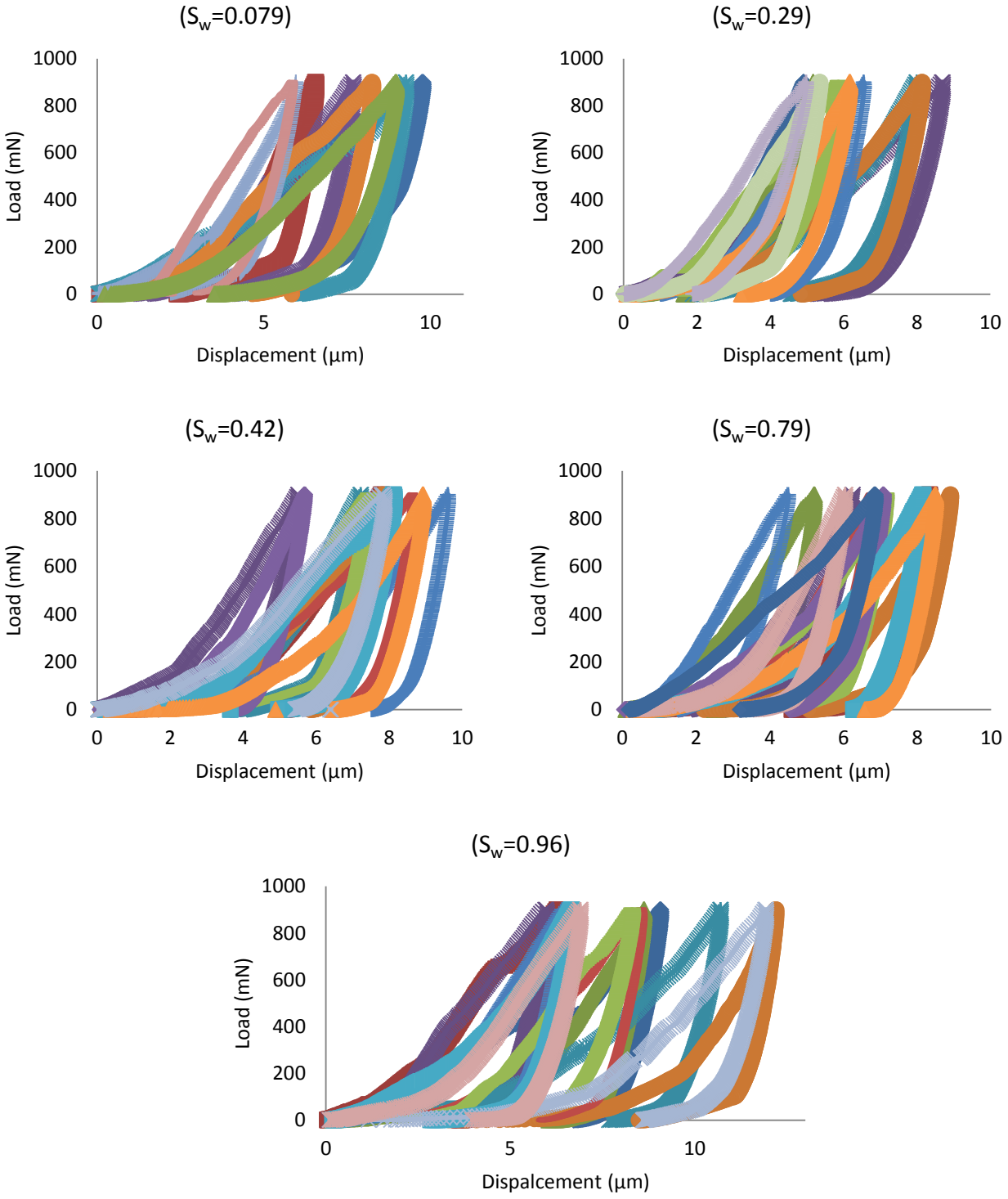

Figure 4-44. Indentation load-displacement curves in different saturations along the clay-rich beds. Each curve (color) is related to one indentation loading-unloading cycle.

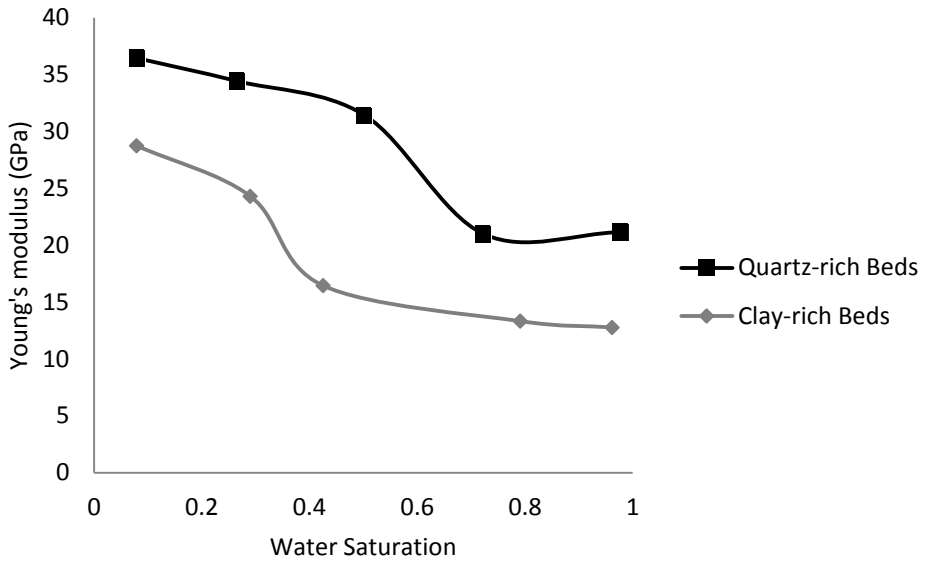

Figure 4-45. Changes in Young's modulus as a function of water saturation in quartz-rich and clay-rich beds.

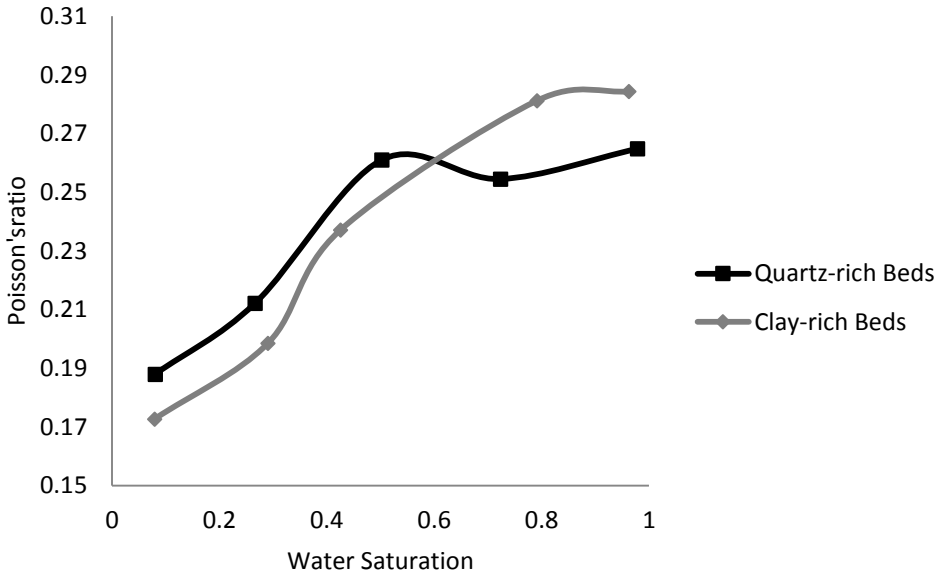

Figure 4-46. Changes in Poisson's ratio as a function of water saturation in quartz-rich and clay-rich beds.

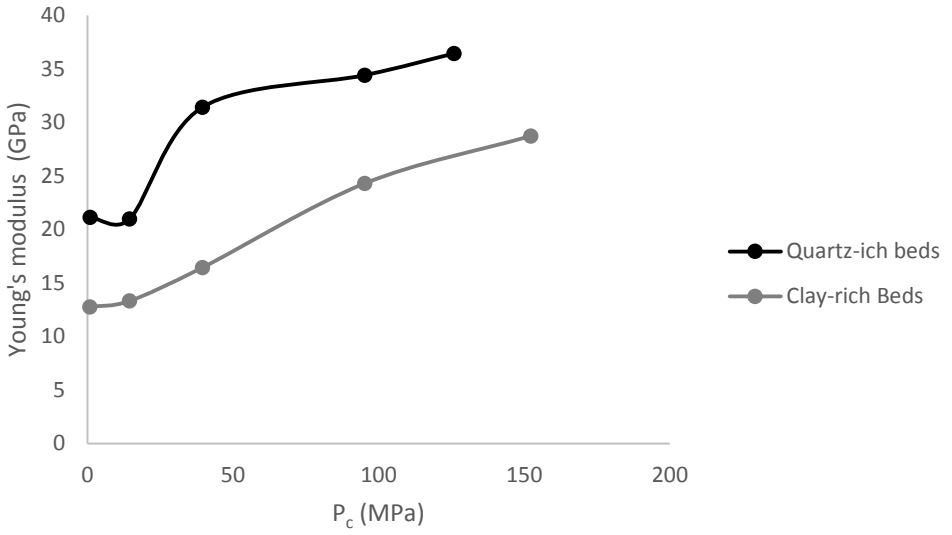

Figure 4-47. Changes in Young's modulus as a function of capillary suction in quartz-rich and clay-rich beds.

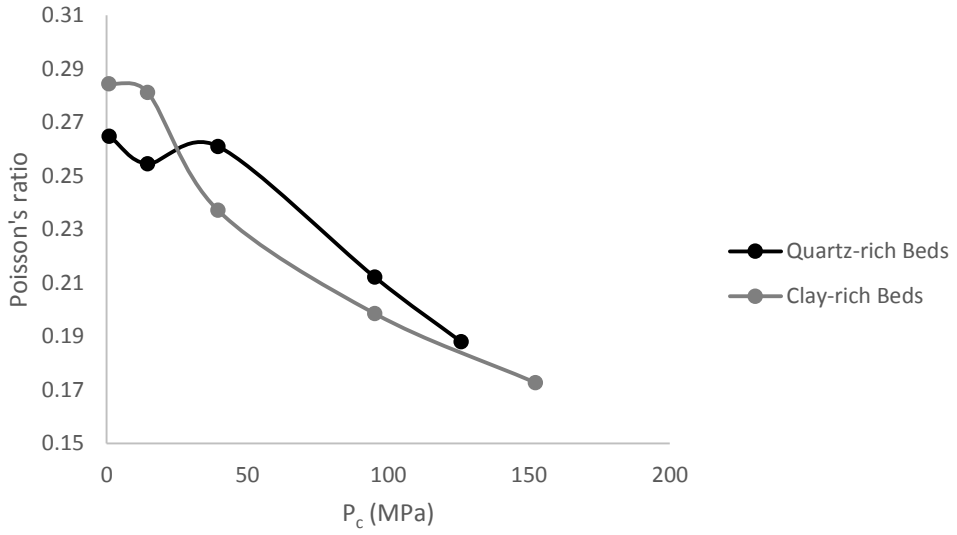

Figure 4-48. Changes in Poisson's ratio as a function of saturation in quartz-rich and clay-rich beds.

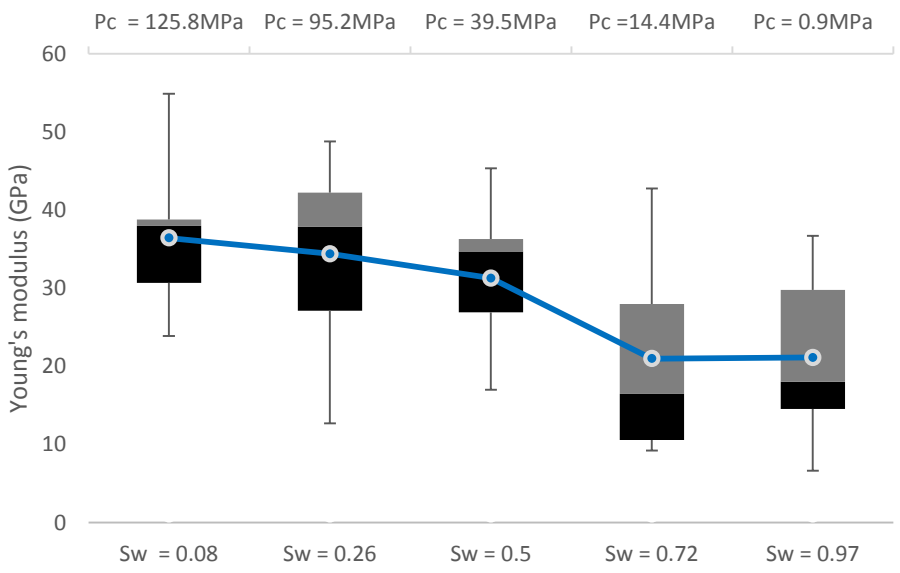

Figure 4-49. Distribution of Young's modulus measurements as well as the mean response on quartz-rich beds at different water saturation and capillary suction values. The middle line in the boxes shows the median, the boxes indicate the range between the first quartile and the third quartile. Whiskers above and below the boxes indicate the maximum and minimum values, respectively. The filled circles show the arithmetic mean.

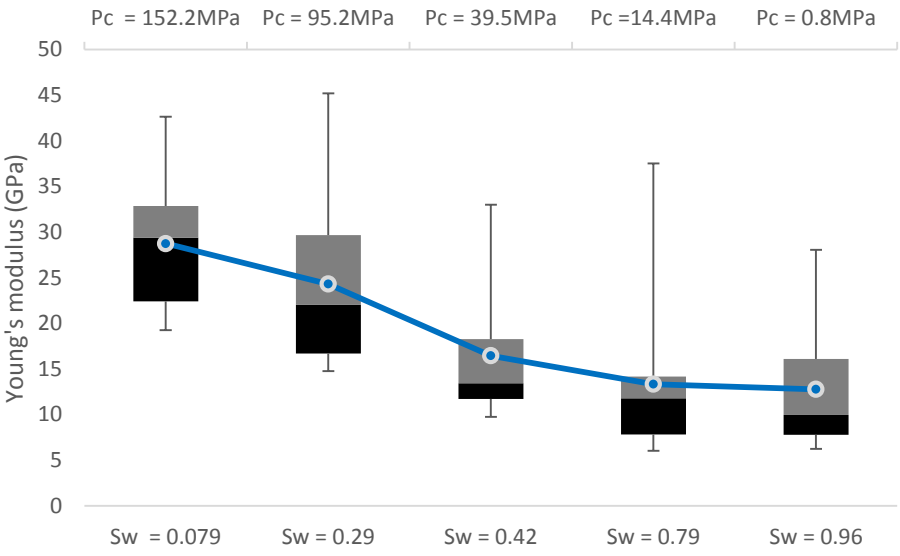

Figure 4-50. Distribution of Young's modulus measurements as well as the mean response on clay-rich beds at different water saturation and capillary suction values. The middle line in the boxes shows the median, the boxes indicate the range between the first quartile and the third quartile. Whiskers above and below the boxes indicate the maximum and minimum values, respectively. The filled circles show the arithmetic mean.

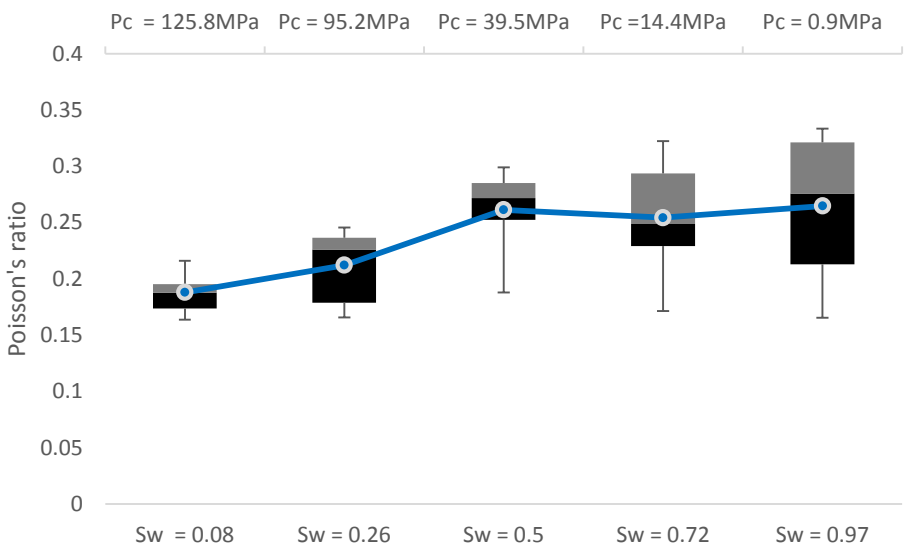

Figure 4-51. Distribution of Poisson's ratio measurements as well as the mean response on quartz-rich beds at different water saturation and capillary suction values. The middle line in the boxes shows the median, the boxes indicate the range between the first quartile and the third quartile. Whiskers above and below the boxes indicate the maximum and minimum values, respectively. The filled circles show the arithmetic mean.

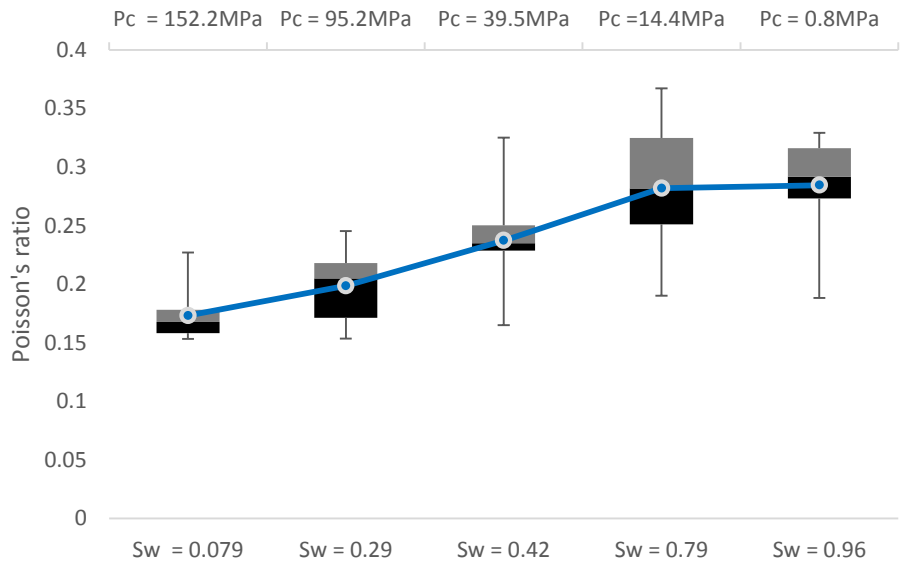

Figure 4-52. Distribution of Poisson's ratio measurements as well as the mean response on clay-rich beds at different water saturation and capillary suction values. The middle line in the boxes shows the median, the boxes indicate the range between the first quartile and the third quartile. Whiskers above and below the boxes indicate the maximum and minimum values, respectively. The filled circles show the arithmetic mean.

The results imply that initially Young's modulus in quartz-rich beds is 21.1% higher than clay-rich beds. As the water saturation is increasing and capillary suction is decreasing the values of Young's modulus in both quartz-rich and clay-rich would decrease. Sharp reduction in Young's modulus of clay-rich beds begins from 29% water saturation after 37.5% reduction in capillary suction while the same behavior is observed in quartz-rich beds but after 50.2% water saturation and 68.6% reduction in capillary suction. The maximum difference between the values of Young's modulus in quartz-rich and clay-rich beds takes place at around 50.2% water saturation where Young's modulus in quartz-rich beds is 52% higher than clay-rich beds. Regarding Poisson's ratio, initially it is 8.1% higher in quartz-rich beds. Although Poisson's ratio in both quartz-rich and clay-rich beds are increasing as a result of water saturation increase and capillary suction decrease but rate of increase is higher in clay-rich beds and after around 60% water saturation the values of Poisson's ratio become higher in clay-rich beds while no significant change is observed in the values of Poisson's ratio for quartz-rich beds. Based on the changes in elastic properties at around 50-60% water saturation and according to the results of capillary condensation experiments where at 58% water saturation capillary suction would reduce more in clay-rich beds, one may conclude that at around 50-60% water saturation geomechanical behaviors would be triggered and progressed.

The observations noted above would suggest that brittle to ductile transitional behavior happens sooner in clay-rich beds than quartz-rich beds. Also, Figure 4-53 and Figure 4-54 represent the percentage of each Young's modulus and Poisson's ratio range within micro-indentation experiments for each water saturation level. It can be observed that at low saturation degrees the majority of tested points have Young's modulus range between 20-40GPa while the tested points with 30-40GPa range in quartz-rich beds are higher than clay-rich beds. As the saturation is increasing and capillary suction is decreasing Young's modulus ranges of the majority of the tested points drop to 5-20GPa for both quartz-rich and clay-rich beds while 5-10GPa range is higher in clay-rich beds and the tested points with 10-20GPa range are higher in quartz-rich beds. For Poisson's ratio the majority of the tested points in both quartz-rich and clay-rich beds for low water saturation are within 0.15-0.2 range while at higher water saturation the dominated range for clay-rich beds is 0.25-0.35 and for quartz-rich beds is 0.2-0.3.

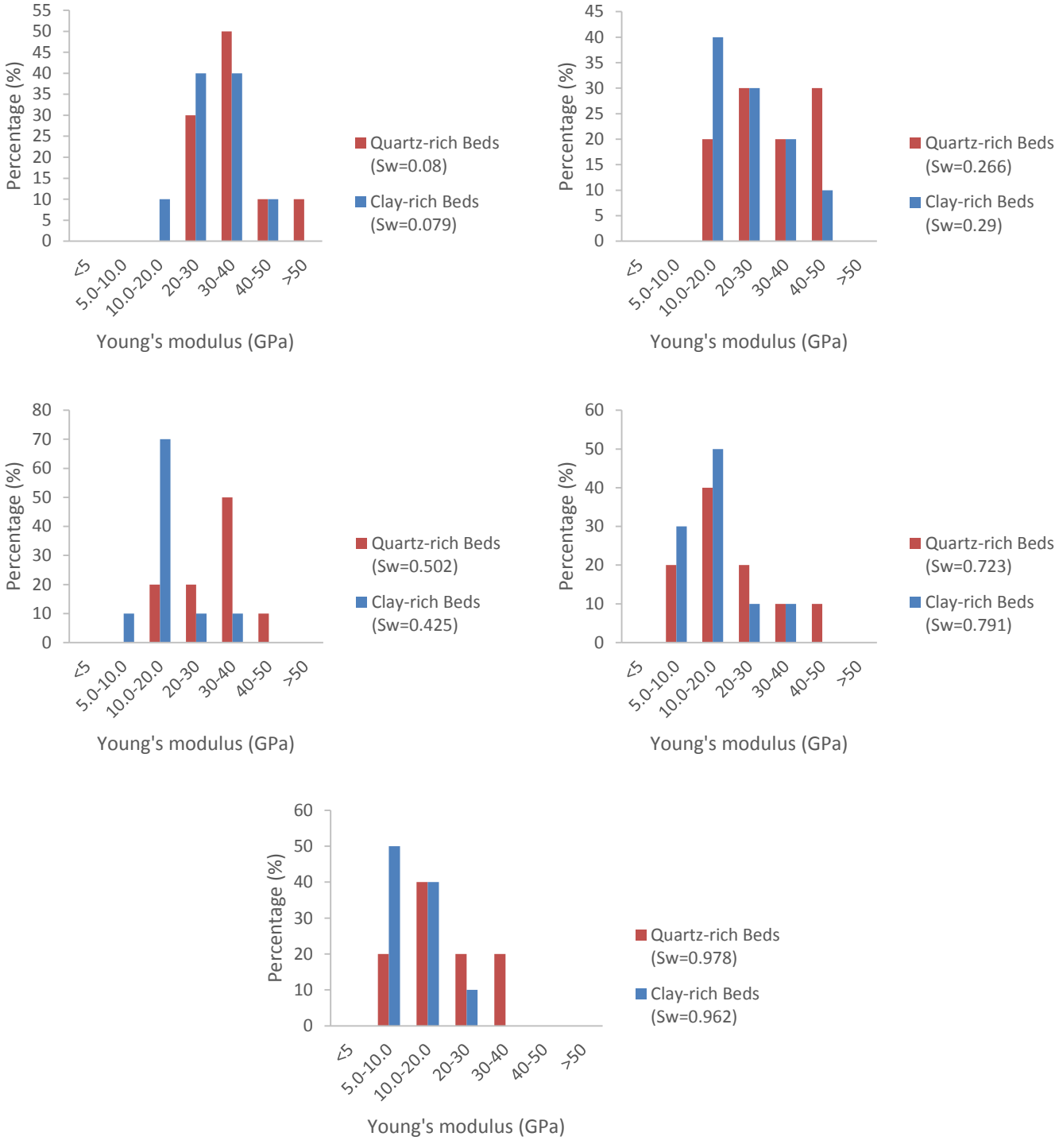

Figure 4-53. Percentage of Young's modulus values for the measured points in different saturations.

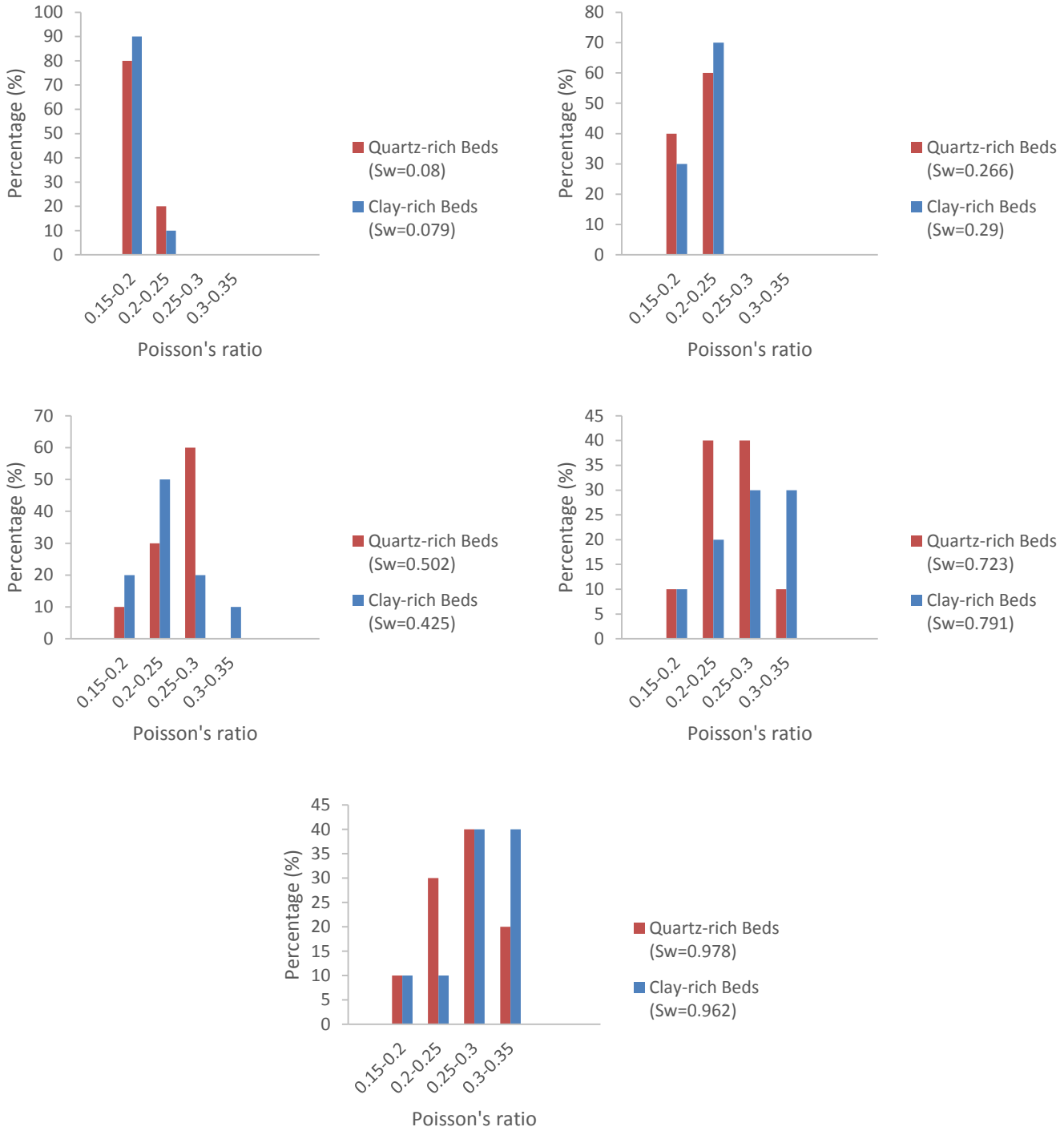

Figure 4-54. Percentage of Poisson's ratio values for the measured points in different saturations.

The results imply that at any water saturation level the rock mechanical behavior of clay-rich beds and quartz-rich beds are different. Table 4-7 shows a summary of micro-indentation along quartz-rich and clay-rich beds.

Table 4-7. Summary of Young's modulus and Poisson's ratio values captured by micro-indentation along quartz-rich and clay-rich beds.

Sample	S_w	P_c (MPa)	Young's modulus (GPa)	Poisson's ratio
Quartz-rich Beds	0.08	125.8	36.4	0.18
	0.26	95.2	34.4	0.21
	0.50	39.5	31.4	0.26
	0.72	14.4	20.9	0.25
	0.97	0.9	21.1	0.26
Clay-rich Beds	0.079	152.2	28.7	0.17
	0.29	95.2	24.2	0.19
	0.42	39.5	16.4	0.23
	0.79	14.4	13.3	0.28
	0.96	0.8	12.77	0.28

4.1.3.5.2. Micro-scratch

An analytical approach to interpret the results from micro-scratch testing was developed to determine the strength parameters on quartz-rich and clay-rich beds. For failure analysis, the Mohr-Coulomb criterion has been considered for unsaturated porous cohesive-frictional materials which can be written in terms of effective stress (Equation (4-36)). Also, unconfined compressive strength (UCS) can be derived as represented in Equation (4-37).

$$\sigma_1' = \sigma_3' \left(\frac{1+sin\varphi'}{1-sin\varphi'}\right) + \frac{2Ccos\varphi'}{1-sin\varphi'} + \left(\frac{2sin\varphi'}{1-sin\varphi'}\right) S\alpha P_c \quad (4\text{-}36)$$

$$UCS = \frac{2Ccos\varphi'}{1-sin\varphi'} + \left(\frac{2sin\varphi'}{1-sin\varphi'}\right) S\alpha P_c \quad (4\text{-}37)$$

where σ_1' and σ_3' are the maximum and minimum principal stresses, φ' is friction angle and c is cohesion. Considering the blade scratching the surface as shown in Figure 4-55. Based on the concept of bearing capacity (Michalowski 2001) which is a magnitude of stress required to cause plastic flow, the scratching area can be divided into three main regions: active (shown in blue), passive (shown in red) and the region between them.

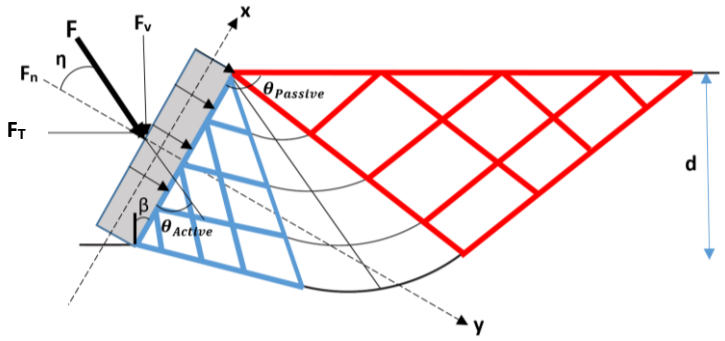

Figure 4-55. Schematic view of the scratching area.

Based on Figure 4-55, η is interface friction angle ($\delta = \tan(\eta + \beta)$ where δ is the ratio of normal to horizontal components of the cutting load), β is the back rake angle, d is depth of cut, F_v and F_T are the vertical and horizontal load components, F_n is the component normal to the blade, θ_{Active} and $\theta_{Passive}$ are the major principle stress inclination in active and passive zones. According to the concept of bearing capacity (q) (Michalowski 2001) the relationship between the scratch hardness (H_T) and UCS can be derived.

$$q = C\ cot\varphi' \left[\frac{1-sin\varphi' cos2\theta_{Active}}{1-sin\varphi'}\ e^{(2\theta_{fan}\ tan\varphi')} - 1\right] = C * \Delta \quad (4\text{-}38)$$

$$\theta_{fan} = \theta_{Passive} - \theta_{Active} \quad (4\text{-}39)$$

$$\theta_{Passive} = \frac{\pi}{2} + \beta$$

For unsaturated $C = C' + \alpha S P_c\ tan\varphi'$

$$F_n = q\,A_p = q\,\frac{d\,w}{cos\beta} \;\rightarrow\; F = \frac{F_n}{cos\eta} \;\rightarrow\; F_T = F\cos(\beta+\eta) = q\,\frac{d\,w}{cos\beta cos\eta}\cos(\beta+\eta) \quad (4\text{-}40)$$

where *w* is width of cut and *Ap* is the projected area in horizontal force (*Fs*) direction = d*w.

$$\frac{H_T}{UCS} = \frac{{}^{F_T}/_{dw}}{\frac{2Ccos\varphi'}{1-sin\varphi'}+\left(\frac{2sin\varphi'}{1-sin\varphi'}\right)S\alpha P_c} = \frac{\frac{q}{cos\beta cos\eta}\cos(\beta+\eta)}{\frac{2Ccos\varphi'}{1-sin\varphi'}+\left(\frac{2sin\varphi'}{1-sin\varphi'}\right)S\alpha P_c} = \Delta\frac{(1-sin\varphi')\cos(\beta+\eta)}{2cos\varphi' cos\beta cos\eta} \quad (4\text{-}41)$$

Based on Equation (4-41) it is observed that for unsaturated porous cohesive-frictional materials there is not necessarily a 1:1 correlation between H_T and UCS. In Equation (4-41) there are two parameters θ_{Active} and θ_{fan} that needs to be calculated. Therefore, the Michalowski (2001) approach has been considered to obtain θ_{Active} and θ_{fan}. The effective mean stress (σ'_m) in the passive zone would be calculated and then based on the relationship between the effective mean stress in the passive and active zones, θ_{Active} and θ_{fan} can be determined.

$$\sigma'_{m\,(Passive)} = \frac{c'cot\varphi'+\alpha SP_c}{1-sin\varphi'} \quad (4\text{-}42)$$

$$\theta_{Active} = 0.5\left[\pi-\eta-\arcsin\left(\frac{sin\eta}{sin\varphi'}\left(1-\frac{1-sin\varphi'}{e^{2(\beta+\frac{\pi}{2}-\theta_{Active})tan\varphi'}}\right)\right)\right] \quad (4\text{-}43)$$

$$\sigma'_{m\,(Active)} = \sigma'_{m\,(Passive)}\,e^{(2\theta_{fan}\,tan\varphi')} \quad (4\text{-}44)$$

Finally, based on Equation (4-42), (4-43) and (4-44), θ_{Active} and θ_{fan} can be obtained and then by replacing these values in Equation (4-41), the UCS can be calculated. To evaluate the accuracy of the developed analytical approach, Dagrain (2001) scratch and UCS experiments were considered, and the results obtained from the developed analytical approach were compared with Dagrain (2001) experiments (shown in Figure 4-56). Following this, two sets of micro-scratch tests were completed using Rockwell (half-apex angle 60°) and conical (half-apex angle 30°) tips in 8%, 26.6%, 5.2%, 72.3% and 97.8% water saturation for quartz-rich beds and 7.9%, 29%, 42.5%, 79.1% and 96.2% water saturation for clay-rich beds. The scratching rate was 0.05mm/s under a constant 10N normal load. Figure 4-57 represents the scratches in low and high water saturations along quartz-rich and clay-rich beds.

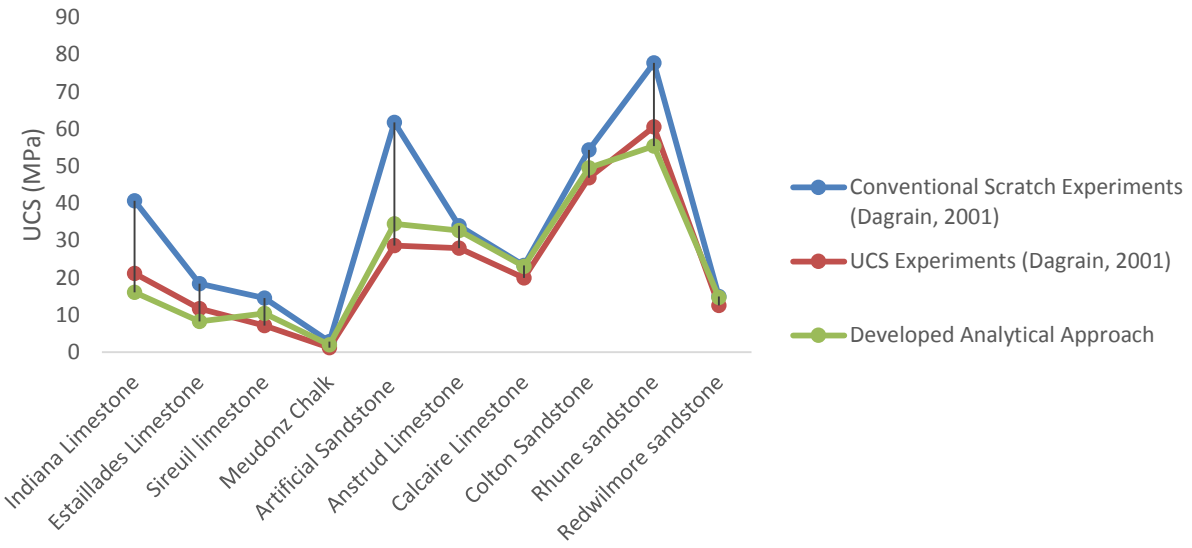

Figure 4-56. Comparing the values for UCS of different rocks obtained by Dagrain (2001) scratch and UCS experiments with the UCS obtained by the developed analytical approach.

As it can be seen in Figure 4-57, as the water saturation increases the scratches become smoother in both quartz-rich and clay-rich beds which can be an indication of the reduction in the strength. Also, the depths of points along the scratches in quartz-rich and clay-rich beds for different saturations are represented in Figure 4-58 and Figure 4-59. Figure 4-60 and Figure 4-61 show the average depth of cut using conical and Rockwell tips in different degrees of water saturation. The depth of cut with conical tip in clay-rich beds are 11.8% higher than quartz-rich beds in low water saturation and high capillary suction and as the water saturation is increasing (capillary suction is decreasing), the difference between the depth of cut in quartz-rich and clay-rich beds decreases. These figures also show that the depth of cut by the conical tip shows greater sensitivity to the variation in capillary suction which can be the result of softening related to capillary-suction reduction and water saturation increase. The same behavior can be observed while scratching with Rockwell tip but the difference between the depth of cut along quartz-rich and clay-rich beds in low and high water saturations is less than conical tip scratching.

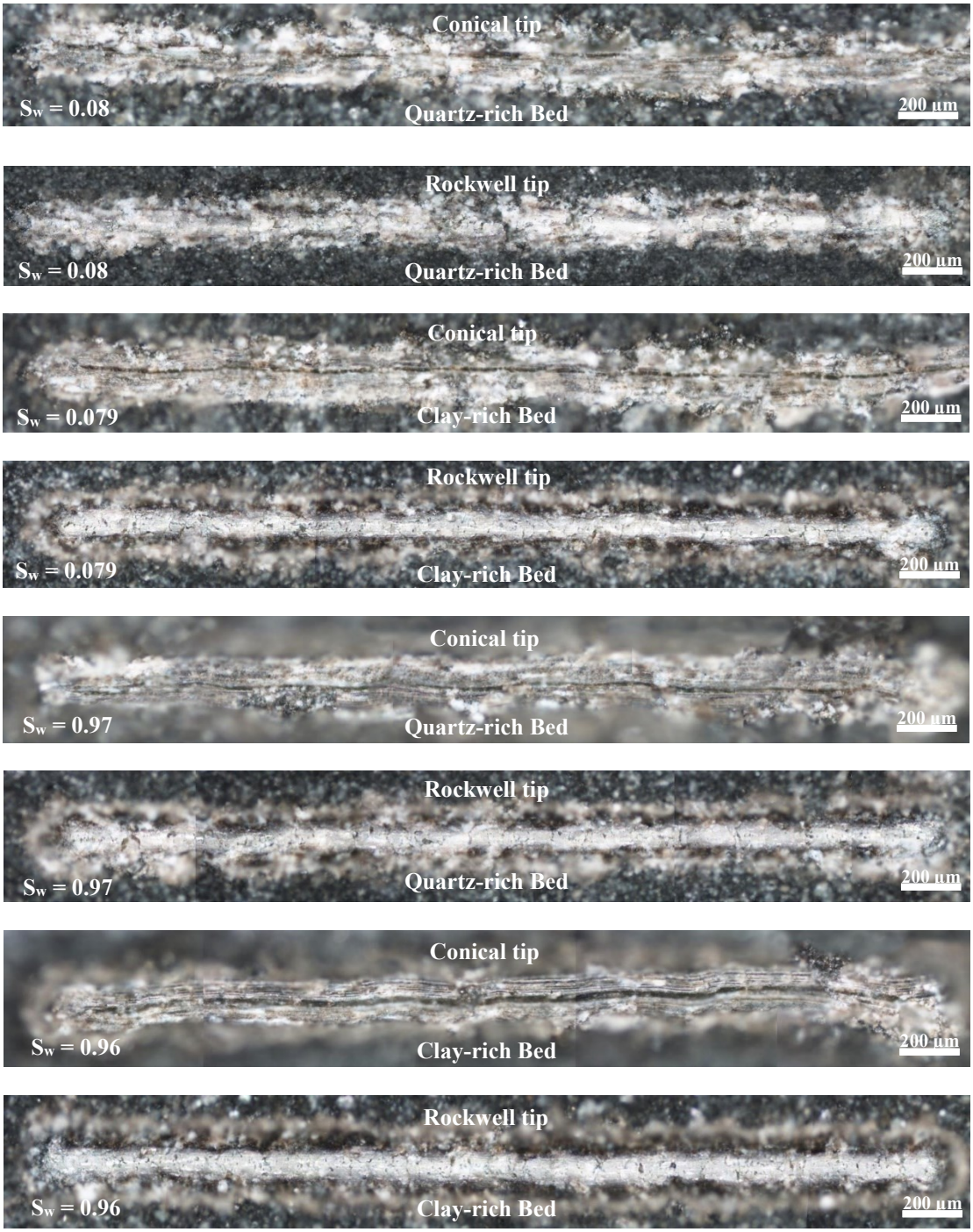

Figure 4-57. 3mm scratches along quartz-rich and clay-rich beds at low and high water saturation with conical and Rockwell tips.

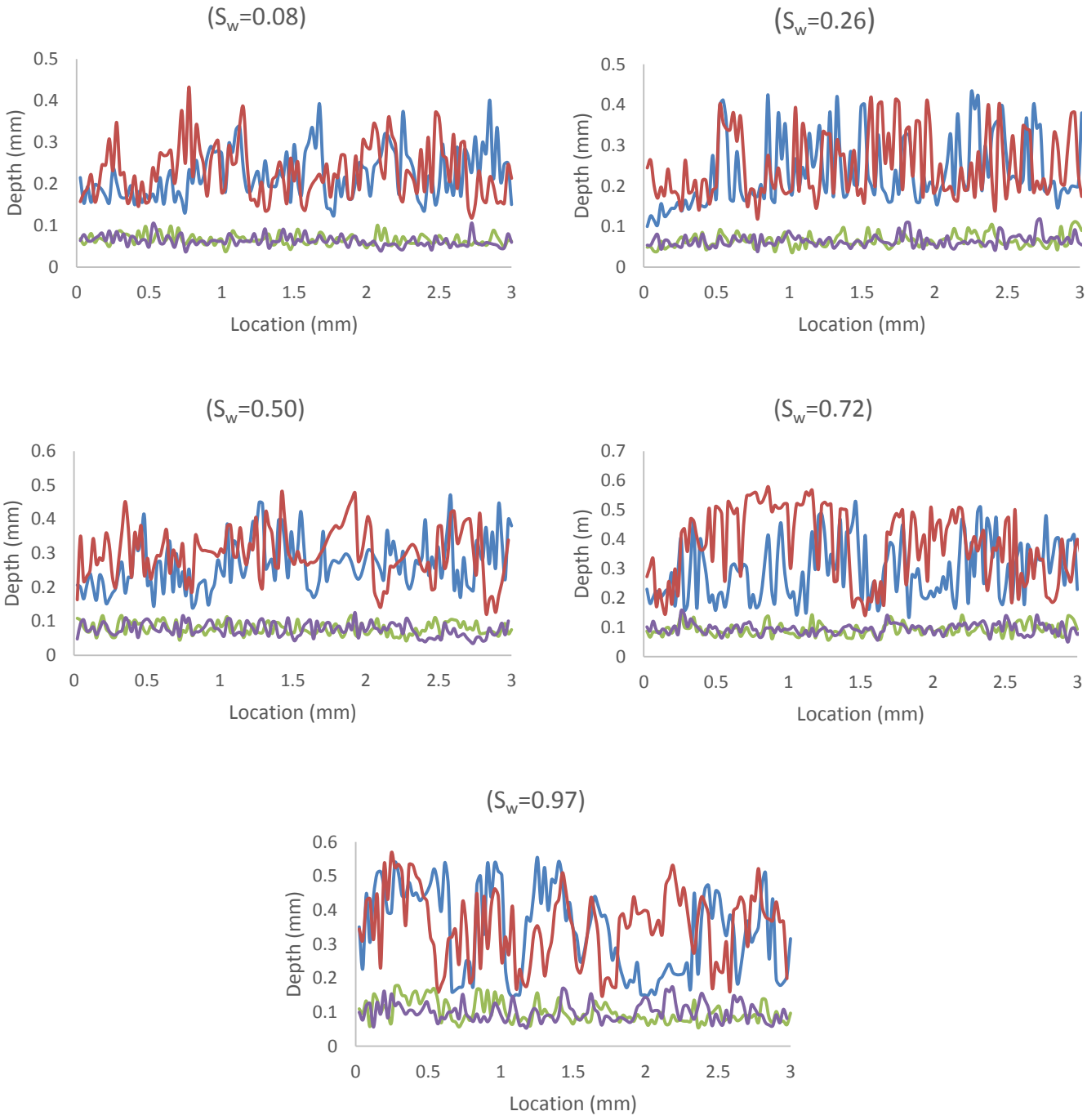

Figure 4-58. Depth of points along the scratches in quartz-rich beds. Blue and red plots are related to two sets of scratches made by conical tip and green and purple plots are related to Rockwell tip.

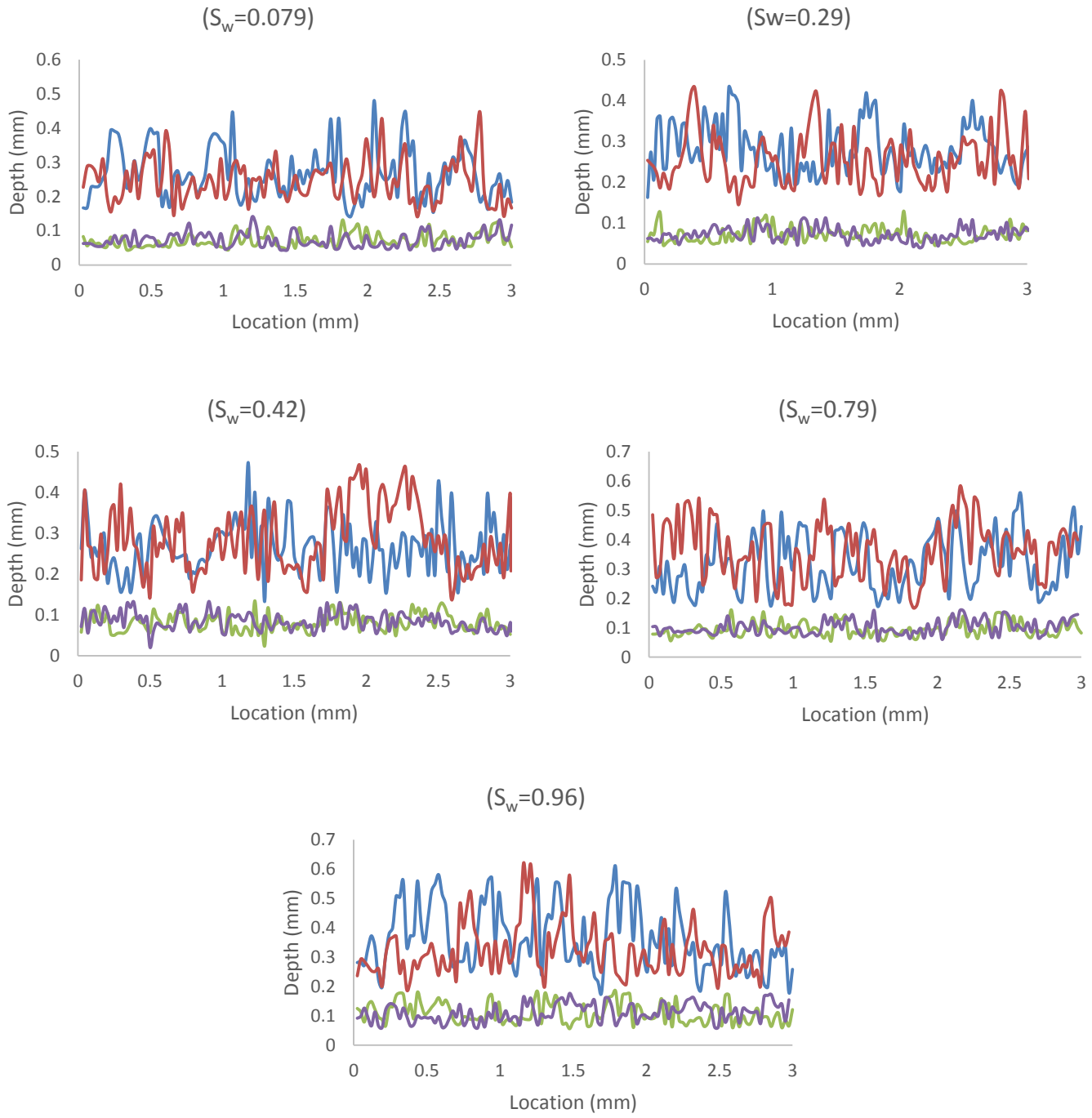

Figure 4-59. Depth of points along the scratches in clay-rich beds. Blue and red plots are related to two sets of scratches made by conical tip and green and purple plots are related to Rockwell tip.

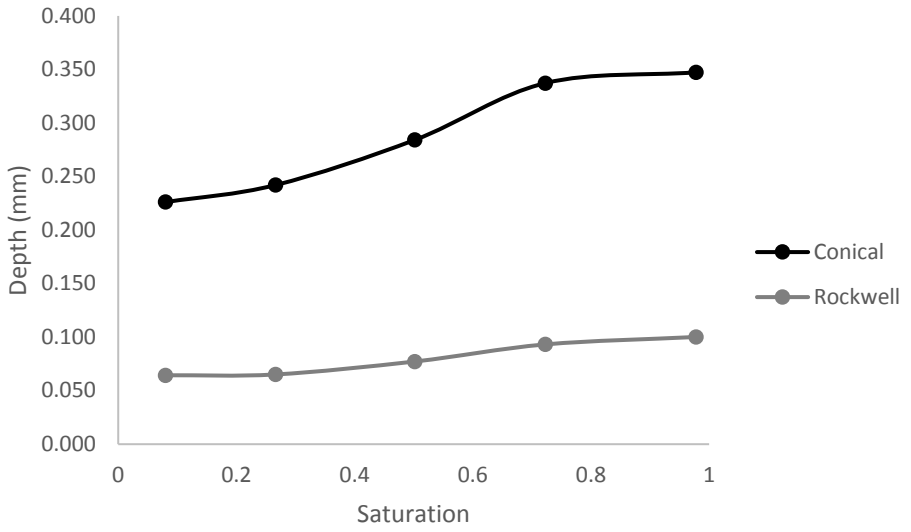

Figure 4-60. Changes in the average depth of cut as a function of water saturation in quartz-rich beds.

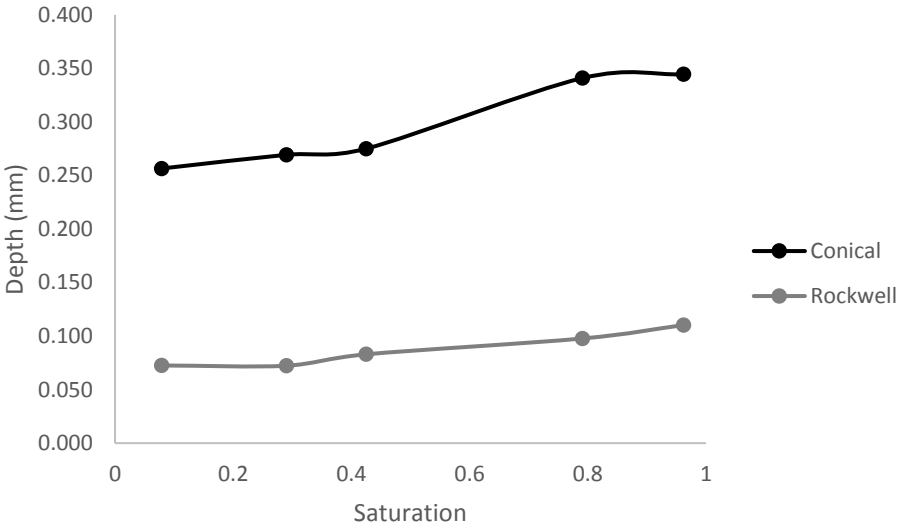

Figure 4-61. Changes in the average depth of cut as a function of water saturation in clay-rich beds.

Figure 4-62 and Figure 4-63 show the horizontal force (F_T) along the scratches in quartz-rich and clay-rich beds for different saturation levels. The results indicate that as the water saturation increases and capillary suction decreases, the horizontal force imposed to conical and Rockwell

tips decrease which can be attributed to the softening (also shown in micro-indentation experiments) and local effective stress change taking place as a result of water saturation increase and capillary suction decrease. The average horizontal forces measured through using conical tip in quartz-rich beds in low (8%) and high water saturation (97.8%) are 11.6N and 10.2N, respectively while they are 11.9N and 9.73N for clay-rich beds which means that horizontal force imposed to the conical tip in quartz-rich beds are higher than clay-rich beds. The same behavior can be observed while using the Rockwell tip where for low (7.9%) and high (96.2%) water saturation tests, the average horizontal forces are 4.64N and 4N for quartz-rich beds, respectively and 4.59N and 4.1N for clay-rich beds, respectively, where measured. Comparing the measured horizontal force values in quartz-rich and clay-rich beds by conical and Rockwell tips in different saturation and capillary suction levels imply that quartz-rich beds are stiffer than clay-rich beds. Table 4-8 represents a summary of the average depth and horizontal force in different water saturation and capillary suction values for quartz-rich and clay-rich beds. Based on the assumption that both scratching tips would result in the same internal friction angle and applying Equation (4-42), (4-43) and (4-44), the values of internal friction angle for the points along the scratches in quartz-rich and clay-rich beds were determined shown in Figure 4-64 and Figure 4-65. Figure 4-66 and Figure 4-67 illustrate the distribution of internal friction angle measurements as well as the mean response on quartz-rich and clay-rich beds at different water saturation levels and capillary suction values. According to Figure 4-68 and Figure 4-69, initially in low water saturation and high capillary suction, the average friction angle for quartz-rich beds is 38^{o} while for clay-rich beds it is 36^{o} (5.3% lower than quartz-rich beds). As the water saturation increases and capillary suction decreases the average values of internal friction angles for quartz-rich and clay-rich beds gradually merge to each other. Comparing the average values of internal friction angles at low and high water saturation levels implies that for quartz-rich and clay-rich beds it drops 20.1% and 16.4%, respectively. Figure 4-70 represents the percentage of each internal friction angle range within micro-scratch experiments along quartz-rich and clay-rich beds for each water saturation level.

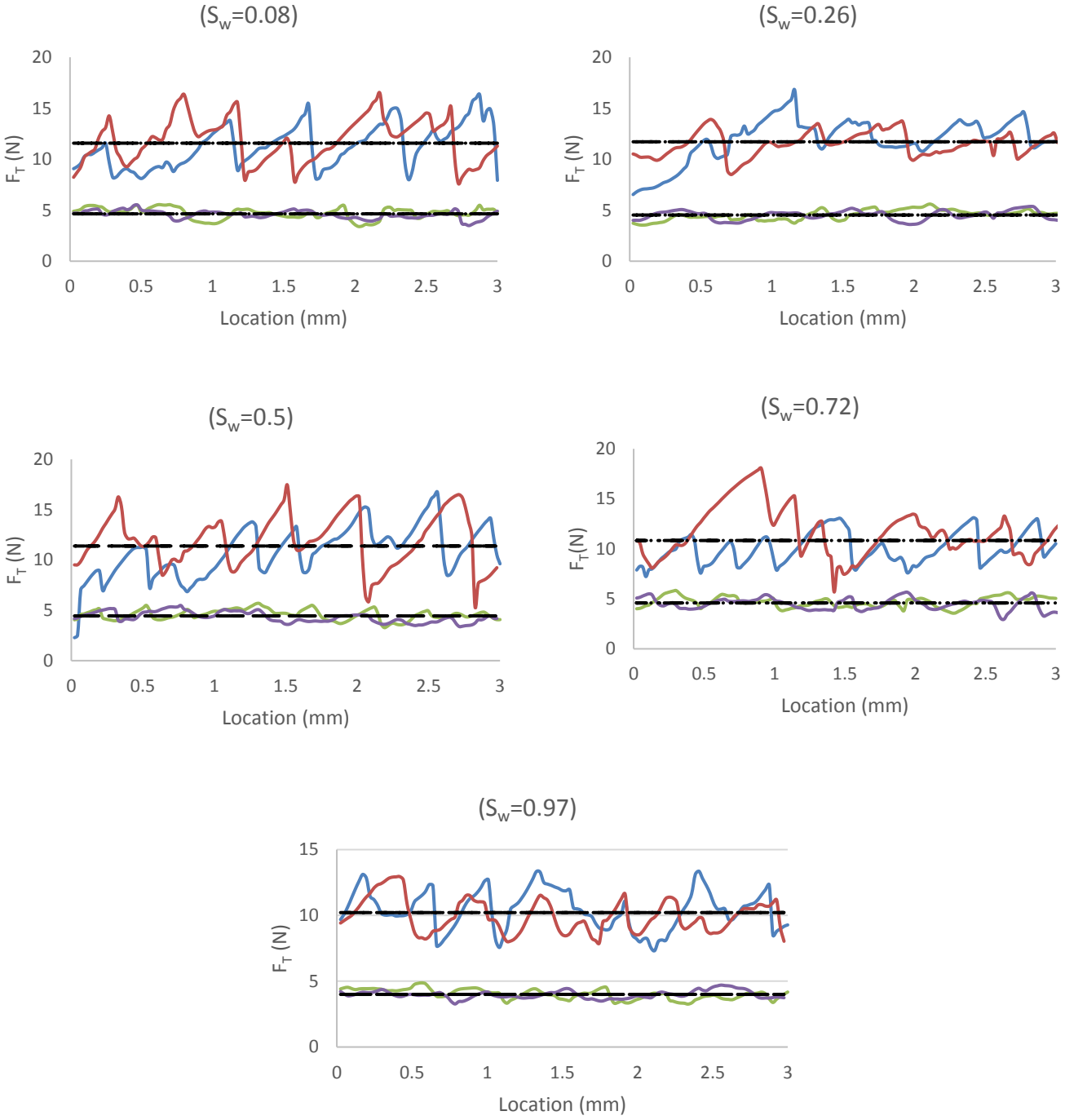

Figure 4-62. Horizontal force values while scratching in quartz-rich beds. Blue and red plots are related to two sets of scratches made by conical tip and green and purple plots are related to Rockwell tip. Dashed line is the average value for horizontal force.

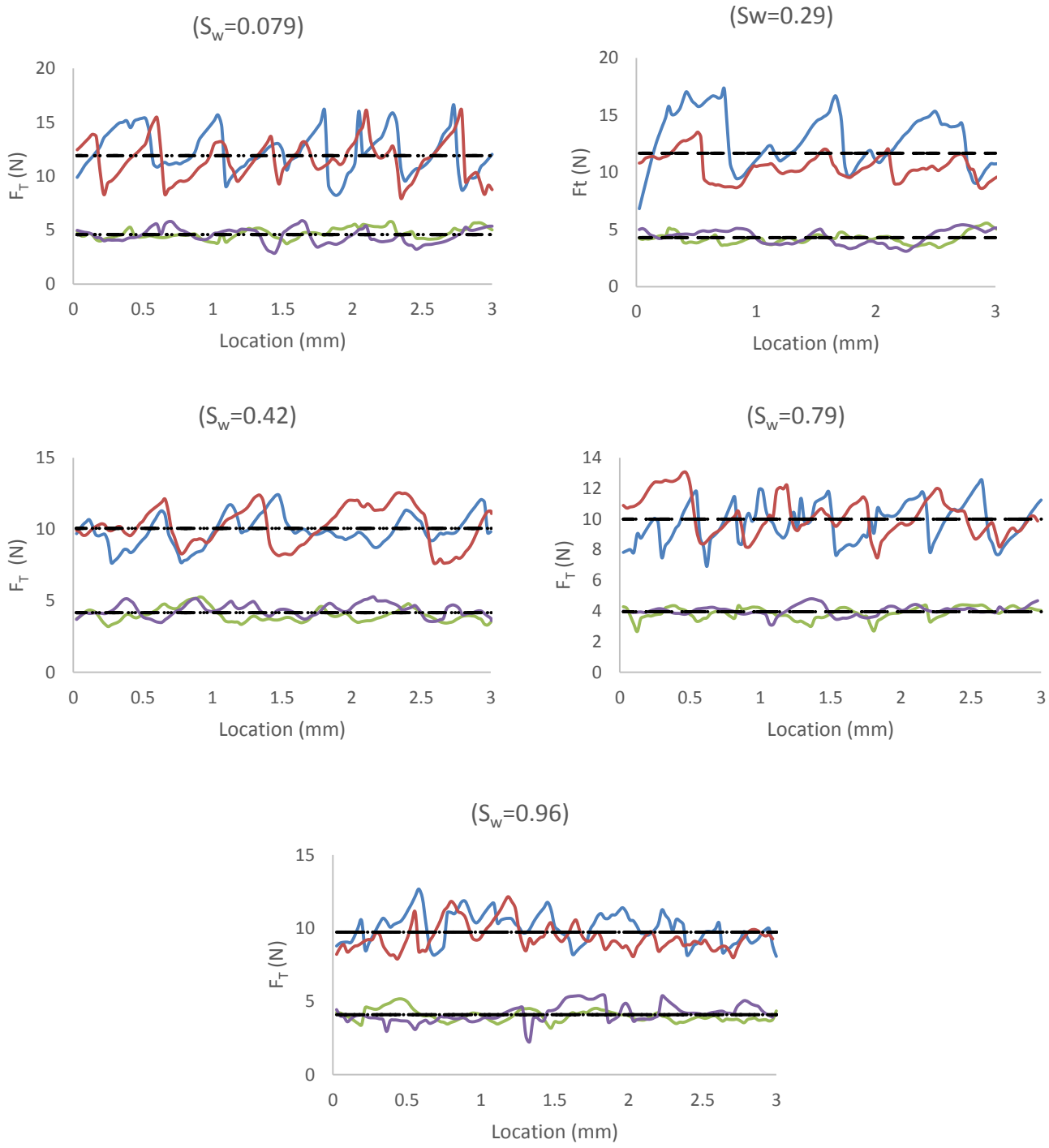

Figure 4-63. Horizontal force values while scratching in clay-rich beds. Blue and red plots are related to two sets of scratches made by conical tip and green and purple plots are related to Rockwell tip. Dashed line is the average value for horizontal force.

Table 4-8. Summary of the average depth and horizontal force in different water saturation and capillary suction values for quartz-rich and clay-rich beds ("C" and "R" superscripts represents conical and Rockwell tips, respectively).

Sample	S_w	P_c (MPa)	$Depth^C$ (mm)	$Depth^R$ (mm)	F_T^C (N)	F_T^R (N)
Quartz-rich Beds	0.08	125.8	0.226	0.064	11.58	4.64
	0.26	95.2	0.242	0.065	11.71	4.53
	0.50	39.5	0.284	0.077	11.39	4.45
	0.72	14.4	0.337	0.093	10.83	4.59
	0.97	0.9	0.347	0.100	10.21	4.00
Clay-rich Beds	0.079	152.2	0.257	0.073	11.90	4.59
	0.29	95.2	0.269	0.072	11.67	4.29
	0.42	39.5	0.275	0.083	10.06	4.17
	0.79	14.4	0.341	0.098	9.99	3.95
	0.96	0.8	0.344	0.110	9.73	4.09

At low water saturation the majority of the measured points for internal friction angle along quartz-rich beds are between 31° to 45° while it is between 26° to 40° for clay-rich beds. At high water saturation levels the majority of the points for quartz-rich beds are within 26° to 40° while the range for clay-rich beds is mainly within 25° to 35°. UCS can also be determined by Equation (4-41) which is not only dependent on internal friction angle but also on interfacial friction angle, θ_{Active} , $\theta_{Passive}$ and H_T which are different in conical and Rockwell tips. Therefore, UCS and cohesion values as well as fracture toughness would not be the same based on the results from conical and Rockwell tips analysis.

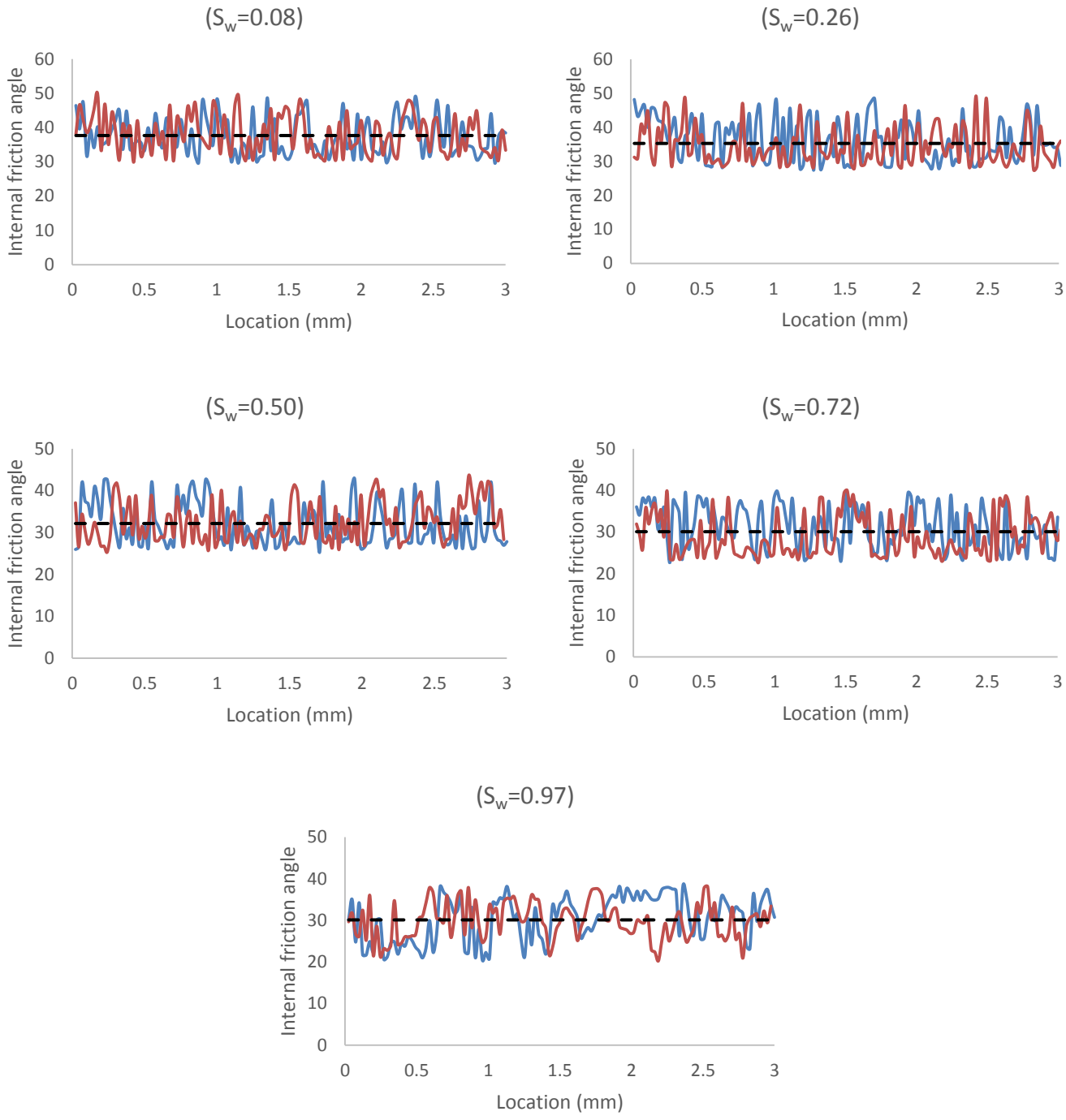

Figure 4-64. Internal friction angle in different water saturation along two sets of scratches in quartz-rich beds. Dashed line is the average value for Internal friction angle.

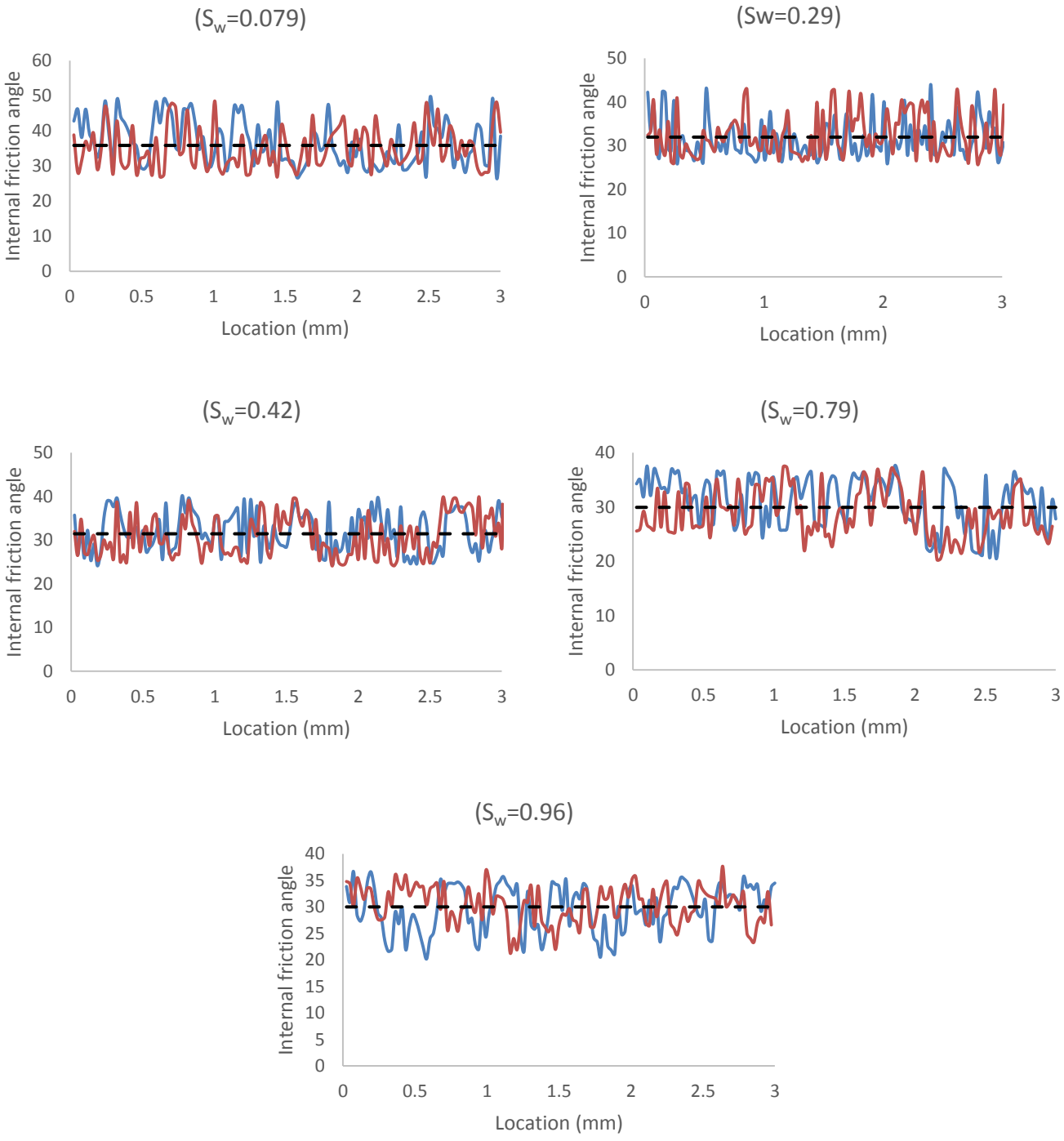

Figure 4-65. Internal friction angle in different water saturation along two sets of scratches in clay-rich beds. Dashed line is the average value for Internal friction angle.

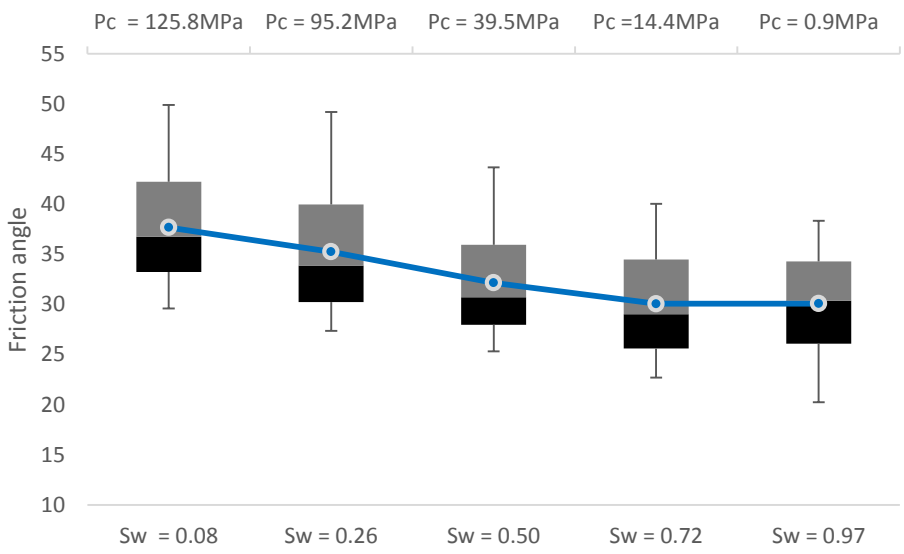

Figure 4-66. Distribution of internal friction angle measurements as well as the mean response on quartz-rich beds at different water saturation and capillary suction values. The middle line in the boxes shows the median, the boxes indicate the range between the first quartile and the third quartile. Whiskers above and below the boxes indicate the maximum and minimum values, respectively. The filled circles show the arithmetic mean.

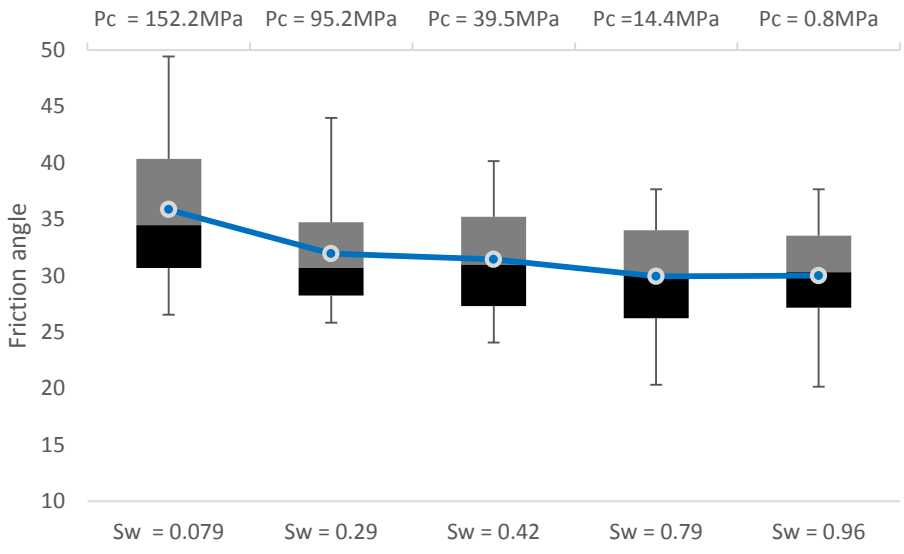

Figure 4-67. Distribution of internal friction angle measurements as well as the mean response on clay-rich beds at different water saturation and capillary suction values. The middle line in the boxes shows the median, the boxes indicate the range between the first quartile and the third quartile. Whiskers above and below the boxes indicate the maximum and minimum values, respectively. The filled circles show the arithmetic mean.

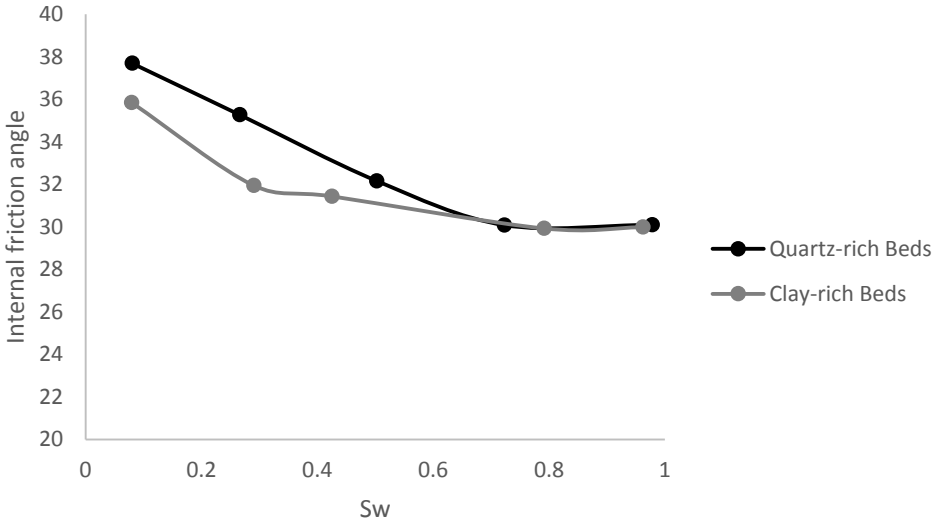

Figure 4-68. Changes in the average internal friction angle as a function of water saturation in quartz-rich and clay-rich beds.

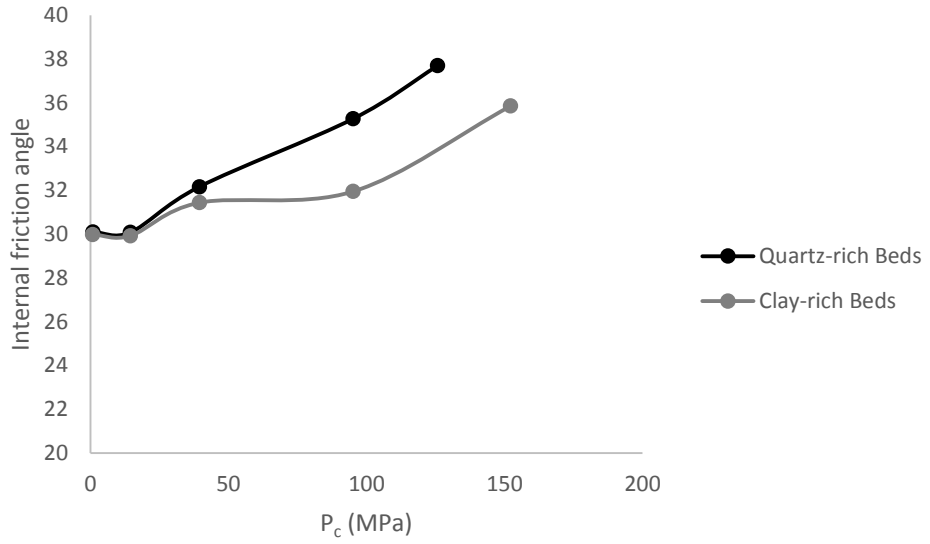

Figure 4-69. Changes in the average internal friction angle as a function of capillary suction in quartz-rich and clay-rich beds.

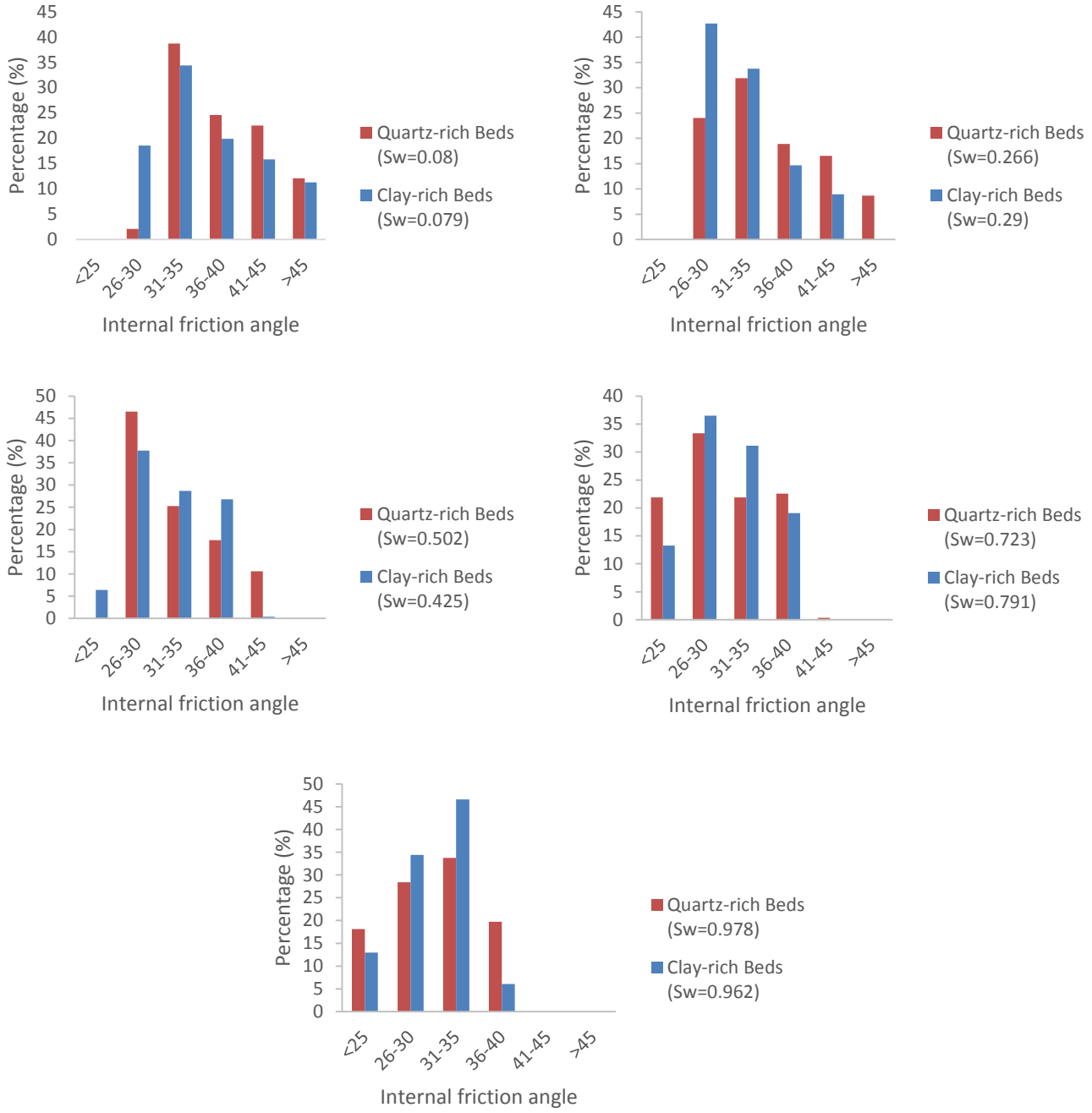

Figure 4-70. Percentage of internal friction angle values for the measured points along the scratches within quartz-rich and clay-rich beds in different water saturations.

The results indicate that the values of UCS obtained from Rockwell tip are 5.8% to 21.4% higher than conical tip results which can be also attributed to the flow of the removed rock in different back rake angles. According to Figure 4-75, in low water saturation the average UCS in quartz-rich beds are 7.8% (with conical tip) and 2.1% (with Rockwell tip) higher than clay-rich beds. As the capillary suction decreases (or water saturation increases) the average UCS values also decrease for both quartz-rich and clay-rich beds (Figure 4-76). Average UCS value for quartz-rich beds in high (72.3% and 97.8%) water saturation drops by 46.3% and 50% (with conical tip) and 35.7% and 46.4% (with Rockwell tip). For clay-rich beds it drops by 50.9% and 53.8% (with conical tip) and 43.6% and 49% (with Rockwell tip) in 79.1% and 96.2% water saturation. The former results can be justified by Equation (4-5) where capillary suction reduction would lead to UCS reduction. Figure 4-77 and Figure 4-78 represent the percentage of each UCS range along the scratches in quartz-rich and clay-rich beds for different water saturation levels. In low water saturation the majority of the measured points for UCS values along the scratches made by conical tip in quartz-rich and clay-rich beds are between 76MPa to 150MPa. In high water saturation levels the majority of the points for quartz-rich and clay-rich beds are within 26MPa to 75MPa. For UCS values measured by Rockwell tip, in low water saturation the majority of the measured points in quartz-rich beds are between 101MPa to 200MPa while for clay-rich beds the majority of the points are between76MPa to 200MPa. Also, in high water saturation levels the majority of the points for both quartz-rich and clay-rich beds are within 26MPa to 75MPa range.

Based on the values for friction angle and UCS, the values of cohesion can be determined by Equation (4.37). Initially the average value of cohesion along the scratches made by conical tip in quartz-rich beds is 26.38MPa which is 8% higher than clay-rich beds. For Rockwell tip the average values of UCS are almost the same (Figure 4-83). Also, the difference between the average values of cohesion with conical and Rockwell tips are 6.8%. The average value of cohesion along the scratches made by conical tip in quartz-rich beds drops by 67% and 73% in 72.3% and 97.8% water saturation. For clay-rich beds it drops by 75% and 79% in 79.1% and 96.2% water saturation. For the Rockwell tip measurements the same behavior observed but the average value of cohesion in quartz-rich beds drops by 48% and 64% in 72.3% and 97.8% water saturation while for clay-rich beds it drops by 60.4% and 68% in 79.1% and 96.2% water saturation.

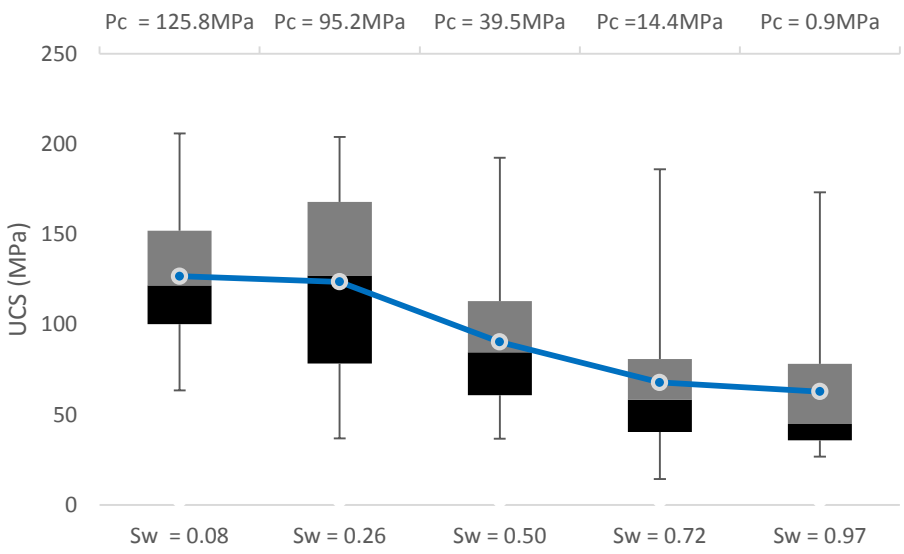

Figure 4-71. Distribution of UCS measurements as well as the mean response on quartz-rich beds done by conical tip at different water saturation and capillary suction values. The middle line in the boxes shows the median, the boxes indicate the range between the first quartile and the third quartile. Whiskers above and below the boxes indicate the maximum and minimum values, respectively. The filled circles show the arithmetic mean.

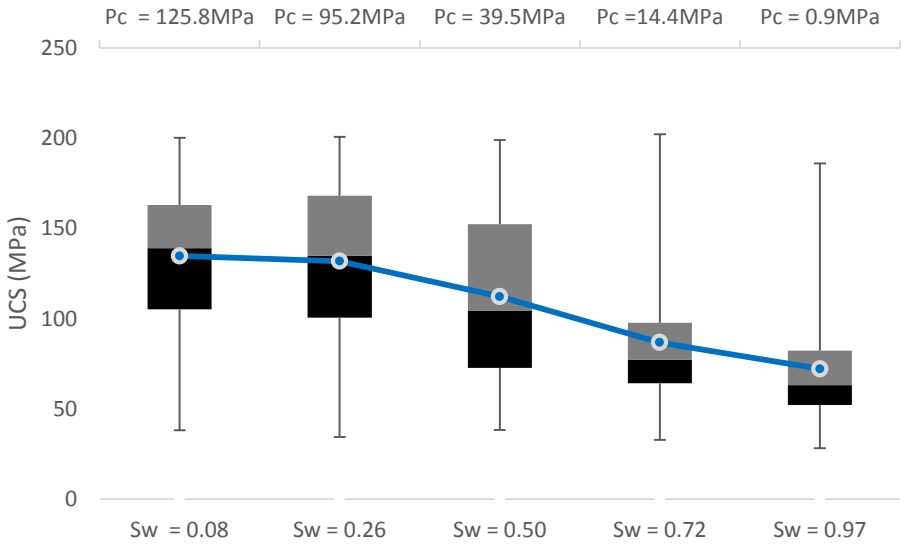

Figure 4-72. Distribution of UCS measurements as well as the mean response on quartz-rich beds done by Rockwell tip at different water saturation and capillary suction values. The middle line in the boxes shows the median, the boxes indicate the range between the first quartile and the third quartile. Whiskers above and below the boxes indicate the maximum and minimum values, respectively. The filled circles show the arithmetic mean.

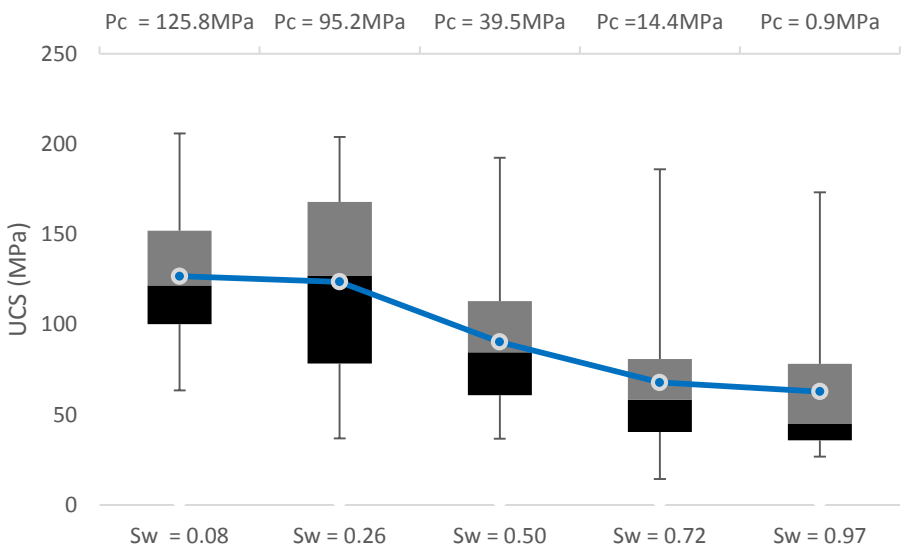

Figure 4-73. Distribution of UCS measurements as well as the mean response on clay-rich beds done by conical tip at different water saturation and capillary suction values. The middle line in the boxes shows the median, the boxes indicate the range between the first quartile and the third quartile. Whiskers above and below the boxes indicate the maximum and minimum values, respectively. The filled circles show the arithmetic mean.

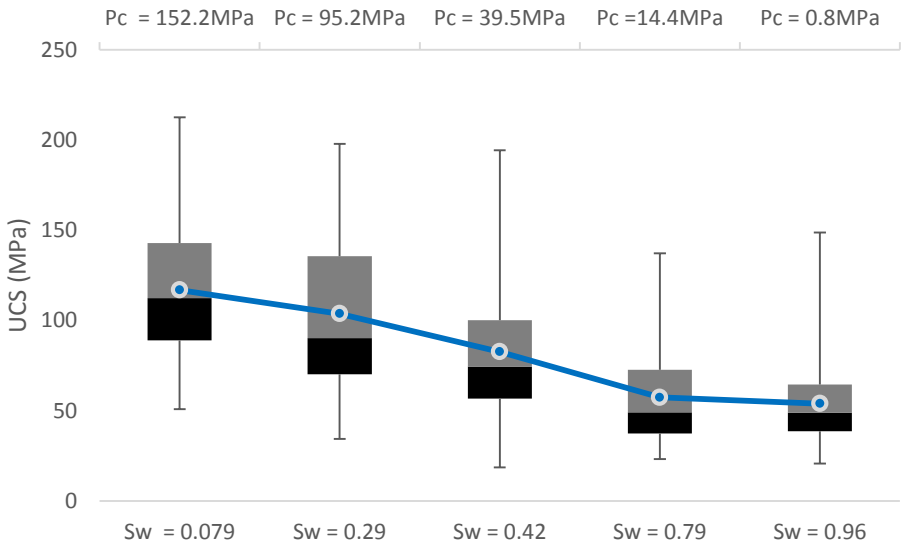

Figure 4-74. Distribution of UCS measurements as well as the mean response on clay-rich beds done by Rockwell tip at different water saturation and capillary suction values. The middle line in the boxes shows the median, the boxes indicate the range between the first quartile and the third quartile. Whiskers above and below the boxes indicate the maximum and minimum values, respectively. The filled circles show the arithmetic mean.

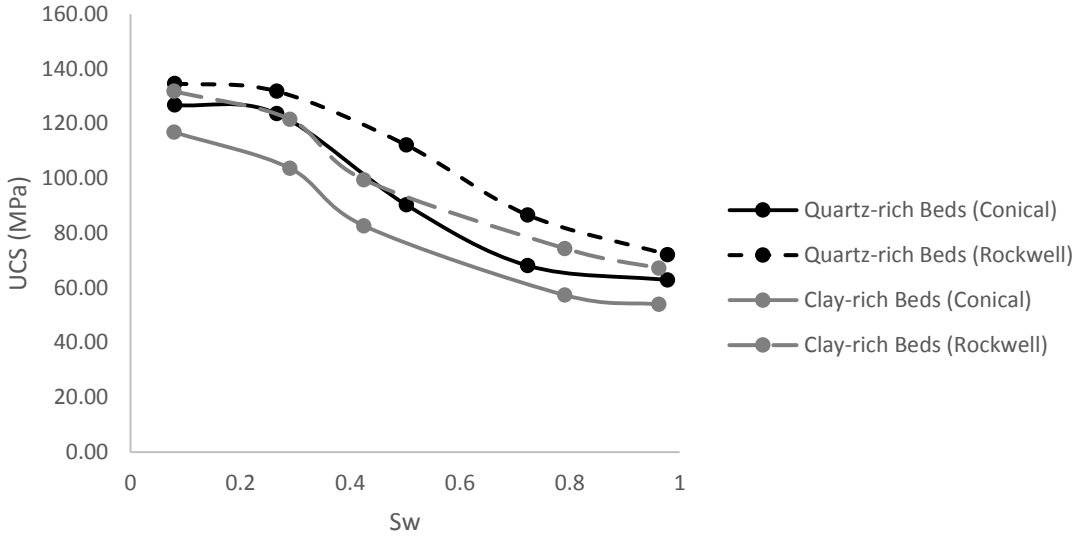

Figure 4-75. Changes in the average UCS as a function of water saturation in quartz-rich and clay-rich beds.

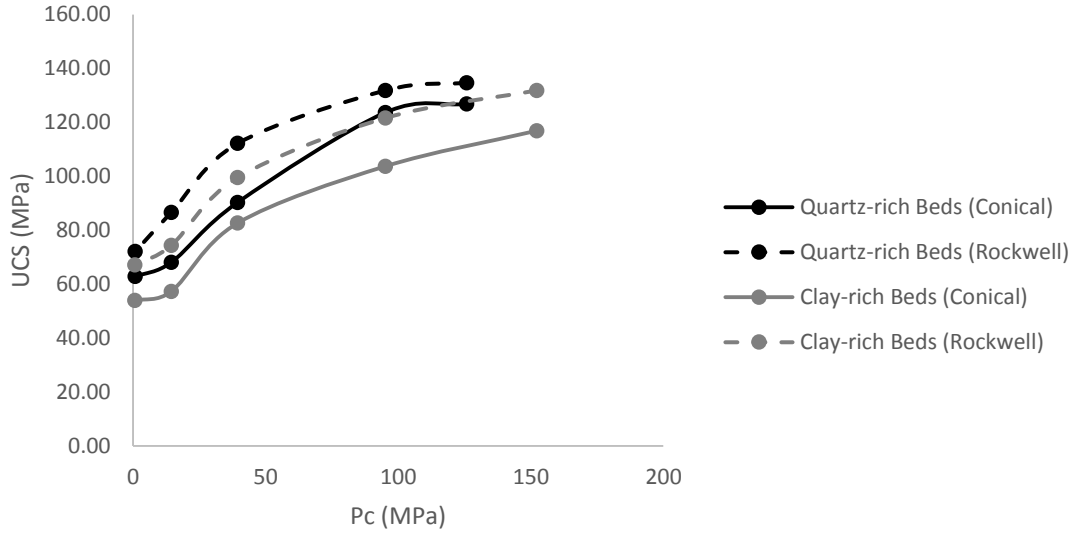

Figure 4-76. Changes in the average UCS as a function of capillary suction in quartz-rich and clay-rich beds

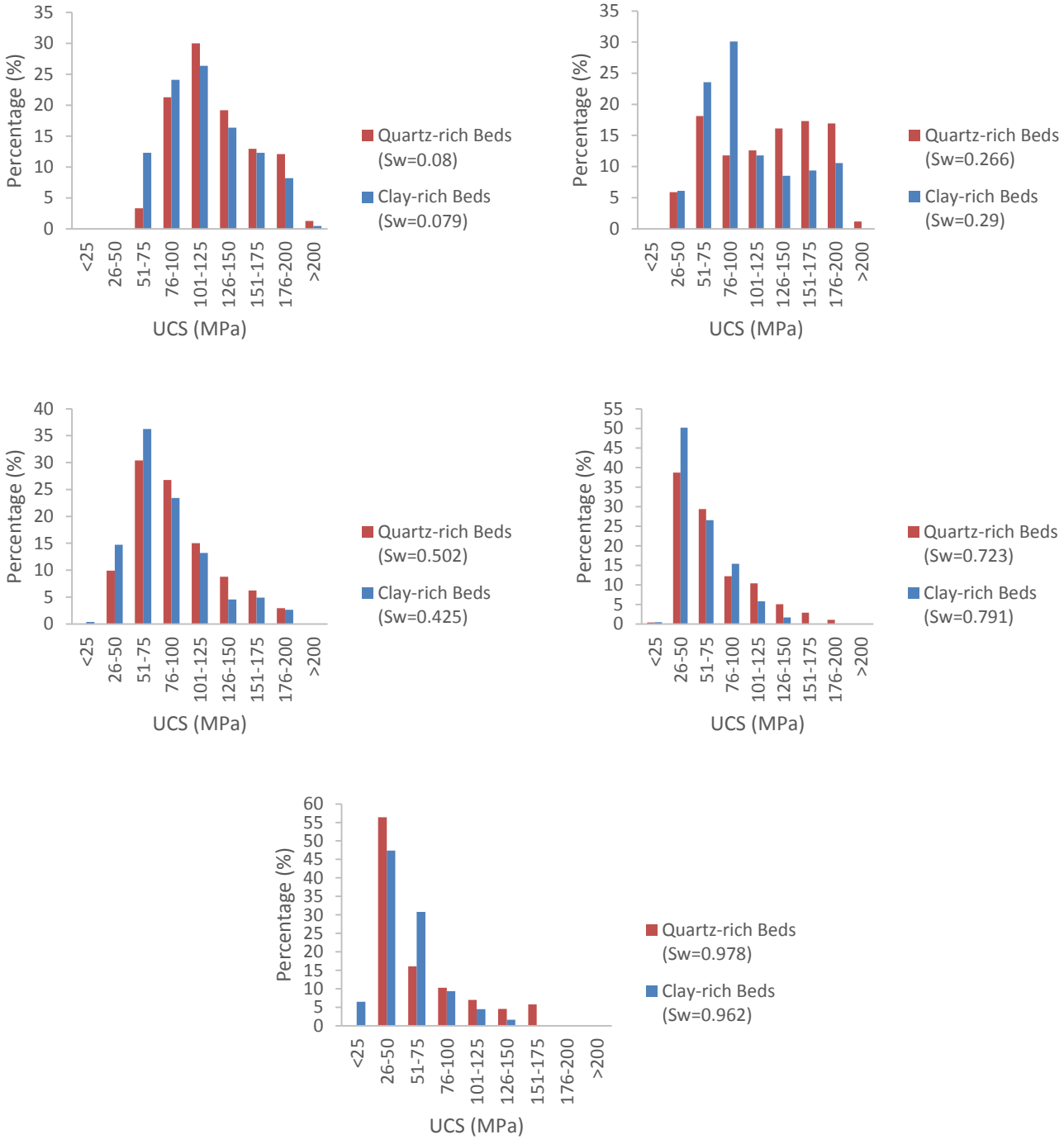

Figure 4-77. Percentage of UCS values for the measured points along the scratches made by conical tip within quartz-rich and clay-rich beds in different water saturations.

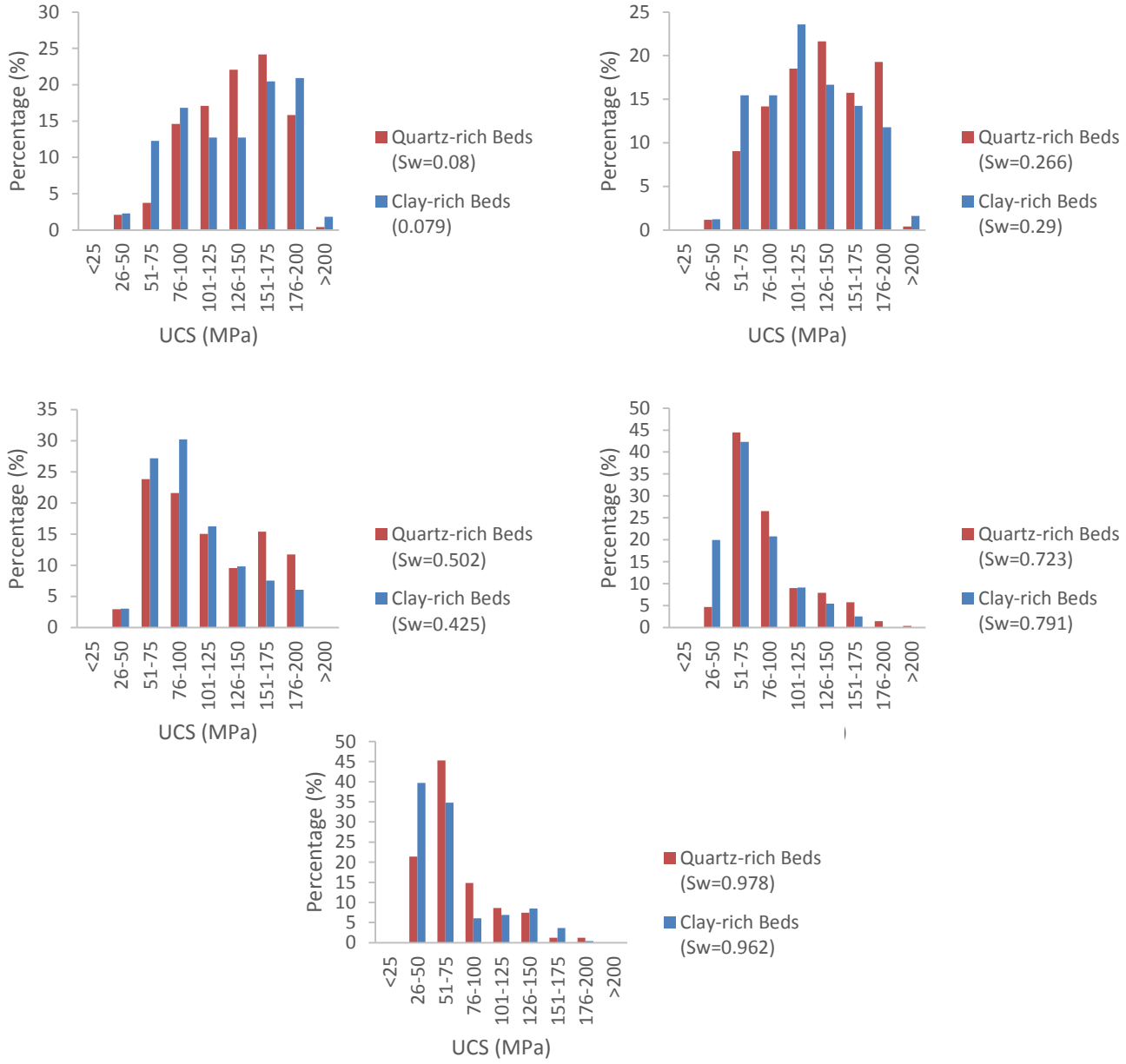

Figure 4-78. Percentage of UCS values for the measured points along the scratches made by Rockwell tip within quartz-rich and clay-rich beds in different water saturations.

Figure 4-79 to Figure 4-82 present the distribution of cohesion measurements done by conical and Rockwell tips on quartz-rich and clay-rich beds at different water saturation levels and capillary suction values.

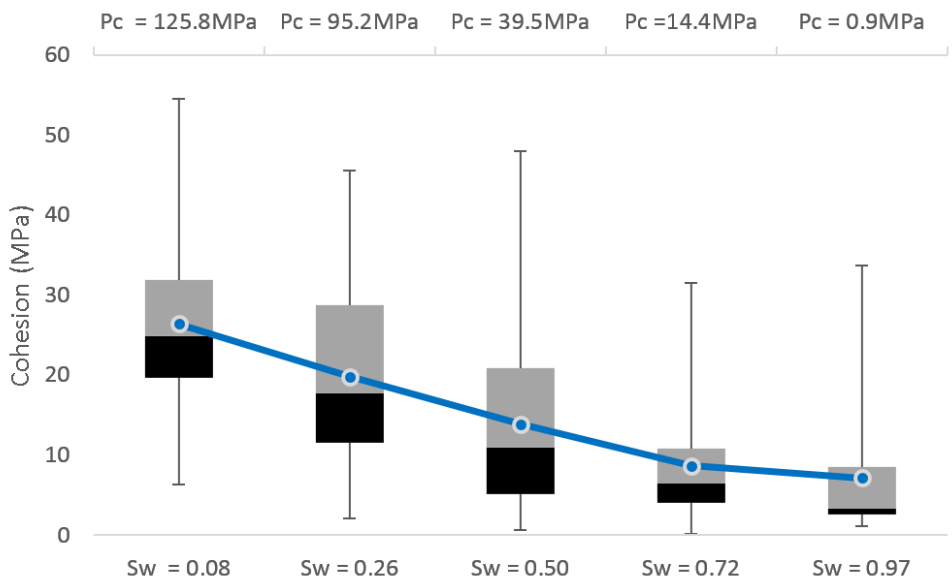

Figure 4-79. Distribution of cohesion measurements as well as the mean response on quartz-rich beds done by conical tip at different water saturation and capillary suction values. The middle line in the boxes shows the median, the boxes indicate the range between the first quartile and the third quartile. Whiskers above and below the boxes indicate the maximum and minimum values, respectively. The filled circles show the arithmetic mean.

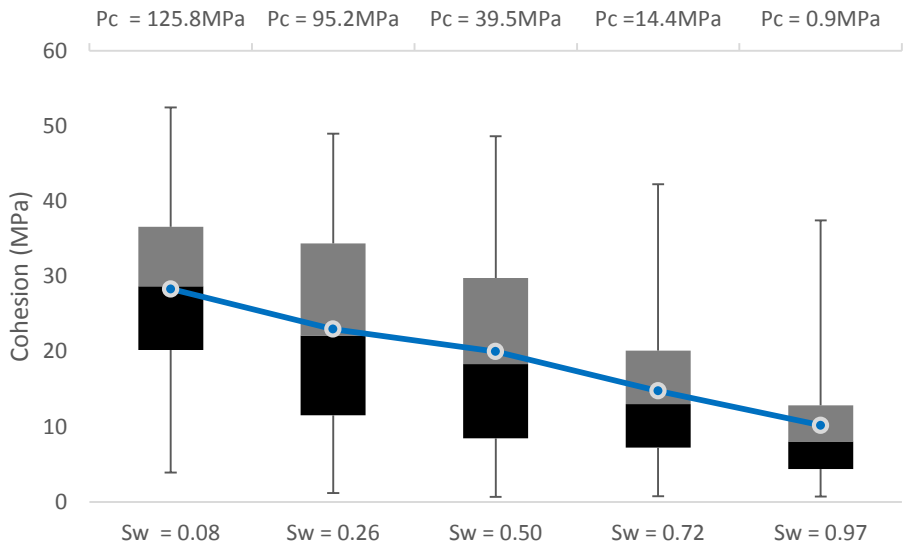

Figure 4-80. Distribution of cohesion measurements as well as the mean response on quartz-rich beds done by Rockwell tip at different water saturation and capillary suction values. The middle line in the boxes shows the median, the boxes indicate the range between the first quartile and the third quartile. Whiskers above and below the boxes indicate the maximum and minimum values, respectively. The filled circles show the arithmetic mean.

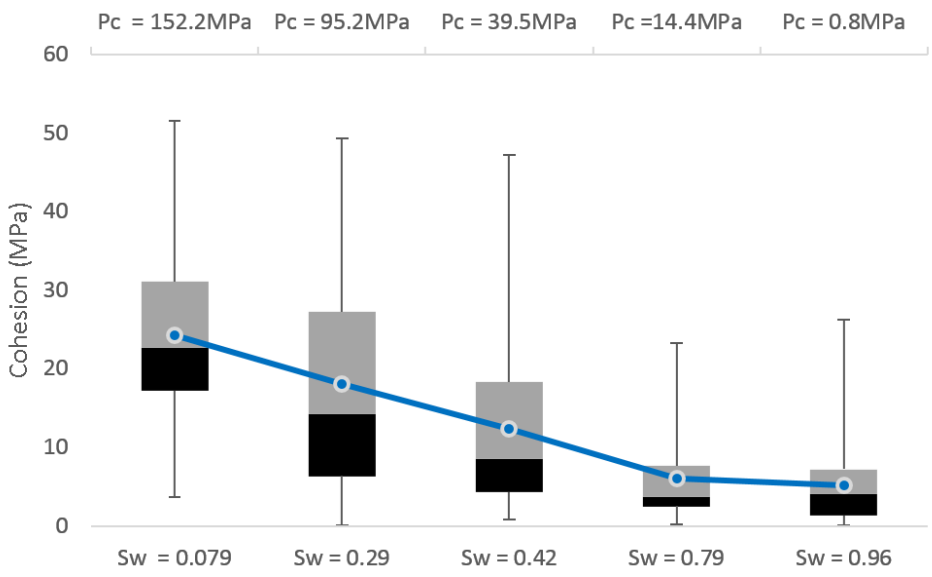

Figure 4-81. Distribution of cohesion measurements as well as the mean response on clay-rich beds done by conical tip at different water saturation and capillary suction values. The middle line in the boxes shows the median, the boxes indicate the range between the first quartile and the third quartile. Whiskers above and below the boxes indicate the maximum and minimum values, respectively. The filled circles show the arithmetic mean.

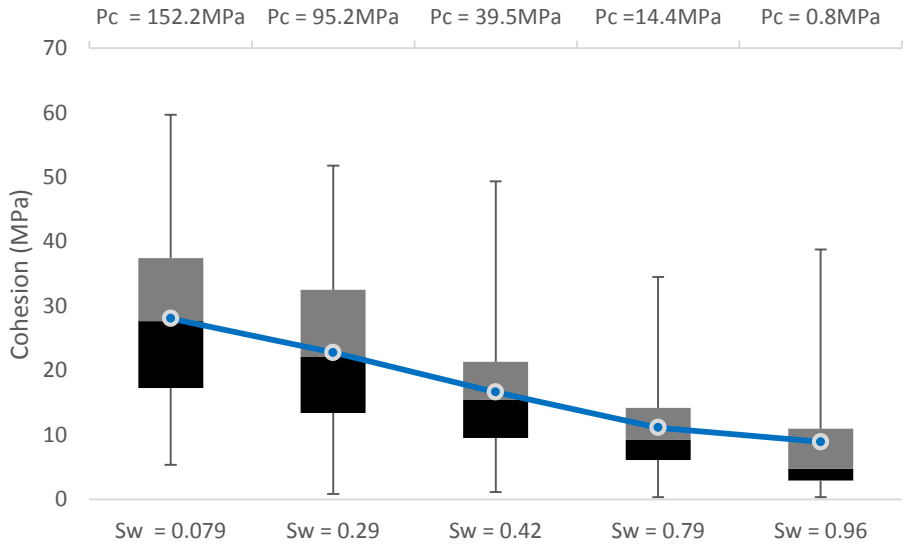

Figure 4-82. Distribution of cohesion measurements as well as the mean response on clay-rich beds done by Rockwell tip at different water saturation and capillary suction values. The middle line in the boxes shows the median, the boxes indicate the range between the first quartile and the third quartile. Whiskers above and below the boxes indicate the maximum and minimum values, respectively. The filled circles show the arithmetic mean.

Based on Equation (3-15) and (3-16) capillary suction would give an apparent cohesion to the beds and as it reduces (as a result of increasing the water saturation) the total cohesion would decrease (Figure 4-84). Figure 4-85 and Figure 4-86 represent the percentage of each cohesion range along the scratches in quartz-rich and clay-rich beds for different water saturation levels. The results indicate that in low water saturation the majority of the measured points for cohesion values in quartz-rich and clay-rich beds are between 10MPa to 40MPa. In high water saturation levels the majority of the points for quartz-rich and clay-rich beds are within >5MPa to 10MPa range.

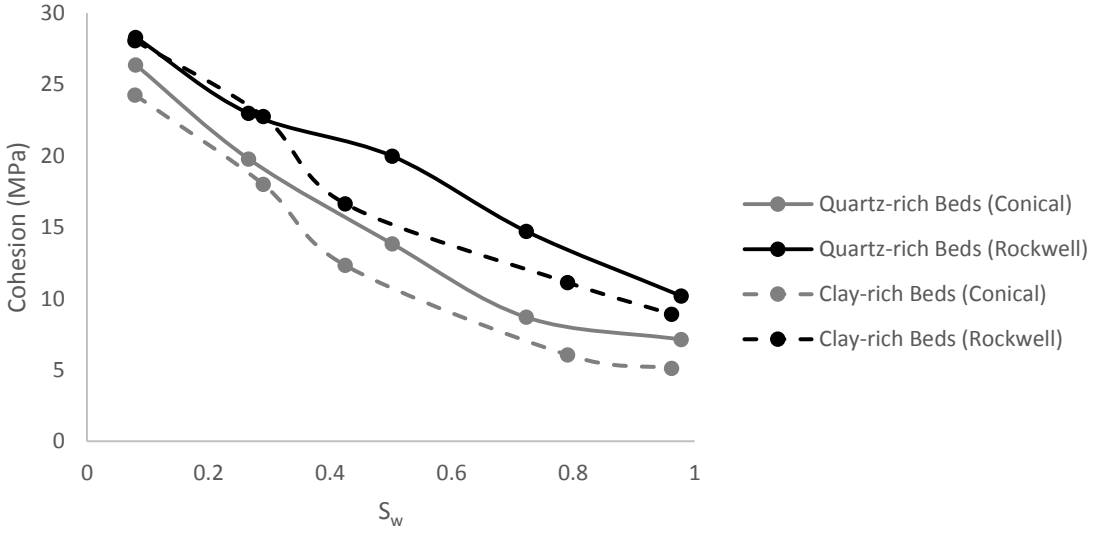

Figure 4-83. Changes in the average cohesion as a function of water saturation in quartz-rich and clay-rich beds.

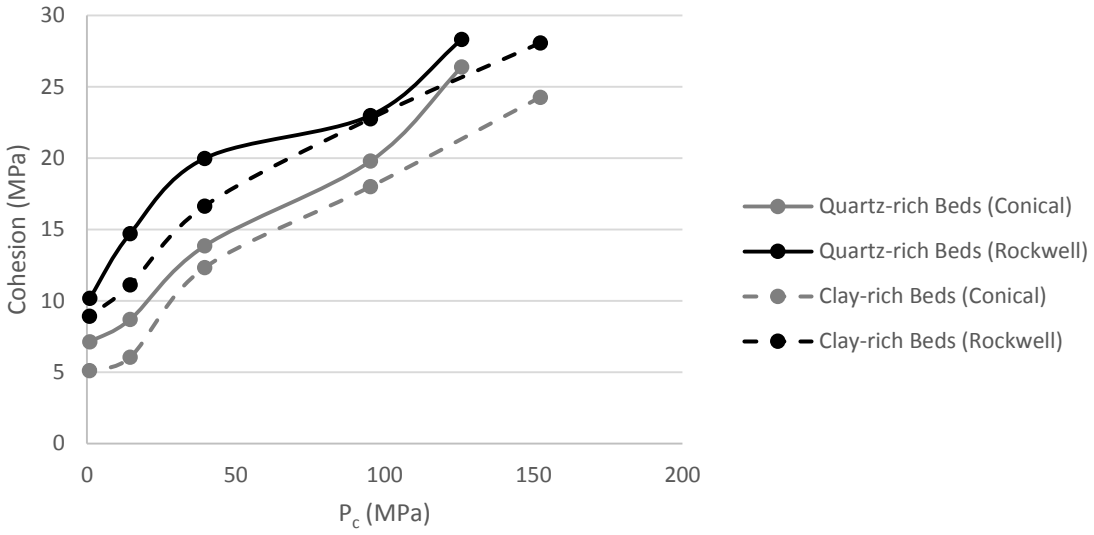

Figure 4-84. Changes in the average cohesion as a function of capillary suction in quartz-rich and clay-rich beds.

Fracture toughness can be also determined by using Equation (4-10). Figure 4-87 to Figure 4-90 illustrate the distribution of fracture toughness measurements done by conical and Rockwell tips on quartz-rich and clay-rich beds at different water saturation levels and capillary suction values. Also, Figure 4-91 and Figure 4-92 show the changes of the average fracture toughness on quartz-rich and clay-rich beds as water saturation and capillary suction are changing. The results imply that the average values of fracture toughness in both quartz-rich and clay-rich beds are higher in the measurements by Rockwell tip in comparison with conical tip measurements (44.9% higher for quartz-rich beds and 47.8% higher for clay-rich beds). Initially, at low water saturation level (8% for quartz-rich beds and 7.9% for clay-rich beds) the average values of fracture toughness measured by conical and Rockwell tips in quartz-rich beds are 2.77MPa.m$^{1/2}$ and 5.02MPa.m$^{1/2}$ while for clay-rich beds they are 2.33MPa.m$^{1/2}$ and 4.46MPa.m$^{1/2}$, respectively. As the water saturation increases, the average fracture toughness measured by conical tip for quartz-rich decreases 41% and 45% in 72.3% and 97.8% water saturations, respectively. The same measurements by Rockwell tip in quartz-rich beds show 42.2% and 46% reduction in fracture toughness for 72.3% and 97.8% water saturation. Regarding the average values of fracture toughness for clay-rich beds using conical tip the results indicate that it would drop by 38.6% and 41% in 79.1% and 96.2% water saturation, respectively while the reductions in the average fracture toughness in 72.3% and 97.8% water saturations using Rockwell tip are 39.1% and 45%.

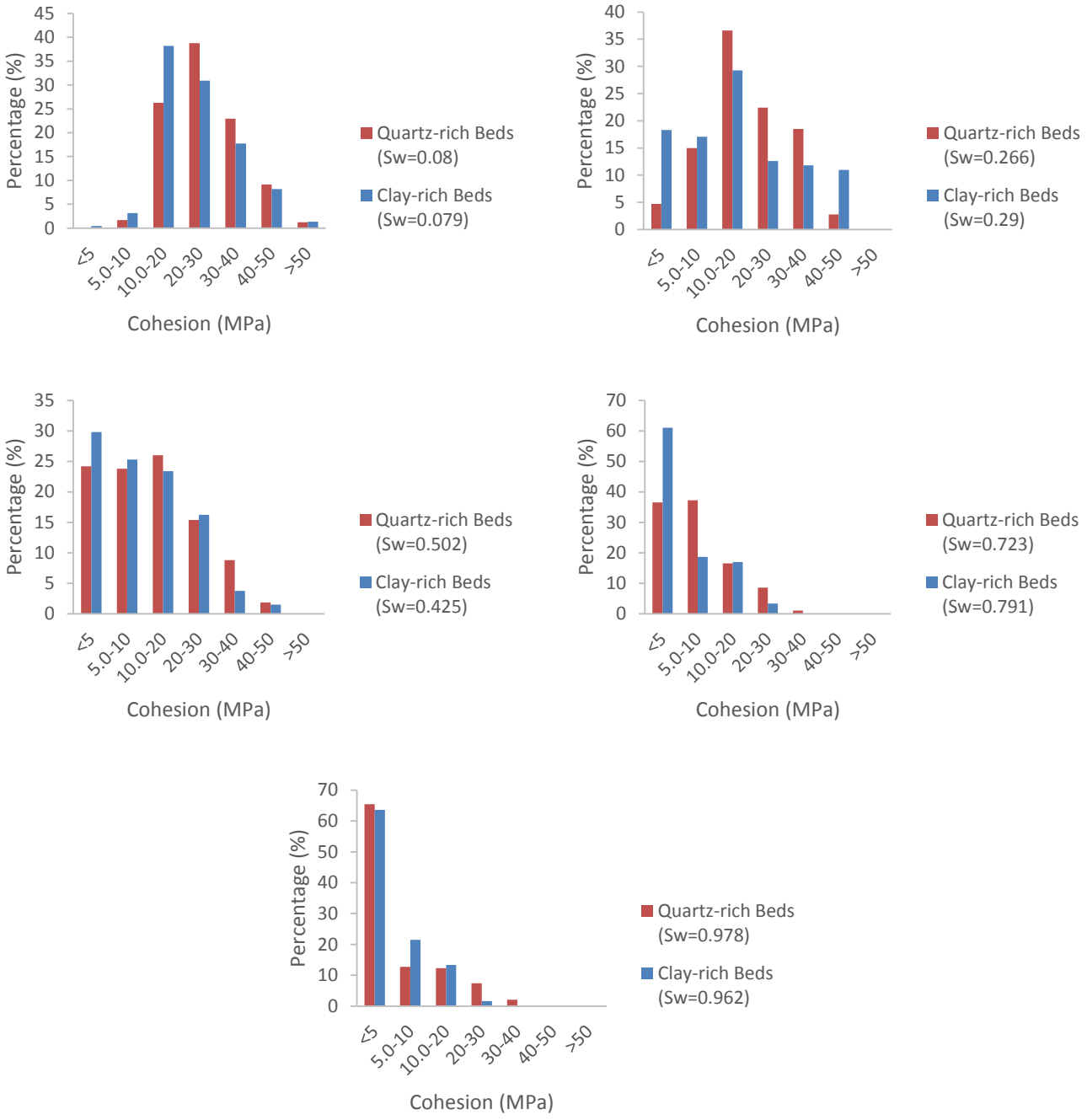

Figure 4-85. Percentage of cohesion values for the measured points along the scratches made by conical tip within quartz-rich and clay-rich beds in different water saturations.

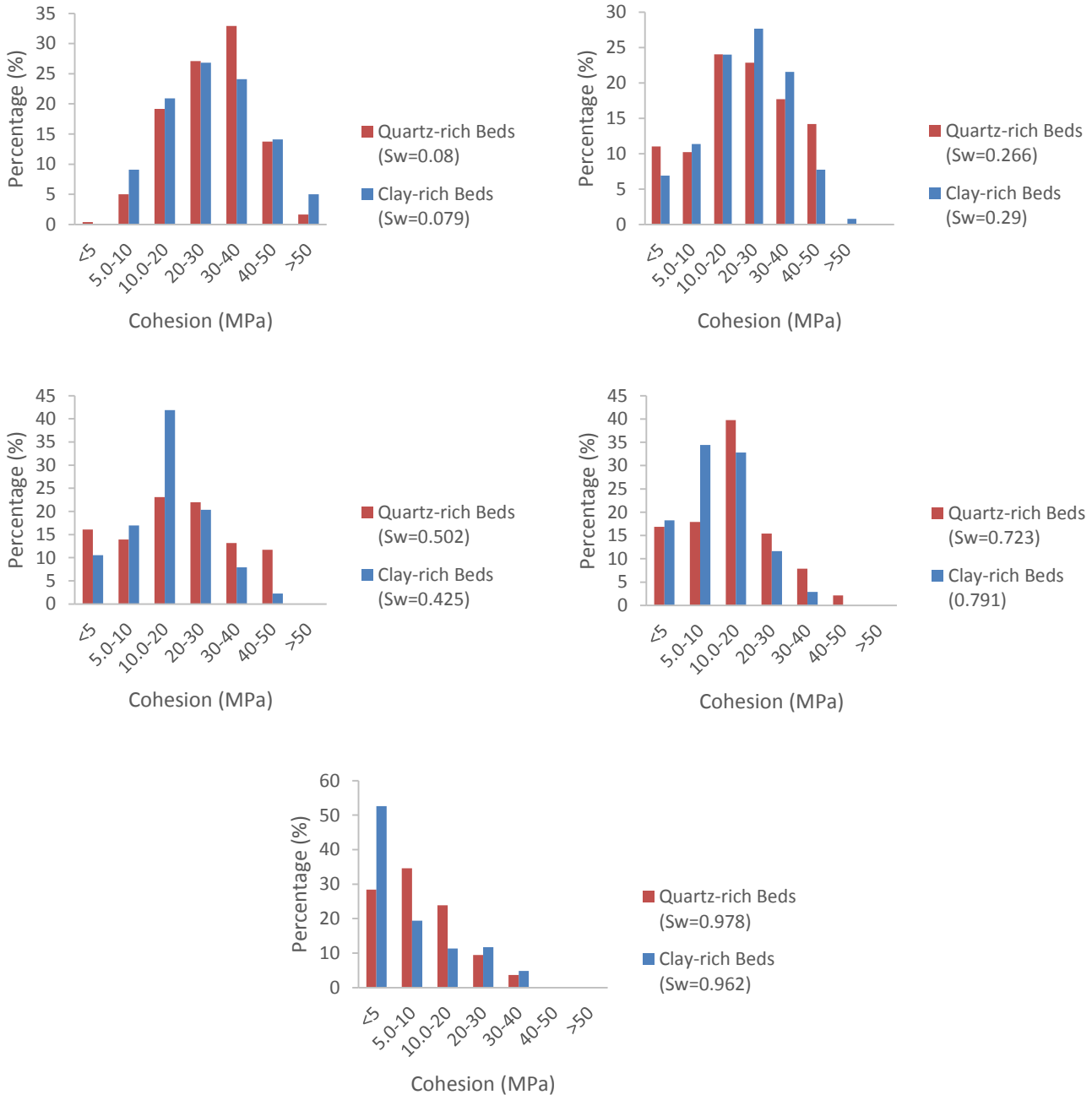

Figure 4-86. Percentage of cohesion values for the measured points along the scratches made by Rockwell tip within quartz-rich and clay-rich beds in different water saturations.

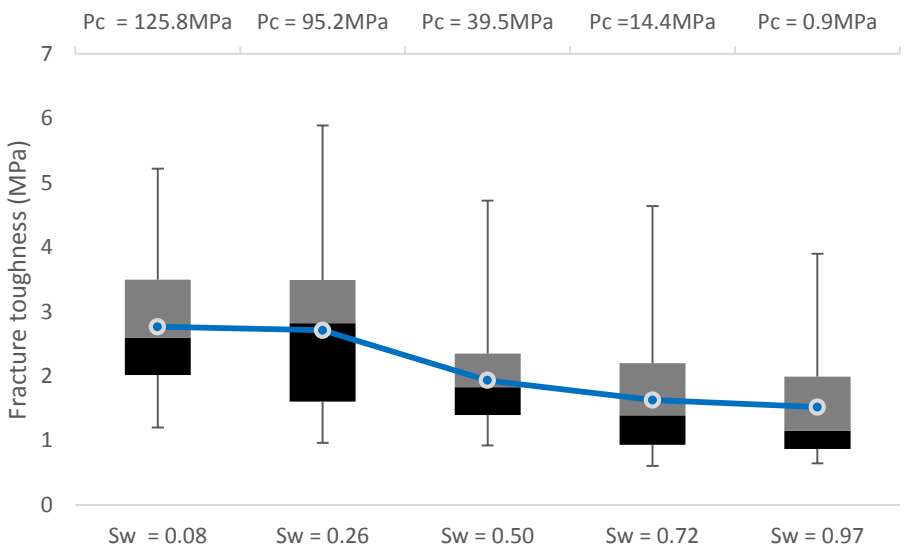

Figure 4-87. Distribution of fracture toughness measurements as well as the mean response on quartz-rich beds done by conical tip at different water saturation and capillary suction values. The middle line in the boxes shows the median, the boxes indicate the range between the first quartile and the third quartile. Whiskers above and below the boxes indicate the maximum and minimum values, respectively. The filled circles show the arithmetic mean.

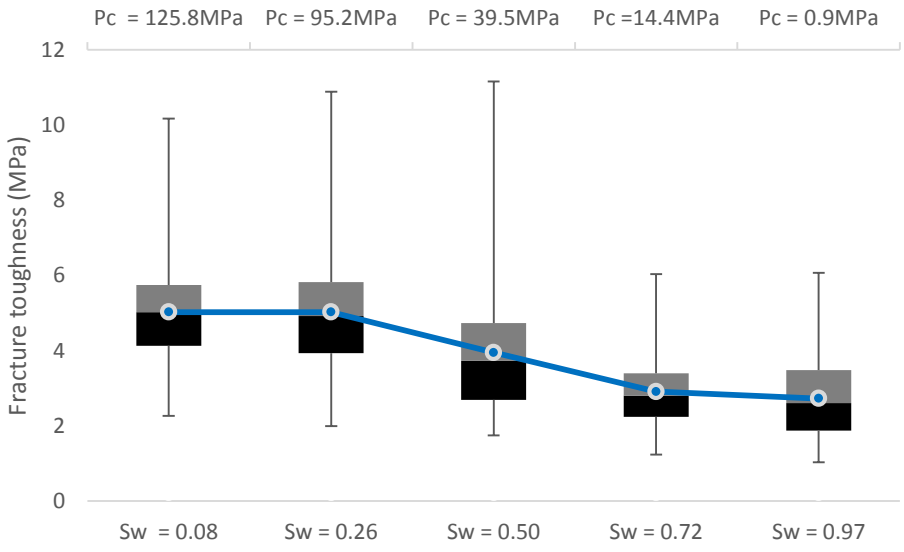

Figure 4-88. Distribution of fracture toughness measurements as well as the mean response on quartz-rich beds done by Rockwell tip at different water saturation and capillary suction values. The middle line in the boxes shows the median, the boxes indicate the range between the first quartile and the third quartile. Whiskers above and below the boxes indicate the maximum and minimum values, respectively. The filled circles show the arithmetic mean.

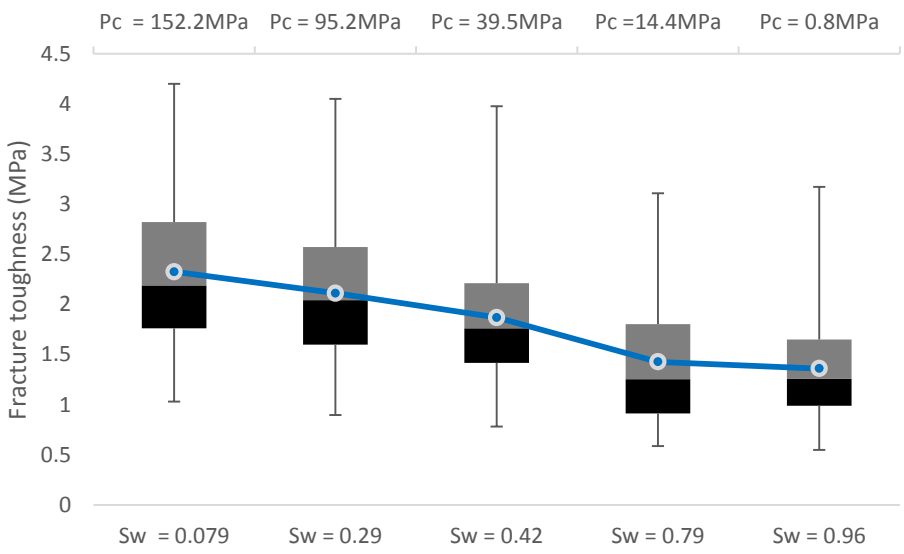

Figure 4-89. Distribution of fracture toughness measurements as well as the mean response on clay-rich beds done by conical tip at different water saturation and capillary suction values. The middle line in the boxes shows the median, the boxes indicate the range between the first quartile and the third quartile. Whiskers above and below the boxes indicate the maximum and minimum values, respectively. The filled circles show the arithmetic mean.

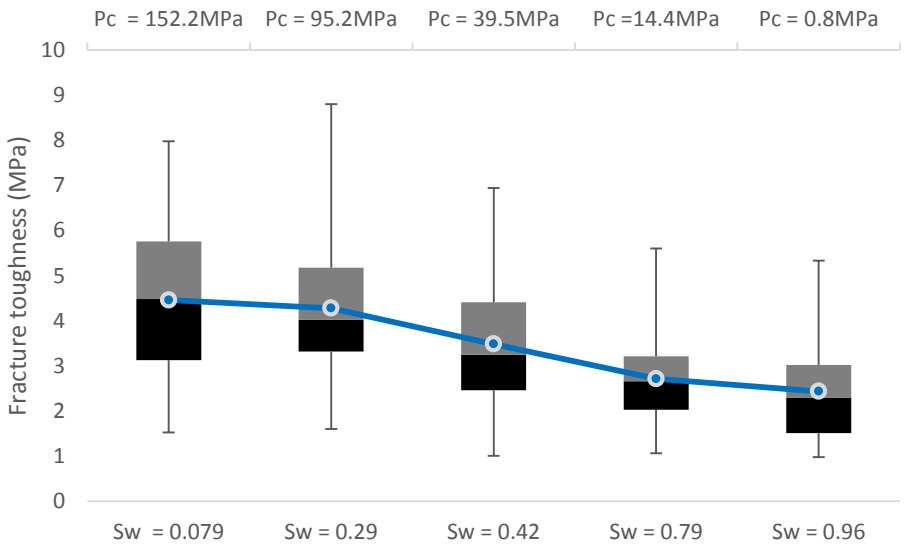

Figure 4-90. Distribution of fracture toughness measurements as well as the mean response on clay-rich beds done by Rockwell tip at different water saturation and capillary suction values. The middle line in the boxes shows the median, the boxes indicate the range between the first quartile and the third quartile. Whiskers above and below the boxes indicate the maximum and minimum values, respectively. The filled circles show the arithmetic mean.

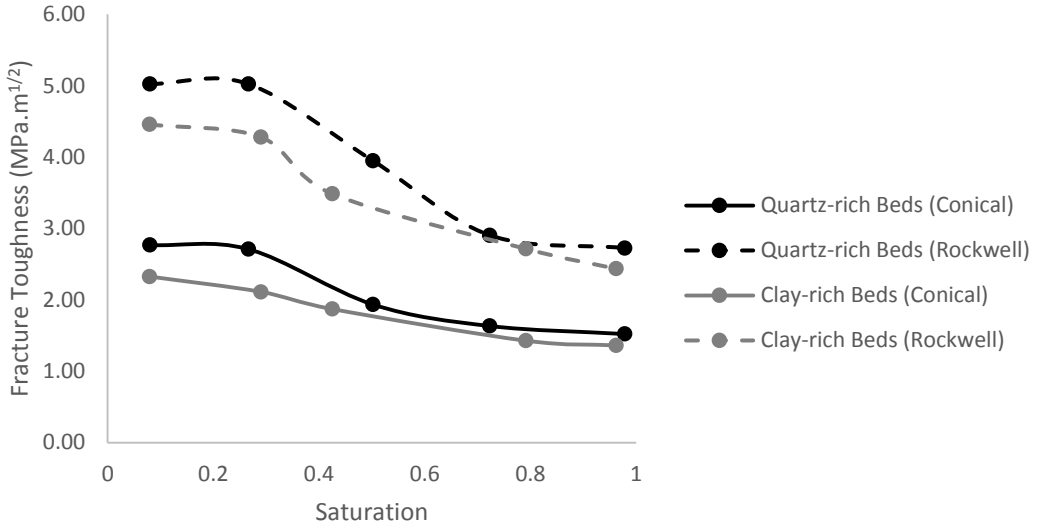

Figure 4-91. Changes in the average fracture toughness as a function of water saturation in quartz-rich and clay-rich beds.

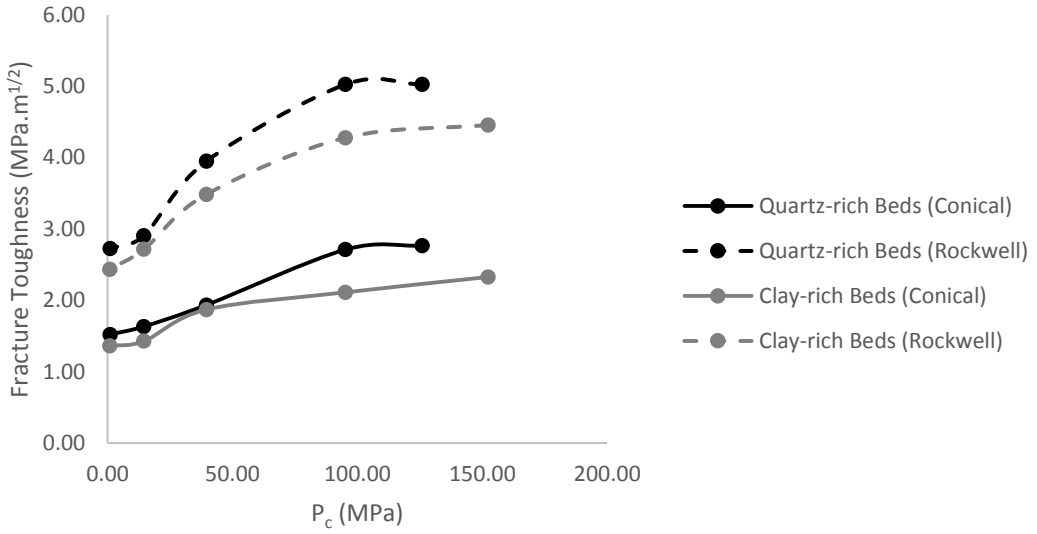

Figure 4-92. Changes in the average fracture toughness as a function of capillary suction in quartz-rich and clay-rich beds.

Figure 4-93 and Figure 4-94 represent the percentage of each fracture toughness range along the scratches in quartz-rich and clay-rich beds for different water saturation levels.

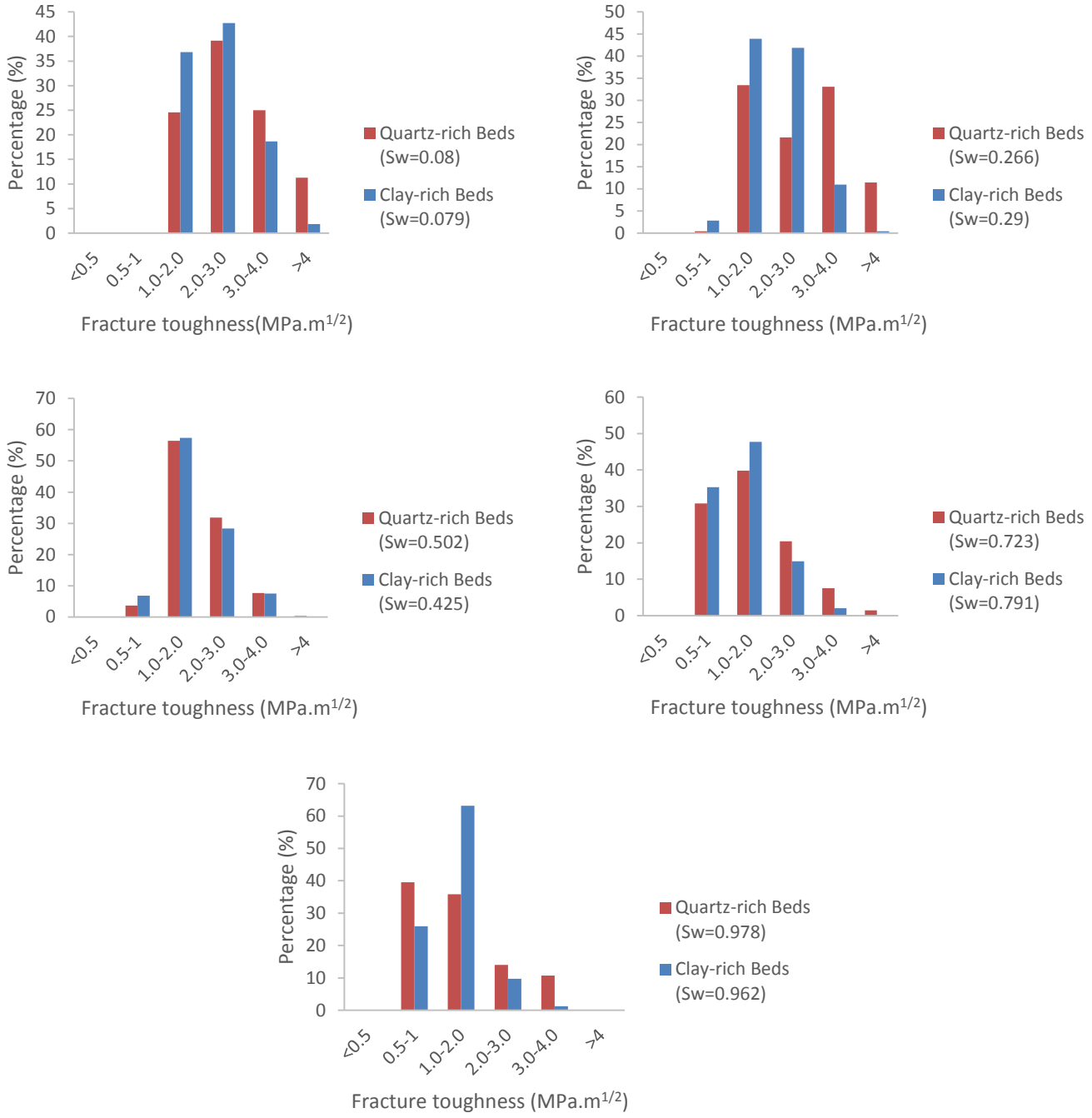

Figure 4-93. Percentage of fracture toughness values for the measured points along the scratches made by conical tip within quartz-rich and clay-rich beds in different water saturations.

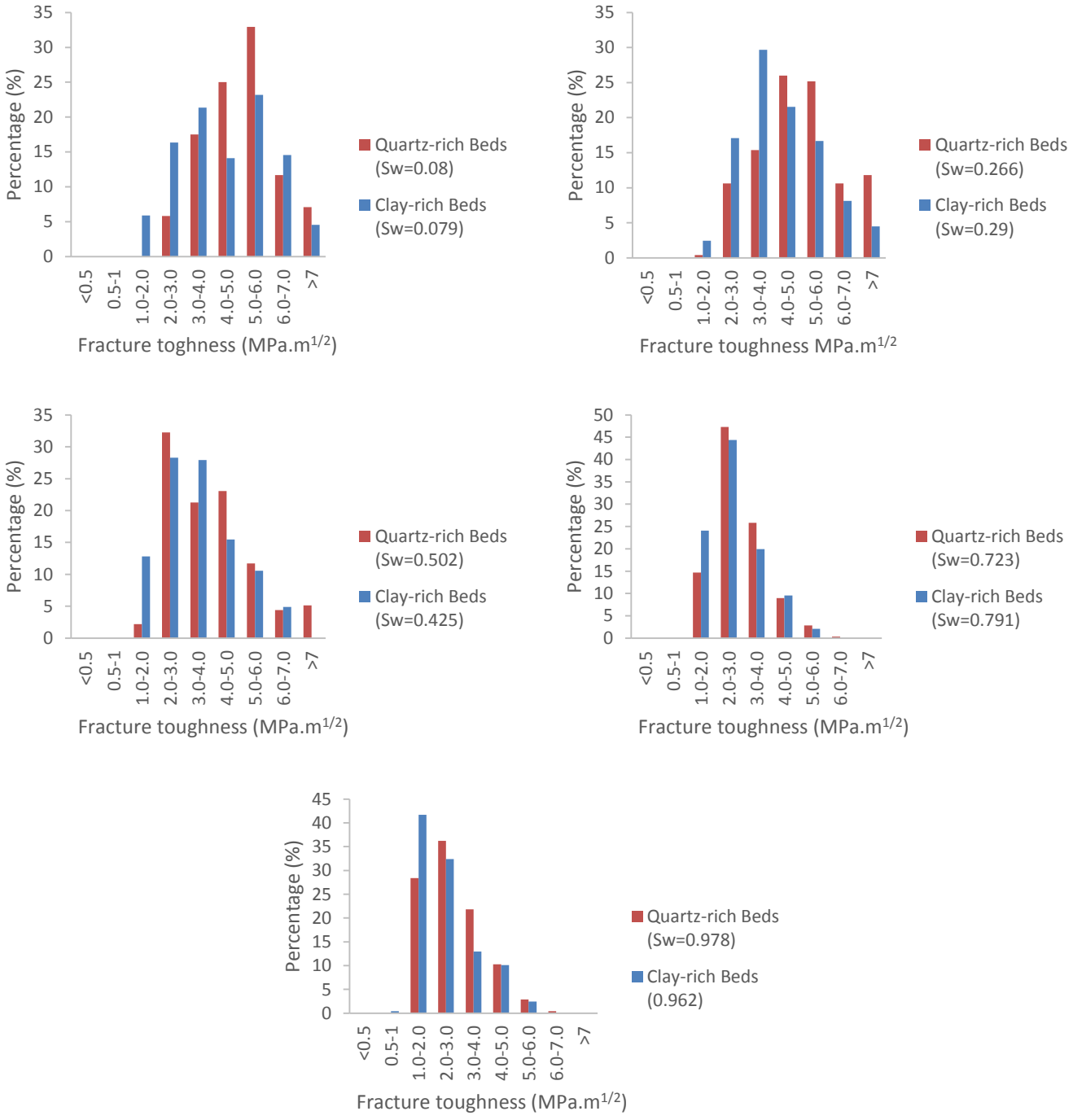

Figure 4-94. Percentage of fracture toughness values for the measured points along the scratches made by Rockwell tip within quartz-rich and clay-rich beds in different water saturations.

Summary of the parameters captured by micro-scratch experiments is shown in Table 4-9. The results imply that since the changes in strength parameters and fracture toughness in clay-rich and quartz-rich beds as a result of increasing the water saturation (or decreasing the capillary suction) are different it would be expected that these bed types would behave differently during water imbibition: clay-rich beds would become weaker in both strength parameters and fracture toughness values in comparison with quartz-rich beds. This implies that the failure progress and fracture propagation as a result of water imbibition would be most likely from the interface between the beds toward the clay-rich beds rather than quartz-rich beds. The same behavior was observed in Figure 3-40 where the failure initiation and fracture propagation would take place in the interface between the beds and then it turned into the clay-rich beds.

Table 4-9. Summary of the parameters captured by micro-scratch experiments ("C" and "R" superscripts represents conical and Rockwell tips, respectively).

Sample	S_w	P_c (MPa)	φ	UCS^C (MPa)	UCS^R (MPa)	C^C (MPa)	C^R (MPa)	K_c^C (MPa.m$^{1/2}$)	K_c^R (MPa.m$^{1/2}$)
Quartz-rich Beds	0.08	125.8	37.69	126.82	134.70	26.38	28.31	2.77	5.02
	0.26	95.2	35.27	123.67	131.83	19.78	22.98	2.71	5.02
	0.50	39.5	32.17	90.35	112.21	13.85	19.98	1.93	3.95
	0.72	14.4	30.08	68.13	86.65	8.69	14.71	1.63	2.91
	0.97	0.9	30.10	62.84	72.15	7.13	10.18	1.52	2.73
Clay-rich Beds	0.079	152.2	35.85	116.90	131.85	24.26	28.06	2.33	4.46
	0.29	95.2	31.95	103.73	121.62	18.00	22.76	2.11	4.28
	0.42	39.5	31.44	82.70	99.54	12.33	16.64	1.87	3.48
	0.79	14.4	29.93	57.35	74.40	6.05	11.12	1.43	2.72
	0.96	0.8	29.98	53.95	67.20	5.12	8.91	1.36	2.43

4.1.3.6. Permeability Measurements

To capture the permeability values in quartz-rich and clay-rich beds pressure-decay (unconfined) and pulse-decay (confined) measurements were conducted on Montney samples.

4.1.3.6.1. Pressure-decay

A length of slabbed core, from 2415m to 2415.5m was selected for pressure-decay permeability measurements. The surface area of the core slab was divided into 6 zones, as shown in Figure 4-95, and the quartz-rich and clay-rich beds were identified in each zone. The results of pressure decay experiments (pressure versus time) on different zones along the core slab are shown in Figure 4-96. By using Equation 4.14 the values of slip-corrected gas permeability were determined. Based on the respective surface areas of quartz-rich and clay-rich beds (Figure 4-97), the ratio of permeability in quartz-rich to clay-rich beds was determined by solving $K_{avg} = \frac{\sum_{i=1}^{n} K_i A_i}{A_t}$ for each two adjacent zones. Figure 4-98 shows the area percentage of quartz-rich and clay-rich beds in each zone.

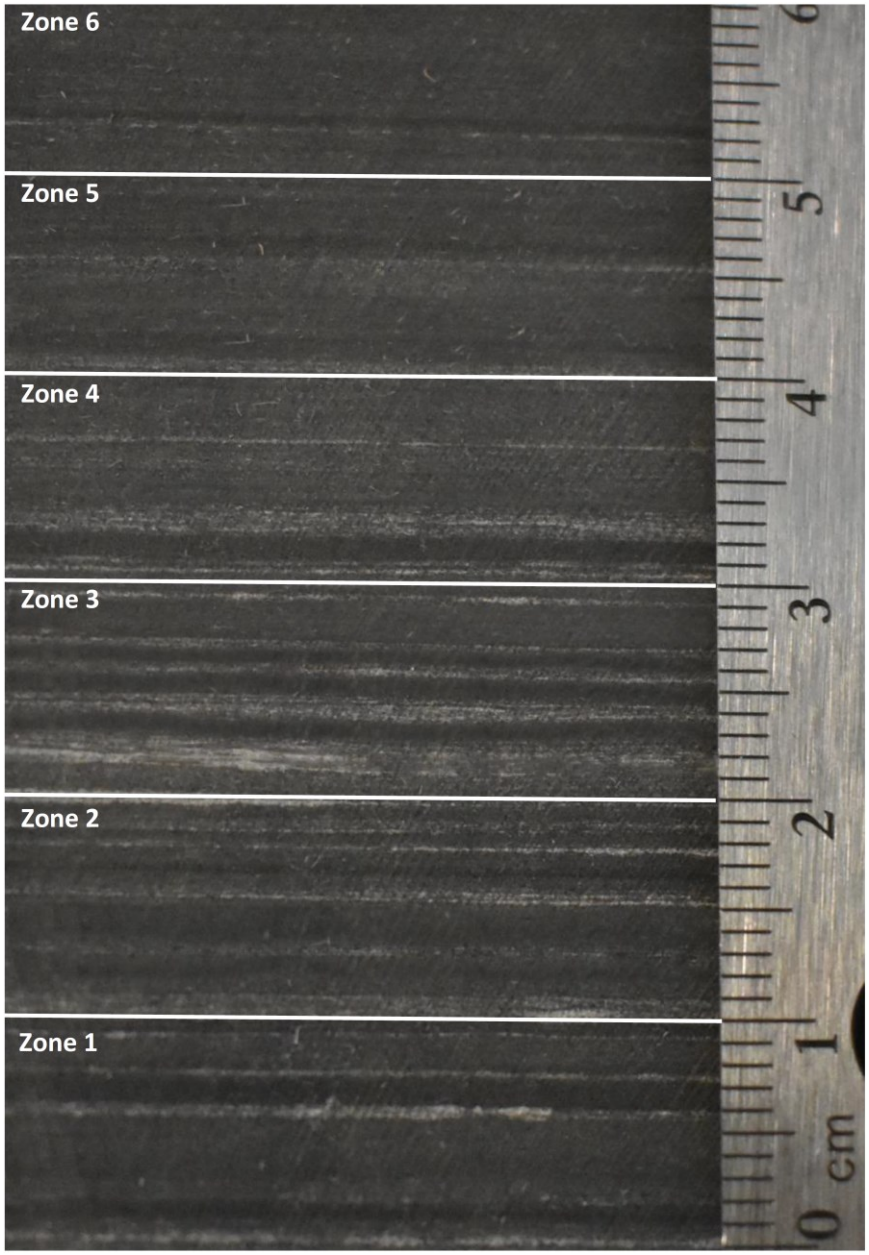

Figure 4-95. Dividing the considered core slab into different zones for pressure-decay permeability measurements.

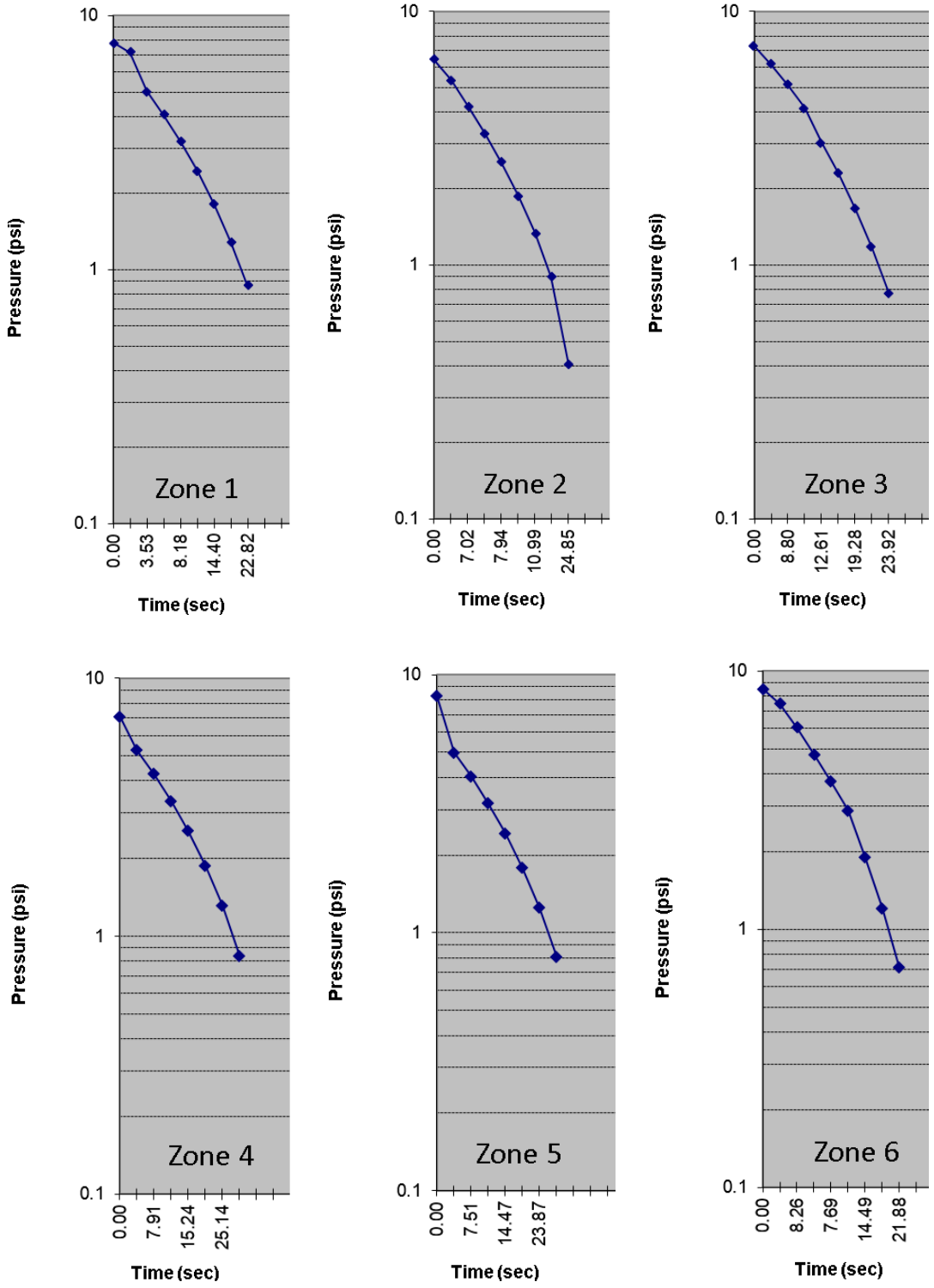

Figure 4-96. Pressure versus time related to pressure decay tests measured for zone 1 to 6 on Montney core slab (the higher the permeability of the zone, the faster the pressure will decay).

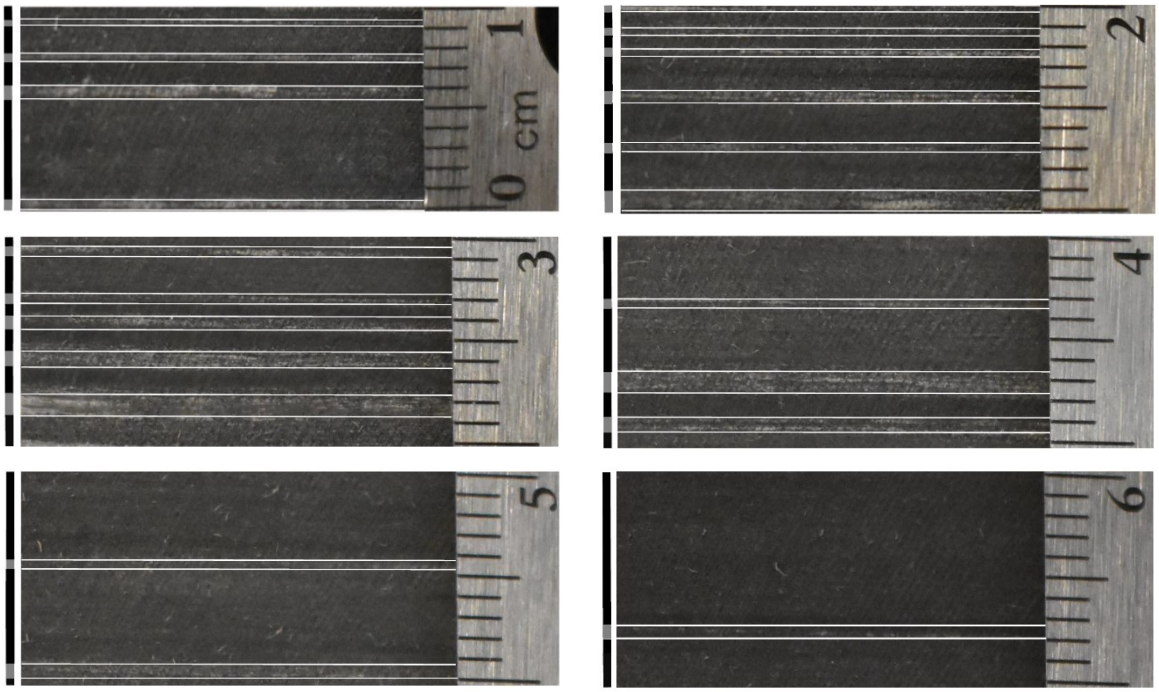

Figure 4-97. Quartz-rich and clay-rich beds in each zone (the number related to each zone is the top right number in each image)

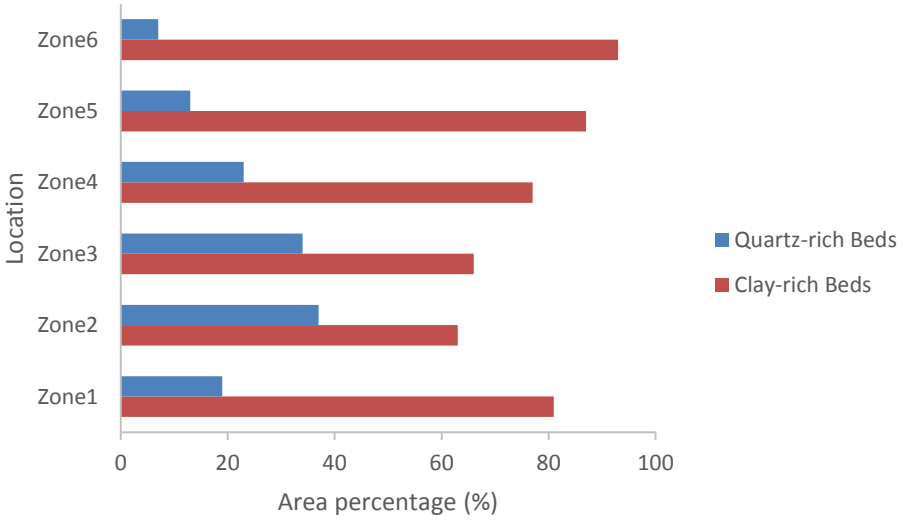

Figure 4-98.Area percentage of quartz-rich and clay-rich beds in each zone.

As shown in Figure 4-99 as the number of quartz-rich beds increases the slip-corrected gas permeability of the zones increase as well which indicates that there is a strong correlation between the portion of quartz- rich beds and the permeability of each zone. Zone 2 and Zone 6 have the maximum and minimum portions of quartz-rich beds with 0.01mD and 0.0052mD slip-corrected gas permeability while for all of the zones the average permeability is 0.0077mD. These results also imply that the permeability of quartz-rich beds are higher than clay-rich beds. Figure 4-100 shows the ratio of permeability in quartz-rich to clay-rich beds in each zone by considering the adjacent zone slip-corrected gas permeability. For example, "Zone1-2" means by solving $K_{avg} = \frac{\sum_{i=1}^{n} K_i A_i}{A_t}$ for Zone 1 and Zone 2 the ratio of quartz-rich beds slip-corrected gas permeability to clay-rich beds slip-corrected gas permeability were determined.

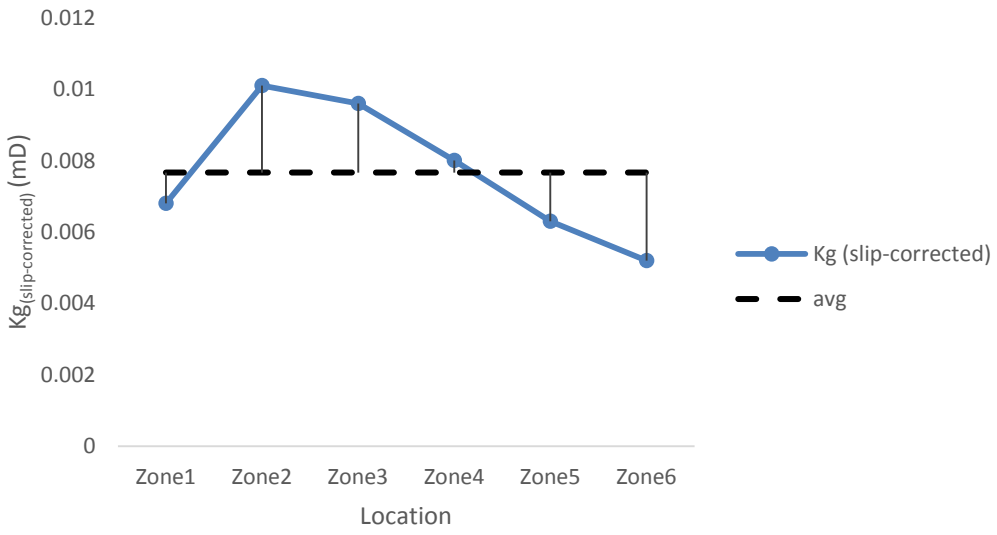

Figure 4-99. Slip-corrected gas permeability of each zone and the average slip-corrected gas permeability of all zones.

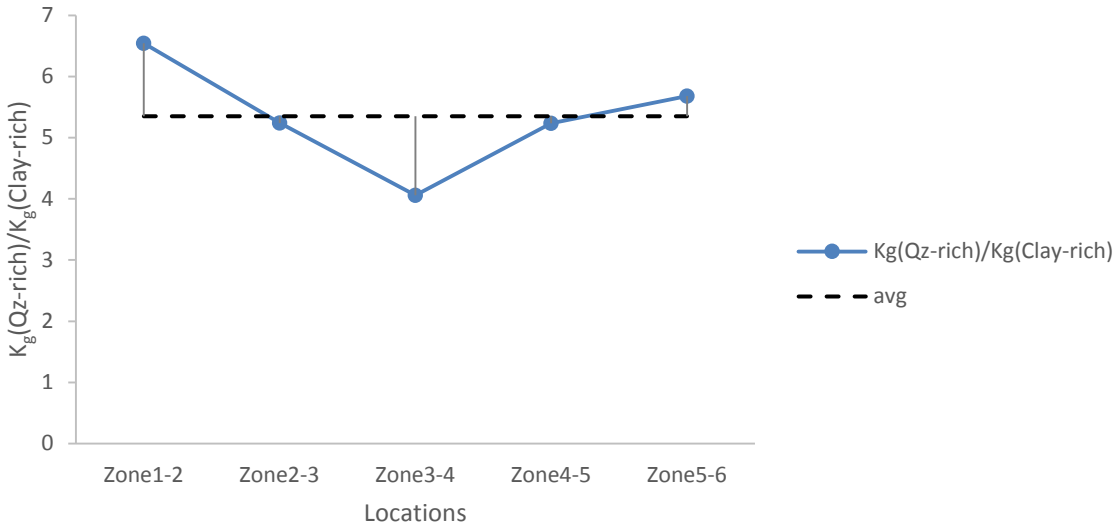

Figure 4-100. Determining the ratio of quartz-rich to clay-rich beds slip-corrected gas permeability in each zone by considering the adjacent zone.

The results indicate that on average, the slip-corrected gas permeability of quartz-rich beds are approximately five times higher than clay-rich beds, as shown in Figure 4-100. Table 4-10 represents the results of pressure-decay permeability measurements in each zone as well as the ratio of quartz-rich beds slip-corrected gas permeability to clay-rich beds slip-corrected gas permeability.

Table 4-10. Summary of pressure-decay permeability measurements.

Zone	Area Percentage (Quartz-rich Beds) (%)	Area Percentage (Clay-rich Beds) (%)	Slip-corrected gas Permeability (K_g) (mD)	K_g(Quartz-rich)/K_g(Clay-rich)
Zone 1	19.1	80.9	0.0068	6.54
Zone 2	37.7	62.3	0.0101	
Zone 3	34	66	0.0096	5.24
Zone 4	23.3	76.7	0.008	4.06
Zone 5	13.1	86.9	0.0063	5.24
Zone 6	7.2	92.8	0.0052	5.68

4.1.3.6.2. Pulse-decay

To capture the permeability of quartz-rich and clay-rich beds under confinement, pulse-decay permeability measurements were done. In a similar manner to the pressure-decay experiments, the surface areas of quartz-rich and clay-rich beds were computed (Figure 4-101) on specimen from the same core slab that pressure decay tests were performed on it. The surface areas of quartz-rich and clay-rich beds was 12.1% for quartz-rich beds and 87.9% for clay-rich beds. The upstream and downstream pressure were kept constant at 1MPa and 6MPa while the flow rate was monitored untill it reached to a constant value for each confining pressure. The results of pulse decay experiments (comulative volume versus time) are shown in Figure 4-102. The experiment was started with 10MPa confining pressure and gradually it increased to 38.5MPa. Figure 4-103 shows the flow rate for each confining pressure. By using Equation 4-17 apparent permeability for each confining stress were calculated. The results of apparent permeability as a function of effective stress for the samples can be found in Figure 4-104.

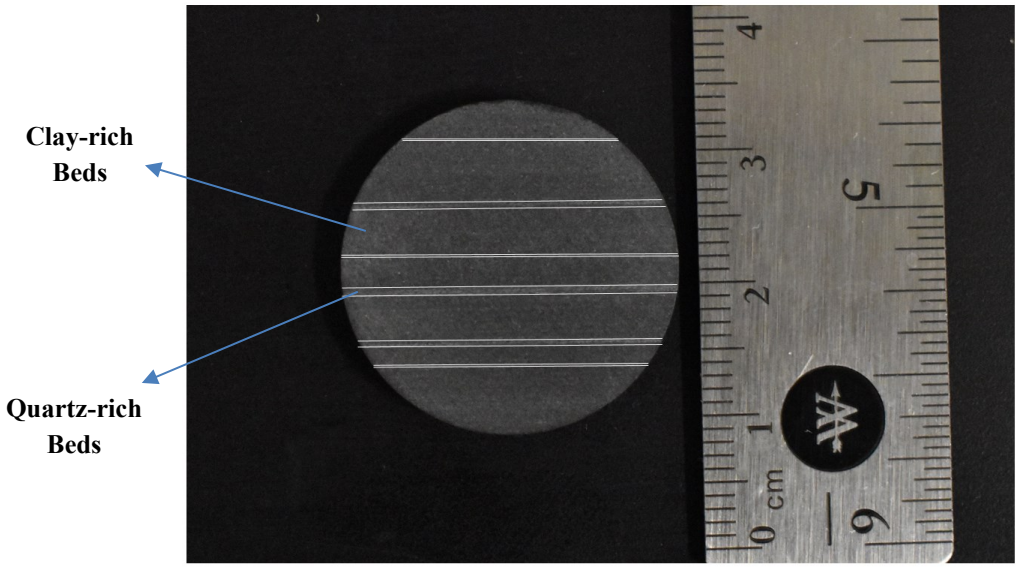

Figure 4-101. Quartz-rich and clay-rich beds in the sample for pulse-decay experiment.

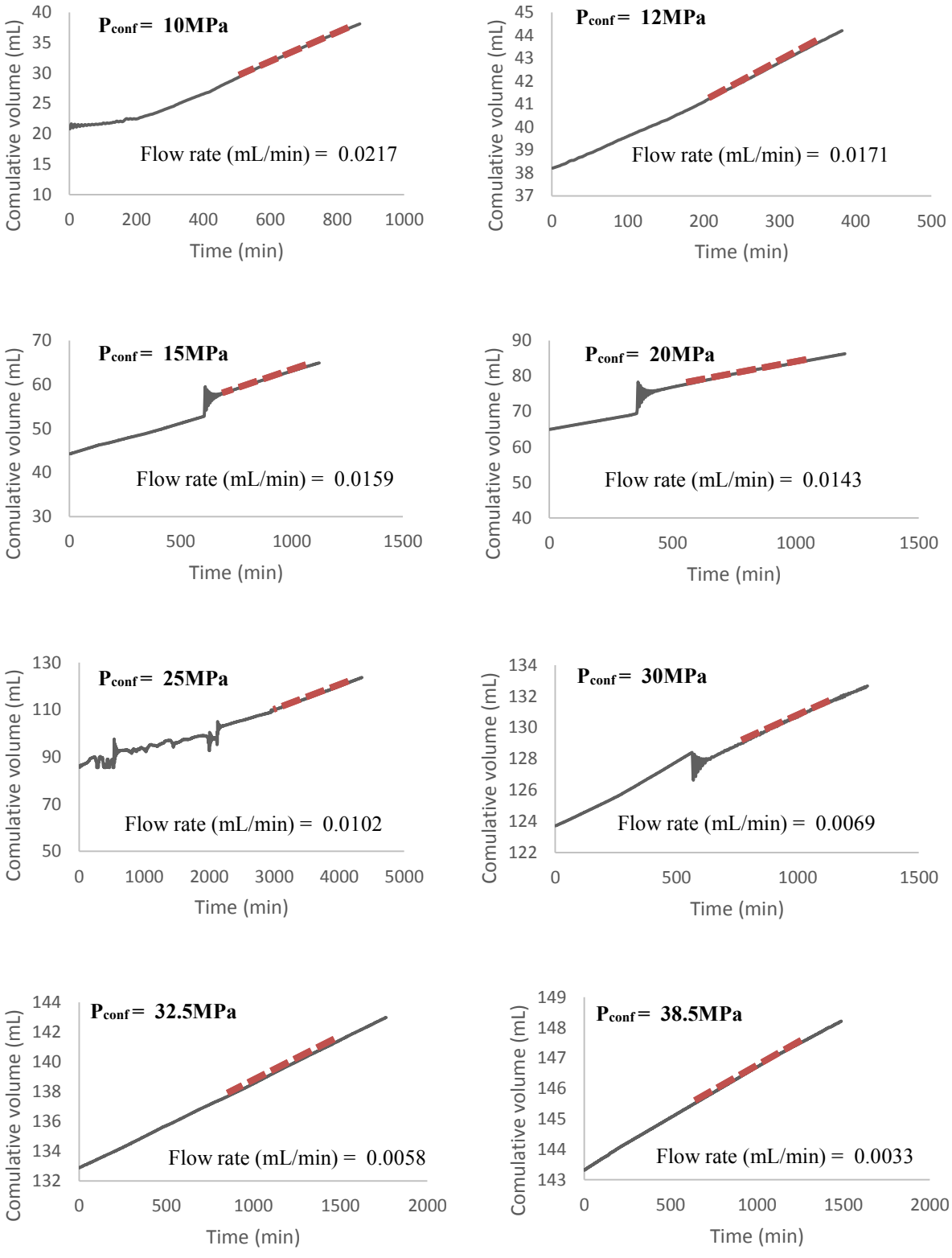

Figure 4-102. The results of pulse decay experiments in different confining stresses on Montney sample. Dotted line indicates the linear part of the curve that is used to calculate the flow rate.

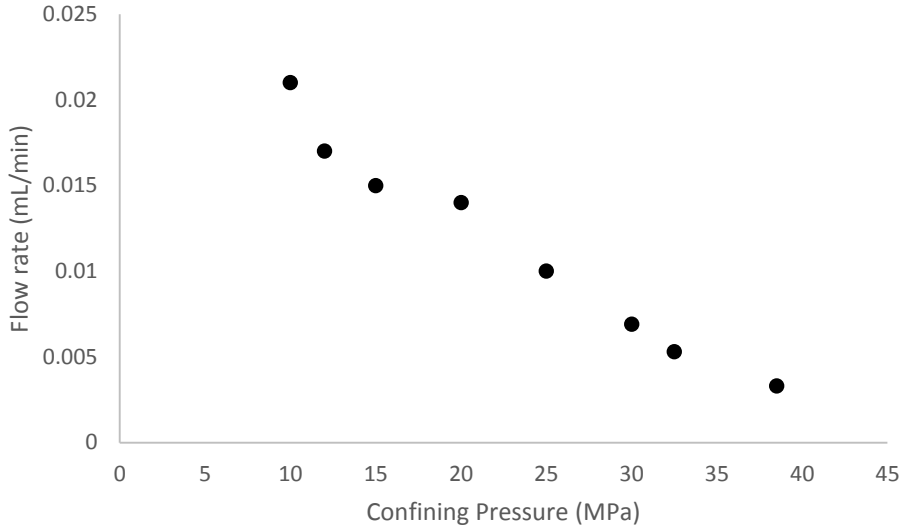

Figure 4-103. Flow rate for each confining pressure during pulse-decay permeability measurements.

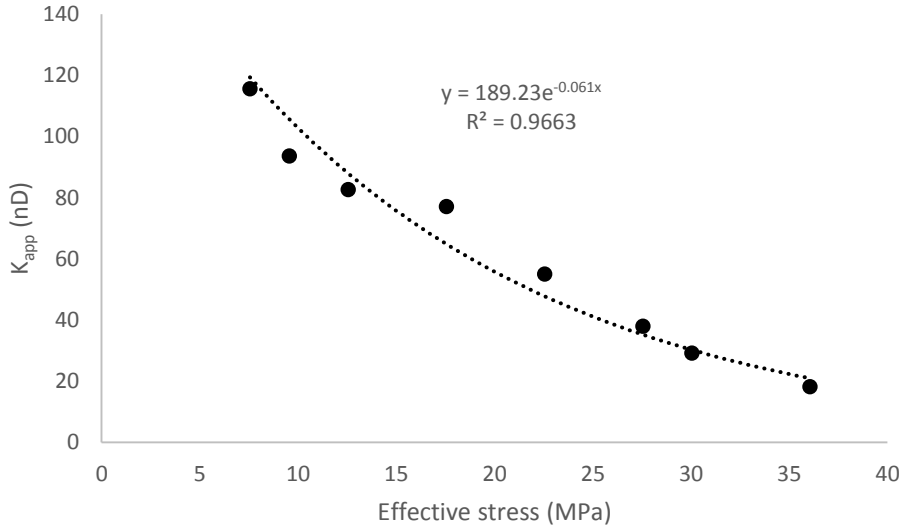

Figure 4-104. Apparent permeability measurements in each effective stress.

According to $K_{avg} = \frac{\sum_{i=1}^{n} K_i A_i}{A_t}$ and the results from pressure-decay experiments where apparent permeability of quartz-rich beds are 5.35 times higher than clay-rich beds, the values of apparent permeability in quartz-rich and clay-rich beds at different effective stress values could be

computed, as shown in Figure 4-105. Apparent permeability at zero effective stress for quartz-rich and clay-rich beds was determined based on the correlation equation shown in Figure 4-105 which is 1065nD for quartz-rich beds and 199.07nD for clay-rich beds. By using Equation (4-18) and considering a = 3.5 and b = 26.6 according to Ashrafi (2016) experiments on Montney samples, the absolute permeability in zero effective stress could be calculated which is 128.1nD for quartz-rich beds and 23.94nD for clay-rich beds. To determine the absolute permeability in different effectivee stresses Equation (4-21) was applied (Figure 4-106) where for the compressibility coefficient, the values of bulk modulus for quartz-rich and clay-rich beds were calculated and reversed. The compressibility coefficients are 0.051 and 0.068 for quartz-rich and clay-rich beds, respectively and 0.065 for the whole sample. The values for permeability obtained from pressure-decay profile permeability measurements were higher than pulse-decay measurements which is in agreement with other studies (Ghanizadeh et al., 2015; Clarkson et al., 2012b) where it was concluded that pressure-decay profile permeability measurements and pulse-decay method would

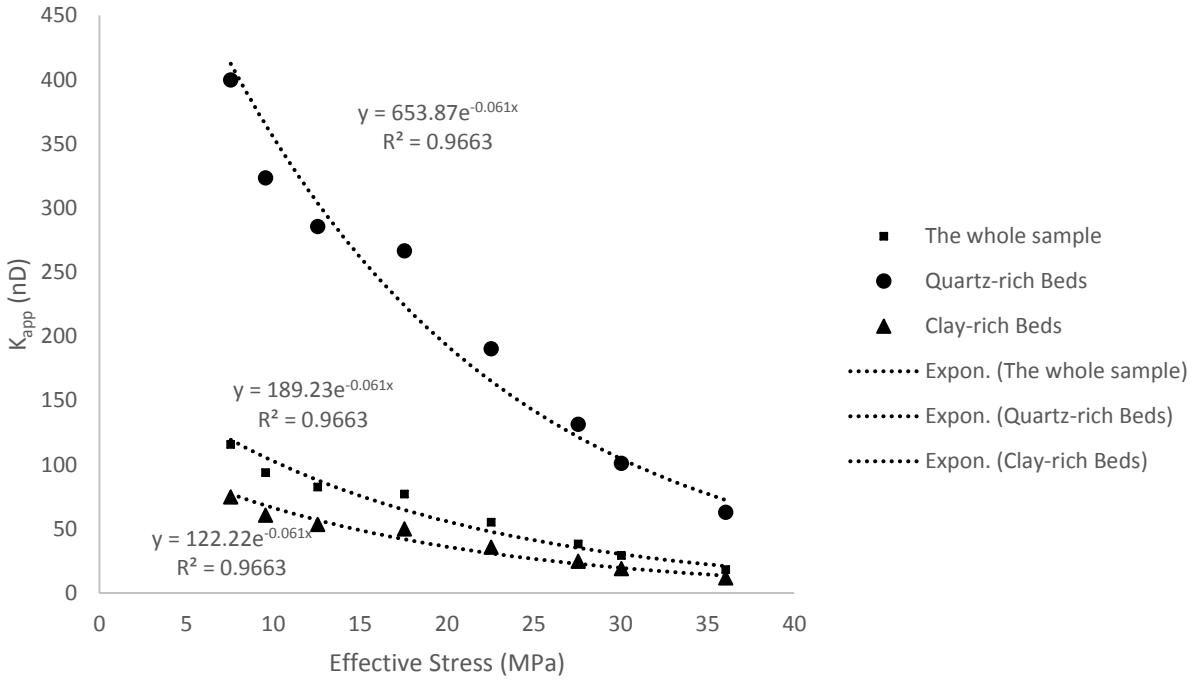

Figure 4-105. Apparent permeability in quartz-rich and clay-rich beds as a function of effective stress.

yield different values for permeability and higher permeability values would be captured from pressure-decay compared to pulse-decay method.

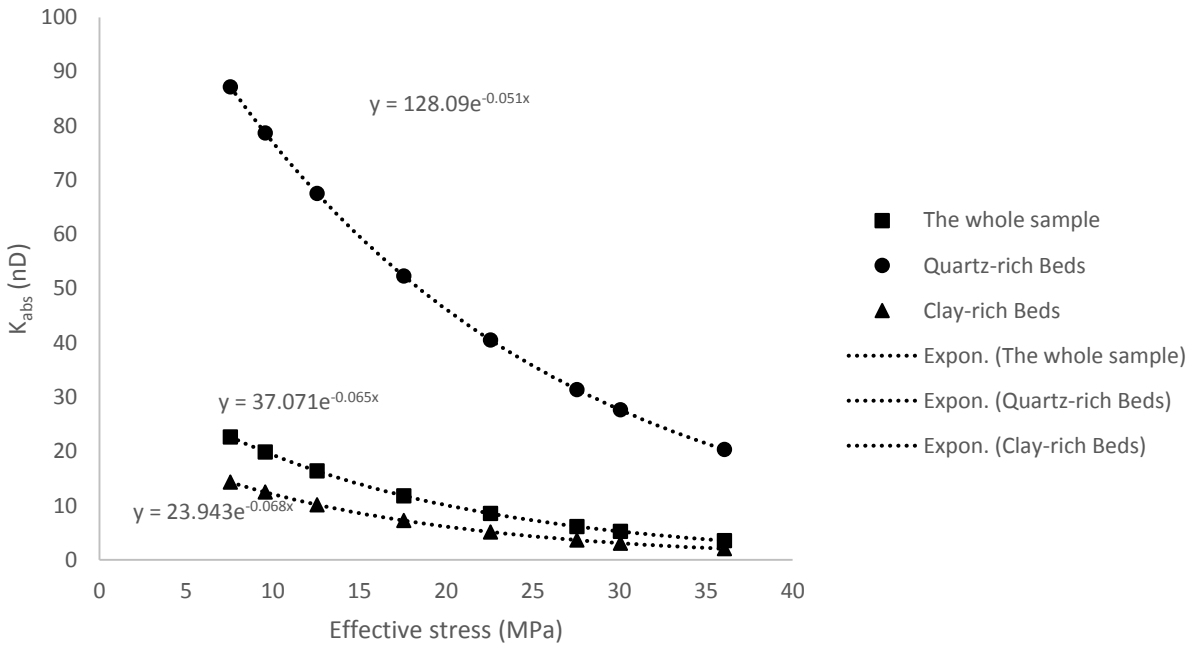

Figure 4-106. Absolute permeability in quartz-rich and clay-rich beds as a function of effective stress.

4.1.3.7. Direct Shear Measurements

For direct shear tests $MgCl_2$ (S_w = 7.8% and P_c = 152MPa), $Mg(NO_3)_2$ (S_w = 31.1% and P_c = 95MPa), NaCl (S_w = 51.9% and P_c = 39MPa) and K_2SO_4 (S_w = 81.8% and P_c = 7MPa) were used. The values of saturation were determined based on the results obtained in capillary condensation experiments. The normal stress values in the tests on samples with parallel beds were 5MPa, 10Mpa and 25MPa and for the samples with perpendicular beds with respect to the loading direction the normal stress values were 5MPa, 25MPa and 50MPa. The results of direct shear tests in different water saturation for the perpendicular samples with 5MPa, 25MPa and 50MPa normal stresses are shown in Figure 4-107, Figure 4-108 and Figure 4-109, respectively and for parallel samples with 5MPa, 10MPa and 25MPa normal stresses the results are shown in Figure 4-110, Figure 4-111 and Figure 4-112, respectively.

For some of the parallel and perpendicular samples at the initial shear loading stage, the initial non-linearity is a result of closure of inner spaces between the sample and shearing box. This initial data is not used in computing strength or stiffness properties of the specimens. With increasing shear displacement, the slope of the curve increases rapidly and by increasing the shearing force micro-fractures are generated in the sample. These fractures for perpendicular samples are initiated

and propagated along the interface between the beds and the shear plane would be the interface between the beds while for parallel samples it can be both the intended shear plane in the beds and/or the interface between the beds. Therefore, the results from perpendicular samples would reveal the strength parameters in the interface between the beds while the results from parallel samples would reflect the strength parameters related to both beds and interfaces.

Once peak shear stress is reached, in all cases there is an abrupt shear stress drop after the peak, reflecting the brittle nature of shear failure for these materials. The former would suggest that the interfaces between the beds would act as weak planes and they have a lower shear strength. It can also imply a weaker cohesion in the interface between the beds which is released within the abrupt shear stress drop. After the shear stress decreases to a certain degree it reaches to post-peak strength. During the first increments of strain, in the pre-peak region, the samples show a strain-hardening behavior which is followed by a post-peak stage of strain-softening behavior that leads to a residual strength value.

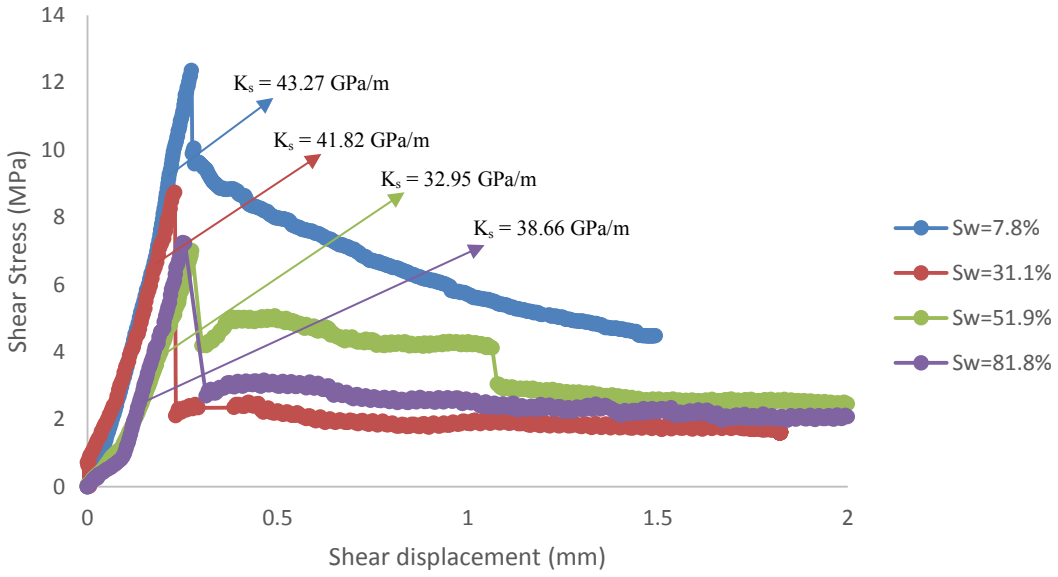

Figure 4-107.. Direct shear tests on perpendicular samples in different water saturation levels under 5MPa normal stress. "K_s" represents shear stiffness.

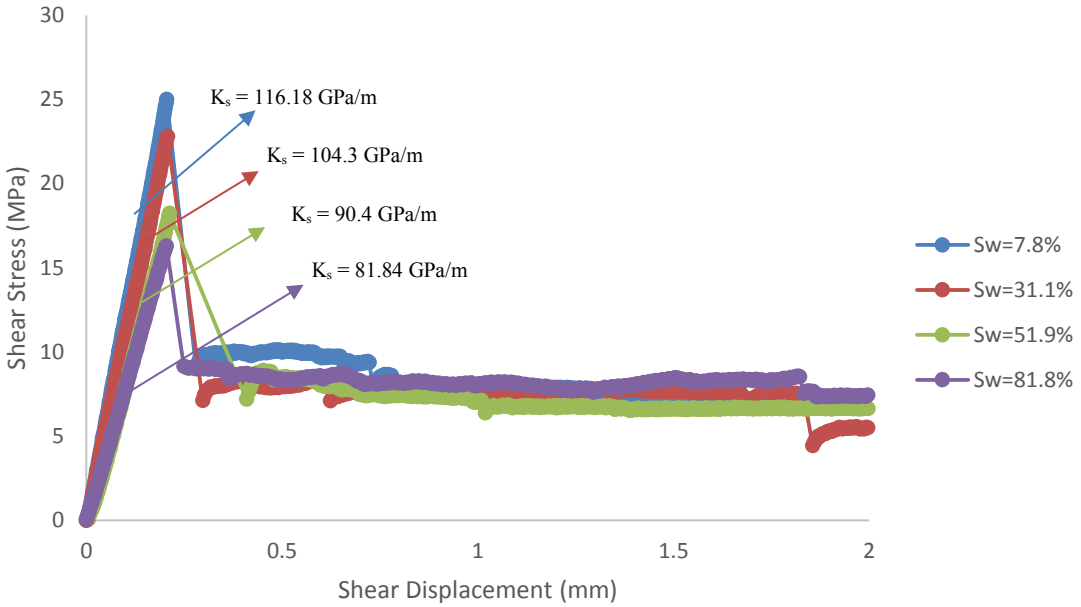

Figure 4-108. Direct shear tests on perpendicular samples in different water saturation levels under 25MPa normal stress. "K_s" represents shear stiffness.

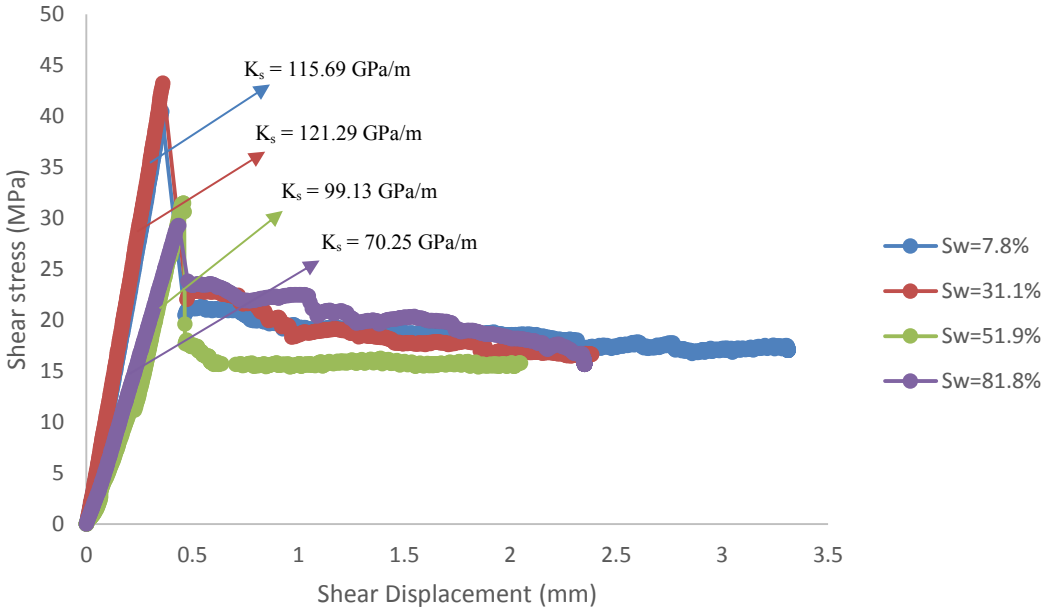

Figure 4-109. Direct shear tests on perpendicular samples in different water saturation levels under 50MPa normal stress. "K_s" represents shear stiffness.

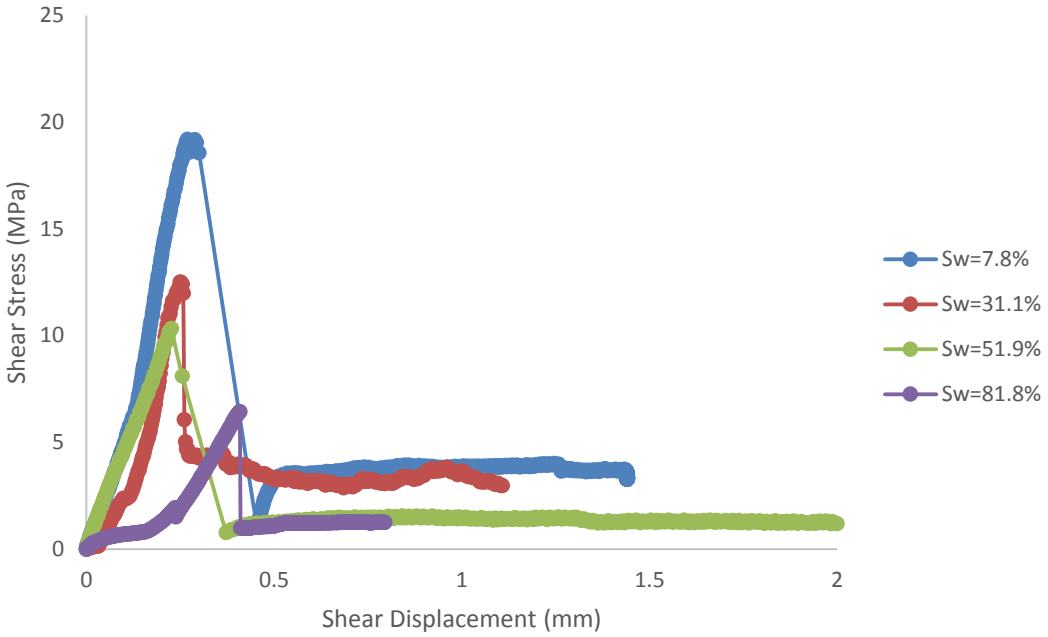

Figure 4-110. Direct shear tests on parallel samples in different water saturation levels under 5MPa normal stress.

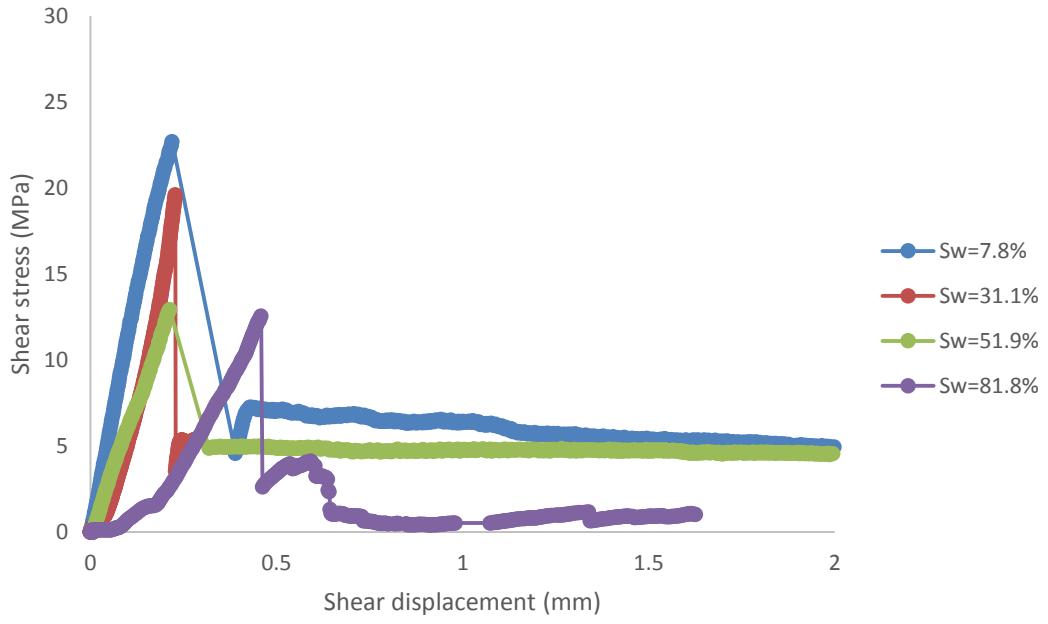

Figure 4-111. Direct shear tests on parallel samples in different water saturation levels under 10MPa normal stress.

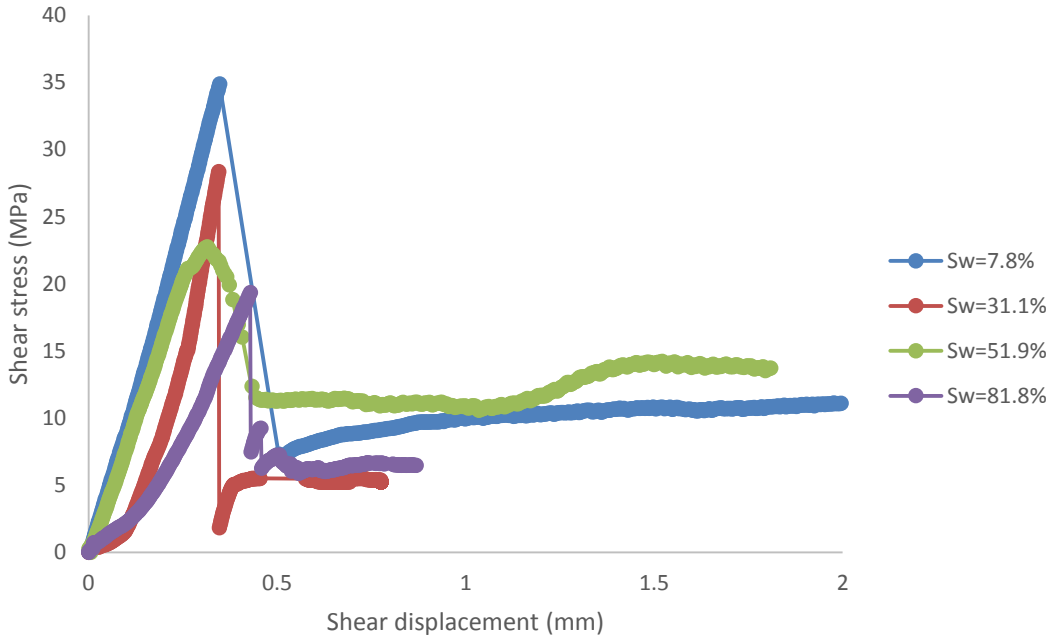

Figure 4-112. Direct shear tests on parallel samples in different water saturation levels under 25MPa normal stress.

Based on the results for both perpendicular and parallel samples, as the normal stress increases the curves become stiffer with higher slope in the strain hardening region. For tests at increasing water saturation, specimens display a more ductile response with lower stiffness and lower strength. As shown in Figure 4-107, Figure 4-108 and Figure 4-109 in high water saturation (81.8%) the slope of the shear stress versus shear displacement (shear stiffness) at 5MPa, 25MPa and 50MPa normal stresses reduces by 10.6%, 29.5% and 39.3%, respectively, in comparison with 7.8% water saturation cases. These results show that shear stiffness shows a decreasing trend as the water saturation increases which is an indication of softening in the presence of water. For perpendicular samples, as the water saturation level increases to 81.8%, the peak shear strength values of the samples (interface between the beds) would decrease by 41.3%, 34.8% and 32.6% for 5MPa, 25MPa and 50MPa normal stresses, respectively (Figure 4-113).

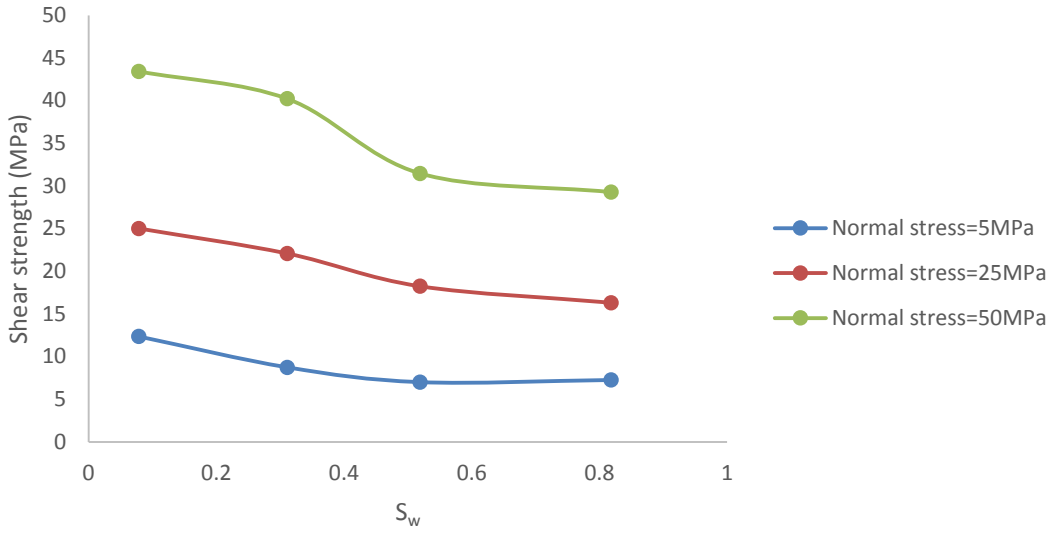

Figure 4-113. Peak shear strength of perpendicular samples (interface between the beds) in different water saturation levels and normal stresses.

Also, based on Figure 4-114 which is related to direct shear tests on parallel samples, the peak shear strength values of the samples (beds and interfaces) would reduce by 66.4%, 44.7% and 44.6% for 5MPa, 10MPa and 25MPa normal stresses, respectively, in 81.8% water saturation.

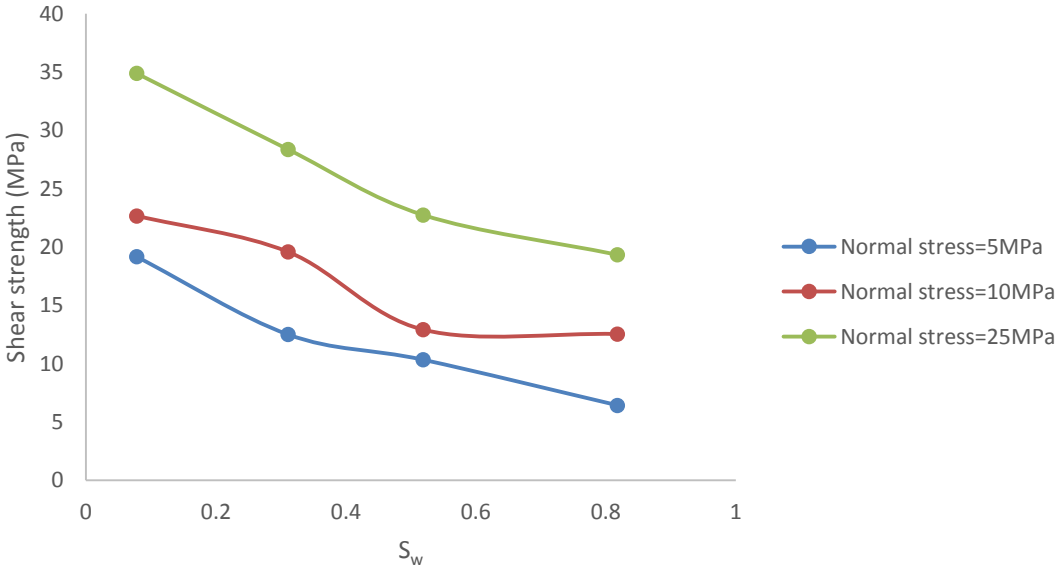

Figure 4-114. Peak shear strength of parallel samples in different water saturation levels and normal stresses.

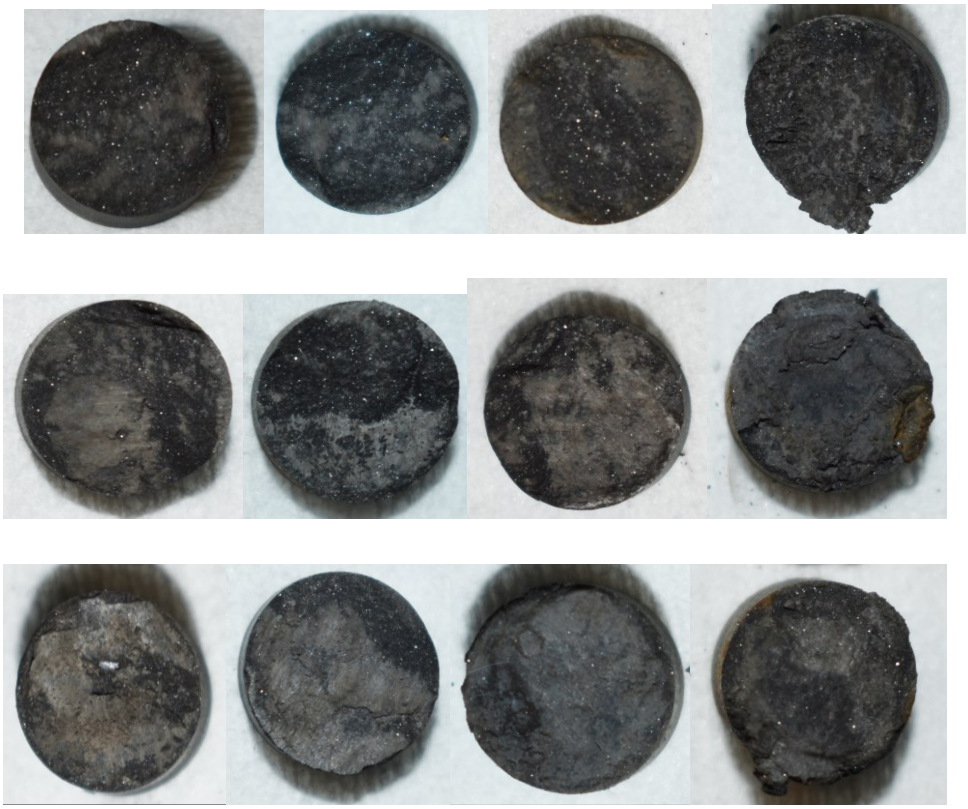

Figure 4-115. Sheared perpendicular samples in different water saturations. Top, middle and bottom images are related to 5MPa, 25MPa and 50MPa normal stress. In each normal stress from left to right the images are related to the water saturations of 7.8%, 31.3%, 51.9% and 81.8%.

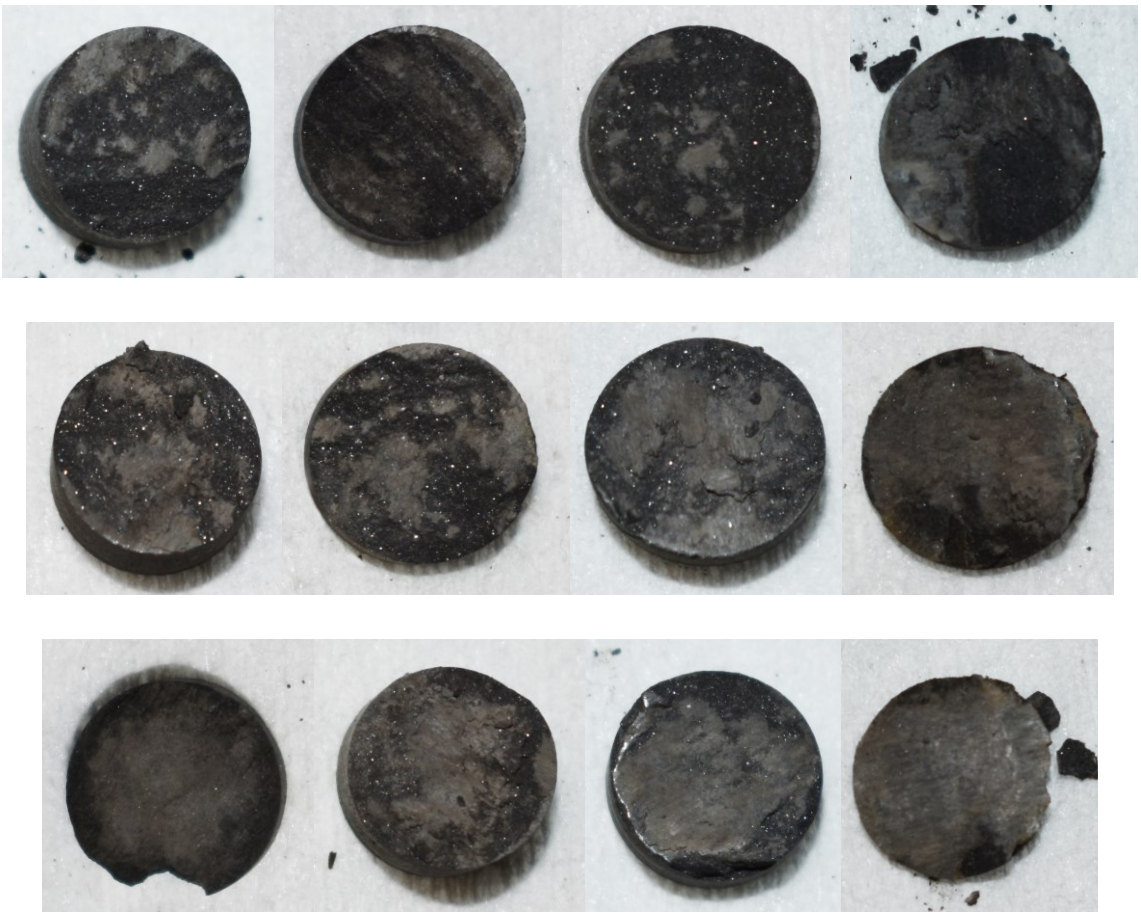

Figure 4-116. Sheared parallel samples in different water saturations. Top, middle and bottom images are related to 5MPa, 10MPa and 25MPa normal stress. In each normal stress from left to right the images are related to water saturations of 7.8%, 31.3%, 51.9% and 81.8%.

Figure 4-115 and Figure 4-116 represent the sheared perpendicular and parallel samples which imply that as the water saturation increases the shear surface becomes smoother. Also, the results indicate that at low water saturation (7.8%) the peak shear strength of parallel samples (beds and interfaces) under 5MPa and 25MPa are 19.17MPa and 34.89MPa, respectively, while the values of peak shear strength in the same conditions for perpendicular samples (interface between the beds) are 12.36MPa and 25.02MPa. For high water saturation (81.8%) the peak shear strength for perpendicular samples (interface between the beds) under 5MPa and 25MPa normal stresses are 7.25MPa and 16.21MPa while the values of peak shear strength in the same conditions for parallel samples (beds and interfaces) are 6.44MPa and 12.55MPa which indicates that the rate of decrease in the shear strength of the interface between the beds is lower than the beds. Table 4-11summarizes the changes in shear strength for both perpendicular samples (interface

between the beds) and parallel samples (beds and interfaces) in different water saturations and capillary suctions.

Table 4-11. Changes in peak shear strength in perpendicular samples (interface between the beds) and parallel samples (beds & interfaces) as a function of water saturation and capillary suction.

Sample	S_w	P_c (MPa)	τ_{peak} (MPa) (σ_n=5MPa)	τ_{peak} (MPa) (σ_n=25MPa)	τ_{peak} (MPa) (σ_n=50MPa)
Perpendicular samples	0.078	152.27	12.36	25.02	43.43
	0.31	95.2	8.74	22.08	40.22
	0.52	39.51	7	18.24	31.47
	0.82	7.04	7.25	16.31	29.28
Parallel samples	S_w	P_c (MPa)	τ_{peak} (MPa) (σ_n=5MPa)	τ_{peak} (MPa) (σ_n=10MPa)	τ_{peak} (MPa) (σ_n=25MPa)
	0.078	152.27	19.17	22.68	34.89
	0.31	95.2	12.51	19.59	28.37
	0.52	39.51	10.34	12.92	22.75
	0.82	7.04	6.44	12.55	19.34

Figure 4-117 and Figure 4-118 show the peak shear strength as a function of normal stress in different water saturations for perpendicular samples (interface between the beds) and parallel samples (beds and interfaces) which can be used to capture the cohesion and friction angle values. Figure 4-119 and Figure 4-120 represent the cohesion and friction angles in low to high water saturation levels for perpendicular samples (interface between the beds) and parallel samples (beds and interfaces). The results indicate that initially at low water saturation levels the cohesion in perpendicular samples (the interface between the beds) is 8.47MPa and in the parallel samples (beds and interfaces) is 15.01MPa (the cohesion is 77.2% lower in the interface between the beds).

As the water saturation increases, cohesion in both the beds and the interface between the beds would decrease and tends to converge to similar values at high water saturation although the rate of the reduction in the cohesion of the interface between the beds is lower. In addition, the friction angle at the interface between the beds decreases from 34.7° to 26.1° as the water saturation reaches 81.8%. For parallel samples, in low water saturation (7.8%) and high capillary suction, the internal friction angle is 38.4° and it reduces to 31° in low capillary suction and high water

saturation (81.8%). The results imply that the interface between the beds would act as a weak plane that becomes progressively weaker during post- fracturing spontaneous imbibition.

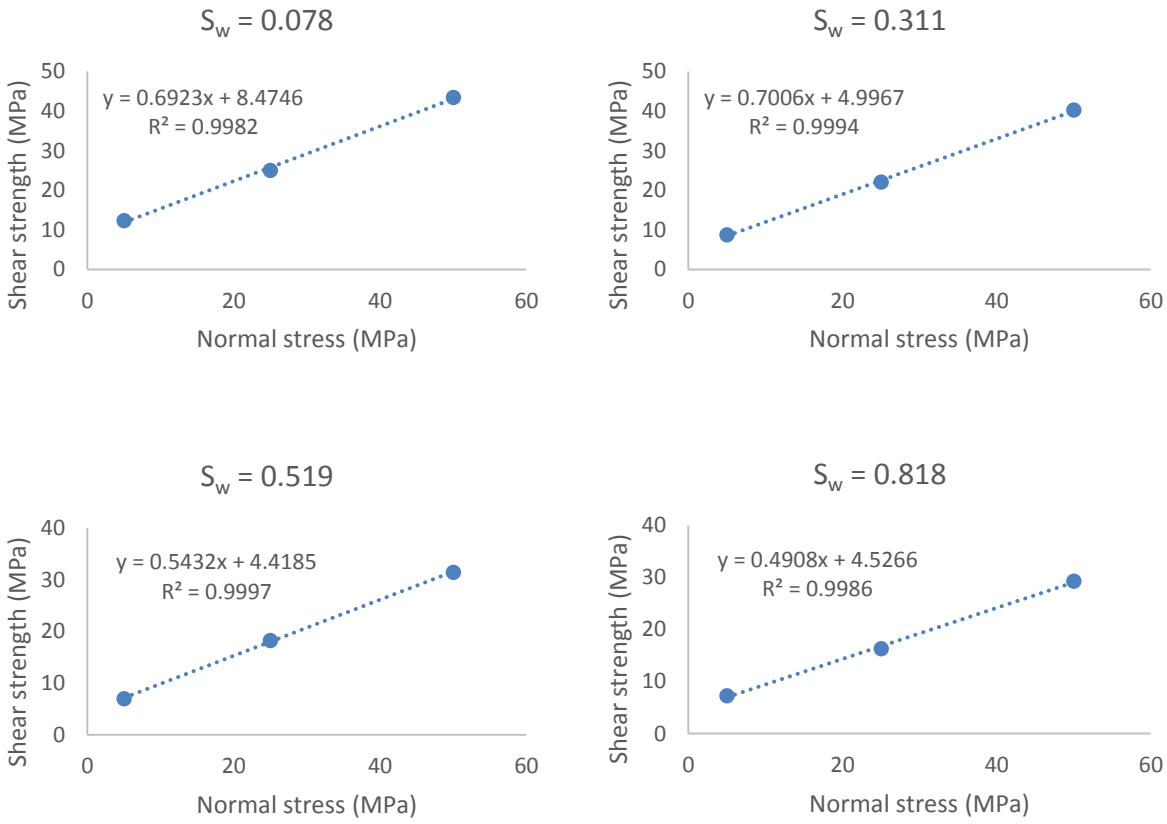

Figure 4-117. Shear strength as a function of normal stress for perpendicular samples (interface between the beds)

Table 4-12 represents the changes in cohesion and friction angle for both perpendicular samples (interface between the beds) and parallel samples (beds and interfaces) in different water saturations and capillary suctions.

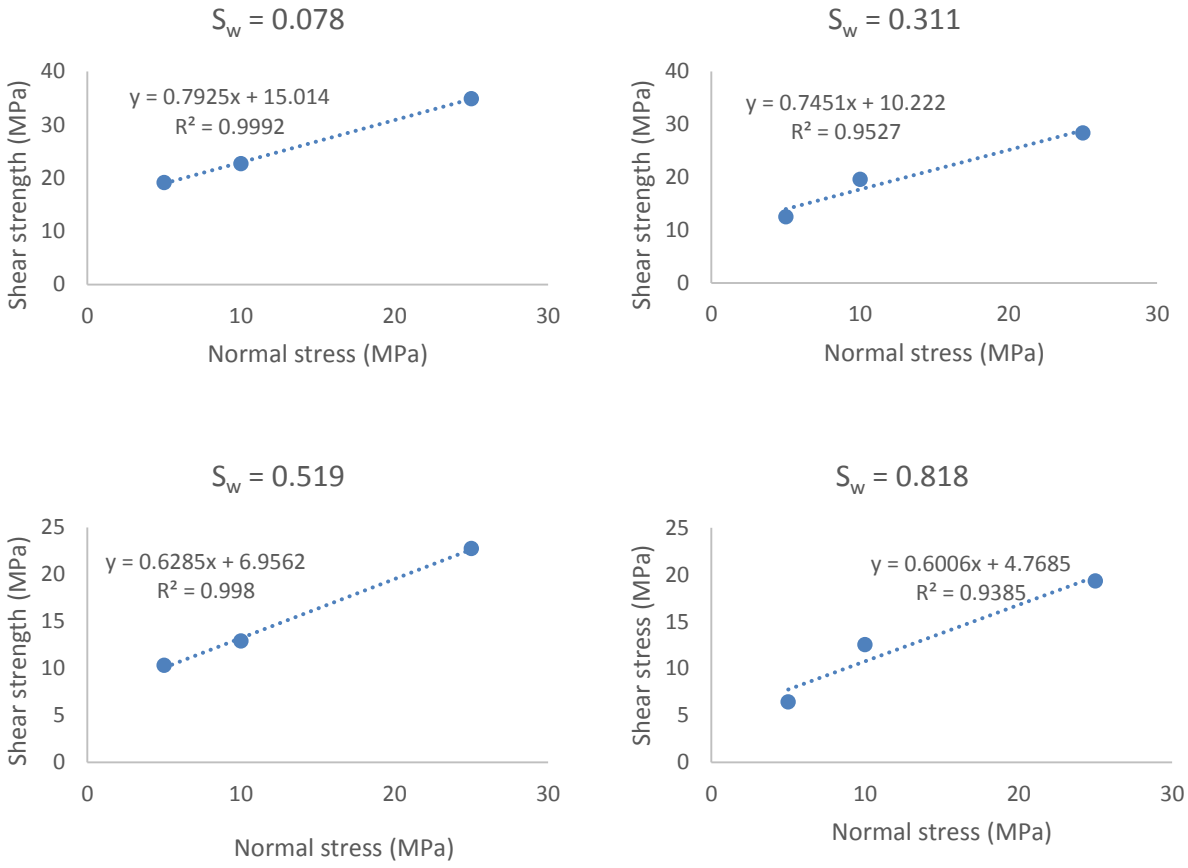

Figure 4-118. Shear strength as a function of normal stress for parallel samples (beds and interfaces)

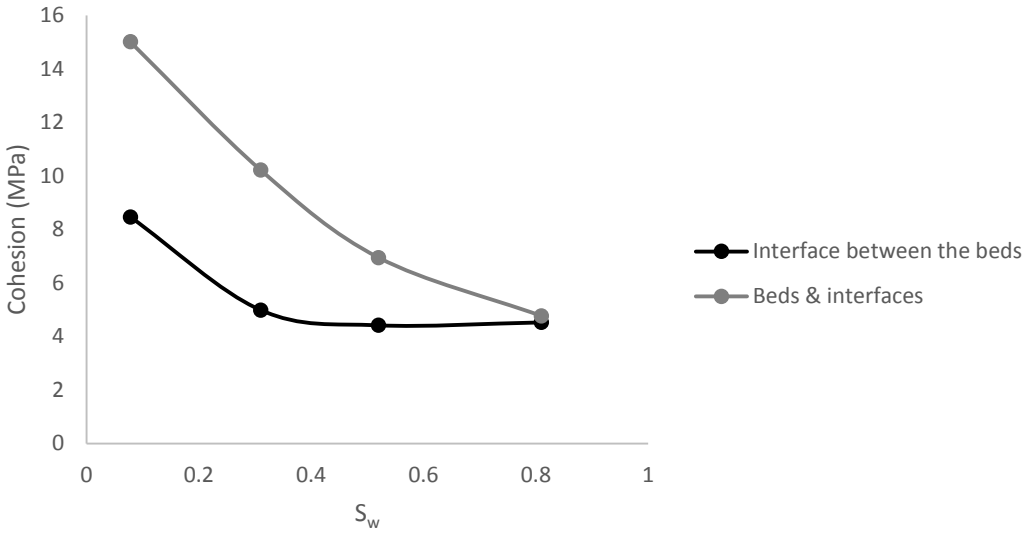

Figure 4-119. Changes in the cohesion of perpendicular samples (interface between the beds) and parallel samples (beds & interfaces) as a function of water saturation.

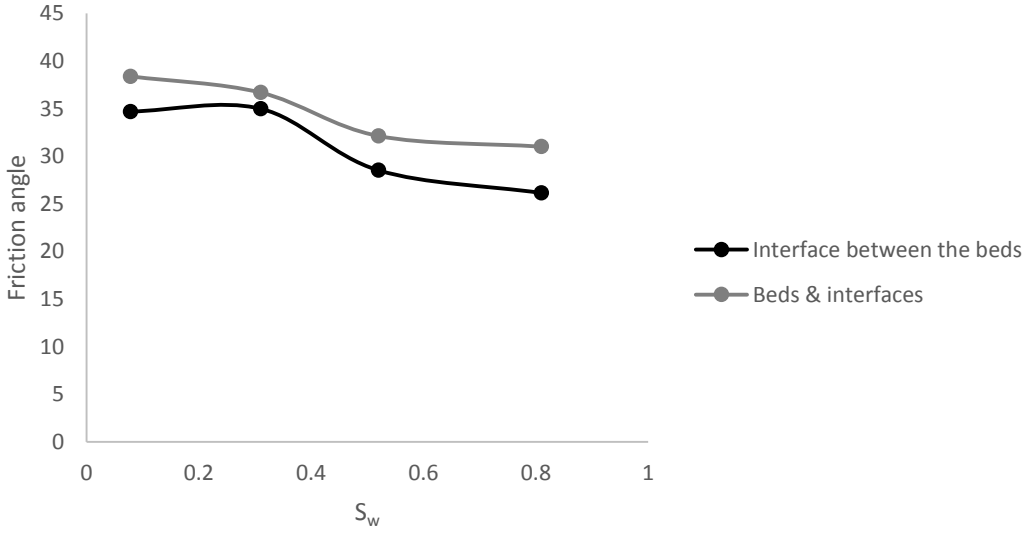

Figure 4-120. Changes in the friction angle of perpendicular samples (interface between the beds) and parallel samples (beds & interfaces) as a function of water saturation.

Table 4-12. Changes in cohesion and friction angle values in perpendicular samples (interface between the beds) and parallel samples (beds & interfaces) as a function of water saturation and capillary suction.

Sample	S_w	P_c (MPa)	C (MPa)	φ
Perpendicular samples	0.078	152.27	8.47	34.69
	0.31	95.2	4.99	34.99
	0.52	39.51	4.41	25.52
	0.82	7.04	4.52	26.14
Parallel samples	S_w	P_c (MPa)	C (MPa)	φ
	0.078	152.27	15.01	38.40
	0.31	95.2	10.22	36.68
	0.52	39.51	6.95	32.13
	0.82	7.04	4.77	31

4.2. Summary

To better analyze the spontaneous water imbibition in tight formations from geomechanical point of view, bed-scale investigations were completed. To determine the properties in the bed-scale an integrated experimental and analytical approach has been developed for partially saturated porous media. The results reveal that:

- According to QEMSCAN analysis the mineralogy and even the mineral sizes in the beds are different. Based on that the beds can be categorized into quartz-rich beds and clay-rich beds. Different mineralogy and mineral sizes in quartz-rich and clay-rich beds would lead to different rock mechanical and strength responses.
- Based on nitrogen adsorption-desorption isotherm analysis it is clearly observed that quartz-rich beds are dominated by slit-like pores and wedge-shaped pores and in clay-rich beds parallel plate shaped pores and slit-like pores are dominant. Also, quartz-rich and clay-rich beds are different in pore size distribution, pore volume and porosity.
- The results of TGA would suggest that initial water saturation (free water and water in pores) in quartz-rich and clay-rich beds are almost the same and it is 7.23% for clay-rich bed and 7.24% for quartz-rich bed.

- Direct shear tests reveal that, as the water saturation increases the strength parameter values of the interface between the beds would decrease significantly which would suggest that the interface between the beds would act as a plane of weakness where the failure can get initiated during spontaneous water imbibition.
- Comparing the results of capillary condensation experiments related to quartz-rich and clay-rich beds indicate that in low water saturation levels the capillary suction in clay-rich beds is higher than quartz-rich beds but as the water saturation is increasing the rate of capillary suction decrease in clay-rich beds is getting higher than quartz-rich beds. This suggests that the local change in the effective stress in quartz-rich and clay-rich beds as a matter of spontaneous water imbibition would be different which would lead to different volumetric responses followed by increasing the possibility of failure especially near the interface between the adjacent beds.
- According to micro-indentation analysis, initially Young's modulus and Poisson's ratio are higher in quartz-rich beds. The maximum difference between the values of Young's modulus in quartz-rich and clay-rich beds takes place at around 50.2% water saturation where Young's modulus in quartz-rich beds is 52% higher than clay-rich beds. After around 60% water saturation the values of Poisson's ratio become higher in clay-rich beds while no significant change is observed in the values of Poisson's ratio for quartz-rich beds. The observations would suggest that as the spontaneous water imbibition is taking place and the local effective stress is changing because of capillary suction decrease, brittle to ductile transitional behavior occurs which would increase the possibility of more planar fracture propagation.
- Based on micro-scratch measurements, initially in low water saturation and high capillary suction, the average friction angle, UCS, cohesion and fracture toughness for quartz-rich beds are higher than clay-rich beds. As the water saturation increases these values in both quartz-rich and clay-rich beds decrease significantly but the rate of reduction in quartz-rich and clay-rich beds are different and in most cases, it drops more in clay-rich beds. In other words, capillary suction would give an apparent strength to the beds and as it reduces (as a result of increasing the water saturation) the strength would decrease. The results imply that during spontaneous water imbibition clay-rich beds would become weaker in both strength parameters and fracture toughness values in comparison with quartz-rich beds which would suggest that the failure progress and fracture propagation as a result of water imbibition would be most

likely from the interface between the beds toward the clay-rich beds rather than quartz-rich beds.

- The results of pressure-decay and pulse-decay permeability measurements imply that the apparent and absolute permeability for quartz-rich and clay-rich beds are different which can lead to different flow behaviors during spontaneous water imbibition.

Chapter 5 : Design, Calibration and Application of Mini-cell

Based on the results obtained in the previous observations, it is concluded that significant changes in Montney rock properties can be initiated within bed-scale features. Therefore, an innovative experimental approach and procedure is needed to study the mechanisms under which the fracturing fluid and bedded-structure tight rock interaction would affect the rock properties. Since the scale of beds is very small (millimeter or less), capturing the mechanisms while the sample is under loading, small size samples (1cmx2cm) would be considered. Therefore, a mini triaxial cell has been designed and built in Reservoir Geomechanics Research Group (RG2) for this purpose through which the loading tests on Montney would be done. Design, calibration and application of the mini-cell are discussed in this chapter. Applying the mini triaxial cell can answer the question that how the rock mass behavior can be affected as a result of smaller scale responses and what are the mechanisms behind those responses.

5.1. Mini-cell Design and Specification

The mini-cell has been designed for performing experiments on small samples to not only capture the rock behavior and properties but also investigate the fundamental responses that cannot be answered or captured in larger scale tests. Regarding the design, the mini-cell has two main parts which are lower body and upper body as shown in Figure 5-1. In the lower body there is stepper motor and worm gear box. Once the stepper motor starts to move the driving shaft, the rotation would be transferred to a worm wheel through which the horizontal movement would be changed to vertical movement. The movement would be transferred to the upper part internal load cell to capture the amount of load as a result of the movement. The load cell is connected to the bottom end cap of the location where the sample would sit. The upper part also includes the top end cap and six tie rods to withstand the load. The tie rods can withstand 950KN load and the mini-cell can handle up to 70MPa confining pressure and 70MPa pore pressure. The outside dimension of the mini-cell is 18cm (diameter) x 28cm (height) and the diameter of the rods is 16mm.The sample diameter range is 5-25mm and the maximum axial displacement is 10mm. Also, ram stroke length per driving shaft revolution is 12.5 micron. An instrumentation socket is considered to pass the wires from the inner space of the mini-cell to the outside. To control the rate of displacement the stepper motor is connected to a controlling box where the exact rate of displacement could be achieved. Also, there is a switch in the controlling box to change the direction of movement from

upward to downward and vice versa for loading-unloading-reloading tests. Table 5-1 represents some specifications of the mini-cell.

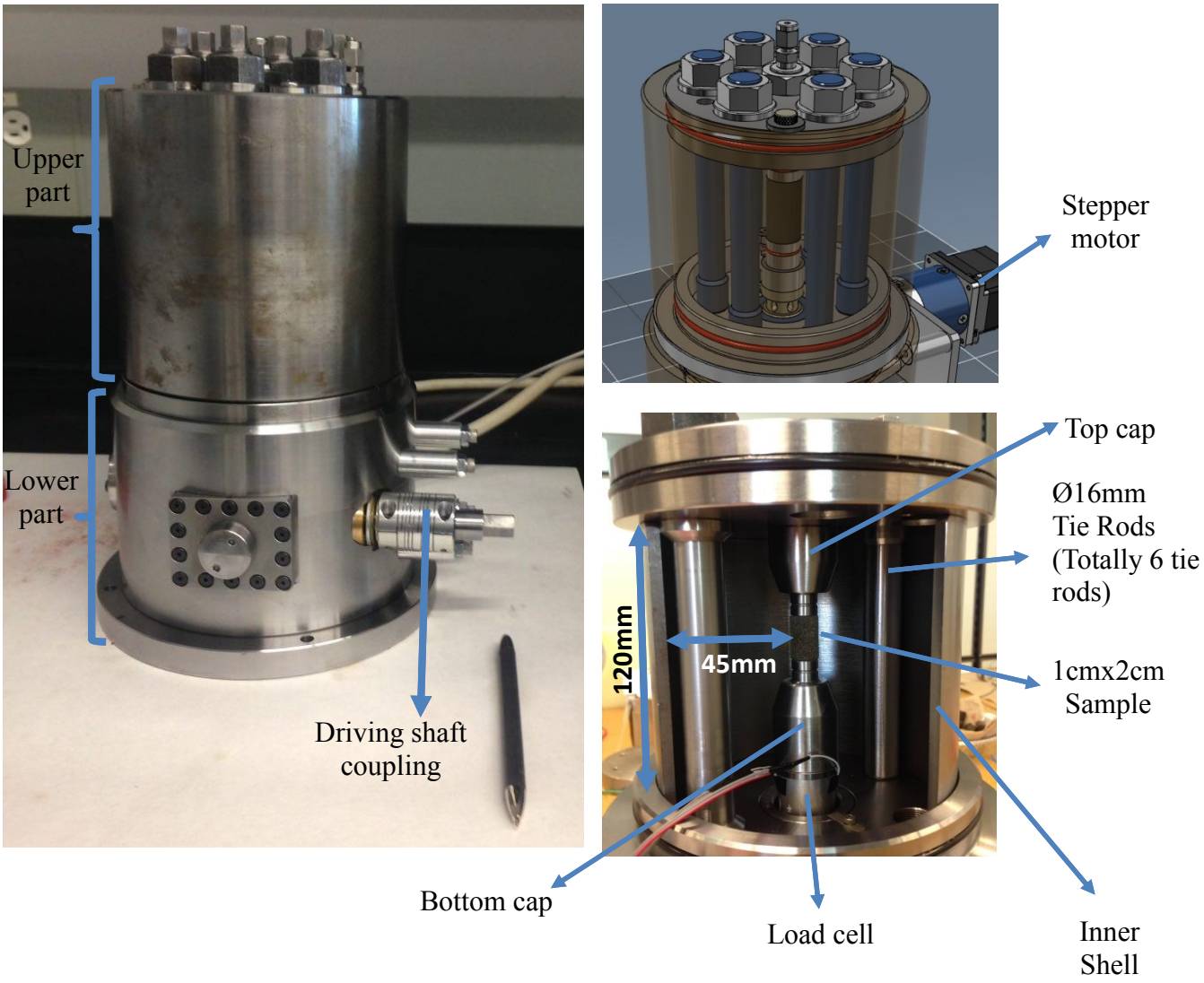

Figure 5-1. Design and specifications of the mini-cell.

To capture the axial strain MHR LVDT with a diameter of 9.5mm and an extremely lightweight core was initially considered. The MHR LVDT is shock and vibration tolerant and is ideal for applications where excessive core weight could influence the motion with less inertia and accurate measurements are easier to achieve. Also the load cell is Model LFH-7I which is a low profile force transducer for applications with minimal space and high capacity requirements. This transducer utilizes foil strain gages to measure compression loads of up to 10,000 lb and achieves accuracy of ±0.7 %. The top of the load cell is the area where the force is applied and the base ring

of the load cell must be placed on a hard and flat surface to obtain optimum accuracy. Figure 5-2 shows the LVDT and load cell assembly in the mini-cell setup.

Table 5-1. Some specifications of the mini-cell.

Outside Dimension (cm)	Maximum confining pressure (MPa)	Maximum Pore Pressure (MPa)	Sample Diameter (mm)	Maximum Axial Displacement (mm)	Ram Mechanism
18 x 28	70	70	5 to 25	10	Stepper Motor & Worm Gear box

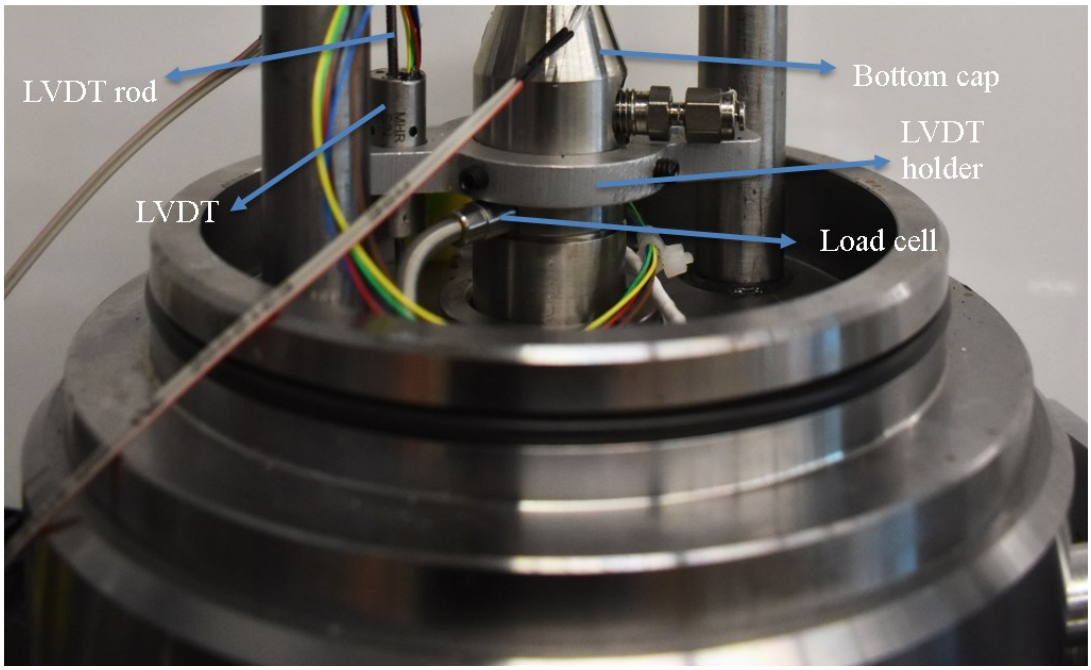

Figure 5-2. LVDT and load cell assembly in the mini-cell.

5.2. Mini-cell Calibrations and Preparation

The first step before performing the tests by mini-cell is the calibration procedures for the parts and setup followed by validation by the parameters captured during the tests on the known samples.

5.2.1. Load cell

To calibrate the load cell to be applied in the mini-cell setup, measurements were done using the proving ring (Figure 5-3) which was based on the correlation between the readings on the proving ring and the load as well as the voltage generated by the load cell in each reading (or load).

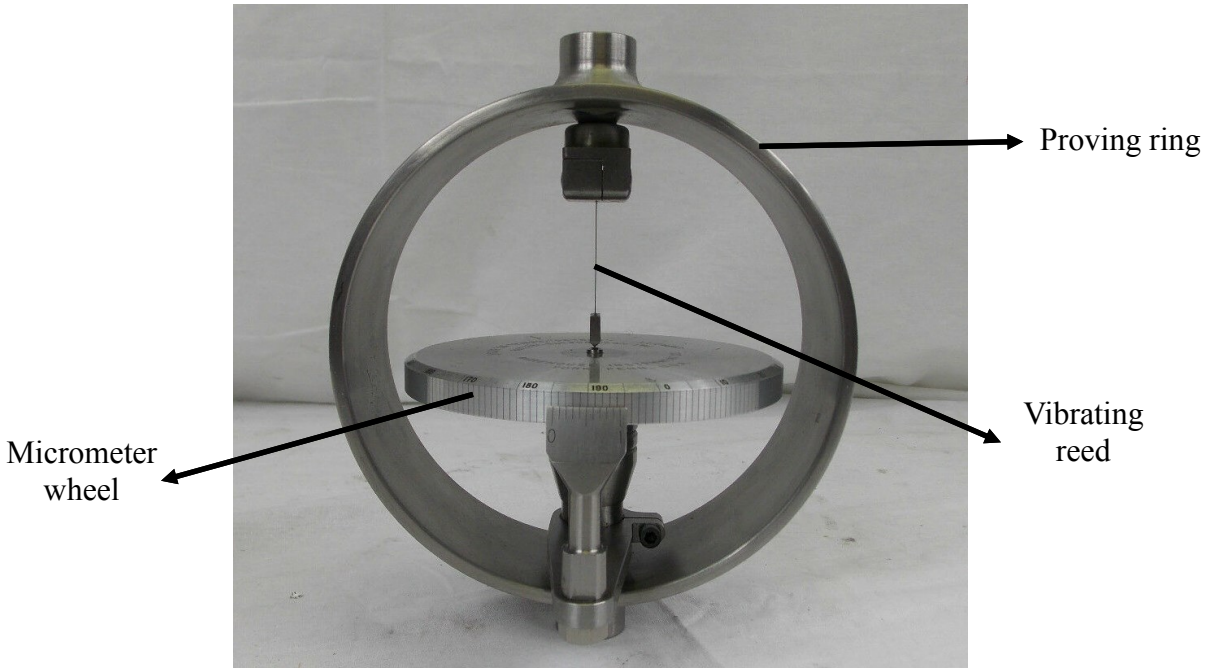

Figure 5-3. Proving ring applied for load cell calibration.

Then, the values of the load were correlated against the voltage generated by the load cell. The measurements were done three times and then the correlation of the overall values of load versus voltage were considered for load cell calibration. Figure 5-4 represents the values of load and voltage versus the deflection read in the proving ring and Figure 5-5 shows the overall calibration of load cell which is voltage versus load.

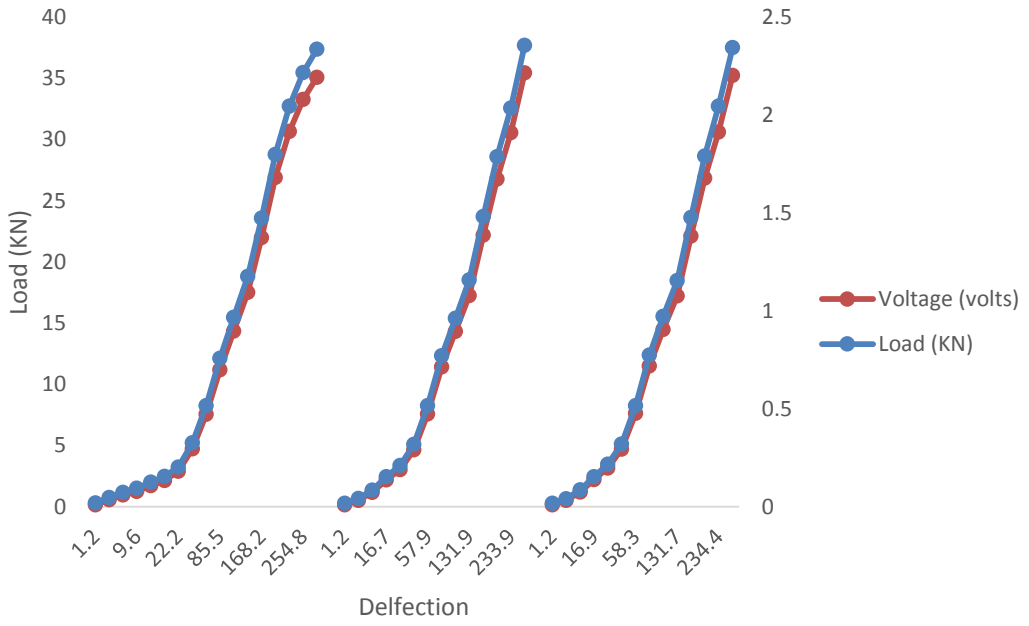

Figure 5-4. The results of three loading tests for calibration of the load cell.

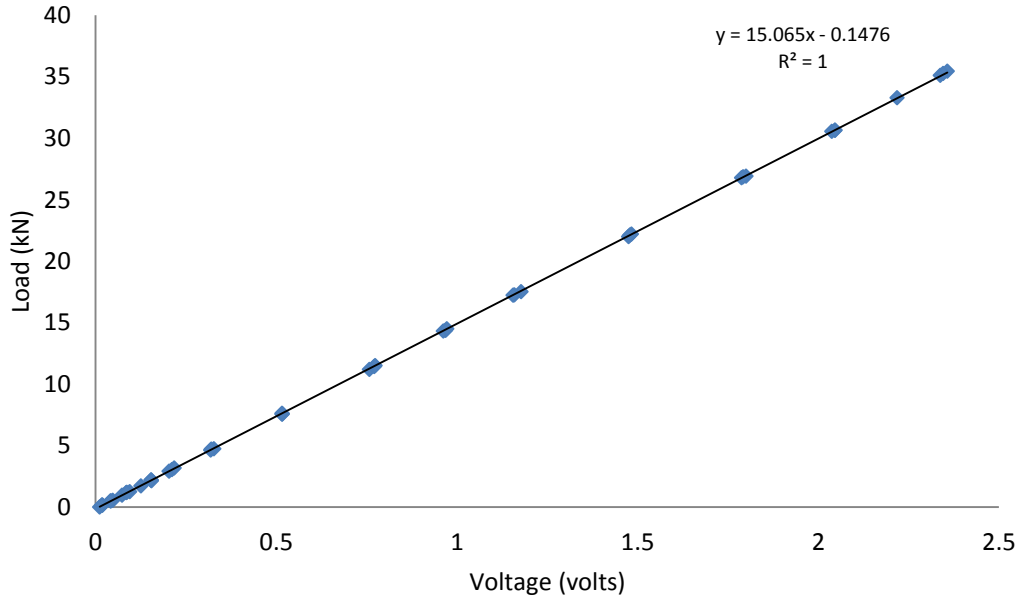

Figure 5-5. The overall result of load cell calibration.

5.2.2. LVDT Calibration

LVDT calibrator was used to calibrate the LVDT which has an adjustable mounting bracket. Once the bracket is displaced, the rod in the LVDT would move and the voltage would be generated. Based on the high accuracy displacement display on the calibration tool and the voltage generated the values of displacement would be calibrated against the voltage. The results of LVDT calibration indicated that the best working range for the LVDT would be between -2mm to 4.5mm. Figure 5-6 show the results of LVDT calibration.

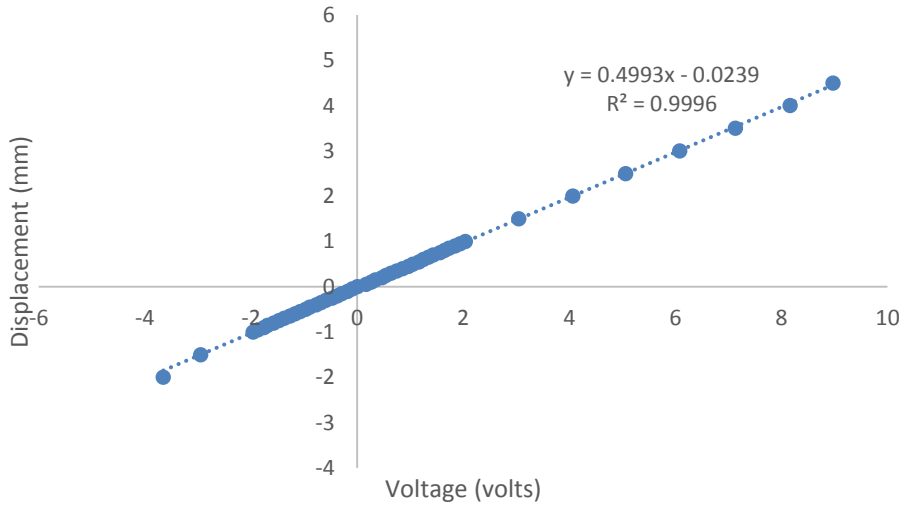

Figure 5-6. The result of LVDT calibration which shows that the best working range is -2mm to 4.5mm displacement.

5.2.3. Wheatstone Bridge Circuit

Wheatstone bridge circuit (shown in Figure 5-7) is a common circuit to achieve the high accuracy needed in strain gauge systems and because of its high sensitivity, it is the most frequently used circuit for static strain measurement. In Figure 5-7, V_{IN} is the input voltage to the bridge, R_g is the resistance of the strain gage, R_1, R_2 and R_3 are the resistances of the bridge and V_{OUT} is the bridge output voltage. Ideally, the strain gage (R_g) is the only resistor in the circuit that varies only due to a change in strain on the surface of the sample to which it is attached.

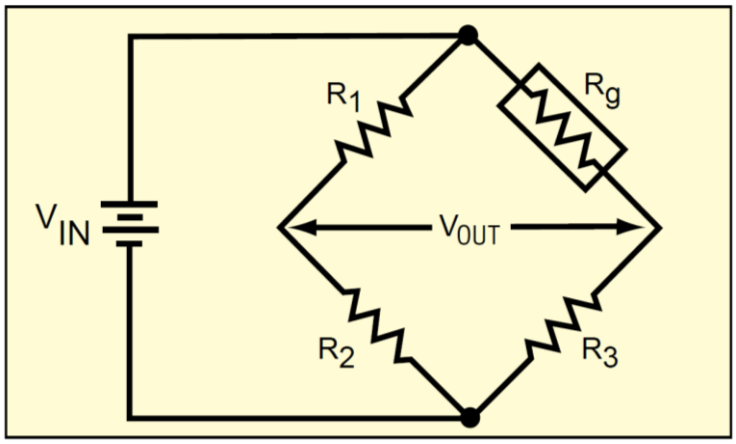

Figure 5-7. A typical Wheatstone bridge circuit. V_{IN} is the input voltage to the bridge, R_g is the resistance of the strain gage, R_1, R_2 and R_3 are the resistances of the bridge and V_{OUT} is the bridge output voltage.

The relationship between V_{OUT} and V_{IN}, R_1, R_2, R_3 and R_g is shown in Equation (5-1) (Button, 2015).

$$V_{OUT} = V_{IN}\left[\frac{R_3}{R_3+R_g} - \frac{R_2}{R_1+R_2}\right] \tag{5-1}$$

Eventually by rearranging Equation (5-1) and defining V_r as the difference of the ratios of V_{OUT} to V_{IN} from the unstrained to the strained state Equation (5-2) can be achieved which can be used to calculate the strain.

$$\varepsilon = \frac{-4V_r}{GF\ (1+2V_r)} \tag{5-2}$$

$$V_r = \left[\frac{V_{OUT}}{V_{IN\ (Strained)}} - \frac{V_{OUT}}{V_{IN\ (Unstrained)}}\right] \tag{5-3}$$

GF is gauge factor which is 2.01 in the strain gauges applied. Since the strain values in the rock samples are sometimes very small, an amplifier circuit for a strain gauge was considered to better capture the small strain responses. First, a Wheatstone bridge was made by a strain gauge and three discrete resistors. This circuit is then connected to LMC6482 op-amp. Figure 5-8 shows the schematic of the interface circuit which contains two amplifiers followed by a Wheatstone bridge.

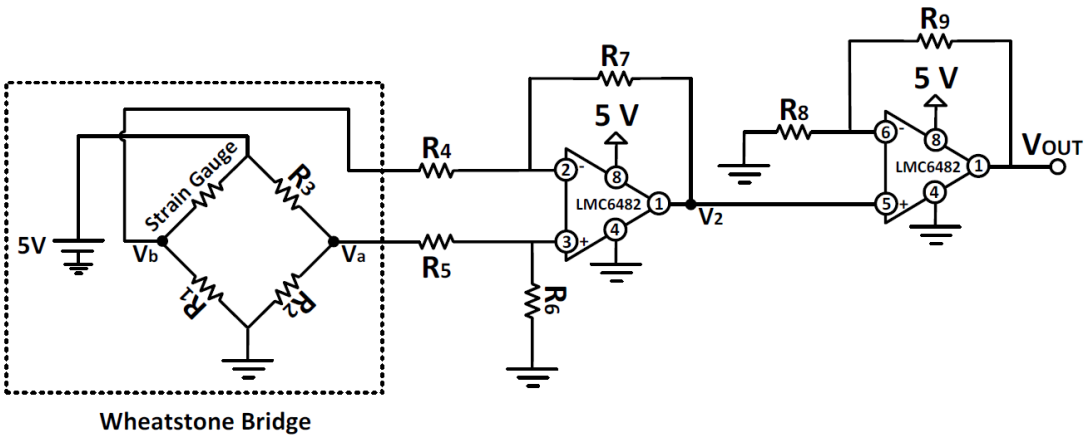

Figure 5-8. An amplifier interface circuit for strain gauge system.

Based on the amplifier interface circuit the total gain of the circuit would be 210 which means that the results would be amplified by 210 and after capturing the voltage from the strain gauge it should be divided by 210. Since the rock samples that were considered for the experiments were 1cm x 2cm a small size strain gauges were taken into account. Therefore, 120ohm KFH series pre-wired strain gauges were used for the tests. This type of strain gauge has a linear grid with active gauge length 3mm, active gauge width 2mm, matrix length 7.4mm and matrix width 3.9mm (Figure 5-9).

Figure 5-9. KFH series strain gauge used for strain measurements in the experiments

5.3. Mini-cell Application

After the load cell and LVDT calibration, the tests on samples with the properties known would be done to compare and validate the results. The loading procedure and the corresponding calculations of stress, strain and elastic properties were performed following the standards proposed by ASTM D7012-14.

5.3.1. 3D Printed Samples

UCS experiments were performed on 1cm (diameter) to 2cm (height) 3D printed sandstone samples (shown in Figure 5-10) manufactured by using the Ex-One MFlex^{TM} 3D Printer System in the GeoPRINT facility at the University of Alberta with the displacement rate of 0.02mm/min. The binder saturation in 3D printed samples were 10% and the tests were done under 22.5ºC. The measured data was recorded automatically by the GeoREF data logger software developed within Reservoir Geomechanics Research Group (RG2).

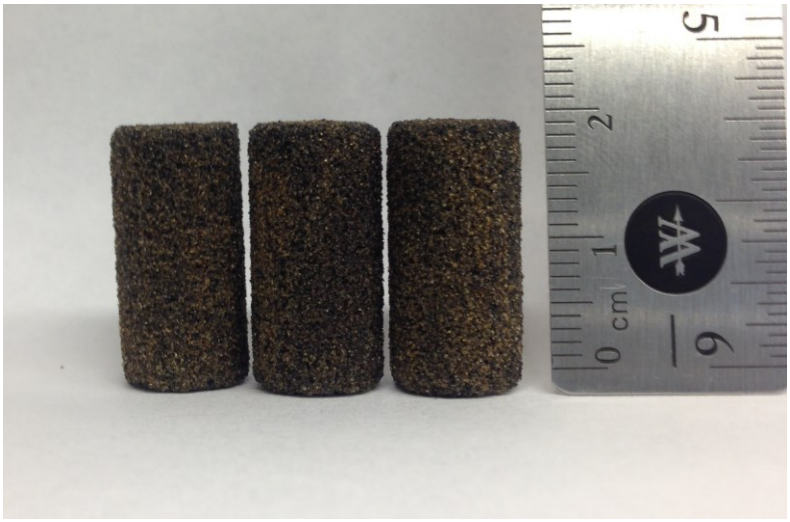

Figure 5-10. 1cm x 2cm 3D printed sandstone samples used for UCS tests.

Figure 5-11 shows the results of UCS tests on 3D printed samples where the average values of Young's modulus and UCS are 1.4GPa and 12.44MPa which agree with Primkulov (2016) and (Gomez, 2017) studies. Based on Gomez (2017) studies it is concluded that the UCS range for 2.54cm to 5cm samples is 14.57MPa to 15.01MPa and for Young's modulus the range is 1.43GPa

to 2.1GPa. The average UCS and Young's modulus values for the tested 3D 2.54cm to 5cm samples are 14.78MPa and 1.7GPa while it is shown that the UCS values in 3D printed samples were decreasing as the sample is getting smaller in size (Primkulov, 2016).

Figure 5-12 show the failure in 3D printed samples in the UCS experiment and Table 5-2, represents the UCS and Young's modulus values for the tested 3D printed samples.

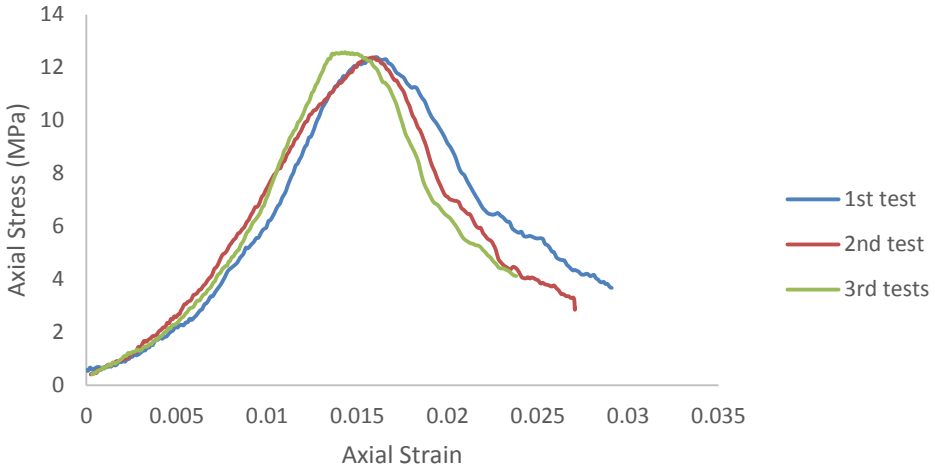

Figure 5-11. The results of UCS experiments on 3D printed samples by mini-cell.

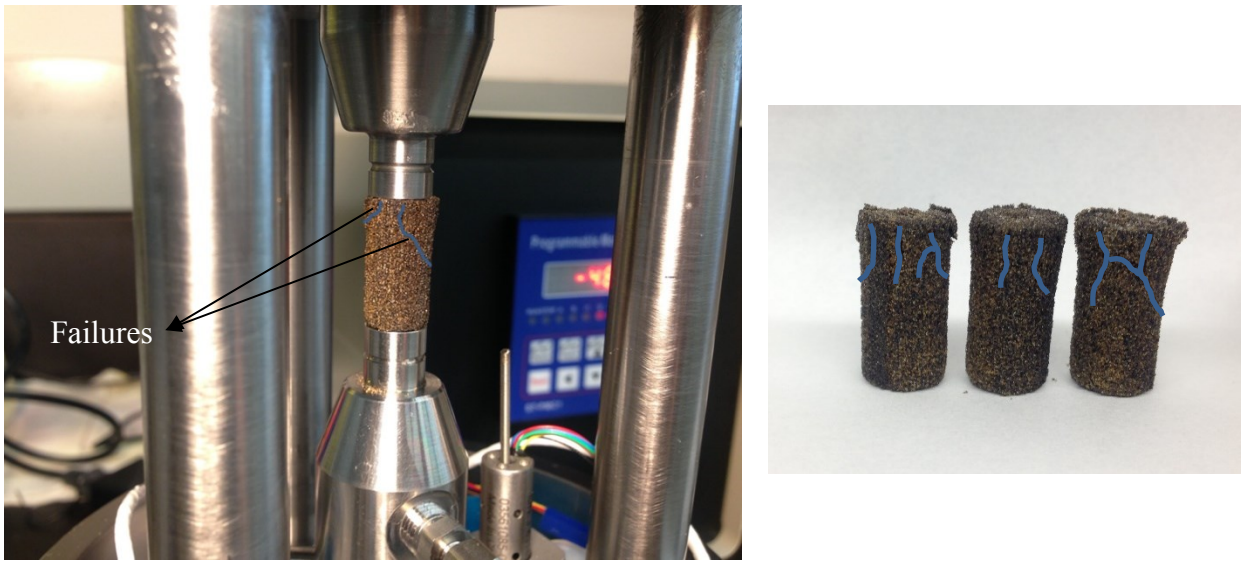

Figure 5-12. 3D printed samples failure under UCS experiments (failures are shown in blue colour).

Table 5-2. A summary of UCS tests on 3D printed samples by mini-cell.

Test no.	Young's modulus (GPa)	UCS (MPa)	Axial strain (at Peak)	Humidity (%)	Temperature (°C)	Binder Saturation (%)
1st	1.45	12.39	0.0161	23%	22.5	10
2nd	1.16	12.37	0.0159	23%	22.5	10
3rd	1.6	12.57	0.0143	23%	22.5	10
Avg	1.40	12.44				

5.3.2. Berea Sandstone Samples

To assess the mini-cell performance on stiffer rocks UCS experiments were performed on 1cm (diameter) to 2cm (height) Berea sandstone samples. In this phase the results are also compared with a UCS test on a sample with the strain gauge. At first, Berea sandstone samples were prepared and the top and bottom surfaces were polished and leveled while for one of the samples the strain gauge was also attached as shown in Figure 5-13. The results of UCS tests on the samples without strain gauge are shown in Figure 5-14.

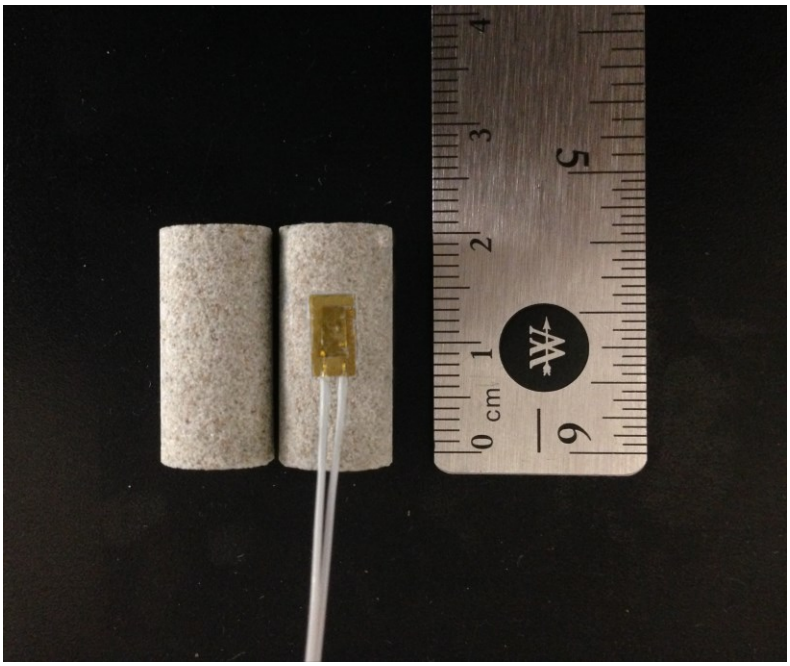

Figure 5-13. Berea sandstone samples for UCS experiments. The left sample is without strain gauge and the right sample is with the strain gauge.

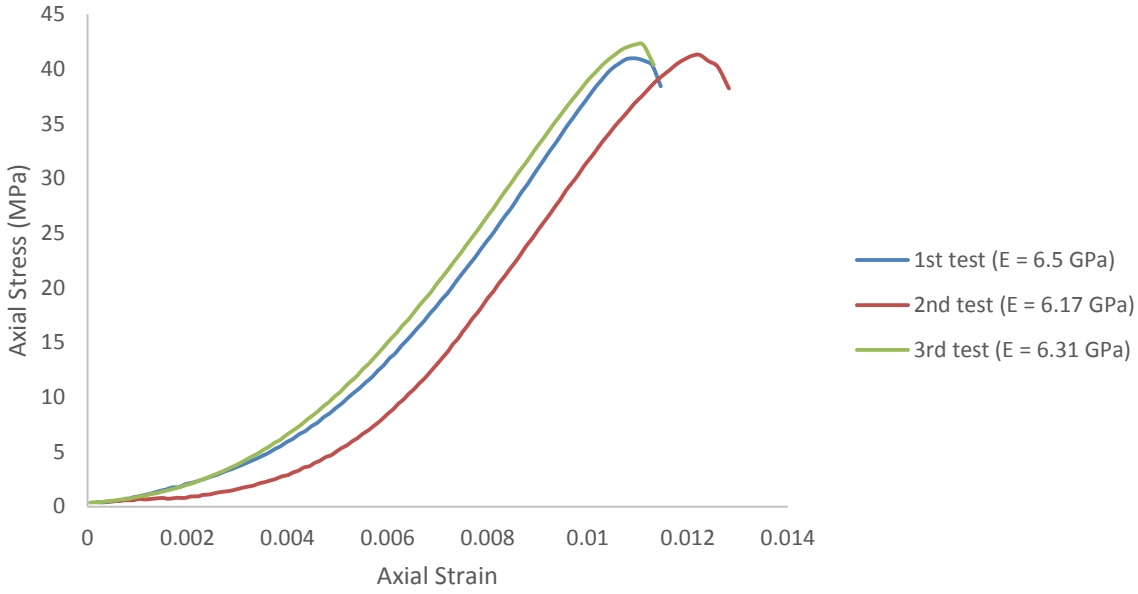

Figure 5-14. The results of UCS experiments of Berea sandstone 1cm x 2cm samples.

The values of UCS for the samples are 40.93MPa, 41.29MPa and 42.23MPa and the average value of UCS for all of the Berea sandstones are 41.49MPa which is in a good agreement with Makhnenko et al. (2015) experiments where the UCS values measured on Berea sandstones were reported between 41-43MPa. The values of Young's modulus for the tested Berea sandstone samples were 6.5GPa, 6.17GPa and 6.31GPa and the average value would be 6.33GPa which is consistent with Batzle et al. (2007) studies where the values of Young's modulus for Berea sandstone are within 6-7GPa range. Table 5-3 shows a summary from UCS experiments on Berea sandstone by mini-cell.

Table 5-3. A summary of UCS tests on Berea sandstone samples by mini-cell.

Test no.	Young's modulus (GPa)	UCS (MPa)	Axial strain (at Peak)	Humidity (%)	Temperature (°C)
1st	6.5	40.93	0.011	28%	24
2nd	6.17	41.29	0.0122	28%	24
3rd	6.31	42.23	0.0109	28%	24
Avg	6.33	41.49			

The UCS results of the sample with strain gauge can be found in Figure 5-15 where the curves obtained by LVDT and strain gauge don't generate the same values of Young's modulus and UCS. According to Figure 5-15, the axial strain values obtained from strain gauge is lower than LVDT which would affect the Young's modulus value (7.37GPa) to be higher by 6.8% than LVDT-based Young's modulus (6.87GPa). Based on LVDT measurements the peak strength is observed in 42.7MPa while the strain gauge failed in 41.96MPa. Although the values obtained from the strain gauge-based test is close to LVDT-based measurements but the difference between the LVDT and strain gauge values in rock testing have been reported in other studies (Acar et al., 2014; Kumurlu et al., 2016) which can be related to the strain gauge attachment procedure through which an adhesive is applied. Thin and homogenous adhesive interlayer between the strain gauge and specimens would generate the most accurate results. Failure in Berea sandstone samples after UCS experiments can be observed in Figure 5-16 which indicate that the failure surface in the samples with and without strain gauge could be also different.

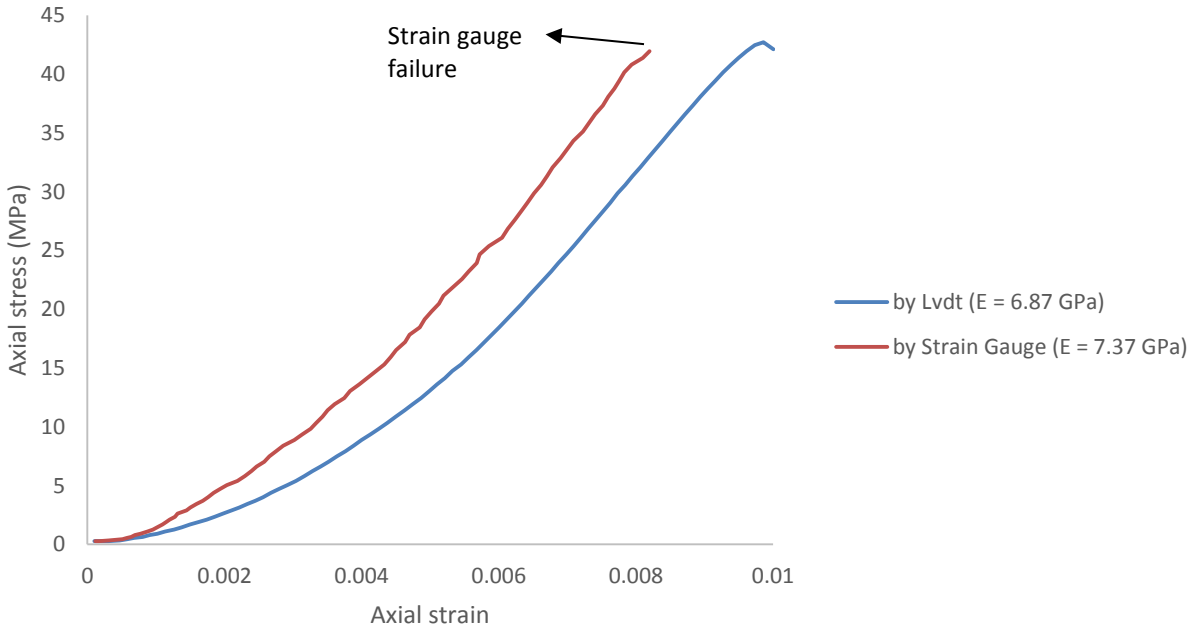

Figure 5-15. The result of UCS experiment on Berea sandstone with strain gauge attached. Different axial strain values obtained from strain gauge and LVDT results.

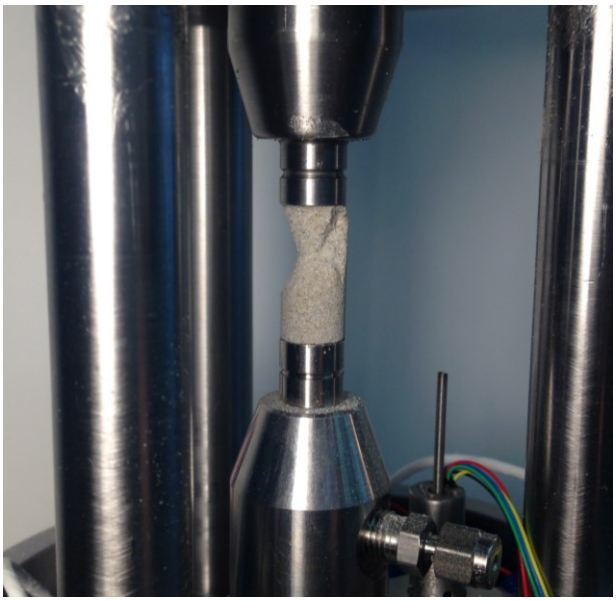

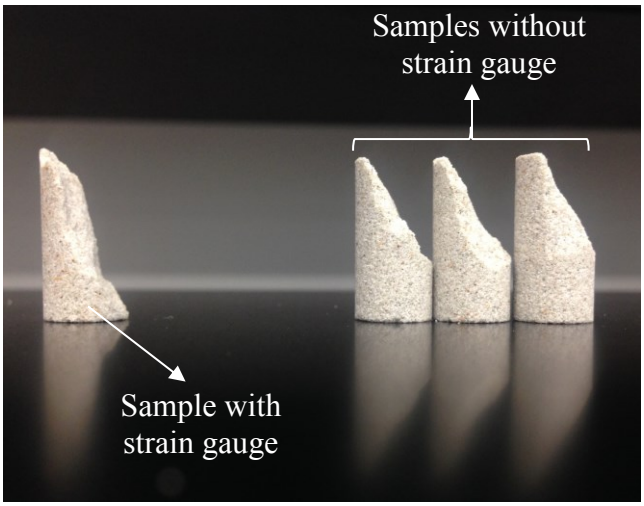

Figure 5-16. Berea sandstone samples failure under UCS experiments (with and without strain gauge attached).

5.3.3. Initial UCS Tests on Montney Sample

In this phase, a 1cm x 2cm Montney sample from the same core used in Chapter 4 experiments with the beds parallel to the direction of loading was prepared and strain gauge was also attached to it. Based on the previous experiments performed on Montney samples (Chapters 3 and 4), Montney samples are stiff rocks with Young's modulus values in excess of 30GPa. The UCS experiment was completed on a Montney sample. Preliminary analyses of the test data showed that values of strain obtained from the LVDT were not as what expected and strain gauge values provided more reasonable (as shown in Figure 5-17) estimates of Young's modulus. Young's modulus from LVDT-based readings was 8.73GPa and it was 46GPa based on strain gauge axial strain measurements. As this was a critical element of assessing variations in properties with changes in capillary suction, the test was stopped to investigate the issue.

5.3.3.1. Mini-cell Troubleshooting

Subsequent assessment of the mini-cell components did not identify issues either mechanically or within the electronic systems. Consequently, a troubleshooting program was developed to explore possible reasons for the discrepancy between LVDT and strain gauge-based measurements. Samples 1cm diameter x 2cm length were prepared from aluminum, brass, copper and steel

(Figure 5-18) for uniaxial compressive loading tests since the values of Young's modulus for these materials are well known (aluminum = 69GPa, brass = 97GPa, copper = 117GPa and steel = 200GPa).

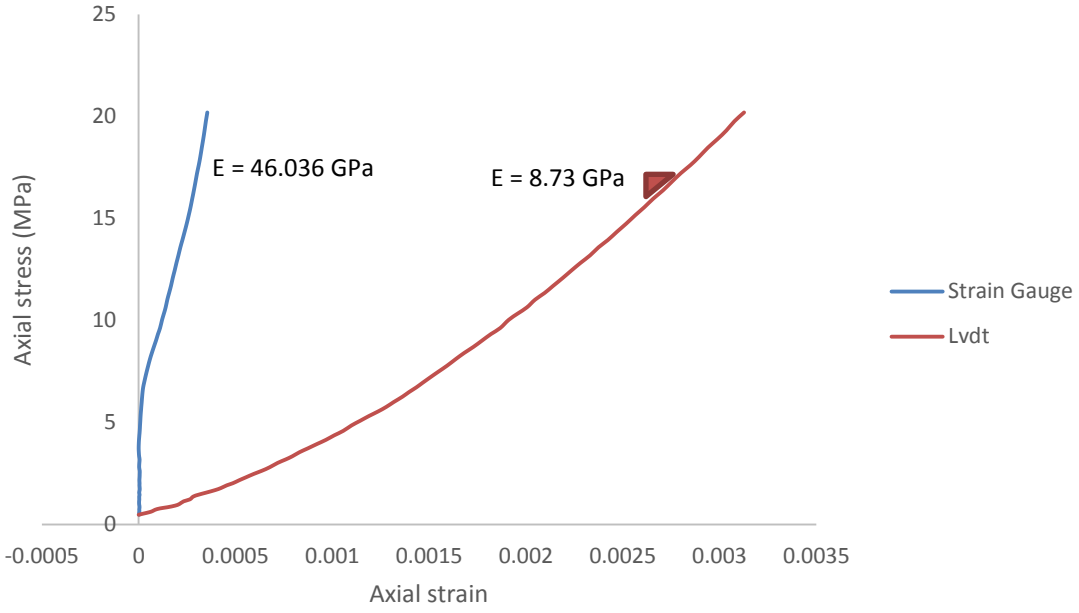

Figure 5-17. Comparing the Axial strain and Young's modulus values captured by LVDT and strain gauge through loading on Montney sample.

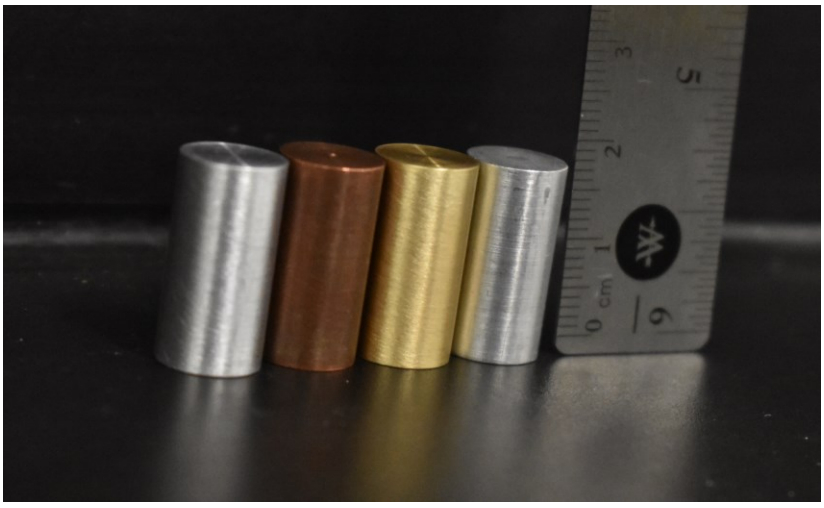

Figure 5-18. 1cm x 2cm samples. From left to right: aluminum, brass, copper and steel samples.

The aluminum, brass, copper and steel samples were subjected to axial loading steps up to 120MPa and axial displacement was measured using the LVDT. The results for aluminum indicate that from 10-20MPa axial loading the slope of axial load versus axial strain (which is by definition Young's modulus) is 20GPa which means that the correction factor to obtain 69GPa Young's modulus is 3.45. Between 20-60MPa loading, the slope of the curve is 28.8GPa and the correction factor would be 2.39. Also, for 60-120MPa loading, the slope of axial load versus axial strain is 33.07GPa with the correction factor of 2.08. Based on the results on aluminum it can be observed that the correction factor in each loading range is different. Figure 5-19 shows the difference between the slope of axial load versus axial strain curve as well as the slope expected (which is Young's modulus value of the sample).

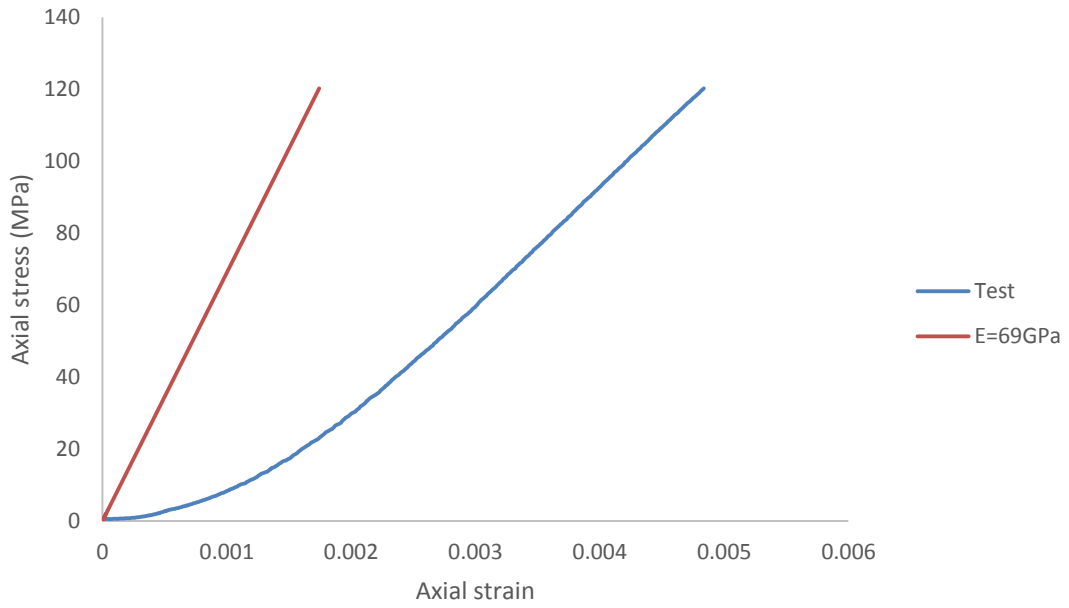

Figure 5-19. Comparing the results of aluminum loading test with the expected slope of axial load versus axial strain.

The loading test was done on brass sample where the correction factors for 10-20MPa, 20-60MPa and 60-120MPa were 10.14, 5.15 and 3.35. Figure 5-20 represents the expected slope of the curve and the values of axial stress versus axial strain obtained in the brass sample loading test.

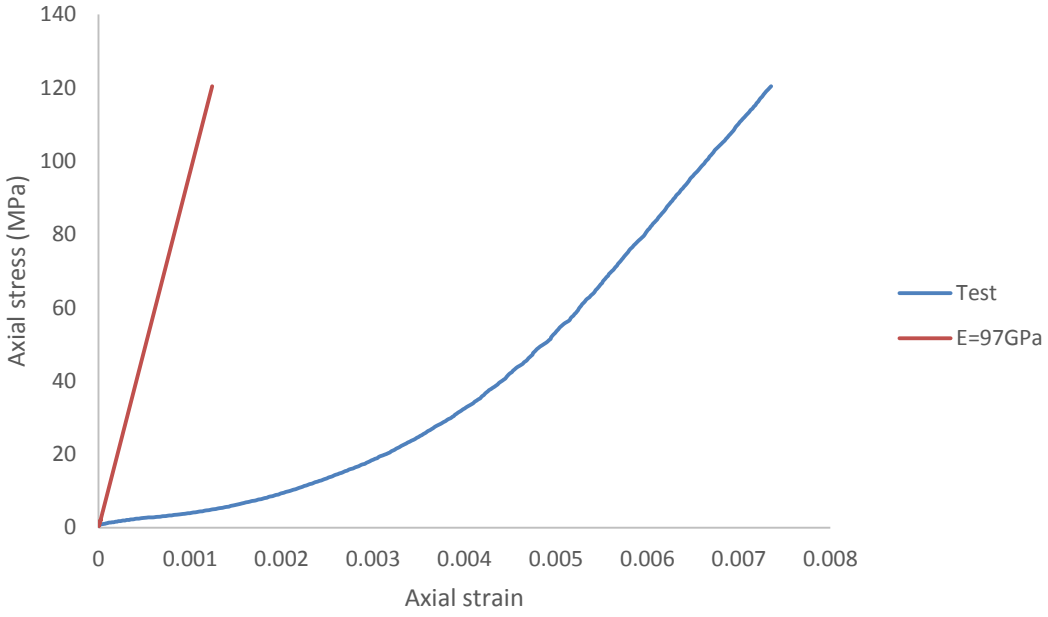

Figure 5-20. Comparing the results of brass loading test with the expected slope of axial load versus axial strain.

The results on copper and steel samples also imply that the correction factors would not be the same in each loading range and the samples correction factors in the same loading range for different samples are not the same as well. Figure 5-21 and Figure 5-22 show the difference between the slope of axial load versus axial strain curve with the slope expected for copper and steel samples. A summary of the loading tests on aluminum, brass, copper and steel can be found in Table 5-4. The results on aluminum, brass, copper and steel samples imply that there is not a fixed correction factor that can be used to correct the values of strain and there other factors directly or indirectly impacting the LVDT measurements. Several additional tests were conducted with the LVDT located near the top cap but this did not resolve the strain issue. Consequently, additional tests using strain gauged specimens were conducted to ensure the overall performance of the mini-cell was satisfactory.

Table 5-4. A summary of LVDT-based measurements in loading tests on 1cm x 2cm aluminum, brass, copper and steel samples.

Sample	Axial stress range (MPa)	Δaxial stress/Δaxial strain (E) (GPa)	Correction factor
Aluminum	10-20	20	3.45
	20-60	28.81	2.39
	60-120	33.07	2.08
Brass	10-20	9.57	10.13
	20-60	18.83	5.15
	60-120	29	3.34
Copper	10-20	24.18	4.83
	20-60	33.78	3.46
	60-120	33.2	3.52
Steel	10-20	14	14.28
	20-60	21.8	9.17
	60-120	38.5	5.19

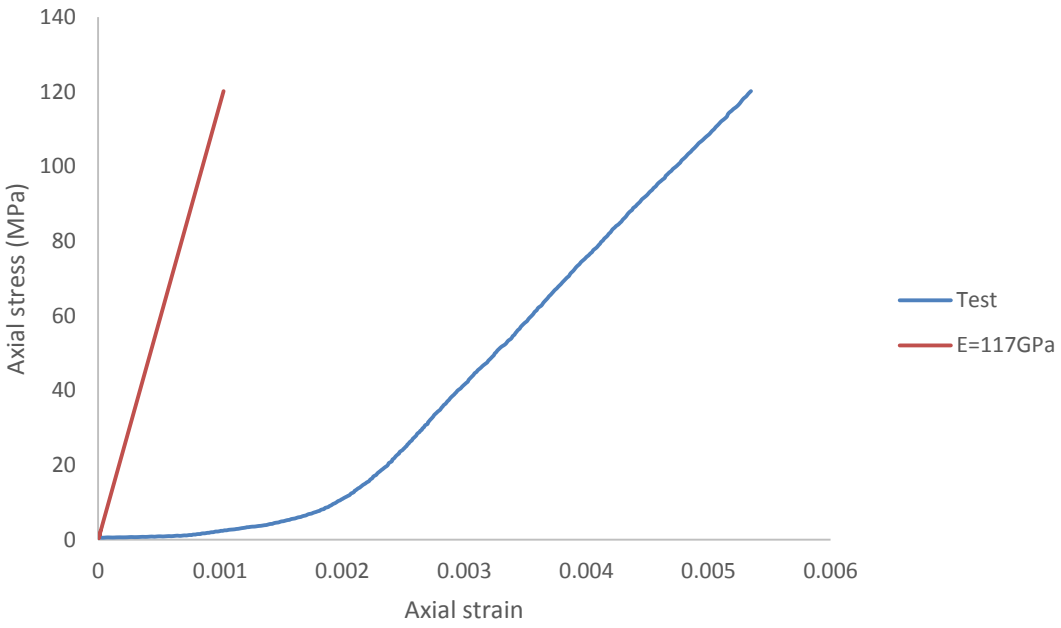

Figure 5-21. Comparing the results of copper loading test with the expected slope of axial load versus axial strain.

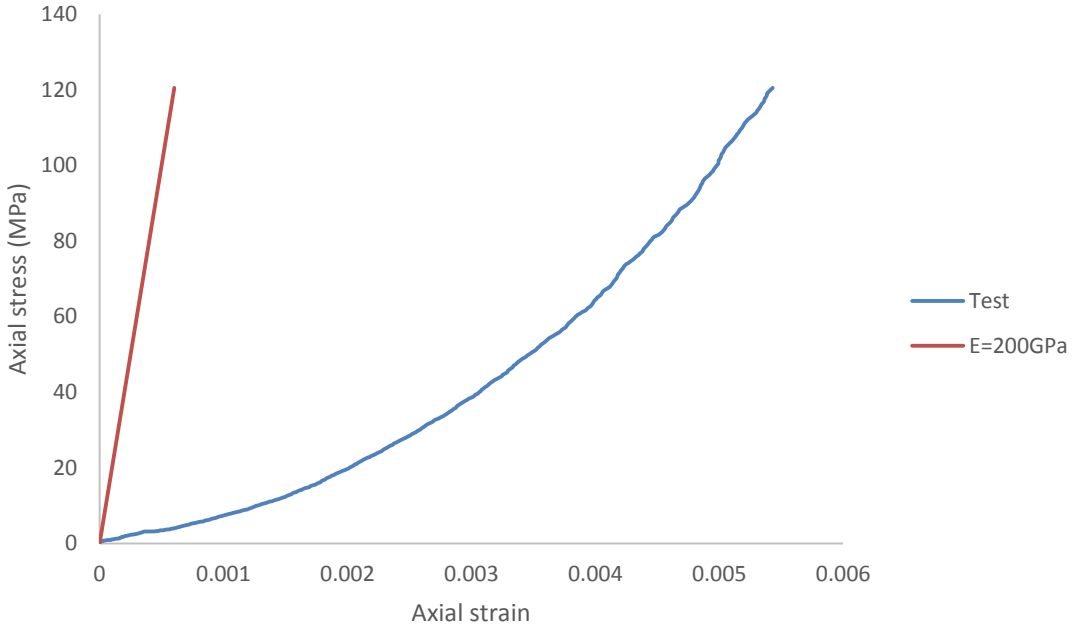

Figure 5-22. Comparing the results of steel loading test with the expected slope of axial load versus axial strain.

For the strain-gauged aluminum sample, Young's modulus was very close to the expected Young's modulus value of aluminum where the known Young's modulus of aluminum sample was 69GPa and the measured value based on strain gauge was 71.1GPa. Figure 5-23 depicts the result of loading test on aluminum sample with the strain gauge attached which can be compared with the LVDT result. Therefore, a new design with two LVDT holders was considered to reduce the instability (Figure 5-24). With a new LVDT design, first a loading test was done on aluminum sample. Figure 5-25. The results of loading test on aluminum sample with new LVDT design. The result for Young's modulus was 43.8GPa which was a little closer to the known value of Young's modulus for aluminum sample (69GPa) but still the difference is high. The same test was performed on brass sample and the result for Young's modulus increased from 29GPa in the previous LVDT design to 32.1GPa in the new design but still the issue wasn't solved and the difference between the real and measured values of Young's modulus based on LVDT is significant.

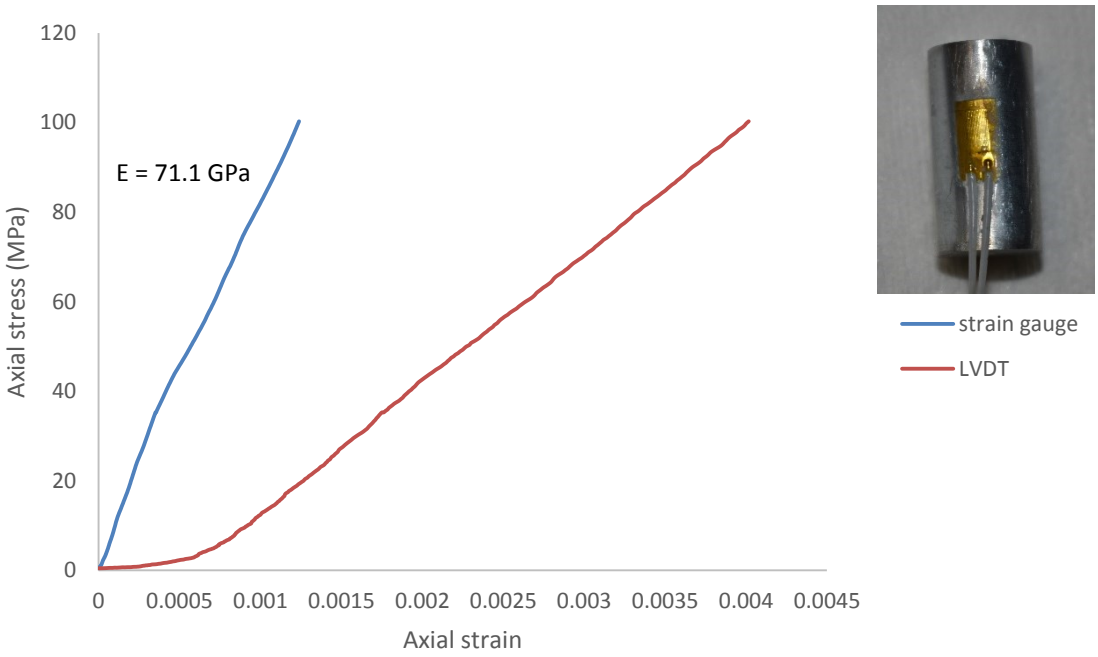

Figure 5-23. The result of uniaxial loading experiment on aluminum sample with strain gauge attached. Different axial strain values obtained from strain gauge and LVDT results.

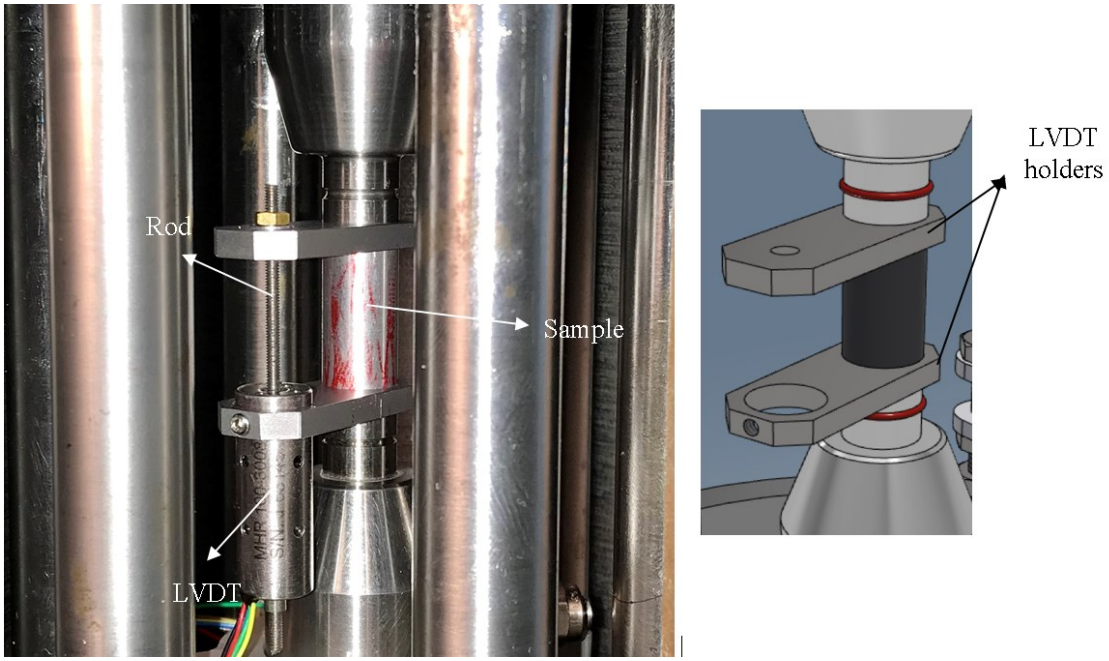

Figure 5-24. New LVDT setup design for the mini-cell.

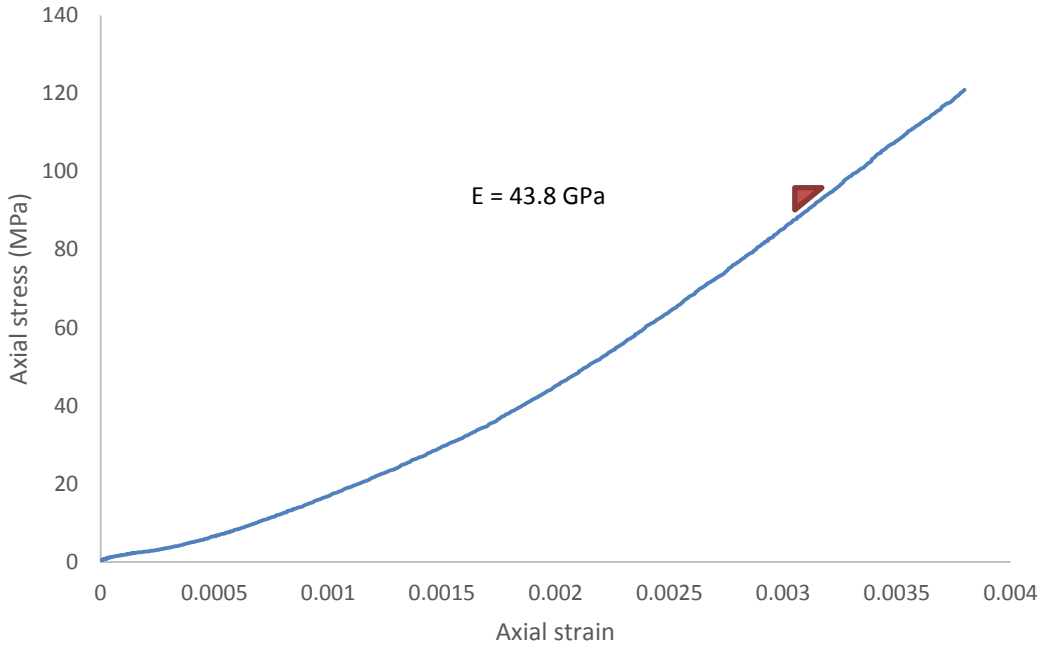

Figure 5-25. The results of loading test on aluminum sample with new LVDT design.

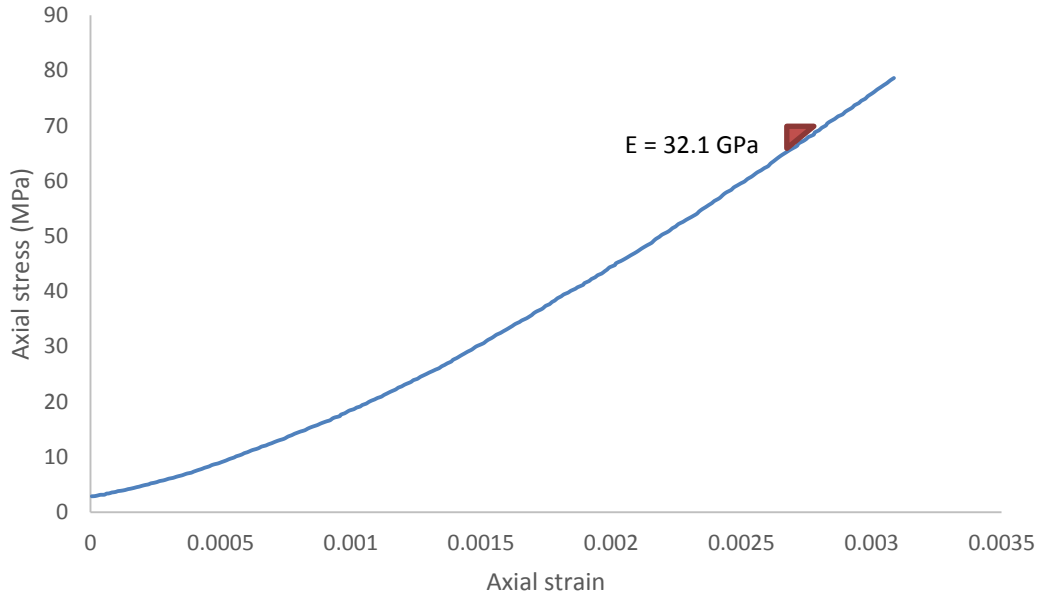

Figure 5-26. The results of loading test on brass sample with new LVDT design.

To capture the strain values several methods such as fiber optics and laser displacement sensors as well as camera-based volume determination system were considered to solve the issue and substituting the LVDT. Regarding the fiber optics it is worth mentioning that based on the available sizes for fiber optics systems and the space that is available inside the mini-cell as well as the accuracy that is needed no commercial option was found, and it needs a collaboration with industry to design a specific fiber optics tool for the mini-cell which would take time and out of the scope of this research. The next option which was discussed was laser displacement sensor system (Figure 5-27) which had been already being used in one of RG2 experimental setups to capture the strain values and it was among the most accurate systems for capturing small changes in displacement. In this system, the position of the target can be calculated by determining the location of the reflected beam spot on the RS-CMOS as shown in Figure 5-27. There were two main challenges with the existing laser displacement sensor. The first issue was related to the size of the existing laser sensor which was not small enough to get fitted inside the mini-cell near the sample. The sizes of the laser displacement sensor is shown in Figure 5-28.

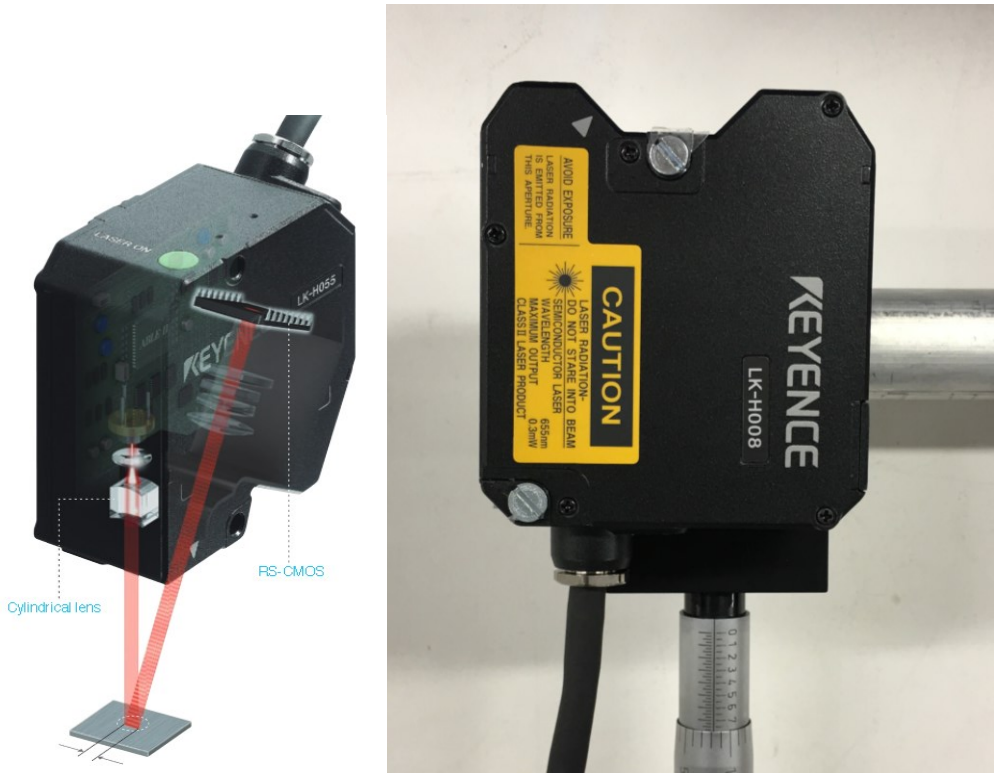

Figure 5-27. Laser displacement sensor considered to be tried in the mini-cell. The position of the target can be calculated by determining the location of the reflected beam spot on the RS-CMOS.

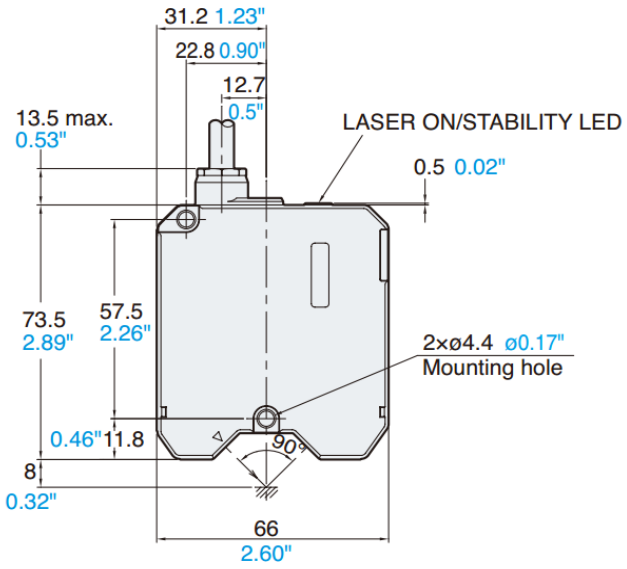

Figure 5-28. Dimensions of the laser displacement sensor system.

The second challenge was laser refraction phenomenon as it enters from one media to another (e.g. air to liquid) originated from displacing the propagation axis. Since for triaxial condition the cell is supposed to be filled with oil and the sample is covered, laser refraction would not only affect the emitted beam but also the reflection beam which in turn can lead to errors in measurements. Once these two challenges can be solved laser displacement sensor system would be one of the best choices for strain measurements. The next option was camera-based volume determination system which is based on utilizing a camera instrumentation located within the mini-cell as illustrated in Figure 5-29.

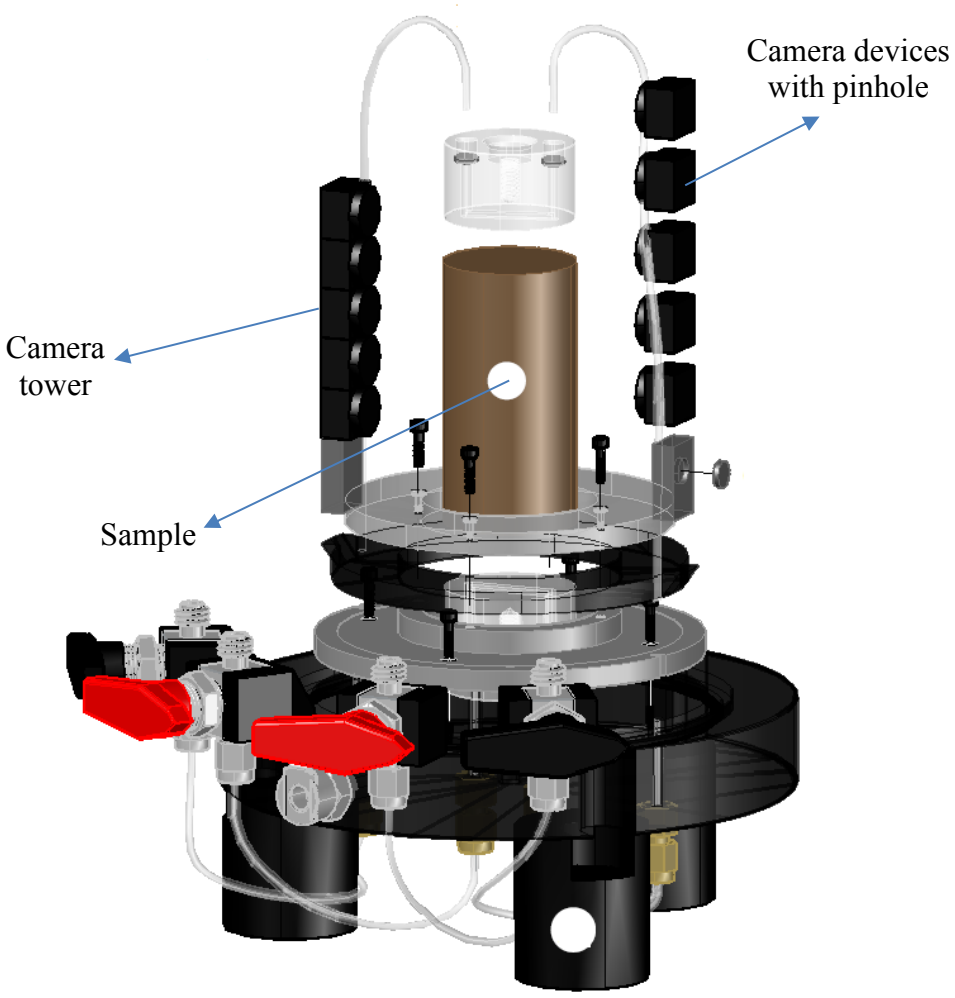

Figure 5-29. A camera instrumentation for a digital image-based deformation measurements (Salazar, 2017)

Then based on the post-image processing the strain values would be captured. There were several issues with camera-based methods. One of the challenges is the correction required for refraction of the light as well as installation a source of light inside the mini-cell. Although camera-based methods would yield good results on measuring the strain values in soil samples but based on Montney properties and the expected strain values under loading there are uncertainties about the operational effectiveness of camera-based methods for stiff rocks such as Montney. Therefore, for the rest of the tests strain gauges were used to determine the axial and radial strain values while the sample is under loading.

5.4. Summary

Design, calibration and application of mini-cell which is going to be applied for the loading tests on small size Montney samples, were discussed.

- Loading tests on small size samples (5-25mm in diameter) with maximum 10mm axial strain can be performed by the mini-cell.
- The mini-cell is able to withstand up to 70MPa confining pressure and pore pressure.
- The mini-cell is equipped with a stepper motor which is connected to a controlling box where the exact rate of displacement could be achieved.
- The load cell was successfully calibrated by three sets of individual tests using proving ring. Applying LFH-7I load cell with high capacity and accuracy and GeoREF data logger software enable the mini-cell to capture the load accurately at any loading step.
- MHR LVDT was first considered and calibrated. Based on the calibration the best working range for the LVDT was determined to be -2mm to 4.5mm.
- The mini-cell is capable of doing the tests with strain gauge since a Wheatstone bridge circuit with amplifier interface was designed and built for the mini-cell.
- The performance of the mini-cell was tested by 3D printed samples and Berea sandstones where there is a good agreement between the results of the tests done by mini-cell and other studies results.
- Uniaxial loading tests on Berea sandstone samples based on LVDT and strain gauge imply that values for Young's modulus and UCS are very close and they are not exactly the same.
- For Montney samples the LVDT didn't return the expected strain values but the strain gauge-based results were more reasonable.
- The troubleshooting phase were performed on the materials with the known values and properties (aluminum, brass, copper and steel) and the results indicated that there was a factor which made instability in LVDT measurements while the strain gauge measurements are reasonable.
- The location of the LVDT changed and even a new design for LVDT holder was considered and built. The instability reduced but still the problem resisted.
- Alternatives such as fiber optics, ultra high-speed and high-accuracy laser displacement sensor as well as camera-based volume determination system were considered for LVDT substitution

but due to several technical reasons and also time-consuming process of preparing and applying them, it was concluded to use strain gauges to capture the strain during the loading tests on Montney samples in the next phase.

Chapter 6 : Complex Reservoir Geomechanical Responses during Spontaneous Water Imbibition in Tight Formations

Since Montney samples have shown to have high capillary suction and bed-scale experiments have implied that rock mechanical properties and strength parameters will change as a function of capillary suction, this chapter investigates the geomechanical responses of small size Montney samples (1cm x 2cm) for unconfined compression with controlled capillary suction and water saturation changes. Montney samples in both parallel and perpendicular directions were prepared and loading experiments were completed using the mini-cell in a humidity-controlled loading setup. Strain gauges were attached to the samples to capture the axial and radial strain while the sample was under loading-unloading-reloading experiments in each water saturation level. Numerical simulations were also undertaken using fully coupled poro-elastoplastic partially saturated models and implementing the developed user defined subroutine to investigate how the changes in capillary suction and water saturation might result in different geomechanical and failure responses. Inputs of the numerical modeling were based on rock mechanical and strength properties as a function of water saturation and capillary suction obtained in bed-scale experiments in Chapter 4. The geometry and the beds locations as well as the width of each bed in each case (sample with parallel or perpendicular beds) based on core measurements were replicated in the numerical modeling. Also, the vertical and confining stress values were based on the reservoir in-situ stress conditions at the sampling depths.

6.1. Laboratory Experiments

6.1.1. Sample Description and Preparation

The samples, as discussed in Chapter 3 and Chapter 4, are from Farrell Creek field, northeast British Columbia from a depth of 2415m. The mineralogy was discussed in Chapter 4 and the details were indicated in Table 4-1and Figure 4-31. The preparation procedure of 1cm x 2cm samples were the same as illustrated in Chapter 4 where the coring was done by air and every effort was taken to obtain perpendicular and parallel samples from the same piece of core. Figure 6-1 depicts the preparation of the sample with parallel and perpendicular beds.

Figure 6-1. Preparing the samples parallel (right sample) and perpendicular (left sample) to the beds for loading tests on Montney samples by mini-cell.

6.1.2. Experimental Procedures

To perform the loading tests on Montney samples with perpendicular and parallel beds while controlling the water saturation and capillary suction, a new setup was designed which was attached to the mini-cell. A chamber was designed, and manufactured by using Stratasys (Eden 260VS) polyjet 3D Printer System in the GeoPRINT facility at the University of Alberta to accommodate 1cm x 2cm specimens. The chamber isolated the sample in order to control relative humidity and provided feedthrough ports for the strain gauge wires (Figure 6-2). Humidity surrounding the specimen was controlled by connecting the sample chamber to a saturated salt solution container, which was also 3D printed. All of the joints, connections and the holes for passing the strain gauges wires were sealed to avoid any leakage of humidity to the outside of the chamber. To maintain and control the capillary suction and water saturation in each step the container was filled with the relevant saturated salt solution. Relative humidity can be converted to water saturation and capillary suction using the results of the tests and relevant correlations discussed in Chapter 4. To ensure equilibrium conditions were achieved, a second twin sample outside of the chamber was subjected to the same saturated salt solution and once the weight of this sample stabilized, it was assumed that an equilibrium moisture content was reached, which typically took 4 to 5 days. To capture the response of the specimen in both axial and radial directions and continuous recording of the deformation during the loading, strain gauges were

used. One of them was glued horizontally (to capture the radial strain) and the other one was glued vertically (to record the axial strain). Figure 6-3 illustrated the setup designed for loading tests on perpendicular and parallel samples while the capillary suction was under control.

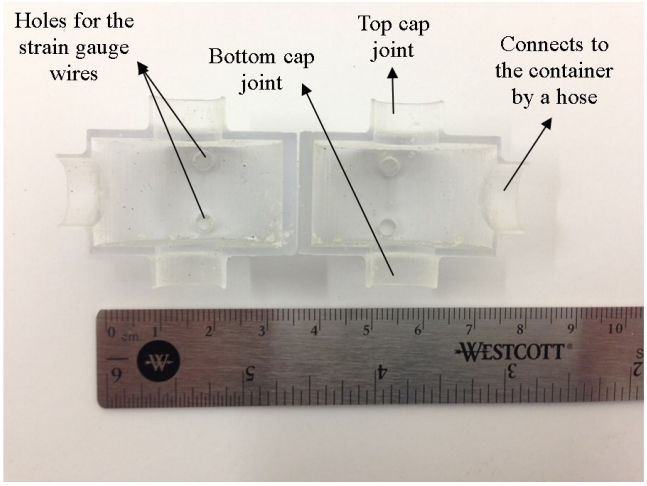

Figure 6-2. A specific chamber designed and made by 3D printer to isolate the sample while it was exposed to a certain humidity degree.

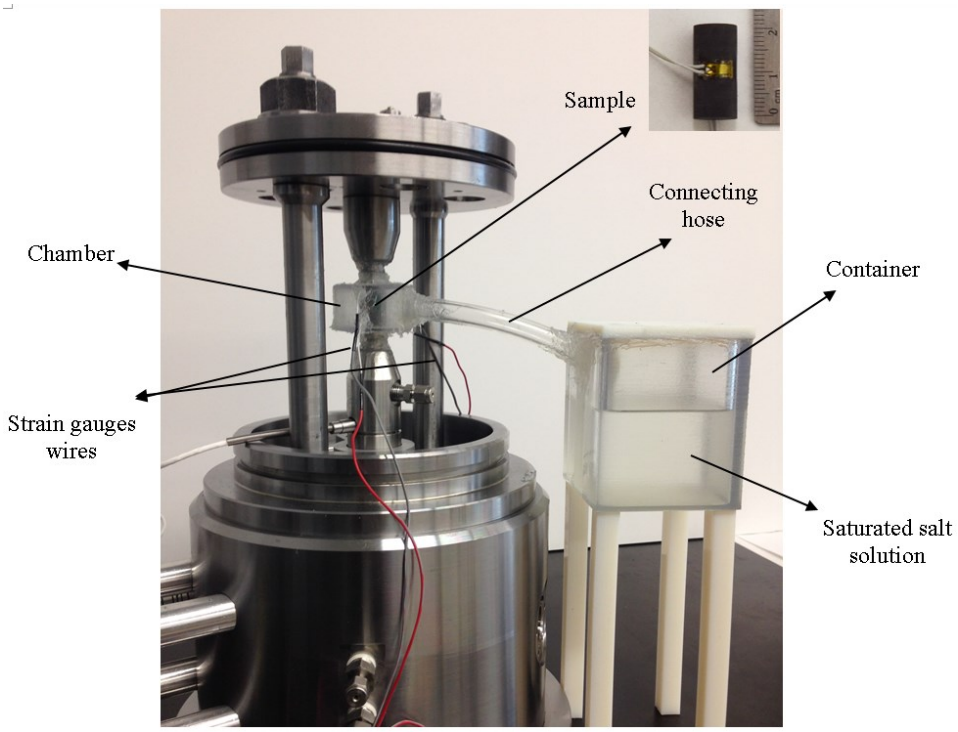

Figure 6-3. Setup designed for the loading tests on 1cm x 2cm Montney samples by mini-cell.

The first round of loading tests was done on samples subjected to $MgCl_2$ (S_w = 7.8% and P_c = 152MPa) and K_2SO_4 (S_w = 81.8% and P_c = 7MPa) and the values of UCS and rock mechanical properties (Young's modulus and Poisson's ratio) were determined. Low displacement rate of 0.002 mm/min was chosen to minimize any potential effect of generating excess pore pressures during loading. Load-unload-reload tests were done in four stages while the capillary suction in the samples was gradually decreased by getting subjected to different saturated salt solutions: $MgCl_2$ (S_w = 7.8% and P_c = 152MPa), $Mg(NO_3)_2$ (S_w = 31.1% and P_c = 95MPa), NaCl (S_w = 51.9% and P_c = 39MPa) and K_2SO_4 (S_w = 81.8% and P_c = 7MPa). As shown in Figure 6-4 the stress path for the load-unload- reload experiments for different capillary suctions would adhere to the following steps:

- Once reaching saturation equilibrium conditions (while the sample was exposed to $MgCl_2$ (S_w = 7.8% and P_c = 152MPa)), the specimen was initially loaded to 20MPa of axial stress and unloaded to 10MPa followed by reloading to 20MPa.
- Then the sample was exposed to $Mg(NO_3)_2$ (S_w = 31.1% and P_c = 95MPa) and once equilibrium conditions were reached, it was unloaded to 10MPa and then reloaded to 20MPa.
- The same procedure would repeated for NaCl (S_w = 51.9% and P_c = 39MPa) and K_2SO_4 (S_w = 81.8% and P_c = 7MPa).

All data was recorded electronically using the GeoREF data acquisition system.

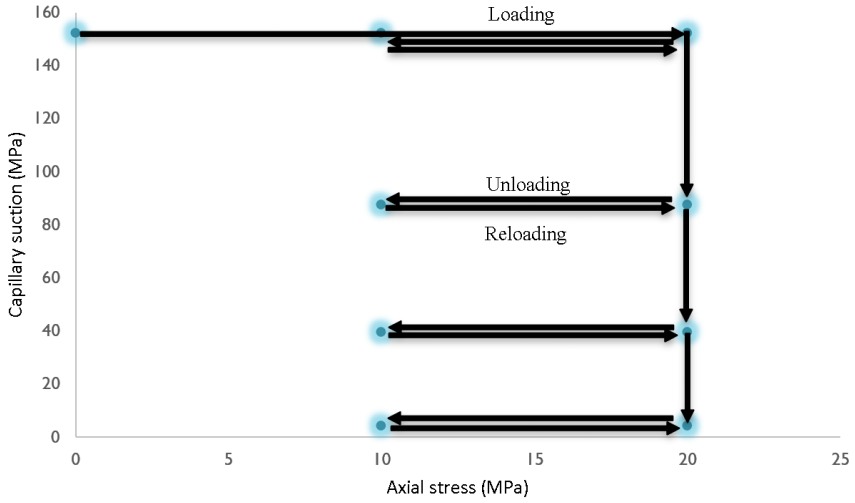

Figure 6-4. Stress path for unloading-reloading experiments in different capillary suction values.

6.1.3. Experimental Results and Discussions

Experimental results on Montney samples under controlled capillary suction conditions are presented in this section. First, the behavior of the Montney samples during the capillary suction variations from high to low and under loading are discussed followed by a discussion on the behavior during load-unload-reload cycles.

6.1.3.1. Uniaxial Compressive Loading in High and Low Capillary Suction

6.1.3.1.1. Stress-strain Curves

For the axial stress-strain curves (Figure 6-5), after the initial pre-existing fractures closure which are aligned at an angle to the loading direction, the slope becomes almost constant, corresponding to the elastic stage. Then the slope is getting smaller indicating the failure initiation (shown by circles in Figure 6-5) until the peak strength is reached which is related to the damaging process. For the radial (lateral) stress-strain curves, increasing the axial stress would lead to accelerating the rate of reduction of the slope. Therefore, in the later stages before failure, both axial and radial strain increase quickly with small change in the axial stress which is more obvious in parallel samples. It is noteworthy that for both the axial and radial stress-strain curves the slope decreased with decreasing the capillary suction and the axial stress magnitude for failure initiation was lower in the samples with low capillary suction (Figure 6-5) the failure axial stress was around 30.3MPa for the parallel sample with high capillary suction (152MPa) and 19.5MPa for low capillary suction (7MPa). The same trend was observed in the perpendicular samples where the failure initiation stress level in high capillary suction was about 58.0MPa and it was around 33.7MPa for the low capillary suction case. Comparing the curves related to parallel and perpendicular samples in Figure 6-5 and the onset of accelerating displacement as well as abrupt change in the slope of stress-strain curves would imply that micro crack initiation and propagation would take place in lower axial stresses in parallel samples in comparison with perpendicular samples.

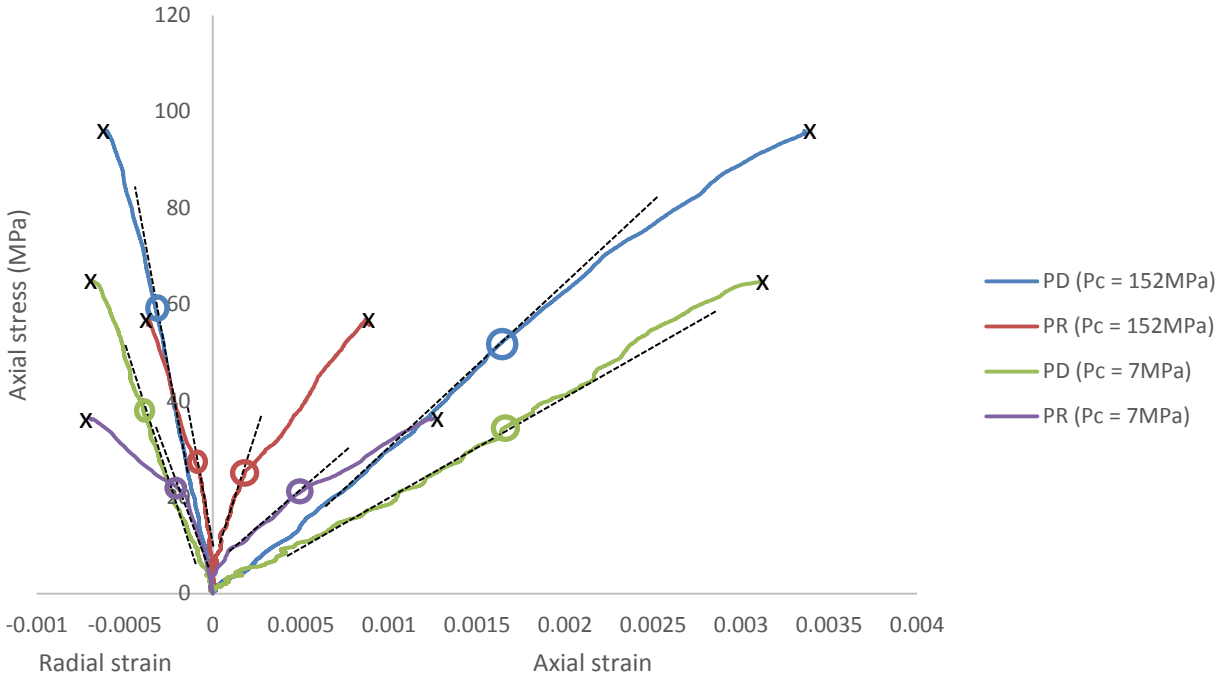

Figure 6-5. Axial stress versus axial and radial strain for both perpendicular and parallel samples in UCS experiments at high (152MPa) and low (7MPa) capillary suctions. "PD" and "PR" represent perpendicular and parallel samples, respectively. The circles show the stress level where the slope is getting smaller indicating the failure initiation."x" indicates the strain gauge failure.

This can be attributed to the interfaces between the beds which were shown in Chapter 4 to be weaker than the quartz-rich and clay-rich beds. This means that most likely in parallel samples most of the failures were initiated from or adjacent to the interface between the beds and as the water saturation increased and capillary suction dropped, the strength of the interfaces reduced significantly (as shown in Table 4-11) which led to triggering additional regions of failure and propagation along the interfaces between the beds. Figure 6-6 shows the parallel and perpendicular samples after UCS experiments where it is clearly observed that most of the failures in parallel samples were initiated along and adjacent to the interfaces between the beds. Micro fractures propagation along and in adjacent to the interface between the beds and opening in the lateral direction would lead to higher radial deformation in parallel samples than perpendicular samples at the same capillary suction level.

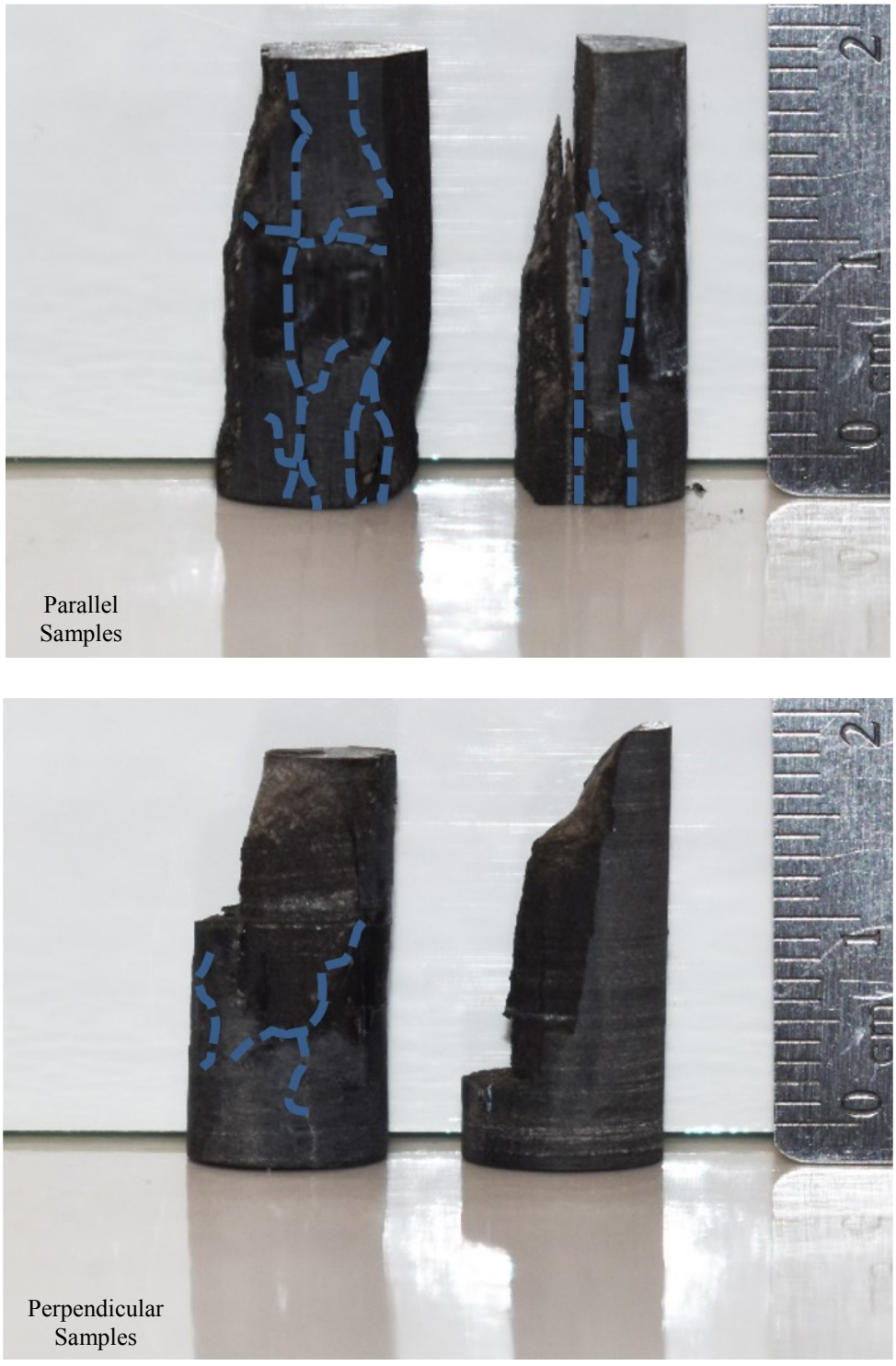

Figure 6-6. Failures in parallel and perpendicular samples after UCS experiments at high (152MPa) and low (7MPa) capillary suctions. In both images, the right and left samples are related to low and high capillary suctions, respectively.Blue lines represent the failures and fractures.

The volumetric strain versus stress for both parallel and perpendicular samples under different capillary suctions are shown in Figure 6-7. Following the pre-existing fracture closure stage, the volumetric strain developed linearly, after which, due to newly created fractures, the behavior became nonlinear. As the newly created micro-fractures intersected with each other and macro-fractures started to form and propagate, the volumetric strain behavior became less compression dominated and more dilation dominated which could be clearly observed in parallel samples especially at low capillary suction where the volumetric strain at failure was found to get shifted from positive to negative. This implies that decreasing the capillary suction may cause the volumetric deformation to change from compression to dilation in the parallel samples. For perpendicular samples, the transition from compression dominated to dilation dominated was not observed until the strain gauges failure (which was most likely caused by a small local failure of the sample) during the UCS experiments.

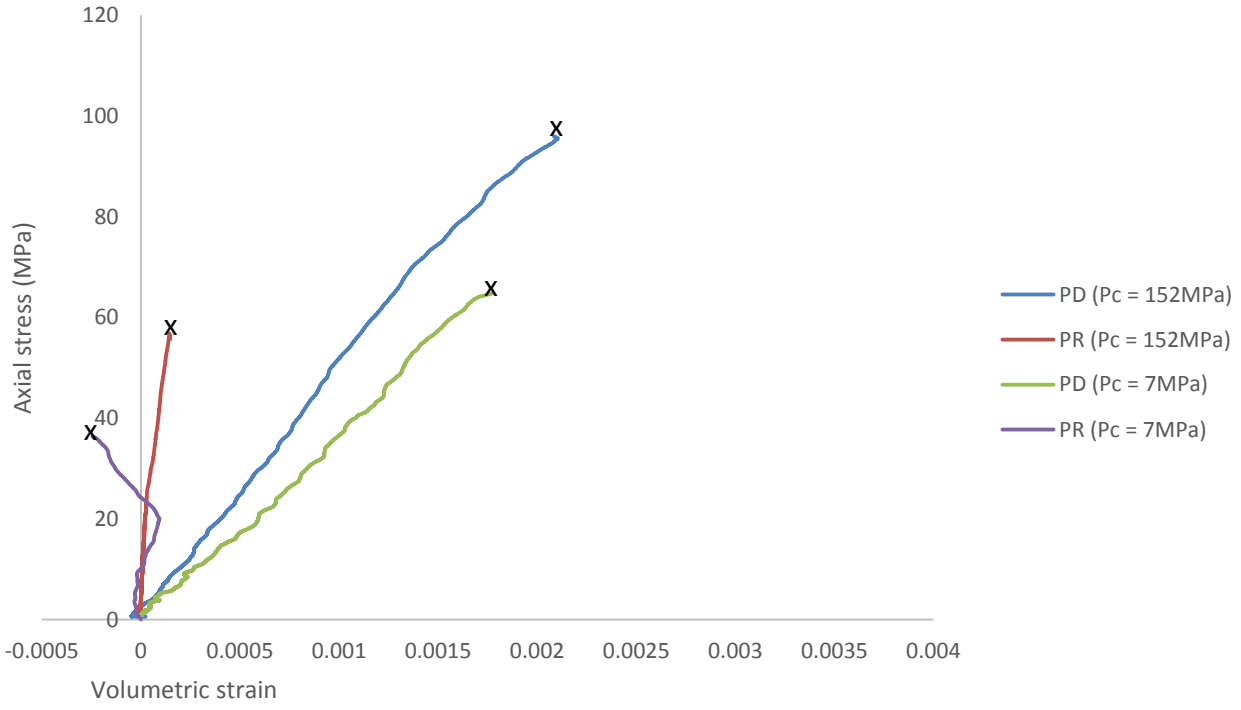

Figure 6-7. Axial stress versus volumetric strain for both perpendicular and parallel samples in UCS experiments at high (152MPa) and low (7MPa) capillary suctions. “PD” and “PR” represent perpendicular and parallel samples, respectively. ”x” indicates the strain gauge failure.

6.1.3.1.2. Failure and Rock Mechanical Responses

Figure 6-5 illustrates the UCS experiments completed on Montney samples with parallel and perpendicular beds at high (152MPa) and low (7MPa) capillary suction values. Based on these results, UCS values for high and low capillary suction in perpendicular samples were 42% and 44% higher than parallel samples. It was observed that the value of UCS in high capillary suction was 96.0MPa while for low capillary suction it was 64.8MPa. This means that a total decrease of nearly 32.6% in UCS was observed as the capillary suction decreased by 95.4% in perpendicular sample. The same behavior was observed in the parallel samples where the UCS value in high capillary suction was 55.7MPa and it dropped by 34.6% to 36.4MPa in low capillary suction. The reasons for lower UCS values in low capillary suction can be attributed to apparent cohesion that capillary suction would give to the media and as it decreases the total cohesion term ($(S_r b(u_a - u_w) tan\varphi'')$ in Equation (3-15)) would decrease followed by a reduction in the rock strength. Additionally, as illustrated previously in Figure 3-38 and Figure 3-39, decreasing the capillary suction would increase the possibility of the stress state reaching the failure envelope as a result of decreasing the cohesion (shift the failure envelope downward) and reducing the effective stress (shift the circle to the left). Young's modulus and Poisson's ratio were computed from the stress-strain curves.

Although based on ASTM D7012-14 (2014) recommended approach, it was assumed that an almost linear behavior (elastic zone) occurred at around half (40-60%) of the peak compressive strength and this stress zone can be used to determine Young's modulus and Poisson's ratio. Eberhardt et al. (1998) and Amann et al. (2011) suggested that the stress zone between fracture closure and fracture initiation where the fracture initiation threshold ranges between 30% and 50% of the peak strength should be considered for Young's modulus and Poisson's ratio determination as it may be a better representative of the rock elastic behavior. Therefore, three stress zones of 20-40%, 40-60% and 60-80% peak compressive strength was evaluated to capture the Young's modulus and Poisson's ratio as shown in Figure 6-8.

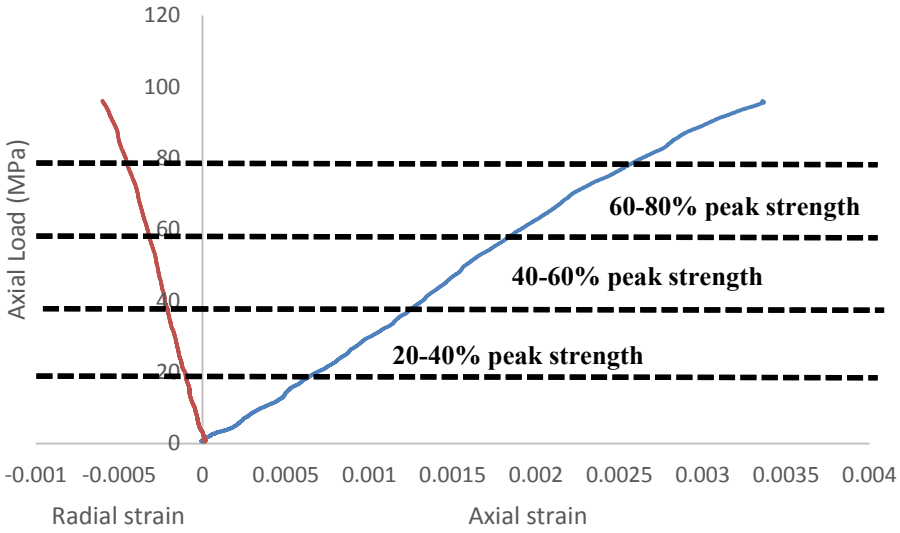

Figure 6-8. Different stress zones for Young's modulus and Poisson's ratio determination.

Figure 6-9 and Figure 6-10 show the slope of axial stress versus axial strain (Young's modulus) and axial stress versus radial strain (lateral stiffness) for both perpendicular and parallel samples at high and low capillary suction.

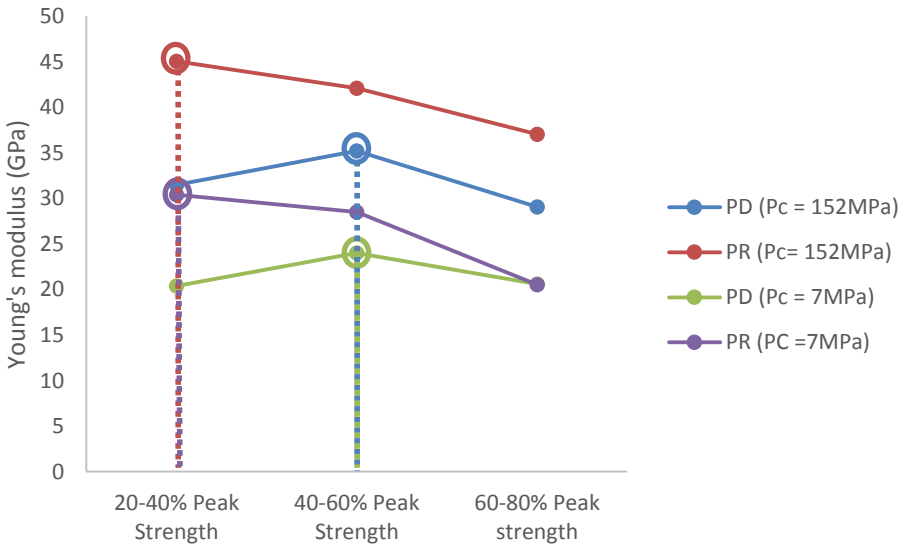

Figure 6-9. Young's modulus in different stress zones. The maximum value of Young's modulus in each sample is highlighted by a circle and the dashed line indicates the relevant stress zone.

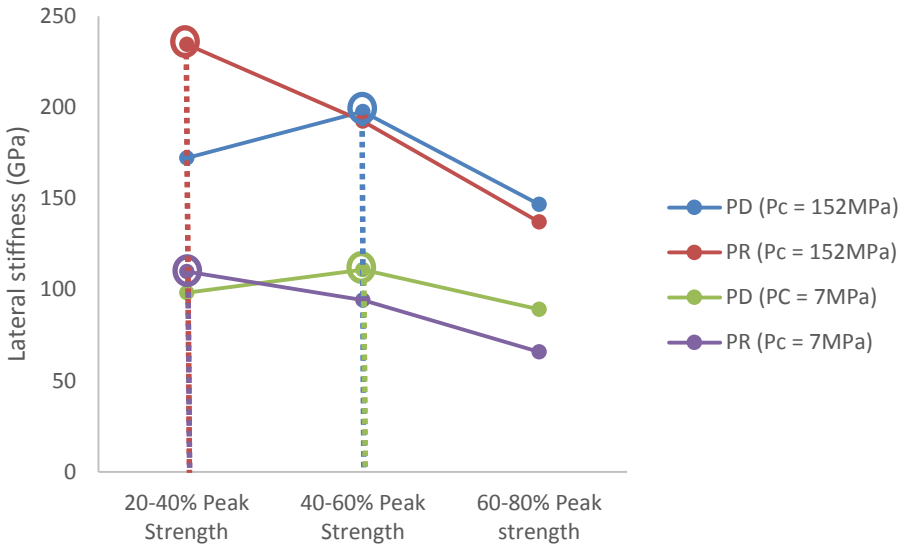

Figure 6-10. Lateral stiffness in different stress zones. The maximum value of lateral stiffness in each sample is highlighted by a circle and the dashed line indicates the relevant stress zone.

As shown in Figure 6-9 and Figure 6-10 for parallel samples at high and low capillary suction using the axial stress zone of 20-40% peak compressive strength would represent stiffer behavior than the axial stress zone of 40-60% peak compressive strength. In 20-40% peak compressive strength stress zone, the Young's modulus values at high and low capillary suction were 45.0GPa and 30.3GPa while these values were 42.1GPa and 28.4GPa for the stress zone of 40-60% peak compressive strength. Also, the values of lateral stiffness (slope of axial stress versus lateral strain) in the stress zone of 20-40% peak compressive strength were higher than the stress zone of 40-60% peak compressive strength.

The results indicated that for perpendicular samples Young's modulus and lateral stiffness of the stress zone of 40-60% peak compressive strength was higher than the stress zone of 20-40% peak compressive strength where Young's modulus and lateral stiffness in high capillary suction were 31.5GPa and 172.2GPa in the stress zone of 40-60% peak compressive strength while they were 35.2GPa and 197.8GPa in 20-40% peak compressive strength stress zone. Based on the values of Young's modulus and lateral stiffness for parallel samples the stress zone of 20-40% peak compressive strength seems to be a better representation of the elastic region to determine the elastic properties and the stress zone of 40-60% peak compressive strength shows to be a better

stress region for elastic properties measurements in perpendicular samples. The reason behind such behaviors is most likely connected to the strength of the interface between the beds. As the axial loading in parallel samples was aligned with the direction of the interfaces between the beds and these interfaces were weaker than both quartz-rich and clay-rich beds, they would act as planes of weakness, would fail sooner and would result in micro failure initiation and propagation in lower stress zone than perpendicular samples where the failure of the stiffer beds would most likely dominate the strength.

The values of calculated Poisson's ratio (dividing the Young's modulus by lateral stiffness) for perpendicular and parallel samples at high and low capillary suction in different stress zones are shown in Figure 6-11. An overall increasing trend can be observed for the Poisson's ratio from the stress zone of 20-40% to 60-80% peak compressive strength where in parallel and perpendicular samples with high capillary suction a gentle increase in Poisson's ratio can be seen from stress zone 20-40% to 40-60% peak compressive strength and a more noted increase from stress zone 40-60% to 60-80% peak compressive strength. The rate of increase is higher in parallel samples and on top of that in the samples with high capillary suction the rate of increase in Poisson's ratio is higher than the samples with low capillary suction. The former can be attributed to more complex and multi stranded micro fracture and failure generation in the sample with high capillary suction and less complex and planar micro fractures in the sample with low capillary suction. Table 6-1 summarizes the results of uniaxial compressive loading in different stress zones at high and low capillary suctions.

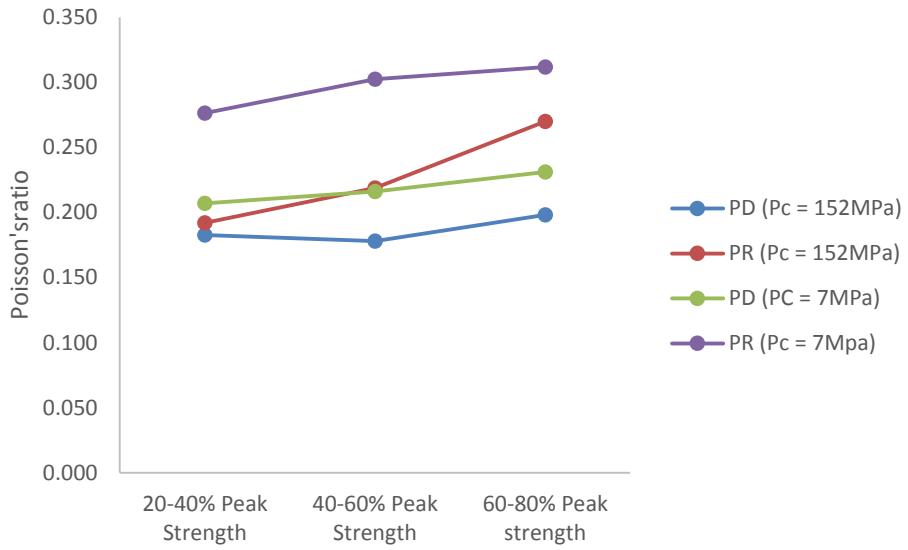

Figure 6-11. Poisson's ratio in different stress zones at high (152MPa) and low (7MPa) capillary suction values.

Table 6-1. Summary of uniaxial compressive loading experiments on parallel and perpendicular Montney samples in different stress zones at high (152MPa) and low (7MPa) capillary suctions. Subscript "H" and "L" indicate high and low capillary suction, respectively.

Sample	$E_{(20\text{-}40\%)}$ (GPa)	$E_{(40\text{-}60\%)}$ (GPa)	$E_{(60\text{-}80\%)}$ (GPa)	$\nu_{(20\text{-}40\%)}$	$\nu_{(40\text{-}60\%)}$	$\nu_{(60\text{-}80\%)}$	Lateral Stiffness (20-40%) (GPa)	Lateral Stiffness (40-60%) (GPa)	Lateral Stiffness (60-80%) (GPa)	UCS (MPa)
$PD_{(H)}$	31.4	35.2	29.0	0.183	0.178	0.198	172.2	197.7	146.7	96.0
$PR_{(H)}$	45.0	42.1	37.0	0.192	0.219	0.27	234.5	192.3	137.2	55.7
$PD_{(L)}$	20.3	23.9	20.6	0.207	0.216	0.231	98.3	110.9	89.1	64.7
$PR_{(L)}$	30.3	28.4	20.5	0.276	0.302	0.312	109.9	94.2	65.8	36.4

Comparing the stress zone of 20-40% and 40-60% peak compressive strength for Young's modulus and Poisson's ratio determination in parallel and perpendicular samples respectively, indicates that Young's modulus and Poisson's ratio of parallel sample in high capillary suction was 21.8% and 7.3% higher than perpendicular sample. Young's modulus of perpendicular sample reduced from 35.2GPa to 24.0GPa as the capillary suction decreased from 152MPa to 7MPa which was 31.86% reduction in Young's modulus value. Also, Poisson's ratio of perpendicular sample in high capillary suction was 0.178 and it reached to 0.216 in low capillary suction. For parallel sample Young's modulus and Poisson's ratio in high capillary suction were 45.0GPa and 0.192 while in low capillary suction these values were 30.4GPa and 0.276. Several mechanisms might

be considered responsible for decreasing the Young's modulus and increasing Poisson's ratio as a result of capillary suction reduction (or water saturation increase). While the low displacement rate of 0.002 mm/min was expected to minimize the potential effect of pore pressure generation during loading, a decrease in capillary suction and an increase in water saturation, small pore pressure changes because of water in the pores and pre-existing micro fractures, would attenuate mechanisms that would trigger damage and failure initiation. In other words, according to Equation (3-13), as the effective stress reduces as a result of capillary suction decrease, the media tends to respond in a form of volumetric strain which would cause an expansion that may lead to the generation of micro fractures as well as the opening of the interface between the beds (especially in parallel samples) which is then responsible for the lower stiffness of the samples.

Based on the values of Young's modulus and Poisson's ratio for parallel and perpendicular samples at high and low capillary suction levels, it is clearly observed that the behavior of Montney samples would become less brittle as the capillary suction decreases. This is more highlighted in parallel samples since they show the higher percentage of Young's modulus reduction and Poisson's ratio growth as a result of decreasing the capillary suction than perpendicular samples. Also, having less brittle behavior in low capillary suction levels would suggest less complex and more planar micro to macro failures and fractures.

As shown in Figure 6-6 in parallel and perpendicular samples the failure patterns are different. Although in both parallel and perpendicular samples, pre-existing micro fracture propagation and coalescence would take place under uniaxial compressive loading, for parallel samples, the failure consisted of tensile micro fractures with propagation along the interface and these tensile micro fractures would then coalesce together or with pre-existing neighboring micro fractures. In perpendicular samples, the failures consisted of a combination of tensile micro fractures which propagated across the beds as well as shear fractures which propagated along the beds. As compressive loading is taking place, the differing mechanical properties of quartz-rich and clay-rich beds would result in varying induced stress within the beds and would result in local stress contrast and development of a local shear stress at the interface between the beds. As the load is increasing, tensile micro-fractures across the beds as well as pre-existing micro fractures propagation would trigger and once the tensile micro fractures reach the interface between the beds, local slip along the interface happens which would possibly connect the tensile micro

fractures in the adjacent beds. Figure 6-12 illustrates a schematic failure patterns in parallel and perpendicular samples during uniaxial compressive loading.

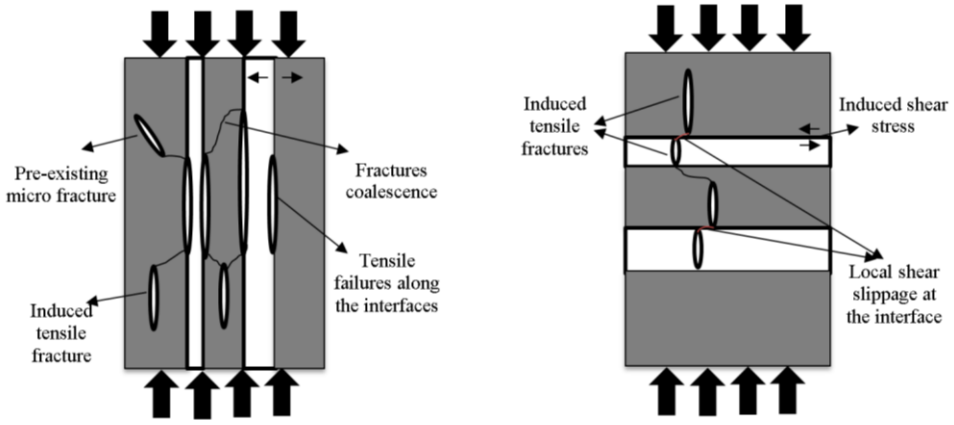

Figure 6-12. Schematic failure mechanism and fracture coalescence patterns in parallel (left image) and perpendicular (right image) samples under uniaxial compressive loading.

6.1.3.2. Loading-Unloading Cycle at Varying Capillary Suction

To better understand the rock elastic and volumetric behavior as a function of capillary suction, four-stage unload-reload tests under controlled capillary suction level were completed. Capillary suction in the samples was controlled by exposing the specimen to a different saturated salt solution in each step. Then, by analyzing the stress–strain curves during the unload/reload paths the observed behaviors as a result of changing the capillary suction would be investigated.

6.1.3.2.1. Rock Mechanical Responses upon Capillary Suction Variation

In the first stage the sample with 152MPa capillary suction was loaded up to 20MPa and then unloaded to 10MPa followed by reloading to 20MPa. The stress-strain curves of loading-unloading-reloading phase on perpendicular and parallel samples for this stage (P_c = 152MPa) are illustrated in Figure 6-13 and Figure 6-14.

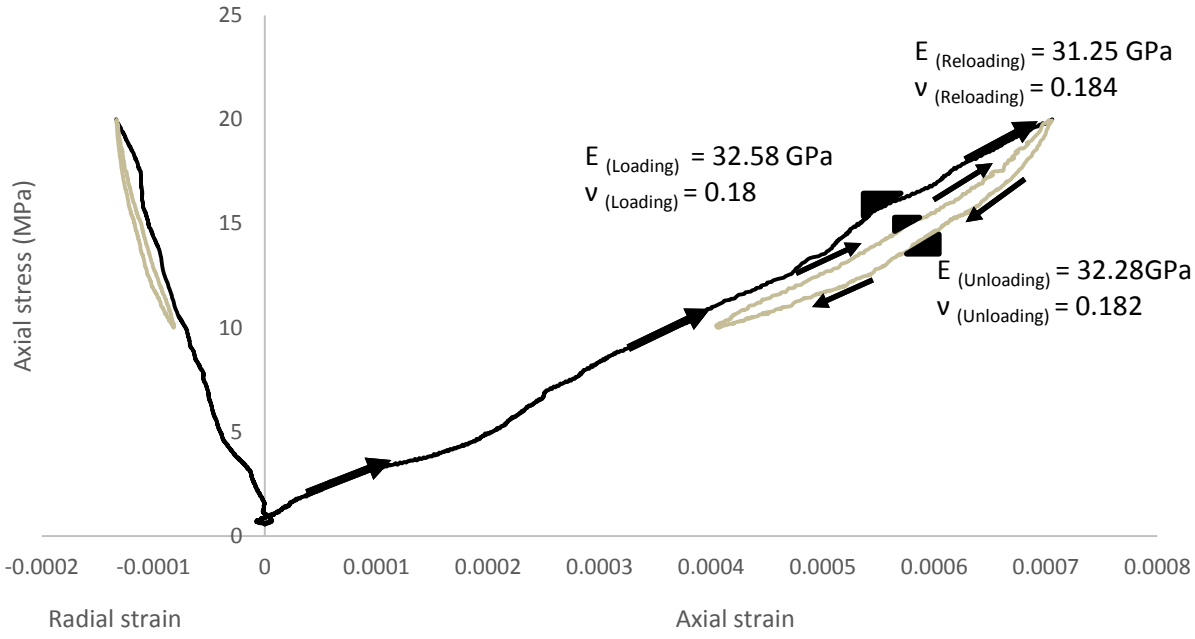

Figure 6-13. Load-unload-reload phase on the perpendicular sample at 152MPa capillary suction.

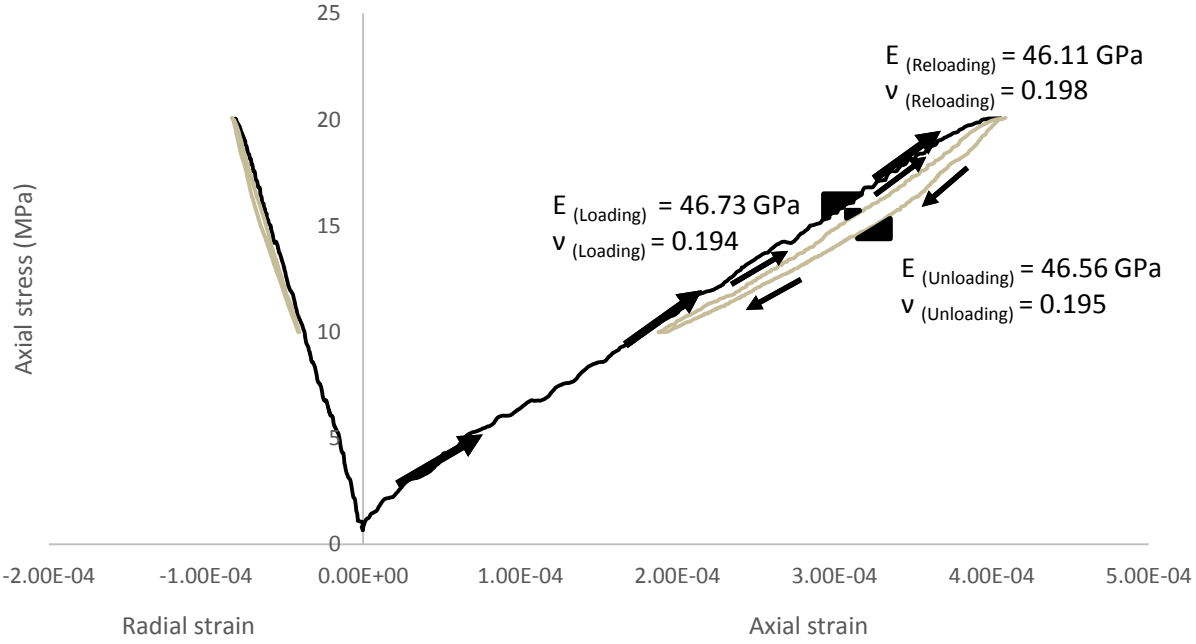

Figure 6-14. Load-unload-reload phase on the parallel sample at 152MPa capillary suction.

As shown in Figure 6-13 and Figure 6-14, in the first loading stage due to closure of the pre-existing micro fractures as a result of increasing the axial stress, the specimens display a stiffer response. Depending on the strength of the pre-existing micro-fractures and their direction with respect to the loading direction, a further increase in axial loading may lead to micro fracture propagation/sliding. To better investigate the former issue, Figure 6-15 depicts a media containing a micro fracture under a triaxial loading stage. Equation (6-1) and (6-2) represents the normal and shear stress components acting on the fracture plane and Equation (6-3) is the shear strength as a function of principles stresses (σ_1 and σ_3) which is based on Equation (3-15). To investigate the possibility of the propagation/sliding in micro fractures, shear and tensile failure indicators were defined as shown in Equation (6-4) and (6-5). The shear failure would occur once the absolute shear failure indicator (SFI) exceeds 1 which means the shear stress exceeds the shear strength. Similarly, where the tensile failure indicator (TFI) is higher than 1 the tensile failure would take place.

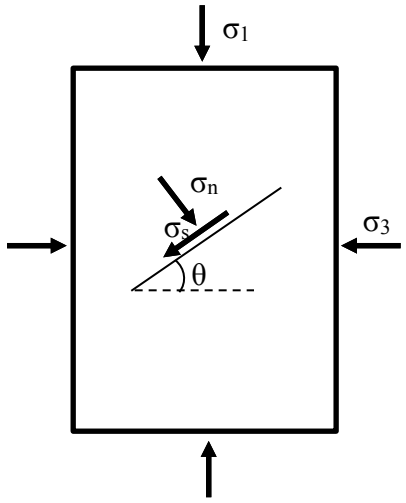

Figure 6-15. Schematic representation of the typical micro fracture and the related normal and shear stress components acting on it in a triaxial loading condition.

$$\sigma_n' = \frac{\sigma_1+\sigma_3}{2} + \frac{\sigma_1-\sigma_3}{2}\, cos2\theta - \alpha u_a + S\alpha P_c \quad (6\text{-}1)$$

$$\sigma_s = \frac{\sigma_1-\sigma_3}{2}\, sin2\theta \quad (6\text{-}2)$$

$$\tau = \left[\frac{\sigma_1+\sigma_3}{2} + \frac{\sigma_1-\sigma_3}{2}\, cos2\theta - \alpha u_a\right] tg\varphi' + C \quad (6\text{-}3)$$

$$SFI = \frac{\sigma_s}{\tau} = \frac{(\sigma_1-\sigma_3)sin2\theta}{[(\sigma_1+\sigma_3)+(\sigma_1-\sigma_3)cos2\theta-2\alpha u_a]\, tg\varphi\prime+2C} \quad (6\text{-}4)$$

$$TFI = \frac{\sigma_n\prime}{\sigma_t} = \frac{(\sigma_1+\sigma_3)+(\sigma_1-\sigma_3)cos2\theta-2\alpha u_a+2S\alpha P_c}{2\sigma_t} \quad (6\text{-}5)$$

Where σ_n' is the effective normal stress and σ_s is the shear stress acting on the fracture plane. Considering the uniaxial compressive loading ($\sigma_3 = 0$), zero total cohesion in the micro fracture and atmospheric air pressure in the experiments ($u_a = 0$) SFI and TFI would be as shown in Equation (6-6) and (6-7).

$$SIF_{Uniaxial} = \frac{\sigma_1 sin2\theta}{\sigma_1(1+cos2\theta)\, tg\varphi\prime} = \frac{sin2\theta}{(1+cos2\theta)\, tg\varphi\prime} = \frac{tg\theta}{tg\varphi\prime} \quad (6\text{-}6)$$

$$TIF_{Uniaxial} = \frac{(\sigma_1+\sigma_3)+(\sigma_1-\sigma_3)cos2\theta-\alpha u_a+S\alpha P_c}{2\sigma_t} = \frac{\sigma_1(1+cos2\theta)+2S\alpha P_c}{2\sigma_t} \quad (6\text{-}7)$$

Equation (6-6) indicates that the orientation of the pre-existing micro fracture with respect to the loading direction and the internal friction angle of the surrounding media have a great impact on the occurrence of shear failure. It is worth mentioning that based on the results of the direct shear tests in Chapter 4, the values of internal friction angle for high and low capillary suctions are 38.4° and 31° which means that SFI exceeds 1 for $\theta>38.4$ and $\theta>31$, respectively. This would suggest that due to the softening behavior as a result of capillary suction reduction, internal friction angle would decrease which can result in the shear failure initiation from the pre-existing micro fractures with lower inclination (θ). Also, based on Figure 6-13 and Figure 6-14 the Young's modulus and Poisson's ratio values related to loading, unloading and reloading stages don't have significant difference which implies that most likely no pre-existing micro fracture propagation /sliding has not occurred. Figure 6-16 and Figure 6-17 represent the unloading-reloading stages for perpendicular and parallel samples in each capillary suction and water saturation level.

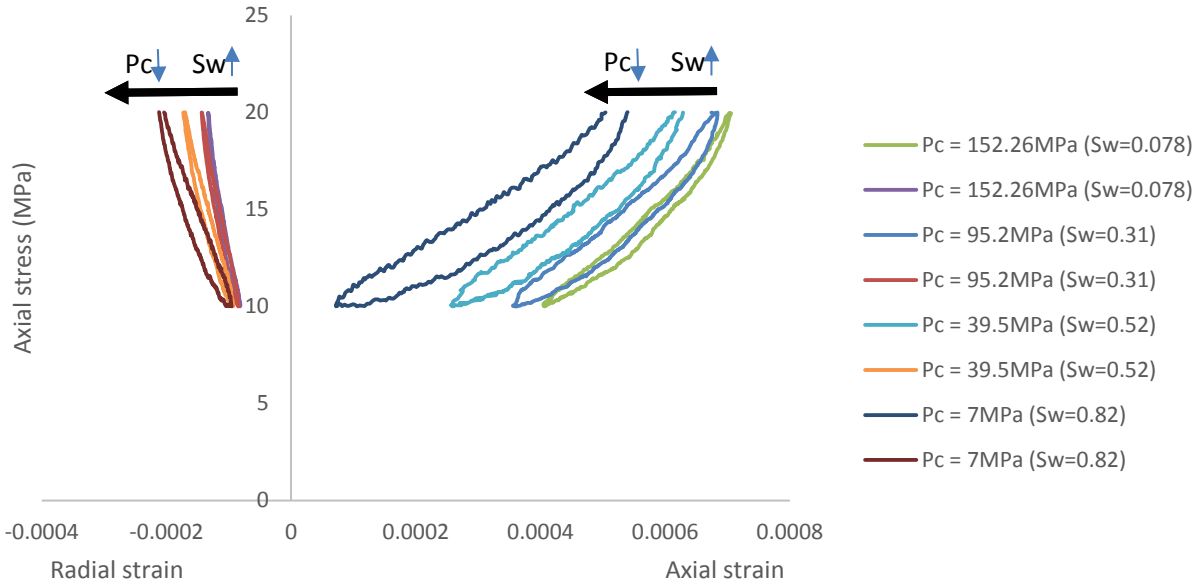

Figure 6-16. Axial and radial response of perpendicular sample subjected to unloading-reloading path during the wetting process (capillary suction change) under a constant stress.

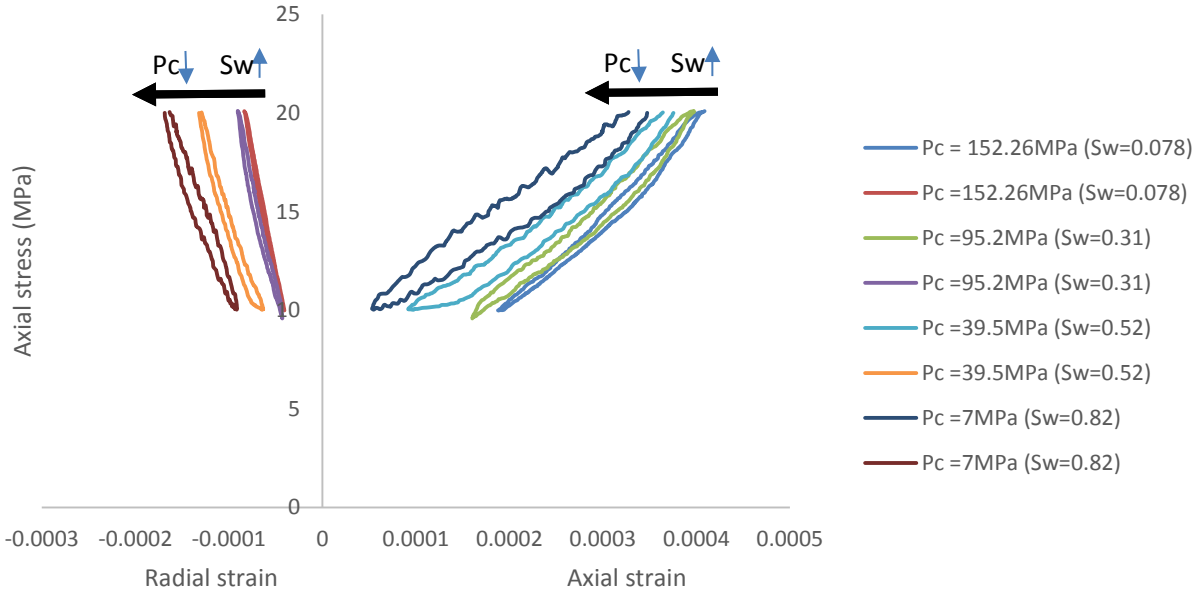

Figure 6-17. Axial and radial response of parallel sample subjected to unloading-reloading path during the wetting process (capillary suction change) under a constant stress.

As shown in Figure 6-16 and Figure 6-17, in each capillary suction level there is a hysteresis loop as a result of the unloading-reloading path. Capillary suction decrease would shift the axial and radial stress–strain hysteresis to the left which can be attributed to effective stress reduction. Based on Equation (3-13), as the effective stress reduces, the media tends to respond in a form of volumetric strain which would cause an expansion. Additionally, in both perpendicular and parallel samples as the capillary suction is decreasing, widening of the loop in the unloading-reloading path can be observed which is a sign of a permanent deformation at the end of the reloading step. Also, the hysteresis in unloading-reloading paths becomes wider as the capillary suction decreases. These observations can be related to swelling (volumetric stain) and softening occurrence followed by the initiation of micro fractures or propagation of the pre-existing micro fractures especially those which are aligned parallel to the loading direction. This may also be the reason the occurrence of a relatively higher rate of radial strain change in the parallel sample and axial strain change in the perpendicular sample. For parallel samples, the direction of loading and interfaces between the beds (as the weak planes) are aligned and any failure along the interfaces would increase the rate of water uptake and mobilization along the interfaces followed by higher rate of radial strain growth than the perpendicular sample. The same mechanism would take place for the perpendicular sample where the failure along the interfaces between the beds would lead to more water uptake along the interfaces and the rate of axial strain change is higher in comparison with the parallel sample.

Figure 6-18 to Figure 6-21 represent the axial and radial strain change in the perpendicular and parallel samples during the wetting steps which also imply that as a result of capillary suction reduction a higher rate of radial strain growth can be observed in parallel sample while the higher rate of axial strain change would take place in a perpendicular sample. The process of achieving equilibrium at a capillary suction of 95MPa induced a very small change in axial and radial strain values in both perpendicular and parallel samples but a more significant change was experienced as the capillary suction decreased to 39.5MPa and 7MPa.

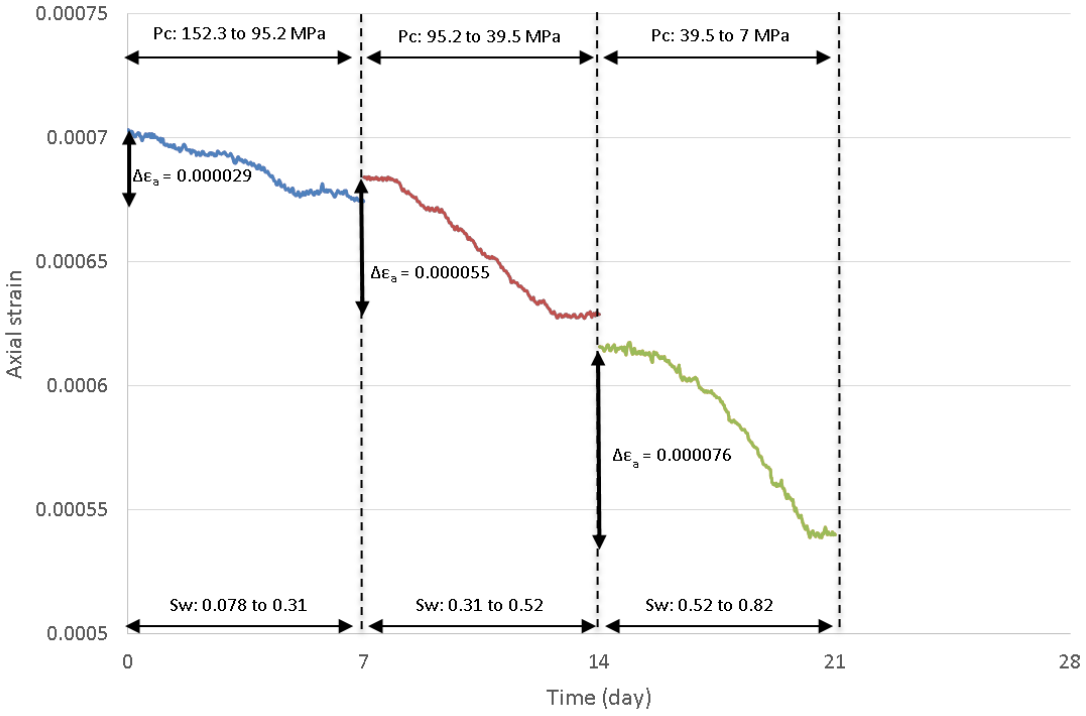

Figure 6-18. Axial strain change in the perpendicular sample during the wetting steps.

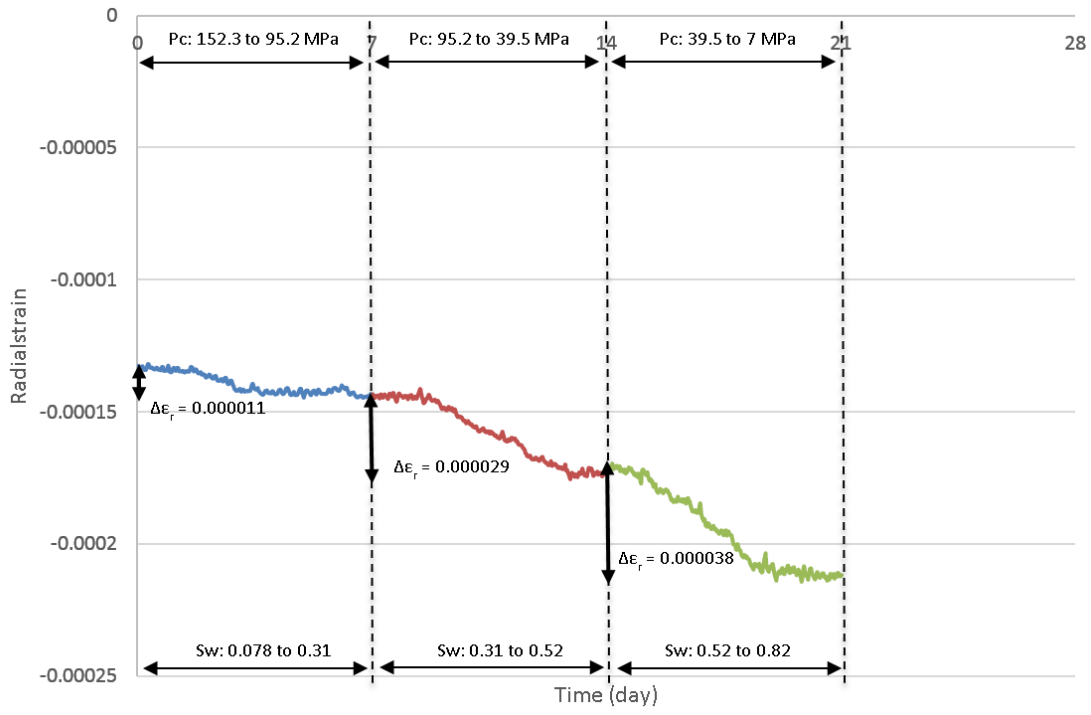

Figure 6-19. Radial strain change in the perpendicular sample during the wetting steps.

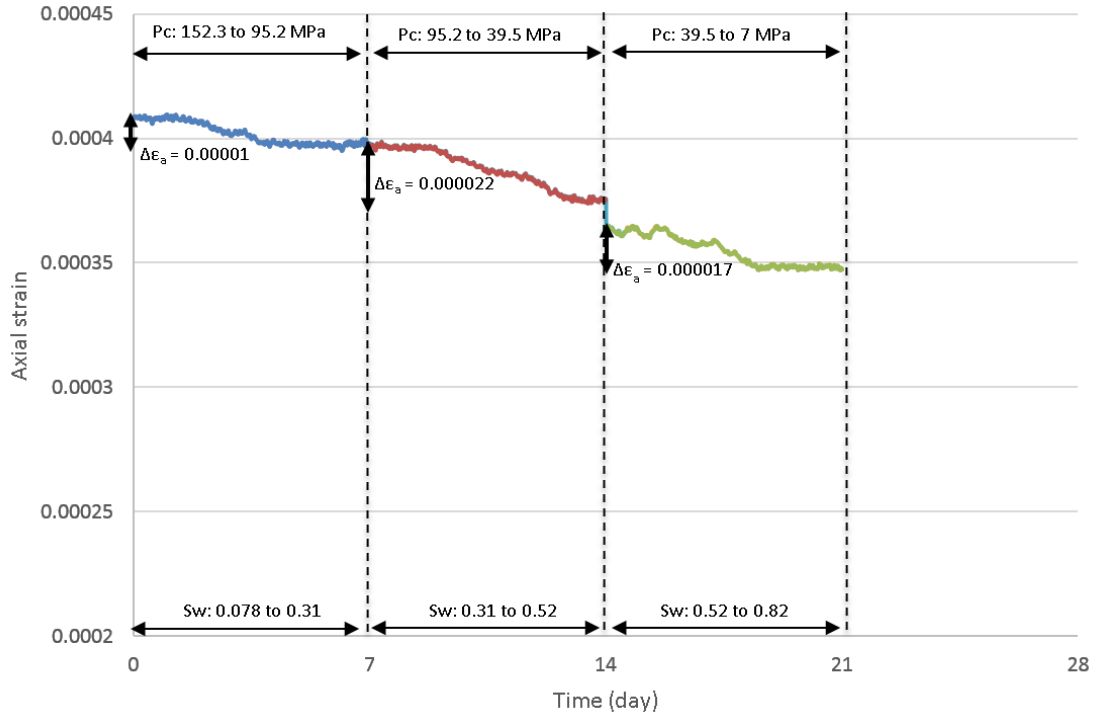

Figure 6-20. Axial strain change in the parallel sample during the wetting steps.

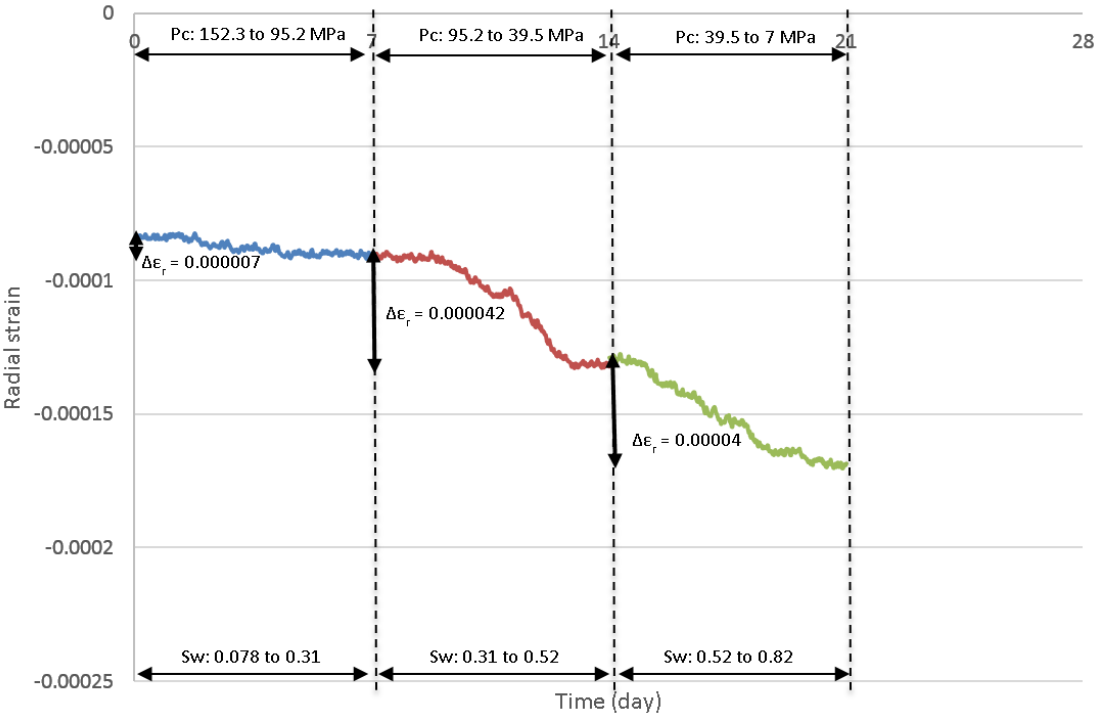

Figure 6-21. Radial strain change in the parallel sample during the wetting steps.

In addition, Figure 6-22 to Figure 6-25 depict the rock mechanical responses (Young's modulus and Poisson's ratio) in unloading-reloading steps after each capillary suction equilibrium for perpendicular and parallel samples. These results clearly show that decreasing the capillary suction results in a reduction in Young's modulus and an increase in Poisson's ratio. In perpendicular samples, Young's modulus in unloading path reduced by 26.1% and 36.9% while for reloading path it reduced by 17.6% and 28.7% after capillary suction reduction to 39.5MPa and 7MPa. Young's modulus of parallel sample in unloading path reduced by 23.6% and 33.8% while Young's modulus reduction in reloading path as the capillary suction decreased from 152MPa to 39.5MPa and 7MPa were 17.7% and 30%, respectively. Poisson's ratio in unloading path of perpendicular sample increased from 0.18 (in 152MPa capillary suction) to 0.21 (39.5MPa) and 0.24 (7MPa) while for the reloading path it increased from 0.18 to 0.22 and 0.25. Also, in the unloading path of the parallel sample Poisson's ratio growth was from 0.19 (152MPa capillary suction) to 0.24 (39.5MPa capillary suction) and 0.27 (7MPa capillary suction) and for the reloading path it increased from 0.2 to 0.25 and 0.28. These observations would imply that the rock response has become less brittle while at the same time these observations represent a nonlinear response with hysteresis.

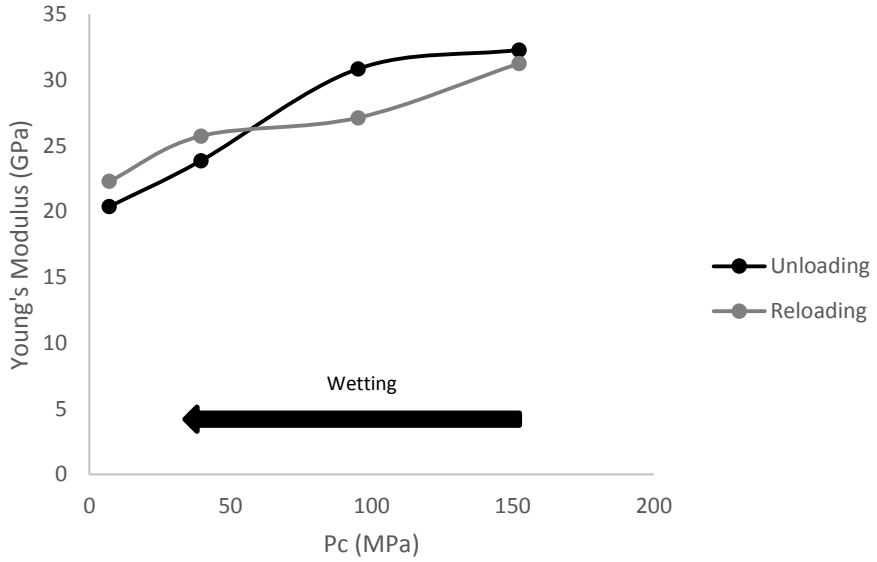

Figure 6-22. Young's modulus values captured in unloading-reloading paths during the wetting phase (capillary suction reduction) performed on perpendicular sample.

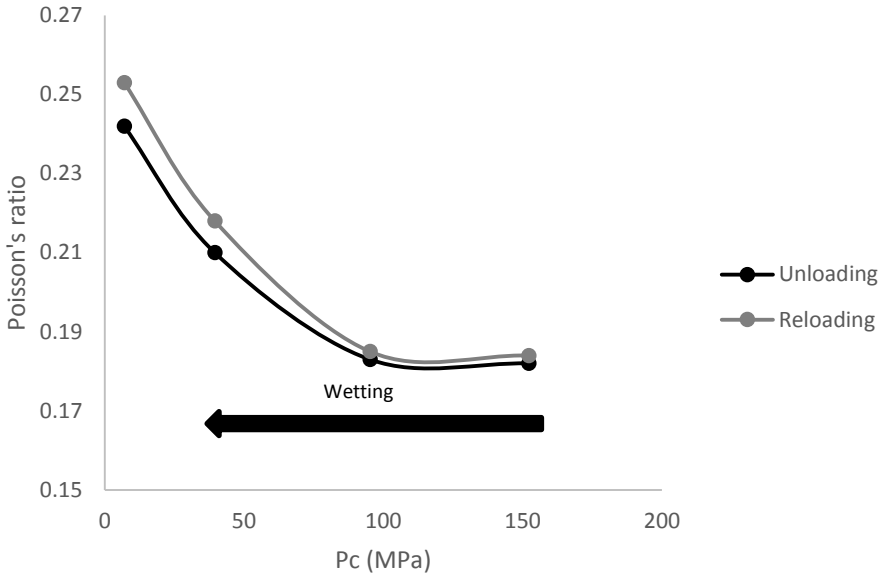

Figure 6-23. Poisson's ratio values captured in unloading-reloading paths during the wetting phase (capillary suction reduction) performed on perpendicular sample.

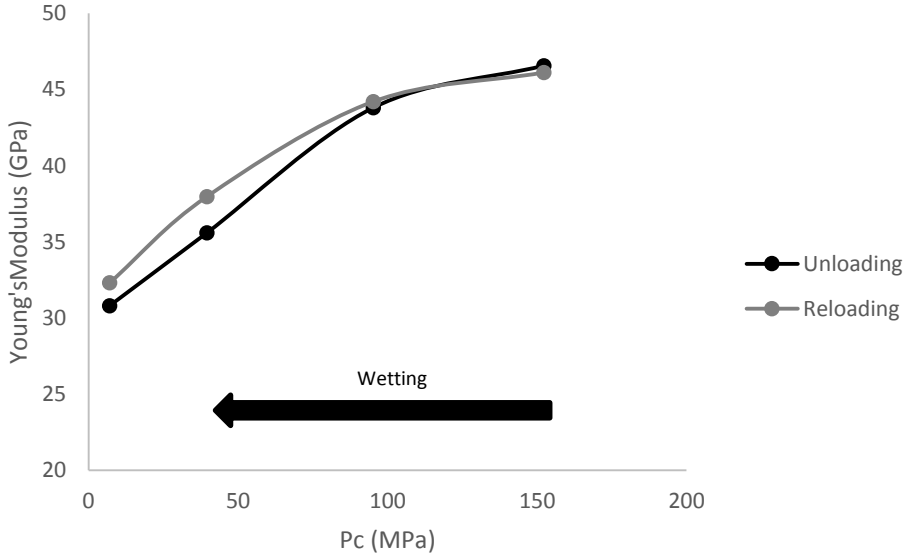

Figure 6-24. Young's modulus values captured in unloading-reloading paths during the wetting phase (capillary suction reduction) performed on parallel sample.

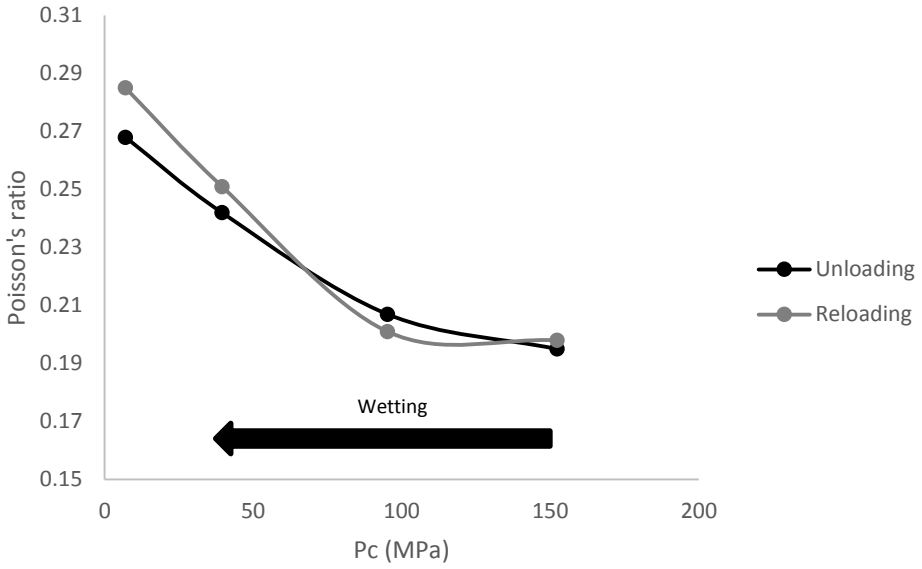

Figure 6-25. Poisson's ratio values captured in unloading-reloading paths during the wetting phase (capillary suction reduction) performed on perpendicular sample.

A closer look at Figure 6-22 to Figure 6-25 also shows that Young's modulus values of the reloading path in both perpendicular and parallel samples are lower or very close to unloading path in higher capillary suction values (152MPa and 95MPa). In lower capillary suction values (39MPa and 7MPa) Young's modulus values of the reloading path are higher in comparison with the unloading path. Also, Figure 6-18 to Figure 6-21 indicated that sample expansion mainly occurred when the capillary suction reduced to in 39MPa and 7MPa. Accordingly, one may conclude that at higher capillary suction values (152MPa and 95MPa) the dominating mechanism for a reduction in Young's modulus values in the reloading path would be triggering the failure in pre-existing micro fractures (sliding/propagation). The expansion during the equilibrium phase to 152MPa and 95MPa was probably not sufficient to trigger the failure in the pre-existing micro fractures during the unloading path. As the capillary suction value was decreasing to 39MPa and 7MPa and the expansion in the samples was increasing, some of the micro fractures might already experience sliding/propagation even before the beginning of the unloading path after the wetting phase which would reduce Young's modulus in unloading path. In other words, the dominating mechanism to reduce the Young's modulus in unloading path would be an expansion that takes place during the wetting phase (equilibrium phase) which can induce micro fracture failure. Also, once the

unloading step begins micro fractures are reopened. This causes the mobilized water to refill the micro fractures. Therefore, micro fractures could not be completely closed in the reloading step (Jiang et al., 2018). This may be the reason why in low capillary suction values (high water saturation) Young's modulus of the unloading path becomes lower than reloading path. It should be noted that although at low capillary suction levels the pore-water pressure hindered the closure of micro fractures, at the same time failures can be mobilized which can result in generation of secondary micro fractures. Young's modulus of the unloading path lower than reloading path coincides with opening of the stress–strain hysteresis loop. Table 6-2 represents a summary of unloading-reloading rock mechanical responses in both perpendicular and parallel samples.

Table 6-2. Summary of unloading-reloading rock mechanical responses of perpendicular and parallel samples during the wetting phase (capillary suction decrease)

	P_c	S_w	$E_{(unloading)}$	$\nu_{(unloading)}$	$E_{(reloading)}$	$\nu_{(reloading)}$
Perpendicular sample	152.26	0.078	32.2	0.182	31.2	0.184
	95.2	0.31	30.8	0.183	27.1	0.185
	39.5	0.52	23.8	0.21	25.7	0.218
	7	0.82	20.3	0.242	22.2	0.253
Parallel sample	152.26	0.078	46.5	0.195	46.1	0.198
	95.2	0.31	43.8	0.207	44.2	0.201
	39.5	0.52	35.5	0.242	37.9	0.251
	7	0.82	30.8	0.268	32.3	0.285

6.1.3.3. Revisiting Rock Mechanical and Strength Responses Captured by Micro-indentation and Micro-scratch tests

Comparing the results of micro-indentation tests to capture rock mechanical responses (Young's modulus and Poisson's ratio) with the results obtained from 1cm x 2cm samples tested by mini-cell indicate that while both of them show a reduction in Young's modulus as a function of a decreasing capillary suction, the results of the experiments on 1cm x 2cm samples show higher values for Young's modulus in comparison with the results of micro-indentation test. As an example, the average Young's modulus of quartz-rich and clay-rich beds in high capillary suction (125.9MPa for the quartz-rich beds and 152.3MPa for clay-rich beds) captured by micro-indentation test were 36.4GPa and 28.7GPa respectively while the overall Young's modulus of the

perpendicular and parallel samples in the reloading path of the cyclic tests in high capillary suction (152.3MPa) were 31.3GPa and 46.1GPa. It is postulated that these differences would arise not only different loading mechanisms but also different loading rates. Consequently, additional micro-indentation tests at higher loading rates (90mN/s) were completed using the FISCHERSCOPE HM2000 at high (125.9MPa for the quartz-rich beds and 152.3MPa for clay-rich beds) and low capillary suctions (0.92MPa for the quartz-rich beds and 0.8MPa for clay-rich beds). Based on Equation (4-6) and assuming the same Poisson's ratio values shown in Table 4-7, Young's modulus values for quartz-rich and clay-rich beds in high and low capillary suctions were determined. Table 6-3 represents the results of micro-indentation test with a higher loading rate.

Table 6-3. Micro-indentation tests on quartz-rich and clay-rich beds in high and low capillary suctions with higher loading rate.

Sample	P_c (MPa)	S_w	Number of indentation points	Min E (GPa)	Max E (GPa)	Average E (GPa)
Quartz-rich beds	125.85	0.08	21	32.4	93.4	55.75
Clay-rich beds	152.27	0.079	8	29.9	47.8	36.96
Quartz-rich beds	0.92	0.97	15	7.3	45.1	22.64
Clay-rich beds	0.8	0.96	15	11.6	29.8	20.48

The results shown in Table 6-3 imply that as the loading rate in the micro-indentation tests increased the results were getting closer to the Young's modulus values obtained in the tests by mini cell. To better investigate the results captured by micro indentation and compare it with larger scale test results performed by mini cell an equivalent model of several Hooke spring elements were considered (Ligang et al., 2017) to determine Young's modulus in parallel sample (as shown in Figure 6-26) based on Young's modulus values of quartz-rich and clay-rich beds.

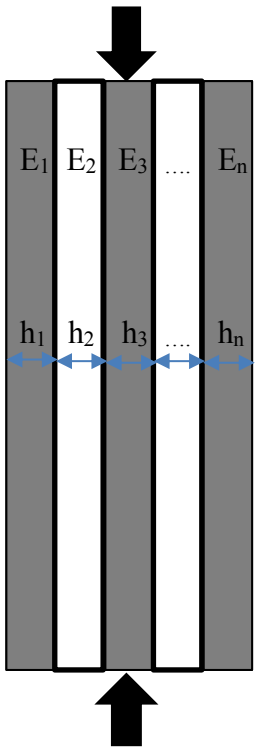

Figure 6-26. Layered rock mass with different parallel beds.

The Young's modulus of layered rock mass (E_r) with parallel beds would be determined by Equation (6-6) (Ligang et al., 2017):

$$E_r = E_1 \frac{h_1}{h} + E_2 \frac{h_2}{h} + E_3 \frac{h_3}{h} + \cdots + E_n \frac{h_n}{h} \quad (6\text{-}6)$$

where Ei (i = 1, 2, . . . , n) is the elastic modulus, of i layer, h is the sum thickness of the layers and hi (i = 1, 2, . . . , n) is the thickness of i layer.

Based on Equation (6-6) and the results of micro-indentation tests with lower loading rate (45 mN/s) shown in Table 4-7 and considering h_{quartz} = 0.3h and h_{clay} = 0.7h, Young's modulus of the parallel sample in high capillary suction would be estimated as 31.04GPa while by substituting Young's modulus values of quartz-rich and clay-rich beds obtained from micro indentation test with higher loading rate (90 mN/s), Young's modulus of the parallel sample in high capillary suction (152MPa) were determined to be 42.6GPa which is close to Young's modulus value of 1cm x 2cm parallel sample tested by mini-cell. Therefore, based on Young's modulus values of

quartz-rich and clay-rich beds captured through a higher loading rate in high and low capillary suctions, Young's modulus values measured in lower loading rate (45 mN/s) are modified which are shown in Table 6-4.

Table 6-4. Modified Young's modulus values measured in micro-indentation tests

Sample	S_w	P_c (MPa)	Young's modulus (GPa)
Quartz-rich Beds	0.08	125.85	55.75
	0.26	95.2	51.39
	0.50	39.51	38.58
	0.72	14.47	28.1
	0.97	0.92	22.64
Clay-rich Beds	0.079	152.27	36.96
	0.29	95.2	32.18
	0.42	39.51	25.10
	0.79	14.47	21.08
	0.96	0.8	20.48

The results of micro-scratch tests in high capillary suction indicated that UCS values for quartz-rich (Pc = 125.9MPa) and clay-rich beds (Pc = 152.3MPa) are 126.8MPa and 116.9MPa. Also, the results of UCS test on a perpendicular sample (which is more beds-strength dominated) in high capillary suction is 96.0MPa and by considering the effect of weaker interfaces between the beds, the values of UCS captured based on micro-scratch tests are in the acceptable range. In addition, for low capillary suction (Pc = 7MPa) the UCS test done by mini cell on 1cm x 2cm perpendicular sample is 64.8MPa. The results of micro-scratch tests on quartz-rich beds in 14.5MPa and 0.92MPa capillary suctions are 68.1MPa and 62.8MPa while the results of micro-scratch tests for clay-rich beds in 14.5MPa and 0.8MPa are 57.4MPa and 54.0MPa which implies that the results of micro-scratch tests at low capillary suction are in the acceptable range as well.

6.2. Numerical Analysis

To investigate the possibility of micro fracture (failures) occurrence at reservoir in-situ stress conditions as a result of post-fracturing spontaneous imbibition in parallel and perpendicular Montney samples, beds-included three-dimensional fully coupled poro-elastoplastic partially saturated finite element models were developed using Abaqus/CAE. The crucial step of the

numerical model is to achieve the water saturation and capillary suction dependency of rock mechanical properties and strength parameters while spontaneous water imbibition is taking place. This adds more complexity to numerical modeling. Therefore, Abaqus/CAE should be first linked to Intel Visual Fortran to develop user defined subroutine (USDFLD) for defining the water saturation and capillary suction dependent parameters and updating them in each time increment. This means that in each increment based on water saturation defined as a field variable in Abaqus/CAE, rock mechanical properties and strength parameters are updated. Also, based on the relationship between saturation and capillary suction which is defined in Abaqus/CAE the effective stress in each increment would be calculated. The input parameters including rock mechanical properties, strength parameters and suction pressure as a function of water saturation for quartz-rich and clay-rich beds are based on the bed-scale experiments and analysis which can be found in Table 6-4, Table 4-9 and Table 4-6.

The porosity values for quartz-rich and clay-rich beds are based on Table 4-2 and the permeability values are calculated according to the correlation in Figure 4-106. For the depth of 2415m in Farrell Creek Montney reservoir, an overburden stress gradient, fracture closure gradient and pore pressure gradient of 25.3MPa/km, 21.3 MPa/km and 17.2MPa/km (McLellan et al., 2014) were assumed. Also, Biot's coefficient was assumed to be 0.7 (Song, 2012). The sample size in both parallel and perpendicular numerical models were 1cm by 2cm (shown in Figure 6-27).

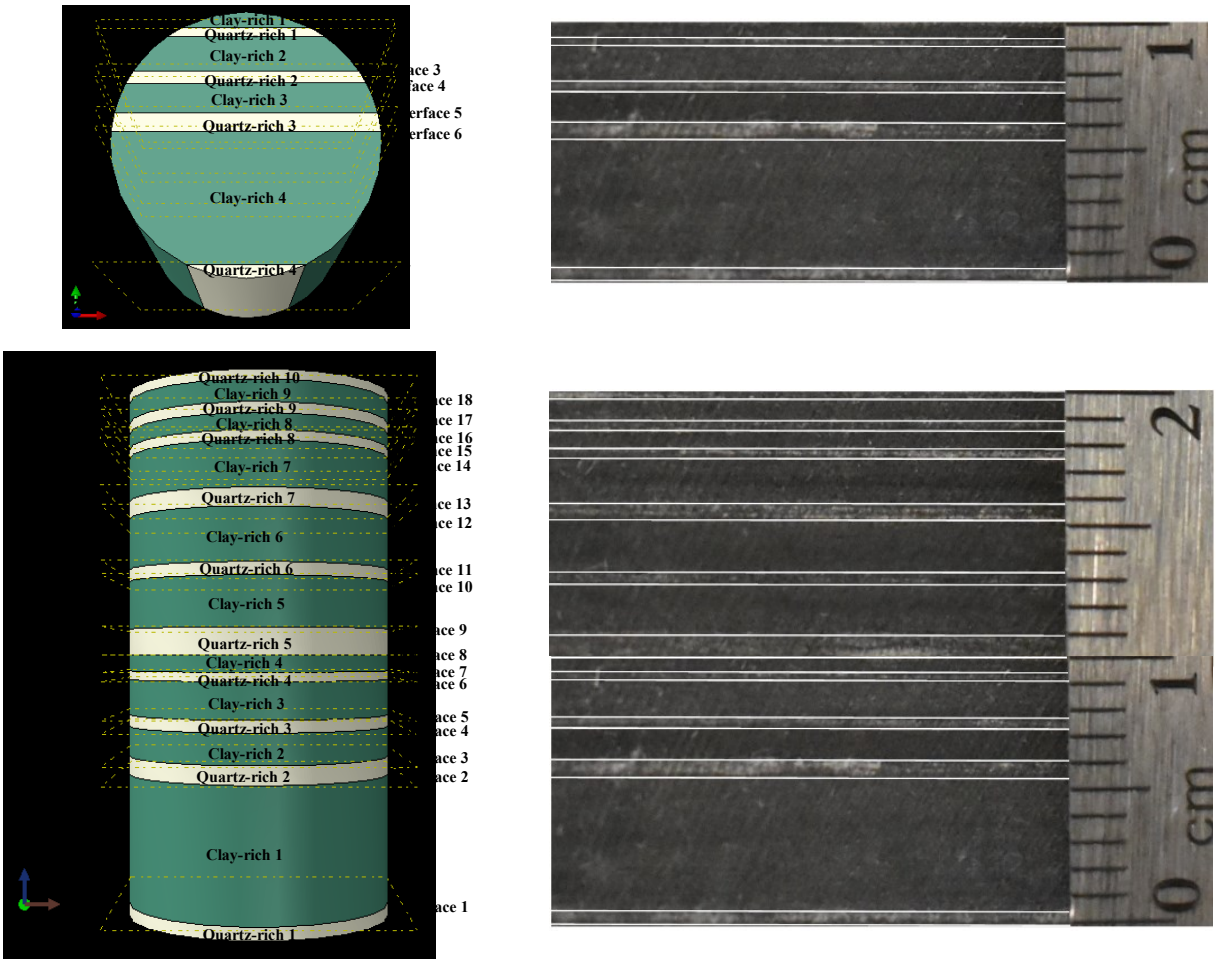

Figure 6-27. Geometry of parallel (top images) and perpendicular (bottom images) numerical models replicated from real Montney sample.

The boundary condition for both parallel and perpendicular samples (as shown in Figure 6-28) is established to allow water to be imbibed from the bottom surface through a pressure difference. The bottom surface is also a pinned (zero deformation) boundary condition (U1=U2=U3=0). Pore fluid/stress type element with displacement and pore pressure degrees of freedom was used where thicker and thinner beds were meshed using hexahedral and tetrahedral elements, respectively (Figure 6-29). The failure criteria is Drucker-Prager. In addition, based on Equation (3-21) the gas phase pressure was estimated and then used for the calculation of shear strength of the interface between the beds (Equation (3-15)). The cohesion and coefficient of friction values for the interfaces between the beds were based on the results of direct shear tests on perpendicular samples which can be found in Table 4-12.

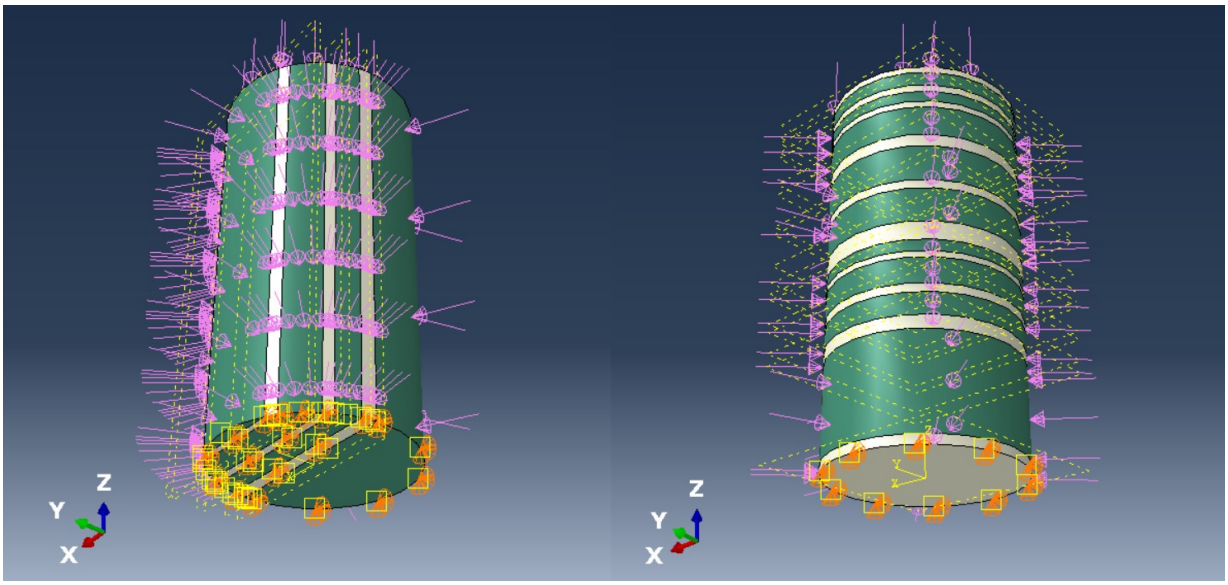

Figure 6-28. Boundary conditions in parallel and perpendicular Montney samples.

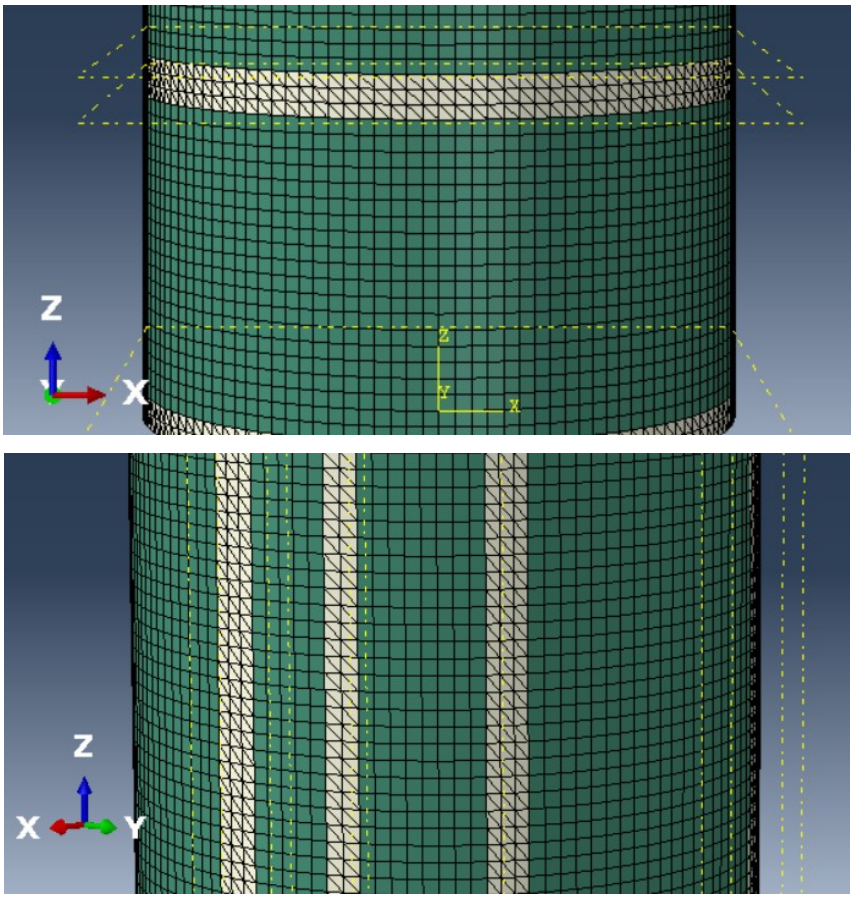

Figure 6-29. Hexahedral and tetrahedral elements used for thicker and thinner beds meshing.

6.2.1. Parallel Sample

Numerical modeling for the parallel sample was able to capture the differential movement of water within the quartz-rich and clay-rich beds as water was imbibed from the base of the specimen. As shown in Figure 6-30, in each time increment the water saturation of the same elevation in the adjacent clay-rich and quartz-rich beds were different which was related to the difference between capillary suction values of the beds as a function of water saturation as well as different pore volume and permeability values. Figure 6-31 and Figure 6-32 represent the differential water saturation (difference between water saturations in adjacent beds at the same elevation) and differential capillary suction (difference between capillary suctions in adjacent beds at the same elevation) along each interface originated from different water saturation and capillary suction values of the adjacent quartz-rich and clay-rich beds. Different water saturation and capillary suction values in quartz-rich and clay-rich beds will result in local stress development which is illustrated in Figure 6-30. As a result of spontaneous water imbibition, water saturation and capillary suction values would be locally affected in both quartz-rich and clay-rich beds and according to Equation (3-14) the local effective stress in the beds would change. The reduction in the local effective stress as well as changes in quartz-rich and clay-rich beds rock mechanical properties as a function of water saturation and capillary suction were not the same which produce different strain responses (as shown in Figure 6-33). Different volumetric responses of the adjacent clay-rich and quartz-rich beds would result in differential volumetric strain along each interface between the beds illustrated in Figure 6-34. As shown in Figure 6-34, “interface 1” experienced the minimum differential volumetric strain while “interface 6” and “interface 7” had the highest differential volumetric strain values. This could be attributed to the difference between the volumetric portion of “Clay-rich 4” and the adjacent quartz-rich beds. In parallel Montney samples, a higher volumetric difference between the clay-rich beds and the adjacent quartz-rich beds would lead to higher differential volumetric strain values along the interface between the beds. Also, for a given clay-rich bed (with quartz-rich beds on both sides), the interface with a quartz-rich bed which had a higher volumetric portion (thicker quartz-rich bed) would generate higher differential volumetric strain. As a result of lateral expansion in clay-rich beds, the thicker adjacent quartz-rich bed would experience lower strain than the thinner quartz-rich bed. Based on the results it could be noted that thicker clay-rich and quartz-rich beds were dominating the results.

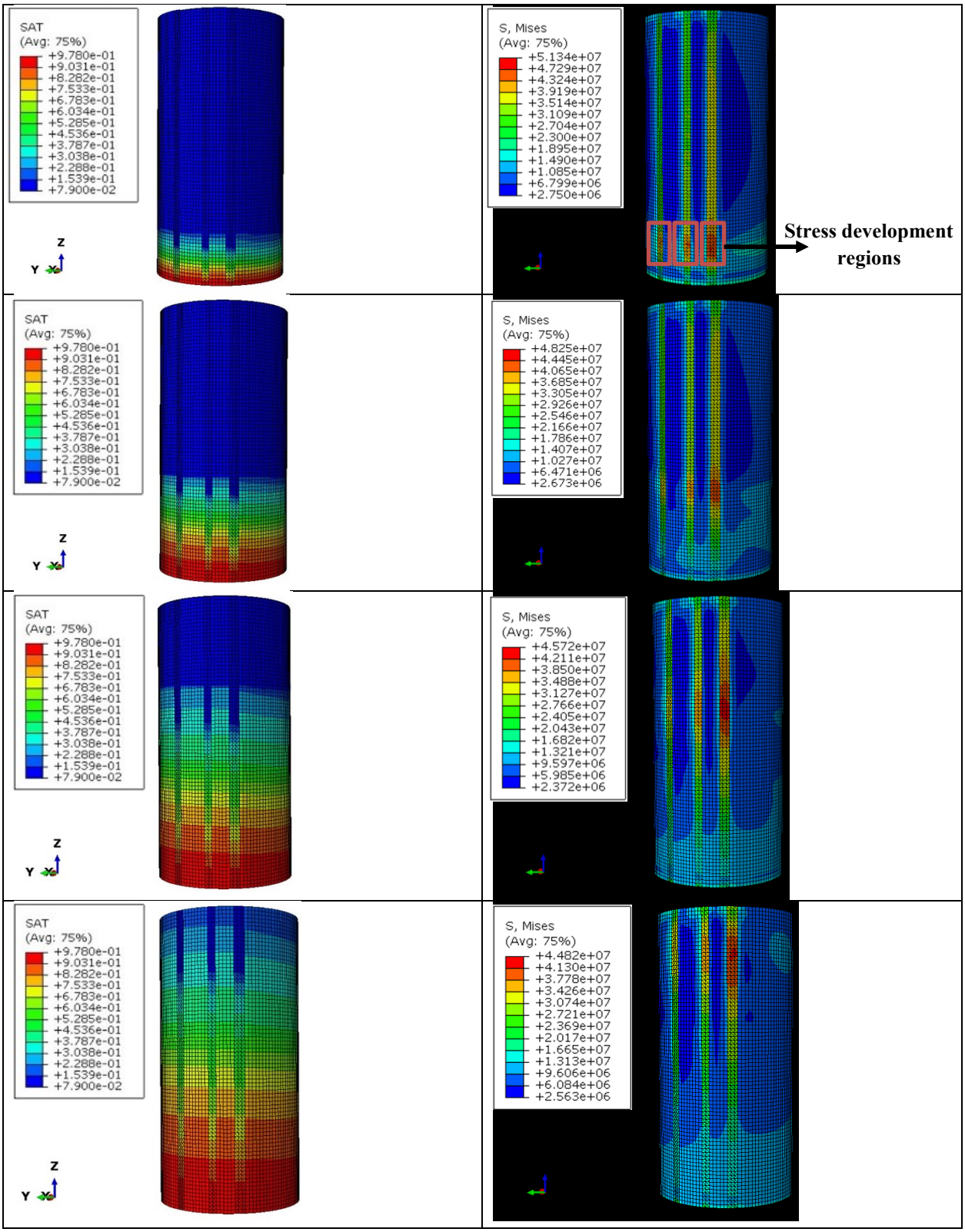

Figure 6-30. Changes in water saturation (on the left) and Mises stress (on the right) in quartz-rich and clay-rich beds during spontaneous water imbibition in parallel Montney sample.

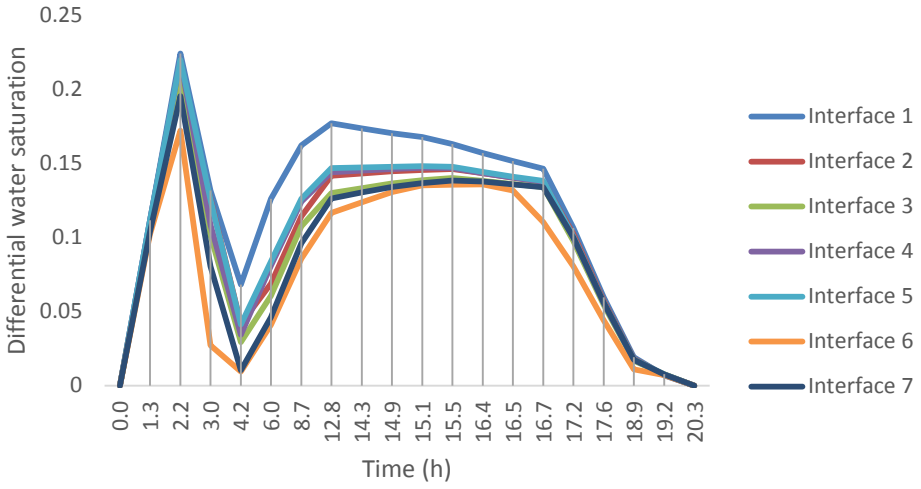

Figure 6-31. Differential water saturation along each interface during spontaneous water imbibition in parallel Montney sample.

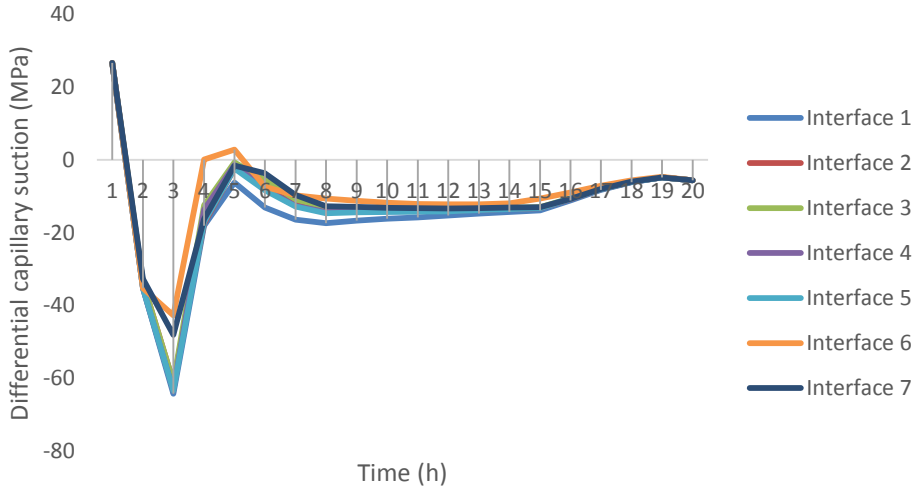

Figure 6-32. Differential capillary suction along each interface during spontaneous water imbibition in parallel Montney sample.

As a result of differential volumetric strain along each interface, induced shear stress components would be generated. Since the normal direction relative to the interfaces between the beds would be in the "X" direction, the shear stress S_{12} and S_{13} which were shear stresses in "XY" and "XZ" direction would be considered and the resultant of these two vectors that are perpendicular to each other would be calculated to investigate any potential failure along the interface between the beds.

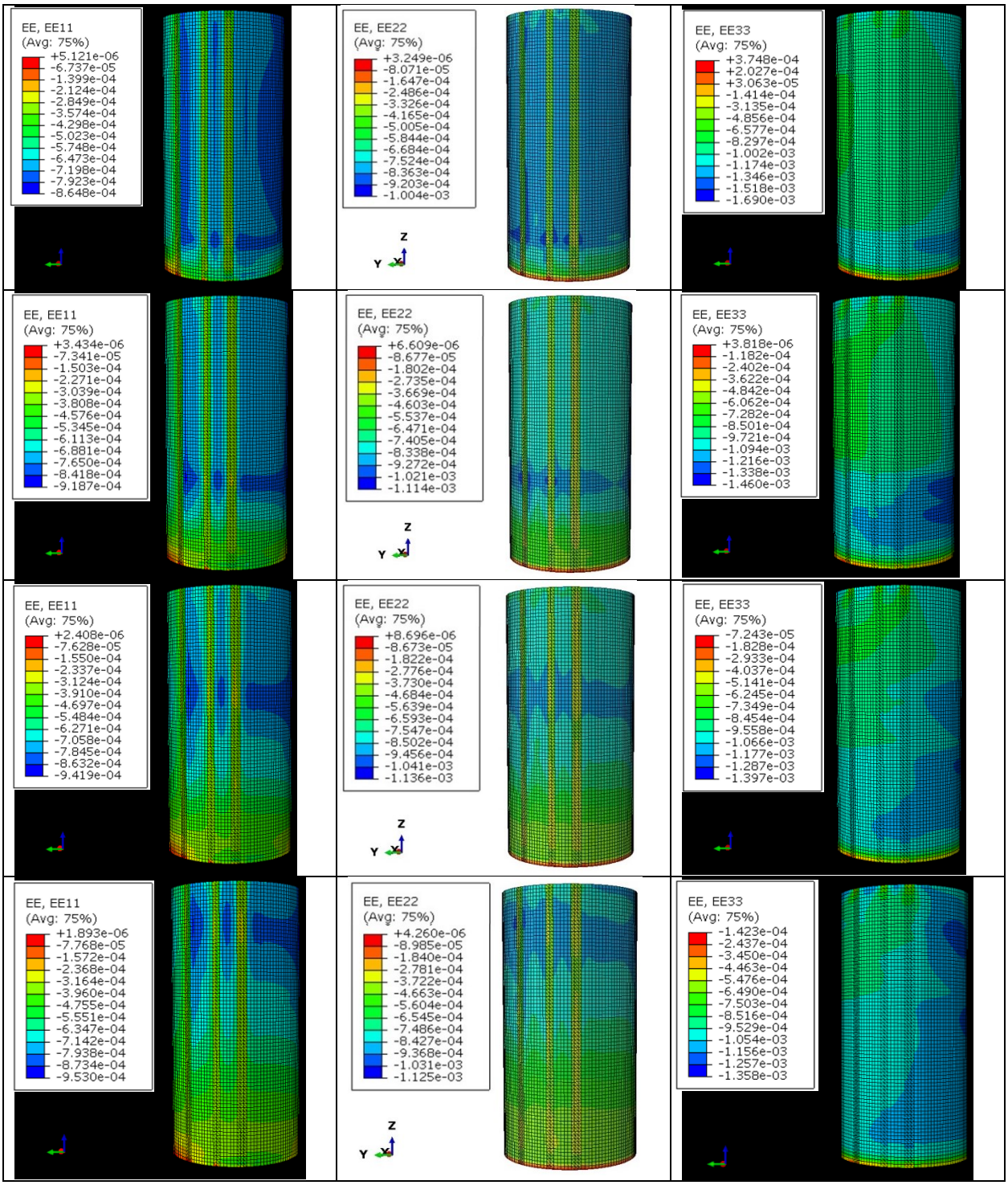

Figure 6-33. Changes in elastic strain values along clay-rich and quartz-rich beds during spontaneous water imbibition in parallel Montney sample: E11 (on the left), E22 (in the middle) and E33 (on the right). "1", "2"and"3" represent "X", "Y" and "Z" directions.

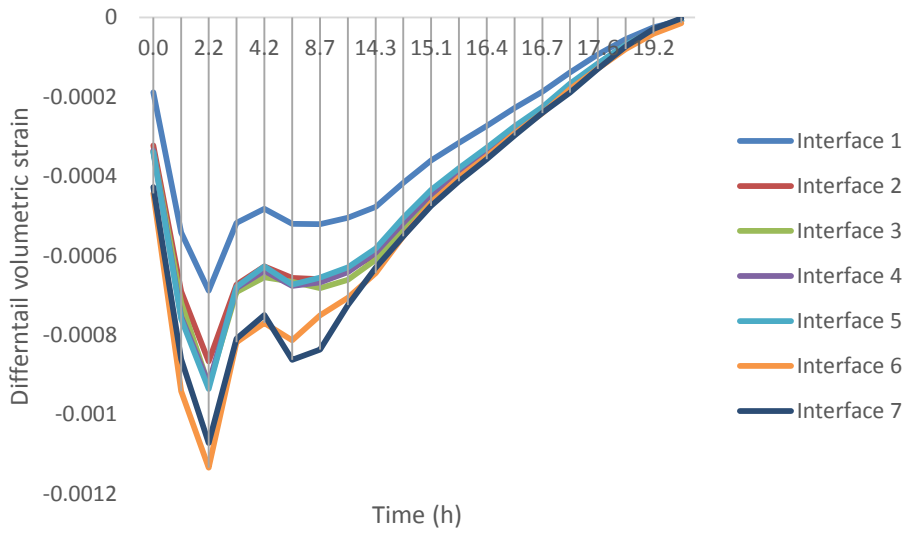

Figure 6-34. Differential volumetric strain along each interface during spontaneous water imbibition in parallel Montney sample.

Figure 6-35 illustrates how S12 and S13 were induced especially near the interfaces during spontaneous water imbibition. In addition, Figure 6-36, Figure 6-37 and Figure 6-38 show S12, S13 and the resultant shear stress acting on the interface planes between quartz-rich and clay-rich beds. As the water saturation in quartz-rich and clay-rich beds were getting closer to each other (especially in higher water saturation levels), induced shear stress along the interface between the beds reduced which could be related to lower differential volumetric strain originating from a lower difference in rock mechanical properties, water saturation and capillary suction values. During spontaneous water imbibition in parallel Montney sample, the minimum and maximum shear stresses along the interfaces were 13.6MPa and 19.52MPa which were respectively related to “interface 1” and “interface 6”. To investigate if the induced shear stress values along each interface might lead to failure, shear strength of the interfaces were calculated by using Equation (3-15) and based on the strength parameters obtained from direct shear test. Then, the best correlation among those points were determined (Figure 6-39) and used for shear strength calculation of the interface. Based on the values of shear stress acting on the interface between the beds and the shear strength values of the interfaces, it was observed that the failure would take place along all interfaces except “interface 1” Figure 6-40).

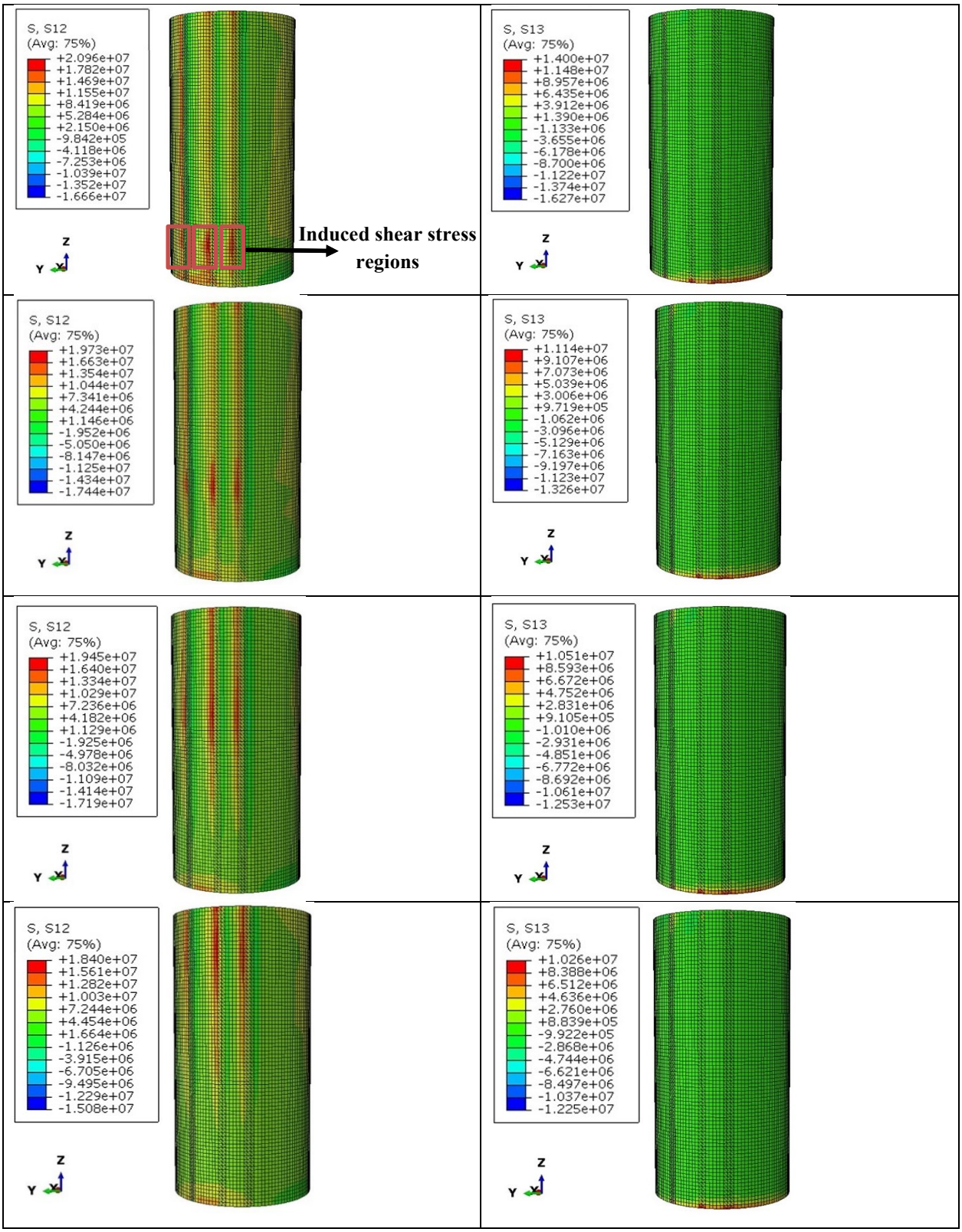

Figure 6-35. Induced shear stress components along the interface between the beds during spontaneous water imbibition in parallel samples: S12 (on the left) and S13 (on the right).

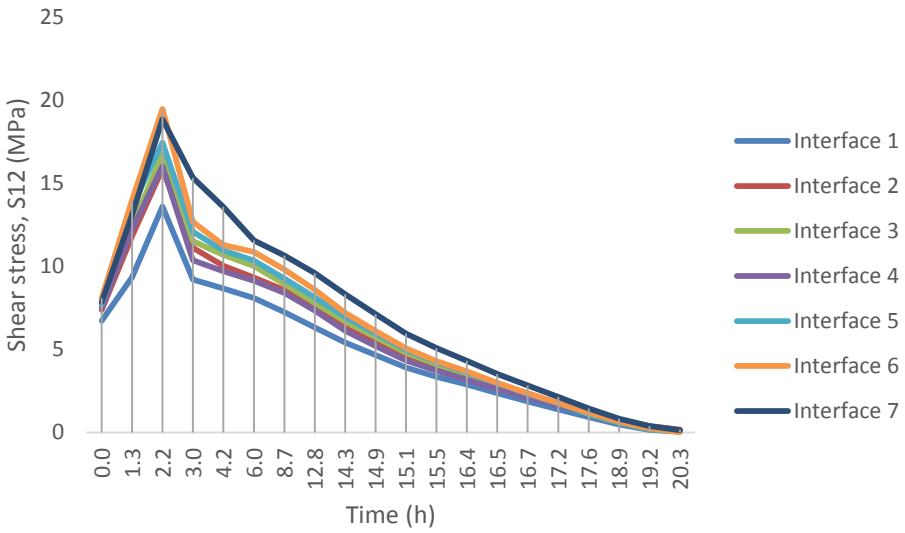

Figure 6-36. Induced S12 along the interfaces between quartz-rich and clay-rich beds during spontaneous water imbibition in parallel Montney sample.

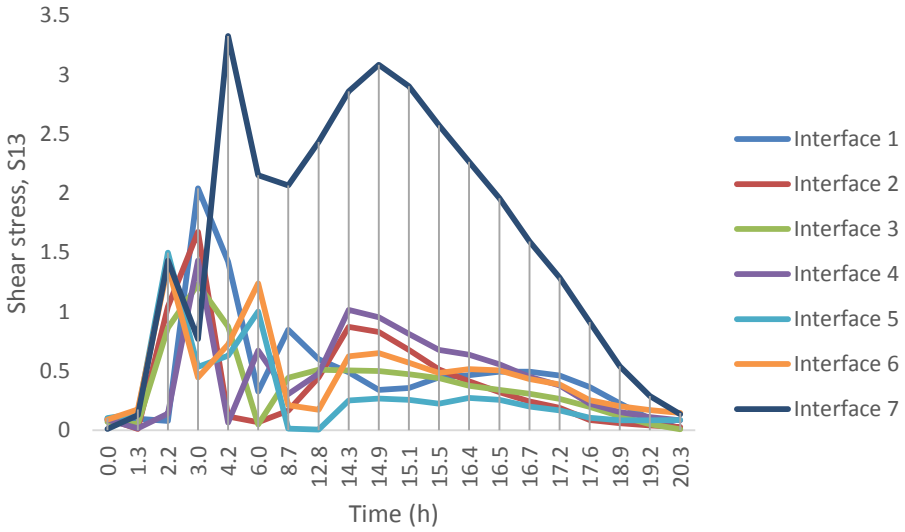

Figure 6-37. Induced S13 along the interfaces between quartz-rich and clay-rich beds during spontaneous water imbibition in parallel Montney sample.

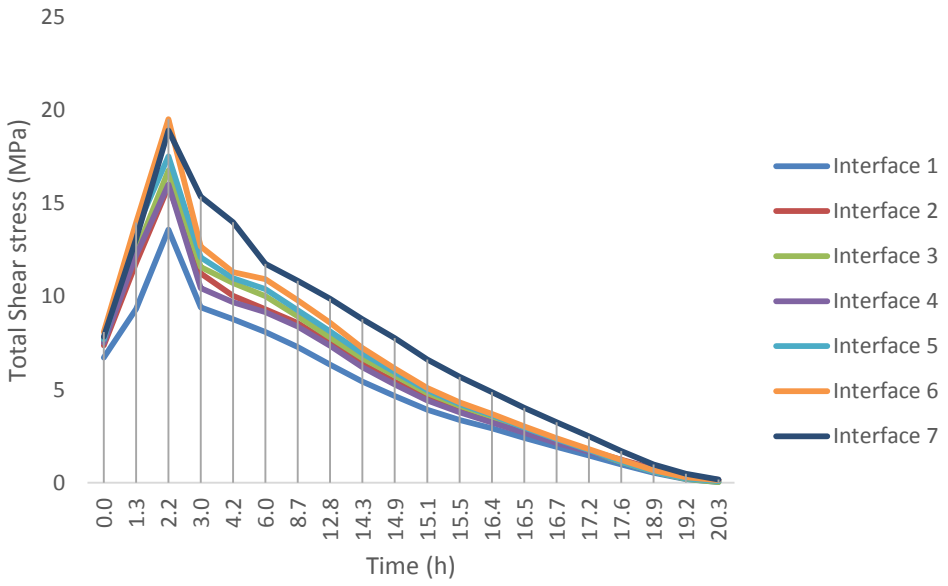

Figure 6-38. Total induced shear stress along the interfaces between quartz-rich and clay-rich beds during spontaneous water imbibition in parallel Montney sample.

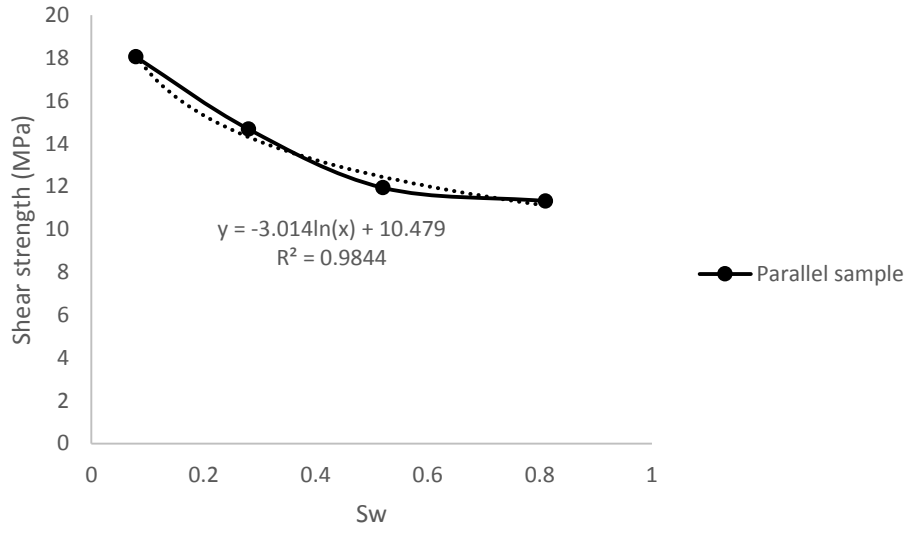

Figure 6-39. Shear strength as a function of water saturation for the interfaces in parallel Montney sample.

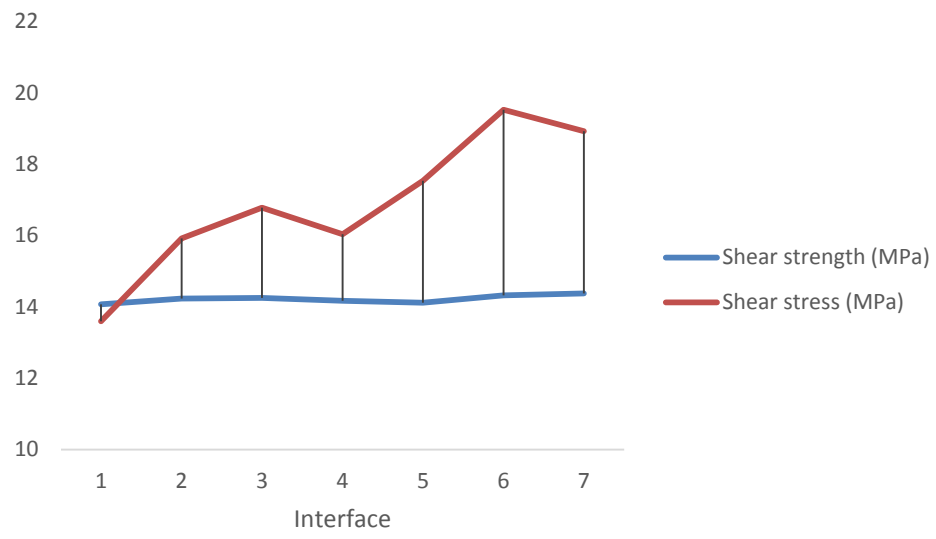

Figure 6-40. Comparing induced shear stress and shear strength values to evaluate the possibility of failure along the interfaces during spontaneous imbibition in parallel Montney sample.

6.2.2. Perpendicular Sample

The procedure for numerical modeling of perpendicular Montney sample was the same as the numerical modeling of spontaneous water imbibition in parallel sample but in this case the beds are horizontal. Since "interface 1" and "interface 18" were very close to the boundaries (shown in Figure 6-27) and the results obtained from them might be affected, the numerical analysis was mainly done for all of the interfaces except "interface 1" and "interface 18". According to the results, once the water front reached to the vicinity of "interface 2" due to the differences in water saturation and capillary suction, local stress development would take place as shown in Figure 6-41. Since the pore volume and capillary suction of the adjacent clay-rich and quartz-rich beds were different the change in water saturation would be different as well. Once the water front reached to the interface between the beds, due to lower porosity and higher capillary suction in clay-rich beds, it would take less time for the clay-rich bed than quartz-rich bed to imbibe a certain volume of water and reach to a certain level of saturation.

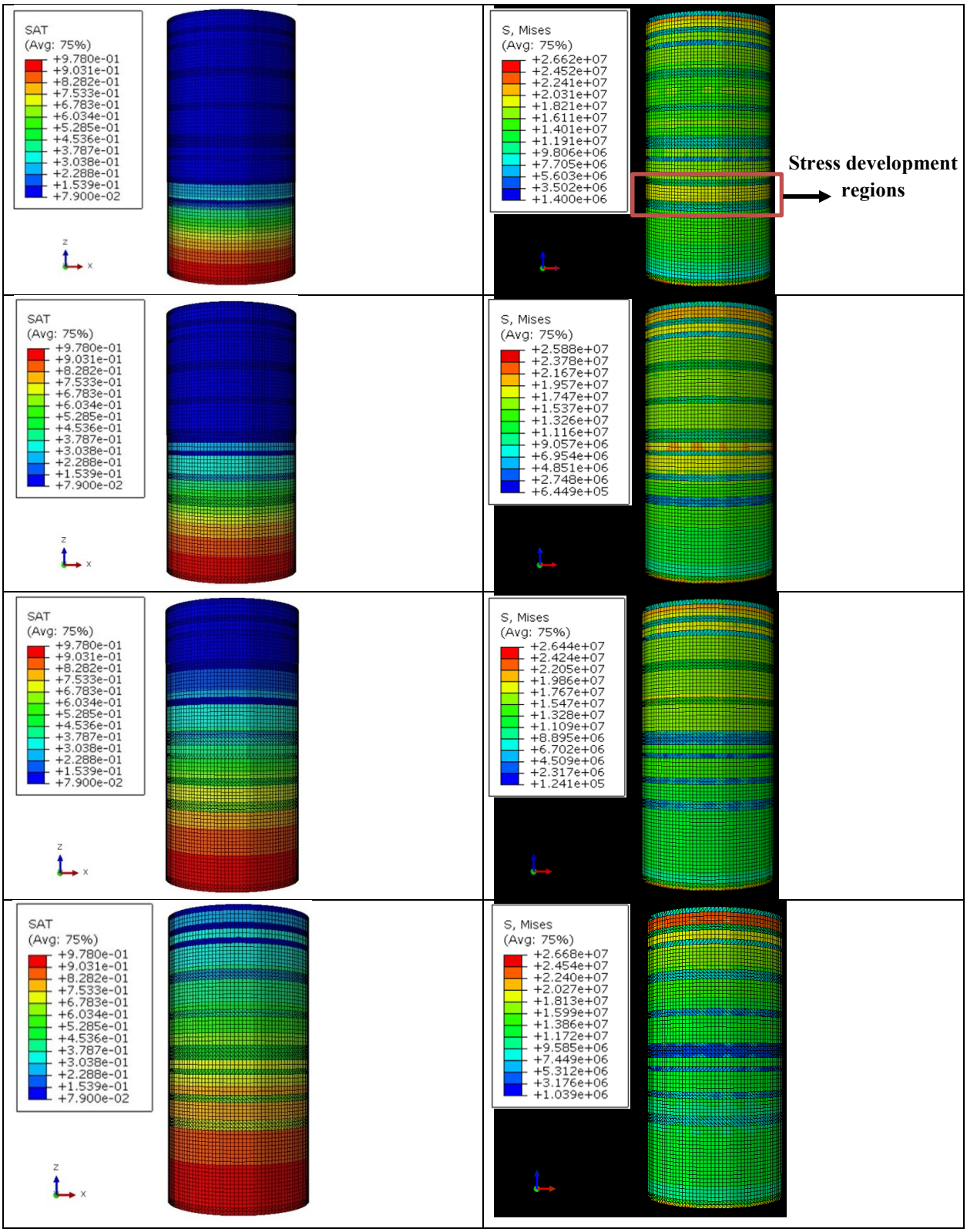

Figure 6-41. Changes in water saturation (on the left) and Mises stress (on the right) in quartz-rich and clay-rich beds during spontaneous water imbibition in perpendicular Montney sample.

In addition, if the water front reached to the interface and the capillary suction of the clay-rich bed was still higher than the initial capillary suction of quartz-rich bed, the water wouldn't enter the quartz-rich bed unless the water saturation in clay-rich bed increased and the capillary suction reached to a value which was lower than the initial capillary suction in quartz-rich bed. Figure 6-42 and Figure 6-43 represent the differential water saturation and capillary suction along each interface originated from different water saturation and capillary suction values of the adjacent quartz-rich and clay-rich beds during spontaneous water imbibition.

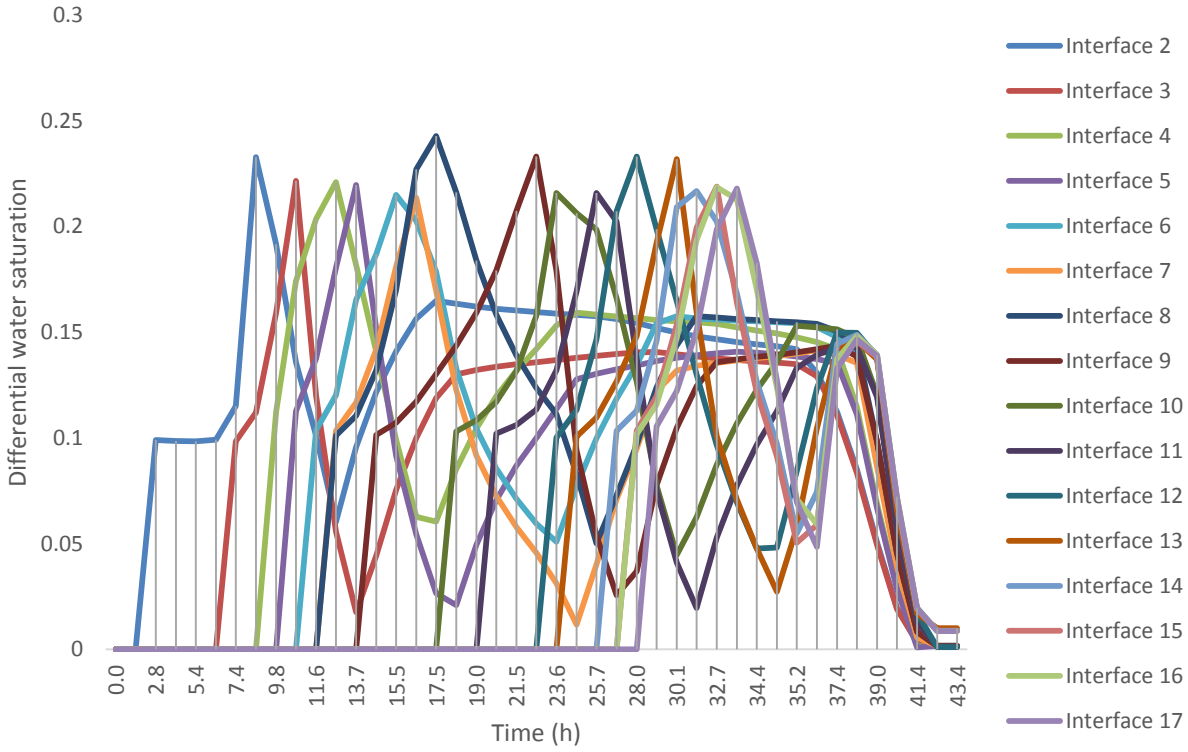

Figure 6-42. Differential water saturation along each interface during spontaneous water imbibition in perpendicular Montney sample.

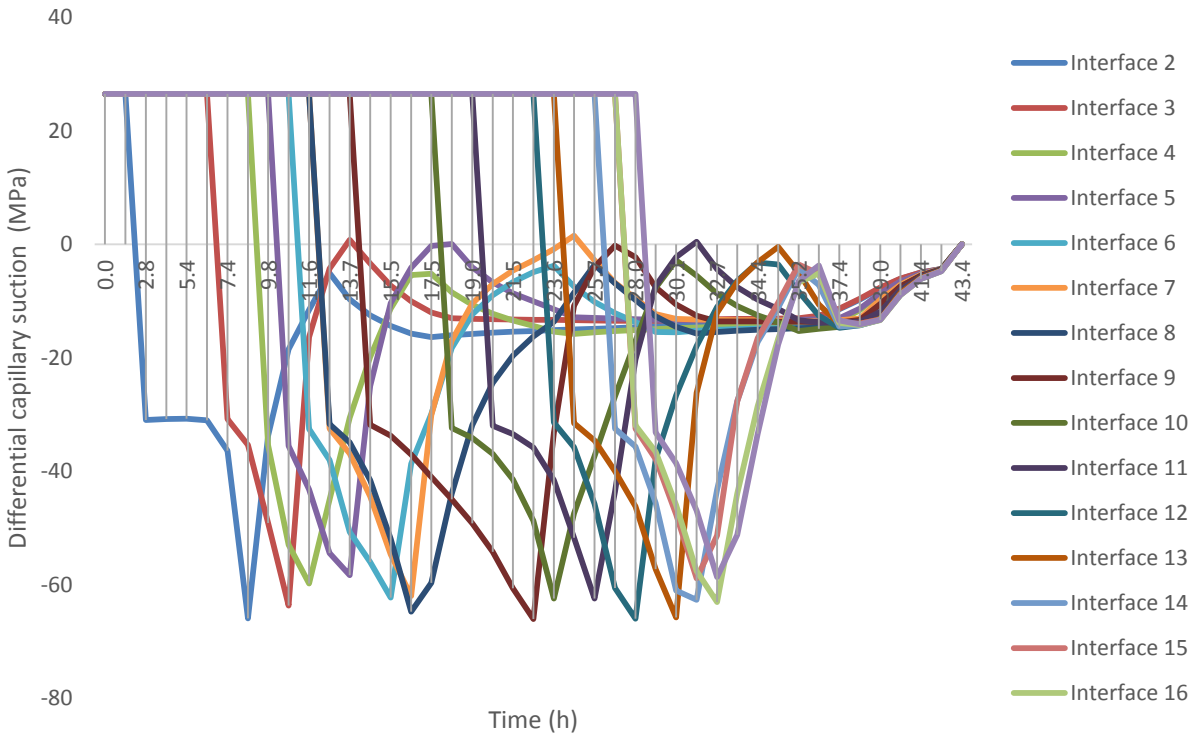

Figure 6-43. Differential capillary suction along each interface during spontaneous water imbibition in perpendicular Montney sample.

As a result of spontaneous water imbibition, the local effective stress in the beds (especially near the interfaces) would change and since these changes as well as changes in rock mechanical properties were not the same in clay-rich and quartz-rich beds it results in different strain responses (as shown in Figure 6-44). Different volumetric responses of the adjacent clay-rich and quartz-rich beds as the imbibition was taking place would results in differential volumetric strain along each interface between the beds shown in Figure 6-45. Based on Figure 6-45, "interface 2", "interface 8", "interface 9", "interface 12", and "interface 13" showed the highest values of differential volumetric strain throughout spontaneous water imbibition in perpendicular Montney sample. These interfaces had also experienced the highest differential water saturation during spontaneous water imbibition (Figure 6-46). Also, these beds were related to the quartz-rich beds with high volumetric portion (thickness). Since quartz-rich and clay-rich beds have different rock mechanical properties, the induced stress in them would be different as a result of loading. This would result in local stress contrast and development of a local stress in the interface between the beds (even before spontaneous imbibition).

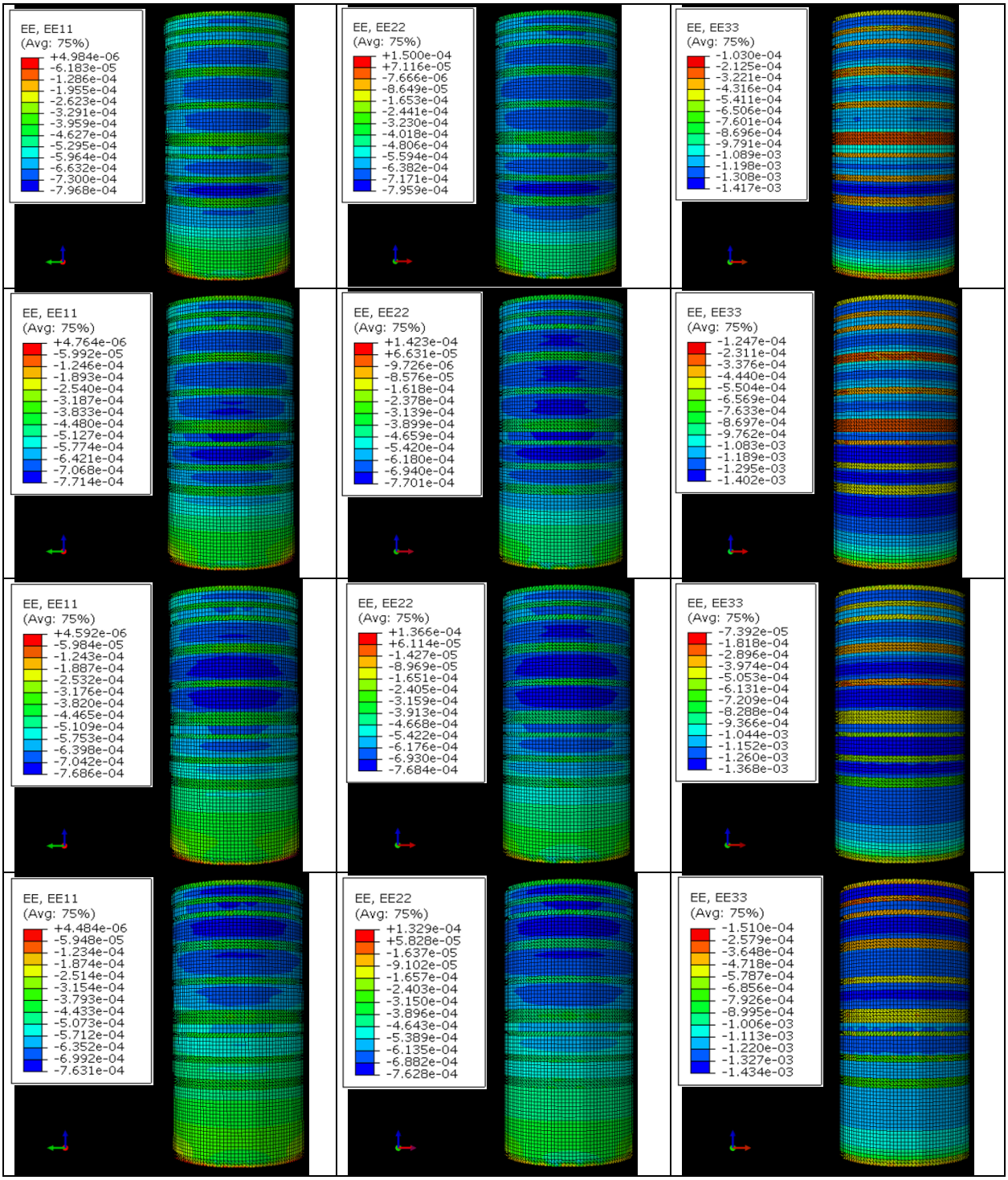

Figure 6-44. Changes in elastic strain values along clay-rich and quartz-rich beds during spontaneous water imbibition in perpendicular Montney sample: E11 (on the left), E22 (in the middle) and E33 (on the right). “1”, “2”and”3” represent “X”, “Y” and “Z” directions.

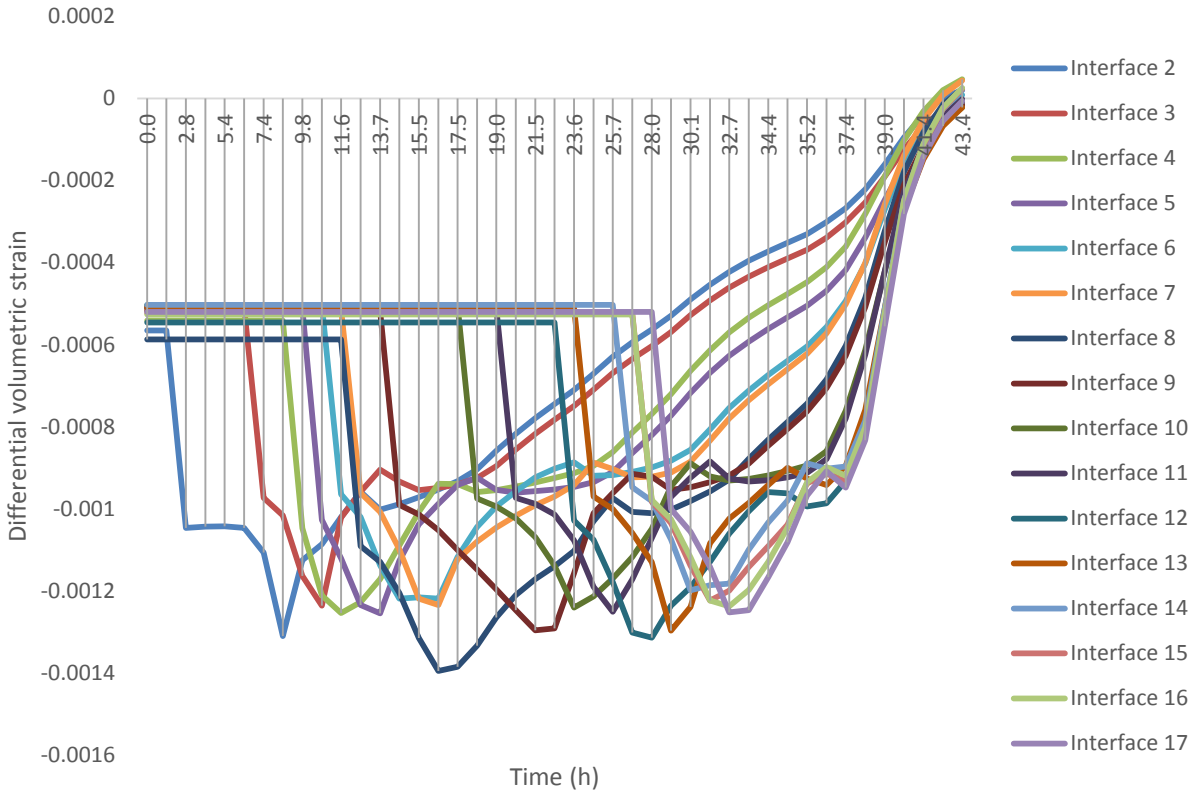

Figure 6-45. Differential volumetric strain along each interface during spontaneous water imbibition in perpendicular Montney sample.

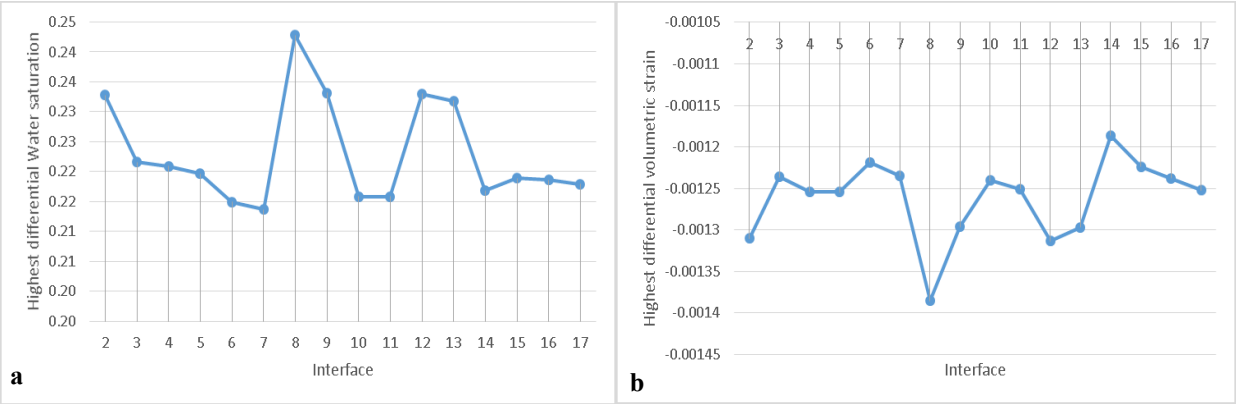

Figure 6-46. a) Highest differential water saturation and b) highest differential volumetric strain in the interfaces during spontaneous water imbibition.

As spontaneous imbibition is taking place, Young's modulus reduction and an increase in Poisson's ratio occur sooner in clay-rich bed leading to the development of an increasing local stress contrast. Higher volumetric portion (thickness) of quartz-rich bed would result in higher local stress contrast followed by higher volumetric strain. The former implies that not only the difference between the volumetric portion of neighboring clay-rich and quartz-rich beds but also the volumetric portion of the quartz-rich bed (as a stiffer part) adjacent to the interface, would play a critical role in generating higher differential volumetric strain values. Differential volumetric strain along each interface would generate induced shear stress components on the interface plane.

In the perpendicular Montney sample, the normal direction relative to the interfaces would be the "Z" direction. Therefore, to find out if any failure along the interfaces happened, total shear stress acting on the interface planes which would be the resultant of S13 (shear stresses in "XZ") and S23 (shear stresses in "YZ" direction) would be considered. Figure 6-47 represents the development of induced S13 and S23 during spontaneous water imbibition in perpendicular Montney sample. Based on Figure 6-47, induced shear stress components were generated near the interfaces which were almost the same for S13 and S23 in each time increment. The former can be attributed to the same confining stress values in "X" and "Y" directions. Figure 6-48, Figure 6-49 and Figure 6-50 illustrate S13, S23 and the resultant shear stress acting on the interface planes between quartz-rich and clay-rich beds as the water was getting imbibed spontaneously.

According to Figure 6-50, induced shear stress values on the interface planes in perpendicular Montney sample were between 17.3MPa and 21.9MPa. The interfaces with the highest induced shear stress values were the same interfaces with the highest differential volumetric strain. The same as parallel sample, as the difference between water saturation degrees and capillary suctions in quartz-rich and clay-rich beds were decreasing, induced shear stress along the interface between the beds diminished. This could be the result of lower differences in local effective stress change in quartz-rich and clay-rich beds which would lead to decreasing differential volumetric strain (as shown in Figure 6-45). The same procedure as the parallel model was followed to determine the shear strength of the interfaces in perpendicular Montney sample (Figure 6-51) and to evaluate the possibility of failure in each interface during spontaneous water imbibition.

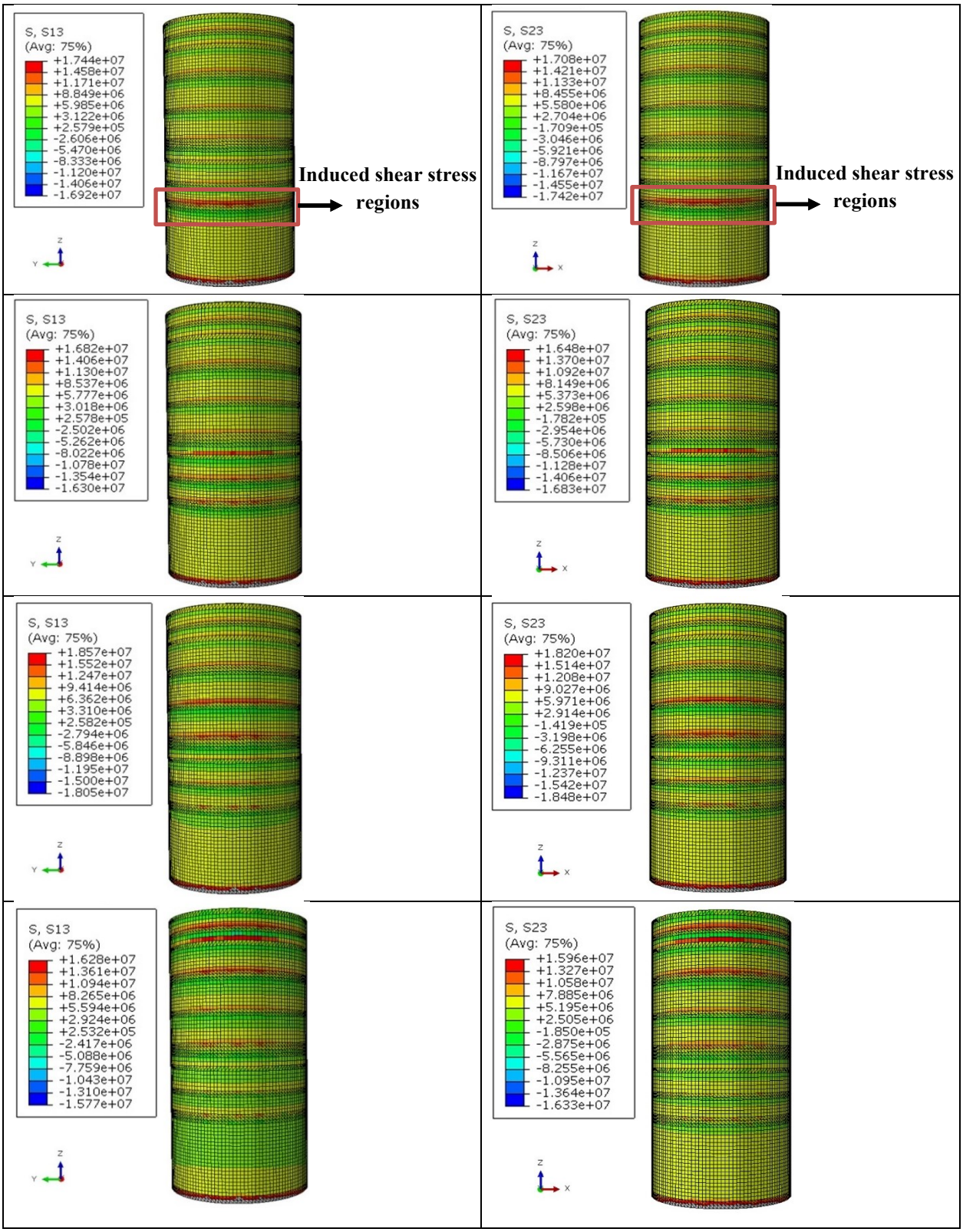

Figure 6-47. Induced shear stress components along the interface between the beds during spontaneous water imbibition in perpendicular sample: S13 (on the left) and S23 (on the right).

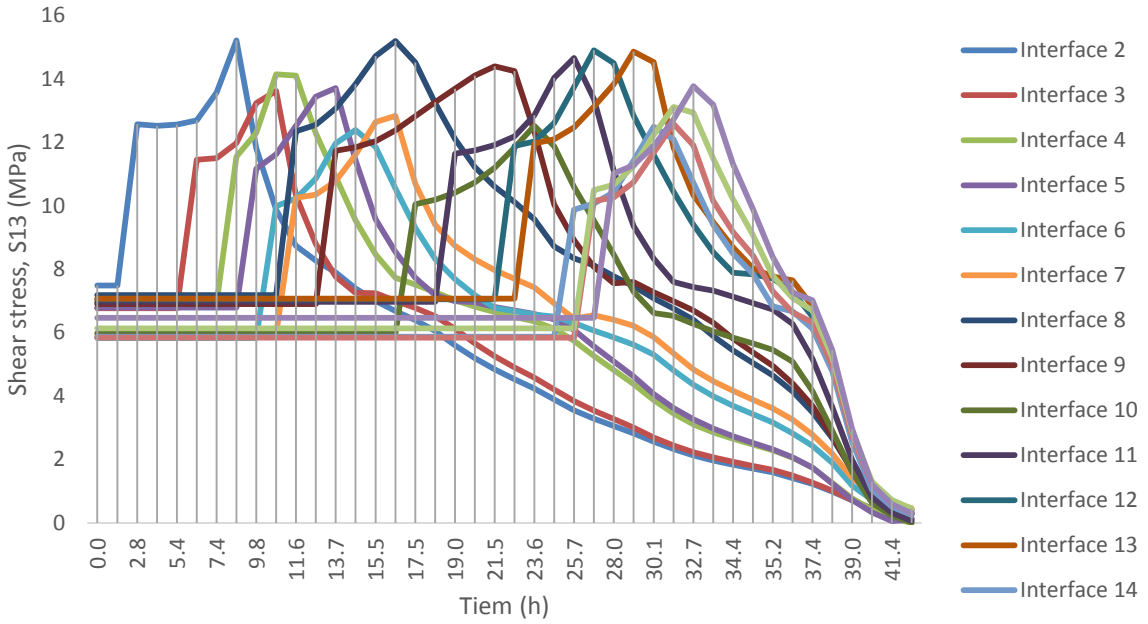

Figure 6-48. Induced S13 along the interfaces between quartz-rich and clay-rich beds during spontaneous water imbibition in perpendicular Montney sample.

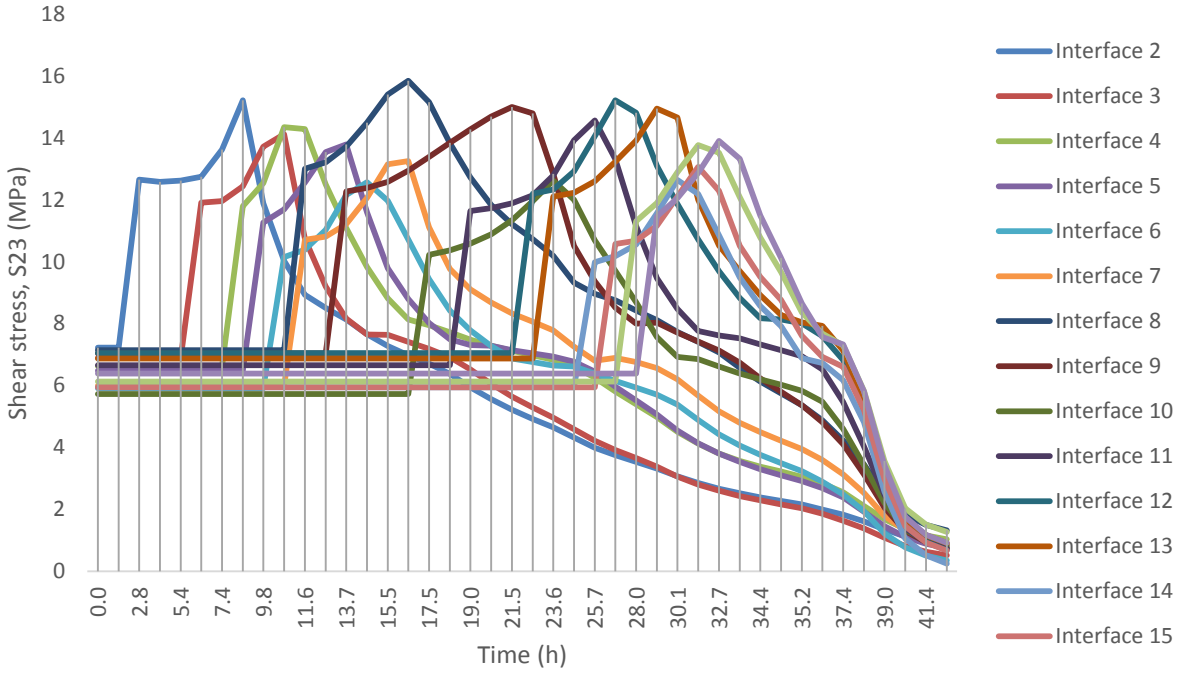

Figure 6-49. Induced S23 along the interfaces between quartz-rich and clay-rich beds during spontaneous water imbibition in perpendicular Montney sample.

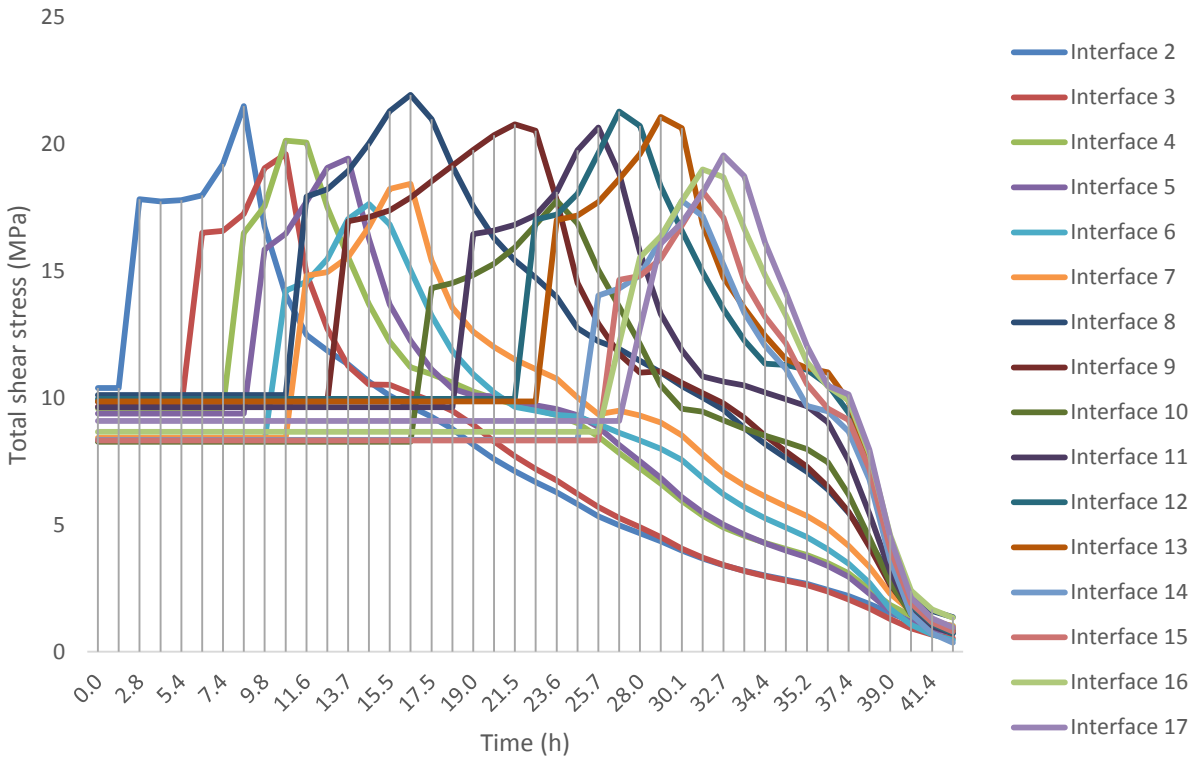

Figure 6-50. Total Induced shear stress along the interfaces between quartz-rich and clay-rich beds during spontaneous water imbibition in perpendicular Montney sample.

According to the values of shear stress obtained for each interface and comparing it with the shear strength values, it was observed that failure would occur in “interface 2”, “interface 8”, “interface 9”, “interface 12” and “interface 13” during spontaneous water imbibition in perpendicular sample at reservoir in-situ stress condition (Figure 6-52). It is worth mentioning that for some other interfaces including “interface 3”, “interface 4” and “interface 5” the values of shear stress and shear strength are very close which implies that there is a great possibility that even these interfaces experience the failure as the water imbibition is taking place at reservoir in-situ stress condition. Basically, there are various parameters that affect the failure in the interface simultaneously including not only the water saturation and capillary suction values in the adjacent beds and changes in beds and interface geomechanical properties but also the difference between the volumetric portion of the adjacent clay-rich and quartz-rich beds as well as the volumetric portion of the quartz-rich bed (as a stiffer part) adjacent to the interface. The failed interfaces are related to the quartz-rich beds with higher volumetric portion. This is consistent with the results of spontaneous water imbibition experiments in Chapter 3 where induced failures were more

highlighted near the thicker quartz-rich beds (Figure 3-40). The former would play a critical role in generating higher differential volumetric strain values and increasing the possibility of failure along the interface.

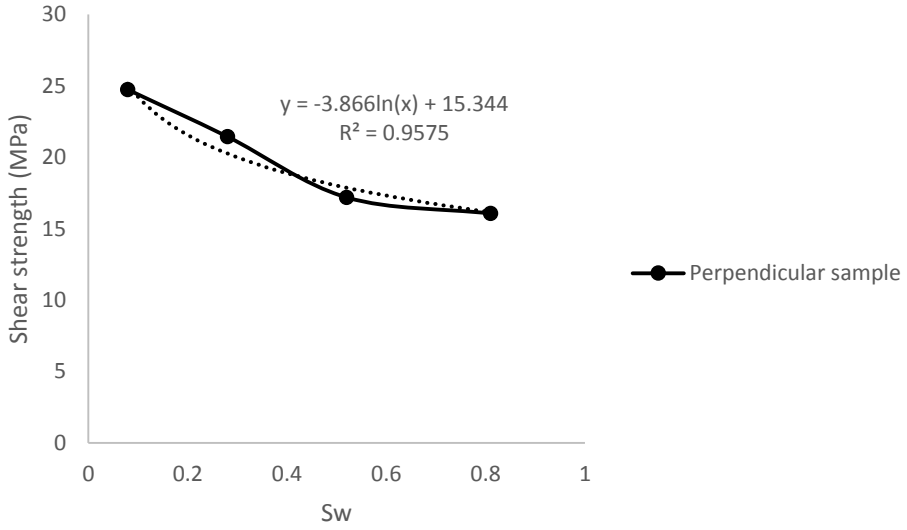

Figure 6-51. Shear strength as a function of water saturation for the interfaces in perpendicular Montney sample.

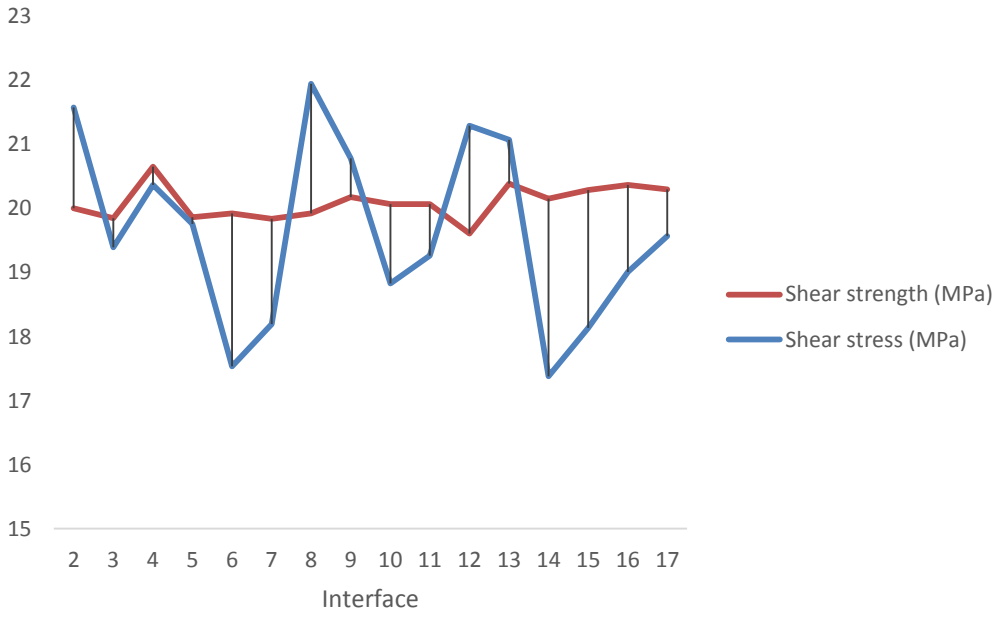

Figure 6-52. Comparing induced shear stress and shear strength values to evaluate the possibility of failure along the interfaces during spontaneous water imbibition in perpendicular Montney sample.

6.3. Summary

Uniaxial compressive loading in high and low capillary suction were done on parallel and perpendicular Montney samples followed by loading-unloading cycle experiments at varying capillary suction to capture Montney geomechanical behaviors. In addition, to investigate the possibility of micro fracture (failures) occurrence at reservoir in-situ stress conditions as a result of post-fracturing spontaneous imbibition in parallel and perpendicular Montney samples, beds-included three-dimensional fully coupled poro-elastoplastic partially saturated finite element models were developed and analyzed.

- In uniaxial compressive loading experiment, increasing the axial stress would lead to accelerating the rate of reduction of the slope in radial stress-strain curves. Therefore, in the later stages before failure, both axial and lateral strain increase quickly with small change in the axial stress which is more obvious in parallel samples.
- For both axial and lateral stress-strain curves the slope decreased with decreasing the capillary suction and the axial stress level under which the failure got initiated was lower in the Montney samples with low capillary suction.
- Comparing the curves related to parallel and perpendicular samples and the onset of accelerating displacement as well as abrupt change in the slope of stress-strain curves would imply that micro failures initiation and propagation would take place in lower axial stresses in parallel samples in comparison with perpendicular samples.
- In both parallel and perpendicular samples as the water saturation increased and capillary suction dropped the strength of the interfaces (as weak planes) reduced significantly which led to triggering more failure initiation and propagation near or along the interfaces between the beds.
- Micro fractures propagation along and in adjacent to the interface between the beds and opening in the lateral direction would lead to higher radial deformation in parallel samples than perpendicular samples at the same capillary suction level.
- UCS values for high and low capillary suction values in perpendicular samples were higher than parallel samples. Also, in high capillary suction UCS were higher than low capillary suction condition.

- The reasons for lower UCS values in low capillary suction can be attributed to increasing the possibility of touching the failure envelope by the Mohr- Coulomb circle as a result of decreasing the cohesion (shift the failure envelop downward) and reducing the effective stress (shift the circle to the left).
- Based on the values of Young's modulus and lateral stiffness at high and low capillary suctions for parallel samples the stress zone of 20-40% peak compressive strength seems to be a better representation of the elastic region to determine the elastic properties while the stress zone of 40-60% peak compressive strength represents to be a better stress region for elastic properties measurements in perpendicular samples.
- Young's modulus and Poisson's ratio of parallel sample in high and low capillary suctions were higher than perpendicular sample. The samples with high capillary suction showed higher Young's modulus and lower Poisson's ratio than the samples with low capillary suction.
- According to the values of Young's modulus and Poisson's ratio for parallel and perpendicular Montney samples at high and low capillary suction levels, it was clearly observed that the behavior of Montney samples would become less brittle as the capillary suction decreased which would suggest the generation of less complex and more planar micro to macro failures and fractures.
- For unloading-reloading experiments, in each capillary suction level there was a hysteresis loop as a result of the unloading-reloading path. In both of the perpendicular and parallel samples as the capillary suction was decreasing, opening of the loop in the unloading-reloading path could be observed which implied that permanent deformations (pre-existing micro fracture propagation or induced micro fractures) occurred at the end of the reloading step.
- The hysteresis in unloading-reloading paths became wider as the capillary suction was decreasing. These observations can be related to volumetric response and softening occurrence followed by the initiation of micro fractures.
- Although considering the unloading and reloading path would reflect the changes in Young's modulus and Poisson's ratio as a result of capillary suction reduction but these changes were not the same in unloading and reloading path which represented a nonlinear response with hysteresis.
- In parallel Montney sample numerical modeling, in each time increment the water saturation of the same elevation in the adjacent clay-rich and quartz-rich beds were different which was

related to the difference between capillary suction values of the beds as a function of water saturation as well as different pore volume and permeability values.

- ❖ According to numerical modeling at in-situ conditions spontaneous water imbibition would result in the change in local effective stress as well as local stress development. This can in turn lead to differential volumetric strain along the interfaces between quartz-rich and clay-rich beds.
- ❖ Differential volumetric strain along each interface would generate induced shear stress components on the interface plane. The interfaces with the highest induced shear stress values were the same as those interfaces with the highest differential volumetric strain.
- ❖ There are various parameters that affect the failure in the interface simultaneously including not only the water saturation and capillary suction values in the adjacent beds (which can affect the local effective stress change) and changes in beds and interface geomechanical properties but also the difference between the volumetric portion of the adjacent clay-rich and quartz-rich beds as well as the volumetric portion of the quartz-rich bed (as a stiffer part) adjacent to the interface. This would play a critical role in generating higher differential volumetric strain values and increasing the possibility of failure along the interface.
- ❖ Comparing the total shear stress along each interface (in the numerical modeling) with the shear strength of it (obtained from the experimental results) indicates that there is a high possibility of the failure occurrence along the interfaces during post-fracturing spontaneous water imbibition at reservoir in-situ stress conditions which can contribute to form a failure/fracture complexity (through coalescence to the pre-existing activated micro fractures) in the imbibed zone.

Chapter 7 : Conclusions and Recommendations

7.1. Conclusions

Hydraulic fracturing to unlock shale plays and tight unconventional reservoirs has been a challenging topic since a large portion of the injected fracturing fluid would remain in the formation. To investigate the effect of the remaining fracturing fluid on the Montney Formation rock properties, an integrated analytical-experimental-numerical workflow was introduced and developed.

- In the first phase of this resarch, experimental and analytical analysis have been performed on Montney samples to investigate the role of spontaneous water imbibition on geomechanical parameters and how the changes may affect the rock behavior. Then, two numerical approaches have been introduced, developed, and analyzed to deal with micro fracture (failure) generation during spontaneous water imbibition in triaxial conditions.
  - According to the results of the experiments, the capillary suction change (as the water content was increasing through a controlled humidity condition) in Montney samples from various depths, was different which implied that different Montney samples from different depths could yield different geomechanical results. Based on spontaneous water imbibition experiments, capillary suction and pre-existing/induced micro fractures were working together for water uptake.
  - Additionally, as the number of beds increased the volume imbibed also increased. Micro fracture generation near the interface between the beds would suggest that most likely the volumetric response of different components (such as beds) as a result of interaction with water might not be the same which could contribute to trigger the failure in the planes of weaknesses (such as the interface between the beds).
  - The rate of reduction in dynamic Young's modulus and shear modulus during spontaneous water imbibition in parallel samples were higher than perpendicular samples. The highest and lowest reduction in dynamic Young's modulus and shear modulus as a result of spontaneous water imbibition were related to the samples with the highest and lowest number of the beds. In addition, as the water content is increasing, dynamic Poisson's ratio parallel and perpendicular to the beds would generally increase which can be attributed to formation of longitudinal and transverse micro fractures followed by more water uptake.

- Brittleness index in both perpendicular and parallel samples were decreasing as the water content was increasing. The former was more highlighted in parallel samples with higher number of beds.
- Based on the results of dynamic changes in rock mechanical properties and converting them to static values for Montney samples from different depths, an analytical approach was applied to evaluate the changes in in-situ stress conditions where a reduction in in-situ stress calculation as a result of considering the effects of spontaneous imbibition was observed.
- From numerical point of view, beds-included numerical approach gives better analysis options than transversely isotropic approach to investigate the failure occurrence during spontaneous water imbibition. Beds-included numerical modeling shows the stress development and any possible failure especially along the interface between the beds (as a result of different water levels and capillary suctions in the adjacent beds) which is not possible to get captured in transversely isotropic approach.
- Based on the results and observations in this phase, one could conclude that as a result of spontaneous water imbibition in Montney samples, rock properties would be affected which could in turn change the rock mass response. Meanwhile, the mechanisms through which rock behavior could be affected would initiate at the beds scale.

❖ In the second phase, to determine the properties in the bed-scale an integrated experimental and analytical approach was applied.

- Based on QEMSCAN analysis the mineralogy and even the mineral sizes in the beds were not the same. Accordingly, the beds could be categorized into quartz-rich beds and clay-rich beds.
- Nitrogen adsorption-desorption isotherm analysis revealed that quartz-rich and clay-rich beds were different in pore size distribution, pore volume and porosity. Also, quartz-rich beds were dominated by slit-like pores and wedge-shaped pores while in clay-rich beds parallel plate shaped pores and slit-like pores were dominant.
- The results of TGA would suggest that initial water saturation in quartz-rich and clay-rich beds were almost the same.

- Capillary condensation experiments indicated that in low water saturation levels the capillary suction in clay-rich beds was higher than quartz-rich beds but as the water saturation was increasing the rate of capillary suction decrease in clay-rich beds was getting higher than quartz-rich beds. This would suggest that the local change in the effective stress in quartz-rich and clay-rich beds as a matter of spontaneous water imbibition would be different. This would lead to different volumetric responses followed by increasing the possibility of failure especially near the interface between the beds.
- The results of pressure-decay and pulse-decay permeability measurements implied that the apparent and absolute permeability for quartz-rich and clay-rich beds are different which can lead to different flow behaviors during spontaneous water imbibition.
- Based on micro-indentation experiments, Young's modulus and Poisson's ratio were higher in quartz-rich beds. After around 60% water saturation the values of Poisson's ratio became higher in clay-rich beds while no significant change was observed in the values of Poisson's ratio for quartz-rich beds.
- Additionally, micro-scratch measurements indicated that initially in low water saturation and high capillary suction, the average internal friction angle, UCS, cohesion and fracture toughness for quartz-rich beds were higher than clay-rich beds. As the water saturation increased these values in both quartz-rich and clay-rich beds decreased significantly but the rate of reduction in quartz-rich and clay-rich beds were different and in most cases it reduced more in clay-rich beds. The results implied that during spontaneous water imbibition clay-rich beds would become weaker in both strength parameters and fracture toughness values in comparison with quartz-rich beds which would suggest that the failure progress and fracture propagation as a result of water imbibition would be most likely from the interface between the beds toward the clay-rich beds rather than quartz-rich beds.
- According to direct shear tests, the strength parameter values of the interface between the beds decreased significantly as the water saturation increased which would imply that the interface between the beds would act as a plane of weakness where the failure could get initiated during spontaneous water imbibition.

- In the next phase of the research, since the scale of the beds were very small (millimeter or less) to capture the mechanisms while the sample was under loading, small size samples (1cmx2cm) were considered.
  - Loading tests on small size samples (5-25mm in diameter) with maximum 10mm axial strain could be performed by the mini-cell while it was able to withstand up to 70MPa confining pressure and pore pressure.
  - The mini-cell was equipped with a stepper motor which was connected to a controlling box where the exact rate of displacement could be achieved.
  - Applying LFH-7I load cell with high capacity and accuracy and GeoREF data logger software enabled the mini-cell to capture the load accurately at any loading step.
  - The mini-cell was capable of doing the tests with strain gauge since a Wheatstone bridge circuit with amplifier interface was designed and built for the mini-cell.
  - The performance of the mini-cell was tested by 3D printed samples and Berea sandstones where there was a good agreement between the results of the tests done by mini-cell and other studies results.
  - For Montney samples the LVDT didn't return the expected strain values but the strain gauge-based results were more reasonable.
  - One of the main advantages of applying the mini triaxial cell was that it was applicable to explain and study the basic mechanisms which were taking place in small scale (e.g. bed-scale) but would affect the rock mass properties.
  - Applying the mini triaxial cell can answer the question of how the rock mass behavior can be affected as a result of smaller scale responses and what are the mechanisms behind those responses.

- In the final phase of the research, geomechanical responses of small size Montney samples (1cm x 2cm) while the sample was under loading and controlled capillary suction and water saturation change, were investigated. To do so, the loading experiments were done in a humidity-controlled loading setup by mini-cell. Uniaxial compressive loading in high and low capillary suction were done on parallel and perpendicular Montney samples followed by loading-unloading cycle experiments at varying capillary suction to capture Montney geomechanical behaviors. In addition, to investigate the possibility of micro fracture (failures)

occurrence at reservoir in-situ stress conditions as a result of post-fracturing spontaneous imbibition in parallel and perpendicular Montney samples, beds-included three-dimensional fully coupled poro-elastoplastic partially saturated finite element models were developed and analyzed.

- According to the results of uniaxial compressive loading in high and low capillary suction, for both axial and lateral stress-strain curves the slope decreased with decreasing the capillary suction and the axial stress level under which the failure got initiated was lower in the Montney samples with low capillary suction. Comparing the curves related to parallel and perpendicular samples and the onset of accelerating displacement as well as abrupt change in the slope of stress-strain curves would imply that micro failures initiation and propagation would take place in lower axial stresses in parallel samples in comparison with perpendicular samples. In both parallel and perpendicular Montney samples as the water saturation increased and capillary suction dropped, the strength of the interfaces (as weak planes) reduced significantly which led to triggering more failure initiation and propagation near or along the interfaces between the beds.
- Uniaxial compressive strength values for high and low capillary suctions in perpendicular samples were higher than parallel samples. Also, in high capillary suction pressure uniaxial compressive strength were higher than low capillary suction pressure condition which could be related to increasing the possibility of touching the failure envelope by the Mohr-Coulomb circle as a result of decreasing the cohesion (shift the failure envelop downward) and reducing the effective stress (shift the circle to the left).
- Based on the values of Young's modulus and lateral stiffness at high and low capillary suctions for parallel Montney samples the stress zone of 20-40% peak compressive strength seems to be a better representative of the elastic region to determine the elastic properties while the stress zone of 40-60% peak compressive strength shows to be a better stress region for elastic properties measurements in perpendicular Montney samples.
- Young's modulus and Poisson's ratio of parallel sample in high and low capillary suctions were higher than perpendicular sample. The samples with high capillary suction showed higher Young's modulus and lower Poisson's ratio than the samples with low capillary suction.

- According to the values of Young's modulus and Poisson's ratio for parallel and perpendicular Montney samples at high and low capillary suction levels, it was observed that the behavior of Montney samples would become less brittle as the capillary suction decreased which would suggest the generation of less complex and more planar micro to macro failures and fractures.
- For unloading-reloading experiments, in each capillary suction level there was a hysteresis loop as a result of the unloading-reloading path. In both of the perpendicular and parallel samples, as the capillary suction was decreasing, opening of the loop in the unloading-reloading path could be observed which could be an indication of permanent deformations. The hysteresis in unloading-reloading paths became wider as the capillary suction was decreasing. These observations could be related to volumetric response and softening occurrence followed by the initiation of micro fractures or propagation of the pre-existing micro fractures especially those which were aligned with the loading direction.
- Although considering the unloading and reloading path would reflect the changes in Young's modulus and Poisson's ratio as a result of capillary suction reduction but these changes were not the same in unloading and reloading path which represented a nonlinear response with hysteresis. This nonlinear response came from the volumetric responses and initiation/propagation of micro fractures as the capillary suction dropped during wetting phase. The former would suggest the activation/propagation of pre-existing micro fractures as a result of water softening.
- In parallel Montney sample numerical modeling, in each time increment the water saturation of the same elevation in the adjacent clay-rich and quartz-rich beds were different which was related to the difference between capillary suction values of the beds as a function of water saturation as well as different pore volume and permeability values.
- Based on the results of numerical modeling at in-situ conditions spontaneous water imbibition would result in a change in local effective stress and rock mechanical properties in the beds. This can in turn lead to differential volumetric strain along the interfaces between quartz-rich and clay-rich beds. Meanwhile, differential volumetric strain along each interface would generate induced shear stress components on the interface plane. The interfaces with the highest induced shear stress values were the same interfaces with the highest differential volumetric strain.

- According to the numerical modeling results of spontaneous water imbibition on both parallel and perpendicular Montney samples, not only water saturation and capillary suction values in the adjacent beds (which can affect the local effective stress change) but also changes in beds and interface geomechanical properties, the difference between the volumetric portion of the adjacent clay-rich and quartz-rich beds and the volumetric portion of the quartz-rich bed (as a stiffer part) adjacent to the interface, would play a critical role in generating higher differential volumetric strain values and increasing the possibility of failure along the interface.

❖ Finally, comparing the result of a) micro-geomechanical analysis at the bed scale (which suggests different weakening responses in quartz-rich and clay-rich beds), b) loading-unloading experiments at varying capillary suction (which shows the activation and propagation of the pre-existing micro fractures) and c) the results of beds-included numerical modeling at reservoir in-situ conditions (which indicate the failure along the interface between the beds) would suggest that as a result of post-fracturing spontaneous water imbibition in the studied Montney Formation, the failures/micro fractures would be generated along the interfaces. Then, the induced failures/micro fractures most likely coalesced to the pre-existing neighboring activated micro fractures which at the end of the day would form a complex micro fracture network. This can affect the rock mass properties in the reservoir and also can lead to increasing the local permeability followed by production increase.

❖ From reservoir analysis point of view, ignoring the changes in rock mechanical and capillary suction as a result of spontaneous imbibition would lead to miscalculations in stress measurements and fracture geometry/propagation prediction as well as stress shadowing analysis. Also, according to the results obtained, geomechanical analysis of spontaneous imbibition in tight bedded-structure rocks needs to be revisited and conventional transversely isotropic approach would not yield accurate results especially when it comes to failure occurrence analysis. In other words, if the rock mass properties would be affected within or after fracturing then any numerical modeling or analytical approach to account for the production, refracturing, frac hit analysis and any other reservoir-related analysis without considering this fact is under question mark.

7.2. Recommendations

The recommendations would be mainly related to experimental phases.

- Generally strain gauges were applied in this study to capture the strain values in Montney samples. Although this approach yielded good results but dealing with strain gauge on the samples coming from tight unconventional reservoirs would be challenging since during the sample preparation for attaching the strain gauge on the sample, pre-conditioning chemicals should be applied after each phase of surface polishing. The strain gauge should be attached to the sample by glue which would locally enter the sample and might change the wettability. For example, as shown in Figure 7-1, in one of the Montney samples, as a result of applying excess pre-conditioning chemicals followed by applying glue, the sample didn't absorb water in that affected region. Therefore, it is very critical to apply the pre-conditioning chemicals and the glue cautiously.

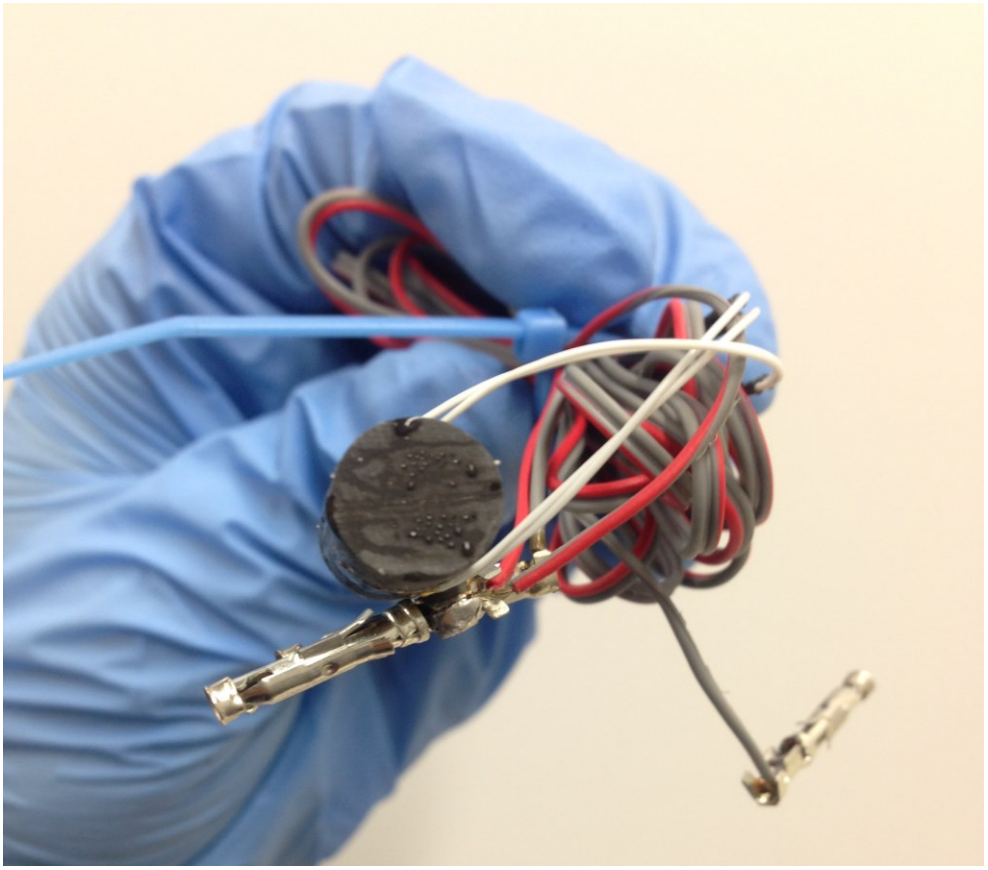

Figure 7-1. How applying excessive pre-conditioning chemicals and glue may affect the rock properties (e.g. wettability).

❖ Meanwhile, the thickness of the glue where the strain gauge would sit on play an important role to capture the acceptable results. If the thickness of glue is high, it would give extra stiffness and strength to the sample. For example, in Figure 7-2 which was related to a dry perpendicular sample with higher thickness of glue the strain gauge results returned a higher Young's modulus value (the test was canceled before failure).

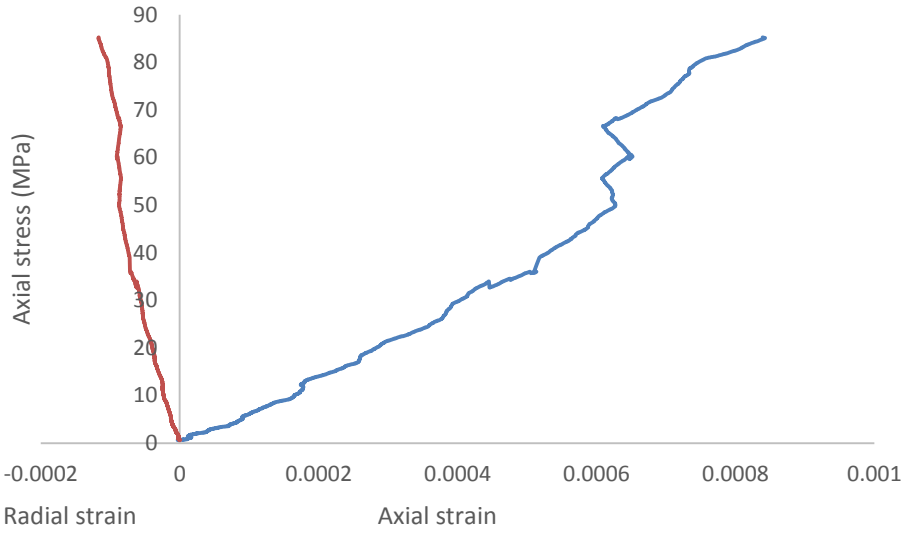

Figure 7-2. Results related to strain gauges with higher glue thickness.

Also, if the glue is not properly applied the strain gauge it would return some messy results (Figure 7-3). Alternatives such as fiber optics, ultra-high-speed and high-accuracy laser displacement sensor as well as camera-based volume determination system could be considered as a substitution for strain gauge or LVDT in the mini-cell testing.

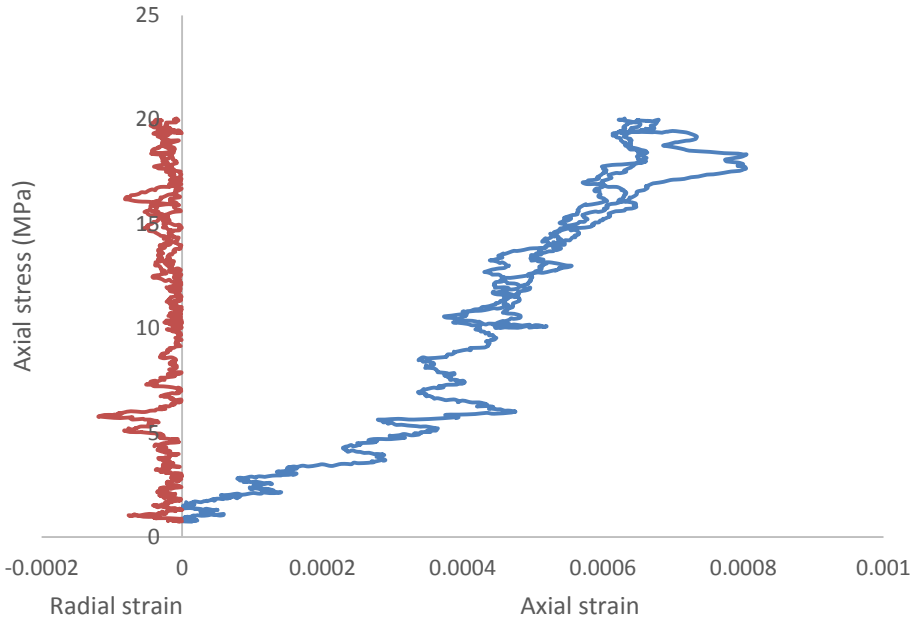

Figure 7-3. Results related to the strain gauges with glue which was not properly applied on sample surface.

7.2.1. Future work

- Investigating the role of post-fracturing spontaneous imbibition on refracturing in a form of numerical modeling or experimental studies.
- Detailed experimental procedures to study the optimum micro-indentation loading rate and micro-scratch cutting rate to get a better micro-geomechanical analysis.
- Working on fiber optics, ultra-high-speed and high-accuracy laser displacement sensor as well as camera-based volume determination system as the options for the strain measurements in the mini-cell.
- Performing triaxial spontaneous water imbibition experiments on Montney samples by mini-cell.
- Studying the effect of post-fracturing spontaneous water imbibition on rock mass properties in a reservoir-scale through numerical modeling.
- Investigating the effect of temperature to on post-fracturing spontaneous imbibition in the Montney formation.

Chapter 8 : References

Abaqus. (2017). Abaqus Analysis User's Manual. Dassault Systemes Simulia Corp., Providence, RI, USA.

Abedi-Koupai, J. and Mehdizadeh, H. (2008). Estimation of Osmotic Suction from Electrical Conductivity and Water Content Measurements in Unsaturated Soils. *Geotechnical Testing Journal, 31*(2): 142-148.

Acar, M. C. , Gündüz, Z. & KARA, H. B. (2014).Modulus of Elasticity Determination of Rocks Using Comressometer, Strain Gauge and Lvdt. ACE 2014 11'th International Congress on Advances in Civil Engineering, Turkey, Istanbul, 21-25 October.

Ahmad, KM., Kristály, F., Turzo, Z. (2018). Effects of clay mineral and physico-chemical variables on sandstone rock permeability. *J Oil Gas Petrochem Sci*. *1*(1): 18-26.

Ahmad, M., & Haghighi, M. (2012). Mineralogy and Petrophysical Evaluation of Roseneath and Murteree Shale Formations, Cooper Basin, Australia Using QEMSCAN and CT Scanning. SPE Asia Pacific Oil and Gas Conference and Exhibition, Perth, Australia, 22-24 October.

Agrawal, S., & Sharma, M. M., (2013). Impact of Liquid Loading in Hydraulic Fractures on Well Productivity. Paper SPE-1638837-MS presented at SPE Hydraulic Fracturing Technology Conference, The Woodlands, Texas, USA, 4-6 February.

Akai, T., Wood, J.M., Otomo, C., Hanyu, A., & Okada, K. (2014). Observation of nano-scale pore structure in a tight gas siltstone reservoir. *Journal of The Japanese Association for Petroleum Technology, 79*, 428-433.

Akono, A.T. & Ulm, F.J. (2012). Fracture scaling relations for scratch tests of axisymmetric shape. *J Mech Phys Solids*, *60*(3):379–390.

Akrad, O., Miskimins, J. and Prasad, M. (2011). The Effects of Fracturing Fluids on Shale Rock Mechanical Properties and Proppant Embedment. SPE Annual Technical Conference and Exhibition held in Denver, Colorado, USA, 30 October–2 November.

Aksu, I., Bazilevskaya, E., Karpyn, ZT. (2015). Swelling of clay minerals in unconsolidated porous media and its impact on permeability. *Geo ResJ*. 7:1−13.

Amann, F., Kaiser, P.K. & Button, E.A. (2012). Experimental Study of the Brittle Behavior of Clay Shale in Rapid Confined Compression. *Rock Mechanics Rock Engineering*, *44*(1): 21–33.

Amann, F., Wild, K. & Wymann, L. (2014). Dependency of Deformability, Strength and Failure Characteristics of Clay Shales on Total Suction. EUROCK 2014, ISRM European Regional Symposium, Vigo, Spain, 26-28 May.

Amanna, F., Martinb,C.D. & Wild, K.M. (2015). The Role of Capillary Suction and Dilatancy on the Interpretation of the Confined Strength of Clay Shales. ISRM 2015 - Shale Symposium, Montreal, May 10-13.

Ambrose, J. (2014). Failure of Anisotropic Shales under Triaxial Stress Conditions. PhD Thesis, Department of Earth Science and Engineering, Imperial College, London.

Anderson, R. L., Ratcliffe, I., Greenwell, H. C., Williams, P. A., Cliffe, S., & Coveney, P. V. (2010). Clay swelling—A Challenge in the Oilfield. *Earth-Science Reviews*, *98*(3), 201-216.

Andreev, G.E. (1995). Brittle Failure of Rock Materials: Test Results and Constitutive Models. Brookfield Press: Rotterdam, Netherlands.

Anovitz, LM and Cole, DR. (2015). Characterization and Analysis of Porosity and Pore Structures. Reviews in Mineralogy & Geochemistry, 80: 61-164.

Ashrafi Moghadam, A. (2016). Analytical and Experimental Study of Gas Flow Regime in the Matrix and Fractures of Shale Gas Reservoirs. PhD Thesis, The University of Alberta, Canada.

ASTM International. (2019). Standard Test Methods for Laboratory Determination of Water (Moisture) Content of Soil and Rock by Mass. D2216-19, West Conshohocken, PA.

ASTM International. (2016). Standard Test Method for Performing Laboratory Direct Shear Strength Tests of Rock Specimens Under Constant Normal Force. D5607-16, West Conshohocken, PA.

ASTM International. (2014). Standard test methods for compressive strength and elastic moduli of intact rock core specimens under varying states of stress and temperatures. D7012–14. West Conshohocken, PA.

ASTM International. (2007). Standard Practice for Instrumented Indentation Testing. E2546–07, West Conshohocken, PA.

Bai, M. (2016). Why are brittleness and fracability not equivalent in designing hydraulic fracturing in tight shale gas reservoirs. *Petroleum, 2*, 1-19.

Barrett, EP., Joyner, LG. & Halenda, PP.(1951). The determination of pore volume and area distributions in porous substances. I. Computations from nitrogen isotherms. *J Am Chem Soc*, *73*:373–380.

Barsotti, E., Tan, S., Saraji, S., Piri, M., & Chen, J. (2016). A review on capillary condensation in nanoporous media: Implications for hydrocarbon recovery from tight reservoirs. *Fuel, 184*, 344-361.

Batzle, M., Duranti, L., Rector, J., & Pride, S. (2007). Measurement and interpretation of seismic attenuation for hydrocarbon exploration. Technical Report No. FC26-04NT15505.

Bertoncello, A., Wallace, J., Blyton, C., Honarpour, M. M., and Kabir, S. 2014. Imbibition and Water Blockage in Unconventional Reservoirs: Well-Management Implications During Flowback and Early Production. *SPE Reservoir Evaluation & Engineering*, *17* (4): 497-506.

Bishop A.W. (1959). The Principle of Effective Stress. *Teknisk ukeblad*, *106* (39): 859-863.

Bostrom, N., Chertov, M., Pagels, M., Willberg, D., Chertova, A., Davis, M., & Zagorski, W. (2014). The Time-Dependent Permeability Damage Caused by Fracture Fluid. SPE International Symposium and Exhibition on Formation Damage Control, 26-28 February, Lafayette, Louisiana, USA.

Button, V.L. (2015). Principles of measurement and transduction of biomedical variables. Amsterdam: Elsevier.

Cabrera Nunez, J., Beaucaire, C., Bruno, G., De Windt, L., Genty, A., Ramambasoa, N., Rejeb, A., Savoye, S., & Volant, P. (2001). Projet Tournemire: synthe`se des programmes de recherché 1995/1999. Rapport IPSN, 202 pp.

Caenn, R., Darley, H.C.H., Gray, G.R. (2011). Clay Mineralogy and the Colloid Chemistry of Drilling Fluids. Composition and Properties of Drilling and Completion Fluids (Sixth Edition), pp: 137-177.

Campbell, C.V. (1967). Lamina, Laminaset, Bed and Bedset. *Sedimentology, 8*: 7-26.

Camuffo, D. (1984). CONDENSATION-EVAPORATION CYCLES IN PORE AND CAPILLARY SYSTEMS ACCORDING TO THE KELVIN MODEL. *Water, Air and Soil Pollution*, *21*:151-159.

Chen, X., Yi, H., Gao, L., Shi, X., & Liu, Y. (2020). Effects of inhibitor KCl on hydration swelling and softening of a smectite-poor mudstone. *Journal of Petroleum Exploration and Production Technology*, *10*: 2685 - 2692.

Chen, S., Zuo, Z., Moore, T.A., Han, Y. & Uwamahoro, C. (2018). Nanoscale Pore Changes in a Marine Shale: A Case Study Using Pyrolysis Experiments and Nitrogen Adsorption. *Energy & Fuels* , *32*(9): 9020-9032.

Cheng, Y. (2012). Impact of Water Dynamics in Fractures on the Performance of Hydraulically Fractured Wells in Gas-Shale Reservoirs. *J. of Can. Pet. Technol. 51* (2): 143-151. SPE-127863-PA.

Chong, K.K., Grieser, W.V., Passman, A., Tamayo, H.C., Modeland, N., & Burke, B. (2010). A Completions Guide Book to Shale-Play Development: A Review of Successful Approaches toward Shale-Play Stimulation in the Last Two Decades. Canadian Unconventional Resources and International Petroleum Conference, Calgary, Alberta, Canada, 19–21 October.

Clarkson, C. R., Wood, J., Burgis, S., Aquino, S., & Freeman, M. (2012a). Nanopore-Structure Analysis and Permeability Predictions for a Tight Gas Siltstone Reservoir by Use of Low-Pressure Adsorption and Mercury-Intrusion Techniques. *Reservoir Eval Eng*,*15*(6):648–661.

Clarkson, C.R., Jensen, J.L., Pedersen, P.K. & Freeman, M. (2012b). Innovative Methods for Flow Unit and Pore Structure Analysis in a Tight Siltstone and Shale Gas Reservoir. *AAPG Bulletin*, *96*(2): 355-374.

Cosenza, P., Ghoreychi, M., de Marsily, G., Vasseur, G. & Violette, S. (2002). Theoretical Prediction of Poroelastic Properties of Argillaceous Rocks from In Situ Specific Storage Coefficient. *Water Resour Res, 38* (10): 25-1–25-12.

Cottin, C., Bodiguel, H. and Colin, A. (2010). From Capillary Fingering to Viscous Flow in Two-Dimensional Porous Media: Role of the Wetting Properties. Multiflow 2010, Bruxelles 8-10 November.

Dagrain, F. (2001). Infuence of the Cutter Geometry in Rock Cutting: An Experimental Approach. PhD Thesis. The University of Minnesota. USA.

Dehghanpour, H., Lan, Q., Saeed, Y., Fei, H., & Qi, Z. (2013). Spontaneous imbibition of brine and oil in gas shales: Effect of water adsorption and resulting micro fractures. *Energy & Fuels*, *27*(6): 3039–3049.

Dehghanpour, H., Zubair, H. A., Chhabra, A., & Ullah, A. (2012). Liquid Intake of Organic Shales. Energy *& Fuels*, 26(9): 5750-5758.

Detournay, E. (2014). Determination of Shear Strength of Rocks from Scratch Tests: Theoretical Justification. American Geophysical Union, Fall Meeting, San Francisco, USA, 15-19 December.

Ding, Y., Liu, X., & Luo, P. 2020. The Analytical Model for Horizontal Wellbore Stability in Anisotropic Shale Reservoir. *Geotechnical and Geological Engineering*, 1-18.

Dusseault, M.B.; Loftsson, M.; Russell, D. (1986). The mechanical behavior of the Kettle Point oil shale. *Can. Geotech. J.*, *23*: 87–93.

Dutta, R., Lee, C.-H., Odumabo, S., Ye, P., Walker, S.C., Karpyn, Z.T., Ayala, L.F. (2014). Experimental investigation of fracturing-fluid migration due to spontaneous imbibition in fractured low-permeability sands. *SPE Reserv. Eval. Eng*. *17* (1): 74-81.

Dyke, C.G., Dobereiner, L., (1991). Evaluating the strength and deformability of sandstones. *Q. Eng. Geol*. *24*: 123–134.

Economides, M. J. and Nolte, K. G. (2000). Reservoir Stimulation, third edition. New York: John Wiley and Sons, Ltd.

Ehlig-Economides, C. A., & Economides M. J. (2011). Water As Proppant, SPE Annual Technical Conference and Exhibition, Denver, Colorado, USA, 30 October-2 November.

Eitzenberger A (2012) Wave propagation in rock and the influence of discontinuities. Doctoral Thesis, Luleal University of Technology, Sweden.

Engelder, T.; Cathles, L.M.; Bryndzia, L.T. (2014). The fate of residual treatment water in gas shale. *Journal of Unconventional Oil and Gas Resources*, *7*: 33-48.

Fairhurst, C. (2014). The Scratch Test — An Innovative and Inexpensive Method to Determine the Compressive Strength and Mohr-Coulomb Failure Envelope for Sedimentary Rock. ISRM International Symposium - 8th Asian Rock Mechanics Symposium, 14-16 October, Sapporo, Japan.

Fan, L., Thompson, J.W., & Robinson, J.R. (2010). Understanding Gas Production Mechanism and Effectiveness of Well Stimulation in the Haynesville Shale Through Reservoir Simulation. Canadian Unconventional Resources and International Petroleum Conference, Calgary, Alberta, Canada, 19-21 October.

Fauria, K.E., Rempel, A.W. (2011). Gas invasion into water-saturated, unconsolidated porous media: Implications for gas hydrate reservoirs. *Earth and Planetary Science Letters*, *312*: 188–193.

Fink, R., Krooss, B.M., Amann-Hildenbrand, A. (2017). Stress-dependence of porosity and permeability of the Upper Jurassic Bossier shale: an experimental study. From: Rutter, E. H., Mecklenburgh, J. & Taylor, K. G. (eds) Geomechanical and Petrophysical Properties of Mudrocks. Geological Society, London.

Fjær, E., Holt, R.M., & Horsrud, P. (2008). Petroleum Related Rock Mechanics, Elsevier, 2nd edition.

Frederic, L.P., Geraldine, F. (2007). Damage Evaluation with P-Wave Velocity Measurements during Uniaxial Compression Tests on Argillaceous Rocks. *International Journal of Geomechanics*, *7*(6): 431-436

Fredlund D.G., Morgenstern N.R. and Widger A. (1978). Shear strength of unsaturated soils. *Canadian Geotechnical Journal. 15*: 313-321.

Fredlund, D.G. and Rahardjo, H. (1993). Soil mechanics for unsaturated soils. John Wiley & Sons: New York.

Fredlund, D.G., Xing, A., Fredlund, M.D., and Barbour, S.L. (1995). The relationship of the unsaturated soil shear strength function to soil-water characteristic curve. *Canadian Geotechnical Journal, 32*: 440–448.

Fredlund, D.G. and Vanapalli, S.K. (2002). Shear strength of unsaturated soils. *Agronomy Soil Testing Manual, Agronomy Society of America*, Madison, 329–361.

Friedheim, J., Guo, Q., Young, S., and Gomez, S. (2011). Testing And Evaluation Techniques For Drilling Fluids-Shale Interaction And Shale Stability. 45th U.S. Rock Mechanics / Geomechanics Symposium, 26-29 June, San Francisco, California.

Ghanbari, E., Abbasi, M., Dehghanpour, H., Bearinger, D. (2013). Flowback Volumetric and Chemical Analysis for Evaluating Load Recovery and Its Impact on Early-Time Production. Unconventional Resource Conference, Calgary, Canada, 5-7 November.

Ghanizadeh,A., Clarkson, C.R., Vahedian,A., Aquino,S., Ardakani, O.H., Wood, J.M., Sanei,H. & Riazi, N. (2016). Petrophysical, geomechanical and geochemical characteristics of the Montney Formation: Implications for hydrocarbon storage and transport. Geo-Convention, Calgary, Alberta, Canada, 7-11 March.

Ghanizadeh, A., Bhowmik, S., Haeri-Ardakani, O., Sanei, H. & Clarkson, C.R. (2015). A Comparison of Shale Permeability Coefficients Derived Using Multiple Non-steady-state Measurement Techniques: Examples from the Duvernay Formation, Alberta (Canada). *Fuel*, *140*: 371-387.

Ghanizadeh, A. 2013. Experimental Study of Fluid Transport Processes in the Matrix System of Organic-rich Shales. PhD Thesis, RWTH Aachen University.

Gomez, J.S. (2017). Mechanical Properties Characterization of 3D Printed Reservoir Sandstone Analogue. Master Thesis. University of Alberta.

Greenspan, L. (1977). Humidity fixed points of binary saturated aqueous solutions. *Journal of Research of the National Bureau of Standards Section A: Physics and Chemistry*, 89-96.

Grieser, W.V. & James, M.B. (2007). Identification of Production Potential in Unconventional Reservoirs. Production and Operations Symposium, March 31–April 3, Oklahoma City, Oklahoma, U.S.A.

Groen, J.C., Peffer, L., & Pérez-Ramírez, J. (2003). Pore size determination in modified micro- and mesoporous materials. Pitfalls and limitations in gas adsorption data analysis. *Microporous and Mesoporous Materials, 60*, 1-17.

Guo, B., Gao, D. (2013). The Significance of Fracture Face Matrix Damage to the Productivity of Fractured Wells in Shale Gas Reservoirs. *Petroleum Science and Technology, 32*(2): 202–210.

Guo, Q., Blue, A., & Friedheim, J. (2015). Testing Methods for Evaluating Drilling Fluid Effects on Gas Shale Stability. 49th U.S. Rock Mechanics/Geomechanics Symposium, 28 June-1 July, San Francisco, California.

Gupta, D. V. S. (2009). Unconventional Fracturing Fluids for Tight Gas Reservoirs. SPE Hydraulic Fracturing Technology Conference, 19-21 January, The Woodlands, Texas. doi:10.2118/119424-MS.

Handwerger, D. A., Willberg, D. M., Pagels, M., Rowland, B., & Keller, J. F. (2012). Reconciling Retort versus Dean Stark Measurements on Tight Shales. SPE Annual Technical Conference and Exhibition, San Antonio, Texas, USA, 8-10 October.

Handwerger, D.A., Suarez-Rivera, R., Vaughn, K.I., and Keller, J.F. (2011). Improved Petrophysical Core Measurements on Tight Shale Reservoirs Using Retort and Crushed Samples. SPE Annual Technical Conference and Exhibition, Denver, CO, USA, 30 October - 2 November.

He, W., Gomez, S. L., Leonard, R. S., & Li, D. T. (2014). Shale-Fluid Interactions and Drilling Fluid Designs. International Petroleum Technology Conference, 19-22 January, Doha, Qatar.

He, S., Liang, L., Zeng, Y., Ding, Y., Lin, Y., & Liu, X. (2016). The influence of water-based drilling fluid on mechanical property of shale and the wellbore stability. *Petroleum, 2*, 61-66.

Heng, S., Guo, Y., Yang, C., Daemen, J.J.K. & Li, Z. (2015). Experimental and theoretical study of the anisotropic properties of shale. *International Journal of Rock Mechanics & Mining Sciences*, *74*: 58–68.

Higgings, S., S. Goodwin, Q. Donald, A. Donald, T. Bratton, & G. Tracy. (2008). Anisotropic stress models improve completion design in the Baxter shale, In Proceedings of SPE ATCE, Denver, 21-24 September.

Holditch, S.A. (1979). Factors Affecting Water Blocking and Gas Flow from Hydraulically Fractured Gas Wells, *JPT, 31*(12):1515–1524.

Holloway, S. (2005). Underground sequestration of carbon dioxide – a viable greenhouse gas mitigation option. *Energy*, *30*: 2318–2333.

Holt, R.M., Fjær, E., Stenebråten, J.F. & Nes, O.M. (2015). Brittleness of shales: Relevance to borehole collapse and hydraulic fracturing. *Journal of Petroleum Science and Engineering*, *131*:200–209.

Holt, R. M., Fjaer, E., Nes, O. M., & Alassi, H. T. 2011. A Shaly Look At Brittleness. 45th U.S. Rock Mechanics / Geomechanics Symposium, 26-29 June, San Francisco, California.

Holtzman, R., Szulczewski, ML. and Juanes, R. (2012). Capillary fracturing in granular media. *Physical Review Letters*. *108*(26):264504.

Honarpour, M. M., Nagarajan, N. R., Orangi, A., Arasteh, F., & Yao, Z. (2012). Characterization of Critical Fluid PVT, Rock, and Rock-Fluid Properties - Impact on Reservoir Performance of Liquid Rich Shales. SPE Annual Technical Conference and Exhibition, 8-10 October, San Antonio, Texas, USA.

Islam, A., Chevalier, S. and Sassi, M. (2013). Experimental and numerical studies of CO2 injection into water-saturated porous medium: capillary to viscous to fracture fingering phenomenon. Energy Procedia 37: 5511 – 5519.

Islam, A., Chevalier, S., Ben Salem, I., Bernabe b, Y., Juanes, R. and Sassi, M. (2014). Characterization of the crossover from capillary invasion to viscous fingering to fracturing during drainage in a vertical 2D porous medium. *International Journal of Multiphase Flow*, *58*: 279–291.

Ji, L., Geehan, T. (2013). Shale Failure around Hydraulic Fractures in Water Fracturing of Shale Gas, Paper SPE 167155 presented at the SPE Unconventional Resources Conference, Calgary, Alberta, 5-7 Noverber.

Jian-chun, G., Bo, L., Cong, L. and Hao, L. (2014). New Model to Evaluate the Brittleness of Shale Reservoir in Western Sichuan Basin. The Electronic Journal of Geotechnical Engineering, 19: 16921-16929.

Jiang, C., Lu, T., Zhang, D., Li, G., Duan, M., Chen, Y., & Liu, C. (2018). An experimental study of deformation and fracture characteristics of shale with pore-water pressure and under triaxial cyclic loading. *Royal Society Open Science, 5*.

Jin, X., Shah, S. N., Roegiers, J.C., & Zhang, B. (2014). Fracability Evaluation in Shale Reservoirs - An Integrated Petrophysics and Geomechanics Approach. SPE Hydraulic Fracturing Technology Conference, 4-6 February, Woodlands, Texas, USA.

Jones, S. C. (1994). A New, Fast, Accurate Pressure-Decay Probe Permeameter. *SPE Formation Evaluation*, *9*(3): 193-199.

Josh, M., Esteban, L., Delle Piane, C., Sarout, J., Dewhurst, D.N. & Clennell, M.B. (2012). Laboratory characterisation of shale properties. *Journal of Petroleum Science and Engineering*, 88–89: 107-124.

Kate, J. M. (2012). Influence of Saturation on Dynamic Elastic Constants of Sandstones. ISRM International Symposium - EUROCK 2012, Stockholm, Sweden, 28–30 May.

King, G.E. (2010). Thirty Years of Gas Shale Fracturing: What Have We Learned. SPE Annual Technical Conference and Exhibition, Florence, Italy, 19-22 September.

Kwon, O., Kronenberg, A.K., Gangi, A.F., Johnson, B., Herbert, B.E. (2004). Permeability of illite-bearing shale: 1. Anisotropy and effects of clay content and loading. *J. Geophys. Res*. *109*: B10205.

Lai, B. T., Li, H., Zhang, J. L., Jacobi, D. and Georgi, D. (2015). Water Content Effects on Dynamic Elastic Properties of Organic-rich Shale. SPE Annual Technical Conference and Exhibition, 28-30 September, Houston, Texas, USA.

Lan, Q., Ghanbari, E., Dehghanpour, H., & Hawkes, R. 2014. Water Loss Versus Soaking Time: Spontaneous Imbibition in Tight Rocks. *Energy technology, 2*, 1033-1039.

Leverett, M.C. (1941). Capillary behavior in porous solids. *Petroleum Transactions AIME*, *27*(3):152–169.

Lan, Q., Dehghanpour, H., Wood, J.M., & Sanei, H. (2015). Wettability of the Montney Tight Gas Formation. *SPE Reservoir Evaluation & Engineering, 18*, 417-431.

Li, W., Wang, C., Shi, Z., Wei, Y., Zhou, H. & Deng, K. (2016). The Description of Shale Reservoir Pore Structure Based on Method of Moments Estimation. *PLoS ONE*, *11*(3): e0151631.

Li, K., Chow, K., & Horne, R. (2006). Influence of initial water saturation on recovery by spontaneous imbibition in gas/water/rock systems and the calculation of relative permeability. *SPE Reservoir Eval. Eng*. *9* (4), 295–301.

Ligang, Zh, Guangqiu, Q., Sining, Q & Zhaoyi, L. (2017). Constitutive model and elastic parameters for layered rock mass based on combined Hooke spring. *Strength, Fracture and Complexity*, *10*: 145–156.

Lovoll, G., Meheust, Y., Maloy, K.J., Aker, E. & Schmittbuhl, J. (2005). Competition of gravity, capillary and viscous forces during drainage in a two-dimensional porous medium, a pore study. *Energy, 30*: 861-872.

Makhanov, K.; Habibi, A.; Dehghanpour, H.; Kuru, E. (2014). Liquid uptake of gas shales: A workflow to estimate water loss during shut-in periods after fracturing operations, *Journal of Unconventional Oil and Gas Resources, 7*: 22-32.

Makhanov, K. Dehghanpour, H. and Kuru, E. (2013). Measuring Liquid Uptake of Organic Shales: A Workflow to Estimate Water Loss during Shut-in Periods. SPE Canadian Unconventional Resources Conference, Calgary, Alberta, 5-7

Makhanov, K. Dehghanpour, H. & Kuru, E. (2012). An Experimental Study of Spontaneous Imbibition in Horn River Shales. SPE Canadian Unconventional Resources Conference, Calgary, Alberta, 30 October-1 November.

Makhnenko, R.Y., Harvieux, J., & Labuz, J.F. (2015). Paul-Mohr-Coulomb failure surface of rock in the brittle regime. *Geophysical Research Letters*, *42* (17): 6975-6981.

McKee, E., & Weir, G.W. (1953). Terminology for stratification and cross-stratification in sedimentary rock. *GSA Bulletin*, *64* (4): 381–390.

McLellan, P. (2012). Direct shear measurements of bedding plane strength and stiffness, Montney and Doig Formations, Farrell Creek Field, Northeast British Columbia. Canadian Rock Mechanics Association Conference, Edmonton, Alberta. May 2012.

McLellan, P., Anderson, I., Wong, J. & Mostafavi, V. (2014). Geomechanical Characterization of the Farrell Creek Montney Reservoir, Northeast British Columbia. CSPG CSEG CWLS GeoConvention 2014, Calgary, Alberta.

Mokhtari, M., Alqahtani, A. A., & Tutuncu, A. N. (2013). Failure Behavior of Anisotropic Shales. 47th U.S. Rock Mechanics/Geomechanics Symposium, 23-26 June, San Francisco, California.

Morgan, S.P. (2015). An Experimental and Numerical Study on the Fracturing Processes in Opalinus Shale. PhD Thesis. Massachusetts Institute of Technology, USA.

Morsy, S. & Sheng, J. J. (2014). Imbibition Characteristics of the Barnett Shale Formation. SPE Unconventional Resources Conference, Woodlands, Texas, USA, 1-3 April.

Nara, Y., Morimoto, K., Hiroyoshi, N., Yoneda, T., Kaneko, K. and Benson, P.M. (2012). Influence of relative humidity on fracture toughness of rock: Implications for subcritical crack growth. *International Journal of Solids and Structures*, *49*: 2471–2481.

Nasseri, M.H.B., & R.P., Young. (2016). Laboratory triaxial and permeability tests on Tournemire Shale and Cobourg Limestone: Report (RSP-413.8), University of Toronto.

Niandou, H., Shao, J., Henry, J., & Fourmaintraux, D. (1997). Laboratory investigation of the mechanical behaviour of Tournemire shale. *International Journal of Rock Mechanics and Mining Sciences, 34*, 3-16.

Oliver, W. C., & Pharr, G. M. (2004). Measurement of hardness and elastic modulus by instrumented indentation: Advances in understanding and refinements to methodology. *Journal of Materials Research*, *19*(1): 3-20.

Padin, A., Tutuncu, A. N., & Sonnenberg, S. (2014). On the Mechanisms of Shale Microfracture Propagation. SPE Hydraulic Fracturing Technology Conference held in The Woodlands, Texas, USA, 4–6 February.

Pagels, M., Willberg, D., Edelman, E., (2011). Chemo-Mechanical Effects of Induced Fluid Invasion into Ultralow Permeability Rocks: AGU Fall Meeting 2011, San Francisco, Poster H21B-1091.

Papamichos, E., Brignoli, M., Santarelli, F.J. (1997). An experimental and theoretical study of a partially saturated collapsible rock. *Mechanics of Cohesive-Frictional Materials*, *2*(3): 251–278.

Pathi, V.M. & Bustin, R.M. (2008). Factors Affecting the Permeability of Shales in the Western Canadian Sedimentary Basin. CSPG CSEG CWLS Convention, Calgary, Alberta, Canada, May 12-15.

Ping, Ch. Qiang, H. Tianshou, M & Dong, L. (2015). The mechanical properties of shale based on micro-indentation test. *Petroleum Exploration and Development*, *42*(5): 723–732.

Polito, P., Bhandari, A. & Flemings, P. (2014). Characterizing Matrix Permeability and Porosity in Barnett Shale. Bureau of Economic Geology, University of Texas at Austin, 2-3 December.

Primkulov, B. (2016). 4D Thermo-Mechanical Properties of Furan-Silica Sand Matrix. Foundation CMG Industrial Research Consortia in Reservoir Geomechanics for Unconventional Resources, May 18.

Qiang, L., Zhang, L., Hongming, T., Zhao, Y., Chen, M., & Xie, C. (2020). Describing the Full Pore Size Distribution of Tight Sandstone and Analyzing the Impact of Clay Type on Pore Size Distribution. *Geofluids, 2020*.

Richard, T., Gadrain, F., Poyol, E., & Detournay, E. (2012). Rock Strength determination from Scratch Tests. *Engineering Geology*, *147*: 91-100.

Rickman, R., Mullen, M., Petre, J., Grieser, W.V., & Kundert, D.P. (2008). A Practical Use of Shale Petrophysics for Stimulation Design Optimization: All Shale Plays Are Not Clones of the Barnett Shale. SPE Annual Technical Conference and Exhibition, Denver, Colorado, USA, 21–24 September.

Roychaudhuri, B., Tsotsis, T., & Jessen, K. (2013). An experimental investigation of spontaneous imbibition in gas shales. *Journal of Petroleum Science and Engineering, 111*, 87-97.

Rozhko, A. (2011a). Capillary Pressure and Apparent Tensile Rock Strength during Drainage and Imbibition. 9th Euroconference on Rock Physics and Geomechanics Trondheim Norway 17 - 21 October.

Rozhko, A. Y. 2011b. Capillary Phenomena In Partially-Saturated Rocks: Theory of Effective Stress. 45th U.S. Rock Mechanics / Geomechanics Symposium, 26-29 June, San Francisco, California.

Roychaudhuri, B., Tsotsis, T., Jessen, K. (2011). An experimental and numerical investigation of spontaneous imbibition in gas shales. In: SPE Annual Technical Conference and Exhibition.

Salazar, S.E. (2017). Development of an Internal Camera-Based Volume Determination System for Triaxial Testing. Master Thesis. University of Arkansas, Fayetteville.

Schmitt, L., Forsans, T., Santarelli, F.J. (1994). Shale testing and capillary phenomena. *International Journal of Rock Mechanics and Mining Sciences & Geomechanics Abstracts, 31*: 411–427.

Shaoul, J., Zelm, L.V., & de Pater C.J. (2011). Damage Mechanisms in Unconventional-Gas-Well Stimulation--A New Look at an Old Problem. *SPE Production & Operations, 26*(04): 388–400.

Sing, K. S. W. (1985). Reporting physisorption data for gas/solid systems with special reference to the determination of surface area and porosity (Recommendations 1984). *Pure Appl. Chem*. *57*:603–619.

Sliwinski, J., Harrington, J., Power, M., Hughes, P. & Yeung., B. (2010). A High-Definition Mineralogical Examination of Potential Gas Shales AAPG Annual Convention and Exhibition, New Orleans, Louisiana, USA, 11-14 April.

Song, L. (2012). Measurement of minimum horizontal stress from logging and drilling data in unconventional oil and gas. Master's thesis, University of Calgary, Calgary, AB.

Song, L., & Hareland, G. (2012). Minimum Horizontal Stress Profile From Logging Data for Montney Formation of North East British Columbia. SPE Canadian Unconventional Resources Conference, Calgary, Alberta, Canada, 30 October-1 November.

Striolo, A., Klaessig, F., Cole, D.R., Wilcox, J., Chase, G.G., Sondergeld, C.H. & Pasquali, M., (2012). Identification of Fundamental Interfacial and Transport Phenomena for the Sustainable Deployment of Hydraulic Shale Fracturing _ Role of Chemicals Used: Workshop Report, NSF Grant Number CBET-1229931.

Taylor, R.S., McIntosh, G., Litun, R., Munn, D., Bennion, B., Piwowar, M., Fyten, G., Romanson, R. & Hoch, O. (2009). Montney fracturing e fluid considerations. In: Paper 2009-154 Presented at Canadian International Petroleum Conference, Calgary, Alberta, 16-18 June.

Vaisblat, N. (2020) Controls on Reservoir Quality in the Lower Triassic Montney Formation. PhD thesis, Department of Earth and Atmospheric Sciences, University of Alberta.

Vale`s, F., Nguyen, D.M., Gharbi, H and Rejeb, A. (2004). Experimental study of the influence of the degree of saturation on physical and mechanical properties in Tournemire shale (France). *Applied Clay Science*, *26*: 197– 207.

Vanorio, T., Prasad, M., & Nur, A. (2003). Elastic properties of dry clay mineral aggregates, suspensions and sandstones. *Geophysical Journal International, 155*: 319-326.

Vermylen, J.P. (2013). Geomechanical Studies of the Barnett Shale, Texas, USA. PhD Dessertation. Department of Geophysics, Stanford University, USA.

Wang, B., Zhang, Q., Wang, G. & Liu, M. (2018). Analysis on the difference of material composition and reservoir space of Mesoproterozoic dark marine shale in the Yanshan area. *Energy Exploration & Exploitation*, *37*(1): 332-354.

Wang, J., & Rahman, S. S. (2015). An Investigation of Fluid Leak-off Due to Osmotic and Capillary Effects and Its Impact on Micro-Fracture Generation during Hydraulic Fracturing Stimulation of Gas Shale. EUROPEC 2015, 1-4 June, Madrid, Spain.

Wang, Q., Wang, Y., Guo, S., Xing, Zh.& Liu, Zh. (2015). The effect of shale properties on the anisotropic brittleness criterion index from laboratory study, *Journal of Geophysics and Engineering*, *12*(5): 866–874.

Wang, Q., Guo, B., Gao, D. (2012). Is Formation Damage an Issue in Shale Gas Development? SPE International Symposium and Exhibition on Formation Damage Control, Lafayette, Louisiana, 15-17 February.

Wang, X., Schubnel, A., Fortin, J., David, E., Guéguen, Y., & Ge, H. (2012). High Vp/Vs ratio: Saturated cracks or anisotropy effects? *Geophysical Research Letters, 39*.

White, J. (2012). CFD Simulation of Silica Gel and Water Adsorbent Beds Used in Adsorption Cooling System. PhD Thesis, The University of Birmingham.

Wild, K.M., Wymann, L.P., Zimmer, S., Thoeny, R. & Amann, F. (2014). Water Retention Characteristics and State-Dependent Mechanical and Petro-Physical Properties of a Clay Shale. *Rock Mechanics and Rock Engineering,* 48 (2): 427- 439. DOI 10.1007/s00603-014-0565-1.

Wood, P. (2013). From Core to Pore. *Geoexpero*. *10* (2).

Wood, J. (2012). Water Distribution in the Montney Tight Gas Play of the Western Canadian Sedimentary Basin: Significance for Resource Evaluation. SPE Canadian Unconventional Resources Conference, 30 October-1 November, Calgary, Alberta, Canada.

Wood, J.M., Sanei, H., Curtis, M.E., & Clarkson, C. (2015). Solid bitumen as a determinant of reservoir quality in an unconventional tight gas siltstone play. *International Journal of Coal Geology*, 287-295.

Xia, L., Zeng, Y., Luo, R., & Liu, W. (2018). Influence of Bedding Planes on the Mechanical Characteristics and Fracture Pattern of Transversely Isotropic Rocks in Direct Shear Tests. *Shock and Vibration, 2018*, 1-14.

Xu, L., Zhang, J., Ding, J., Liu, T., Shi, G., Li, X., Dang, w., Cheng, y. & Guo, R. (2020). Pore Structure and Fractal Characteristics of Different Shale Lithofacies in the Dalong Formation in the Western Area of the Lower Yangtze Platform. *Minerals*, *10*(1): 72-97.

Xu, Y., Adefidipe, O. A., Dehghanpour, H., and Virues, C. J. (2015). Volumetric Analysis of Two-Phase Flowback Data for Fracture Characterization. SPE Western Regional Meeting, 27-30 April, Garden Grove, California, USA.

Yan, Q, Lemanski, C., Karpyn, Z.T. and Ayala, L.F. 2015. Experimental investigation of shale gas production impairment due to fracturing fluid migration during shut-in time. *Journal of Natural Gas Science and Engineering*, *24*: 99-105.

Yang, L., Ge, H., Shen, Y., Zhang, J., Yan, W., Wu. S. & Tang, X. 2015. Imbibition inducing tensile fractures and its influence on in-situ stress analyses: A case study of shale gas drilling. *Journal of Natural Gas Science and Engineering*, *26*: 927-939.

Ye, Y., Tang, S., & Xi, Z. (2020). Brittleness Evaluation in Shale Gas Reservoirs and Its Influence on Fracability. *Energies, 13*, 388.

Yu, B., Tan, Q., Deng, J. & Feng, Y. (2013). The Permeability Property and Borehole Stability in Bedding Shale. *Petroleum Science and Technology*, *31*(22).

Yuan, J. L., Deng, J. G., & Zhang, D. Y. (2013). Fracability Evaluation of Shale-Gas Reservoirs. *Acta Petrolei Sinica*, *34* (3): 523–527.

Ž Tonžetić, I., Butcher, A.R., Cropp, A.F. & Pudmenzky, C. (2006). Automated SEM Analysis - Measurement & Characterisation -of Dust Using QEMSCAN. 2nd Aerosol Workshop, School of Physical and Chemical Sciences, Queensland University of Technology, Brisbane, Australia, 5 May.

Zhang, J. (2019). Applied Petroleum Geomechanics. Amsterdam, Netherlands: Gulf Professional Publishing, Elsevier.

Zhang, Y., Shao, D., Yan, J., Jia, X., Li, Y., Yu, P. & Zhang, T. (2016). The pore size distribution and its relationship with shale gas capacity in organic-rich mudstone of Wufeng-Longmaxi Formations, Sichuan Basin, China. *Journal of Natural Gas Geoscience*, *1*(3): 213-220.

Zhang, C., Oostrom, C., Wiestsma, T., Grate, J. & Warner, M. (2011). Influence of Viscous and Capillary Forces on Immiscible Fluid Displacement: Pore-Scale Experimental Study in a Water-Wet Micromodel Demonstrating Viscous and Capillary Fingering. *Energy & Fuels, 25*: 3493-3505.

Zhang, J., Chenevert, M. E., AL-Bazali, T., & Sharma, M. M. (2004). A New Gravimetric - Swelling Test for Evaluating Water and Ion Uptake in Shales. SPE Annual Technical Conference and Exhibition, 26-29 September, Houston, Texas.

Zhao, Y., Wang, Ch., & Bi, J. (2020). A method for simultaneously determining axial permeability and transverse permeability of tight reservoir cores by canister degassing test. *Energy Sci Eng. 8*: 1220-1230.

Zhou, Z., Hoffman, B. T., Bearinger, D., & Li, X. (2014). Experimental and Numerical Study on Spontaneous Imbibition of Fracturing Fluids in Shale Gas Formation. SPE/CSUR Unconventional Resources Conference – Canada, 30 September–2 October, Calgary, Alberta, Canada.